*Edited by*
*Avraam I. Isayev*

**Encyclopedia of**
**Polymer Blends**

## *Related Titles*

Elias, H.-G.
**Macromolecules**
**Volume 4: Applications of Polymers**
727 pages with 295 figures and 193 tables
2008
Hardcover
ISBN: 978-3-527-31175-0

Elias, H.-G.
**Macromolecules**
**Volume 3: Physical Structures and Properties**
699 pages with approx. 360 figures and approx. 100 tables
2007
Hardcover
ISBN: 978-3-527-31174-3

Matyjaszewski, K., Gnanou, Y., Leibler, L. (eds.)
**Macromolecular Engineering**
**Precise Synthesis, Materials Properties, Applications**
2982 pages in 4 volumes with 1047 figures and 97 tables
2007
Hardcover
ISBN: 978-3-527-31446-1

Elias, H.-G.
**Macromolecules**
**Volume 2: Industrial Polymers and Syntheses**
664 pages with 169 figures and 143 tables
2007
Hardcover
ISBN: 978-3-527-31173-6

Elias, H.-G.
**Macromolecules**
**Volume 1: Chemical Structures and Syntheses**
698 pages with 271 figures and 144 tables
2005
Hardcover
ISBN: 978-3-527-31172-9

Kemmere, M. F., Meyer, T. (eds.)
**Supercritical Carbon Dioxide**
**in Polymer Reaction Engineering**
358 pages with 153 figures and 40 tables
2005
Hardcover
ISBN: 978-3-527-31092-0

Meyer, T., Keurentjes, J. (eds.)
**Handbook of Polymer Reaction Engineering**
**1137 pages in 2 volumes with 373 figures and 96 tables**
2005
Hardcover
ISBN: 978-3-527-31014-2

Xanthos, M. (ed.)
**Functional Fillers for Plastics**
451 pages with 161 figures and 116 tables
2005
Hardcover
ISBN: 978-3-527-31054-8

Advincula, R. C., Brittain, W. J., Caster, K. C., Rühe, J. (eds.)
**Polymer Brushes**
**Synthesis, Characterization, Applications**
501 pages with 202 figures and 6 tables
2004
Hardcover
ISBN: 978-3-527-31033-3

Elias, H.-G.
**An Introduction to Plastics**
409 pages with 163 figures and 111 tables
2003
Hardcover
ISBN: 978-3-527-29602-6

*Edited by*
*Avraam I. Isayev*

# Encyclopedia of Polymer Blends

Volume 1: Fundamentals

WILEY-VCH Verlag GmbH & Co. KGaA

**The Editor**

***Prof. Avraam I. Isayev***
The University of Akron
Inst. of Polymer Engineering
Akron, OH 444325-0301
USA

All books published by Wiley-VCH are carefully produced. Nevertheless, authors, editors, and publisher do not warrant the information contained in these books, including this book, to be free of errors. Readers are advised to keep in mind that statements, data, illustrations, procedural details or other items may inadvertently be inaccurate.

**Library of Congress Card No.:** applied for

**British Library Cataloguing-in-Publication Data**
A catalogue record for this book is available from the British Library.

**Bibliographic information published by the Deutsche Nationalbibliothek**
The Deutsche Nationalbibliothek lists this publication in the Deutsche Nationalbibliografie; detailed bibliographic data are available on the Internet at http://dnb.d-nb.de.

© 2010 WILEY-VCH Verlag GmbH & Co. KGaA, Boschstr. 12, 69469 Weinheim, Germany

All rights reserved (including those of translation into other languages). No part of this book may be reproduced in any form – by photoprinting, microfilm, or any other means – nor transmitted or translated into a machine language without written permission from the publishers. Registered names, trademarks, etc. used in this book, even when not specifically marked as such, are not to be considered unprotected by law.

**Cover** Adam Design, Weinheim
**Typesetting** Thomson Digital, Noida, India
**Printing and Binding** Strauss GmbH, Mörlenbach

Printed in the Federal Republic of Germany
Printed on acid-free paper

**ISBN:** 978-3-527-31929-9

# Contents

**Preface** *XI*
**List of Contributors** *XV*

**1 Molecular Simulation of Polymer Melts and Blends: Methods, Phase Behavior, Interfaces, and Surfaces** *1*
*Peter Virnau, Kurt Binder, Hendrik Heinz, Torsten Kreer, and Marcus Müller*
1.1 Introduction *1*
1.2 Molecular Models for Polymers and Monte Carlo Simulations *6*
1.2.1 Modeling Polymers in Molecular Simulations *6*
1.2.2 Basics of Monte Carlo Simulations *8*
1.2.3 Determination of Phase Behavior *9*
1.3 Wetting and Phase Diagrams in Confined Geometries *14*
1.3.1 Length and Energy Scales of Minimal, Coarse-Grained Models for Polymer–Solid Contacts *14*
1.3.2 Measuring the Surface Free Energy Difference, $\Delta\gamma$, by Computer Simulation *18*
1.3.3 Application to Polymer–Solvent Mixtures *20*
1.4 Molecular Dynamics Method *21*
1.4.1 Basic Molecular Dynamics *21*
1.4.2 Non-equilibrium Molecular Dynamics Simulations of Coarse-Grained Polymer Systems *23*
1.5 Atomistic Simulation of Polymer Melts and Blends Using Molecular Dynamics Techniques *28*
1.5.1 Polymer Melts *28*
1.5.2 Polymer Blends *30*
1.5.3 Reversible Mapping between Atomistic, Coarse Grained, and Field Models *33*
1.5.4 Comparison to Experiment and Future Challenges *34*
1.6 Concluding Remarks *35*
Symbols *37*
References *38*

*Encyclopedia of Polymer Blends, Volume 1: Fundamentals.* Edited by Avraam I. Isayev
Copyright © 2010 WILEY-VCH Verlag GmbH & Co. KGaA, Weinheim
ISBN: 978-3-527-31929-9

**2 Thermodynamics of Flexible and Rigid Rod Polymer Blends** *45*
*Akihiko Matsuyama*
2.1 Introduction *45*
2.2 Fundamentals of a Nematic Phase *46*
2.2.1 Scalar Orientational Order Parameter *46*
2.2.2 Free Energy of Rigid Rod Solutions *47*
2.2.3 Nematic–Isotropic Phase Separations *51*
2.2.4 Entropy- and Energy-Driven Nematic Ordering *54*
2.3 Mixtures of a Flexible Polymer and a Rigid Rod *56*
2.3.1 Free Energy of Flexible and Rigid Rod Polymer Blends *59*
2.3.2 Nematic–Isotropic Phase Transition *63*
2.3.3 Landau–de Gennes Expansion of the Free Energy *64*
2.3.4 Phase Separations *65*
2.3.5 Phase Diagrams in Solutions of Rigid Rod-Like Polymers *70*
2.3.6 Smectic-Nematic–Isotropic Phase Separations *71*
2.3.7 Conformation of a Polymer Dissolved in a Liquid Crystalline Phase *76*
2.4 Phase Separation Dynamics *78*
2.4.1 Kinetic Equations *80*
2.4.2 Linearized Analysis of Spinodal Decomposition *82*
2.4.3 Morphologies *88*
2.5 Summary *93*
Symbols *94*
References *96*

**3 Amorphous Polymer Blends: Recent Developments** *101*
*Jeffery L. White*
3.1 Introduction *101*
3.2 Miscible Blend Dynamics and Length Scales of Mixing *102*
3.3 Amorphous Biopolymer Blends *108*
3.4 Conclusions *109*
References *109*

**4 Phase Field Modeling on Polymer Crystallization and Phase Separation in Crystalline Polymer Blends** *113*
*Thein Kyu, Haijun Xu, Taiming Guo, and Guoxiang Wang*
4.1 Phase Field Theory of Crystal Solidification of a Pure Substance *113*
4.2 Phase Field Modeling on Morphology Development *114*
4.3 Application of Phase Field Approach to Crystallization of a Homopolymer *122*
4.4 Thermodynamics of Crystalline Polymer Solutions and Blends *129*
4.4.1 Prigogine's Model *129*
4.4.2 Flory Diluent Theory *130*
4.5 Phase Diagrams of Crystalline Polymer Blends *132*

4.5.1 Phase Diagram Calculation of a Crystalline/Amorphous Polymer Blend *132*
4.5.2 Determination of Crystal–Amorphous Interaction in Crystalline/Amorphous Blends *135*
4.5.3 Phase Diagram Calculation for Binary Crystalline Polymer Blends *137*
4.5.4 Morphology Development in Relation to Phase Diagram of Crystalline/Amorphous Polymer Blends *139*
4.5.5 Morphology Development in Relation to the Phase Diagram of Crystalline/Crystalline Polymer Blends *142*
4.5.6 Phase Field Modeling on Phase Separation and Morphology Evolution *145*
Symbols *148*
References *149*

**5 Miscibility Criterion in Polymer Blends and its Determination** *153*
*Valeria Arrighi, John M.G. Cowie, Steven Fuhrmann, and Abdelsallam Youssef*
5.1 Introduction *153*
5.2 Thermodynamics *154*
5.3 Glass Transition of Polymer Blends *158*
5.3.1 Determination of the Glass Transition of Polymer Blends *160*
5.4 Phase Equilibria Methods *162*
5.4.1 Scattering Techniques *163*
5.4.1.1 Turbidity Measurements and Light Scattering *165*
5.4.1.2 Small-Angle Neutron Scattering *168*
5.4.1.3 Small-Angle and Wide-Angle X-Ray Scattering *173*
5.4.1.4 Neutron Reflectivity *175*
5.4.2 Microscopy *176*
5.4.2.1 Transmission Electron Microscopy *177*
5.4.2.2 Scanning Electron Microscopy *177*
5.4.2.3 Scanning Probe Microscopy – Atomic Force Microscopy (AFM) and Scanning Tunneling Microscopy (STM) *178*
5.5 Spectroscopic Methods *180*
5.5.1 Dynamics above the Glass Transition *180*
5.5.2 Sub-$T_g$ Relaxations *185*
5.5.3 Infrared and Raman Spectroscopy *186*
5.6 Summary and Conclusions *189*
Abbreviations and Symbols *189*
References *192*

**6 Physical Aging of Polymer Blends** *199*
*John M.G. Cowie and Valeria Arrighi*
6.1 Introduction to Physical Aging *199*
6.2 Experimental Measurements *200*
6.2.1 Enthalpy Relaxation *200*

6.2.2 Theoretical Approaches *202*
6.2.2.1 Phenomenological Models *202*
6.2.2.2 Petrie–Marshall and Cowie–Ferguson Models *204*
6.2.2.3 Molecular Models *204*
6.2.3 Enthalpic Relaxation in Polymer Blends *205*
6.2.4 Volume Relaxation *212*
6.2.5 Mechanical Relaxation *214*
6.2.6 Positron Annihilation Lifetime Spectroscopy *216*
6.2.7 Other Spectroscopic Techniques *218*
6.2.8 Scattering Techniques *219*
6.3 Discussion of Physical Aging in Blends *220*
6.3.1 Effect of Intermolecular Interactions *220*
6.3.2 Phase Separated Blends *223*
6.4 Concluding Comments *223*
Abbreviations and Symbols *224*
References *226*

**7 Nanoparticle/Polymer Blends: Theory and Modeling** *233*
*Valeriy V. Ginzburg*
7.1 Introduction *233*
7.2 Morphology of Polymer Blends with Nanoparticles *235*
7.2.1 Phase Behavior of Binary Polymer Blends *235*
7.2.2 Simple Arguments for Nanoparticles as Compatibilizers *237*
7.2.3 Influence of Nanoparticles on the Dynamics of Phase Separation in Polymer Blends *239*
7.2.4 Thermodynamics of Binary Nanoparticle/Polymer Blends *242*
7.2.5 Phase Behavior of Ternary Nanoparticle/Polymer/Polymer Mixtures *245*
7.2.6 Phase Behavior of Nanoparticle/Block-Copolymer Mixtures *248*
7.2.7 Determination of Polymer–Particle Flory–Huggins Interaction Parameters *254*
7.3 Physical Properties of Filled Polymer Blends *255*
7.3.1 Mechanical Properties (Modulus, Strength, and Toughness) *255*
7.3.2 Electrical Conductivity *257*
7.4 Summary and Outlook *260*
Abbreviations and Symbols *261*
References *263*

**8 Modeling the Self-Assembly of Ternary Blends that Encompass Photosensitive Chemical Reactions: Creating Defect-Free, Hierarchically Ordered Materials** *269*
*Olga Kuksenok, Rui D.M. Travasso, Pratyush Dayal, and Anna C. Balazs*
8.1 Introduction *269*
8.2 The Model *272*
8.3 Results and Discussion *275*

8.3.1 Combing with Light: Creating Patterned, Defect-Free Thin Films *275*
8.3.2 Modeling the Bulk Behavior of Photosensitive Blends under Non-uniform Illumination *278*
8.3.3 Combing Out Defects in Bulk Binary Blends *286*
8.3.4 Creating Order within the Ternary Mixtures *290*
8.3.5 Relating the Dimensionless Simulation Parameters to Physical Values *293*
8.3.6 Using a Single Photomask to Create Multiple Patterns in the Ternary Films *295*
8.4 Conclusions *300*
Abbreviations and Symbols *303*
References *305*

**Index** *307*

# Preface

The *Encyclopedia of Polymer Blends* includes scientific publications in various areas of blends. Polymer blends are mixtures of two or more polymers and/or copolymers. Polymer blending is used to develop new materials with synergistic properties that are not achievable with individual components, without the need to synthesize and scale up new macromolecules. Along with a classical description of polymer blends, articles in the encyclopedia will describe recently proposed theories and concepts that may not be accepted yet but reflect future development. Each article provides current points of view on the subject matter. These up-to-date reviews are very helpful for understanding the present status of science related to polymer blends.

The encyclopedia will be the source of existing knowledge related to polymer blends and will consist of five volumes. Volume 1 describes the fundamentals, including the basic principles of polymer blending, thermodynamics, miscible, immiscible, and compatible blends, kinetics, and composition and temperature dependence of phase separation. Volume 2 covers the principles, equipment, and machinery for polymer blend processing. Volume 3 deals with the structure of blended materials that governs their properties. Volume 4 describes various properties of polymer blends. Volume 5 discusses the blended materials and their industrial, automotive, aerospace, and other high technology applications. Individual articles in the encyclopedia describe the topics in terms of historical perspective, the state-of-the-art science, and technology and its future.

This encyclopedia is intended for use by academicians, scientists, engineers, researchers, and graduate students working on polymers and their blends.

Volume 1 is devoted to fundamental principles of polymer blends and is divided into eight chapters. These chapters cover the basic thermodynamic principles defining the miscible, immiscible, or compatible nature of amorphous, semi-crystalline and liquid crystalline polymer blends, and temperature and composition dependent phase separation in polymer blends. They are detailed below and build upon each other.

Chapter 1 is devoted to molecular simulation of polymer melts and blends, including methods, phase behavior, interfaces, and surfaces that are currently the

*Encyclopedia of Polymer Blends, Volume 1: Fundamentals.* Edited by Avraam I. Isayev
Copyright © 2010 WILEY-VCH Verlag GmbH & Co. KGaA, Weinheim
ISBN: 978-3-527-31929-9

subject of active research. This chapter describes molecular models for polymers, Monte Carlo simulations, and wetting and phase diagrams in confined geometries, techniques that are commonly used to determine the phase behavior of oligomer melts and blends. It also describes molecular dynamics methods, including basic and non-equilibrium molecular dynamics and atomistic simulations of polymer melts and blends, reversible mapping between atomistic, coarse grained, and field models, and comparison with experiments and future challenges.

Chapter 2 is devoted to the thermodynamics of flexible and rigid rod polymer blends. The fundamentals of nematic phase, scalar orientational order parameter, free energy of rigid rod solutions, nematic–isotropic phase separations, entropy- and energy-driven nematic ordering are introduced. Then, the phase separations of mixtures of flexible polymers and rigid rod-like molecules and low molecular weight liquid crystalline molecules in a thermal equilibrium state are discussed. Recent theoretical models to describe phase behavior, combining Flory–Huggins theory of isotropic mixing for polymer blends, Onsager theory, and the Maier–Saupe model of a nematic phase are presented. Based on time-dependent Landau–Ginzburg equations, the thermal instabilities of the phase separations and morphologies with the interplay between orientation and concentration fluctuations are described. Through recent theoretical and experimental studies, the phase separation dynamics of inhomogeneous mixtures consisting of conserved and nonconserved order parameters are considered.

Chapter 3 provides a brief review of recent developments in areas of amorphous polymer blends. Differential mixing, chain dynamics, and glass transition properties for individual polymer components in miscible binary blends, as well as new methods to experimentally acquire such information, are considered. Miscible blend dynamics and length scales of mixing of amorphous polymer blends are discussed. Amorphous biopolymer blends involving polymers obtained from renewable feedstocks is also briefly reviewed.

Chapter 4 considers the phase field modeling of polymer crystallization and phase separation in crystalline polymer blends. In particular, recent advances in establishing thermodynamic phase diagrams of binary crystalline polymer blends and concomitant dynamics of solid–liquid phase transformation coupled with liquid–liquid phase separation driven by thermal-quenching are described. A general free energy description of the phase field theory of the crystal solidification of pure substances is introduced with emphasis on the formation of a single crystal and spherulitic growth. Then, the approach is extended to crystallization of semicrystalline polymers and their blends by coupling with Flory–Huggins theory of liquid–liquid demixing. Various phase diagrams obtained by solving the combined Flory–Huggins and phase field free energy equations are compared with measured phase diagrams. This combined free energy is further utilized in the framework of the time-dependent Ginzburg–Landau (TDGL-Model C) dynamics pertaining to the concentration and crystal order parameters to elucidate the competition between the pattern formation and dynamics of liquid–liquid phase separation and solid–liquid phase transition. Effects of thermal, molecular orientation, and concentration field on the crystalline morphology development are discussed.

Chapter 5 is devoted to miscibility criterion in polymer blends and its determination, including experimental and theoretical considerations. A general and theoretical background to the experimental determination of miscibility based on thermodynamics, glass transition, and phase equilibria is given. Scattering and microscopy techniques and spectroscopic techniques, including infrared and Raman spectroscopy, to determine dynamics above and below the glass transition relaxations are described.

Chapter 6 deals with theoretical and experimental developments in the physical aging of polymer blends. In particular, aging data for polymer blends are reviewed and compared to the relevant homopolymer data. The past and present phenomenological, empirical and molecular models of aging are discussed. Enthalpic, volume, and mechanical relaxation, positron annihilation lifetime spectroscopy and other spectroscopic and scattering techniques are also considered. Then, specific examples on aging of blends are presented in systems where the effects of intermolecular interactions are important. Finally, complex behaviors of aging of phase separated blends are considered.

Chapter 7 provides a review of recent developments in the theory and modeling of nanoparticle-filled polymer blends. The influence of nanoparticles on the dynamics of phase separation in binary polymer blends, depending on the nanoparticle size, shape anisotropy, and surface treatment, is discussed. Theoretical methods of description of the phase diagrams in polymer/nanoparticle blends are considered, with special emphasis on the discussion of mesoscale field-based models (extended Flory–Huggins lattice theory) allowing one to calculate various hybrid particle/polymer structures. Finally, experimental and theoretical data on the influence of particles, their loading, and composite morphology on specific material properties, including the modulus of elasticity and electrical conductivity, are presented.

Chapter 8 details the modeling of the self-assembly of ternary blends encompassing photosensitive chemical reactions that create defect-free, hierarchically ordered materials. Starting with a brief review of literature, this chapter provides a description of theoretical models and then shows how one can control the evolution of such systems by varying the reaction rate coefficients in a specified manner. A further discussion on the formation of defect-free structures in the binary and ternary systems via a combination of stationary and moving light sources is given. Then, description is provided on the use of a photomask to control the structure formation within thin films of ternary blends.

Each chapter provides a summary and outlook for future development in blends followed by a list of abbreviations and symbols and then references.

There are many people who contributed to the completion of this volume. I wish to express my profound appreciation to the contributors of the various chapters for being patient with my requests for revisions and corrections. I would also like to thank Dr. Gustavo Carri, Dr. Valeriy Ginzburg, Dr. Dmitry Golovaty, Dr. Hendrik Heinz, Dr. Alamhir Karim, Dr. Thein Kyu, Dr. Akihiko Matsuyama, Dr. Sindee Simon and Dr. Victor Yashin for providing excellent reviews of various chapters. Their inquisitive reviews were very helpful in improving the quality of this volume.

I am thankful to Wiley-VCH Publishers for undertaking this project and for their patience, understanding, and cooperation with the authors at all stages of preparation. Finally, the support and patience of my family and the families of all the chapter authors contributed to the completion of this volume.

January 2010 *Avraam I. Isayev*
Akron, Ohio, USA

## List of Contributors

***Valeria Arrighi***
Heriot-Watt University
Chemistry School of Engineering and
Physical Sciences
Riccarton
Edinburgh EH14 4AS
UK

***Anna C. Balazs***
University of Pittsburgh
Chemical Engineering Department
Pittsburgh, PA 15261
USA

***Kurt Binder***
Johannes Gutenberg-Universität Mainz
Institut für Physik
Staudinger Weg 7
55099 Mainz
Germany

***John M.G. Cowie***
Heriot-Watt University
Chemistry School of Engineering and
Physical Sciences
Riccarton
Edinburgh EH14 4AS
UK

***Pratyush Dayal***
University of Pittsburgh
Chemical Engineering Department
Pittsburgh, PA 15261
USA

***Steven Fuhrmann***
Heriot-Watt University
Chemistry School of Engineering and
Physical Sciences
Riccarton
Edinburgh EH14 4AS
UK

***Valeriy V. Ginzburg***
The Dow Chemical Company
Research and Development
Building 1710
Midland, MI 48674
USA

***Taiming Guo***
University of Akron
Department of Mechanical Engineering
Akron, OH 44325-3903
USA

***Hendrik Heinz***
University of Akron
Department of Polymer Engineering
Akron, OH 44325-0301
USA

*Encyclopedia of Polymer Blends, Volume 1: Fundamentals.* Edited by Avraam I. Isayev
Copyright © 2010 WILEY-VCH Verlag GmbH & Co. KGaA, Weinheim
ISBN: 978-3-527-31929-9

***Torsten Kreer***
Institut Charles Sadron
23, rue des Loess
67034 Strasbourg
France

***Olga Kuksenok***
University of Pittsburgh
Chemical Engineering Department
Pittsburgh, PA 15261
USA

***Thein Kyu***
University of Akron
Department of Polymer Engineering
Akron, OH 44325-301
USA

***Akihiko Matsuyama***
Kyushu Institute of Technology
Faculty of Computer Science and
System Engineering
Department of Bioscience and
Bioinformatics
Kawazu 680-4, Iizuka
Fukuoka 820-8502
Japan

***Marcus Müller***
Georg-August-Universität
Institut für Theoretische Physik
Friedrich-Hund-Platz 1
37077 Göttingen
Germany

***Rui D.M. Travasso***
Universidade de Coimbra
Centro de Física Computacional
Departamento de Física
3004-516 Coimbra
Portugal

***Peter Virnau***
Johannes Gutenberg-Universität Mainz
Institut für Physik
Staudinger Weg 7
55099 Mainz
Germany

***Guoxiang Wang***
University of Akron
Department of Mechanical Engineering
Akron, OH 44325-3903
USA

***Jeffery L. White***
Oklahoma State University
Department of Chemistry
Stillwater, OK 74078
USA

***Haijun Xu***
University of Akron
Department of Polymer Engineering
Akron, OH 44325-301
USA

***Abdelsallam Youssef***
Heriot-Watt University
Chemistry School of Engineering and
Physical Sciences
Riccarton
Edinburgh EH14 4AS
UK

# 1
# Molecular Simulation of Polymer Melts and Blends: Methods, Phase Behavior, Interfaces, and Surfaces

*Peter Virnau, Kurt Binder, Hendrik Heinz, Torsten Kreer, and Marcus Müller*

## 1.1
## Introduction

Understanding thermodynamic properties, including also the phase behavior of polymer solutions, polymer melts, and blends, has been a long-standing challenge [1–7]. Initially, the theoretical description was based on the lattice model introduced by Flory and Huggins [1–7]. In this model, a flexible macromolecule is represented by a (self-avoiding) random walk on a (typically simple cubic) lattice, such that each bead of the polymer takes one node of the lattice, and a bond between neighboring beads of the chain molecule takes a link of the lattice. For a binary polymer blend (A,B), two types of chains occur on the lattice (and possibly also "free volume" or vacant sites, which we denote as $V$). The model (normally) does not take into account any disparity in size and shape of the (effective) monomeric units of the two partners of a polymer mixture. Between (nearest neighbor) pairs AA, AB, and BB of effective monomers, pairwise interaction energies, $\varepsilon_{AA}$, $\varepsilon_{AB}$ and $\varepsilon_{BB}$, are assumed. Thus, this model disregards all chemical detail (as would be embodied in the atomistic modeling [8–10], where different torsional potentials and bond-angle potentials of the two constituents can describe different chain stiffness).

Despite the simplicity of this lattice model, it is still a formidable problem of statistical mechanics, and its "numerically exact" treatment already requires large-scale Monte Carlo simulations [11–13]. Consequently, the standard approach has been [1–7] to treat this Flory–Huggins lattice model in mean-field approximation, which leads to the following expression for the excess free energy density of mixing [4]:

$$\frac{\Delta F}{k_B T} = \frac{\phi_A \ln \phi_A}{N_A} + \frac{\phi_B \ln \phi_B}{N_B} + \phi_V \ln \phi_V + \chi_{AB}\phi_A\phi_B + \tfrac{1}{2}\chi_{AA}\phi_A^2 + \tfrac{1}{2}\chi_{BB}\phi_B^2. \tag{1.1}$$

Here $\phi_A$, $\phi_B$ and $\phi_V = 1-\phi_A-\phi_B$ are the volume fractions of monomers of type A, B and of vacant sites, respectively. Every lattice site has to be taken by either

*Encyclopedia of Polymer Blends, Volume 1: Fundamentals.* Edited by Avraam I. Isayev
Copyright © 2010 WILEY-VCH Verlag GmbH & Co. KGaA, Weinheim
ISBN: 978-3-527-31929-9

an A monomer, a B monomer, or a vacancy, and for simplicity the (fixed) lattice spacing is taken as our unit of length. $N_A$ and $N_B$ are chain lengths of the two types of polymers (we disregard possible generalizations that take polydispersity into account [5]). Thus, the first three terms on the right-hand side of Eq. (1.1) represent the entropy of mixing terms, while the last three terms represent the enthalpic contributions ($\chi_{AB}$, $\chi_{AA}$ and $\chi_{BB}$ are the phenomenological counterparts of the pairwise interaction energies $\varepsilon_{AB}$, $\varepsilon_{AA}$ and $\varepsilon_{BB}$, respectively). Note that in the entropic terms the (translational) entropy of a polymer is reduced by a factor $1/N$ in comparison to a corresponding monomer because of chain connectivity. In deriving this simple expression for the entropy, the fact that polymer chains on the lattice cannot intersect either themselves or other chains has not been explicitly taken care of: the excluded volume constraint is only taken into account via the constraint that a lattice site can be taken by at most one monomer, but only the average occupation probabilities $\phi_A$, $\phi_B$ and not the local concentrations $c_i^A$, $c_i^B$ of a lattice site $i$ enter: while $c_i^A = 1$ or 0 and $c_i^B = 1$ or 0, $\phi_A = \langle c_i^A \rangle_T$, $\phi_B = \langle c_i^B \rangle_T$. By $\langle Q \rangle_T$ we denote a thermal average of an observable $Q$ in the sense of statistical mechanics at a given temperature, $T$, that is:

$$\langle Q \rangle_T = (1/Z) \sum_C Q(C) \exp\left[-E(C)/k_B T\right] \tag{1.2}$$

$$Z = \sum_C \exp\left[-E(C)/k_B T\right], \quad F = -k_B T \ln Z \tag{1.3}$$

where the sums are extended over all configurations $C$ ("microstates") of the considered statistical system, $E(C)$ is the corresponding energy function (the "Hamiltonian" of the system [4, 9, 10]), and $Z$ its partition function.

From these definitions it should be clear that in the exact expression for the enthalpy one should expect terms of the type:

$$\chi_{AB} \left(\frac{1}{2q}\right) \sum_{j(n.n.\text{ of } i)} \left( \left\langle c_i^A \, c_i^B \right\rangle_T + \left\langle c_i^B \, c_j^A \right\rangle \right)$$

where $q$ is the number of nearest neighbors of a site $i$ on the lattice, rather than $\chi_{AB}\phi_A\phi_B$. The latter expression results, of course, if this correlation function is factorized, $\left\langle c_i^B \, c_j^A \right\rangle_T \approx \left\langle c_i^A \right\rangle \left\langle c_j^B \right\rangle = \phi_A \phi_B$. This neglect of correlations in the occupancy of lattice sites would become accurate in the limit $q \to \infty$, but turns out to be rather inaccurate for the simple cubic lattice, which has $q = 6$ only. Moreover, as far as unmixing of a polymer blend is concerned, only interchain contacts and not intrachain contacts contribute (strongly attractive intrachain interactions can cause contraction or even collapse of the random coil configurations).

We shall not discuss Eq. (1.1) further for the general case, but rather focus on the two most important special cases, namely incompressible blends and incompressible polymer solutions. Taking $\phi_V = 0$ one can reduce Eq. (1.1) to a simpler expression [1–4], where $\phi_A = \phi$, $\phi_B = 1 - \phi$:

$$\frac{\Delta F}{k_B T} = \frac{\phi \ln \phi}{N_A} + \frac{(1-\phi) \ln (1-\phi)}{N_B} + \chi \phi \, (1-\phi) \tag{1.4}$$

where in the mean-field approximation the Flory–Huggins parameter $\chi$ is related to the pairwise energies by:

$$\chi = q\,[\varepsilon_{AB} - (\varepsilon_{AA} + \varepsilon_{BB})/2]/k_B T \tag{1.5}$$

As an example for the predictions that follow from Eqs. (1.4) and (1.5), we note that the stability limit ("spinodal curve") of the homogenous phase is given by the vanishing of the second derivative of $\Delta F$ with respect to $\phi$:

$$\partial^2(\Delta F/k_B T)/\partial\phi^2 = 0 \tag{1.6}$$

which yields the equation:

$$\chi = \chi_s(\phi) = \{[\phi N_A]^{-1} + [(1-\phi)N_B]^{-1}\}/2 \tag{1.7}$$

Equation (1.7) describes the spinodal curve in the plane of variables $(\chi, \phi)$. The maximum of the spinodal curve for such a binary incompressible mixture yields the critical point, that is:

$$\phi^{crit} = \left(\sqrt{N_A/N_B} + 1\right)^{-1},\ \chi_{crit}^{-1} = 2\left(N_A^{-1/2} + N_B^{-1/2}\right)^{-2} \tag{1.8}$$

For the simplest case of a symmetric mixture ($N_A = N_B = N$), this reduces to $\phi^{crit} = \frac{1}{2}$, and $\chi_{crit} = 2/N$.

The case of an incompressible polymer solution results if we interpret B as a solvent molecule in Eq. (1.4) by putting $N_B = 1$ [or alternatively put $\phi_B = 0$ in Eq. (1.1) and reinterpret $V$ as solvent molecule]. However, while for polymer mixtures in the state of dense melts incompressibility is often a reasonable first approximation, for polymer solutions in some cases such an assumption is inadequate, for example, if one uses supercritical carbon dioxide as a solvent for the polymers [7, 14].

When one tries to account for real polymer systems in terms of models of the type of Eqs. (1.1)–(1.8) the situation is rather unsatisfactory; however, when one fits data on the coexistence curve or on $(\partial^2(\Delta F/k_B T)/\partial\phi^2)_T$, the latter quantity being experimentally accessible via small angle scattering, one finds that one typically needs an effective $\chi$-parameter that does not simply scale proportional to inverse temperature, as Eq. (1.5) suggests. Moreover, there seems to be a pronounced $\phi$-dependence of $\chi$, in particular for $\phi \to 1$. Near $\phi = \phi^{crit}$, on the other hand, there are critical fluctuations (which have been intensely studied by Monte Carlo simulations [11–13, 15] and also in careful experiments of polymer blends [16–18] and polymer solutions [19]). Sometimes in the literature a dependence of the $\chi$ parameter on pressure [18] or even chain length is reported, too. Thus, there is broad consensus that the Flory–Huggins theory and its closely related extensions [20] are too crude as models to provide predictive descriptions of real polymer solutions and blends. A more promising approach is the lattice cluster approach of Freed and coworkers [21–23], where effective monomers block several sites on the lattice and have complicated shapes to somehow "mimic" the local chemical structure. However, this approach requires rather cumbersome numerical calculations, and is still of a mean-field character, as

far as critical phenomena are concerned. We shall not address this approach further in this chapter.

A very popular approach to describe polymer chains in the continuum is the Gaussian thread model [24–26], and if one treats interactions among monomers in a mean-field-like fashion this leads to the so-called "self-consistent field theory" [27–33] of polymers. This theory is an extension of the Flory Huggins theory to spatially inhomogeneous systems (like polymer interfaces or microphases-separated copolymer systems), with respect to the description of the phase diagrams of polymer solutions and blends. However, it still lacks chemical detail and is on a mean-field level; hence we shall not dwell on it further here.

An alternative approach that combines the Gaussian thread model of polymers with liquid-state theory is known as the polymer reference interaction site model (PRISM) approach [34–38]. This approach has the merit that phenomena such as the de Gennes [3] correlation hole phenomena and its consequences are incorporated in the theoretical description, and also one can go beyond the Gaussian model for the description of intramolecular correlations of a polymer chain, adding chemical detail (at the price of a rather cumbersome numerical solution of the resulting integral equations) [37, 38]. An extension to describe the structure of colloid–polymer mixtures has also become feasible [39, 40]. On the other hand, we note that this approach shares with other approaches based on liquid state theories the difficulty that the hierarchy of exact equations for correlation functions needs to be decoupled via the so-called "closure approximation" [34–38]. The appropriate choice of this closure approximation has been a formidable problem [34–36]. A further inevitable consequence of such descriptions is the problem that the critical behavior near the critical points of polymer solutions and polymer blends is always of mean-field character.

There have been many other attempts to base the description of polymer solutions, melts, and blends on liquid-state theory (e.g., [41–44]) and we shall not mention all of them. Perhaps the most widely used and successful approaches are based on Wertheim's [45, 46] perturbation theory devised to deal with the equation of state of associating fluids. Theories based on this approach, where attractive interactions between different monomers or monomers and solvent particles are treated in first order thermodynamic perturbation theory, often appear under acronyms like TPT1 or SAFT (statistical associating fluid theory). Comparisons with computer simulations [7, 47, 48] have shown that TPT1-MSA [49, 50] (here MSA stands for a closure approximation known [51] as "mean spherical approximation") yields rather reasonable results on phase coexistence, but typically a large overestimation of the two-phase region occurs, and the critical behavior is described as mean-field like; so the correct Ising-type criticality [11–15] cannot be described as expected. The latter comment applies to the many variants of SAFT (e.g., [52–56]) as well. However, as a caveat, apart from this shortcoming and other systematic errors resulting from the fact that thermodynamic perturbation theory [57] becomes generally inadequate at low temperatures and errors from the closure approximations [51] occur, we mention that some variants of such theories invoke additional uncontrolled approximations that may lead to further

uncontrolled errors. For example, the now rather popular perturbed chain (PC)-SAFT approach [56] relies on an expansion of isotherms as sixth-order polynomials of the monomer density and this may give rise to completely spurious gas–gas and liquid–liquid phase equilibria [58, 59] in the equation of state of a homopolymer, in addition to the standard liquid–gas two-phase region, which is the only physically meaningful phase separation of typical homopolymers at high temperatures.

A general conclusion that can be drawn from this short survey on the many attempts to develop analytical theories to describe the phase behavior of polymer melts, polymer solutions, and polymer blends is that this is a formidable problem, which is far from a fully satisfactory solution. To gauge the accuracy of any such approaches in a particular case one needs a comparison with computer simulations that can be based on exactly the same coarse-grained model on which the analytical theory is based. In fact, none of the approaches described above can fully take into account all details of chemical bonding and local chemical structure of such multicomponent polymer systems and, hence, when the theory based on a simplified model is directly compared to experiment, agreement between theory and experiment may be fortuitous (cancellation of errors made by use of both an inadequate model and an inaccurate theory). Similarly, if disagreement between theory and experiment occurs, one does not know whether this should be attributed to the inadequacy of the model, the lack of accuracy of the theoretical treatment of the model, or both. Only the simulation can yield "numerically exact" results (apart from statistical errors, which can be controlled, at least in principle) on exactly the same model, which forms the basis of the analytical theory. It is precisely this reason that has made computer simulation methods so popular in recent decades [58–64].

Consequently, we focus here on computer simulations exclusively. The outline of the remainder of this chapter is as follows: Section 1.2 presents on overview of polymer models (from lattice models to atomistic descriptions) and will also describe the most important aspects of Monte Carlo simulations of these models. As an example, recent work on simple short alkanes and solutions of alkanes in supercritical carbon dioxide [47, 48] will be presented, to clarify to what extent a comparison of Monte Carlo results on phase behavior and experimental data is sensible, and which experimental input into the models is indispensable to make them predictive.

In Section 1.3 we continue the discussion of Monte Carlo simulations of polymer blends and polymer solutions, but with the emphasis on interfaces that result in the context of phase separation: interfaces between coexisting phases in the bulk (liquid–liquid interfaces in a blend, liquid–vapor-type interfaces in a solution) and at solid external walls. It will be shown how all the surface free energies entering Young's formula for the contact angle of droplets can be determined, and how one can estimate the location of wetting transitions. Coarse-grained models are the focus of this section.

Section 1.4 discusses the basic aspects of molecular dynamics simulation of polymer melts and blends with both coarse-grained and chemically detailed models. While the first part of this section emphasizes the basic aspects of the technique, Section 1.4.2 emphasizes non-equilibrium aspects such as the response to shear deformation, and the special techniques necessary to simulate such phenomena

(non-equilibrium molecular dynamics, NEMD). Since shear deformations create heat, the proper thermostating of the system in the context of a NEMD simulation needs to be carefully considered, and this will be explained in this section. Of course, the processing of polymer solutions, melts, and blends in their molten state is always an indispensable step prior to the production of (typically solid) polymeric materials, and hence addressing such problems by the theoretical modeling is clearly adequate and necessary.

While most sections in this chapter emphasize coarse-grained models, it must be stressed that such models can elucidate qualitative trends, but a quantitative prediction of properties of specific polymeric materials is not achieved. The latter task is attempted by molecular dynamics simulations of chemically realistic atomistic models (Section 1.5). Although the feasibility of this "brute force" approach is limited due to excessive demands of computer resources to equilibrate melts of macromolecules with high molecular weights, and there are also uncertainties about the force fields, nevertheless various encouraging results have been obtained, and some examples of them will be reviewed in this section. The "mapping" between atomistic and coarse-grained models will be discussed briefly.

Finally, Section 1.6 gives a short summary of the state of the art and outlook on closely related problems that were not covered in this chapter.

## 1.2
## Molecular Models for Polymers and Monte Carlo Simulations

### 1.2.1
### Modeling Polymers in Molecular Simulations

If generic properties of polymers need to be determined, it is often sufficient to rely on lattice models. For comparison with experiments of particular melts and blends, more sophisticated off-lattice models are typically applied. These models are described by force fields that determine the interactions between atoms or groups of atoms, and the quality of the modeling is essential for the predictive quality of the simulations. Force field parameters can be derived from direct comparison with experimental data, from quantum mechanical calculations, or both. In the first part of this section, we present generic polymer models that are commonly used in molecular simulations without focussing on any particular substance. Emphasis is placed on lattice and simple off-lattice models that will also be discussed in the next three sections. Section 1.5 is dedicated to chemically realistic descriptions.

The first model that took into account excluded volume effects was the self-avoiding-walk (SAW), which was introduced about 60 years ago [65, 66]. Each monomer occupies a lattice site on a simple cubic lattice. The bond length between adjacent monomers is fixed by the lattice constant and the bond angles are restricted by the geometry of the lattice. This model is well-suited to describe generic polymers in dilute, good solvent conditions and exhibits the correct scaling behavior

($R_g^2 \propto N^{2\nu}$, $\nu \approx 0.588$). Variations of this model, like the interacting SAW (iSAW), allow for interactions between non-adjacent beads and can even undergo a phase transition to a globular state, reproducing the generic behavior of a single chain under bad solvent conditions. A particularly popular extension of the iSAW to two types of beads is even able to describe generic properties of proteins. In the HP (hydrophobic–polar) model [67], non-adjacent hydrophobic beads attract each other, whereas interactions between hydrophobic and polar beads and between two polar beads are restricted to excluded volume. These simple conditions suffice to form a hydrophobic core as observed in crystal structures of proteins. Likewise, polymer blends can be readily implemented in such simple models if we allow for a second type of chains and specified interactions between monomers of like and unlike species. Polymers on a simple cubic lattice exhibit two major disadvantages. On the one hand, both bond length and bond angles are fixed and, on the other hand, Monte Carlo simulations on the simple cubic lattice are often plagued with ergodicity problems [68]. The bond fluctuation model [69] was introduced to address these issues while preserving the computational efficiency of lattice models. Again, the basic idea is simple: instead of occupying a simple lattice site, a monomer now occupies a whole lattice cell. Neighboring beads are only allowed to move such that the bond does not stretch or compress too much. Specifically, bond vectors are chosen to prevent overlaps of adjacent monomers and intersection of bonds during simulation. Note that, due to this additional flexibility, the bond fluctuation model already resembles to some extent a coarse-grained continuum model.

A simple and very popular example of a coarse-grained off-lattice model is given by the bead-spring chain of Kremer and Grest [70, 71]. In this model monomers interact via a Lennard-Jones potential:

$$V_{\mathrm{LJ}}(r) = \begin{cases} 4\varepsilon\left[\left(\frac{\sigma}{r}\right)^{12} - \left(\frac{\sigma}{r}\right)^{6} + \text{const.}\right], & \text{if } r < r_c \\ 0, & \text{else} \end{cases} \tag{1.9}$$

To increase computational efficiency the Lennard-Jones potential usually is cut and shifted at either twice the minimum value, or $2.5\sigma$. The constant in Eq. (1.9) is chosen such that $V_{\mathrm{LJ}}$ is continuous at $r = r_c$. The value of $\varepsilon$ sets the scale of energy (and temperature $T$, which is often normalized as $T^* = k_B T/\varepsilon$), and the size $\sigma$ of effective monomers sets the scale of length. In addition, adjacent beads interact with the so-called FENE potential:

$$V_{\mathrm{FENE}}(r) = -\text{const.} \cdot \varepsilon \cdot \ln\left[1 - \left(\frac{r}{r_{\max}}\right)^2\right] \tag{1.10}$$

Constants in Eq. (1.10) are chosen such that the most favorable distance between bonded monomers is slightly smaller than the distance between non-bonded monomers to prevent crystallization. Alternatively, a harmonic potential can be used for bonded monomers instead of Eqs. (1.9, 1.10). As indicated for lattice models, polymer blends can be implemented by adjusting the interaction strength $\varepsilon$ for monomers of

type A and B and between A and B. By mapping ε and σ to experimental energy and length scales, simulations of this model can be compared with experiments of specific polymers. In these scenarios, single Lennard-Jones beads typically represent groups of carbon atoms [47].

The next steps towards a more chemically detailed description are so-called united atom models. In this class hydrogen atoms are grouped together with the heavier atoms to which they are attached. These potentials typically contain both bond bending and torsional terms. Fully atomistic models, which frequently are used in simulations of biopolymers [72], consider hydrogen as a separate particle and often contain electrostatic terms as well. Section 1.5 presents a few selected examples of atomistic polymer models in comparison with experiments.

At the end of this introductory section we emphasize that the model should be adequate for the problem in question. Adding additional parameters to describe the system in a chemically realistic manner increases the computational cost and does not necessarily lead to better agreement with experiments. This should be considered, especially because on today's computers fully atomistic molecular dynamics simulations are typically limited to box sizes of a few nanometers and 10s or 100s of nanoseconds of simulated time.

### 1.2.2 Basics of Monte Carlo Simulations

Classical molecular simulations are dominated by two classes of algorithms: Monte Carlo and molecular dynamics [62, 63]. Monte Carlo generally aims at generating independent configurations of a statistical system that contributes to the Boltzmann-weighted statistical average of an observable. This information can also be obtained from molecular dynamics simulations in which a starting configuration is evolved according to Newton's equations of motion. In addition, molecular dynamics generates information about the dynamical evolution of a system. In the following, we give a short overview and present a selection of several techniques important for studying polymer blends and melts. After a brief introduction to basic Monte Carlo algorithms we focus on grand-canonical simulations, which are commonly used to determine phase diagrams of polymer melts and blends. Molecular dynamics simulations are introduced in Section 1.4.

Monte Carlo simulations are, as indicated by the name, based on the idea of evolving a system by drawing random numbers. Unfortunately, statistically meaningful configurations are typically confined to a small volume of phase space. To evolve a system within this volume we apply importance sampling, that is, we only sample states that actually contribute to statistical averages.

To derive the relevant equations we consider our system to be in a particular state *i*. This state is in equilibrium with its environment if the probability flows in and out of this state are equal:

$$\sum_j P(i) a_i \omega_{ij} = \sum_j P(j) a_j \omega_{ji} \quad \forall j \tag{1.11}$$

where $P(i)$ is the probability of residing in state $i$, which is typically given by the Boltzmann distribution;
$\omega_{ij}$ is the probability of jumping from $i$ to $j$ as given by the algorithm;
$a_{i,j}$ is the probability of selecting or placing a particular particle for the move.

The system is in equilibrium if Eq. (1.11) applies to all states. Equation (1.11) is always fulfilled if the stricter condition:

$$P(i)a_i\omega_{ij} = P(j)a_j\omega_{ji} \quad \forall i,j \tag{1.12}$$

is met, which is known as detailed-balance. Several ways to fulfill detailed-balance are conceivable. The Metropolis criterion [83] was historically the first implementation of detailed balance, and remains by far the most popular choice today:

$$w_{ij} = \min\left(1, \frac{a_j P_j}{a_i P_i}\right). \tag{1.13}$$

For example, consider a local Monte Carlo scheme for a Lennard-Jones liquid in the NVT (constant particle number, volume, and temperature) ensemble: We choose one particle at random, and move it a fixed distance away from the previous position in an arbitrary direction. For the reverse move (from $j$ to $i$) $a_j = a_i$ the two prefactors cancel out. $P_i \propto \exp[-\beta E(i)]$ according to the canonical Boltzmann distribution. Equation (1.13) indicates that the move is always accepted if the energy of the system is lowered by the displacement. If the energy increases, the move is accepted with probability $\exp(-\beta\Delta E)$, that is, we draw a random number between 0 and 1 and accept the move if the random number is smaller than $\exp(-\beta\Delta E)$.

Apart from local displacements, a wide variety of Monte Carlo moves can already be formulated using Eq. (1.13). For instance, an end-monomer can be cut from a polymer chain and reattached at the other end. In this case the movement of the chain resembles a slithering snake, from which the name of the algorithm is derived [73, 74]. In dilute systems, a monomer can be selected at random, around which one side of the polymer is rotated by an arbitrary angle (or an angle allowed by the lattice geometry). This so-called pivot algorithm is currently the most efficient way to simulate single chains in good solvent conditions [75, 76]. For globular states, various end- [77] and internal-rebridging [78, 79] algorithms have been developed in which the chain is cut and reconnected internally. A version that cuts and rebridges two chains in a melt also exists [80]. From this list it becomes immediately clear that Monte Carlo moves do not have to mimic physically feasible moves of a real polymer chain. This characteristic is oftentimes advantageous as it allows for a fast and efficient sampling of configuration space. On the downside, information about the physical evolution of the system is lost.

### 1.2.3 Determination of Phase Behavior

In the following, we focus on a set of techniques commonly used to determine the phase behavior of oligomer melts [47, 48] and blends [81] to give an example of how

MC techniques are applied in practice. The methodology is rather general and in principle can be applied to any molecular liquid [82] or spin system. It also has advantages over techniques like Gibbs ensemble Monte Carlo [83] because it can be combined with finite-size scaling in the vicinity of the critical point. In addition, the method yields interfacial properties. Our presentation follows Reference [47]. Simulations are typically performed in the grand canonical $\mu VT$ ensemble with periodic boundary conditions, that is, we fix the chemical volume and temperature but allow for particle insertions or deletions. For a simple Lennard-Jones liquid, Eq. (1.13) becomes:

$$w_{ij} = \min\left(1, \frac{V}{n+1}\exp\left(-\beta\Delta E + \beta\mu\right)\right) \tag{1.14}$$

for insertion from $n$ particles to $n+1$ particles in the system, and:

$$w_{ji} = \min\left(1, \frac{n}{V}\exp\left(+\beta\Delta E - \beta\mu\right)\right) \tag{1.15}$$

for deletion attempts from $n$ to $n-1$; $V$ denotes the volume of the simulation box. The simulation of polymer melts is slightly more involved because insertions of whole chains are typically rejected in a melt due to overlaps. To attenuate this problem, more advanced schemes like configurational bias Monte Carlo [85–88] need to be implemented. Again, the basic idea is simple: the first particle is inserted at random. Subsequent particles of the chain are inserted after the surrounding area is scanned for favorable vacancies. The bias, however, has to be considered when final acceptance probabilities are calculated. This algorithm, combined with local updates schemes introduced above, works very well for oligomers. Melts containing larger chains remain challenging and the efficiency of the grand canonical insertion attempt still limits the applicability of the whole approach.

In a typical simulation run, a joint histogram of particle number and energy is accumulated. The system is at coexistence when an unweighted simulation spends an equal amount of time in the coexisting phases. If we plot the probability distribution as a function of particles in the melt, we obtain a double-peaked distribution at coexistence and the areas below the two peaks are equal [88, 90]. Coexistence densities can be calculated by determining the average particle numbers in the gas and the liquid peak and dividing the respective numbers by the volume of the simulation box.

In practice, it is difficult to estimate the coexistence chemical potential ahead of time. However, if two distributions at $\mu$, $T$ and $\mu'$, $T'$ overlap sufficiently, it is possible to extrapolate data from $\mu, T$ to $\mu', T'$ and avoid a second simulation [91]. The probability of a certain configuration $c$ at $\mu', T'$ is given by:

$$P_{\mu',T'}(c) = \frac{Z}{Z'} P_{\mu,T}(c) \quad \mathrm{e}^{-(\beta'-\beta)E + (\mu'\beta' - \mu\beta)n} \tag{1.16}$$

where $P_{\mu',T'}(n_0)$ is the sum over all configurations $c_i$ at $n_0$.

$\sum_{\{c_i\}|n=n_0} P_{\mu,T}(c_i) \propto \sum_{\{c_i\}} \delta(n-n_0)$ can be determined from the original data set. After a suitable normalization, the grand canonical partition sums $Z$ and $Z'$

disappear and we obtain:

$$P_{\mu',T'}(n_0) = \frac{\sum_{\{c_i\}} \delta(n-n_0) \quad e^{-(\beta'-\beta)E_i + (\mu'\beta'-\mu\beta)n}}{\sum_{\{c_i\}} \quad e^{-(\beta'-\beta)E_i + (\mu'\beta'-\mu\beta)n}} \tag{1.17}$$

From a statistical mechanics viewpoint, molecular systems share several properties with Ising spin systems if density fluctuations are substituted with spin flips. Polymer melts and blends without long-range interactions typically belong to the 3d-Ising universality class [92, 93], and critical points can be determined with techniques that were originally derived for spin systems [94]. To this extent we can calculate second- or fourth-order cumulants [94]:

$$U_2 = \frac{\langle M^2 \rangle}{\langle |M| \rangle^2}, \quad U_4 = \frac{\langle M^4 \rangle}{\langle M^2 \rangle^2} \tag{1.18}$$

which become system size independent and cross at the critical point (Figure 1.1). $M$ denotes the order parameter of the transition. For liquid–vapor phase coexistence it is given by:

$$M \equiv \varrho - \langle \varrho \rangle \tag{1.19}$$

In practice, we perform several simulations close to the critical point for different simulation box volumes and determine the coexistence chemical potential as indicated above. These simulations can be extrapolated to different temperatures close to $T_c$ to obtain $U_K(V,T)(K=2,4)$. The critical point is the intersection point of the cumulants. The computation of cumulants is closely related to finite-size effects [95–97] that haunted computer simulations in the early days but are now under firm control: In a macroscopic system the correlation length diverges at the

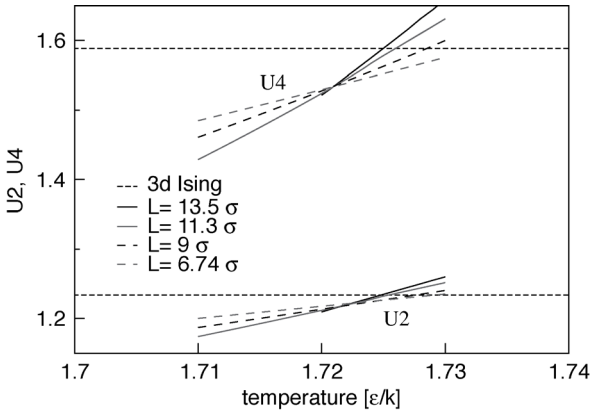


**Figure 1.1** Second- and fourth-order cumulants for a LJ + FENE pentamer in comparison to the corresponding values for the 3d Ising distribution at criticality (horizontal straight lines). Each line has been extracted from a single simulation by extrapolating the data set to several temperatures. Adapted from Reference [47].

critical point. In a system of finite size, the correlation length can at most be equal to half of the linear dimension of the simulation box, which has to be considered in the vicinity of $T_c$. Definition (1.19) is sufficient for most purposes. Note, however, that an exact mapping of fluid criticality to Ising criticality has to consider field-mixing effects [92] and $M$ becomes a linear combination of density and energy. Owing to higher order effects and corrections to scaling the values of $U_4$ and $U_2$ at the intersection points of the curves in Figure 1.1 deviate slightly from the asymptotic values obtained for the 3d Ising model (dotted horizontal lines). Note, however, that the intersections of both $U_2$ and $U_4$ occur at about the same temperature, which can be determined with good accuracy.

Away from the critical point, that is, at low temperatures, both phases are separated by a free energy barrier that corresponds to a region of low probability. This barrier cannot be overcome by thermal fluctuations. Several sophisticated schemes have been devised to address this issue. Multicanonical methods [98] modify the Hamiltonian in order to sample a range of densities uniformly. To this end, a weight function $w[n]$ is added to the original Hamiltonian. The simulated distribution $P_{\text{sim}}(n) = P(n)\exp(-w[n])$ becomes flat for the choice of $w(n) \approx \ln P(n)$. Unfortunately, $P(n)$ is a priori unknown, but can be estimated by extrapolating an overlapping data set [91]. A sequence of simulations and extrapolations typically starts close to the critical point where barriers between both peaks are small and no weighting is required for the first run. The weight function $w(n)$ can also be self-adjusted during simulation [99–102]. Note, that some of these schemes violate detailed balance and bear the risk of systematic errors. However, they are well-suited to generate an educated guess for the probability distribution, which can be used in a weighted simulation with fixed weights. A detailed discussion of methods to overcome free energy barriers can be found in Reference [103].

In the following we focus on a scheme that is based on umbrella sampling [104] and circumvents most of these problems. In successive umbrella sampling [105] the relevant range of states is subdivided into small windows that are sampled consecutively. This allows us to simulate without a weight function or to generate a weight function on the fly from previous windows by means of extrapolation. In the simplest implementation, we start with an empty box and allow the system to change only between 0 and 1 particle. A histogram $H(n)$ monitors how often each state is visited ($n$ denotes the number of particles in the simulation box). After a predetermined number of insertion/deletion Monte Carlo moves, the ratio $H(1)/H(0)$ is determined, and we move the window to the right (to allow 1 and 2 particles). This procedure is repeated until all relevant states have been sampled. Then, the (unnormalized) probability distribution can be estimated recursively:

$$\frac{P(n)}{P(0)} = \frac{H(1)}{H(0)} \cdot \frac{H(2)}{H(1)} \cdots \frac{H(n)}{H(n-1)} \tag{1.20}$$

or:

$$\ln \frac{P(n)}{P(0)} = \ln \frac{H(1)}{H(0)} + \ln \frac{H(2)}{H(1)} + \cdots + \ln \frac{H(n)}{H(n-1)} \tag{1.21}$$

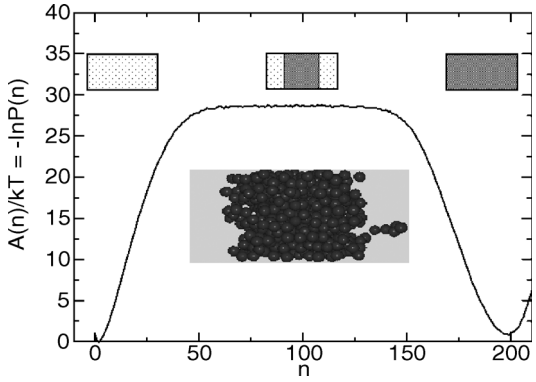


**Figure 1.2** Free energy as a function of the number of LJ + FENE pentamers ($n$) in the simulation box ($T = 1.38\,\varepsilon/k_B$, $V = 9 \times 9 \times 18\,\sigma^3$). Inset: typical configuration for $n = 100$ pentamers. With permission from Reference [47].

Logarithms are used to increase numerical accuracy as probabilities can become very low. The efficiency of the algorithm can be increased by combining the scheme with the multicanonical concept. In a weighted simulation we replace $H(n)$ in Eq. (1.20) by $H(n)\exp[-w(n)]$. After $P(n)$ is determined according to Eq. (1.20), $w(n) = \ln[P(n)]$ is extrapolated to the next window and used as an educated guess for $w(n+1)$.

Once the probability distribution is determined, information about interfacial properties can be extracted. Half way in between the gas and the liquid phase we typically observe configurations in which half of the simulation box is filled with liquid and half of the box is filled with gas at coexistence density (Figure 1.2 inset). As the free energy of the coexisting phases is the same, the difference in free energy can be attributed to the presence of the interface [106]:

$$\gamma = \frac{k_B T}{2L^2} \ln \frac{P(n_{max})}{P(n_{min})} \tag{1.22}$$

The interface area is $L^2$; the factor of 2 arises from periodic boundary conditions. $P(n_{max})$ is the average height of both peaks and $P(n_{min})$ the minimum in between. For these measurements an elongated box is preferred to ensure that the two interfaces do not interact [107, 108].

Finally, we briefly mention an example that combines a coarse-grained modeling ansatz with grand canonical simulations. In this particular case, hexadecane is modeled as a chain of five coarse-grained Lennard-Jones beads [Eq. (1.9)] that are connected by FENE [Eq. (1.10)] springs [48]. The solvent, carbon dioxide, is represented by a simple Lennard-Jones bead that contains an additional $r^{-10}$ term to account for the (spherically averaged) quadrupolar moment of $CO_2$ [82, 111]. Simulation parameters ε, σ, and $q$ (for $CO_2$) are derived by equating the critical temperature, the critical density, and the quadrupolar moment (in the case of $CO_2$) of simulation and experiment for the pure components. Mixture parameters $\varepsilon_{AB}$ and

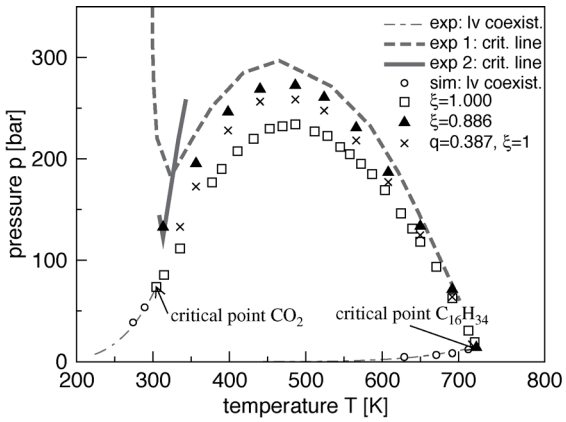


**Figure 1.3** Projection of the global mixture phase diagram of a hexadecane–$CO_2$ mixture onto the pressure–temperature plane. Simulation results for the liquid–vapor coexistence of the pure components are shown by circles. Thick lines mark two different experimental observations of the critical line from References [109, 110]. The thin dash-dotted lines indicate the experimental liquid–vapor coexistence of the pure fluids. Crosses mark the critical mixture line obtained for a $CO_2$ model that includes a spherically averaged quadrupolar moment, and no modification of the Lorentz–Berthelot mixing rule. Triangles and squares denote the critical line for a $CO_2$ model without quadrupolar moment with (triangles) and without modification (squares) of the Lorentz–Berthelot rule.

$\sigma_{AB}$ are given by the Lorentz–Berthelot combining rule ($\varepsilon_{AB} = \xi\sqrt{\varepsilon_A \varepsilon_B}$, $\xi = 1$, $\sigma_A = 0.5(\sigma_A + \sigma_B)$). Figure 1.3 shows a projection of the phase diagram and the critical line onto the pressure–temperature plane. Even though the model is very simple and lacks atomistic details it can describe adequately the phase behavior of the mixture without additional fitting parameters. If, however, the quadrupolar moment of $CO_2$ is not taken into account, a modification of the Lorentz–Berthelot rule is required ($\xi < 1$). This emphasizes that atomistic detail is not always required to describe the phase behavior correctly. However, it is advisable to include physically relevant quantities like the quadrupolar moment of $CO_2$.

## 1.3
## Wetting and Phase Diagrams in Confined Geometries

### 1.3.1
### Length and Energy Scales of Minimal, Coarse-Grained Models for Polymer–Solid Contacts

While previous sections have focused on the bulk phase behavior and the properties of interfaces between coexisting bulk phases, the polymer material is often confined in a container or a thin polymer film is supported by a substrate. This confinement

can give rise to wetting phenomena and these effects may profoundly alter the phase behavior in confined geometry [112].

In the following, we assume that the confining walls of the container or the supporting substrate (e.g., a wafer) are hard and non-deformable, that is, the properties of the solid do not change as it is brought into contact with the polymer material. If one measures the density profile of the polymer material at the polymer–solid contact, one will typically observe a steep rise of the density from zero (in the solid, confining wall) to the bulk density of the polymer material. The spatial extension of this polymer–solid interface is only a few ångström, that is, its width is dictated by the size of the atomistic constituents. On the other hand, in multicomponent polymer materials (i.e., polymer blends or polymer–solvent mixtures) one component will enrich at the solid surface, and the width of these enrichment layers may extend far away from the solid surface.

Two different enrichment phenomena can be distinguished [113]:

1) If the multicomponent material is completely miscible in the bulk, then a component will typically adsorb at the preferential, solid surface. This phenomenon alters the composition profile near the polymer–solid contact on a length scale that is set by the molecular extension. The enrichment layers are much larger than the width of the polymer–solid interface but they cannot grow macroscopically large.
2) If the multicomponent material exhibits two coexisting phases in the bulk, then one phase will be enriched at the polymer–solid contact and, provided that the solid is sufficiently preferential, this wetting layer of the preferred phase will grow macroscopically thick. One says that the preferred phase of the polymer material wets the solid [114].

In both situations the polymer–solid interface is much thinner than the width of the enrichment layer or the interphase. Since previous sections have dealt with phase coexistence in multicomponent polymer materials, we restrict ourselves to the wetting phenomena (2) and refer the reader to References [115–117] for simulation studies of adsorption phenomena within the framework of coarse-grained models.

The properties of the polymer–solid interface are most suitably investigated by atomistic modeling approaches. Atomistic modeling can address the complex interactions between polymer and solid materials and study the subtle conformational changes and structuring effects of the polymer liquid in the ultimate vicinity of the solid. However, atomistic approaches cannot address the length and time scales required to build up and equilibrate wetting layers.

Systematic coarse-graining schemes have been applied to one-component polymer melts in contact with solid surfaces. In this framework, one starts with an atomistic modeling approach and systematically devises effective free energies of interaction between coarse-grained segments along the polymer. In this way, information on the atomistic scale may be transferred into coarse-grained models. An interesting example of this strategy is the investigation of polycarbonate at a nickel surface where a strong, specific adsorption of the chain ends to the solid

surfaces has been revealed by atomistic modeling and this specific adsorption has been incorporated in the coarse-grained model [118]. Without the underlying atomistic modeling this specific interactions could have been easily overlooked. This example highlights the (rather special) case of a coupling between atomistic surface properties and long-range conformational properties. Typically, however, the surface tension of a polymer melt exhibits only a weak dependence on molecular weight.

If one uses a coarse-grained approach, one has to identify the relevant properties that the description on the coarser scale has to capture. In the following, we specifically consider wetting phenomena in a binary AB polymer blend that exhibits liquid–liquid phase separation between an A-rich and a B-rich phase. The thermodynamics of the surface enrichment layers is dictated by the free energies of the solid in contact with the two coexisting phases, $\gamma_{AW}$ and $\gamma_{BW}$, and their interfacial tension, $\gamma_{AB}$. If the solid surface, W, attracts the A-rich phase, then a domain of the A-rich phase, which is embedded in the B-rich phase, will form a drop at the solid surface. The AB-interface at the boundary of the domain will make the contact angle, $\Theta$, with the solid wall, W. Young's equation describes the balance of forces at the three-phase contact line parallel to the solid surface and dictates [119]:

$$\gamma_{WB} - \gamma_{WA} = \gamma_{AB} \cos \Theta \tag{1.23}$$

Note that the surface tensions, $\gamma_{WB}$ and $\gamma_{WA}$, are large. On the atomistic scale there are strong forces and, consequently, the energy of a segment with the surface can exceed the thermal energy scale, $k_B T$, by far. Moreover, the steep rise in density at the narrow polymer–solid contact gives rise to important changes of the conformational entropy (Lifshitz entropy [27]). In contrast, the interfacial free energy, $\gamma_{AB}$, is very small on the length scale of a coarse-grained segment. For a strongly segregated, symmetric binary polymer blend, one obtains [28]:

$$\gamma_{AB} = k_B T \varrho b^2 \sqrt{\chi/6} \tag{1.24}$$

where $b$ denotes the statistical segment length, $\varrho$ the number density of coarse-grained segments, and $\chi$ the Flory–Huggins parameter, which describes the repulsion between segments of the different polymer species of the blend.

Typically, the Flory–Huggins parameter is very small, that is, of the order $1/N$. Therefore, the left-hand side of Young's equation, Eq. (1.23), consists of a cancellation of two large contributions. It is a formidable task to predict via atomistic modeling the difference $\Delta\gamma = \gamma_{WB} - \gamma_{WA}$ or the Flory–Huggins parameter, $\chi$ with an accuracy of the order $k_B T/N$ per segment.

The behavior of polymer solutions, which exhibit phase coexistence between a polymer-rich liquid (L) and a polymer-poor vapor (V), is qualitatively similar. Only the separation of energy scales between the surface tensions of the polymer and vapor in contact with the solid and the liquid–vapor interfacial tension is less pronounced because the liquid–vapor interface also is narrow and the cohesive van der Waals interactions inside the liquid are strong.

The idea of a minimal coarse-grained model for polymer–solid contacts consists in not describing the structural details of the polymer–solid contact on the length scale of Ångströms because this length scale is not resolved. Instead, the aim is to tailor the interactions at the surface in order to match the difference in surface tension, $\Delta\gamma$, of the coarse-grained model to the experimental data. In this way, the macroscopic interfacial thermodynamics is parameterized.

Another important ingredient, which determines the wetting behavior, is the interaction between the outer, liquid–vapor interface of the wetting layer and the solid surface. This interaction (per unit area) is denoted as the interface potential [114] and it dictates, *inter alia*, the order of the wetting transition and the way, in which the thickness of the wetting layer grows as one approaches the bulk phase coexistence by varying the pressure.

Generally, the interface potential consists of a short-ranged and long-ranged contribution. The short-ranged potential stems from the distortion of the density profile at the interface. It decays exponentially as the thickness of the wetting layer increases and its length scale is set by the decay length in the wings of the interfacial profile, that is, the bulk correlation length, $\xi \sim R_e$.

The long-ranged part of the interface potential arises from the integrated van der Waals interactions inside the polymer material and between the solid surface and the polymer. This long-ranged interaction can be described by an external potential, which decays like [32]:

$$V_{\text{wall}}^{\text{lr}}(z) = \underbrace{\frac{\Delta A}{6\pi\varrho}}_{\varepsilon_{\text{wall}}} \cdot \frac{1}{z^3} \tag{1.25}$$

The strength, $\varepsilon_{\text{wall}}$, is parameterized by the Hamaker constant, $A$, which is proportional to the energy parameter, $\varepsilon$, of the Lennard-Jones potential. Typically, in a coarse-grained model, the Lennard-Jones interactions are cut-off at a finite distance, cf. Eq. (1.9). Therefore, the strength, $\Delta A$, is the difference between the Hamaker constant of the interactions inside the polymer liquid and that between polymer and solid.

To describe the thermodynamics and structure of wetting layers at a polymer–solid contact within the framework of a minimal, coarse-grained model, one has to identify the bulk properties, Flory–Huggins parameter, $\chi N$, the mean-squared end-to-end distance, $R_e$, and the molecular density, $\varrho/N$. $R_e$ characterizes the gross features of the molecular shape on large length scales, and $\chi N$ and $\varrho/N$ can be identified, for example, by matching the critical point of the blend or solution to experimental data. The structure and thermodynamics of the polymer–solid contact requires (at least) two additional, coarse-grained parameters – the difference in the surface tension, $\Delta\gamma$, between the two coexisting phases and the strength of the long-ranged interactions. The former can be identified by the macroscopic contact angle that a drop of the A-rich phase or polymer-rich phase embedded in a B-rich matrix or vapor makes with the solid surface. The latter can be estimated from experimental data on the Hamaker constants.

### 1.3.2
### Measuring the Surface Free Energy Difference, $\Delta\gamma$, by Computer Simulation

Here we discuss how to determine the additional coarse-grained parameters that characterize the coarse-grained model of the polymer–solid contact using the example of a one-component polymer material, which exhibits liquid–vapor phase coexistence. Knowing the bulk phase behavior and the interfacial tension between the coexisting phases, one could determine the difference, $\Delta\gamma$, by measuring the contact angle of a cap-shaped drop on the solid surface. This procedure mimics the experimental measurement but, unfortunately, the small droplet sizes accessible in simulations gives rise to significant finite-size effects:

1) If a drop is formed on the surface, the chemical potential of the system will be shifted away from the bulk coexistence value (Kelvin equation). Drops of a given size are only stable for a certain range of system sizes. If the system size is too large, the system will rather dissolve the excess material homogeneously in the volume than pay the free energy cost of the liquid–vapor interface [121]. This is the analog of the droplet condensation–evaporation transition in the bulk [122].
2) The contact angle of a small droplet may significantly be affected by the effects of the line tension that describes the free energy costs of the three-phase contact between liquid, vapor, and solid. This effect can be greatly reduced by considering cylindrical droplets that span the simulation box in one direction via the periodic boundary condition. In this case, the length of the three-phase contact line is twice the width of the system independent from the droplet size or contact angle [123].
3) The contact angle is defined by the asymptotic behavior of the liquid–vapor interface approaching the surface. At short distances from the surface, the interaction between the interface and the surface – the interface potential – distorts the interface away from its asymptotics and, thus, it may be very difficult to identify the asymptotic behavior from simulation data of small drops [31].

These difficulties will be avoided if one directly computes the surface free energy difference. To measure surface free energies, we apply the same grand-canonical Monte Carlo technique that we used for the bulk thermodynamics (Section 1.2.3), now in the presence of two surfaces [120, 124]. We fix the chemical potential to its coexistence value and, using the re-weighting method, we can make the simulation sample all densities between the vapor phase (V) and the liquid phase (L) in contact with the surface. Again the logarithm of the probability distribution, $P$, yields the free energy as a function of the density. Figure 1.4 displays the results for the Lennard-Jones bead-spring model with $N = 10$ effective segments at temperature $k_B T/\varepsilon = 1.68$. The free energy exhibits two minima, corresponding to configurations where either a vapor (low density) or a liquid (high density) phase is in contact with the surface. The ratio of the probability for finding the system in one of these phases yields the difference

in the surface free energies:

$$\Delta\gamma \equiv \gamma_{VW} - \gamma_{LW} = \frac{k_B T}{2L^2} \ln\left[\frac{P(\phi_L)}{P(\phi_V)}\right] \tag{1.26}$$

where $2L^2$ denotes the area of the two surfaces. Note that the bulk does not yield any contribution to the difference because, at coexistence, the grand-canonical free energies (i.e., pressure) of the two coexisting phases – liquid and vapor – are identical.

At intermediate densities the typical conformations consist of a liquid slab at each wall. If the system size is sufficiently large the distance between the liquid–vapor interfaces and the wall and their mutual distance become large. In this limit the interfaces neither interact with the walls nor with each other, and we expect only a weak dependence of the free energy on the density, that is, a plateau in the probability distribution, $P$, at intermediate values of the average density. The liquid will wet the surface if the difference in surface tensions equals the interfacial tension, $\Delta\gamma = \gamma_{LV}$. In a sufficiently large system, the wetting transition corresponds to the point where the plateau value of $P$ equals $P(\phi_V)$.

For the system size studied in Figure 1.4, we do not observe a plateau, that is, once the interfaces have reached a distance from the wall, which is large enough

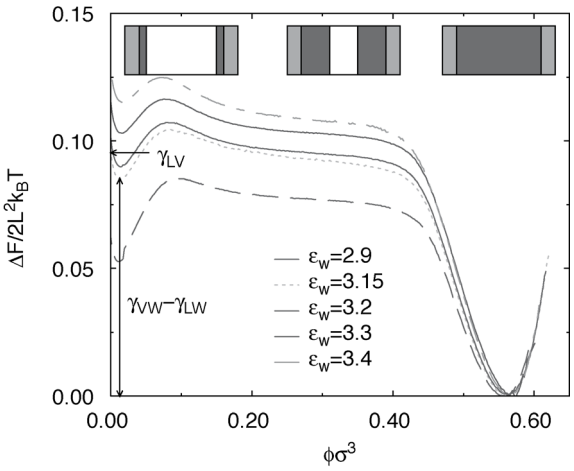


**Figure 1.4** Illustration of the simulation technique for a one-component, bead-spring model at temperature $k_B T/\varepsilon = 1.68$ and $\mu_{coex}$. A cuboidal system geometry $13.8\sigma \times 13.8\sigma \times 27.6\sigma$ with periodic boundary conditions in the two short directions and two confining surfaces in the long direction is used. The curves are shifted such that the free energy of the liquid phase vanishes. The horizontal arrow on the left marks the value of the interfacial tension $\gamma_{LV}$, while the vertical arrow marks the difference in the surface tension between the vapor/wall and liquid/wall for $\varepsilon_w = 3.15$. Typical system configurations are sketched schematically. Adapted from Reference [120].

for the interface potential between the interface and the surface to decay, they already begin to interact mutually. This indicates that our simulation cell is too small to accommodate two non-interacting solid–liquid and liquid–vapor interfaces. Nevertheless, we can reliably determine $\gamma_{VW} - \gamma_{LW}$. In these limiting states, the container is either completely filled with vapor or liquid, and there are no liquid–vapor interfaces present. The perturbation of the density profile in the liquid extends only over a few segmental diameters, σ, which is much smaller than the extension of the simulation cell.

To parameterize the coarse-grained model to a specific physical realization, one has to tune the interactions, $V_{wall}$, between solid and polymer to reproduce the experimental value of the surface free energy difference, $\Delta\gamma$. Once $\Delta\gamma$ has been obtained via the method described above for a particular strength, $\varepsilon_{wall}$, of $V_{wall}$, the dependence on the attractive strength of the wall can be obtained via thermodynamic integration [120, 124]:

$$\Omega(\varepsilon_{wall}) = \Omega(\varepsilon_o) + \int_{\varepsilon_o}^{\varepsilon_{wall}} d\varepsilon_{w'} \frac{\langle E_{wall}(\varepsilon_{w'})\rangle}{\varepsilon_{w'}} \tag{1.27}$$

where $\Omega$ is the grand canonical potential and $E_{wall} = L^2 \int dz\, \phi(z) V_{wall}(z)$ denotes the interaction energy associated with the monomer–wall interaction potential. Like any thermodynamic integration, this procedure can be efficiently carried out in the framework of an expanded ensemble.

### 1.3.3
### Application to Polymer–Solvent Mixtures

To illustrate these techniques, we consider the coarse-grained model for hexadecane and carbon dioxide, which we have discussed in Section 1.2. The correction of the Lorentz–Berthelot rule is set to $\xi = 0.9$ and the temperature is fixed at $k_B T/\varepsilon = 0.92$. (In this case carbon dioxide was modeled as a simple Lennard-Jones bead without quadrupolar moment.) The short- and long-ranged interactions at the polymer–solid contact are described by a 9-3-potential of the form:

$$V_{wall} = \varepsilon_{WS(P)} \left[ \left( \frac{\sigma_{S(P)}}{\Delta z} \right)^9 - \left( \frac{\sigma_{S(P)}}{\Delta z} \right)^3 \right] \tag{1.28}$$

where $\varepsilon_{WS}$ and $\varepsilon_{WP}$, denote the strength of the surface interaction acting on solvent and polymer, respectively.

Using the technique illustrated in Figure 1.4 for the one-component system, one can accurately locate the strength of the surface interaction, $\varepsilon_{WP}^{wet}$, at which the polymer film will wet the substrate, as a function of the vapor pressure, $P$. Figure 1.5 depicts the results for different values of the attraction, $\varepsilon_{WS}$, of the substrate to the solvent, carbon dioxide. If the substrate does not strongly attract the solvent, increasing the vapor pressure, $P$ will stabilize the polymer film because of the concomitant decrease of the liquid–vapor interfacial tension, $\gamma_{LV}$. If the substrate strongly attracts the solvent, however, the solvent will form a layer at the substrate and will displace the

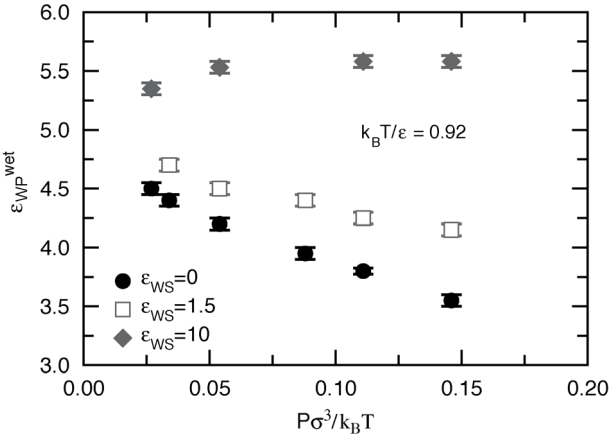


**Figure 1.5** Dependence of the wetting transition $\varepsilon_{WP}^{wet}$ on pressure, $P$, estimated by grand-canonical Monte-Carlo simulations of a polymer–solvent mixture. Adapted from Reference [125].

polymer. The excess of solvent at the surface may lead to dewetting of the polymer film upon increasing the pressure. This effect has also been corroborated by self-consistent field calculations [125, 126].

## 1.4
## Molecular Dynamics Method

### 1.4.1
### Basic Molecular Dynamics

Molecular dynamics [127] (MD) is a numerical technique to approximate the static and dynamic properties of classical many-body systems. MD techniques are commonly employed alongside Monte Carlo techniques because dense packing reduces the acceptance probability of translation and chain rotation moves to very low values, particularly when using all-atom models.

The key idea is simple: if $U(\{\boldsymbol{r}_i\})$ is the total potential acting on particle $i$ with mass $m_i$ and position $\boldsymbol{r}_i(t)$ at time $t$, then Newton's equations of motion (EOM):

$$m_i \frac{\partial^2}{\partial t^2} \boldsymbol{r}_i(t) = -\nabla_i U(\{\boldsymbol{r}_i\}) \tag{1.29}$$

are solved iteratively. The main justification of the MD method is based on the ergodic hypothesis that time averages are equal to statistical ensemble averages. However, MD simulations generate cumulative errors that cannot be suppressed entirely, but are minimized using adequate integration schemes. Various algorithms have been suggested to solve Eq. (1.29).

The Verlet algorithm uses the Taylor expansions of the position vectors in different time directions. With $\Delta t$ the "time-step" of the simulation, adding the expansions for $\boldsymbol{r}_i(t+\Delta t)$ and $\boldsymbol{r}_i(t-\Delta t)$ leads to:

$$\boldsymbol{r}_i(t+\Delta t) = 2\boldsymbol{r}_i(t) - \boldsymbol{r}_i(t-\Delta t) + \boldsymbol{a}(t)\Delta t^2 + O(\Delta t^4) + \cdots \tag{1.30}$$

where $\boldsymbol{a}_i(t) = -\nabla_i U(\{\boldsymbol{r}_i\})/m_i$ denotes the acceleration. When terms larger than $O(\Delta t^3)$ are neglected one obtains positions that are correct to $O(\Delta t^4)$, whereas velocities are correct to order $O(\Delta t^2)$.

A commonly applied modification is the velocity Verlet algorithm. It explicitly incorporates the particle's velocity, $\boldsymbol{v}_i$, such that:

$$\begin{aligned} \boldsymbol{r}_i(t+\Delta t) &= \boldsymbol{r}_i(t) + \boldsymbol{v}_i(t)\Delta t + \frac{\boldsymbol{a}_i \Delta t^2}{2} \\ \boldsymbol{v}_i(t+\Delta t) &= \boldsymbol{v}_i(t) + \frac{\boldsymbol{a}_i(t) + \boldsymbol{a}_i(t+\Delta t)}{2}\Delta t \end{aligned} \tag{1.31}$$

This approach produces errors that are of the same order as the Verlet algorithm. Its advantage lies in symmetric coordinates for "past" and "future" and conservation of the phase-space volume, that is, the velocity Verlet algorithm is consistent with Liouville's theorem. Although energy is not conserved perfectly on short time scales, there are no energy drifts for large times. The stability of the method can be increased, for example, using "Beeman's algorithm" [128] or the "leap-frog" [129] method, which calculate the velocities more accurately.

In predictor–corrector algorithms time derivatives of the position vectors at time $t$ are used to predict the positions and their derivatives at time $t+\Delta t$. The predicted variables then are corrected according to the difference from those at time $t$, where a set of "Gear constants" are used. The latter are chosen to balance accuracy and stability, that is, short- and long-time conservation of energy. Optimized values depend on the order of the Taylor expansion ("order of the algorithm").

Predictor–corrector algorithms are only time reversible for $\Delta t \to 0$ and therefore violate Liouville's theorem. However, in the canonical ensemble they can be tuned to be more accurate than the Verlet integration.

The main computational effort in MD simulations is to evaluate the interatomic forces. For pair-wise additive and short-range potentials geometrical composition algorithms have been proposed to optimize the force calculation. Mostly applied are the "cell linked-lists" or the "Verlet list" algorithm. Examples for efficient methods to compute forces from long-range potentials are "Ewald summation" [130], "particle-mesh Ewald" [131], "particle-particle-particle-mesh" [132], and "generalized Born" [133] algorithms.

The MD method has become a powerful tool to simulate even millions of particles and arbitrarily complex molecules in confined systems or in the bulk using periodic boundary conditions. Modifications of the original approach allow for MD simulations at constant pressure, chemical potential, or temperature. "*Ab initio*" MD simulations [134], using first-principles to evaluate interatomic forces for quantum electronic systems, have led to remarkable accomplishments in simulating the properties of real materials.

### 1.4.2 Non-equilibrium Molecular Dynamics Simulations of Coarse-Grained Polymer Systems

Computational studies of polymeric liquids under non-equilibrium conditions have been performed intensively in recent decades [135–152]. This is not only related to the advancing computational resources that have made such studies possible, but mainly to the distinct advantages of numerical investigations. While experiments usually only provide information on macroscopic properties, non-equilibrium molecular dynamics (NEMD) simulations allow one to explore structural features, which can be related to the phenomenological coefficients that describe the transport of mass, momentum, and energy. NEMD simulations have reproduced successfully many qualitative features of polymer solutions under stationary (steady) shear, such as "shear thinning" (decreasing viscosity with shear rate), "shear alignment" or effects on the normal stress [137, 139–142, 144, 145, 147, 149, 150]. Meanwhile, many numerical studies have been performed even for nonstationary flow fields [140, 145, 146, 150]. However, a reliable characterization of systems out of equilibrium requires careful numerical approaches, where special attention must be paid to coarse-graining, boundary conditions, and thermostat issues. In this section we discuss some of these technical aspects in mesoscopic NEMD simulations for coarse-grained polymer systems.

A presentation that covers the entire field of NEMD simulation techniques would greatly extend the length of this section. Here, we focus mainly on the case of confined polymer systems, where shear deformation is induced by displacement of the confining boundaries. The simulation of bulk systems usually invokes other techniques than discussed here, which are often better suited to reveal homogeneous fluid dynamics. For instance, homogeneous flow fields can be generated by deterministic (e.g., SLLOD [135, 136, 138, 148, 152]) EOM, which have been shown to reveal rather accurate transport properties for atomic liquids [138]. However, complex fluids, such as polymer solutions or melts, tend to "align" under strong shear-deformation due to hydrodynamic instabilities. Homogeneous methods that enforce a linear shear profile therefore have to be applied with care. Simulation methods for atomistic and molecular fluids in homogeneous flow fields have been reviewed in detail [152].

The rigorous solution of the time-dependent, quantum-mechanical, many-body problem is numerically unfeasible. The problem thus must be reduced to classical mechanics and coarse-grained models have to be introduced. In particular for NEMD simulations, the modeling of solvent effects can be crucial and the complexity of the problem is highly dependent on whether the external stimuli are strong or weak and whether they are constant in time or nonstationary.

When hydrodynamic effects are not expected to be important, it is often convenient to simulate without explicit solvent molecules. This approach can still be justified even when hydrodynamic flow becomes relevant, but solvent-related degrees of freedom have to be incorporated on a certain coarse-grained level. To reproduce hydrodynamic effects in the continuum limit, mesoscale hydrodynamic techniques

have been developed that conserve local mass and momentum. Such methods, for example, dissipative particle dynamics [143, 147, 149–151, 153–172], stochastic rotational dynamics [173–181], and the lattice Boltzmann method [182–185], can reproduce hydrodynamic behavior described by the Navier–Stokes equation on the relevant (large) length scales. In these approaches, monomers interact via conservative and thermal forces, where the latter are introduced via a thermostat.

Upon using a thermostat, one assumes that heat transport within the system occurs instantaneously. This is not strictly correct but often it is convenient to simulate at constant temperature. Fluctuation relations are derived more straightforwardly than for the micro-canonical ensemble and the thermostat helps to stabilize particle trajectories, allowing the use of larger time steps. In NEMD simulations, the thermostat is of great importance, as it is used to remove the viscous heat due to the entropy production from external stimuli. However, it is a non-trivial challenge in many NEMD simulations of complex fluids to maintain the temperature and simultaneously avoid an undesired influence of the thermostat on transport properties. For simulations far beyond static equilibrium, the specific choice of the thermostat and its parameters are often crucial. One example, where complications may arise easily, is the shear deformation of confined polymer systems, which is often simulated at shear rates much larger than typical experimental values (see References [142–144]) in order to obtain statistically meaningful results.

Owing to its simplicity, the Langevin (LGV) thermostat is one of the most applied methods to perform simulations in the canonical ensemble. In this approach, the simulated particles are coupled to an external heat bath at constant temperature. The dissipative force acting on particle $i$ is proportional to its velocity:

$$\boldsymbol{F}_i^{\mathrm{d}} = -m_i \Gamma \boldsymbol{v}_i \tag{1.32}$$

where $\Gamma$ is a friction constant. The random force follows from the fluctuation–dissipation theorem, which defines the temperature of the simulation. The LGV thermostat acts on a local scale. Particles that are too fast are damped by the viscous background, whereas the stochastic heat bath increases the velocity of particles that are too slow. As this method stabilizes the trajectories of monomers very efficiently, the LGV thermostat has been applied for many previous studies [137, 139, 141, 142, 144, 145, 150] of polymeric systems, both in static equilibrium and in NEMD simulations. However, the LGV thermostat does not conserve momentum and screens hydrodynamic interactions beyond a length [170, 186]:

$$\varkappa = \sqrt{\frac{\eta}{\varrho \Gamma}} \tag{1.33}$$

where $\eta$ and $\varrho$ are viscosity and density, respectively.

Galilean invariance is lost due to the coupling of monomers to the heat bath, which mimics a solvent that rests in the laboratory frame. Therefore, the method belongs to the class of "profile-biased" thermostats [138]. This can be demonstrated easily: Let us consider a film of linear polymers confined by two adsorbing substrates. Shear is applied by moving the upper substrate with a constant velocity, $w$, while the lower

substrate remains at rest. For a large film thickness, $L$, the density inhomogeneities close to the substrates are negligible. With $\eta_{\text{bulk}}$ as the bulk viscosity, the Navier–Stokes equation reads [145]:

$$\eta_{\text{bulk}}\Delta\boldsymbol{v}(z) = \Gamma\varrho\boldsymbol{v}(z) \tag{1.34}$$

where $z$ denotes the gradient direction, $\boldsymbol{v}(z)$ is the velocity profile, and $\varrho$ the monomer mass density.

Solving Eq. (1.34) with stick boundary conditions at the lower substrate, $v_x(0) = 0$ ($x$ the shear direction), and assuming $v_x(L) \leq w$ for the upper, leads to [145, 170]:

$$\frac{v_x(z)}{v_x(L)} = \frac{\sinh\left(\sqrt{\Gamma\varrho/\eta_{\text{bulk}}}z\right)}{\sinh\left(\sqrt{\Gamma\varrho/\eta_{\text{bulk}}}L\right)} \tag{1.35}$$

for the monomer velocity profile. The shear stress, $\sigma_{xz}$, can be obtained from integrating over the dissipated force [right-hand side of Eq. (1.34)], and for $L \gg \sqrt{\eta_{\text{bulk}}/\Gamma\varrho}$ one finds $\sigma_{xz} \sim \Gamma^{1/2}$. Simulations [145] confirmed this scaling behavior and revealed velocity profiles as given in Eq. (1.35). This outcome obviously is determined by the thermostat, as Eq. (1.34) describes the coupling of monomers to a solvent that remains at rest in the laboratory frame, independent of shear rate [145, 170].

To circumvent a biasing of flow profiles in shear simulations, the LGV thermostat is often applied anisotropically [137, 139, 141, 145, 150]. For instance, the thermostat force may be applied only in gradient and vortex directions, but "deactivated" along the direction of shear. Recent results [150] indicate that, under certain circumstances, a good agreement between this implementation and a method that intrinsically provides Galilean invariance can be achieved (see below). However, the coupling between the shear and gradient directions in complex fluids demands special attention whenever this feature becomes relevant for the transport properties of the confined fluid.

The most straightforward modification of the LGV thermostat is to relate the thermostat forces to the relative velocity of interacting particle pairs. Such an approach is based on the dissipative particle dynamics (DPD) method. Originally, DPD was proposed in conjunction with "soft" interaction potentials, which would represent clusters of atoms, increasing the stability of particle trajectories and allowing the use of larger MD time steps than for "hard" potentials. It has been applied to various problems, for example, phase separation [161, 164, 166], the flow around complex objects [153], and colloidal [154, 162] and polymeric [143, 147, 149–151, 157, 158, 167, 170] systems.

When DPD is applied as a thermostat, dissipative and random forces are added to the total conservative force in a pair-wise form. The sum of thermostat forces acting on a particle pair vanishes such that the microscopic dynamics fulfills Newton's third law. This method provides momentum conservation and Galilean invariance.

At large densities, the DPD thermostat reveals the coupling between the shear and gradient directions and hence is well suited for shear simulations of polymer melts. However, it is important to note that DPD cannot describe hydrodynamic behavior at arbitrary densities when solvent effects are not otherwise incorporated. This affects the applicability of the DPD thermostat already in static equilibrium, where it fails to reproduce Zimm dynamics [189] due to the missing long-range interaction between monomers transmitted by the solvent. To account for hydrodynamic correlations in the dilute regime, solvent effects have to be included on whatever coarse-grained level [143, 147, 157, 165, 167–169, 171], for example, by introducing explicit solvent monomers.

Modified versions of DPD are frequently proposed and the advantages and shortcomings of such modifications are a current issue of research [150, 172, 187]. DPD can be transformed into "smooth-particle hydrodynamics" [188], where the Navier–Stokes equation is solved in a Lagrangian form, or by the application of a splitting algorithm [169] into an Andersen's-thermostat version [165]. The DPD method can also be applied in the micro-canonical ensemble [159, 160, 163]. An extension of DPD has been introduced recently to allow for damping along the parallel and perpendicular components of the relative particle velocities independently [187]. This enables one to tune the transport properties of coarse-grained liquids to better match atomistic NEMD simulations, whenever the latter are feasible. However, the new approach does not conserve local angular momentum and hence should be used with care.

LGV and DPD thermostat have been compared recently [150] for NEMD simulations of polymer brushes. A polymer brush forms when linear polymers are adsorbed on substrates with one chain end, such that the steric repulsions between monomers force the chains to stretch away perpendicularly from the substrate. Systems of two polymer-brush bearing surfaces in contact can sustain large normal loads, simultaneously revealing small friction forces under shear deformation due to shear induced chain inclination. Polymer brushes therefore are very important lubricants and hence are the subject of many NEMD studies [137, 139–142, 144, 145, 147, 151].

For steady-state shear deformation similar transport properties are found at large and intermediate monomer densities, but systematic differences between the two methods arise at small densities. DPD and LGV thermostat also reveal somewhat different results for nonstationary flows [150].

NEMD simulations of polymer brushes at constant shear motion have also been performed with explicit solvent molecules, which are typically introduced as "single monomers." Both the LGV thermostat [139] and DPD [143, 147] exhibit significantly enhanced lubrication properties as compared to simulations of "dry" brushes, revealing the importance of solvent-induced effects on the macroscopic transport coefficients.

Complex polymer systems, such as polymer melts [149, 150] or star polymers [190] embedded between two polymer brushes, have been the subject of recent investigations. Simulations of these systems under nonstationary stimuli are extremely rare.

Alternative approaches to account for hydrodynamic interactions are based on so-called "hybrid" methods, where the polymers are coupled to a dynamical

background. The latter can be introduced either by collisions of ideal-gas particles or by a lattice-based solution of the Boltzmann equation [184], known from the kinetic theory of gases.

The first technique is known as the stochastic rotational dynamics (SRD) method or multiparticle collision dynamics, which is a particle-based algorithm suited to account for hydrodynamic interactions on the mesoscale. The coarse-grained solvent is described as ideal-gas particles that propagate via streaming and collision steps, which are constructed such that the dynamics conserves mass, momentum, and energy.

In the streaming step, the solvent particle trajectories are ballistic. Collisions are introduced by sorting the particles into cubic lattice cells and performing a stochastic rotation of the relative velocities in each cell. In contrast to DPD, the SRD method acts on all particles within the same collision cell.

In SRD, the environment of a particle depends on the superimposed velocity field. This breaks Galilean invariance, because the particles that participate in a collision differ between moving and resting frame. However, when the mean free path length of particles is large compared to the mesh size of the lattice, colliding particles arrive from different cells and are therefore uncorrelated. This reflects the conditions of "molecular chaos," where Galilean invariance is negligible. It has been shown [175] that Galilean invariance can be restored by a randomization of the collision environment, for example, by random shifts of the cells before each collision step.

To simulate polymer solutions, the monomers have to be coupled to the SRD fluid. Different strategies to achieve this aim have been proposed [173, 174, 176–179, 181]. Typically, the EOM of the polymers themselves are integrated with the standard MD method. The monomers are included into the collision step, thereby exchanging momentum with the SRD fluid. This is carried out under conservation of the total momentum. Often it is sufficient to treat the monomers as hydrodynamic point sources and to neglect the excluded volume interaction between solvent and monomers [173]. This method reproduces hydrodynamic behavior on large length scales and therefore reveals Zimm dynamics for dilute linear polymers in static equilibrium [173, 176, 177].

SRD appears to be a very promising (rather new) approach for future NEMD simulations, as it is a very efficient mesoscale technique. It reflects the characteristic shear deformation of solute macromolecules, for example, for shear flows of star polymers [180] or DNA molecules [181].

Hydrodynamic flow also can be incorporated via a discretized version of the Boltzmann equation. This approach is known as the lattice Boltzmann (LB) method. The idea is to solve the linearized Boltzmann equation on an underlying lattice to propagate molecular populations ("fictitious" solvent particles), which define the density and velocity on each lattice site. Similar to SRD, the monomers are treated as hydrodynamic point sources in the continuous space. The flow velocity at the monomer positions follows from a linear interpolation between neighboring lattice sites.

Coupling a stochastic version of LB with standard MD has allowed the reproduction of Zimm dynamics for dilute polymers in static equilibrium [183]. It has been

applied recently to study polymer migration in confined geometries for pressure driven flows [191]. LB also can be used in somewhat different "hybrid" methods [182], where the "point-particle" assumption for the solute is no longer valid, for example, in colloidal systems [185].

The applicability of thermostat implementations and mesoscale hydrodynamic techniques depend strongly on the specific system under consideration and general recommendations in favor of one method cannot be made. However, some guidelines shall be given:

- The LGV thermostat can be ruled out, even in its "profile-unbiased" version, whenever momentum transport is relevant, either in the form of hydrodynamic interactions or, for instance, due to a coupling between the shear and gradient directions. However, the LGV thermostat can be a powerful tool, as it stabilizes the particle trajectories very efficiently and allows the study of systems far from equilibrium. Excellent examples are investigations of polymer brushes at sufficiently large density, where situations far beyond linear response [137, 139, 141, 142, 144, 145, 150] and nonstationary shear deformation [144, 145, 150] could be studied.
- The DPD thermostat is the most straightforward and natural way to introduce Galilean invariance and momentum conservation. Whenever feasible, NEMD simulations with DPD and explicit solvent molecules would yield reasonable mesoscale hydrodynamics. Simulations far beyond static equilibrium [143, 147, 149–151] and nonstationary flows [150] have been performed. However, the level of coarse-graining for the explicit solvent still is a relevant issue.
- The usage of monomers as hydrodynamic point sources coupled to a SRD or LB fluid invokes problems for some systems in NEMD simulations. For instance, shear induced instabilities related to compositional fluctuations at polymer–liquid interfaces cannot be described properly when excluded volume effects are neglected. For nonstationary flow fields, a problem arises matching the time scales of polymer system and background fluid. When adjusted incorrectly, effects stemming from the finite solvent inertia may not be covered.

## 1.5 Atomistic Simulation of Polymer Melts and Blends Using Molecular Dynamics Techniques

### 1.5.1 Polymer Melts

Molecular dynamics simulations of polymer melts and blends in full atomistic detail are computationally demanding and a relatively recent approach to complement experimental observations and advance polymer theory [192–201]. The numerical simulation of Newton's equation of motion with suitable interatomic potentials (force fields) for polymers and other common constituents [202, 203] contributes to

understanding of the structural, dynamic, thermal, and mechanical properties of polymer melts. First attempts employed rotational isomeric state models to generate an initial structure and energy minimization (a predecessor method to MD to minimize atomic overlaps), combined with "blowing up" interatomic potentials, to obtain independent static equilibrium models of polymer melts [192]. The system size has since increased from the simulation of a single atactic polypropylene chain in a box of 1.8 $nm^3$ volume with a few independent configurations to complex polymer systems of 10 $nm^3$ volume over periods of nanoseconds (millions of time steps of femtoseconds) using desktop computers and over periods of microseconds (billions of time steps of femtoseconds) using supercomputers. The exponentially increasing amount of computational resources opens up new avenues to obtain insight into the dynamics of molten polymers.

In polyisoprene melts, the local polymer dynamics were shown to be independent of initial configurations [193]. Ratios of correlation times for different C–H vectors in the chain backbone match NMR data very well, while absolute values were more than twice as long. The spatial extent of cooperative motion accompanying conformational transitions was found to be about 1–2 repeat units. Diffusion coefficients, friction coefficients, and zero-shear viscosities in models of linear polyethylene melts were computed in very good agreement with experiment [194]. Systems of several chains of length $C_{24}$ to $C_{156}$ were first equilibrated using an efficient end-bridging Monte Carlo algorithm, and then subjected to MD simulation in the NVE and NVT ensembles up to 12 ns. The resulting series of melt properties as a function of chain length significantly expanded the understanding of polymer melts, including radii of gyration and relaxation times. Most importantly, the friction coefficient $\xi$ was found to be constant above a chain length of $C_{60}$, which is consistent with the Rouse model for an unentangled polymer melt (Figure 1.6).

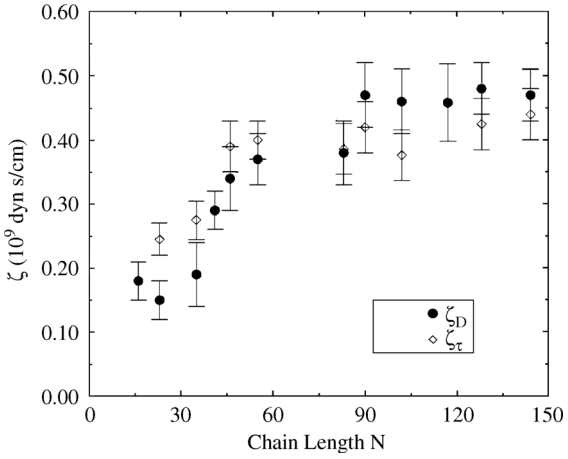


**Figure 1.6** Friction coefficient $\xi$ versus chain length $N$ of polyethylene, as obtained from the Rouse relation between $\xi$ and diffusion coefficient $D$ ($\xi_D$, full symbols) and from the Rouse relation between $\xi$ and the longest relaxation time $\tau_1$ ($\xi_\tau$, open symbols). After Reference [194].

Molecular dynamics methods have been further applied in industrial contexts [195] to gain qualitative insight into viscoelastic properties of polydisperse polymer melts, interface tensions between polymer melts, and the Izod impact strength. Nanoparticles of up to 16 nm diameter composed of chains of length $C_{50}$ to $C_{200}$ of various polymers (PE, PEP, aPP, PIB) were simulated by large-scale parallel MD to estimate glass transition and melting temperatures [196]. According to experiment, the thermal expansion coefficient and the heat capacity increase at the glass transition temperature; both increases were also observed in MD simulation at, however, two distinct temperatures of 50 K below and 50 K above the experimental glass transition. Nevertheless, a qualitative relation between increasing transition temperature and increasing size of the polymer particles has been found. Results obtained so far have been insufficient to demonstrate conclusively the ability to simulate glass transitions reliably and routinely, owing to the long time scales of the transitions and limitations in accuracy of the atomistic models [197, 198]. Several chains of atactic polystyrene of composition $C_{400}H_{402}$ were simulated to investigate the surface structure of thin films [199]. An end-bridging Monte Carlo algorithm was first invoked using a coarse-grained model for equilibration of the melt, followed by mapping onto the full atomistic detail, and molecular dynamics simulation. A preferred orientation of the phenyl rings normal to the surface was found and a surface energy 38 mJ $m^{-2}$ was computed in agreement with experiment. Moreover, dielectric properties of poly (butadiene) [200], glass transitions of various polymers [198], and force field parameters for silamethylene polymers [201] were investigated.

### 1.5.2 Polymer Blends

The simulation of polymer blends includes mixtures of polymers in the molten and solid states [204–218]. We can distinguish miscible, partially miscible, and immiscible blends as well as mixtures of very specifically interacting biopolymers. For example, direct contacts between residues in a protein (homeodomain of Antennapedia) and DNA bases, as well as the role of water molecules at the interface, have been analyzed during a 2 ns trajectory [204]. Dynamical observations by NMR spectroscopy were consistent with specific interactions derived from the simulation, and the critical role of the Gln-50 residue (pink) for protein–DNA binding, as previously known through genetic and biochemical analysis, could be linked to the interaction with four base pairs and bases in both DNA strands (Figure 1.7). The simulation of similar specific protein–protein interactions [206] and protein–polymer interactions [213] is an interesting extension of the simulation of homopolymers and block-copolymers.

After an efficient initial Monte Carlo equilibration with chain scission and fusion moves, the diffusion of binary liquid blends of *n*-alkanes and polymers was investigated for chain lengths of $C_5/C_{78}$, $C_{10}/C_{78}$, and $C_{12}/C_{60}$ using molecular dynamics simulation [207]. Diffusion coefficients of both components increased with increasing weight fraction of the short chain component, which was attributed to the increase in free volume contributed by these solvent-like chains. Results were found

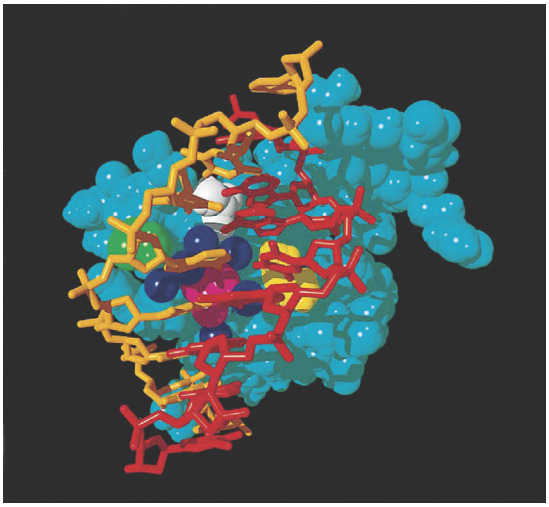

**Figure 1.7** Snapshot of a protein–DNA interface (Antennapedia homeodomain–DNA complex). The protein is represented by a space-filling model, with all atoms in cyan except for the side chains of Ile-47 (yellow), Gln-50 (pink), Asn-51 (gray) and Met-54 (green). The DNA is shown as a wireframe model. Positions of interfacial water molecules are given by dark blue spheres. After Reference [204].

to be in good agreement with free volume theory for low and medium fractions of the short alkane, with Rouse theory for all volume fractions, and with measurements of diffusion constants for the $C_{12}/C_{60}$ system across the range of volume fractions and temperatures.

More recently, glass transition temperatures were computed in semi-quantitative agreement with experiment for a cationic polymethacrylate blended with triethyl citrate plasticizer as a function of plasticizer weight content using medium size simulation boxes ($3.4\,nm^3$) in the NPT ensemble (Figure 1.8) [212]. Results of similar quality were also obtained for hydroxyl-terminated poly(butadiene) and poly(glycidyl azide) with various amounts of plasticizers [218]. The findings illustrate the current ability and limitation of all-atom simulations to characterize the phase behavior of polymers and blends as a function of chemistry. The reliability might be further improved through more accurate force fields, particularly with a focus on the precise modeling of polarity [219] and torsion barriers. In addition, stress tensors at interfaces and in arbitrarily shaped volumes within the system can be computed to describe the detailed dynamic mechanical behavior, including additive contributions from bonded, Coulomb, and van der Waals interactions to the total stress [220]. Notably, however, the quantitative prediction of glass transition temperatures meets the principal problem that the structural relaxation time of the polymer melt slows down dramatically in the temperature region slightly above the glass transition, where it reaches typically about 1 s. Molecular dynamics studies can equilibrate atomistic models of polymer melts often only on the nanosecond timescale, and hence one observes that the polymer melt falls out of equilibrium already at

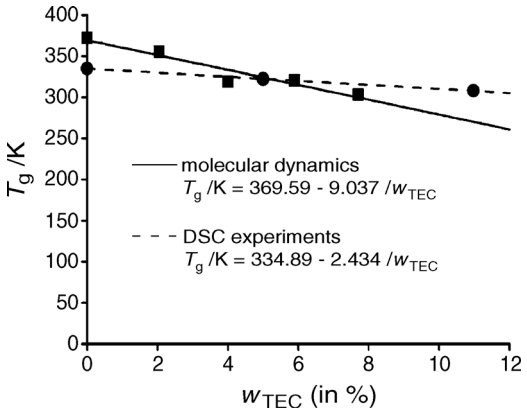


**Figure 1.8** Dependence of the glass transition temperature $T_g$ of a cationic polymethacrylate on the weight proportion of plasticizer $w_{TEC}$. A comparison of experimental values from DSC (dashed line) and computed values from all-atom simulation (full line) is shown. After Reference [212].

temperatures clearly above the glass transition temperature. This effect has been demonstrated by variation of the cooling rate for coarse-grained models [221]. Therefore, one would expect that normally the glass transition temperature found in simulations is an overestimate (the absolute difference is largest for the so-called "strong glassformers" and weakest for the so-called "fragile glassformers"). In view of this fact, the good agreement between experimental results and simulations sometimes reported in the literature is somewhat surprising. Partially, this may be due to a lucky cancellation of errors (the potentials used in the modeling may not always be very accurate, and if they underestimate the real glass transition temperature this may partially offset the systematic shift to higher temperatures due to the too short observation times in the simulation). In any case, more systematic studies will be needed to clearly resolve these problems.

Several studies also underline the importance of very efficient equilibration algorithms and long trajectories to understand the miscibility of long polymer chains in blends and at interfaces. Using relatively short MD trajectories without a significant equilibration algorithm, computed surface and interface tensions of various thin film interfaces of polyethylene, polypropylene, poly(ethylpropylene), and short copolymers of chain length $C_{200}$ lead to uncertainties in excess of $20\,\mathrm{mJ\,m^{-2}}$ [205]. In comparison, computed surface and interface tensions of shorter surfactants, such as attached to inorganic filler components, lead to uncertainties of only $2\,\mathrm{mJ\,m^{-2}}$ [222]. Similarly, MD simulations of a poly(vinylphenol)/poly(vinyl methyl ether) blend with long chains of $N = 250$ for each polymer without a significant equilibration algorithm did not result in uniform mixing [209]. Nevertheless, local structural correlations such as the gauche-to-anti ratio and the formation of hydrogen bonds can be understood, as further demonstrated for poly(vinylphenol)/poly(ethylene terephthalate) [210] and polystyrene/polyisoprene blends [211]. As discussed in the introduction, the standard elementary description of miscibility in polymer blends uses the concept of the "Flory–Huggins

χ-parameter" and for large molecular weights (degree of polymerization of the order of 1000 or more) partial miscibility occurs only if χ is rather small, of the order of 1 part in a thousand. Such small values need an almost perfect compensation between effective interactions of like and unlike monomeric units (taking also the steric arrangements of these units in the blend into account). Although it would be very desirable to be able to predict these χ-parameters accurately from simulation, one cannot yet expect that the models are accurate enough for this purpose in the general case. In addition, polymer blends are characterized by spatial correlations on rather large scales and slow relaxation of concentration fluctuations, and therefore, so far, many studies have relied on coarse-grained models exclusively [9]. Going beyond such coarse-grained descriptions clearly is desirable, of course, and the mapping between coarse-grained and atomistic models, discussed in the next subsection, is a promising direction towards this goal.

Further results of all-atom molecular dynamics simulations have also been reported for PEO/PMMA blends [214], POSS/PE blends [215], blends of hydroxyl-terminated polybutadiene with explosive plasticizers [217], as well as a novel force field for PDMS and mixtures with alkanes [216]. The simulation of multiphase polymer systems has also been reviewed [208].

### 1.5.3
### Reversible Mapping between Atomistic, Coarse Grained, and Field Models

Understanding the complex phase properties of polymer blends benefits from simulation methods at different length scales, and efforts to achieve compatibility and convertibility between these length scales have been made [223–227]. A common approach involves the iterative match of radial distribution functions from atomistic simulations of an oligomer to those calculated in a coarse-grained simulation for the same oligomer (Figure 1.9) [223]. Similarly, coarse-grained models representing an oligomer of few repeat units in one bead can be mapped to yet coarser models representing many repeat units in one bead to simulate high polymers. In addition, to match structural information such as radial distribution functions, a match of free energies such as surface tensions and solubility parameters is required. The difference in length and time scales also necessitates suitable scale factors to interpret distance and time consistently at both scales. The neglect of numerous degrees of freedom from the atomistic to the coarse-grained scale makes it difficult to compare

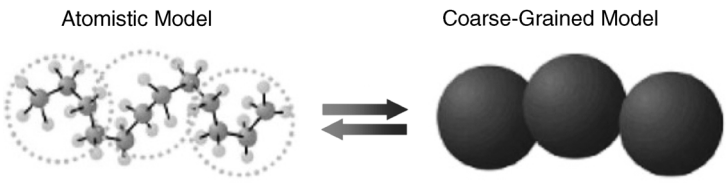


**Figure 1.9** Conversion between atomistic and coarse-grained models. A 4 : 1 coarse-graining scheme is shown. After Reference[226].

time scales more accurately than within an order of magnitude [224]. First estimates for an appropriate scale factor and dynamic mapping approaches can be derived from a comparison of computed diffusion constants at both scales and the conversion of Lennard-Jones (reduced) time in the coarse-grained simulation into real time.

The efficiency of a reversible mapping approach also depends on a well-defined (or even automatic) parametrization method such as the simplex method or iterative Boltzmann inversion [223]. A useful route to relaxed high polymer structures can be (i) an atomistic simulation, (ii) the derivation of a coarse-grained model, (iii) a coarse-grained simulation using suitable algorithms, (iv) reverse mapping to the atomistic level, and (v) local relaxation of the atomistic structure (Figure 1.9). For example, iterative Boltzmann inversion has been applied to study the phase separation in a polystyrene/polyisoprene blend and leads to qualitative agreement with experiment [225].

Further methods to study mesoscopic structures include time dependent Ginzburg–Landau theory, dynamic density functional theory, lattice-gas automata, and the lattice Boltzmann equation [226]. Some of these simulation methods, such as the dynamic mean field theory (Mesodyn) and dissipative particle dynamics (DPD), utilize coarse-grained molecular models to study the morphology of inhomogeneous materials using Flory–Huggins $\chi$ parameters between components and can be reversibly linked to atomistic simulation. For example, Flory–Huggins $\chi$ parameters between two components, characteristic ratios ($C_\infty$) of the Gaussian chains, and self-diffusion coefficients ($D$) have been estimated through atomistic simulation and fed into coarse-grained models in the mesoscopic simulation [226]. Trends in thermodynamically preferred morphology, phase separation, mechanical properties, and the behavior under shear were obtained in good agreement with experiment for various polymer blends, including polyethylene/polypropylene, poly(ethylene terephthalate)/poly(ethylene naphthalate), poly(vinyl chloride)/polyethylene, poly (methyl methacrylate)/polycarbonate, and polycarbonate/acrylonitrile/butadiene/ styrene [226], as well as composites [227]. The mesoscale morphologies and structures can be converted into atomistic models for continued analysis at a chemically specific level.

### 1.5.4
### Comparison to Experiment and Future Challenges

The previous sections indicate the ability of chemically detailed simulations to explain experimental data and the potential for predictions in unknown systems. All-atomic simulation often bridges the gap between indirect structural information obtained from spectroscopic, thermal, and mechanical measurements and molecular level details. The local dynamics of polymer chains [193] agrees with C-H NMR relaxation data on a relative scale [2]; however, absolute correlation times in the simulation appear to be $\sim$2.5 times the real value. This mismatch could be associated with overestimated torsion barriers in atomistic models, such as an eclipsed barrier of 5–6 kcal mol$^{-1}$ for *n*-butane (from *ab initio* calculations) in comparison to the experimental value of 4.0 kcal mol$^{-1}$ [228]; such differences can

be corrected in future force fields. Nevertheless, diffusion coefficients, friction coefficients, and zero-shear viscosities have been computed in very good agreement with experiment [194], and model predictions both at the atomistic and coarse-grained level can be considered reliable over significant temperature and pressure ranges for non-polar polymers such as polyethylene, polypropylene, or polyisobutylene. The availability of high-performance computing resources [195, 196, 199] further aids in obtaining equilibrium structures and in the application of new equilibration algorithms for large systems.

In polar polymers, the exact balance of charges and the description of specific interactions such as hydrogen bonds are critical [219]. Often, X-ray diffraction data, NMR data, and binding constants are valuable experimental input to identify specific van der Waals, π-stacking, and polar interactions on the basis of molecular simulation [204]. Therefore, atomic-level simulations have great potential in the design of complex interfaces or "mixtures" of biological and bioinspired polymers in combination with experiment. Properties such as gas diffusion constants, elastic constants, and possibly glass transition temperatures as well as solubility parameters could be simulated in approximate agreement with experiment, as recently shown for chitosan [229]. Self-diffusion coefficients for short-chain polymer blends have been obtained in quantitative agreement with experiment [207], and current limitations on chain length ($10^2$–$10^3$ main chain atoms) will be pushed back as computational power becomes more readily available. In the same way, it is likely that surface and interface properties in polymer blends will be computed quantitatively in the near future. In addition to the previously mentioned techniques, electron paramagnetic resonance spectroscopy (EPR) also constitutes a helpful tool in combination with all-atom simulations to monitor the dynamics in spin-probe labeled polymers at a length scale of 1–10 nm, which is of interest in chain dynamics [230]. Ultimately, the phase behavior and mechanical properties of long-chain polymer blends can be most effectively simulated through multiscale approaches, for example, coarse-grained models and field-based descriptions, which can be parameterized on the basis of atomistic models and converted from the atomistic into the simplified scale as well as vice versa.

## 1.6 Concluding Remarks

The subject of molecular simulation and thermodynamics of polymers is an active area of research and encouraging results have been obtained. The interplay between the refinement of computer simulation methods and the rapid growth of computer resources (the speed of the hardware is doubling roughly about every two years) has led to a rapid growth of successful applications of simulation methods.

While for the first 30 years after the introduction (in 1941) of the Flory–Huggins theory of polymer blends (and polymer solutions) experimentalists had to exclusively rely on this approach and its refinements for the interpretation of their data, in the two decades from about 1970 to about 1990 basic steps were taken to go beyond this phenomenological description, both via the formulation of more detailed and refined

theories [e.g., the self-consistent field theory (SCFT) of polymeric systems, the statistical associating fluid theory (SAFT) for the description of the equation of state, and the polymer reference interaction site model (PRISM), etc.] and via computer simulation methods. Owing to lack of computer resources, the first successful applications focused on Monte Carlo simulations of lattice models (such as self-avoiding walks on the simple cubic lattice, or the bond fluctuation model), providing crucial tests of the Flory–Huggins theory of polymer mixtures, elucidating their limitations, and of the random phase approximation applied to polymer blends and block copolymers, and so on. Alternative coarse-grained off-lattice models such as the Kremer–Grest bead-spring model were also introduced, offering the important advantage that via molecular dynamics simulations dynamical aspects of polymer blends, melts, and solutions also became accessible (interdiffusion and spinodal decomposition in blends and solutions; selfdiffusion in melts and the entanglement problem; glass transition in polymeric systems).

Of course, while work along such lines can elucidate basic theoretical questions, provide general insight into the problems, and give guidance to experiments, the important task of predicting properties of polymeric materials from "first principles" (i.e., only the knowledge of chemical structure is used as the input) cannot be addressed using such coarse-grained models alone. It must also be stressed that a theoretically fully satisfactory treatment would require us to solve the many-body Schrödinger equation for all the electrons plus nuclei in the system and use the resulting energy eigenvalues and associated eigenfunctions in a quantum statistical mechanics framework; unfortunately, such an approach is still far from feasible. Consequently, all simulations of "chemically realistic" models rely on approximate descriptions, which again need to be validated by comparison to experiment. In fact, for polymeric materials, in most cases effects due to electrons are not explicitly considered, and one uses effective potentials ("force fields") as input in molecular dynamics simulations (which amount to the solution of Newton's equations of motion, i.e., classical mechanics rather than quantum mechanics). While some parts of such potentials (e.g., torsional potentials) can be derived from presumably very reliable quantum chemistry approaches, the non-bonded dispersion forces cannot be deduced reliably from any "first principles"-theories. Thus, both coarse-grained and atomistic models describe the latter often by the phenomenological Lennard-Jones potential, with parameters chosen such that the model correctly reproduces selected experimental data in a simulation. Of course, great care is necessary so that in such applications the "technical" limitations of simulations (polymeric systems often involve large length scales and hence one needs to watch out for finite size effects; polymeric systems often involve huge relaxation times, and hence the question of whether equilibrium has been reached needs to be addressed) are adequately considered. As a general rule, we stress that sound simulation work needs a careful "education" of the simulator in the techniques that he or she is using, and in their theoretical background; the present chapter could only give the flavor of this background, and has hopefully "whetted the appetite" of the reader to study this background more thoroughly. Any would-be practitioner of such techniques must realize that it would be completely wrong and misleading to think that simulation

methods are already a standard tool that everybody can use without prior knowledge, just as experimentalists can use standard instruments (microscopes, light or X-ray scattering apparatus, etc.). The idea that computer simulation belongs to this category of "standard tools" is clearly a vision but not yet reality.

Owing to the problem that one needs to connect quantum-mechanical input (sub-ångström length scale, sub-picosecond time scale) to the scales of coarse-grained models (many nanometers and many nanoseconds) and the latter to the mesoscopic scales of interest for many problems (many micrometers or even millimeters and time scales up to seconds are the length- and time-scales of interest for the processing of real polymeric materials), it is clear that a straightforward brute-force approach (if ever feasible at all) is not the most economical approach to the problem. Hence the idea of a hierarchical "multiscale modeling" approach is clearly attractive and the first promising steps in this direction can be found in the literature. In the present chapter we have, hence, illustrated this very interesting development. However, we also emphasize that at present this is still a very active area of research, and universally applicable methods (including also an understanding of the accuracy of the approach under various circumstances) have yet to emerge.

## Symbols

| | |
|---|---|
| $<>_T$ | thermal average |
| $A$ | Hamaker constant or Helmholtz free energy |
| $\boldsymbol{a}_i$ | acceleration (molecular dynamics) |
| $a_{ij}$ | probability of selecting or placing a particular particle for the move (Monte Carlo) |
| $b$ | statistical segment length |
| $c_i^{\mathrm{A,B}}$ | local concentrations (Flory–Huggins model) |
| $C_\infty$ | characteristic ratio |
| $D$ | self-diffusion coefficient |
| $F_i$ | force acting on particle $i$ |
| $H(n)$ | number of occurrence in state n (successive umbrella sampling) |
| $F$ | Helmholtz free energy |
| $k_\mathrm{B}$ | Boltzmann constant |
| $L$ | linear box size |
| $m_i$ | mass of particle $i$ |
| $M$ | order parameter |
| $n$ | number of particles |
| $N_{\mathrm{A,B}}$ | chain length of polymer type A or B (Flory–Huggins model) |
| $p$ | pressure |
| $P(i)$ | probability of residing in state in state $i$ (Monte Carlo) |
| $P_{\mathrm{sim}}$ | simulated probability (multicanonical sampling) |
| $q$ | number of nearest neighbors (Flory–Huggins model) |
| $R_\mathrm{g}$ | radius of gyration |
| $\boldsymbol{r}_i$ | position of particle |

| | |
|---|---|
| $T$ | temperature |
| $T_c$ | critical temperature |
| $U$ | potential |
| $U_2$ | second-order cumulant |
| $U_4$ | fourth-order cumulant |
| $V$ | volume |
| $V_{FENE}$ | FENE potential |
| $\boldsymbol{v}_i$ | velocity of particle $i$ |
| $V_{LJ}(r)$ | Lennard-Jones potential |
| $w(n)$ | weight function (multicanonical sampling) |
| $Z$ | partition sum |

### Greek Symbols

| | |
|---|---|
| $\beta = 1/k_B T$ | |
| $\gamma$ | interfacial tension |
| $\Gamma$ | friction constant |
| $\varepsilon_{AA}, \varepsilon_{AB}$ *and* $\varepsilon_{BB}$ | interaction energies (Flory–Huggins model) |
| $\varepsilon, \sigma$ | interaction parameters in Lennard-Jones model |
| $\eta$ | viscosity |
| $\Theta$ | contact angle |
| $\mu$ | chemical potential |
| $\xi$ | friction coefficient or empirical modification parameter in Lorentz–Berthelot rule or correlation length |
| $\varrho$ | density |
| $\sigma_{xz}$ | shear stress |
| $\varphi_A, \varphi_B$ *and* $\varphi_V$ | volume fractions (Flory–Huggins model) |
| $\chi_{AB}, \chi_{AA}$ *and* $\chi_{BB}$ | Flory–Huggins parameters |
| $\omega_{ij}$ | probability of jumping from state $i$ to $j$ (Monte Carlo simulation) |
| $\Omega$ | grand canonical potential |

### References


1 Huggins, M.J. (1941) *J. Chem. Phys.*, **9**, 440; Flory, P.-J. (1941) *J. Chem. Phys.*, **9**, 660.
2 Flory, P.-J. (1953) *Principles of Polymer Chemistry*, Cornell University Press, Ithaca, N.Y.
3 de Gennes, P.G. (1979) *Scaling Concepts in Polymer Physics*, Cornell University Press, Ithaca, N.Y.
4 Binder, K. (1994) *Adv. Polym. Sci.*, **112**, 181.
5 Koningsveld, R., Stockmayer, W.-H., and Nies, E. (2001) *Polymer Phase Diagrams*, Oxford University Press, Oxford.
6 Rubinstein, M. and Colby, R.H. (2003) *Polymers Physics*, Oxford University Press, Oxford.
7 Binder, K., Müller, M., Virnau, P., and MacDowell, L.G. (2005) *Adv. Polym. Sci.*, **173**, 1.
8 Bicerano, J. (ed.) (1992) *Computational Modeling of Polymers*, Marcel Dekker, New York.
9 Binder, K. (ed.) (1995) *Monte Carlo and Molecular Dynamics Simulations in Polymer Science*, Oxford University Press, New York.

**10** Kotelanskii, M. and Theodorou, D.N. (eds) (2004) *Simulation Methods for Polymers*, Marcel Dekker, New York.

**11** Sariban, A. and Binder, K. (1987) *J. Chem. Phys.*, **86**, 5859; Sariban, A. and Binder, K. (1988) *Macromolecules*, **21**, 711.

**12** Binder, K.,in (1995) *Monte Carlo and Molecular Dynamics Simulations in Polymer Science* (ed. K. Binder), Oxford University Press, New York, p. 356.

**13** Müller, M. (1995) *Macromolecules*, **28**, 1825; Müller, M. (1999) *Macromol. Theory Simul.*, **8**, 343.

**14** Kemmere, M.F. and Meyer, Th. (eds) (2005) *Supercritical Carbon Dioxide in Polymer Reaction Engineering*, Wiley-VCH Verlag GmbH, Weinheim.

**15** Deutsch, H.-P. and Binder, K. (1992) *Macromolecules*, **25**, 6214; Deutsch, H.-P. and Binder, K. (1993) *J. Phys. (Paris) II*, **3**, 1049.

**16** Bates, F.S., Rosedale, J.H., Stepanek, P., Lodge, T.P., Fredrickson, G.H., and Helm, P.P. Jr (1990) *Phys. Rev. Lett.*, **65**, 1893; Stepanek, P., Lodge, T.P., Kredowski, C., and Bates, F.S. (1991) *J. Chem. Phys.*, **94**, 8289.

**17** Meier, G., Schwahn, D., Mortensen, K., and Janssen, S. (1993) *Europhys. Lett.*, **22**, 577; Schwahn, D., Meier, H., Mortensen, K., and Janssen, S. (1994) *J. Phys. II (Paris)*, **4**, 837.

**18** Schwahn, D. (2005) *Adv. Polym. Sci.*, **183**, 1.

**19** Melnichenko, Y.B., Anisimov, M.A., Povodyrev, A.A., Wignall, G.D., Sengers, J.V., and Van Hook, W.A. (1977) *Phys. Rev. Lett.*, **79**, 5266.

**20** Sanchez, I.C. and Lacombe, R.H. (1976) *J. Phys. Chem.*, **80**, 2352; Lacombe, R.H., and Sanchez, I.C. (1978) *Macromolecules*, **11**, 1145.

**21** Bawendi, M.G. and Freed, K.F. (1988) *J. Chem. Phys.*, **88**, 2741; Freed, K.F. and Bawendi, M.G. (1989) *J. Phys. Chem.*, **93**, 2194.

**22** Dudowicz, J., Freed, K.F., and Madden, W.-G. (1990) *Macromolecules*, **23**, 4803; Dudowicz, J. and Freed, K.F. (1991) *Macromolecules*, **24**, 5076–5112.

**23** Freed, K.F. and Dudowicz, J. (1995) *Trends Polym. Sci.*, **3**, 248; Freed, K.F. and Dudowicz, J. (1998) *Macromolecules*, **31**, 6681; Freed, K.F. and Dudowicz, J. (2005) *Adv. Polym. Sci.*, **183**, 63; Dudowicz, J. and Freed, K.F. (1995) *Macromolecules*, **28**, 6625; Dudowicz, J. and Freed, K.F. (1996) *Macromolecules*, **29**, 8960; Foreman, K.W. and Freed, K.F. (1998) *Adv. Chem. Phys.*, **103**, 335.

**24** Edwards, S.F. (1965) *Proc. Phys. Soc. London*, **85**, 613.

**25** Doi, M. and Edwards, S.F. (1986) *Theory of Polymer Dynamics*, Academic Press, New York.

**26** Grosberg, A.Yu. and Khokhlov, A.R. (1994) *Statistical Physics of Macromolecules*, AIP, New York,Helfand, E. and Tagami, Y. (1971) *J. Polym. Sci., Part B, Polym. Lett.*, **9**, 741.

**27** Helfand, E. (1975) *J. Chem. Phys.*, **62**, 999.

**28** Scheutjens, J.M.H.M. and Fleer, G.J. (1973) *J. Phys. Chem.*, **83**, 1619.

**29** Hong, K.M. and Noolandi, J. (1981) *Macromolecules*, **14**, 727; Noolandi, J. and Hong, K.M. (1983) *Macromolecules*, **15**, 483; 1983, **16**, 1443; Whitemore, D.M. and Noolandi, J. (1985) *Macromolecules*, **18**, 657; Whitemore, D.M. and Noolandi, J. (1995) *Macromoleclues*, **28**, 5763.

**30** Matsen, M.W. (1995) *Macromolecules*, **28**, 5763; Matsen, M.W. (1999) *J. Chem. Phys.*, **110**, 4658.

**31** Müller, M. and MacDowell, L.G. (2003) *J. Phys.: Condens. Matter*, **15**, R609.

**32** Fredrickson, G.H. (2006) *The Equilibrium Theory of Inhomogeneous Polymers*, Oxford University Press, New York.

**33** Hamley, I.W. (1998) *The Physics of Block Copolymers*, Oxford University Press, Oxford.

**34** Schweizer, K.S. and Curro, J.G. (1987) *Phys. Rev. Lett.*, **58**, 246; Schweizer, K.S. and Curro, J.G. (1988) *Phys. Rev. Lett.*, **60**, 809; Schweizer, K.S. and Curro, J.G. (1988) *J. Chem. Phys.*, **88**, 7242; Schweizer, K.S. and Curro, J.G. (1989) *J. Chem. Phys.*, **91**, 5059.

**35** Curro, J.G. and Schweizer, K.S. (1990) *Macromolecules*, **23**, 1402; Curro, J.G. and Schweizer, K.S. (1991) *Macromolecules*, **24**, 6736; Curro, J.G., Schweizer, K.S., Grest, G.S., and Kremer, K. (1989) *J. Chem. Phys.*, **91**, 1357.

**36** Yethiraj, A. and Schweizer, K.S. (1992) *J. Chem. Phys.*, **97**, 5927; Yethiraj, A. and

Schweizer, K.S. (1993) *J. Chem. Phys.*, **98**, 9080; Schweizer, K.S. and Yethiraj, A. (1993) *J. Chem. Phys.*, **98**, 9053; Yethiraj, A. (1995) *J. Chem. Phys.*, **102**, 6874.
**37** Schweizer, K.S. and Curro, J.G. (1994) *Adv. Polym. Sci.*, **116**, 319.
**38** Schweizer, K.S. and Curro, J.G. (1997) *Adv. Chem. Phys.*, **98**, 1.
**39** Fuchs, M. and Schweizer, K.S. (2000) *Europhys. Lett.*, **51**, 621; Fuchs, M. and Schweizer, K.S. (2001) *Phys. Rev. E*, **64**, 021514.
**40** Fuchs, M. and Schweizer, K.S. (2002) *J. Phys.: Condens. Matter*, **14**, R239.
**41** Lipson, J.E.G. (1991) *Macromolecules*, **24**, 1334; Lipson, J.E.G. (1992) *J. Chem. Phys.*, **96**, 1418; Sevian, H.M., Brazhink, P.K., and Lipson, J.E.G. (1993) *J. Chem. Phys.*, **99**, 4112.
**42** Taylor, M.P. and Lipson, J.E.G. (1998) *J. Chem. Phys.*, **102**, 2118.
**43** Dickman, R. and Hall, C.K. (1986) *J. Chem. Phys.*, **85**, 4108; Honnell, K.G. and Hall, C.K. (1989) *J. Chem. Phys.*, **90**, 1841; Yethiraj, A. and Hall, C.K. (1991) *J. Chem. Phys.*, **95**, 8494.
**44** Costa, L.A., Zhou, Y., Hall, C.K., and Carra, S. (1995) *J. Chem. Phys.*, **102**, 6212.
**45** Wertheim, M.S. (1984) *J. Stat. Phys.*, **35**, 19; Wertheim, M.S. (1984) *J. Stat. Phys.*, **35**, Wertheim, M.S. (1986) *J. Stat. Phys.*, **42**, 459; Wertheim, M.S. (1986) *J. Stat. Phys.*, **42**, 477.
**46** Wertheim, M.S. (1986) *J. Chem. Phys.*, **85**, 2929; Wertheim, M.S. (1987) *J. Chem. Phys.*, **87**, 7323.
**47** Virnau, P., Müller, M., MacDowell, L.G., and Binder, K. (2004) *J. Chem. Phys.*, **121**, 2169.
**48** Mognetti, B.M., Virnau, P., Yelash, L., Paul, W., Binder, K., Müller, M., and MacDowell, L.G. (2009) *J. Chem. Phys.*, **130**, 044101.
**49** MacDowell, L.G., Müller, M., Vega, C., and Binder, K. (2000) *J. Chem. Phys.*, **113**, 419.
**50** MacDowell, L.G., Virnau, P., Müller, M., and Binder, K. (2002) *J. Chem. Phys.*, **117**, 6360.
**51** Hansen, J.P. and McDonald, I.R. (1986) *Theory of Simple Liquids*, Academic, New York.
**52** Chapman, W.G., Gubbins, K.E., Jackson, G., and Radosz, M. (1989) *Fluid Phase Equilib.*, **52**, 31; Chapman, W.G., Gubbins, K.E., Jackson, G., and Radosz, M. (1990) *Ind. Eng. Chem. Res.*, **29**, 1709.
**53** Blas, F.J. and Vega, L.F. (1997) *Mol. Phys.*, **92**, 135; Blas, F.J. and Vega, L.F. (1998) *Ind. Eng. Chem. Res.*, **37**, 660.
**54** Müller, E.A. and Gubbins, K.E. (2001) *Ind. Eng. Chem. Res.*, **40**, 2198.
**55** Economou, L.G. (2002) *Ind. Eng. Chem. Res.*, **41**, 953.
**56** Gross, J. and Sadowski, G. (2001) *Ind. Eng. Chem. Res.*, **40**, 1244; Gross, J. and Sadowski, G. (2002) *Ind. Eng. Chem. Res.*, **41**, 1084.
**57** Barker, J.A. and Henderson, D. (1967) *J. Chem. Phys.*, **47**, 4714.
**58** Yelash, L., Müller, M., Paul, W., and Binder, K. (2005) *J. Chem. Phys.*, **123**, 014908.
**59** Yelash, L., Müller, M., Paul, W., and Binder, K. (2005) *Phys. Chem. Chem. Phys.*, **7**, 3728.
**60** Binder, K. (ed.) (1979) *Monte Carlo Methods in Statistical Physics*, Springer, Berlin.
**61** Binder, K. and Cicotti, G. (eds). (1996) *Monte Carlo and Simulations of Condensed Matter*, Societa Italiana di Fisica, Bologna.
**62** Frenkel, D. and Smit, B. (2002) *Understanding Molecular Simulation: From Algorithms to Applications*, 2nd edn, Academic Press, San Diego.
**63** Landau, D.P. and Binder, K. (2005) *A Guide to Monte Carlo Simulations in Statistical Physics*, 2nd edn, Cambridge University Press, Cambridge.
**64** Ferrario, M., Ciccotti, G. and Binder, K. (eds) (2006) *Computer Simulations in Condensed Matter: From Materials to Chemical Biology*, vols 1, 2, Springer, Berlin.
**65** Orr, W.J.C. (1947) *Trans. Faraday Soc.*, **43**, 12.
**66** Montroll, E.W. (1950) *J. Chem. Phys.*, **18**, 734.
**67** Dill, K.A. (1985) *Biochemistry*, **24**, 1501.
**68** Baschnagel, J., Wittmer, J., and Meyer, H. (2004) *NIC Ser.*, **23**, 83.
**69** Carmesin, I. and Kremer, K. (1988) *Macromolecules*, **21**, 2819.
**70** Grest, G.S. and Kremer, K. (1986) *Phys. Rev. A*, **33**, 3628.

**71** Kremer, K. and Grest, G.S. (1990) *J. Chem. Phys.*, **92**, 5057.

**72** MacKerell, A.D., Banavali, N., and Foloppe, N. (2001) *Biopolymers*, **56**, 257.

**73** Kron, A.K. (1965) *Polym. Sci. U.S.S.R.*, **7**, 1361.

**74** Wall, F.T. and Mandel, F. (1975) *J. Chem. Phys.*, **63**, 4592.

**75** Madras, N. and Sokal, A. (1998) *J. Stat. Phys.*, **50**, 109.

**76** Kennedy, T. (2002) *J. Stat. Phys.*, **106**, 407.

**77** Mansfield, M.L. (1982) *J. Chem. Phys.*, **77**, 1554.

**78** Deutsch, J.M. (1997) *J. Chem. Phys.*, **106**, 8849.

**79** Reith, D., Virnau, P. (2010) *Comput. Phys. Commun.* **181**, 800.

**80** Karayiannis, N.C., Mavrantzas, V.G., and Theodorou, D.N. (2002) *Phys. Rev. Lett.*, **88**, 105503.

**81** Cavallo, A., Müller, M., and Binder, K. (2003) *Europhys. Lett.*, **61**, 214.

**82** Mognetti, B.M., Virnau, P., Yelash, L., Paul, W., Binder, K., Müller, M., and MacDowell, L.G. (2008) *J. Chem. Phys.*, **128**, 104501.

**83** Panagiotopoulos, A.Z. (1987) *Mol. Phys.*, **61**, 813.

**84** Metropolis, N., Rosenbluth, A.W., Rosenbluth, M.N., Telleri, A.H., and Teller, E. (1953) *J. Chem. Phys.*, **21**, 1087.

**85** Harris, J. and Rice, S.A. (1988) *J. Chem. Phys.*, **88**, 1298.

**86** Frenkel, D., Mooij, G.C.A.M., and Smit, B. (1992) *J. Phys. Condens. Matter*, **4**, 3053.

**87** Siepmann, J.I. and Frenkel, D. (1992) *Mol. Phys*, **75**, 59.

**88** de Pablo, J.J., Laso, M., and Suter, U.W. (1992) *J. Chem. Phys.*, **96**, 2395.

**89** Binder, K. and Landau, D. (1984) *Phys. Rev. B*, **30**, 1477.

**90** Borgs, C. and Kotecky, R. (1990) *J. Stat. Phys.*, **60**, 79.

**91** Ferrenberg, A.M. and Swendsen, R.H. (1988) *Phys. Rev. Lett.*, **61**, 2635.

**92** Wilding, N.B. and Bruce, A.D. (1992) *J. Phys. Condens. Matter*, **4**, 3087–3108.

**93** Lee-Koo, M. and Green, M.S. (1981) *Phys. Rev. A*, **23**, 2650.

**94** Binder, K. (1981) *Z. Phys. B*, **43**, 119.

**95** Privman, V. (ed.) (1990) *Finite-Size Scaling Theory Finite Size Scaling and Numerical Simulation of Statistical Systems*, World Scientific, p. 1.

**96** Barber, M.E., Domb, C. and Lebowitz, J.L. (eds) (1983) *Finite-Size Scaling Phase Transitions and Critical Phenomena*, vol. **8**, Academic Press, p. 146.

**97** Fisher, M.E. and Green, M.S. (eds) (1971) *Critical Phenomena*, Academic Press, London, p. 1.

**98** Berg, B.A. and Neuhaus, T. (1992) *Phys. Rev. Lett.*, **68**, 9.

**99** Wang, F. and Landau, D.P. (2001) *Phys. Rev. Lett.*, **86**, 2050.

**100** Wang, F. and Landau, D.P. (2001) *Phys. Rev. E*, **64**, 056101.

**101** Yan, Q. and de Pablo, J.J. (2003) *Phys. Rev. Lett.*, **90**, 035701.

**102** Hansmann, U.H.E. and Wille, L.T. (2002) *Phys. Rev. Lett.*, **88**, 068105.

**103** Binder, K. and Heermann, D.W., 4th ed. (2002) *Monte Carlo Simulations in Statistical Physics: An Introduction*, Springer, Berlin.

**104** Torrie, G.M. and Valleau, J.P. (1977) *J. Comput. Phys.*, **23**, 187.

**105** Virnau, P. and Müller, M. (2004) *J. Chem. Phys.*, **120**, 10925.

**106** Binder, K. (1982) *Phys. Rev. A*, **25**, 1699.

**107** Grossmann, B. and Laursen, M.L. (1993) *Nucl. Phys. B*, **408**, 637.

**108** Müller, M. and Schick, M. (1996) *J. Chem. Phys.*, **105**, 8885.

**109** Schneider, G., Alwani, Z., Heim, W., Horvath, E., and Franck, E.U. (1967) *Chem.-Ing.-Tech.*, **39**, 649.

**110** Charoensombut-Amon, T., Martin, R.J., and Kobayashi, R. (1986) *Fluid Phase Equilib.*, **31**, 89.

**111** Mognetti, M., Oettel, M., Yelash, L., Virnau, P., Paul, W., and Binder, K. (2008) *Phys. Rev. E*, **77**, 041506.

**112** Binder, K., Landau, D.P., and Müller, M. (2003) *J. Stat. Phys.*, **110**, 1411.

**113** Metzger, S., Müller, M., Binder, K., and Baschnagel, J. (2003) *J. Chem. Phys.*, **118**, 8489.

**114** Schick, M. (1990) *Liquids at Interfaces*, (eds J. Charvolin, J.F. Joanny, and J. Zinn-Justin) Elsevier Science Publishers B.V., Amsterdam, p. 415.

**115** Eisenriegler, E., Kremer, K., and Binder, K. (1982) *J. Chem. Phys.*, **77**, 6296.

**116** Metzger, S., Müller, M., Binder, K., and Baschnagel, J. (2002) *Macromol. Theory Simul.*, **11**, 985.

**117** Descas, R., Sommer, J.U., and Blumen, A. (2004) *J. Chem. Phys.*, **120**, 8831.

**118** delle Site, L., Abrams, C.F., Alavi, A., and Kremer, K. (2002) *Phys. Rev. Lett.*, **89**, 156103.

**119** Young, T. (1805) *Philos. Trans. R. Soc. London*, **5**, 65.

**120** Müller, M. and MacDowell, L.G. (2000) *Macromolecules*, **33**, 3902.

**121** MacDowell, L.G., Müller, M., and Binder, K. (2002) *Colloids Surf., A*, **206**, 277.

**122** MacDowell, L.G., Virnau, P., Müller, M., and Binder, K. (2004) *J. Chem. Phys.*, **120**, 5293.

**123** Servantie, J. and Müller, M. (2008) *J. Chem. Phys.*, **128**, 014709.

**124** Müller, M. and Binder, K. (1998) *Macromolecules*, **31**, 8323.

**125** Lin, Y.C., Müller, M., and Binder, K. (2004) *J. Chem. Phys.*, **121**, 3816.

**126** Müller, M., MacDowell, L.G., Virnau, P., and Binder, K. (2002) *J. Chem. Phys.*, **117**, 5480.

**127** Allen, M.P. and Tildesley, D.J. (1987) *Computer Simulation of Liquids*, Clarendon Press, Oxford.

**128** Beeman, D. (1976) *J. Comput. Phys.*, **20**, 130.

**129** Noakes, J.L. (1998) *J. Aust. Math. Soc. A*, **64**, 37.

**130** Ewald, P. (1921) *Ann. Phys.*, **369**, 253.

**131** Darden, T.A., York, D.M., and Pedersen, L.G. (1993) *J. Chem. Phys.*, **98**, 8345.

**132** Hockney, R. and Eastwood, J. (1981) *Computer Simulation using Particles*, McGraw-Hill, New York.

**133** Constanciel, R. and Contreras, R. (1984) *Theor. Chim. Acta*, **65**, 1.

**134** Car, R. and Parrinello, M. (1985) *Phys. Rev. Lett.*, **55**, 2471.

**135** Evans, D.J. and Morriss, G.P. (1984) *Phys. Rev. A*, **30**, 1528.

**136** Ladd, A.J.C. (1984) *Mol. Phys.*, **53**, 459.

**137** Murat, M. and Grest, G.S. (1989) *Phys. Rev. Lett.*, **63**, 1074.

**138** Evans, D.J. and Morriss, G.P. (1990) *Statistical Mechanics of Nonequilibrium Liquids*, Academic Press, London.

**139** Grest, G.S. (1997) *Curr. Opin. Colloid Interface Sci.*, **2**, 271.

**140** Doyle, P.S., Shafeh, E.S.G., and Gast, A.P. (1997) *Phys. Rev. Lett.*, **78**, 1182; Doyle, P.S., Shafeh, E.S.G., and Gast, A.P. (1998) *Macromolecules*, **31**, 5474.

**141** Grest, G.S. (1999) *Advances in Polymer Science*, vol. **138** (ed. S. Granick), Springer, Berlin, p. 149.

**142** Kreer, T., Müser, M.H., Binder, K., and Klein, J. (2001) *Langmuir*, **17**, 7804.

**143** Irfachsyad, D., Tildesley, D., and Malfreyt, P. (2002) *Phys. Chem. Chem. Phys.*, **4**, 3008.

**144** Kreer, T. and Müser, M.H. (2003) *Wear*, **254**, 827.

**145** Kreer, T., Binder, K., and Müser, M.H. (2003) *Langmuir*, **19**, 7551.

**146** Cifre, J.G.H., Hess, S., and Kröger, M. (2004) *Macromol. Theory Simul.*, **13**, 748.

**147** Goujon, F., Malfreyt, P., and Tildesley, D.J. (2004) *Phys. Chem. Chem. Phys.*, **5**, 457; Goujon, F., Malfreyt, P., and Tildesley, D.J. (2005) *Mol. Phys.*, **103**, 2675; Goujon, F., Malfreyt, P., and Tildesley, D.J. (2008) *J. Chem. Phys.*, **129**, 034902.

**148** Daivis, P.J. and Todd, B.D. (2006) *J. Chem. Phys.*, **124**, 194103.

**149** Pastorino, C., Binder, K., Kreer, T., and Müller, M. (2006) *J. Chem. Phys.*, **124**, 064902.

**150** Pastorino, C., Kreer, T., Müller, M., and Binder, K. (2007) *Phys. Rev. E*, **76**, 026706.

**151** Dimitrov, D.I., Milchev, A., and Binder, K. (2007) *J. Chem. Phys.*, **127**, 084905.

**152** Todd, B.D. and Daivis, P.J. (2007) *Mol. Simul.*, **33**, 189.

**153** Hoogerbrugge, P.J. and Koelman, J.M.V.A. (1992) *Europhys. Lett.*, **19**, 155.

**154** Koelman, J.M.V.A. and Hoogerbrugge, P.J. (1993) *Europhys. Lett.*, **21**, 369.

**155** Espanol, P. (1995) *Phys. Rev. E*, **52**, 1734.

**156** Espanol, P. and Warren, P. (1995) *Europhys. Lett.*, **30**, 191.

**157** Schlijper, A.G., Hoogerbrugge, P.J., and Manke, C.W. (1995) *J. Rheol.*, **39**, 567.

**158** Kong, Y., Manke, C.M., Madden, W.G., and Schlijper, A.G. (1997) *Baltzer. Tribol. Lett.*, **3**, 133.

**159** Bonet Avalos, J. and Mackie, M. (1997) *Europhys. Lett.*, **40**, 141.

**160** Espanol, P. (1994) *Europhys. Lett.*, **40**, 631.

**161** Novik, K.E. and Coveney, P.V. (1997) *Int. J. Mod. Phys. C*, **8**, 909.

**162** Boek, E.S., Coveney, P.V., Lekkerkerker, H.N.W., and van der Schoot, P. (1997) *Phys. Rev. E*, **55**, 3124.

**163** Ripoll, M., Espanol, P., and Ernst, M.H. (1999) *Int. J. Mod. Phys. C*, **9**, 1329.

**164** Jury, S.I., Bladon, P., Krishna, S., and Cates, M.E. (1999) *Phys. Rev. E*, **59**, R2535.

**165** Lowe, C.P. (1999) *Europhys. Lett.*, **47**, 145.

**166** Dzwinel, W. and Yuen, D. (2000) *Int. J. Mod. Phys. C*, **11**, 1.

**167** Spenley, N.A. (2000) *Europhys. Lett.*, **49**, 534.

**168** Besold, G., Vattulainen, I., Karttunen, M., and Polson, J. (2000) *Phys. Rev. E*, **62**, R7611.

**169** Shardlow, T. (2003) *SIAM J. Sci. Comput.*, **24**, 1267.

**170** Soddemann, T., Dünweg, B., and Kremer, K. (2003) *Phys. Rev. E*, **68**, 046702.

**171** Symeonidis, V. and Karniadakis, G.E. (2006) *J. Comput. Phys.*, **218**, 82.

**172** Noguchi, H., Kikuchi, N., and Gompper, G. (2007) *Europhys. Lett.*, **78**, 10005.

**173** Malevanets, A. and Yeomans, J.M. (2000) *Europhys. Lett.*, **52**, 231.

**174** Malevanets, A. and Kapral, R. (2000) *J. Chem. Phys.*, **112**, 7260.

**175** Ihle, T. and Kroll, D.M. (2001) *Phys. Rev. E*, **63**, 020201; Ihle, T. and Kroll, D.M. (2003) *Phys. Rev. E*, **67**, 066705.

**176** Ripoll, M., Mussawisade, K., Winkler, R.G., and Gompper, G. (2004) *Europhys. Lett.*, **68**, 106.

**177** Mussawisade, K., Ripoll, M., Winkler, R.G., and Gompper, G. (2005) *J. Chem. Phys.*, **123**, 144905.

**178** Padding, J.T., Wysocki, A., Löwen, H., and Louis, A.A. (2005) *J. Phys.: Condens. Matter*, **17**, S3393.

**179** Lee, S.H. and Kapral, R. (2006) *J. Chem. Phys.*, **124**, 214901.

**180** Ripoll, M., Winkler, R.G., and Gompper, G. (2006) *Phys. Rev. Lett.*, **96**, 188302; Ripoll, M., Winkler, R.G., and Gompper, G. (2007) *Eur. Phys. J., E*, **23**, 349.

**181** Watari, N., Makino, M., Kikuchi, N., Larson, R.G., and Doi, M. (2007) *J. Chem. Phys.*, **126**, 094902.

**182** Ladd, A.J.C. (1994) *J. Fluid Mech.*, **271**, 285; Ladd, A.J.C. (1994) *J. Fluid Mech.*, **271**, 311.

**183** Ahlrichs, P. and Dünweg, B. (1989) *Int. J. Mod. Phys. C*, **9**, 1429; Ahlrichs, P. and Dünweg, B. (1999) *J. Chem. Phys.*, **111**, 8225.

**184** Succi, S. (2001) *The Lattice Boltzmann Equation for Fluid Dynamics and Beyond*, Oxford University Press, New York.

**185** Chatterji, A. and Horbach, J. (2005) *J. Chem. Phys.*, **122**, 184903.

**186** Dünweg, B. (1993) *J. Chem. Phys.*, **99**, 6977.

**187** Junghans, C., Praprotnik, M., and Kremer, K. (2008) *Soft Matter*, **4**, 156.

**188** Monaghan, J.J. (1992) *Annu. Rev. Astron. Astrophys.*, **30**, 543.

**189** Zimm, B.H. (1956) *J. Chem. Phys.*, **24**, 269.

**190** 189. Spirin, L., Galuschko, A., Kreer, T., and Binder, K., and Baschnagel, J.,in preparation.

**191** Usta, O.B., Butler, J.E., and Ladd, A.J.C. (2007) *Phys. Rev. Lett.*, **98**, 090831.

**192** Theodorou, D.N. and Suter, U.W. (1985) *Macromolecules*, **18**, 1467.

**193** Moe, N.E. and Ediger, M.D. (1996) *Polymer*, **37**, 1787.

**194** Harmandaris, V.A., Mavrantzas, V.G., and Theodorou, D.N. (1998) *Macromolecules*, **31**, 7934.

**195** Yao, S. (2000) *Nihon Reoroji Gakk.*, **28**, 159.

**196** Fukui, K., Sumpter, B.G., Barnes, M.D., and Noid, D.W. (2000) *Macromolecules*, **33**, 5982.

**197** Bicerano, J. (2002) *Prediction of Polymer Properties*, 3rd edn, Marcel Dekker, New York.

**198** Soldera, A. and Metatla, N. (2006) *Phys. Rev. E*, **74**, 061803.

**199** Clancy, T.C., Jang, J.H., Dhinojwala, A., and Mattice, W.L. (2001) *J. Phys. Chem. B*, **105**, 1493.

**200** Smith, G.D., Borodin, O., and Paul, W. (2002) *J. Chem. Phys.*, **117**, 10350.

**201** Makrodimitri, Z.A., Raptis, V.E., and Economou, I.G. (2006) *J. Phys. Chem. B*, **110**, 16047.

**202** Sun, H. (1995) *Macromolecules*, **8**, 701–712.

**203** Heinz, H., Koerner, H., Anderson, K.L., Vaia, R.A., and Farmer, B.L. (2005) *Chem. Mater.*, **17**, 5658.

**204** Billeter, M., Guntert, P., Luginbuhl, P., and Wuthrich, K. (1996) *Cell*, **85**, 1057.

**205** Clancy, T.C. and Mattice, W.L. (1999) *Comp. Theor. Polym. Sci.*, **9**, 261.

**206** Elcock, A.H., Sept, D., and McCammon, J.A. (2001) *J. Phys. Chem. B*, **105**, 1504.

**207** Harmandaris, V.A., Angelopoulou, D., Mavrantzas, V.G., and Theodorou, D.N. (2002) *J. Chem. Phys.*, **116**, 7656.

**208** Jo, W.H. and Yang, J.S. (2002) *Adv. Polym. Sci.*, **156**, 1.

**209** Gestoso, P. and Brisson, J. (2003) *Polymer*, **44**, 2321.

**210** Gestoso, P. and Brisson, J. (2003) *Polymer*, **44**, 7765.

**211** Faller, R. (2004) *Macromolecules*, **37**, 1095.

**212** Wagner, K.G., Maus, M., Kornherr, A., and Zifferer, G. (2005) *Chem. Phys. Lett.*, **406**, 90.

**213** Ganazzoli, F. and Raffaini, G. (2005) *Phys. Chem. Chem. Phys.*, **7**, 3651.

**214** Genix, A.C., Arbe, A., Alvarez, F., Colmenero, J., Willner, L., and Richter, D. (2005) *Phys. Rev. E*, **72**, 031808.

**215** Capaldi, F., Rutledge, G.C., and Boyce, M.C. (2005) *Macromolecules*, **38**, 6700.

**216** Makrodimitri, Z.A., Dohrn, R., and Economou, I.G. (2007) *Macromolecules*, **40**, 1720.

**217** Abou-Rachid, H., Lussier, L.S., Ringuette, S., Lafleur-Lambert, X., Jaidann, M., and Brisson, J. (2008) *Propell. Explos. Pyrotech.*, **33**, 301.

**218** Jaidann, M., Abou-Rachid, H., Lafleur-Lambert, X., Lussier, L.S., Gagnon, N., and Brisson, J. (2008) *Polym. Eng. Sci.*, **48**, 1141.

**219** Heinz, H. and Suter, U.W. (2004) *J. Phys. Chem. B*, **108**, 18341.

**220** Heinz, H. (2007) *Mol. Simul.*, **33**, 747.

**221** Binder, K., Baschnagel, J., and Paul, W. (2003) *Progr. Polym. Sci.*, **28**, 115.

**222** Heinz, H., Vaia, R.A., and Farmer, B. (2006) *J. Chem. Phys.*, **124**, 224713.

**223** Müller-Plathe, F. (2002) *ChemPhysChem*, **3**, 754.

**224** Faller, R. (2004) *Polymer*, **45**, 3869.

**225** Sun, Q. and Faller, R. (2006) *J. Chem. Theor. Comput.*, **2**, 607.

**226** Fermeglia, M. and Pricl, S. (2007) *Prog. Org. Coat.*, **58**, 187.

**227** Cosoli, P., Scocchi, G., Pricl, S., and Fermeglia, M. (2008) *Microporous Mesoporous Mater.*, **107**, 169.

**228** Herrebout, W.A., van der Veken, B.J., Wang, A., and Durig, J.R. (1995) *Phys. Chem.*, **99**, 578.

**229** Prathab, B. and Aminabhavi, T.M. (2007) *J. Polym. Sci B: Polym. Phys.*, **45**, 1260.

**230** Beier, C. and Steinhoff, H.J. (2006) *Biophys. J.*, **91**, 2647.

# 2
# Thermodynamics of Flexible and Rigid Rod Polymer Blends

*Akihiko Matsuyama*

## 2.1
## Introduction

Binary mixtures of a flexible polymer and a low molecular weight liquid crystalline molecule, or a rigid rod-like molecule, are of interest because of their important technological applications in high modulus fibers, nonlinear optics, and electro-optical devices. These blends are basic materials for recent new technologies of liquid crystal displays [1, 2]. The performances of these systems are closely related to phase separations and conformations of polymer chains dissolved in a liquid crystalline phase. One of the main problems is to examine the location of various phases such as isotropic, nematic, and smectic phases, depending on temperature and concentration. To understand the thermodynamics and thermal instability of these blends, it is important to consider the co-occurrences between liquid crystalline ordering and phase separations.

Generally, polymer chains exhibit a variety of flexibility, from flexible to rigid rod-like polymers. Polymer blends containing a liquid crystalline ordering have received considerable attention. The volume of literature on the theories and experiments of liquid crystallinity in polymer blends is now very extensive. There are many theoretical models for liquid crystalline polymers, such as the Flory lattice model [3–8], wormlike chain model [9–11], and Onsager virial theory [12] for rigid rods. An example of a recent review of liquid crystalline polymers is the text book of Donald and Windle [13].

In this chapter we introduce the thermodynamics, or phase behavior, of binary mixtures of a flexible polymer and a rigid rod-like molecule. Here the flexible polymer means that liquid crystalline ordering does not occur in the constituent pure polymer. We first describe the fundamentals of a nematic phase, based on the Onsager theory for a rigid rod, where the entropy-induced nematic ordering is discussed. This will be the basis of the following sections. In Section 2.3, we focus on the phase separations of mixtures of a flexible polymer and a rigid rod-like molecule, or a low molecular weight liquid crystalline molecule, in a thermal equilibrium state. We introduce recent theoretical models to describe phase behavior, combining the Flory–Huggins

*Encyclopedia of Polymer Blends, Volume 1: Fundamentals.* Edited by Avraam I. Isayev
Copyright © 2010 WILEY-VCH Verlag GmbH & Co. KGaA, Weinheim
ISBN: 978-3-527-31929-9

theory of isotropic mixing for polymer blends, Onsager theory, and Maier–Saupe model of a nematic phase. In Section 2.4, based on time-dependent Landau–Ginzburg equations, we consider the thermal instabilities of the phase separations and morphologies, where the interplay between orientation and concentration fluctuations is important. Through recent theoretical and experimental studies, we introduce the phase separation dynamics of inhomogeneous mixtures, consisting of one conserved order parameter (concentration) and one non-conserved order parameter (orientation).

## 2.2
## Fundamentals of a Nematic Phase

In this section, we introduce a basis of the Onsager model for a nematic phase, which will help us to understand subsequent sections.

### 2.2.1
### Scalar Orientational Order Parameter

Liquid crystal molecules have anisotropic shapes such as rod-like and disk-like molecules. One of the most common liquid crystal phases is a nematic, where the molecules have no positional order, but they have long-range orientational order. The preferred direction in a nematic sample is called the director $\boldsymbol{n}$, which has a unit vector. The nematic phase is a uniaxial medium with an optical axis along $\boldsymbol{n}$. Some liquid crystals show biaxial nematics, which mean that they also orient along a secondary axis in addition to orienting their long axis. We focus here on a uniaxial nematic phase. The states of directors $\boldsymbol{n}$ and $-\boldsymbol{n}$ are indistinguishable. Rigid rod-like molecules are the simplest type of objects that allow the nematic phase. Let $\boldsymbol{u}_i$ be a unit vector, labeled for the axis of a rod ($i = 1, 2, \ldots, N_r$), where $N_r$ is the total number of rods in a system. The averaged-orientational order parameter is given by [14]:

$$S = \frac{1}{N_r}\sum_{i=1}^{N_r}\frac{3}{2}\left((\boldsymbol{n}\cdot\boldsymbol{u}_i)^2 - \frac{1}{3}\right) \tag{2.1}$$

and is equivalent for the average of the second Legendre polynomial: $\langle P_2(\cos\theta)\rangle = \langle\frac{3}{2}(\cos^2\theta - \frac{1}{3})\rangle$, where $\theta$ is the angle between the long axis of a rod and the local director. When the rods are completely random and in an isotropic state $S = 0$, whereas for a perfectly aligned sample $S = 1$. For a typical liquid crystal sample, the value of $S$ is on the order of 0.3 to 0.8, and generally increases with decreasing temperature. The order parameter can be experimentally measured by diamagnetism, birefringence, Raman scattering, and NMR [14]. To describe the orientational order parameter dependence on temperature, concentration, and molecular length, we consider molecular theories of the nematic phase in the following.

### 2.2.2
### Free Energy of Rigid Rod Solutions

We consider a dispersion of rigid rod-like molecules in a volume $V$. Let $\varrho_r(\boldsymbol{r}, \boldsymbol{u})$ be the number density of rods with an orientation $\boldsymbol{u}$ (or its solid angle $\Omega$) at a position $\boldsymbol{r}$. The free energy $F$ of the dispersion at the level of second virial approximation is given by:

$$\begin{aligned}\beta F/V = &\int \varrho_r(\boldsymbol{r}, \boldsymbol{u})\,[\beta\mu^\circ + \ln \varrho_r(\boldsymbol{r}, \boldsymbol{u}) - 1]\mathrm{d}\boldsymbol{r}\,\mathrm{d}\Omega \\ &+ \tfrac{1}{2}\int\int \varrho_r(\boldsymbol{r}, \boldsymbol{u})\,\varrho_r(\boldsymbol{r}', \boldsymbol{u}')\beta_1(\boldsymbol{r}, \boldsymbol{u}; \boldsymbol{r}', \boldsymbol{u}')\mathrm{d}\boldsymbol{r}\,\mathrm{d}\Omega\,\mathrm{d}\boldsymbol{r}'\mathrm{d}\Omega'\end{aligned} \tag{2.2}$$

where $\mathrm{d}\Omega$ is the solid angle, $\mu^\circ$ is the standard chemical potential of a rod, $\beta \equiv 1/k_\mathrm{B}T$; $T$ is the absolute temperature and $k_\mathrm{B}$ is the Boltzmann constant, and $\beta_1 \equiv 1 - \exp[-\beta U_{ij}]$ is the Mayer–Mayer function [15] and $U_{ij}$ is the interaction energy between two rods in the configurations $(\boldsymbol{r}, \boldsymbol{u})$ and $(\boldsymbol{r}', \boldsymbol{u}')$. Using the distribution function $f(\boldsymbol{r}, \boldsymbol{u})$ of rods, the density can be expressed as:

$$\varrho_r(\boldsymbol{r}, \boldsymbol{u}) = \varrho f(\boldsymbol{r}, \boldsymbol{u}) \tag{2.3}$$

where $\varrho \equiv N_r/V$ is the average number density of rods. The total number $N_r$ of rigid rods must be conserved, and then we have the normalization condition:

$$\int\int \varrho_r(\boldsymbol{r}, \boldsymbol{u})\,\mathrm{d}\boldsymbol{r}\,\mathrm{d}\Omega = N_r/V \tag{2.4}$$

Substituting Eq. (2.3) into (2.2) we obtain:

$$\begin{aligned}\beta F/V \;=\; &\varrho[\beta\mu^\circ + \ln\varrho - 1] + \varrho\int f(\boldsymbol{r}, \boldsymbol{u}) \ln f(\boldsymbol{r}, \boldsymbol{u})\mathrm{d}\boldsymbol{r}\,\mathrm{d}\Omega \\ &+ \tfrac{1}{2}\varrho^2\int\int f(\boldsymbol{r}, \boldsymbol{u})\,f(\boldsymbol{r}', \boldsymbol{u}')\beta_1(\boldsymbol{r}, \boldsymbol{u}; \boldsymbol{r}', \boldsymbol{u}')\mathrm{d}\boldsymbol{r}\,\mathrm{d}\Omega\,\mathrm{d}\boldsymbol{r}'\,\mathrm{d}\Omega'\end{aligned} \tag{2.5}$$

The first three terms correspond to the translational entropy of rods and the first integral term shows the entropy change due to ordering. In a disordered phase, this term becomes zero because $f(\boldsymbol{r}, \boldsymbol{u}) = 1$. In an ordered phase, we have peaks in $f(\boldsymbol{r}, \boldsymbol{u})$ and then the first integral term remains with nonzero values. The last term shows the interaction between rods.

Although, the third and higher virial coefficients are neglected in Eq. (2.5), it can be applied to describe basic properties of phase behavior in any particle system. The second virial approximation corresponds to the simplest version of density functional theories [16, 17] and is the theoretical instrument responsible for producing a qualitative rather than quantitative understanding.

In the following, we assume that the system is spatially uniform but non-uniform for orientation. Using the orientational distribution function $f(\boldsymbol{u})$, the density is given by $\varrho_r(\boldsymbol{r}, \boldsymbol{u}) = \varrho f(\boldsymbol{u})$ and Eq. (2.5) can be expressed as:

$$\begin{aligned}\beta F/V = &\varrho[\beta\mu^\circ + \ln(\varrho/e) + \int f(\boldsymbol{u}) \ln[4\pi f(\boldsymbol{u})]\mathrm{d}\Omega \\ &+ \tfrac{1}{2}\varrho\int\int \beta_1(\boldsymbol{u}, \boldsymbol{u}')\,f(\boldsymbol{u})f(\boldsymbol{u}')\mathrm{d}\Omega\,\mathrm{d}\Omega']\end{aligned} \tag{2.6}$$

where $d\Omega = 2\pi \sin\theta d\theta$ for a uniaxial nematic phase. In an isotropic phase, all orientations have equal probability, which implies $f(\boldsymbol{u}) = 1/(4\pi)$. The factor $4\pi$ in Eq. (2.6) gives the correct value that the third term becomes zero in an isotropic phase. Equation (2.6) is the free energy obtained by Onsager [12].

The equilibrium distribution is determined by the condition that the free energy is a minimum for the distribution with the normalization condition:

$$\int f(\boldsymbol{u})\, d\Omega = 1 \tag{2.7}$$

The minimum is found by introducing a Lagrange multiplier $\lambda$ and solving:

$$\frac{\delta}{\delta f(\boldsymbol{u})}\left[F[f(\boldsymbol{u})] - \lambda \int f(\boldsymbol{u})\, d\Omega\right] = 0 \tag{2.8}$$

which gives:

$$f(\boldsymbol{u}) = \frac{1}{Z_0}\exp\left[-\varrho \int d\Omega' f(\boldsymbol{u}')\, \beta_1(\boldsymbol{u}, \boldsymbol{u}')\right] \tag{2.9}$$

where the $Z_0$ is the normalization constant satisfied in Eq. (2.7). Using the distribution function, the orientational order parameter $S$ can be calculated by:

$$S = \int P_2(\cos\theta) f(\boldsymbol{u}) d\Omega \tag{2.10}$$

When the orientational distribution function is uniaxial, we have $f(\boldsymbol{u})d\Omega = 2\pi f(\theta)\sin\theta d\theta$.

In the Onsager model, attractive intermolecular forces are not taken into account, rather only the steric interaction energy between two rods is considered. The third term in Eq. (2.6) is an orientational entropy ($S_{or}$) and the last term stands for the packing entropy ($S_p$) related to the excluded volume between two rods. As a model of rigid rods we take a spherocylinder, consisting of cylinder of diameter $D$ and length $L$ capped with two hemispheres. The function $\beta_1$ is the excluded volume of the spherocylinders and depends on the angle $\varphi(\theta, \theta')$ between two spherocylinders:

$$\beta_1(\boldsymbol{u}, \boldsymbol{u}') = 2L^2 D|\sin\varphi| + 2\pi D^2 L + \tfrac{4}{3}\pi D^3 \tag{2.11}$$

where the last two terms are end contributions and are of the order $D/L$. For a spherocylinder with a large aspect ratio, these end effects are of minor importance and the first term dominates; thus it is often assumed that:

$$\beta_1(\boldsymbol{u}, \boldsymbol{u}') = 2L^2 D|\sin\varphi| \tag{2.12}$$

To derive the orientational distribution function in an equilibrium state, Onsager used a trial function [12]. To derive the analytical expression of the free energy, we here expand $|\sin\varphi|$ in the Legendre polynomials $P_{2n}(\cos\theta)$ [18, 19]:

$$|\sin\varphi| = \frac{\pi}{4} - \sum_{n=1}^{\infty} B_{2n} P_{2n}(\cos\theta) P_{2n}(\cos\theta') \tag{2.13}$$

where:

$$B_{2n} \equiv \frac{\pi(4n+1)(2n-3)!!(2n-1)!!}{2^{2n+2}n!(n+1)!} \tag{2.14}$$

and take $n = 1$. We then obtain:

$$|\sin\varphi| = \frac{\pi}{4} - \frac{5\pi}{32} P_2(\cos\theta) P_2(\cos\theta') \tag{2.15}$$

Substituting Eq. (2.12) into (2.9), the distribution function is given by:

$$f(\theta) = \frac{1}{Z_0} \exp\left[\frac{5L}{4D}\phi S P_2(\cos\theta)\right] \tag{2.16}$$

where $\phi = \nu_r \varrho$ is the volume fraction of rods and $\nu_r = (\pi/4)D^2 L$ is the volume of a rod. The normalization constant $Z_0$ is determined from condition (2.7) as:

$$Z_0 = 4\pi \int_0^1 \mathrm{d}(\cos\theta) \exp\left[\frac{5L}{4D}\phi S P_2(\cos\theta)\right] \tag{2.17}$$

Substituting Eq. (2.16) into (2.10), the order parameter is determined by the self-consistent equation:

$$S = I_1[\Gamma_0 S]/I_0[\Gamma_0 S] \tag{2.18}$$

where we define:

$$\Gamma_0 \equiv \tfrac{5}{4}\left(\frac{L}{D}\right)\phi \tag{2.19}$$

$$I_m[\Gamma_0 S] \equiv \int_0^1 \left[\tfrac{3}{2}\left(x^2 - \tfrac{1}{3}\right)\right]^m \exp\left[\tfrac{3}{2}\Gamma_0 S\left(x^2 - \tfrac{1}{3}\right)\right] \mathrm{d}x \tag{2.20}$$

$m = 0, 1, 2, \ldots$, and $x \equiv \cos\theta$. The orientational entropy is given as a function of the orientational order parameter $S$:

$$S_{or}/k_B \equiv -\int f(\theta) \ln 4\pi f(\theta) \mathrm{d}\Omega = -(\Gamma_0 S^2 - \ln I_0[\Gamma_0 S]) \tag{2.21}$$

and the packing entropy is:

$$\begin{aligned} S_{pc}/k_B &\equiv -\frac{\varrho}{2}\int\int \beta_1(\Omega_1, \Omega_2) f(\Omega_1) f(\Omega_2) \mathrm{d}\Omega_1 \mathrm{d}\Omega_2, \\ &= -\tfrac{4}{5}\Gamma_0\left(1 - \tfrac{5}{8}S^2\right) \end{aligned} \tag{2.22}$$

On increasing the orientational order parameter $S$, the orientational entropy decreases and the packing entropy increases.

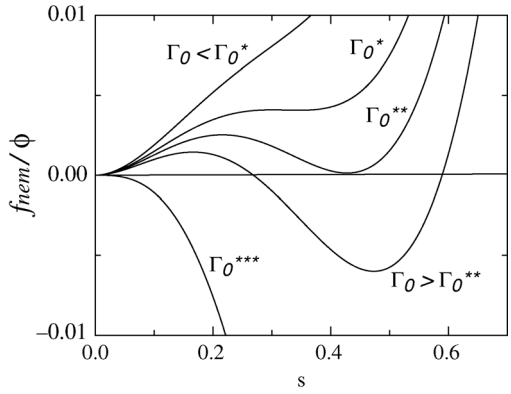


**Figure 2.1** Nematic free energy ($f_{\text{nem}}/\phi$) in Eq. (2.23) versus the order parameter $S$ for various values of $\Gamma_0[\equiv 5L\phi/(4D)]$.

Using Eqs. (2.12) and (2.16), the free energy (2.6) is given by:

$$\nu_r \beta F/V = \phi\left[\beta\mu^\circ + \ln\phi - 1 + \left(\frac{L}{D}\right)\phi + \tfrac{1}{2}\Gamma_0 S^2 - \ln I_0[\Gamma_0 S]\right] \tag{2.23}$$

where the term $\ln\nu_r$ is included in the standard chemical potential $\mu^\circ$ of a rod. The first four terms show the dimensionless free energy density ($f_{\text{iso}}$) for the isotropic liquid phase and the last two terms correspond to the dimensionless nematic free energy density ($f_{\text{nem}}$), where we define $\nu_r \beta F/V = f_{\text{iso}} + f_{\text{nem}}$.

Figure 2.1 shows the nematic free energy ($f_{\text{nem}}/\phi$) plotted against the order parameter $S$ for various values of $\Gamma_0$. For lower values of $\Gamma_0 < \Gamma_0^*(= 4.49)$, the free energy has a single minimum at $S = 0$, which corresponds to an isotropic phase. When $\Gamma_0$ exceeds a certain critical value $\Gamma_0^*$, another minimum appears at a positive $S$, which corresponds to a metastable nematic phase. The first-order phase transition from an isotropic to a nematic phase takes place at $\Gamma_0 = \Gamma_0^{**}(= 4.55)$, where the free energy of the isotropic phase becomes equal to that of the nematic phase. For intermediate values $\Gamma_0^* < \Gamma_0 < \Gamma_0^{***}(= 5)$, two minima are observed: one is metastable and the other is stable. For larger values of $\Gamma_0 > \Gamma_0^{***}$, the free energy has a single minimum at $S > 0$, which corresponds to the nematic phase.

Figure 2.2 shows the order parameter $S$ plotted against $\Gamma_0[\equiv 5L\phi/(4D)]$. The first-order nematic–isotropic phase transition (NIT) occurs at $\Gamma_0^{**}$ and the value of the order parameter increases from 0.427 to 1 with increasing $\Gamma_0$, or concentration. Using Eq. (2.19), the volume fraction at which the NIT takes place is given by $\phi_{\text{NI}} = 3.64D/L$. In concentrated solutions, the excluded volume interaction tends to align the rods and gives rise to the nematic phase, or macroscopic ordering. For $\Gamma_0^* < \Gamma_0 < \Gamma_0^{**}$, the system corresponds to a metastable region where pretransitional behaviors [14] have been observed. For example, the short-range order effect increases with increasing concentration and causes various anomalies in the physical properties such as a steep increase in birefringence, a slowing down of the relaxation process [20], and viscoelasticity [21].

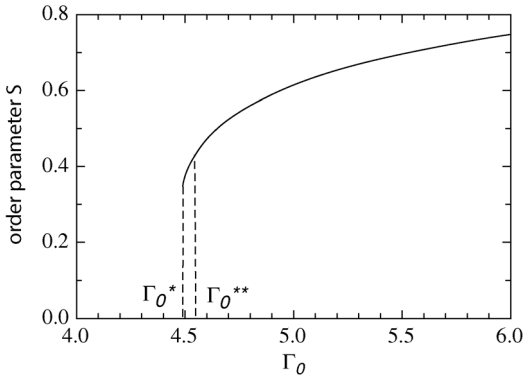


**Figure 2.2** Order parameter $S$ versus $\Gamma_0[\equiv 5L\phi/(4D)]$.

### 2.2.3
### Nematic–Isotropic Phase Separations

To determine whether the system shows macroscopic phase separations, we consider the free energy (2.23). Suppose that a system of volume fraction $\phi$ and volume $V$ is separated into two phases of volume fraction $\phi_1$ and $\phi_2$ with volumes $V_1$ and $V_2$, respectively; we then have two conservation rules. First, the volume must satisfy:

$$V = V_1 + V_2 \tag{2.24}$$

and second, the number of molecules in each phase must comply with:

$$\phi V = \phi_1 V_1 + \phi_2 V_2 \tag{2.25}$$

Now we can write the total free energy $f_p$ of a two-phase system as:

$$\begin{aligned} f_p(\phi) &= [V_1 f(\phi_1) + V_2 f(\phi_2)]/V \\ &= \frac{\phi_2 - \phi}{\phi_2 - \phi_1} f(\phi_1) + \frac{\phi - \phi_1}{\phi_2 - \phi_1} f(\phi_2) \end{aligned} \tag{2.26}$$

where we define the dimensionless free energy density: $f \equiv \nu_r \beta F/V$. Figure 2.3 shows, schematically, free energy $(f)$ plotted as a function of the volume fraction $\phi$. Clearly, Eq. (2.26) is a broken line extending from $\phi_1$ to $\phi_2$. If a system of concentration $\phi$ is separated into two phases of concentration $\phi_1$ and $\phi_2$, the total free energy $f(\phi)$ decreases to $f_p(\phi)$. The total free energy becomes minimum when the broken line coincides with the dash-dotted line, which is tangent to the curve at both concentration $\phi_i$ and $\phi_n$. This thermodynamic statement is embodied as the "common tangent construction." The concentration range between the two tangent points ($\phi_i < \phi < \phi_n$) corresponds to the biphasic region and the lowest free energy for the system corresponds to an isotropic phase of concentration $\phi_i$ in coexistence with a nematic phase of concentration $\phi_n$. When $\phi < \phi_i$, the system is in an isotropic state and when $\phi > \phi_n$ it is in a nematic phase. The free energy (2.23) can not predict

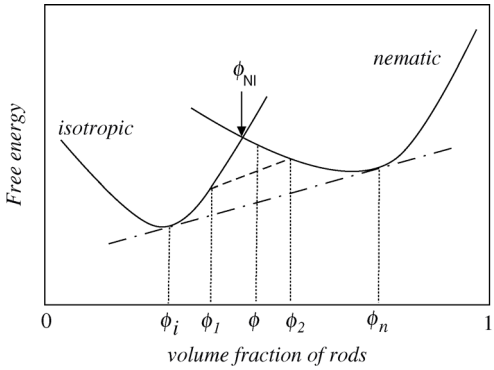


**Figure 2.3** Schematically illustrated free energy density $f(\equiv \nu_r \beta F/V)$ plotted as a function of the volume fraction $\phi$.

phase separations between two isotropic phases and two nematic phases. For two phases to coexist in equilibrium, it is necessary that they have the same chemical potentials for each component. The osmotic pressure $\Pi$ can be calculated by:

$$\Pi = -\left(\frac{\partial F}{\partial V}\right)_{N_r} \tag{2.27}$$

and then we obtain the dimensionless osmotic pressure:

$$\begin{aligned} \tilde{\Pi}(\phi, S) &\equiv \nu_r \beta \Pi \\ &= \phi + \frac{L}{D}\phi^2 - \tfrac{5}{8}\frac{L}{D}\phi^2 S^2 \end{aligned} \tag{2.28}$$

The chemical potential of a rod is given by:

$$\mu = \left(\frac{\partial F}{\partial N_r}\right)_V \tag{2.29}$$

and then we obtain the dimensionless chemical potential:

$$\begin{aligned} \tilde{\mu}(\phi, S) &\equiv \beta \mu \\ &= \beta \mu^\circ + \ln \phi + 2\left(\frac{L}{D}\right)\phi - \ln I_0[\Gamma_0 S] \end{aligned} \tag{2.30}$$

To calculate the concentrations of the coexisting isotropic and nematic phases, both phases must have the same osmotic pressure and the same chemical potential:

$$\tilde{\Pi}(\phi_i, 0) = \tilde{\Pi}(\phi_n, S) \tag{2.31}$$

$$\tilde{\mu}(\phi_i, 0) = \tilde{\mu}(\phi_n, S) \tag{2.32}$$

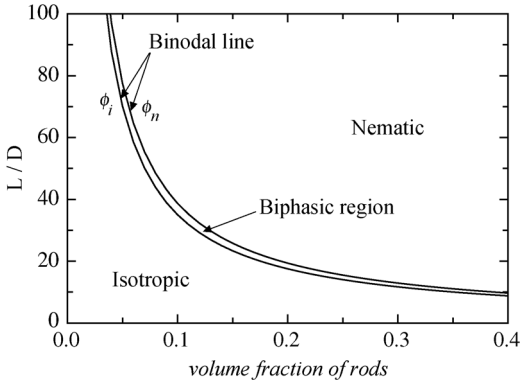


**Figure 2.4** Phase diagram of the ($L/D$)–volume fraction ($\phi$) plane.

It is easy to prove that this has the same meaning as the common tangent construction. The order parameter $S$ can be determined by solving Eq. (2.18). From Eq. (2.31), the volume fraction $\phi_i$ can be given as a function of $\phi_n$:

$$x_i = \tfrac{1}{2}\left[-1 + \sqrt{1+4}\left(x_n + x_n^2 - \tfrac{5}{8}x_n^2 S^2\right)\right] \tag{2.33}$$

where we define $x_i \equiv (L/D)\phi_i$ and $x_n \equiv (L/D)\phi_n$. Substituting Eq. (2.33) into (2.32), we can numerically find the volume fractions $\phi_i$ and $\phi_n$ of the coexisting isotropic and nematic phases, respectively:

$$\phi_i = 3.504\frac{D}{L}, \qquad \phi_n = 3.872\frac{D}{L}, \tag{2.34}$$

and $S_{\mathrm{NI}} = 0.574$ at the NIT point. The binodal volume fractions corresponding to the coexisting phases are proportional to $D/L$, which implies that for shorter rods a large volume fraction is required to form a nematic phase. The NIT concentration $\phi_{\mathrm{NI}} = 3.63D/L$ is hidden inside the binodal region. Figure 2.4 shows binodal compositions of the coexisting isotropic and nematic phases as a function of the axial ratio of the rods. As the axial ratio decreases, the width of the biphasic region increases, but moves to higher volume fractions. The results are qualitatively consistent with experimental observations. In a thermal equilibrium state, whether the system with the concentrations between $\phi_i < \phi < \phi_n$ is metastable or unstable, it depends on the curvature of the free energy. From the thermodynamic inequality, we have the relation $(\partial\Pi/\partial V)_T < 0$, or $(\partial\Pi/\partial\phi)_T > 0$, for a metastable phase. The position of spinodal, which separates metastable and unstable regions, is determined by $\partial\Pi/\partial\phi = 0$, which corresponds to the inflection point of the free energy. The biphasic region of Figure 2.4 corresponds to a metastable region and there is no spinodal region of $(\partial\Pi/\partial\phi)_T < 0$.

According to the Onsager trial function, it gives the following results [12]:

$$\phi_i = 3.34\frac{D}{L}, \qquad \phi_n = 4.486\frac{D}{L}, \qquad S_{\mathrm{NI}} = 0.848. \tag{2.35}$$

The bilinear expansion in Eq. (2.13) with higher order terms yields [19]:

$$\phi_i = 3.290\frac{D}{L}, \qquad \phi_n = 4.191\frac{D}{L}, \qquad S_{\mathrm{NI}} = 0.792 \tag{2.36}$$

The Onsager theory, or second virial expansion, is very successful in predicting the qualitative behavior of the isotropic–nematic phase transition of hard rods. However, it is an exact theory in the limit of $L/D \to \infty$. Straley has estimated that, for $L/D < 20$, the contribution of the third virial coefficient to the free energy in the nematic phase should be at least comparable to that of the second virial coefficient [22]. For more concentrated solutions, an alternative approach such as the Flory lattice model [3, 5] is required. The full phase diagram of rod-like colloidal systems has been obtained in computer simulations [23, 24]. The effects of polydispersity of rods [19, 25] and charged rods [10] are also important in the phase transitions. The comparison between Onsager theory and experimental results has been summarized by Vroege and Lekkerkerker [26].

### 2.2.4
### Entropy- and Energy-Driven Nematic Ordering

Onsager theory is important in understanding why rods are oriented in high concentrations. In Onsager theory, only the steric interaction between rods is taken into account and so the Helmholtz free energy only depends on the entropy: $F = -TS_0$. In a thermal equilibrium state, the free energy is minimized and thus the entropy ($S_0$) has to be maximized, that is, the total entropy, consisting of translational ($S_{\mathrm{pc}}$) and orientational degrees ($S_{\mathrm{or}}$) of freedom, increases when an isotropic phase changes to a nematic phase. The isotropic phase has full translational and orientational entropies. The nematic phase has lower orientational entropy than the isotropic phase since the nematic phase spontaneously breaks the orientational symmetry. On the other hand, the translational entropy in the nematic phase is higher than that in the isotropic phase because the excluded volume is minimized when the rods are parallel. Parallel rods can move each other more easily along a nematic director. The viscosity in the nematic phase along rods becomes lower as concentration increases [27]. On increasing the concentration of rods, two entropy terms compete and the translational entropy dominates over orientational entropy and so the isotropic phase changes to the nematic phase (Figure 2.5). The entropy means that the number ($\omega$) of available states for a system is given in $S_0 = k_{\mathrm{B}} \ln \omega$. Onsager theory gives us the fundamental aspects for entropy and ordering: the number of available state $S_n$ in the stable ordered (nematic) phase is larger than that $S_i$ in the disordered (isotropic) phase at the same concentration, namely, we have $S_i(\phi_n) < S_n(\phi_n)$ at the same concentrations [28].

The same physical picture can be applied to dispersions of spherical colloidal particles. At lower concentrations of the colloidal particles, the system is in an isotropic fluid phase. On increasing the concentration, the colloidal particles contact each other and the space, or free volume where they can freely move, becomes less. The free volume, however, can increase when the colloidal particles form a crystalline

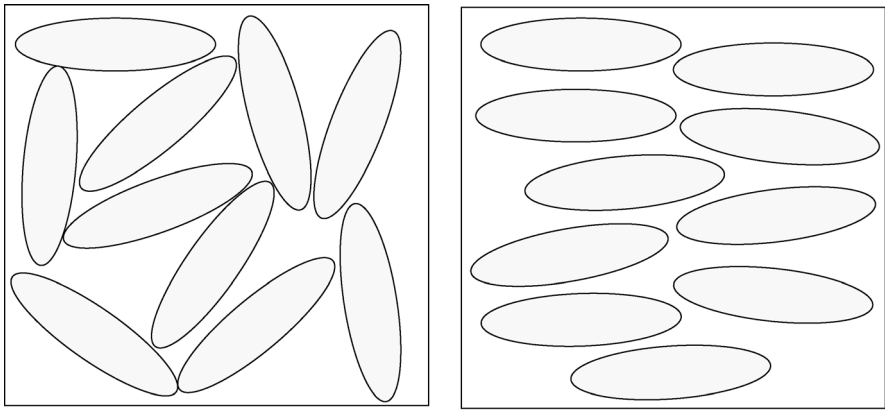


**Figure 2.5** Isotropic (a) and nematic (b) phases at the same concentration. The number of available state in the nematic phase is larger than that in the isotropic phase, where there is competition between translational and orientational degrees of freedom.

phase since they can freely move around the lattice point of a crystalline phase. Then the translational entropy in a crystalline phase becomes higher than that in an isotropic fluid phase. This is known as the entropy-induced fluid-crystalline phase transition (Alder transition) [29]. In contrast, when simple liquids such as metallic elements exhibit a crystalline state the entropy decreases due to attractive interactions between atoms, resulting in a rigid material. We see that the entropy-induced ordering can create soft matter because there is a large number ($\omega$) of available states for the system.

When the interaction between rods is only a short-range attractive interaction, the $\beta_1$ of Eq. (2.6) can be given by:

$$\beta_1(\boldsymbol{u}, \boldsymbol{u}') = -\beta\varepsilon\nu_{\mathrm{rr}} P_2(\cos\theta) P_2(\cos\theta') \tag{2.37}$$

where $\nu_{\mathrm{rr}} \equiv (\pi/4)L^2 D$ is the average excluded volume between two rods in an isotopic phase and $-\varepsilon$ shows the Maier–Saupe [30] attractive interaction energy between rods. Substituting Eq. (2.37) into (2.9), the orientational distribution function is given by:

$$f(\theta) = \frac{1}{Z_0} \exp\left[\frac{L}{D}\beta\varepsilon\phi S P_2(\cos\theta)\right] \tag{2.38}$$

and we can describe the NIT, depending on the temperature and concentration. When $\phi = 1$, the free energy results in the Maier–Saupe free energy for a nematic phase of the pure rods, which is classified as energy-driven nematic ordering. Brochard [14, 31] first described the phase behavior of liquid crystal bends by using this attractive interaction model.

Equation (2.5) can also lead to the McMillan model [32] for a smectic A phase of polymer-rod blends [33] (Section 2.3.5). When the system is spatially non-uniform

but uniform for orientation, the density is given by $\varrho_r(\boldsymbol{r}, \boldsymbol{u}) = \varrho f(\boldsymbol{r})$, where $f(\boldsymbol{r})$ is the positional distribution function, and Eq. (2.5) can be applied to describe crystalline phases such as fcc and bcc [34–36].

These fundamentals will be applied to construct the free energy for flexible and rigid rod polymer blends in the next section.

## 2.3 Mixtures of a Flexible Polymer and a Rigid Rod

Binary mixtures of a flexible polymer and a rigid rod-like molecule (nematogen or liquid crystal) play an important role in electro-optical devices, such as light shutters and displays. Since the miscibility or phase separation controls the performance of the materials, the phase behavior and phase separation kinetics have been of fundamental and practical interests. Liquid crystalline domains dispersed in a polymer matrix are called polymer dispersed-liquid crystals (PDLCs), or polymer-stabilized liquid crystals (PSLCs), where the polymer forces the liquid crystals to phase separate into droplets surrounding by the polymer matrix [2]. Practically, there are many ways to create PDLCs by mixing polymers and liquid crystals: the emulsion method [37] and phase separation method [38], including polymerization-, thermally-, and solvent-induced phase separations. The reader is referred to text books [1, 2] for details of PDLC and a review [39] for the rheological and mechanical properties.

In these blends, a nematic–isotropic phase separation and a isotropic–isotropic one with a critical point have been observed [40–44]. Typical examples are mixtures of (*p*-ethoxybenzylidene)-*p*-*n*-butylaniline (EBBA) and polystyrene (PS) or poly(ethylene oxide) (PEO) [40] and mixtures of 4-cyano-4′-*n*-heptylbiphenyl (7CB) with poly (methyl methacrylate) (PMMA) or PS [44]. Figure 2.6 shows the phase diagrams of EBBA/PEO blends with different molecular weights of the polymer chain [40]. The reduced temperature is $T^* \equiv T/T_{\mathrm{NI}}^{\mathrm{L}}$, where $T_{\mathrm{NI}}^{\mathrm{L}}$ is the NIT temperature of the pure EBBA and $\phi_2$ is the polymer volume fraction. The lower line is the boundary where the isotropic phase first appears on heating, and the upper line is the boundary where the nematic phase first appears on cooling. Filled circles show the direct measurements and the open circles represent a lever rule [40]. The dashed lines are theoretical curves by Kronberg *et al*. The mixtures show that the nematic phase at low concentrations coexists with the isotropic phase at high concentrations between solid lines below $T^* < 1$. On increasing molecular weights of the polymer, the phase boundary at low concentrations shifts to lower concentrations and we have the coexistence of a nematic phase consisting of almost pure EBBA and an isotropic phase consisting of the mixture. PEO(4000) shows a more complex behavior than the other polymers. The open triangles show the phase boundary, corresponding to the phase separation into two isotropic liquid phases. Three phase equilibria of a nematic and two isotropic phases have also been observed in mixtures of liquid crystal PAA (*p*-azoxyanisole) and *n*-alkanes [42]. Figure 2.7 shows schematic illustrations of a stable nematic (N) phase at dilute polymer concentrations and a nematic–isotropic phase separation (N + I). The stable nematic phase at low polymer concentrations

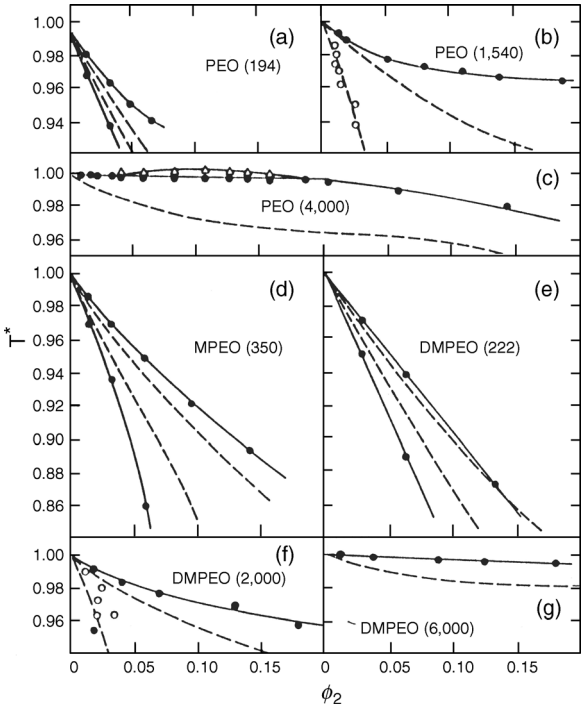


**Figure 2.6** Phase diagrams of EBBA + PEO with different molecular weights. PEO, MPEO, and DPEO indicate 0, 1 and 2 end groups, respectively [40]. Reprinted with permission from Reference [40]. Copyright (1978) American Chemical Society.

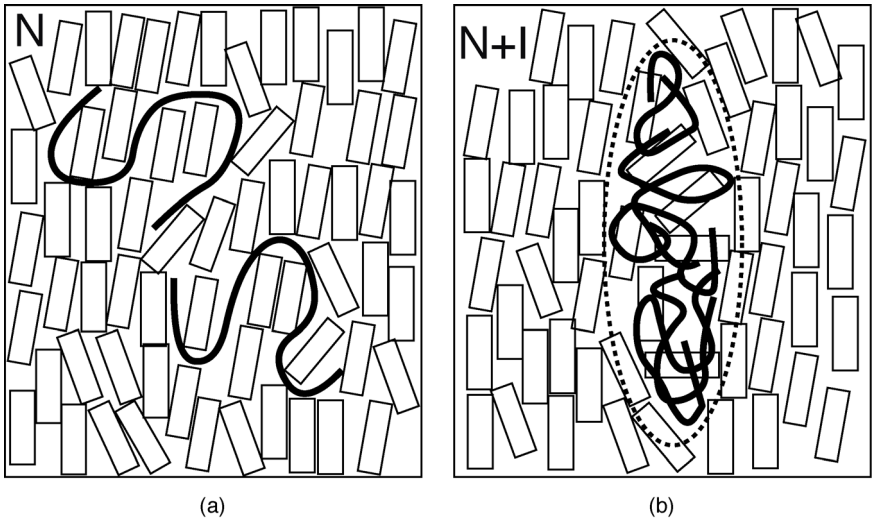


**Figure 2.7** Schematic of (a) a stable nematic (N) phase and (b) a nematic–isotropic phase separation (N + I).

consists of almost pure liquid crystals and it does exhibit macroscopic phase separations. On increasing polymer concentration, below the NIT temperature, polymers are expelled into an isotropic phase from a surrounding nematic phase and these droplets coalesce into large droplets, yielding a nematic–isotopic phase separation (N + I). These polymers affect the relaxation phenomena of liquid crystals. For example, the rotational diffusion coefficient of liquid crystal (8CB) molecules is reduced by at least one order of magnitude in the presence of polymer (polystyrene) chains [45].

These phase separations can also be affected by polymerization of monomer. Figure 2.8 shows a phase diagram of photopolymerization-induced phase separations in PDLC, presented by Kyu *et al.* [46]. The symbols show the experimental cloud points and the curves show the calculated binodal and spinodal curves of the nematogen/monomer mixture and the nematogen/crosslinked polymer mixture. The coexistence curve of the nematogen/monomer mixture is an upper critical

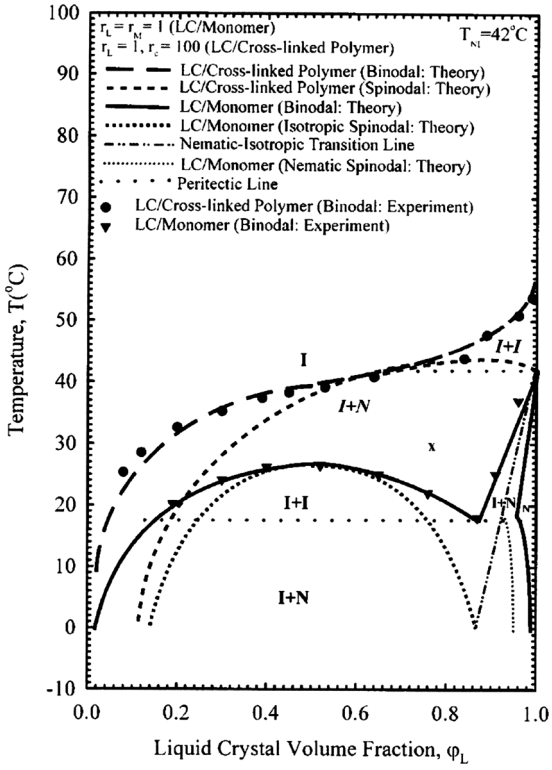


**Figure 2.8** Coexistence and spinodal curves of mixtures of nematogen/monomer and nematogen/crosslinked polymer in comparison with the experimental cloud point phase diagrams [46]. The coexistence regions for the nematogen/network system are labeled with italic letters to distinguish them from those of the nematogen/network mixture. Reprinted with permission from Reference [46]. Copyright (2001) American Physical Society.

solution temperature (UCST) type overlapping with the nematic–isotropic transition of the constituent nematogens. Photopolymerization was carried out on a typical mixture ($\phi_L = 0.75$) in the isotropic phase of the nematogen/monomer mixture. As polymerization advances, the binodal curve moves upward towards the higher nematogen content side. When it crosses the reaction temperature ($T = 30\,^{\circ}C$: point $\times$), the system becomes unstable and undergoes phase separations. The coexistence curve for nematogen/crosslinked polymer makes an upward turn near the pure nematogen axis due to network elasticity. Recently, another type of liquid crystal/polymer composite as a holographic PDLC composite has been developed through pattern photopolymerization-induced phase separation of nematogen/monomer mixtures.

To describe the phase diagrams on the temperature–concentration plane of solutions involving rigid rod-like molecules, Flory and coworkers provided lattice models for liquid crystalline polymer blends [3, 8]. Ballauf has extended the Flory lattice model to mixtures of nematic liquid crystals and flexible polymers by including the isotropic interaction between components [47–49]. The theory successfully described the main features of the phase diagram for mixtures of EBBA and PS [48]. Many theoretical studies have been furnished by a density functional theory [50], Landau–de Gennes expansion [51], and dynamical mean field theory [52]. Shen and Kyu [53] have presented the free energy by taking into account the Flory–Huggins theory for the free energy of mixing of isotropic phases in conjunction with the Maier–Saupe theory [30, 54]. Matsuyama and Kato [55] have presented the mean field theory, taking into account both the excluded volume interaction and the Maier–Saupe attractive interactions between liquid crystals (nematogens) and described the phase behavior of a polymer and liquid crystal mixtures and solutions of a rigid rod-like polymer. In this section, we introduce the phase behavior of a flexible polymer and a rigid rod blends through the Matsuyama–Kato model.

### 2.3.1
### Free Energy of Flexible and Rigid Rod Polymer Blends

We consider mixtures of a rod-like molecule of length $L$ and diameter $D$ and a flexible polymer chain of contour length $an_p$, where $a$ ($a^3$) is the length (volume) of a unit segment on the polymer chain and $n_p$ is the number of segments on the polymer. Let $N_p$ and $N_r$ be the total number of the polymer and rod, respectively. We here assume that the polymer is sufficiently flexible and does not contribute to any nematic ordering. On the basis of the second virial theory, discussed in Section 2.2.2, we take into account here both the excluded volume interaction [Eq. (2.12)] and the orientation-dependent attractive interactions between rods [Eq. (2.37)]. Then the function $\beta_1$ is given by:

$$\beta_1(\boldsymbol{u}, \boldsymbol{u}') = 2L^2 D|\sin\varphi| - \beta\varepsilon\nu_{rr} P_2(\cos\theta) P_2(\cos\theta') \tag{2.39}$$

Extending the second virial approximation [Eq. (2.5)] to a solution consisting of a flexible polymer and a rod, the free energy is given by [19, 55]:

$$\begin{aligned}\beta F(N_{\mathrm{p}}, N_{\mathrm{r}}) = & \sum_{i=\mathrm{p,r}} (N_i \beta \mu_i^{\circ} - N_i + N_i \ln c_i) + \nu_{\mathrm{pp}} N_{\mathrm{p}} c_{\mathrm{p}} + 2\nu_{\mathrm{pr}} N_{\mathrm{p}} c_{\mathrm{r}} \\ & + N_{\mathrm{r}} \int f(\boldsymbol{u}) \ln 4\pi f(\boldsymbol{u}) \mathrm{d}\Omega \\ & + \nu_{\mathrm{rr}} N_{\mathrm{r}} c_{\mathrm{r}} \int\int \left| \frac{4}{\pi} \sin\varphi(\theta, \theta') \right| f(\boldsymbol{u}) f(\boldsymbol{u}') \mathrm{d}\Omega \, \mathrm{d}\Omega' \\ & - \tfrac{1}{2} \chi_{\mathrm{a}} \nu_{\mathrm{rr}} N_{\mathrm{r}} c_{\mathrm{r}} S^2 \end{aligned} \tag{2.40}$$

where

$\mu_i^{\circ}$ shows the standard chemical potential of the pure particle $i(= \mathrm{p}, \mathrm{r})$,
$c_i = N_i/V$ is the number density of the particle $i$,
$\nu_{ij}$ is the average excluded volume of a pair of the particles $i$ and $j$ with random orientations,
$\nu_{\mathrm{r}} \equiv \pi D^2 L/4$ is the volume of the rod.

The last term shows the attractive interaction energy, Eq. (2.37), between rods and the term $|\sin\varphi|$ describes the excluded volume, Eq. (2.12), between rods. We define here the dimensionless anisotropic parameter $\chi_{\mathrm{a}} (\equiv \varepsilon/k_{\mathrm{B}}T > 0)$, where $\varepsilon$ shows the orientation-dependent attractive (Maier–Saupe) interaction between rods [14, 30]. The orientational order parameter $S$ of the rod can be calculated by:

$$S = \int P_2(\cos\theta) f(\Omega) \mathrm{d}\Omega \tag{2.41}$$

where $f(\Omega)$ is the orientational distribution function of the rods, and we have the normalization condition:

$$\int f(\Omega) \, \mathrm{d}\Omega = 1 \tag{2.42}$$

The free energy [Eq. (2.40)] contains compressible fluids, namely, it corresponds to a pseudo-ternary system consisting of a polymer, a rod, and a solvent molecule. We here derive the free energy of mixing for binary mixtures of the flexible polymer and the rigid rod. The free energy of mixing for the blends can be calculated by:

$$\Delta F = F(N_{\mathrm{p}}, N_{\mathrm{r}}) - F_i(N_{\mathrm{p}}, 0) - F_i(0, N_{\mathrm{r}}) \tag{2.43}$$

where the $F_i(N_{\mathrm{p}}, 0)$ and $F_i(0, N_{\mathrm{r}})$ are the reference free energy of the pure polymer and the pure rod in an isotropic phase ($S = 0$), respectively. We here assume the system is incompressible:

$$\phi_{\mathrm{p}} + \phi_{\mathrm{r}} = 1 \tag{2.44}$$

where $\phi_{\mathrm{p}} = \nu_{\mathrm{p}} N_{\mathrm{p}}/V$ and $\phi_{\mathrm{r}} = \nu_{\mathrm{r}} N_{\mathrm{r}}/V$ are the volume fraction of the flexible polymer and rod, respectively. The core volume of the polymer is given by $\nu_{\mathrm{p}} = a^3 n_{\mathrm{p}}$. We here assume $D = a$ and so the volume $\nu_{\mathrm{r}}$ of the rod is given by $\nu_{\mathrm{r}} = a^3 n_{\mathrm{r}}$, where $n_{\mathrm{r}} \equiv L/D$ is the axial ratio of the rod and we omit $\pi/4$ by including in the constant $a$. Then the total

volume of the system is given by:

$$V = v_p N_p + v_r N_r = a^3 (n_p N_p + n_r N_r) = a^3 N_t$$

where $N_t$ is the total number of the segments in the system. We also have $v_{rr} = (\pi/4) L^2 D = n_r v_r$. From Eq. (2.40), we obtain:

$$\beta F_i(N_p, 0) = \beta \mu_p^\circ N_p - N_p - N_p \ln v_p + v_{pp} N_p / v_p \tag{2.45}$$

$$\beta F_i(0, N_r) = \beta \mu_r^\circ N_r - N_r - N_r \ln v_r + v_{rr} N_r / v_r \tag{2.46}$$

Substituting Eqs. (2.40), (2.45), and (2.46) into (2.43), we obtain:

$$\Delta F = F_{mix} + F_{nem} \tag{2.47}$$

$$\beta F_{mix} / N_t = \frac{\phi_p}{n_p} \ln \phi_p + \frac{\phi_r}{n_r} \ln \phi_r + \chi \phi_p \phi_r \tag{2.48}$$

$$\begin{aligned} \beta F_{nem} / N_t \;=\; & \frac{\phi_r}{n_r} \int f(\boldsymbol{u}) \ln 4\pi f(\boldsymbol{u}) \mathrm{d}\Omega \\ & + \phi_r^2 \left[ \int \int \left| \frac{4}{\pi} \sin \varphi(\theta, \theta') \right| f(\boldsymbol{u}) f(\boldsymbol{u}') \mathrm{d}\Omega \, \mathrm{d}\Omega' - 1 \right] - \tfrac{1}{2} \chi_a \phi_r^2 S^2 \end{aligned} \tag{2.49}$$

where:

$$\chi \equiv a^3 \left[ \frac{2 v_{pr}}{v_p v_r} - \frac{v_{pp}}{v_p^2} - \frac{v_{rr}}{v_r^2} \right] \tag{2.50}$$

The first term $F_{mix}$ in Eq. (2.47) shows the isotropic mixing free energy and the second term $F_{nem}$ represents the free energy for nematic ordering of the rods. The first two terms in Eq. (2.48) show the entropy of mixing of the polymer and the rod-like molecule and the third term shows the isotropic interactions between the polymer and rod. The parameter $\chi$ is well-known as the Flory–Huggins interaction parameter between unlike molecules in isotropic mixing. The average excluded volumes $v_{pr}$ and $v_{pp}$ in Eq. (2.50) depend on the conformation of the polymer chain, or temperature. We assume here that the $\chi$ parameter depends only on temperature: $\chi = U_0 / k_B T$, where $U_0$ shows the local interactions, consisting of the entropy and energy terms, between unlike molecules in an isotropic state. Then the mixing free energy $F_{mix}$ results in the Flory–Huggins theory for polymer blends [56]. We note that we extended the Onsager virial theory to blends with the incompressible condition (2.44). As the result, the free energy for the isotropic mixing results in the Flory–Huggins theory. This means that we can use the Flory–Huggins free energy as the free energy of an isotropic mixing for any polymer blend system. Then the theory can be applied to more concentrated solutions than the Onsager theory, although it is a second virial approximation for the nematic ordering.

The orientational distribution function $f(\theta)$ of the rods is determined by minimizing the free energy (2.47) with respect to this function. Using the Legendre polynomial (2.15) for $|\sin\gamma|$ in Eq. (2.49), we obtain:

$$f(\theta) = \frac{1}{Z}\exp[\Gamma S P_2(\cos\theta)] \tag{2.51}$$

where:

$$\Gamma \equiv \left(\chi_a + \tfrac{5}{4}\right)\frac{L}{D}\phi_r \tag{2.52}$$

and $\Gamma$ corresponds to the strength of nematic ordering. The term $\chi_a$ and 5/4 come from the attractive and excluded volume interactions between rods, respectively. Substituting Eq. (2.51) into (2.42), the normalization constant $Z$ is given by $Z = 4\pi I_0[\Gamma S]$, where the function $I_0$ is defined in Eq. (2.20). The orientational order parameter (2.41) of the rods is determined by the self-consistent equation:

$$S = I_1[\Gamma S]/I_0[\Gamma S] \tag{2.53}$$

Substituting Eq. (2.51) into (2.49), we obtain:

$$\int f(\Omega)\ln 4\pi f(\Omega)\mathrm{d}\Omega = \Gamma S^2 - \ln I_0[\Gamma S] \tag{2.54}$$

$$\int\int \sin\varphi(\theta,\theta')f(\Omega)f(\Omega')\mathrm{d}\Omega\mathrm{d}\Omega' = \frac{\pi}{4}\left(1-\tfrac{5}{8}S^2\right) \tag{2.55}$$

and the nematic free energy [Eq. (2.49)] is finally given by:

$$\beta F_{nem}/N_t = \tfrac{1}{2}\left(\chi_a + \tfrac{5}{4}\right)\phi_r^2 S^2 - \frac{\phi_r}{n_r}\ln I_0[\Gamma S] \tag{2.56}$$

The chemical potential of the polymer is given by:

$$\begin{aligned}
\beta\Delta\mu_p &= \beta(\mu_p - \mu_p^\circ) \\
&= \beta\left(\frac{\partial\Delta F}{\partial N_p}\right)_{N_r,T}, \\
&= n_p\beta\left[f + (1-\phi_p)\left(\frac{\partial f}{\partial\phi_p}\right)\right], \\
&= \ln\phi_p + \left(1-\frac{n_p}{n_r}\right)(1-\phi_p) + n_p\chi(1-\phi_p)^2 \\
&\quad + \frac{n_p}{2}\left(\chi_a + \tfrac{5}{4}\right)S^2(1-\phi_p)^2
\end{aligned} \tag{2.57}$$

and that of the rod is given by:

$$\begin{aligned}
\beta\Delta\mu_r &= \beta(\mu_r - \mu_r^\circ) \\
&= \beta\left(\frac{\partial \Delta F}{\partial N_r}\right)_{N_p,T}, \\
&= n_r\beta\left[f - \phi_p\left(\frac{\partial f}{\partial \phi_p}\right)\right], \\
&= \ln(1-\phi_p) + \left(1-\frac{n_r}{n_p}\right)\phi_p + n_r\chi\phi_p^2 \\
&\quad + \frac{n_r}{2}\left(\chi_a + \tfrac{5}{4}\right)S^2(1-\phi_p)^2 - \ln I_0[\Gamma S]
\end{aligned} \tag{2.58}$$

where we define $f \equiv \Delta F/N_t$.

### 2.3.2 Nematic–Isotropic Phase Transition

The nematic free energy $F_{nem}$ [Eq. (2.56)] has the same form as $f_{nem}$ in Eq. (2.23). Then, as discussed in Figure 2.1, the NIT takes place at $\Gamma^{**} = 4.55$. We define here the reduced temperature $\tau \equiv 1/\chi$. Using Eq. (2.52), we obtain the reduced NIT temperature ($\tau_{NI}$) as a function of the polymer volume fraction $\phi_p$:

$$\tau_{NI} = \frac{\alpha n_r(1-\phi_p)}{4.55 - 1.25 n_r(1-\phi_p)} \tag{2.59}$$

where we define the dimensionless nematic interaction parameter $\alpha \equiv \chi_a/\chi$. When $\tau < \tau_{NI}$, the nematic phase is stable and when $\tau > \tau_{NI}$ the isotropic is phase stable. The orientational order parameter $S$ jumps from 0 to 0.44 at $\tau = \tau_{NI}$. The NIT temperature diverges at the concentration $\phi_p^* = (1.25-4.55)/(1.25n_r)$. For the pure rod ($\phi_p = 0$), the reduced NIT temperature $\tau_{NI}^L$ is given by:

$$\tau_{NI}^L = \frac{\alpha n_r}{4.55 - 1.25 n_r} \tag{2.60}$$

Figure 2.9 shows the NIT temperature plotted against the volume fraction $\phi_p$ for various values of $n_r$ with $\alpha = 2.5$. The left- (right-) hand side of the each solid line corresponds to a nematic (isotropic) phase. When $n_r > 3.64$, the temperature $\tau_{NI}^L$ diverges to the high temperature side. For lower $n_r$, or low molecular weight liquid crystals, the attractive interaction $\chi_a$ between rods dominates and so we have the NIT at $\phi_p = 0$. For larger values of $n_r$, or longer rod-like molecules, however, the steric interaction dominates and the attractive interaction plays only an auxiliary role for nematic ordering and then the NIT takes place on increasing concentration $\phi$. When

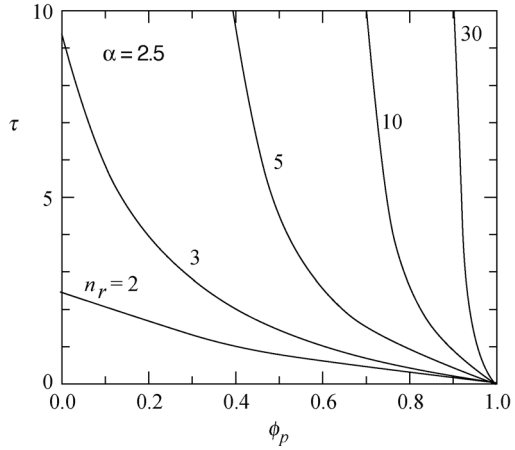


**Figure 2.9** Nematic–isotropic transition temperature ($\tau_{NI}$) versus volume fraction $\phi_p$ of polymers with $\alpha = 2.5$ [55]. The value of $n_r$ is changed. Reprinted with permission from Reference [55]. Copyright (1996) American Institute of Physics.

$n_r < 3.64$, using Eqs. (2.59) and (2.60), we obtain the NIT temperature ($T_{NI}$) as a function of $\phi_p$:

$$T_{NI}/T_{NI}^{L} = \frac{(4.55-1.25n_r)(1-\phi_p)}{4.55-1.25n_r(1-\phi_p)} \tag{2.61}$$

where the temperature is normalized by the NIT temperature $T_{NI}^{L}$ of the pure nematogen.

### 2.3.3
### Landau–de Gennes Expansion of the Free Energy

The function $I_0[x]$ defined by Eq. (2.20) can be expanded in $x$ as:

$$\ln I_0[x] = \frac{1}{10}x^2 + \frac{1}{105}x^3 - \frac{1}{700}x^4 + \cdots . \tag{2.62}$$

where $x \equiv \Gamma S$. Substituting Eq. (2.62) into (2.56), we obtain the nematic free energy as an expansion in the order parameter $S$:

$$\beta F_{nem}/N_t = \left(\chi_a + \tfrac{5}{4}\right)\phi_r^2\left[\tfrac{1}{2}\left(1-\frac{\Gamma}{5}\right)S^2 - \frac{\Gamma^2}{105}S^3 + \frac{\Gamma^3}{700}S^4\right] \tag{2.63}$$

The discontinuous NIT occurs at $\Gamma = \Gamma^{**}(= 4.55)$, where the free energy of the isotropic and that of the nematic phase are equal. The equilibrium value of $S$ is given as a function of $\phi_r$ by minimizing the free energy with respect to $S$, yielding:

$$S = \frac{5}{2\Gamma}\left(1 + \sqrt{6.6 - \frac{28}{\Gamma}}\right) \tag{2.64}$$

for $\Gamma > \Gamma^{**}$ and $S = 0$ otherwise. The equilibrium order parameter starts at $S_{NI} = 0.722$ and gradually approaches 1 with increasing $\Gamma(< 5)$. From Eq. (2.64), the temperature coefficient of the order parameter at the NIT temperature $(T_{NI}^{L})$ of a pure nematogen is given by:

$$\left(\frac{\partial S}{\partial T}\right)_{T=T_{NI}^{L}} = -\left(\frac{4.89\chi_a}{\chi_a + 1.25}\right)\frac{1}{T_{NI}^{L}} \tag{2.65}$$

The parameter $\chi_a$ can be experimentally determined by using this equation.

Equation (2.63) is only correct in the vicinity of the NIT, or $\Gamma < 5$. It is convenient to set the coefficients of Eq. (2.63) to describe for any value of $\Gamma(> 0)$ as follows [21]:

$$\beta F_{nem}/N_t = \left(\chi_a + \tfrac{5}{4}\right)\phi_r^2\left[\tfrac{1}{2}\left(1 - \frac{\Gamma}{3}\right)S^2 - \frac{\Gamma^2}{9}S^3 + \frac{\Gamma^3}{6}S^4\right] \tag{2.66}$$

In this case, the equilibrium value of $S$ is given by:

$$S = \tfrac{1}{4} + \tfrac{3}{4}\sqrt{1 - \frac{8}{3\Gamma}} \tag{2.67}$$

for $\Gamma > \frac{8}{3}$ and $S = 0$ otherwise. The equilibrium order parameter starts at $S_{NI} = 0.33$ and gradually approaches 1 with increasing $\Gamma$. Equation (2.66) can show the same behavior as Eq. (2.56) as a function of $\Gamma$.

### 2.3.4
### Phase Separations

We introduce here the phase behavior of a flexible polymer and a low molecular weight liquid crystal molecule (nematogen) of $n_r < 3.64$. The conditions for binodal curves of two-phase equilibria are given by:

$$\Delta\mu_p(\phi_r') = \Delta\mu_p(\phi_r'') \tag{2.68}$$

$$\Delta\mu_r(\phi_r') = \Delta\mu_r(\phi_r'') \tag{2.69}$$

where $\phi_r'$ and $\phi_r''$ show the volume fraction of nematogens in lower and higher concentrations in coexisting two phases, respectively. The above coupled equations correspond to the common tangent construction (Figure 2.3).

Figure 2.10 shows a typical phase diagram calculated for $\alpha = 3.1$, $n_p = 20$, $n_r = 2$ (a) and $\alpha = 5$, $n_p = 10$, $n_r = 2$ (b). The temperature is normalized by the NIT temperature $T_{NI}^{L}$ of the pure nematogen. The solid curve is referred to the binodal curve and the dotted line shows the NIT temperature, derived in Eq. (2.61). The dashed curve corresponds to the spinodal curve: $(\partial^2 f/\partial\phi_p^2)_T = 0$. The filled circle shows the critical point. In the biphasic region, we have two different metastable regions: an isotropic metastable (Im) and a nematic metastable (Nm), and two unstable regions: an isotropic unstable (Iu) and a nematic unstable (Nu). The metastable and unstable regions are separated by $\partial^2 f/\partial\phi_p^2 = 0$, which corresponds

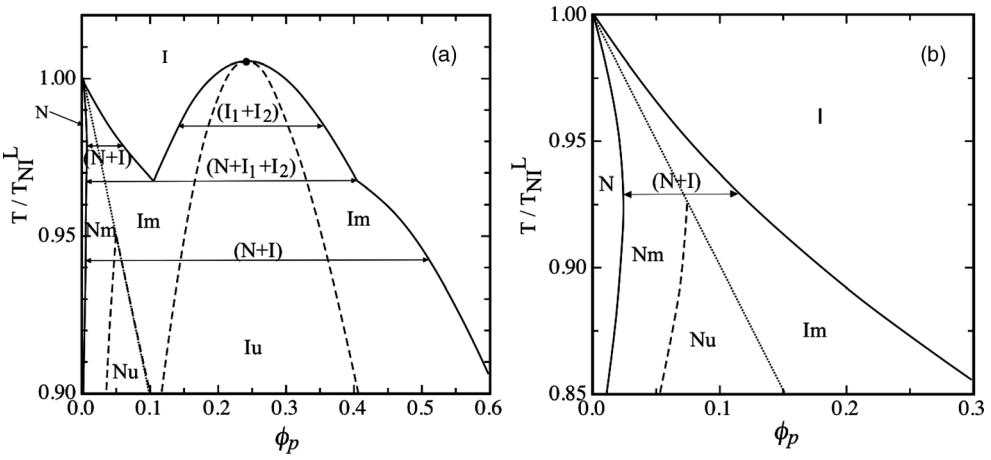


**Figure 2.10** Typical phase diagram for $\alpha = 3.1$, $n_p = 20$, $n_r = 2$ (a) and $\alpha = 5$, $n_p = 10$, $n_r = 2$ (b).

to the inflection point of the free energy. These unstable regions inside the binodal line were first predicted by Shen and Kyu [53]. In Figure 2.10a, we have the triple point (TP), where a nematic phase and two isotropic phases can simultaneously coexist ($N + I_1 + I_2$). Above the triple point, the biphasic region between a nematic and isotropic phase ($N + I$) appears at lower concentrations. We also have the isotopic-isotropic ($I_1 + I_2$) phase separation with a UCST such as observed in PAA and *n*-alkanes blends [42] and PS and 7CB blends [44]. Below the triple point we have the broad biphasic regions between nematic and isotropic phases ($N + I$), where the nematic phase consists almost of the pure nematogens and the coexisting isotropic phase consists of the nematogens and flexible polymers. On increasing the nematic interaction parameter $\alpha$, the isotropic–isotropic phase separation disappears and we only have the nematic–isotropic phase separation (Figure 2.10b).

Figure 2.11 schematically shows the free energy of Figure 2.10a plotted against the concentration ($\phi_p$) of the polymer for a temperature of $T_c > T > T_{NI}^L$ (a), $T_{NI}^L > T > T_{TP}$ (b), $T = T_{TP}$ (c), and $T < T_{TP}$ (d). The $T_c$ shows the UCST and $T_{TP}$ shows the triple point temperature. The figure shows the common tangent construction for phase separations, discussed in Figure 2.3. At high temperatures, as shown in Figure 2.11a, the two isotropic phases at $\phi_p = \phi_1$ and $\phi_2$ can coexist because the $\chi$ parameter between unlike molecules becomes dominant at the concentration between $\phi_1$ and $\phi_2$. On decreasing temperature, the nematic free energy appears in the dilute concentration below $T < T_{NI}^L$ and we have two common tangent lines to the free energy (Figure 2.11b). The nematic free energy merges into the isotropic free energy at the NIT concentration $\phi_{NI}$. Upon further decreasing temperature, the nematic free energy becomes small and we have the triple point at $T = T_{TP}$ (Figure 2.11c), where we have a common tangent to the free energy at three different concentrations: $\phi_N$ (nematic), $\phi_1$ (isotropic), and $\phi_2$ (isotropic). At lower temperatures of the triple point $T < T_{TP}$ (Figure 2.11d), the attractive interaction $\chi_a$

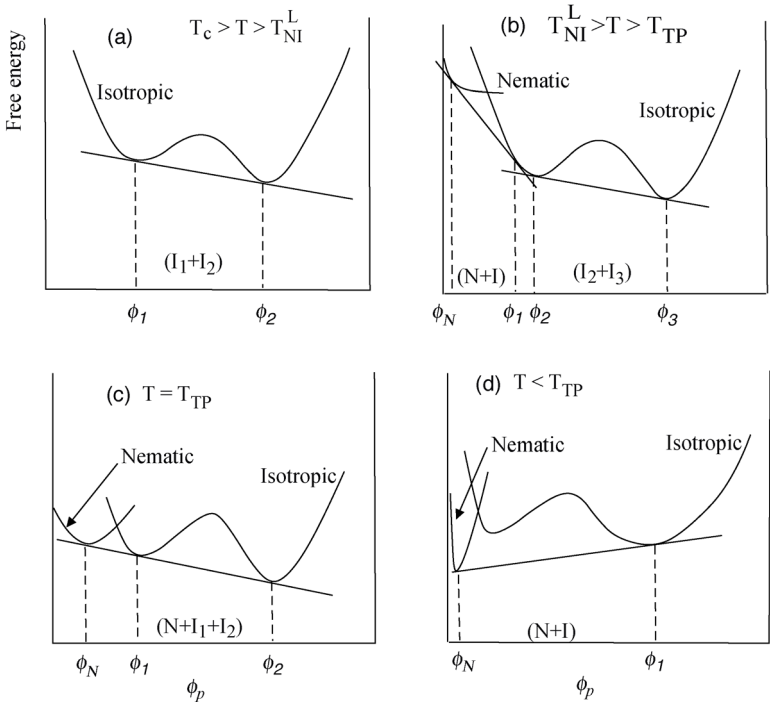


**Figure 2.11** Illustration of the free energy of Figure 2.10 plotted against the concentration of polymer for a temperature of $T_c > T > T_{NI}^L$ (a), $T_{NI}^L > T > T_{TP}$ (b), $T = T_{TP}$ (c), and $T < T_{TP}$ (d).

between nematogens becomes dominant and the nematic free energy becomes smaller and the broad biphasic region N + I appears. The phase behavior also depends on the strength of external fields, such as electric and magnetic fields. Lin *et al.* have found theoretically that, due to the field-induced ordering, the phase boundaries shift to higher temperature [57].

Figure 2.12a shows the phase diagram for $\alpha = 2.5$ and $n_r = 2$ [55]. The number $n_p$ of segments on a polymer chain is varied. For low molecular weight polymers, the biphasic region (N + I) appears at lower temperatures. The stable nematic phase appears in a dilute region of the polymer concentration. The nematic phase consists almost of pure nematogens and the coexisting isotropic phase consists of nematogens and flexible polymers. For larger values of $n_p$, we have the coexistence between two isotropic phases with a UCST and the TP. The critical point (filled circle) in the isotropic phase can be calculated by the condition $(\partial \Delta\mu_r/\partial\phi_p)_T = 0$ and $(\partial^2 \Delta\mu_r/\partial\phi_p^2)_T = 0$. We then have the critical concentration:

$$\phi_p^c = \frac{\sqrt{n_r}}{\sqrt{n_p} + \sqrt{n_r}} \tag{2.70}$$

and the critical temperature:

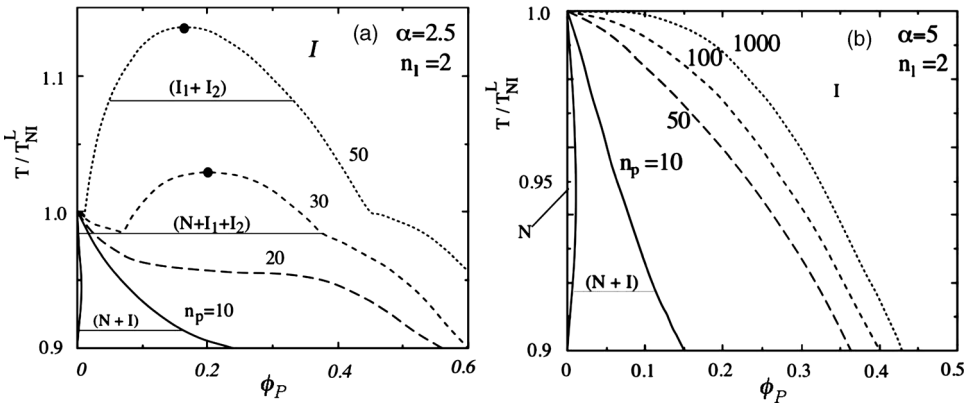


**Figure 2.12** Binodal curves on the temperature–volume fraction ($\phi_p$) plane for $\alpha = 2.5$, $n_r = 2$ (a) and $\alpha = 5$, $n_r = 2$ (b). The number $n_p$ of the segments in a polymer is varied. For larger values of the nematic interaction parameter $\alpha$, the isotropic–isotropic phase separation disappears and we only have the nematic–isotropic phase separation [55]. Reprinted with permission from Reference [55]. Copyright (1996) American Institute of Physics.

$$\tau_c = \frac{2n_p n_r}{\left(\sqrt{n_p} + \sqrt{n_r}\right)^2} \tag{2.71}$$

which result in the Flory–Huggins theory for polymer blends in an isotropic phase. Figure 2.12b shows the phase diagram for $\alpha = 5$ and $n_r = 2$ [55]. The number $n_p$ of segments on a polymer is varied. When the nematic interaction parameter $\alpha$ increases, the isotropic–isotropic phase separation disappears and we only have the nematic–isotropic phase separation. The width of the two-phase region increases with increasing $n_p$.

This type of phase diagram is characterized by the nematic interaction parameter $\alpha$ [33, 55]. As shown in Figures 2.10 and 2.12, there are two generic types of the phase diagram: whether it has the phase separation $I_1 + I_2$ or not. The conditions for the appearance of these phase diagrams are obtained by comparing the NIT temperature $T_{NI}^L$, the UCST, and $T_c$. From Eqs. (2.60) and (2.71), the nematic interaction parameter $\alpha$ is given by:

$$\alpha = \frac{2n_p(4.55 - 1.25n_r)}{\left(\sqrt{n_p} + \sqrt{n_r}\right)^2}\left(\frac{T_{NI}^L}{T_c}\right) \tag{2.72}$$

For $n_p \gg 1$, we have:

$$\alpha = \alpha^*\left(\frac{T_{NI}^L}{T_c}\right) \tag{2.73}$$

where $\alpha^* \equiv 2(4.55 - 1.25n_r)$. When $\alpha < \alpha^*$, or $T_{NI}^L < T_c$, we have phase diagrams as shown in Figure 2.10a with a UCST. If $\alpha > \alpha^*$, or $T_{NI}^L > T_c$, we have diagrams, such as in Figure 2.10b, without a critical point. For example, when $n_r = 2$, we have $\alpha^* = 4.1$.

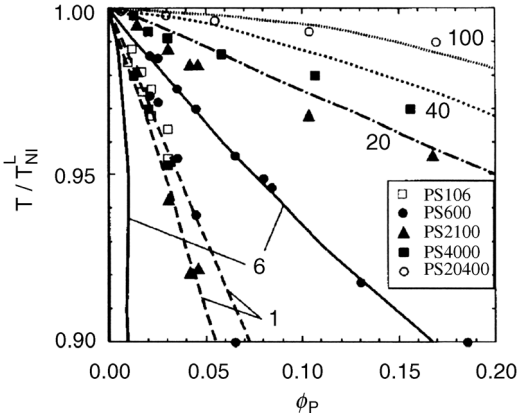


**Figure 2.13** Comparison of theoretical calculations with the observed phase diagram of PS/EBBA mixtures [55]. Reprinted with permission from Reference [55]. Copyright (1996) American Institute of Physics.

Then the $I_1 + I_2$ phase separation does not appear in Figure 2.12b with $\alpha = 5$, even for high molecular weight polymers. Such a threshold of the phase diagrams has also been obtained by Holyst and Schick [51].

Figure 2.13 compares the theoretical binodal curves with the observed phase diagrams of PS/EBBA mixtures [40, 55]. The molecular weight of PS is changed from 106 to 20 400. The number $n_p$ of segments on the polymer is changed from 1 to 100 with $n_r = 1.5$ and we use $\alpha = \alpha^* = 5.35$ to fit the experimental data. The fit of theoretical curves to the experimental data is qualitatively good for the isotropic binodal curves. On increasing $n_p$, however, the calculated binodal curve in a nematic phase is shifted to a lower concentration than the experimental data. Flexible polymers, discussed in this section, almost do not dissolve in a nematic phase below the NIT temperature of the pure nematogens and the broad biphasic region between nematic and isotropic phases appears. The free energy is minimized due to the phase separation rather than the nematic ordering of the polymer chain. This can be classified as polymer-induced phase separation. However, the stiffness of polymer chains can change the phase behavior in polymer and nematogen blends [58, 59]. For instance, the width of the biphasic region between a nematic and an isotropic phase becomes narrow due to the partial orientational ordering of polymer chains induced by nematic fields [60–64]. Liquid crystalline polymers have an anisotropic coupling between the polymer and nematogenic solvent molecules and the blends have a narrower nematic–isotopic biphasic region, as observed experimentally [65]. In this case, the free energy is minimized by the partial orientational ordering of polymer chains dissolved in a nematic solvent rather than phase separations. This can be classified as polymer-induced stabilization of nematic ordering. The stiffness of a polymer chain strongly affects both the nematic ordering of polymer blends and the width of the biphasic region between a nematic and isotopic phase. The mean field theory, introduced in this section, can semi-quantitatively describe the observed phase diagrams of blends of a flexible polymer and a nematogen.

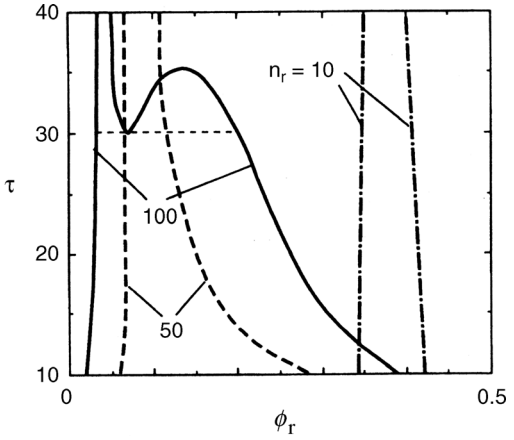


**Figure 2.14** Binodal curves with $n_p = 1$ and $\alpha = 0$. The axial ratio $n_r$ is changed [55]. Reprinted with permission from Reference [55]. Copyright (1996) American Institute of Physics.

### 2.3.5
### Phase Diagrams in Solutions of Rigid Rod-Like Polymers

We here consider binary mixtures consisting of a rigid rod-like polymer and a solvent. When $n_r \gg 1$, the free energy (2.47) can describe the phase behavior. Figure 2.14 shows the binodal curves with $n_p = 1$ and $\alpha = 0$. The axial ratio $n_r$ is varied. The binodal curve of the isotropic phase is on the left (lower volume fraction $\phi_r$) and that of the nematic phase is on the right. When $n_r = 10$ and 50, the isotropic–nematic phase separation appears for all the temperature range. This is known as the biphasic chimney, where the difference in composition between the isotropic and nematic phases is slight. For longer rods, $n_r = 100$ (solid curve), we have a triple point where an isotropic phase and two nematic phases can simultaneously coexist. At the higher temperature of the triple point, we have two phase coexistence between two nematic phases with the UCST, which is induced by the unfavorable interaction $\chi$ between unlike molecules in the nematic phase, and the nematic–isotropic phase separation in dilute regions, which is induced by the excluded volume interaction between rods, discussed in Section 2.2. Below the triple point, the broad biphasic region between the nematic and isotropic phases appears. On increasing the nematic interaction parameter $\alpha$, the width of the broad biphasic region increases and the temperature of the triple point is shifted to higher temperature. Figure 2.15 shows the experimentally determined phase diagram for poly($\gamma$-benzyl-L-glutamate) (PBLG, $M_w = 310\,000$) in dimethylformamide (DMF) [66]. The equilibrium line bounding the liquid crystalline phase was determined by NMR, while the line bounding the isotropic phase was determined from polarizing microscope studies. In the experiments, it showed effects associated with crystallization and gelation at high polymer concentrations [67]. The phase equilibria can be characterized as consisting of a narrow chimney in which there is only a small difference in composition between

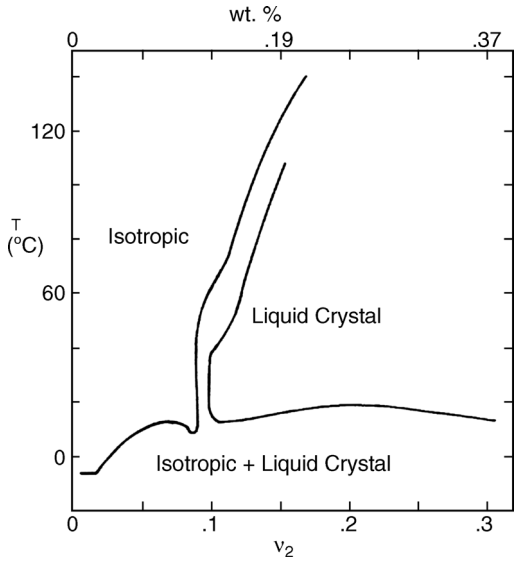


**Figure 2.15** Experimentally determined phase diagram for poly(γ-benzyl-L-glutamate) (PBLG) in dimethylformamide (DMF) [66]. Reprinted with permission from Reference [66]. Copyright (1971) American Chemical Society.

the ordered and disordered phases, connected to a wide biphasic region in which the polymer and solvent mix only slightly. Such phase diagrams have also been predicted by Flory's lattice theory for rod-like polymers [3, 68, 69].

### 2.3.6
### Smectic-Nematic–Isotropic Phase Separations

Mean field theories can also be extended to the phase behavior of smectic A liquid crystal and flexible polymer blends [63, 70–74] by combining the Flory–Huggins theory for isotropic mixing and Kobayashi–McMillan theory [32, 75] for smectic A ordering of liquid crystals.

The free energy is given by $F = F_{\mathrm{mix}} + F_{\mathrm{sm}}$, where $F_{\mathrm{mix}}$ is the free energy of mixing of an isotropic phase and is given by Eq. (2.48). The second term shows the free energy for the smectic A ordering of nematogens. On the basis of the Kobayashi–McMillan theory, it is given by [33, 76]:

$$\begin{aligned}\beta F_{\mathrm{sm}}/N_{\mathrm{t}} = {} & \frac{\phi_{\mathrm{r}}}{n_{\mathrm{r}}}\int\int f(r,\cos\theta)\ln f(r,\cos\theta)\mathrm{d}r\mathrm{d}(\cos\theta) \\ & -\tfrac{1}{2}\chi_{\mathrm{a}}\phi_{\mathrm{r}}^2(S^2+\gamma\eta^2)\end{aligned} \tag{2.74}$$

where θ is the angle between the long axis of the nematogens and the director, $r \equiv z/d$, $d$ is the average distance between smectic layers, and $f(r,\cos\theta)$ is the distribution function of nematogens. The parameter γ shows the dimensionless interaction for a smectic A phase. According to McMillan theory [32], γ is given by

$\gamma = 2\exp[-(r_0/d)]$, which can be vary between 0 and 2 and increases with increasing chain length of alkyl end-chains of nematogens. The smectic condensation is more favored for larger values of $\gamma$. The smectic A order parameter can be calculated by:

$$\eta = \int\int \cos(2\pi z/d)\, P_2(\cos\theta) f(z,\Omega) \mathrm{d}z \mathrm{d}\Omega \tag{2.75}$$

We have an isotropic phase with $S = \eta = 0$, a nematic phase with $S \neq 0, \eta = 0$, and a smectic A phase with $S \neq 0, \eta \neq 0$. The equilibrium distribution function $f(z,\Omega)$ is determined by minimizing the free energy [Eq. (2.74)] with respect to this function. In the original McMillan theory, the order parameter for the smectic A phase is given by $\langle P_2(\cos\theta)\cos(2\pi z)\rangle$. It has been reported that the decoupled approximation:

$$\langle P_2(\cos\theta)\cos(2\pi z)\rangle = \langle P_2(\cos\theta)\rangle\langle\cos(2\pi z)\rangle$$

is in qualitative agreement with the original McMillan theory [77].

Figure 2.16 shows the order parameter $S$ and $\eta$ plotted against the polymer concentration $\phi(\equiv \phi_p)$ for various values of $\gamma$ [33]. In Figure 2.16a, the smectic order parameter $\eta$ continuously decreases to zero with increasing $\phi$ and the smectic

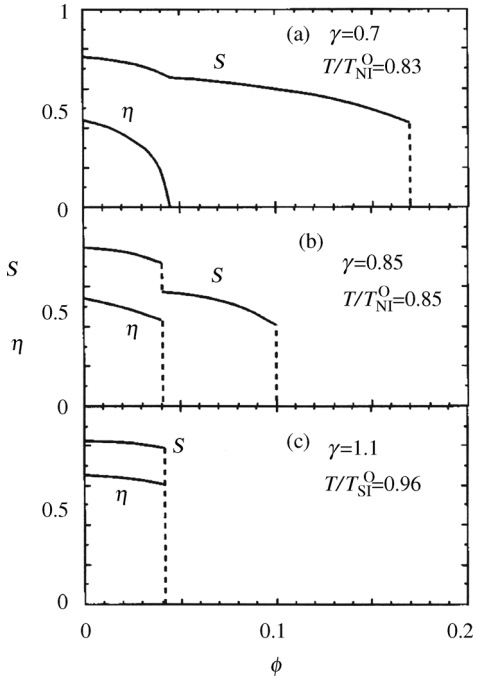


**Figure 2.16** Order parameter $S$ and $\eta$ plotted against the polymer concentration $\phi$ for various values of $\gamma$: (a) $\gamma = 0.7$, $T/T_{NI}^{\circ} = 0.83$; (b) $\gamma = 0.85$, $T/T_{NI}^{\circ} = 0.9$; (c) $\gamma = 1.1$, $T/T_{SI}^{\circ} = 0.96$ [33]. Reprinted with permission from Reference [33]. Copyright (1998) American Institute of Physics.

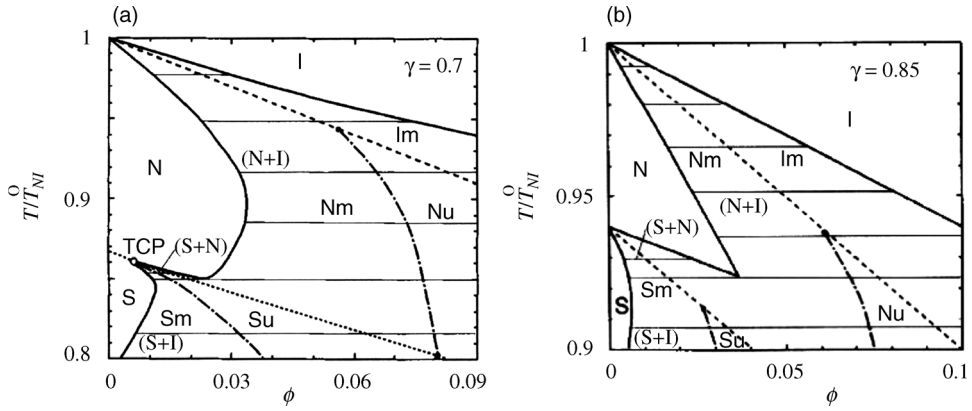


**Figure 2.17** Temperature–composition phase diagram for a mixture of polymer and smectic-A liquid crystal for $\alpha = 8$ and for $\gamma = 0.7$ (a) and $\gamma = 0.85$ (b) [33]. Reprinted with permission from Reference [33]. Copyright (1998) American Institute of Physics.

A-nematic phase transition (SNT) is of second order, while the NIT is of first order. In Figure 2.16b, the smectic order parameter discontinuously drops to zero with increasing $\phi$ and the SNT is of first order. In Figure 2.16c, the nematic phase disappears and we only have the first-order smectic A–isotropic phase transition (SIT). Owing to McMillan theory for a pure nematogen ($\phi = 0$), the SNT should be second order for $T_{SN}^{\circ}/T_{NI}^{\circ} < 0.87$ and first order for larger values of $T_{SN}^{\circ}/T_{NI}^{\circ}$, where $T_{SN}^{\circ}$ shows the SNT temperature of a pure nematogen.

Figure 2.17 shows the phase diagram at dilute regions for $\gamma = 0.7$ (a) and $\gamma = 0.85$ (b). The solid curve refers to the binodal region and the dashed-dotted line shows the spinodal region. The dashed line shows the first-order NIT and the dotted line corresponds to the second-order SNT. The binodal lines at more concentrated regions have been calculated in References [33, 76]. Under the SNT line, we have a smectic metastable (Sm) and a smectic unstable (Su) region. It consists of a coexistence between a nematic–isotropic phase separation (N + I), a smectic–isotropic phase separation (S + I), and a smectic–nematic phase (S + N) at dilute compositions of nematogens [76]. We also have a triple point (three-phase equilibrium), where the smectic A, nematic, and isotropic phases can simultaneously coexist. When $\gamma = 0.7$ (Figure 2.17a), the SNT is second order and then the point where the second-order SNT line meets the binodal at the top of the biphasic region (S + N) is a tricritical point (TCP), although it has not been experimentally observed yet. This TCP resembles the λ-point in the mixtures of liquid $^3$He and liquid $^4$He [78]. On increasing the smectic interaction parameter $\gamma$, the SNT temperature of the pure nematogen is shifted to the higher temperature side as shown in Figure 2.17b. The TCP moves upwards and disappears and the SNT becomes first order. Upon further increasing $\gamma$, the nematic phase disappears and we only have the biphasic region (S + I).

On decreasing the molecular weight $n$ of a polymer, the isotropic–isotropic phase separation appears above the NIT temperature, as shown in Figure 2.12. Figure 2.18

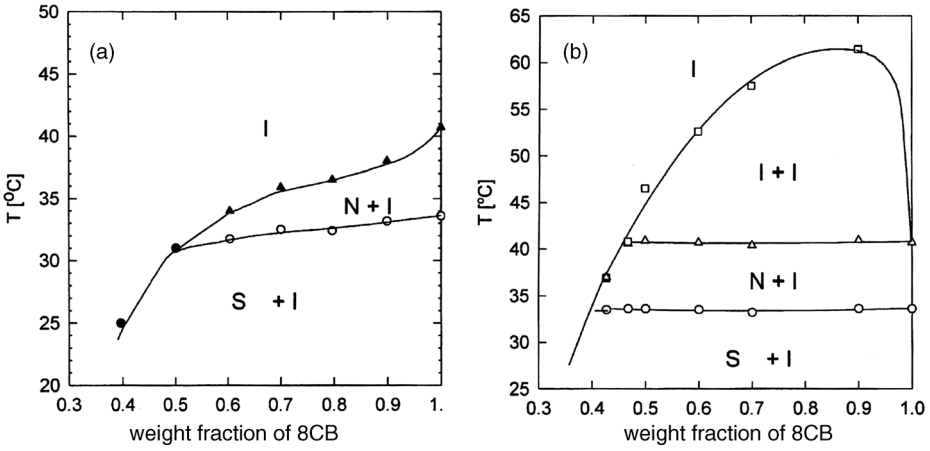


**Figure 2.18** Equilibrium phase diagrams of 8CB/PS mixtures: for PS of molecular weight ($M_w$) (a) 4750 and (b) 65 000 [79]. Reprinted with permission from Reference [79]. Copyright (2005) American Chemical Society.

shows equilibrium phase diagrams of propoxylated glycerol triacrylate and 4-cyano-4′-*n*-octylbiphenyl (8CB)/PS mixtures: (a) for PS of molecular weight $M_w = 4750$; (b) $M_w = 65\,000$ [79]. The different symbols show the experimental transition temperatures obtained by optical microscopy. Note that the horizontal axis corresponds to weight fraction of 8CB. The phase diagrams demonstrate a strong dependence of the phase behavior on the molecular weight of the polymer. For a low molecular weight polymer (Figure 2.18a), the phase diagram has no I + I phase separation. However, the phase diagrams with $M_w = 65\,000$ (Figure 2.18b) indicates the biphasic region I + I with an upper critical solution temperature and the shape is asymmetric. The critical point is located at the weight fraction 85% of 8CB and a temperature of $T_c = 62\,^{\circ}C$. In the upper region of the phase diagram, a single phase is observed where 8CB and PS form a homogeneous isotropic solution (I), while in the lower regions, we have phase separations I + I, N + I, and S + I. These phase separations have also been observed in propoxylated glycerol triacrylate/8CB mixtures [80]. These experimental results are qualitatively consistent with Figures 2.12 and 2.17.

Similar phase separation between a nematic phase and a highly swollen lamellar (smectic) phase has been observed in a suspension composed of rod-like fd virus and the thermosensitive polymer poly(*N*-isopropylacrylamide) (NIPA) [81]. Figure 2.19 shows the melting behavior of fd-virus/NIPA mixtures with high rod concentration. At low temperature (5 °C), the mixture forms a lamellar (smectic) phase where layers of rods are intercalated with layers of polymer (Figure 2.19a). At 7 °C, the dislocation defects act as a nucleation site for formation of nematic tactoids (Figure 2.19b). As nematic tactoids grow, they expel polymer into the coexisting lamellar phase, which leads to swelling of lamellar layers (Figure 2.19c and j). In a swollen lamellar phase, there are regions where individual layers are tightly bound and regions where they

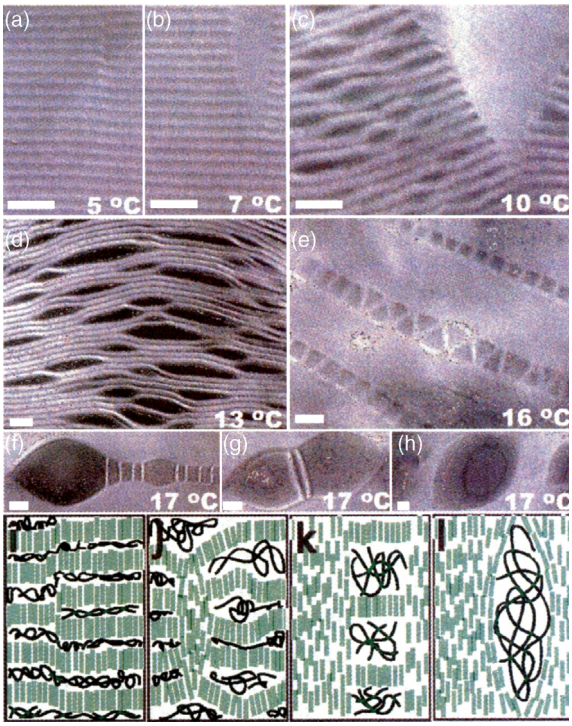


**Figure 2.19** Melting behavior of fd-virus/NIPA mixtures with high rod concentration [81]. (a)–(h) Observations with an inverted microscope; (i)–(l) illustration of the proposed melting processes of the lamellar rod/polymer mixture. Scale bars are 5 μm. Reprinted with permission from Reference [81]. Copyright (2004) American Physical Society.

are well separated (Figure 2.19d). With increasing temperature, most of the sample is melted into a nematic phase that coexists with highly swollen lamellar phase. The lamellar phase has the shape of an elongated stripe while the nematic phase fills the rest of the space. The polymer is expelled into the coexisting lamellar phase from the nematic phase (Figure 2.19e and k). Upon increasing temperature further, the lamellar stripes transform into a polymer-rich isotropic phase (Figure 2.19f–h) and the isotropic–nematic coexistence appears (Figure 2.19h and l).

Combining the Flory–Huggins theory for an isotropic mixing and a free energy for other liquid crystalline phases opens up the possibility of extending the theory to describe other liquid crystalline phases such as smectic C. Such mean field theories have been applied to phase diagrams of colloidal solutions [35], crystal and liquid crystal mixtures [82], and colloid and liquid crystal mixtures [83].

Density functional theory (DFT) is also a powerful approach to describe equilibrium statistical systems of partially ordered phases like liquid crystalline phases. DFT is based on a theorem that the free energy of a system can be written as a function of the single-particle distribution or the density $\phi(\boldsymbol{r})$, which minimize the free energy at the thermal equilibrium state [84]. DFT has been developed to determine the free

energy of isotropic polymer systems [85] and nematic polymers [86]. Maissa *et al.* first used DFT to derive the free energy of binary nematic polymer mixtures, including a nematic polymer/non-nematic solvent mixture and a nematic polymer blend. The calculated phase diagrams are consistent with Figure 2.12. In the case of liquid crystal composites, a complicated factor is the strong anisotropy in the shape of the components. More recently, Schmidt *et al.* have presented a geometry-based DFT to describe ternary mixtures of hard colloidal spheres, ideal polymer spheres, and rigid rods [87]. Ginzburg *et al.* have combined a DFT with a self-consistent field model to calculate the phase behavior of thin, oblate colloidal particles that are coated with surfactants and dispersed in a polymer melt [88].

### 2.3.7
### Conformation of a Polymer Dissolved in a Liquid Crystalline Phase

The conformational properties of a polymer dissolved in a liquid crystalline phase depend on many factors, including polymer concentration, polymer stiffness, and solvent quality. When flexible polymers are added into a nematic phase, the polymers are expelled from the nematic phase and isotropic droplets are dispersed in the nematic matrix. With time these droplets coalesce and the nematic–isotropic phase separation takes place. When the polymer concentration is extremely dilute, the system shows a stable nematic phase consisting of almost pure nematogens (Figure 2.7). In the nematic phase, a flexible polymer shows weak anisotropy in the conformation due to weak coupling between the polymer and the local orientational order [43]. In contrast, liquid crystalline polymers, or stiff polymers, have good miscibility with nematogens due to the strong anisotropic coupling between the polymer and nematogen. Even in case of a flexible polymer, it may be possible that the partial orientational ordering of the polymer in a nematic solvent can give rise to an induced-nematic phase [89]. It has been recognized that a smectic phase can be induced in a nematic liquid crystal mixture by strong mesogenic interactions [71, 76, 90]. Phase separations strongly depend on the conformations of a polymer. In the nematic solvents, long liquid crystalline polymers align along the nematic director to give a much greater degree of translational order. These anisotropic conformations have been inferred from small-angle neutron scattering [91, 92] and viscosity measurements [93] and have been directly measured using single molecular spectroscopy [94].

Figure 2.20 shows images of fluorescently labeled biopolymers in an isotopic solvent (left) and a nematic solvent (right) of fd virus [94]; Figure 2.20a–d shows, respectively, the images of actin, wormlike micelles, neurofilaments, and DNA. In Figure 2.20a–c, the biopolymers are highly elongated, having a rod-like shape in the nematic phase of fd. By contrast, the polymers in an isotropic phase crumple into compact random coils. Just above the NIT, actin filaments and wormlike micelles form hairpin defects [95–97]. DNA dissolved in the nematic phase behaves qualitatively differently (Figure 2.20d): it forms a slightly anisotropic droplet. Each droplet contains many DNA molecules and, with time, these droplets coalesce into large droplets. These observations suggest that the persistence length $l_p$ of the polymer is

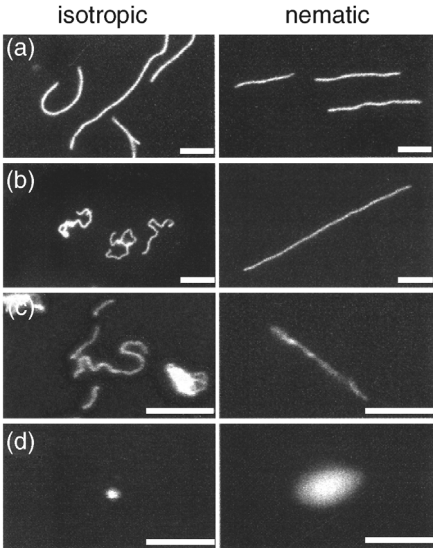


**Figure 2.20** Images of fluorescently labeled biopolymers in an isotropic solvent (left) and a nematic solvent (right) of fd virus [94]. Images (a)–(d) are, respectively, of actin, wormlike micelles, neurofilaments and DNA [94]. Scale bar is 5 μm. Reprinted with permission from Reference [94]. Copyright (2004) American Physical Society.

important in determining its solubility in the nematic phase. DNA has small $l_p$ and is insoluble and then we have nematic–isotopic phase separations (Section 2.2.3). Polymers with a large persistence length undergo a coil–rod transition at the NIT of a solvent molecule. Theoretically, Wang and Warner [98] have investigated the anisotropic conformations of liquid crystalline polymers dissolved in an isotopic solvent, which shows either rod-like or random walk behavior. In a nematic solvent, a discontinuous phase transition from a condensed-rod-like conformation to a swollen one of a polymer chain has been predicted, depending on the stiffness of the polymer [99], although this has not been experimentally observed, yet.

The conformation of rod-like polymer chains dissolved in a smectic phase has also been observed. Link *et al.* examined the effect of smectic solvation on the properties of polymer chains using single molecule spectroscopy of the rod-like polymer poly(2-methoxy-5- 2°-ethylhexyloxy -*p*-phenylene vinylene) (MEH-PPV) dissolved in the smectic phase of 8CB [100]. 8CB is a good solvent for this polymer. Figure 2.21 shows $P$ histograms for MEH-PPV in the nematic (left) and smectic (right) phase of 8CB as well as two typical fluorescence intensities (insets). The sign of $P$ expresses the relative orientation of the main polymer axis: positive values indicate parallel alignment of the polymer chain and negative values show perpendicular alignment. For the nematic phase, all polymer chains are aligned parallel to the director. For the smectic phase, two orthogonal polymer orientations are observed, as indicated by the reversal of intensity ratios for different fluorescent bursts and the appearance of an additional broad distribution in the $P$ histogram peaked at negative $P$ values

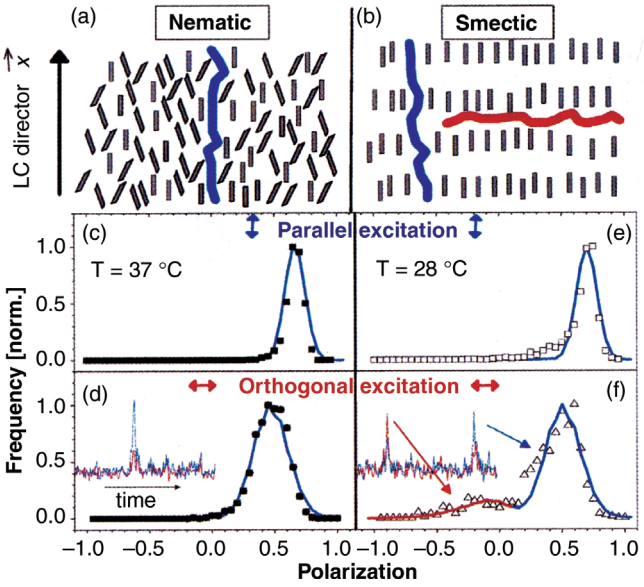


**Figure 2.21** Orthogonal orientations for solvation of a rod-like polymer(MEH-PPV) in a smectic liquid crystal (8CB). Schematic illustration of the nematic (a) and ideal smectic (b) phase; *P* histograms measured with excitation polarized parallel – (c), (e) – and orthogonal – (d), (f) – to the director [100]. Reprinted with permission from Reference [100]. Copyright (2006) American Physical Society.

(Figure 2.21f). The perpendicularly aligned polymer chains occupy the gaps between the smectic layers. The corresponding *P* histogram shows that a small fraction ($\sim$ 10%) of polymer chains is aligned perpendicular with a large degree of disorder. The experimentally observed perpendicular alignment of MEH-PPV implies that the presence of polymers stabilizes the smectic layers at a larger separation than in neat 8CB.

## 2.4 Phase Separation Dynamics

A homogeneous mixture quenched from a stable phase into a thermodynamically unstable state within a phase diagram develops into an inhomogeneous system. Spinodal decomposition (SD) is induced by the instability of an order parameter, which is usually concentration [101]. In the early stages, the SD is interpreted within the framework of the Cahn theory for an isotropic SD [102, 103]. In contrast, in the late stages, the SD is governed by diffusion or hydrodynamic processes and exhibits slow coarsening [104]. There are two types of order parameters that describe a system. One is a conserved order parameter such as concentration of binary mixtures. The other is a non-conserved order parameter such as the polarization of a ferroelectric

solid and the orientational order of a nematic phase. In polymer and liquid crystal mixtures, we can expect co-occurrences between phase separation and liquid crystalline ordering. Such inhomogeneous mixtures, consisting of one conserved order parameter (concentration) and one non-conserved order parameter (orientation), are important for not only fundamental scientific reasons but also technological applications.

For practical use of PDLC, dispersions are mainly prepared by mixing a small amount of miscible monomers with liquid crystals and photo-polymerizing [1], since polymer and liquid crystals tend to be immiscible. As the polymerization evolves, the system undergoes phase separations into a liquid crystalline phase rich in liquid crystals and an isotropic phase rich in polymers. Before the system reaches equilibrium states, however, the polymerization freezes the system into a crosslinked network of polymer-rich domains. Then, the morphologies of the PDLC involve interplay among three kinetic processes: polymerization, phase separation, and phase ordering. These phase separation dynamics have been simulated by some authors [105–108].

In this section, we focus on the interplay between phase separations and phase ordering kinetics in mixtures of a flexible polymer and a liquid crystal (nematogen). When the system is thermally quenched from a stable isotropic phase into an unstable part of the biphasic region, the fluctuations of concentration and orientation take place and isotropic or nematic droplets appear with time [109, 110]. The instability of these systems is driven by the competition between phase separation and nematic ordering. Figure 2.22 shows the phase diagram of the polymer/liquid crystal mixture with $n_p = n_r = 2$ and $\alpha = 1.4$. The solid curve refers to the binodal and the dotted line shows the first-order NIT. The dash-dotted line shows the spinodal. The arrows indicate temperature quenches from a stable isotropic phase

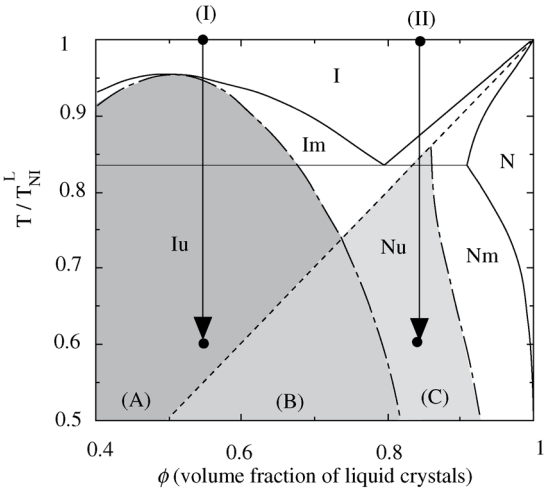


**Figure 2.22** Phase diagram of a polymer/liquid crystal mixture with $n_p = n_r = 2$ and $\alpha = 1.4$. The arrows indicate temperature quenches from a stable isotropic phase into an unstable region.

into an unstable region. In the biphasic region between the nematic and the isotropic phases, we have two different metastable regions: Im and Nm, and two unstable regions: Iu and Nu, discussed in Figure 2.10. The region (A), lying below the isotropic spinodal curve and above the NIT line, corresponds to a system that is initially unstable with respect to concentration fluctuations, but metastable to orientation fluctuations: $(\partial^2 f/\partial\phi^2)_T < 0$ and $(\partial^2 f/\partial S^2)_T > 0$, where we define $f \equiv \beta\Delta F/N_t$ in Eq. (2.47) and $\phi$ is the volume fraction of a nematogen. The region (B), between the isotropic spinodal curve and the NIT line, is initially unstable to both concentration and orientation fluctuations: $(\partial^2 f/\partial\phi^2)_T < 0$ and $(\partial^2 f/\partial S^2)_T < 0$. In region (C), between the isotropic spinodal curve and the nematic spinodal curve, the system is initially unstable with respect to orientation fluctuations but metastable to concentration fluctuations: $(\partial^2 f/\partial\phi^2)_T > 0$ and $(\partial^2 f/\partial S^2)_T < 0$. Thus, if we thermally quench from an isotropic phase to these different regions, we can expect a variety of SD processes even in the early stages.

### 2.4.1 Kinetic Equations

To elucidate the time evolution of the concentration and orientation fluctuations during a SD, we introduce kinetic equations based on the time-dependent Landau–Ginzburg (TDLG) equations for concentration and orientational order parameters.

We consider mixtures of a flexible polymer and a nematogen described by one conserved order parameter (volume fraction $\phi$ of a nematogen) and one non-conserved order parameter (orientational order parameter of a nematogen). Since the orientational order parameter is a traceless symmetric tensor, its components can be expressed as [14]:

$$S_{ij} = \tfrac{3}{2}S(\boldsymbol{r})\left[n_i(\boldsymbol{r})n_j(\boldsymbol{r}) - \tfrac{1}{3}\delta_{ij}\right] \tag{2.76}$$

where

$i, j = x, y, z$ denote the components along three orthogonal coordinate axes,
$\boldsymbol{n}(\boldsymbol{r})$ is a local director,
$\delta_{ij}$ is the Kronecker $\delta$ function,
$S(\boldsymbol{r})$ is the scalar orientational order parameter at a position $\boldsymbol{r}$.

The dynamics of the mixture are described by the coupled TDLG equations for the two order parameters [111, 112]. In inhomogeneous systems under non-equilibrium conditions, spatial variations occur in the two order parameters. The total free energy $(F)$ can be expressed in terms of a local bulk free energy density $f(\phi, S_{ij})$ and the gradients of the two order parameters [111, 113, 114]:

$$F[\phi, S_{ij}] = \int \mathrm{d}r\left[f(\phi, S_{ij}) + \frac{K_0}{2}(\nabla\phi)^2 + L_0(\partial_i\phi)(\partial_j S_{ij}) + \frac{L_1}{2}(\partial_k S_{ij})^2 + \frac{L_2}{2}(\partial_i S_{ik})(\partial_j S_{jk})\right] \tag{2.77}$$

where the free energy $F$ and $f$ are dimensionless quantities (divided by $k_B T$), and $K_0$, $L_0$, $L_1$, $L_2$ are phenomenological coefficients. The coefficient $K_0$ corresponds to

interfacial tension [101], $L_1$ and $L_2$ are related to the Frank elastic constants [14], and $L_0$ is the anchoring strength of nematogens at a NI interface [112]. These coefficients have been derived from a dynamical mean field theory as a function of composition and temperature [112, 115–117]. We here take these coefficients as constant. The indices $i$, $j$, and $k$ are summed over the appropriate number of dimensions and $\partial_i$ shows the vector operator. Using Eq. (2.76), the bulk free energy density [Eq. (2.47)] can be given by [113]:

$$\begin{aligned} f(\phi, S_{ij}) &= \frac{1-\phi}{n_{\mathrm{p}}}\ln(1-\phi)+\frac{\phi}{n_{\mathrm{r}}}\ln\phi+\chi\phi(1-\phi)+\tfrac{1}{2}A(\phi)S_{ij}S_{ji} \\ &\quad -\tfrac{1}{3}B(\phi)S_{ij}S_{jk}S_{ki}+\tfrac{1}{4}C(\phi)(S_{ij}S_{ji})^2 \end{aligned} \tag{2.78}$$

where:

$$A(\phi)=\tfrac{3}{2}\left(1-\tfrac{\xi}{3}\right)\chi_{\mathrm{a}}\phi^2 \tag{2.79}$$

$$B(\phi)=\tfrac{4}{15}\xi\chi_{\mathrm{a}}\phi^2 \tag{2.80}$$

$$C(\phi)=\tfrac{1}{27}\xi\chi_{\mathrm{a}}\phi^2 \tag{2.81}$$

$\xi \equiv n_{\mathrm{r}}\chi_{\mathrm{a}}\phi$, and we here used the nematic free energy [Eq. (2.66)], expressed by the tensor order parameter $S_{ij}$.

In considering the non-equilibrium equations of motion for our system, we adopt a thermodynamic point of view. For simplicity, we neglect hydrodynamic flows. The phenomenological equation of motion for the concentration $\phi$, which ensures local conservation of material, is given by [101]:

$$\begin{aligned} \frac{\partial\phi(\boldsymbol{r},t)}{\partial t} &= \Gamma_{\phi\phi}\nabla^2\left(\frac{\delta F}{\delta\phi}\right) \\ &= \Gamma_{\phi\phi}\nabla^2\left[\frac{\partial f}{\partial\phi}-K_0\nabla^2\phi-L_0\partial_i\partial_j S_{ij}\right] \end{aligned} \tag{2.82}$$

where the thermodynamic force that drives the flux is given by the gradient of the chemical potential $\mu = \delta F/\delta\phi$ and $\Gamma_{\phi\phi}$ is the mobility, assumed constant. On the other hand, for the non-conserved order parameter $S_{ij}$, we take the local rate of change to be linearly proportional to the local thermodynamic force $\partial F/\partial S_{ij}$. The equation of motion for $S_{ij}$ is then given by:

$$\begin{aligned} \frac{\partial S_{ij}(\boldsymbol{r},t)}{\partial t} &= -\Gamma_{\mathrm{SS}}\left(\frac{\delta F}{\delta S_{ij}}+\Lambda(\boldsymbol{r},t)\delta_{ij}\right) \\ &= -\Gamma_{\mathrm{SS}}\left[\frac{\partial f}{\partial S_{ij}}-L_0\partial_i\partial_j\phi-L_1\nabla^2 S_{ij}\right. \\ &\quad \left.-\frac{L_2}{2}(\partial_i\partial_k S_{kj}+\partial_j\partial_k S_{ki})+\Lambda(\boldsymbol{r},t)\delta_{ij}\right] \end{aligned} \tag{2.83}$$

where the transport coefficient $\Gamma_{SS}$ is taken as constant . The kinetic equations could in principle be made more general, by writing the Onsager coefficient $\Gamma_{ij}$ as a matrix. This would allow one order parameter to be driven by gradients in the chemical potential of the other. Fukuda has derived the coefficients as a function of concentration and the molecular length and obtained the kinetic equations by taking into account the off-diagonal kinetic coefficient $\Gamma_{\phi S}$ [115–117]. Here we set the off-diagonal matrix elements to zero, for simplicity. The Lagrange multiplier $\Lambda$ in Eq. (2.83) will be chosen to ensure conservation of the trace of $S_{ij}$. The kinetic equations can be applicable to study binary nematic liquid crystal mixtures [118]. Casagrande *et al.* have studied experimentally the dynamics of a nematic–nematic phase separations [109].

### 2.4.2
### Linearized Analysis of Spinodal Decomposition

We consider here the linearized analysis of the kinetic equations and define variables $\delta\phi(\boldsymbol{r},t) = \phi(\boldsymbol{r},t) - \phi_0$ and $\delta S_{ij}(\boldsymbol{r},t) = S_{ij}(\boldsymbol{r},t) - S_{ij,0}$, where $\phi_0$ and $S_{ij,0}(=0)$ are the values of concentration and orientation in the initial homogeneous (isotropic) system, respectively. Since the initial state is isotropic, the response must be independent of a direction $q_i$ and so we can define a $z$ axis to be oriented along the wavenumber $q$: $q_i = q\delta_{iz}$. In the Fourier representation, the differential Equations (2.82) and (2.83) can be solved as [113]:

$$\delta\phi(q,t) = u_1(q)\exp[\omega_1(q)t] + u_2\exp[\omega_2(q)t] \tag{2.84}$$

$$\delta S_{zz}(q,t) = u_3(q)\exp[\omega_1(q)t] + u_4\exp[\omega_2(q)t] \tag{2.85}$$

where the growth rates $\omega_1$ and $\omega_2$ are given by:

$$\omega_1(q) = \tfrac{1}{2}\left[-a(q) - c(q) + \sqrt{(c(q)-a(q))^2 + 4b(q)d(q)}\right] \tag{2.86}$$

$$\omega_2(q) = \tfrac{1}{2}\left[-a(q) - c(q) - \sqrt{[c(q)-a(q)]^2 + 4b(q)d(q)}\right] \tag{2.87}$$

and the four coefficients $u_1$, $u_2$, $u_3$, and $u_4$ are given as a function of wavenumber $q$. The functions $a(q)$, $b(q)$, $c(q)$, and $d(q)$ are given by:

$$a(q) = \Gamma_{\phi\phi}(f_{\phi\phi} + K_0 q^2)q^2 \tag{2.88}$$

$$b(q) = \Gamma_{\phi\phi}L_0 q^4 \tag{2.89}$$

$$c(q) = \Gamma_{SS}\left[f_{SS} + \left(L_1 + \tfrac{2}{3}L_2\right)q^2\right] \tag{2.90}$$

$$d(q) = \tfrac{2}{3}\Gamma_{SS}L_0 q^2 \tag{2.91}$$

where the required derivatives $f_{\phi\phi}$ and $f_{SS}$ mean the second derivative of the bulk free energy $f$ with respect to $\phi$ and $S$, respectively.

These results can be used to calculate the time evolution of structure factors as measured by small-angle light scattering or X-ray scattering. The structure factor for concentration is defined by:

$$S_\phi(q,t) \equiv \langle |\delta\phi(q,t)|^2 \rangle \tag{2.92}$$

and that for the component $S_{zz}$ of the orientational order parameter is given by:

$$S_S(q,t) \equiv \langle |\delta S_{zz}(q,t)|^2 \rangle \tag{2.93}$$

We first consider the behavior of the SD with $L_0 = 0$ in Eq. (2.77). When $L_0 = 0$, we obtain $b(q) = d(q) = 0$ and then the kinetic equations (2.82) and (2.83) have no cross term between the gradients of the concentration and orientation order parameters. Such behaviors of SD in PDLC have been discussed theoretically [73, 119–122]. The time evolution of the structure factor for the concentration fluctuations falls into the Cahn–Hilliard classical category [102, 103] and Eq. (2.84) results in the Cahn theory of SD for isotropic solutions. The structure factor for concentration in Eq. (2.92) is given by:

$$\langle |\delta\phi(q,t)|^2 \rangle = \langle |\delta\phi(q,0)|^2 \rangle \exp[-2a(q)t] \tag{2.94}$$

When $f_{\phi\phi} > 0$, from Eq. (2.88), the amplitude of any concentration fluctuation decreases with time because $a(q) > 0$ and so the system is stable. If $f_{\phi\phi} < 0$, concentration fluctuations are unstable for the wave vector in the range $0 < q < q_0 = (-f_{\phi\phi}/K_0)^{1/2}$ and the amplitude of the corresponding modes grows exponentially with time. The structure factor $S_\phi$ has a maximum at $q = q_m (= q_0/\sqrt{2})$ and vanishes at all times for $q = 0$ because the concentration is conserved: $\int \delta\phi(r) \mathrm{d}r = 0$. Shimada *et al.* have discussed the dynamics of the formation of liquid crystalline phase of rod-like polymer solutions by using kinetic equations of distribution function of polymer segments for dilute isotopic phases [123]; they found that the growth rates of concentration fluctuation are governed by the translational motion, not the orientational motion in this SD region.

On the other hand, the structure factor $S_{zz}$ in Eq. (2.85) is given by:

$$\langle |\delta S_{zz}(q,t)|^2 \rangle = \langle |\delta S_{zz}(q,0)|^2 \rangle \exp[-2c(q)t] \tag{2.95}$$

The eigenvalue $c(q)$ is nonzero at $q = 0$ because the orientational order parameter $S$ is not conserved. When $f_{SS} > 0$, from Eq. (2.90), the amplitude of any orientation fluctuation decreases with time because $c(q) > 0$ and the system is stable. If $f_{SS} < 0$ orientation fluctuations are unstable for the wavenumber in the range $0 < q < q_1 = [-f_{SS}/(L_1 + 2L_2/3)]^{1/2}$ and the amplitudes of the corresponding modes grow exponentially with time. The structure factor $S_S$ decreases with increasing $q$ because the amplitude $c(q)$ monotonically increases with increasing $q$ [121]. The orientation fluctuation with $q = 0$ corresponds to a macroscopic fluctuation of an orientational order parameter throughout the system.

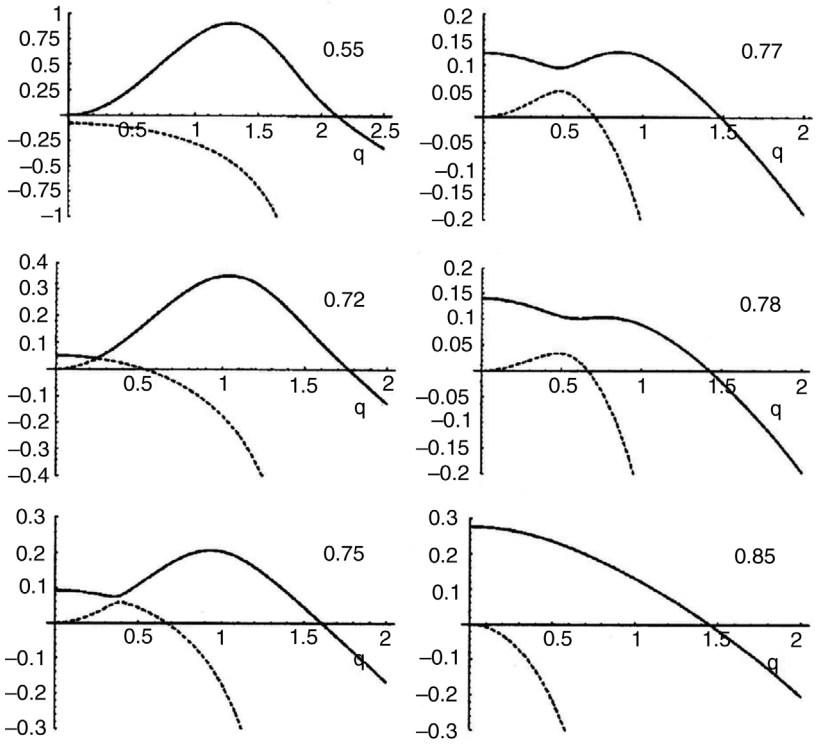


**Figure 2.23** Two growth rates, $\omega_1(q)$ (solid line) and $\omega_2(q)$ (dotted line), are shown against the wavenumber $q$. Concentration $\phi_0$ of the liquid crystal is varied with fixed temperature $T/T_{NI}^L = 0.6$ [113]. Reprinted with permission from Reference [113]. Copyright (2000) American Physical Society.

When $L_0$ has nonzero values, we have a coupling between concentration and orientation. This cross term plays a significant role in phase separation kinetics of solutions containing liquid crystals or liquid crystalline polymers [112, 113, 116]. The structure factors are affected by this cross term even in the linear regime of the SD.

Figure 2.23 shows two growth rates, $\omega_1(q)$ (solid line) and $\omega_2(q)$ (dotted line), of Eqs. (2.86) and (2.87). The initial concentration $\phi_0$ of the liquid crystal is varied with fixed temperature $T/T_{NI}^L = 0.6$. The parameters used are $\Gamma_{\phi\phi} = \Gamma_{SS} = 1$, $K_0 = 0.4$, $L_0 = 0.2$, and $L_1 = L_2 = 0.1$ in this example. When $\phi_0 = 0.55$ in the Iu region (A) in Figure 2.22, the growth rate $\omega_1(q)$ has positive values in the range $0 < q < q_0 (= 2.21)$ and has a maximum at $q_m = 1.3$. This maximum is driven by the instability of the concentration fluctuation: $f_{\phi\phi} < 0$. The other eigenvalue $\omega_2(q)$ has negative values for all $q$ because $f_{SS} > 0$. On increasing the concentration, the growth rate $\omega_1(q)$ has two peaks. One is at $q = 0$, which is induced by the instability of the orientation fluctuations $f_{SS} < 0$ and the other is at $q_m$, which is driven by the instability of the concentration fluctuation $f_{\phi\phi} < 0$. The hybridization of eigenvalues appears at around $\phi_0 = 0.72$. On further increasing the concentration, the value of the peak

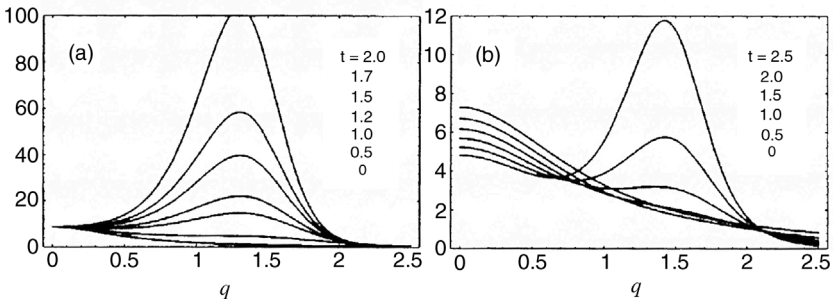


**Figure 2.24** Temporal evolution of the compositional structure factor $S_\phi$ (a) and the orientational structure factor $S_S$ (b) for the temperature quench into Iu region ($T/T_{NI}^{L} = 0.6$, $\phi_0 = 0.55$ in Figure 2.22) [113]. Reprinted with permission from Reference [113]. Copyright (2000) American Physical Society.

at $q = 0$ becomes larger than that at $q_m$. In the Nu region (C) ($\phi_0 = 0.85$) in Figure 2.22, in which the system is outside the isotropic spinodal curve ($f_{SS} < 0$, $f_{\phi\phi} > 0$), the growth rate $\omega_1(q)$ decreases with increasing $q$.

Figure 2.24 shows the temporal evolution of the compositional structure factor $S_\phi$ (a) and the orientational structure factor $S_S$ (b) for the temperature quench into the Iu region ($T/T_{NI} = 0.6$, $\phi_0 = 0.55$) in Figure 2.22. The structure factor for concentration has a maximum at $q_m$, which corresponds to the peak wavenumber of $\omega_1(q)$. With time the corresponding mode grows exponentially and the peak position $q_m$ is invariant. Then the time evolution of the structure factor $S_\phi$ is the same as that of the Cahn–Hilliard theory for isotropic SD [102]. The amplitude of the peak at $q = 0$ decreases with time because $f_{SS} > 0$ and another peak appears at $q_m$. In this quench, the concentration fluctuation initially induces the SD and the orientational ordering within the domain subsequently takes place due to the coupling between the two order parameters: *concentration-induced SD*.

Figure 2.25 shows the temporal evolution of the compositional structure factor $S_\phi$ (a) and of the orientational structure factor $S_S$ (b) for the temperature quench into Nu region ($T/T_{NI} = 0.6$, $\phi_0 = 0.85$) in Figure 2.22. In the very early stages, the concentration fluctuation becomes weak with time because $f_{\phi\phi} > 0$. However, the orientational fluctuations grow exponentially with time because $f_{SS} < 0$. On further increasing time, a peak in $S_\phi$ appears and shifts to lower wavenumbers. There is no longer any time stage in which the peak position in $S_\phi$ is invariant. The instability of the orientation fluctuation induces the SD and the concentration fluctuation is induced by the coupling between two order parameters: *orientation-induced SD*. The time dependence of the average domain size is given by:

$$R = 2\pi/q_m \sim t^\nu \tag{2.96}$$

where the exponent $\nu$ changes with increasing time even in the early stage of SD. The kinetic exponent ($\nu$) has been predicted by various authors for the late stage of SD in binary mixtures of isotropic fluids. The most common value is $\nu = \frac{1}{3}$ [124, 125]. Siggia [126] has obtained an exponent $\nu = \frac{1}{3}$ for the intermediate stage of SD and

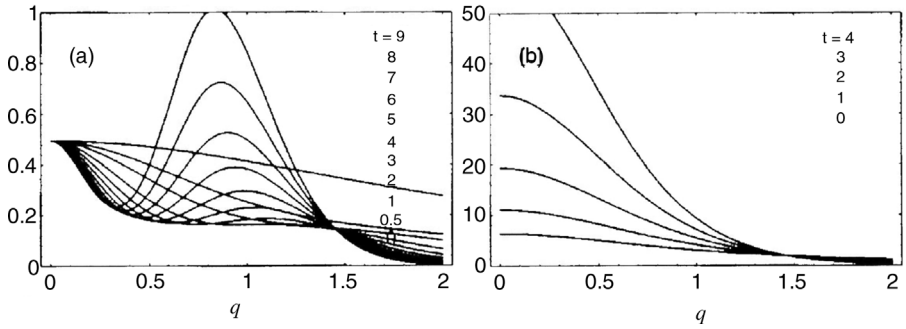


**Figure 2.25** Temporal evolution of the compositional structure factor $S_\phi$ (a) and the orientational structure factor $S_S$ (b) for the temperature quench into Nu region ($T/T_{NI}^L = 0.6$, $\phi_0 = 0.85$ in Figure 2.22) [113]. Reprinted with permission from Reference [113]. Copyright (2000) American Physical Society.

$\nu = 1$ at the late stage where the hydrodynamic flow becomes dominant. Graca *et al.* [127] have observed the growth of polymer domains in the isotropic, nematic, and smectic matrices by the light scattering. In the smectic and isotropic matrices, the growth is diffusive with the exponent $\nu \approx 0.3$ and has a crossover to the hydrodynamic fast-mode growth of the exponent $\nu \approx 1$ with time. In the nematic matrix, it is influenced by the elastic forces. Figure 2.25 means that the SD is advanced by the instability of the orientational ordering and no longer follows Cahn's linear analysis that predicts no shift in the peak $S_\phi$ in the early stages. On increasing the concentration of the liquid crystals, the behavior of the SD is changed from the concentration fluctuation- to orientation fluctuation-induced SD. The cross term $L_0$ between concentration- and orientation-gradients plays a significant role in the early stage SD.

Dhont and Briels have analyzed the initial stage of isotropic–nematic SD on the basis of the Smoluchowski equation for the probability function of the position and orientation of a repulsive rod [128]. They found that demixing due to rotational diffusion is shown to be much faster than translational diffusion and the wave vector where the scattered intensity exhibits a maximum is to be a function of time even during the initial stage of SD. The scattered intensity during demixing by the unstable orientational order parameter is proportional to $\propto \exp[-\lambda^{(-)}t]$ and the eigenvalue related to the unstable mode is given by [128, 129]:

$$\lambda^{(-)} = 6D_r\left(1-\frac{L}{4D\phi}\left[1-\frac{499}{8064}(qL)^2\right]\right) \tag{2.97}$$

where $D_r$ is the rotational diffusion coefficient of a non-interacting rod. When $L/D\phi > 4$, this eigenvalue is negative for small wave vectors and so inhomogeneities with the corresponding wavelength $2\pi/q$ grow in time without any time delay. This concentration marks the location of the nematic spinodal (Nu) regions.

Some experiments have reported such growth of the domain in the early stages [110, 130]. Takenaka *et al.* [131] have investigated the phase separation

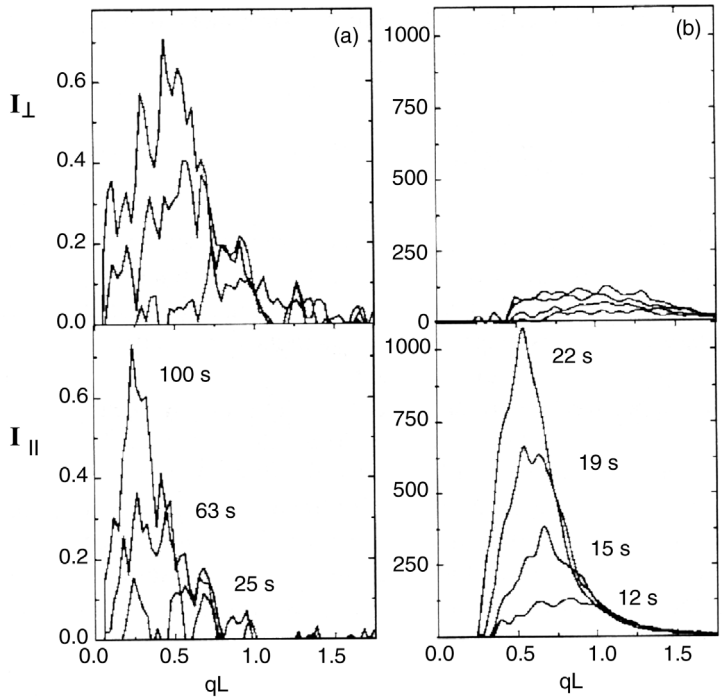


**Figure 2.26** Cross sections of the Fourier transforms of the confocal images parallel and perpendicular to the director for a fd virus concentration of $\phi = 0.52$ (a), and the parallel and perpendicular cross sections of the scattering intensity as found from SALS (b). The wave vector is scaled by the length $L$ of the fd virus and the intensities are given in arbitrary units [129]. Reprinted with permission from Reference [129]. Copyright (2006) American Physical Society.

dynamics of PS/8CB mixtures with small-angle X-ray scattering and presented experimental evidence for the existence of concentration fluctuations induced by orientational fluctuations. More recently, Lettinga *et al.* [129] have presented experimental evidence in a nematic dispersion of rod-like fd viruses that SD is driven by orientation, and found the same $q$ dependence of the growth rate, $\omega_1$, discussed in this section. Figure 2.26 shows cross sections of the Fourier transforms of the confocal images (a) and small-angle light scattering (SALS) patterns (b) parallel and perpendicular to the nematic director. From this figure, we can obtain the wave vector $q_m$ at which the Fourier transform exhibits its maximum, which shows the wavelength of the fastest growing Fourier component of the inhomogeneous morphology. The authors examined the fundamental difference between spinodal decomposition of dispersions of rods and spheres. In the case of rods, the phase separation is dominated by rotational diffusion. As a result the eigenvalue, which quantifies the rate of the phase separation, approaches a nonzero value for $q \to 0$, which is contrary to liquid–liquid phase separations of spherical molecules where the corresponding

eigenvalue becomes zero for $q \to 0$ (Figure 2.23). They also found a minimum in the eigenvalue $\lambda^{(-)}$ as a function of the wave vector. This minimum corresponds to the maximum in Figure 2.23 at high concentration of liquid crystals, or rods. They suggested that the minimum in $\lambda^{(-)}$ is related to the attractive (depletion) interaction between rods induced by adding dextran.

### 2.4.3 Morphologies

When the system is thermally quenched from a stable isotropic phase into an unstable part of the biphasic region in Figure 2.22, the interplay between concentration and orientation fluctuations can lead to very different morphologies. Such morphologies depend on non-equilibrium processes of phase separations. Liu and Fredrickson have suggested that, because of the presence of orientational order, the composition pattern that results from spinodal decomposition can be quite different from the ordinary isotropic case [112]. For instance, even if the concentration of liquid crystals is high, liquid crystal-rich droplets are formed in a polymer-rich isotropic matrix [132, 133]. Figure 2.27 shows a typical optical microscopy image of the polymer poly(2-ethylhexyl acrylate) (PEHA) and the liquid crystal 5CB blend between crossed polarizers [133]. The texture corresponds to the sample prepared with 80 wt% of 5CB. The cross type pattern of the droplets is typical of a radial/axial structure, indicating that the director adopts a homeotropic anchoring at the polymer interface [refer to Eq. (2.99) and the References [134–136] for nematic director configurations].

To calculate morphologies of phase separation of PDLCs, many simulation methods have been developed [137]. Zhu *et al.* [138] have performed a Monte Carlo simulation to investigate the phase behaviors of PDLC by using the Lebwohl–Lasher model for nematogens [139]. One of the methods is to numerically solve the

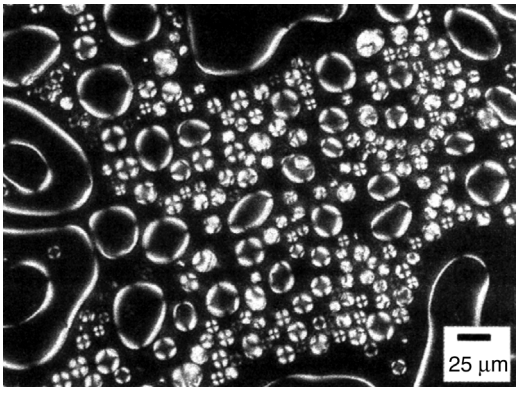


**Figure 2.27** Optical microscopy image of the polymer poly(2-ethylhexyl acrylate) PEHA and the liquid crystal 5CB blend between crossed polarizers. The cross type pattern of the droplets is typical of axial organization in a nematic microdomain [133]. Reprinted with permission from Reference [133]. Copyright (2002) American Physical Society.

kinetic equations. Lapena *et al.* have simulated nonlinear coupled differential equations (2.82) and (2.83) in two spatial dimensions with periodic boundary conditions [140] and found the following dynamics of SD. For the temperature quench into Iu region (A) in Figure 2.22, where the volume fraction of a polymer is slightly higher than that of a nematogen, we first observe the nematogen-rich spherical droplets immersed in a polymer-rich matrix. When the concentration of nematogens in the droplets exceeds the concentration of the NIT, the nematogens in the droplets begin to order. At this time, the droplets expel more polymers because the polymers are less soluble in the nematic phase. A pair of defects forms inside each droplet and separates. With time, the two defects move along the director in opposite directions towards the edges of the droplet, to lower the elastic free energy. Figure 2.28 shows a snapshot of the local composition at a late stage. Black corresponds to pure polymers and white shows pure liquid crystals. The arrows represent the local nematic director (shown for two droplets only). The nematic droplets show an anisotropic shape due to the elastic energy of nematic director. The morphology in Figure 2.28 is consistent with Figure 2.27, except for the concentration of liquid crystals.

Figure 2.29 shows snapshots of local composition as a function of time for the temperature quench into the region (B) in Figure 2.22. In the early stages, small highly ordered nematogen-rich droplets form in a polymer-rich matrix. With time, these nematogen-rich droplets grow and the surrounding polymer-rich region shrinks into a fibrillar network of interconnected domains, even though the polymer-rich phase is the minority phase. This is in contrast to systems with one

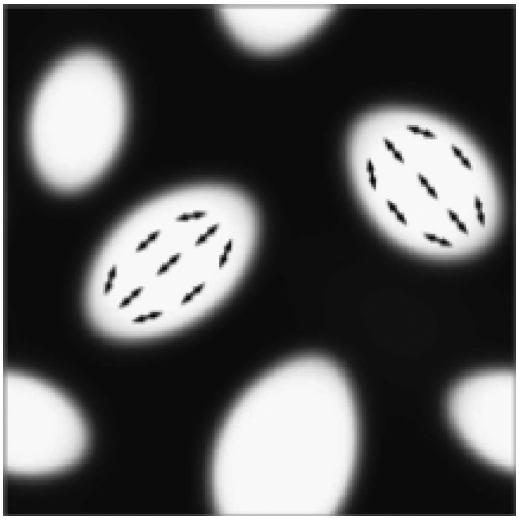

**Figure 2.28** Late-time snapshot of the local composition when quenched into region (A) in Figure 2.22. Black corresponds to pure polymers and white to pure liquid crystals. The arrows represent the local nematic director (shown for two droplets only) [140]. Reprinted with permission from Reference [140]. Copyright (1999) American Physical Society.

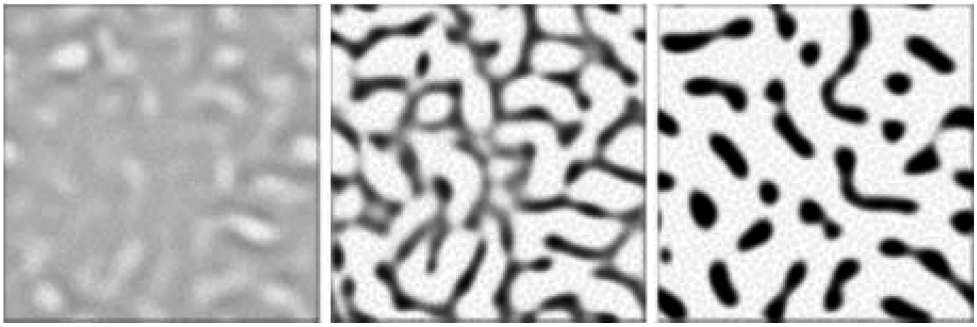

**Figure 2.29** Snapshots of local composition as a function of time when quenched into region (B) in Figure 2.22. Black corresponds to pure polymers while white corresponds to pure rods. Note that ordering drives the system to a fibrillar network morphology of polymer-rich domains at intermediate times [140]. Reprinted with permission from Reference [140]. Copyright (1999) American Physical Society.

compositional order parameter (model B) [141], where the majority phase can form networks. At the late stage, this network breaks up to form polymer-rich noncircular droplets because of defects in the surrounding nematogen-rich matrix. In the experiments, however, the fibrillar network may arrest phase separations due to the viscoelastic effects [142]. Nakazawa *et al.* [143] have studied polymerization-induced phase separations in PDLC by computer simulations in two dimensions, taking into account the viscoelastic effects. The viscoelastic effects and gelation enable the polymer-rich phase to form a stable interconnected domain when the polymer is the minor component. Even in the symmetric components $\phi = 0.5$, when the hydrodynamic flow sets in the kinetic equations, the bicontinuous structure transforms into a nematogen-rich droplet in a polymer-rich isotropic matrix [144].

Nakai *et al.* have observed the SD of 50/50 mixtures of X-7G liquid crystal and poly (ethylene terephthalate)(PET) by polarized light microscopy (PLM) [110]. They observed the following sequences as time evolutions: (i) the self-similar growth of a percolating network of the anisotropic liquid phase rich in X-7G in the isotropic matrix phase rich in PET, (ii) disruption of the percolating network and shrinkage of the disrupted fragments into the nematic droplets, and (iii) diffusion and coalescence of the anisotropic droplets. Figure 2.30 shows binarized PLM images in regime (ii) of the phase separation. The shaded and bright (unshaded) domains correspond to the anisotropic network or droplets, while the dark domains are the isotropic matrix. Here we focus on the time evolution of the bright domains. When $t = 270s$ (a), we have the typical bicontinuous domain structure, while (f) ($t = 600s$) shows the nematic droplet structure. The bright percolated network in parts (a)–(c) is divided into four nematic droplets, as designated by the numbers 1–4.

The director through a nematic–isotropic interface depends on the sign of the coefficient $L_0$ in Eq. (2.77). The cross term in Eq. (2.77) is given by:

$$L_0 \partial_i \phi \partial_j S_{ij} = L_0 (n_i n_j - \delta_{ij}/3) \partial_i \phi \partial_j S + L_0 S \partial_i \phi \partial_j (n_i n_j) \tag{2.98}$$

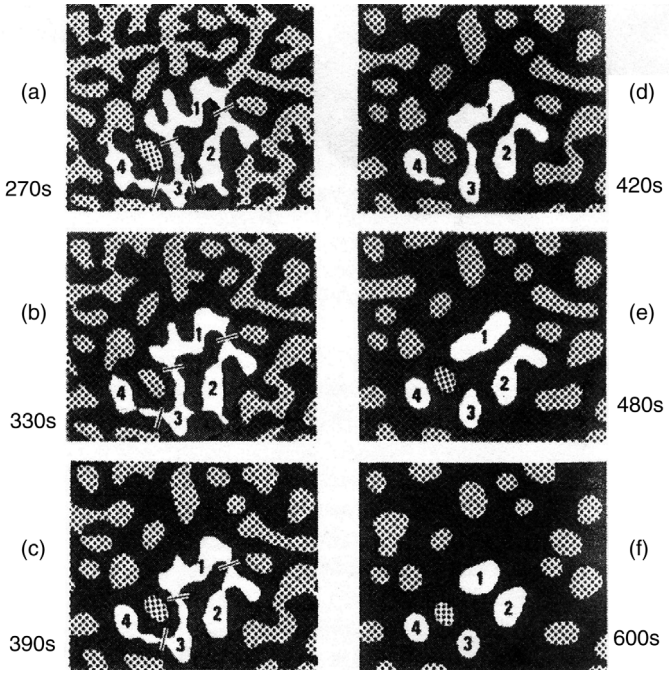


**Figure 2.30** Binarized PLM images obtained for an X-7G liquid crystal/PET polymer mixture. Shaded or bright domains correspond to the anisotropic networks or droplets rich in X-7G, while dark domains show the isotropic matrix rich in PET [110]. Note that the bright bicontinuous network in images (a)–(c) is divided into four nematic fragments, numbered 1–4. Reprinted with permission from Reference [110]. Copyright (1996) American Chemical Society.

Here we consider a two-dimensional system ($i, j = x, y$) for simplicity: $n_z = 0$, or the director is uniform along $z$ axis. Assuming the gradients change along the $x$ axis: $\partial_i = \delta_{ix}\partial_x$, and the director does not rotate: $\partial_i n = 0$. Then the cross term in Eq. (2.98) can be given by:

$$L_0 \partial_i \phi \partial_j S_{ij} = L_0 \left(n_x^2 - \tfrac{1}{3}\right) \partial_x \phi \partial_x S \tag{2.99}$$

where we have $\partial_x \phi \partial_x S > 0$ through a nematic–isotropic interface (note that $\phi$ shows the volume fraction of nematogens). The director at a nematic–isotropic (NI) interface depending on the sign of $L_0$ is shown in Figure 2.31. When $L_0 < 0$, the free energy is minimized when $n_x = 1$, $n_y = 0$. This corresponds to the director $n$ perpendicular to the interface ($y$ axis): homeotropic anchoring. On the other hand, when $L_0 > 0$, the cross term is minimized when $n_x = 0$, $n_y = 1$ and the director $n$ tends to align parallel to the interface ($y$ axis): planar anchoring. The value of $L_0$ corresponds to the strength of anchoring. Director fields in a nematic droplet also depend on the Frank elastic constants [37]. Das and Rey have simulated to resolve defect nucleation, defect–defect interactions, and defect–particle interactions, as well

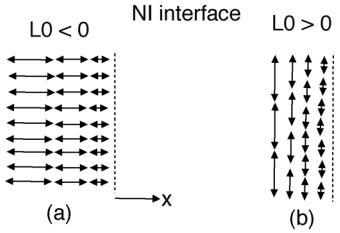


**Figure 2.31** Illustration of the spatial anisotropy of the local director at an NI interface for different values of $L_0$. The nematic phase is represented by double-headed arrows whose length is proportional to the magnitude of the local order. The right-hand side of the dotted line shows an isotropic phase. When $L_0 < 0$ (a) , the director $\boldsymbol{n}$ tends to align perpendicular to the interface ($y$ axis): homeotropic anchoring; when $L_0 > 0$ (b) , the director $\boldsymbol{n}$ tends to align parallel to the interface: planar anchoring.

as global and local morphological features in the concentration and order parameter spatiotemporal behavior [145–147], depending on the sign of $L_0$. They found that the positional order in the crystalline emulsion emerges from orientation-induced SD and the polymer-rich droplets are pinned by a random network of disclination lines.

Morphologies also depend on an external field $e_i$, such as a magnetic and electric field, which is coupled to the orientational order parameter as $-\zeta e_i e_j S_{ij}$, where $\zeta$ represents its susceptibility. Under strong anchoring conditions, a magnetic field leads to a director re-orientation [148] and induces stripe domains in phase separation accompanying orientational ordering [149]. Figure 2.32 shows simulated domain pattern evolution of symmetric mixture ($\phi = 0.5$) under an external field [149]. In the isotropic SD (a) [quenches into region (A) in Figure 2.22], phase separation proceeds

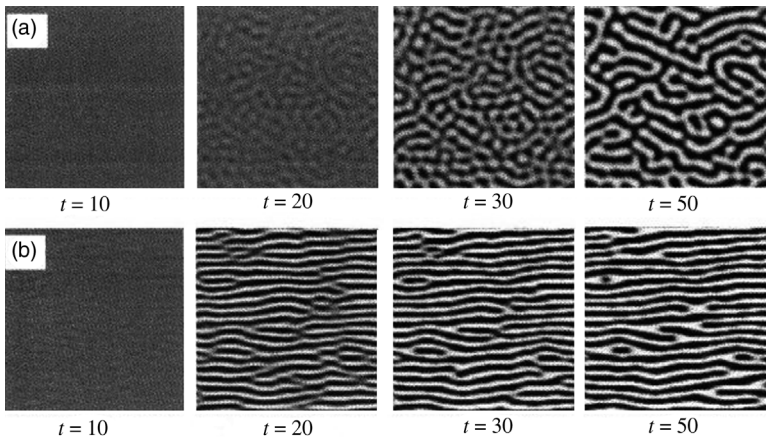


**Figure 2.32** Simulated domain pattern evolution of a symmetric mixture ($\phi = 0.5$) under an external field. White corresponds to nematogen-rich phases. Phase separation in (a) and (b) corresponds to temperature quench into regions (A) and (B) in Figure 2.22, respectively [149]. Reprinted with permission from Reference [149]. Copyright (2006) American Physical Society.

before nematic ordering and thus the isotropic domain pattern is formed. In the nematic SD (b) [quenches into region (B) in Figure 2.22], the nematic order develops before phase separation. The director field is aligned along the external field without interference from concentration fluctuations. Thus the anisotropic stripe pattern emerges from the nematic phase along the external field, as observed experimentally [109]. Essery and Ball have simulated to describe SD in a blend of liquid crystals or polymer solutions under an extensional flow and found the formation of a fibrillar or lamellar (stripe) structure, depending on the symmetry of the system [150]. Such stripe patterns can also be derived by taking into account the off-diagonal coefficient $\Lambda_{\phi S}$ of the kinetic equations in the morphology [115–117]. The phase ordering kinetics of PDLC confined between two parallel walls have also been studied numerically [151]. The ordering of nematogens is found to be accelerated as the separation distance between the walls decreases.

Hydrodynamic effects on phase separations and morphologies are also important [144, 152, 153]. Sulaiman *et al.* [153] have presented a lattice Boltzmann algorithm that includes hydrodynamics to describe the deformations of a drop of isotropic fluid immersed in a nematic liquid crystal solvent, both in the absence and in the presence of an external field. The equilibrium shape of the drop is affected by the elastic constant $K$ of a liquid crystal, the radius $R$ of a droplet, and the anchoring strength $W$ of the director at the surface of a droplet, and the surface tension $\sigma$. As $W/\sigma$, or $|L_0/K_0|$ increases, the anchoring energy dominates over the surface tension and the droplet distorts to more easily allow homeotropic anchoring at its surface.

These results show how the phase separation dynamics in polymer/liquid crystal mixtures are driven by the competition between phase separation and nematic ordering. The nematic ordering can significantly influence the domain morphology.

## 2.5 Summary

In this chapter we have reviewed the phase behavior and phase separation dynamics of blends of a flexible polymer and a rigid rod-like molecule. In Section 2.3, Onsager theory was extended to the blend systems with the incompressible condition, Eq. (2.44). As the result, the free energy for the isotropic mixing results in the Flory–Huggins theory. The mean field theory combining the Flory–Huggins free energy for the isotropic mixing and the Onsager–Maier–Saupe–McMillan model for liquid crystalline ordering can qualitatively describe the observed phase diagrams of polymer and liquid crystal blends. In Section 2.4, we introduced simple kinetic equations for phase separation dynamics and discussed SD and morphologies induced by concentration and orientation fluctuations. The nematic ordering can significantly influence domain morphologies and phase separation dynamics.

From a thermodynamic point of view, a blend of a flexible polymer and a rigid rod-like polymer exhibits less miscibility, because of the unfavorable low entropy of mixing of macromolecules even for athermal mixtures. Moreover, the phase separation is enhanced by the presence of liquid crystalline ordering. The affinity of two

components can be changed through specific intermolecular interactions such as hydrogen bonding and dipole–dipole interactions [154]. When flexible polymers are added into a solution of rigid rod-like molecules, various types of phase separations take place [155–157]. For example, the nematic–isotropic phase separation has been investigated in suspensions of tobacco mosaic virus by adding polymers such as poly (ethylene oxide) [158, 159]. This phase separation has been examined in terms of depletion interaction [160–162], which was not explained in this chapter.

The subject of this chapter will be useful in understanding the phase behavior of liquid crystalline composites such as mixtures of a liquid crystal and a surfactant molecule [163], a liquid crystal and a spherical colloid [164, 165], and a liquid crystal and a carbon nanotube [166, 167]. Volume phase transitions of a liquid crystalline gel immersed in a nematogen [168–172] are also closely related to the phase separations stated in this chapter, where the liquid crystalline ordering induces the volume change of the gel. Polymer–clay nanocomposites are a new class of organic–inorganic hybrid materials, which have good thermal stability in a liquid crystalline phase [173]. Holographic PDLCs [174] form one-, two-, and three-dimensional photonic crystal structures and have been proposed for use in various new devices [175]. The smectic blue phase of liquid crystal also presents interesting possibilities for new materials as polymer stabilized smectic blue phases [176, 177]. New blue phases are made from molecules in which two stiff, rod-like segments are linked by a flexible chain [178]. Studies of thermal stability in liquid crystalline composites, consisting of liquid crystalline molecules and other components, will be more important in not only fundamental fields but also in new technological applications.

## Symbols

| | |
|---|---|
| $a$ | length of a unit segment on a polymer chain |
| $an_{\mathrm{p}}$ | contour length of a polymer |
| $c_{\mathrm{i}} = N_i/V$ | number density of the particle $i$ |
| $D$ | diameter of a rod |
| $D_{\mathrm{r}}$ | rotational diffusion coefficient |
| $d$ | average distance between smectic layers |
| $F$ | Helmholtz free energy |
| $F_i(N_{\mathrm{p}}, 0), F_i(0, N_{\mathrm{r}})$ | reference free energy of the pure polymer and the pure rod |
| $F_{\mathrm{mix}}$ | isotropic mixing free energy |
| $F_{\mathrm{nem}}$ | free energy for nematic ordering |
| $F_{\mathrm{sm}}$ | free energy for smectic A ordering |
| $f(\boldsymbol{r},\boldsymbol{u})$ | distribution function |
| $f(\boldsymbol{r})$ | positional distribution function |
| $f(\boldsymbol{u})$, $f(\theta)$, $f(\Omega)$ | orientational distribution function |
| $f = v_{\mathrm{r}}\beta F/V$ | dimensionless free energy density |
| $f_{\mathrm{iso}}$ | free energy for an isotropic phase |
| $f_{\mathrm{nem}}$ | free energy for a nematic phase |

| | |
|---|---|
| $f_{\mathrm{p}}$ | free energy for a two-phase system |
| $f_{\phi\phi}, f_{SS}$ | second derivative of the bulk free energy $f$ with respect to $\varphi$ and $S$ |
| $K_0, L_0, L_1, L_2$ | phenomenological coefficients |
| $k_{\mathrm{B}}$ | Boltzmann constant |
| $L$ | length of a rod |
| $N_i$ | total number of polymers and rods ($i = \mathrm{p}, \mathrm{r}$) |
| $N_{\mathrm{t}}$ | total number of segments in the system |
| $\boldsymbol{n}$ | director |
| $n_{\mathrm{p}}$ | number of segments on a polymer |
| $n_{\mathrm{r}} = L/D$ | axial ratio of a rod |
| $P_2(\cos\theta)$ | the second Legendre polynomial |
| $P_{2n}(\cos\theta)$ | Legendre polynomial |
| $q$ | wavenumber |
| $q_{\mathrm{m}}$ | wavenumber where a structure factor has a maximum |
| $R = 2\pi/q_{\mathrm{m}}$ | average domain size |
| $\boldsymbol{r}$ | position |
| $S$ | orientational order parameter |
| $S_{\mathrm{i}}$ | entropy in an isotropic phase |
| $S_{ij}$ | tensor order parameter |
| $S_{\mathrm{n}}$ | entropy in a nematic phase |
| $S_{\mathrm{NI}}$ | order parameter at NIT |
| $S_0$ | entropy |
| $S_{\mathrm{or}}$ | orientational entropy |
| $S_{\mathrm{pc}}$ | packing entropy |
| $S_{\mathrm{S}}(q, t)$ | structure factor for orientation |
| $S_{\phi}(q, t)$ | structure factor for concentration |
| $T$ | absolute temperature |
| $T_{\mathrm{c}}$ | UCST |
| $T_{\mathrm{NI}}$ | NIT temperature of the mixture |
| $T_{\mathrm{TP}}$ | triple point temperature |
| $T_{\mathrm{NI}}^{\mathrm{L}}$ | NIT temperature of a pure liquid crystal |
| $T^* = T/T_{\mathrm{NI}}^{\mathrm{L}}$ | reduced temperature |
| $T_{\mathrm{SN}}^{\circ}$ | SNT temperature of a pure liquid crystal |
| $t$ | time |
| $\boldsymbol{u}$ | orientation |
| $u_{ij}$ | interaction energy between two rods |
| $V$ | volume of a system |
| $v_{ij}$ | average excluded volume between the particle $i$ and $j$ with random orientations |
| $v_{\mathrm{p}} = a^3 n_{\mathrm{p}}$ | volume of a polymer |
| $v_{\mathrm{r}} = (\pi/4)D^2 L$ | volume of a rod |
| $v_{\mathrm{rr}} = (\pi/4)L^2 D$ | average excluded volume between two rods |
| $Z_0, Z$ | normalization constants |

## Greek Symbols

| | |
|---|---|
| $\alpha \equiv \chi_a/\chi$ | nematic interaction parameter |
| $\beta = 1/k_B T$ | |
| $\beta_1 = 1 - \exp[-\beta u_{ij}]$ | Mayer–Mayer function |
| $\Gamma$ | strength of nematic ordering |
| $\Gamma_{ij}$ | Onsager's transport coefficients |
| $\gamma$ | smectic interaction parameter |
| $\Delta F$ | free energy of mixing |
| $\Delta\mu_p = (\mu_p - \mu_p^\circ)$ | chemical potential of a polymer |
| $\mu, \Delta\mu_r = (\mu_r - \mu_r^\circ)$ | chemical potential of a rod |
| $\varepsilon$ | Maier–Saupe attractive interaction |
| $\eta$ | smectic A order parameter |
| $\theta$ | angle between the long axis of a rod and the director |
| $\tilde{\mu}$ | dimensionless chemical potential of a rod |
| $\mu^\circ$ | standard chemical potential of a rod |
| $\mu_i^0$ | standard chemical potential of the particle $i$ (= p, r) |
| $\nu$ | kinetic exponent |
| $\Pi$ | osmotic pressure |
| $\tilde{\Pi}$ | dimensionless osmotic pressure |
| $\varrho = N_r/V$ | average-number density of rods |
| $\varrho_r(\boldsymbol{r}, \boldsymbol{u})$ | number density of rods with an orientation $\boldsymbol{u}$ at a position $\boldsymbol{r}$ |
| $\tau = 1/\chi$ | reduced temperature |
| $\tau_c$ | reduced critical temperature |
| $\tau_{NI}$ | reduced NIT temperature |
| $\tau_{NI}^L$ | reduced NIT temperature of a pure rod |
| $\phi$ | volume fraction of rods |
| $\phi_i$ | volume fraction of rods in an isotropic phase |
| $\phi_n$ | volume fraction of rod in a nematic phase |
| $\phi_p$ | volume fraction of polymer |
| $\phi_p^c$ | critical concentration |
| $\phi_r$ | volume fraction of rod |
| $\phi_{NI}$ | NIT concentration |
| $\phi_0$ | concentration in the initial homogeneous system |
| $\varphi(\theta, \theta')$ | angle between two rods |
| $\chi$ | Flory–Huggins interaction parameter |
| $\chi_a = \varepsilon/k_B T$ | dimensionless anisotropic parameter |
| $\Omega$ | solid angle |
| $\omega_1, \omega_2$ | growth rates |

## References


1 Drzaic, P.S. (1995) *Liquid Crystal Dispersions*, World Scientific, Singapore.

2 Crawford, G.P. and Zumer, S. (eds) (1996) *Liquid Crystals in Complex Geometries*, Taylor and Francis, London.

3 Flory, P.J. (1956) *Proc. R. Soc. London A*, **234**, 60.
4 Flory, P.J. (1956) *Proc. R. Soc. London A*, **234**, 73.
5 Flory, P.J. (1978) *Macromolecules*, **11**, 1119.
6 Flory, P.J. (1978) *Macromolecules*, **11**, 1138.
7 Flory, P.J. (1978) *Macromolecules*, **11**, 1141.
8 Flory, P.J. and Ronca, G. (1979) *Mol. Cryst. Liq. Cryst.*, **54**, 289.
9 Khokhlov, A.R. and Semenov, A.N. (1985) *J. Stat. Phys.*, **38**, 161.
10 Sato, T. and Teramoto, A. (1996) *Adv. Polym. Sci.*, **126**, 85.
11 Yamakawa, H. (1997) *Helical Wormlike Chains in Polymer Solutions*, Springer-Verlag, Berlin, Heidelberg.
12 Onsager, L. (1949) *Ann. N. Y. Acad. Sci.*, **51**, 627.
13 Donald, A.M., Windle, A.H., and Hanna, S. (2006) *Liquid Crystalline Polymers*, 2nd edn, Cambridge University Press, Cambridge.
14 de Gennes, P.G. and Prost, J. (1993) *The Physics of Liquid Crystals*, 2nd edn, Oxford Scientific, London.
15 Mayer, J.E. and Mayer, M.G. (1941) *Statistical Physics*, John Wiley & Sons, Inc., New York.
16 Evans, R. (1979) *Adv. Phys.*, **28**, 143.
17 Baus, M. (1990) *J. Phys.: Condens Matter.*, **2**, 2111.
18 Kayser, R.F. and Raveche, H.J. (1978) *Phys. Rev. A*, **17**, 2067.
19 Lekkerkerker, H.M.W., Coulon, P., van der Haegen, R., and Deblieck, R. (1984) *J. Chem. Phys.*, **80**, 3427.
20 Nakamura, H. and Okano, K. (1983) *Phys. Rev. Lett.*, **50**, 186.
21 Doi, M. and Edwards, S.F. (1986) *Theory of Polymer Dynamics*, Academic, New York.
22 Straley, J.P. (1973) *Mol. Cryst. Liq. Cryst.*, **22**, 333.
23 Veerman, J.A.C. and Frenkel, D. (1990) *Phys. Rev. A*, **41**, 3237.
24 Bolhuis, P. and Frenkel, D. (1996) *J. Chem. Phys.*, **106**, 666.
25 Odijk, T. and Lekkerkerker, H.M.W. (1985) *J. Phys. Chem.*, **89**, 2090.
26 Vroege, G.J. and Lekkerkerker, H.N.W. (1992) *Rep. Prog. Phys.*, **55**, 1241.
27 Kiss, G. and Porter, R.S. (1980) *Mol. Cryst. Liq. Cryst.*, **60**, 267.
28 Holyst, R. (2005) *Soft Matter.*, **1**, 329.
29 Alder, B.J. and Wainwright, T.E. (1957) *J. Chem. Phys.*, **27**, 1208.
30 Maier, M. and Saupe, A. (1959) *Z. Naturforsch., Teil A*, **14**, 882.
31 Brochard, F. (1979) *J. Phys.*, **40**, 1049.
32 McMillan, W.L. (1971) *Phys. Rev. A*, **4**, 1238.
33 Matsuyama, A. and Kato, T. (1998) *J. Chem. Phys.*, **108**, 2067.
34 Kirkwood, J.G. and Monroe, E. (1941) *J. Chem. Phys.*, **9**, 514.
35 Matsuyama, A. (2006) *J. Phys. Soc. Jpn.*, **75**, 034604.
36 Matsuyama, A. (2006) *J. Phys. Soc. Jpn.*, **75**, 084602.
37 Drzaic, P.S. (1998) *Liq. Cryst.*, **3**, 1543.
38 Smith, G.W., Ventouris, G.M., and West, J.L. (1992) *Mol. Cryst. Liq. Cryst.*, **213**, 11.
39 Dutta, D., Fruitwala, A., Kohli, A., and Weiss, R.A. (1990) *Polym. Eng. Sci.*, **30**, 1005.
40 Kronberg, B., Bassignana, I., and Patterson, D. (1978) *J. Phys. Chem.*, **82**, 1714.
41 Dubault, A., Casagrande, C., Veyssie, M., and Deloche, B. (1980) *Phys. Rev. Lett.*, **45**, 1645.
42 Orendi, H. and Ballauf, M. (1989) *Liq. Cryst.*, **6**, 497.
43 Dormoy, Y., Gallani, J.L., and Martinoty, P. (1989) *Mol. Cryst. Liq. Cryst.*, **170**, 135.
44 Ahn, W., Kim, C.Y., Kim, H.S., and Kim, C. (1992) *Macromolecules*, **25**, 5002.
45 Wieczorek, S.A., Freyssingeas, E., and Holyst, R. (2005) *J. Phys. Chem.*, **109**, 16252.
46 Kyu, T., Nwabunma, D., and Chiu, H.-W. (2001) *Phys. Rev. E*, **63**, 061802.
47 Ballauf, M. (1986) *Mol. Cryst. Liq. Cryst.*, **136**, 175.
48 Ballauf, M. (1986) *Mol. Cryst. Liq. Cryst. Lett.*, **4**, 15.
49 Ballauf, M. (1986) *Macromolecules*, **19**, 1366.
50 Maissa, P. and Sixou, P. (1989) *Liq. Cryst.*, **5**, 1861.
51 Holyst, R. and Schick, M. (1992) *J. Chem. Phys.*, **96**, 721.
52 Liu, A.J. and Fredrickson, G.H. (1993) *Macromolecules*, **26**, 2814.

**53** Shen, C. and Kyu, T. (1995) *J. Chem. Phys.*, **102**, 556.

**54** Brochard, F., Jouffroy, J., and Levinson, P. (1984) *J. Phys.*, **45**, 1125.

**55** Matsuyama, A. and Kato, T. (1996) *J. Chem. Phys.*, **105**, 1654.

**56** Flory, P.J. (1953) *Principles of Polymer Chemistry*, Cornell University Press, Ithaca.

**57** Lin, Z., Zhang, H., and Yang, Y. (1998) *Phys. Rev. E*, **58**, 5867.

**58** ten Bosch, A., Maissa, P., and Sixou, P. (1983) *J. Chem. Phys.*, **79**, 3462.

**59** ten Bosch, A., Maissa, P., and Sixou, P. (1983) *J. Phys. Lett.*, **44**, L105.

**60** Matsuyama, A., Sumikawa, Y., and Kato, T. (1997) *J. Chem. Phys.*, **107**, 4711.

**61** Matsuyama, A. (2008) *J. Chem. Phys.*, **128**, 224907.

**62** Matsuyama, A. and Kato, T. (1998) *Phys. Rev. E*, **58**, 585.

**63** Matsuyama, A. and Kato, T. (1998) *J. Chem. Phys.*, **109**, 2023.

**64** Matsuyama, A. and Kato, T. (1999) *Phys. Rev. E*, **59**, 763.

**65** Chiu, H.W., Zhou, Z.L., Kyu, T., Cada, L.G., and Chie, L.C. (1996) *Macromolecules*, **29**, 1051.

**66** Wee, E.L. and Miller, W.G. (1971) *J. Phys. Chem.*, **75**, 1446.

**67** Millar, W.G., Kou, L., Tohyama, K., and Voltaggio, V. (1978) *J. Polym. Sci.: Polym. Symp.*, **65**, 91.

**68** Warner, M. and Flory, P.J. (1980) *J. Chem. Phys.*, **73**, 6327.

**69** Matheson, R.R. and Flory, P.J. (1981) *Macromolecules*, **14**, 954.

**70** Kyu, T. and Chiu, H.W. (1996) *Phys. Rev. E*, **53**, 3618.

**71** Chiu, H.W. and Kyu, T. (1997) *J. Chem. Phys.*, **107**, 6859.

**72** Chiu, H.W. and Kyu, T. (1998) *J. Chem. Phys.*, **108**, 3246.

**73** Chiu, H.W. and Kyu, T. (1999) *J. Chem. Phys.*, **110**, 5998.

**74** Benmouna, F., Daoudi, A., Roussel, F., Leclecqcq, L., Buisine, J.M., Coqueret, X., Benmouna, M., Ewen, B., and Maschke, U. (2000) *Macromolecules*, **33**, 960.

**75** Kobayashi, K.K. (1970) *J. Phys. Soc. Jpn.*, **29**, 1010.

**76** Kyu, T., Chiu, H.W., and Kajiyama, T. (1997) *Phys. Rev. E*, **55**, 7105.

**77** Kventsel, G.F., Kuckhurst, G.R., and Zewdie, H.B. (1985) *Mol. Phys.*, **56**, 589.

**78** Knobler, C.M. and Scott, R.L (1984), in *Phase Transition and Critical Phenomena*, vol. 9 (eds C. Domb and J.L. Lebowitz), Academic, New York.

**79** Wieczorek, S.A., Freyssingeas, E., and Holyst, R. (2005) *J. Phys. Chem. B*, **109**, 16252.

**80** Maschke, U., Benmouna, F., Roussel, F., Daoudi, A., Gyselinck, F., Buisine, J.M., Coqueret, X., and Benmouna, M. (1999) *Macromolecules*, **32**, 8866.

**81** Alsayed, A.M., Dogic, Z., and Yodh, A.G. (2004) *Phys. Rev. Lett.*, **93**, 057801.

**82** Dayal, P., Matkar, R.A., and Kyu, T. (2006) *J. Chem. Phys.*, **124**, 224902.

**83** Matsuyama, A. and Hirashima, R. (2008) *J. Chem. Phys.*, **128**, 044907.

**84** Tarazona, P., Cuesta, J.A., and Martinez-Raton, Y. (2008) in *Density Functional Theories of Hard Particle Systems, Lecture Notes in Physics*, vol. **753** (ed. A. Mulero), Springer-Verlag, Berlin, Heidelberg, p. 247.

**85** Hong, K.M. and Noolandi, J. (1981) *Macromolecules*, **14**, 727.

**86** ten Bosch, A., Pinton, J.F., Maissa, P., and Sixou, P. (1987) *J. Phys. A: Math. Gen.*, **20**, 4531.

**87** Schmidt, M. and Denton, A.R. (2002) *Phys. Rev. E*, **65**, 021508.

**88** Ginzburg, V.V., Singh, C., and Balazs, A.C. (2000) *Macromolecules*, **33**, 1089.

**89** Matsuyama, A. and Kato, T. (2000) *J. Chem. Phys.*, **112**, 1046.

**90** De Jeu, W.H. and Demus, D. (1986) *J. Chem. Phys.*, **84**, 6410.

**91** Dallest, J.F., Maissa, P., ten Bosch, A., Sixou, P., Blumstein, A., Blumstein, R., Teixeira, J., and Noirez, L. (1988) *Phys. Rev. Lett.*, **61**, 2562.

**92** Cotton, J.P. and Hardouin, F. (1997) *Prog. Polym. Sci.*, **22**, 795.

**93** Chen, F.L. and Jamieson, A.M. (1994) *Macromolecules*, **27**, 4691.

**94** Dogic, Z., Zhang, J., Lau, A.W.C., Espinoza, H.A., Dalhaimer, P., Discher, D.E., Janmey, P.A., Kamien, R.D.,

Lubensky, T.C., and Yodh, A.G. (2004) *Phys. Rev. Lett.*, **92**, 125503.
**95** de Gennes, P.G. (1982) in *Polymer Liquid Crystals* (eds A. Ciferri, W.R. Krigbaum, and R.B. Meyer), Academic Press, New York.
**96** Odijk, T. (1986) *Macromolecules*, **19**, 2313.
**97** Odijk, T. (1996) *J. Chem. Phys.*, **105**, 1270.
**98** Wang, X.J. and Warner, M. (1992) *Liq. Cryst.*, **12**, 385.
**99** Matsuyama, A. (2003) *Phys. Rev. E*, **67**, 042701.
**100** Link, S., Chang, W.S., Yethiraj, A., and Barbara, P.F. (2006) *Phys. Rev. Lett.*, **96**, 017801.
**101** Langer, J.S. (1992), in *Solids Far from Equilibrium* (ed. C. Godrèche), Cambridge University Press, New York, ch. 13.
**102** Cahn, J.W. and Hilliard, J.E. (1958) *J. Chem. Phys.*, **28**, 258.
**103** Cahn, J.W. (1968) *Trans. Mettal. Soc. AIME*, **242**, 166.
**104** Chaikin, P.M. and Lubensky, T.C. (1995) *Principles of Condensed Matter Physics*, Cambridge University Press, New York.
**105** Kim, J.Y. and Palffy-Muhoray, P. (1991) *Mol. Cryst. Liq. Cryst.*, **203**, 93.
**106** Kim, J.Y., Cho, C.H., Palffy-Muhoray, P., Mustafe, M., and Kyu, T. (1993) *Phys. Rev. Lett.*, **71**, 2232.
**107** Kyu, T. and Chiu, H.W. (2001) *Polymer*, **42**, 9173.
**108** Motoyama, M., Nakazawa, H., Ohta, T., Fujisawa, T., Nakada, H., Hayashi, M., and Aizawa, M. (2000) *Comput. Theor. Polym. Sci.*, **10**, 287.
**109** Casagrande, C., Veyssie, M., and Knobler, C.M. (1987) *Phys. Rev. Lett.*, **58**, 2078.
**110** Nakai, A., Shiwaku, T., Wang, W., Hasegawa, H., and Hashimoto, T. (1996) *Macromolecules*, **29**, 5990.
**111** Langer, S.A. and Glotzer, S.C. (1997) *Phys. A*, **239**, 358.
**112** Liu, A.J. and Fredrickson, G.H. (1996) *Macromolecules*, **29**, 8000.
**113** Matsuyama, A., Evans, R.M.L., and Cates, M.E. (2000) *Phys. Rev. E*, **61**, 2977.
**114** Matsuyama, A., Evans, R.M.L., and Cates, M.E. (2002) *Eur. Phys. J. E*, **9**, 79.
**115** Fukuda, J. (1998) *Phys. Rev. E*, **58**, R6939.
**116** Fukuda, J. (1999) *Phys. Rev. E*, **59**, 3275.
**117** Fukuda, J. (1999) *Eur. Phys. J. B*, **7**, 573.
**118** Matsuyama, A. and Kato, T. (2000) *J. Chem. Phys.*, **113**, 9300.
**119** ten Bosch, A. (1991) *J. Phys. II*, **1**, 949.
**120** Dorgan, J.R. (1993) *J. Chem. Phys.*, **98**, 9094.
**121** Elder, K.R., Drolet, F., Kosterlitz, J.M., and Grant, M. (1994) *Phys. Rev. Lett.*, **72**, 677.
**122** Lin, Z., Zhang, H., and Yang, Y. (1997) *Macromol. Theor. Simul.*, **6**, 1153.
**123** Shimada, T., Doi, M., and Okano, K. (1988) *J. Chem. Phys.*, **88**, 7181.
**124** Lifshitz, I.M. and Slyozov, V.V. (1961) *Chem. Phys. Solids*, **19**, 35.
**125** Binder, K. and Stauffer, D. (1974) *Phys. Rev. Lett.*, **33**, 1006.
**126** Siggia, E. (1979) *Phys. Rev. A*, **20**, 595.
**127** Graca, M., Wieczorek, S.A., and Holyst, R. (2003) *Phys. Rev. Lett.*, **90**, 115504.
**128** Dhont, J.K.G. and Briels, W.J. (2005) *Phys. Rev. E*, **72**, 031404.
**129** Lettinga, M.P., Kang, K., Holmqvist, P., Imhof, A., Derks, D., and Dhont, K.G. (2006) *Phys. Rev. E*, **73**, 011412.
**130** Kim, W.K. and Kyu, T. (1994) *Mol. Cryst. Liq. Cryst.*, **250**, 131.
**131** Takenaka, M., Shimizu, H., Nishitsuji, S., and Hasegawa, H. (1983) *Macromolecules*, **39**, 6226.
**132** Bhargava, R. and Levin, I.W. (2004) *Vib. Spectrosc.*, **34**, 13.
**133** Roussel, F., Canlet, C., and Fung, B.M. (2002) *Phys. Rev. E*, **65**, 021701.
**134** Erdmann, J.H., Zummer, S., and Doana, J.W. (1990) *Phys. Rev. Lett.*, **4**, 1907.
**135** Crawford, G.P. and Doana, J.W. (1992) *Condens. Matter. News*, **1**, 5.
**136** Lansac, Y., Fried, F., and Maissa, P. (1995) *Phys. Rev. E*, **52**, 6227.
**137** Joen, Y.J., Bingzhu, Y., Rhee, T.J., Cheung, D.L., and Jamil, M. (2007) *Macromol. Theor. Simul.*, **16**, 643.
**138** Zhu, J., Xu, G., Ding, J., and Yang, Y. (1999) *Macromol. Theor. Simul.*, **8**, 409.
**139** Lebwohl, P.A. and Lasher, G. (1972) *Phys. Rev. A*, **6**, 426.
**140** Lapena, A.M., Glotzer, S.C., Langer, S.A., and Liu, A.J. (1999) *Phys. Rev. E*, **60**, R29.
**141** Hohenberg, P.C. and Helperin, B.I. (1977) *Rev. Mod. Phys.*, **49**, 435.

**142** Fung, Y.K., Yang, D.K., YiNG, S., Chien, L.C., Zumer, S., and Doana, J.W. (1995) *Liq. Cryst.*, **19**, 797.

**143** Nakazawa, H., Fujinami, S., Motoyama, M., Ohta, T., Araki, T., Tanaka, H., Fujisawa, T., Nakada, H., Hayashi, M., and Aizawa, M. (2001) *Comput. Theor. Polym. Sci.*, **11**, 445.

**144** Araki, T. and Tanaka, H. (2004) *Phys. Rev. Lett.*, **93**, 015702.

**145** Das, S.K. and Rey, A.D. (2004) *J. Chem. Phys.*, **121**, 9733.

**146** Das, S.K. and Rey, A.D. (2005) *Europhys. Lett.*, **70**, 621.

**147** Das, S.K. and Rey, A.D. (2006) *Comput. Mater. Sci.*, **38**, 325.

**148** Das, S.K. and Rey, A.D. (2006) *Macromol. Theor. Simul.*, **15**, 469.

**149** Araki, T. and Tanaka, H. (2006) *J. Phys.: Condens Matter*, **18**, L305.

**150** Essery, R.L.H. and Ball, R.C. (1991) *Europhys. Lett.*, **16**, 379.

**151** Xia, J., Wang, J., Lin, Z., Qui, F., and Yang, Y. (2006) *Macromolecules*, **39**, 2247.

**152** Popa-Nita, V., Sluckin, T.J., and Kralj, S. (2005) *Phys. Rev. E*, **71**, 061706.

**153** Sulaiman, N., Marenduzzo, D., and Yeomans, J.M. (2006) *Phys. Rev. E*, **74**, 041708.

**154** Eisenbach, C.D., Hofmann, J., and Fischer, K. (1994) *Macromol. Rapid. Commun.*, **15**, 117.

**155** van Bruggen, M.P.B., van der Kooij, F.M., and Lekkerkerker, H.N.W. (1996) *J. Phys. Condens. Matter*, **8**, 9451.

**156** Vliegenthart, G.A., van Blaaderen, A., and Lekkerkerker, H.N.W. (1999) *Faraday Discuss.*, **112**, 173.

**157** Urakami, N., Imai, M., Sano, Y., and Takasu, M. (1999) *J. Chem. Phys.*, **111**, 2322.

**158** Adams, M. and Fraden, S. (1998) *Biophys. J.*, **74**, 669.

**159** Adams, M., Dogic, Z., Keller, S.L., and Fraden, S. (1998) *Nature*, **393**, 349.

**160** Asakura, S. and Oosawa, F. (1954) *J. Chem. Phys.*, **22**, 1255.

**161** Warren, P.B. (1994) *J. Phys. I*, **4**, 237.

**162** Matsuyama, A. and Kato, T. (2001) *Eur. Phys. J. E*, **6**, 15.

**163** Yamamoto, J. and Tanaka, H. (2001) *Nature*, **409**, 321.

**164** Lubensky, T.C., Petty, D., Currier, N., and Stark, H. (1998) *Phys. Rev. E*, **57**, 610.

**165** Loudet, J.C., Barois, P., and Pouling, P. (2000) *Nature*, **407**, 611.

**166** Lynch, M. and Patrick, D. (2002) *Nano Lett.*, **2**, 11.

**167** Duran, H., Gazdecki, B., Yamashita, A., and Kyu, T. (2005) *Liq. Cryst.*, **32**, 815.

**168** Warner, M. and Wang, X.J. (1992) *Macromolecules*, **25**, 445.

**169** Urayama, K., Okuno, Y., Nakao, T., and Kohjiya, S. (2003) *J. Chem. Phys.*, **118**, 2903.

**170** Benmouna, F., Maschke, U., Coqueret, X., and Benmouna, M. (2000) *Macromolecules*, **33**, 1054.

**171** Matsuyama, A. and Kato, T. (2001) *J. Chem. Phys.*, **114**, 3817.

**172** Matsuyama, A. and Kato, T. (2001) *Phys. Rev. E*, **64**, R010701.

**173** Lu, C. and Mai, Y.W. (2005) *Phys. Rev. Lett.*, **95**, 088303.

**174** Escuti, M.J. and Crawford, G.P. (2004) *Mol. Cryst. Liq. Cryst.*, **421**, 23.

**175** Fally, M., Drevensek-Olenik, I., Ellabban, M.A., Pranzas, K.P., and Vollbrandt, J. (2006) *Phys. Rev. Lett.*, **97**, 167803.

**176** Kikuchi, H., Yokota, M., Hisakado, Y., Yang, H., and Kajiyama, T. (2002) *Nat. Mater.*, **1**, 64.

**177** Harry, J.C. and Mikhail, N.P. (2005) *Nature*, **436**, 997.

**178** Yamamoto, J., Nishiyama, I., Inoue, M., and Yokoyama, H. (2005) *Nature*, **437**, 525.

# 3
# Amorphous Polymer Blends: Recent Developments

*Jeffery L. White*

## 3.1
## Introduction

The science related to polymer blends has historically enjoyed a productive marriage between intellectual pursuit and economic utility, as recently discussed in a national workshop hosted by the National Science Foundation [1]. The notion that the polymer blend area is a mature science can be challenged by simply assessing the lack of understanding surrounding mixtures of amorphous macromolecules of even the simplest chemical structure. As the polymer science community, both from an intellectual and engineering motivation, pursues increasingly complex systems, tailored composites, hybrid and hierarchical structures, self-assembly, and biologically inspired materials (as outlined in a recent *Macromolecules* "Perspectives" article [2]), we find that the same key questions that continue to characterize problems in mixtures of amorphous polymers arise in these emerging interdisciplinary areas. For example, simply measuring with confidence the length scales within which two polymers are mixed in a binary mixture of two non-crystalline macromolecules can be very challenging, even for very simple polymer chain architectures. In addition, what causes amorphous mixtures to have a homogeneous, intimately mixed arrangement of its constituent chains versus a heterogeneous, phase separated morphology? If intimate mixing of the two polymer species occurs, does this mean that the chains assume new "identities" relative to their pure component characteristics, and if so, in what ways? Can we synthetically manipulate the macroscopic properties of the end-result blend by systematic variation of chemical structure? Amorphous polymer blends, which for the purposes of this chapter mean mixtures of high polymers with no crystalline regions in the final blend, represent the first step in generating complex polymer systems. As such, fundamental understanding of how they behave, and connections between microscopic structure versus end-use properties, is paramount to continued progress in key areas of macromolecular science, ranging from synthetic to engineering to biological materials.

Rather than review the field historically, or provide a tutorial on amorphous polymers and their blends, we will update the reader on key progress in recent years in the area of amorphous polymer blends, with particular emphasis on areas

*Encyclopedia of Polymer Blends, Volume 1: Fundamentals.* Edited by Avraam I. Isayev
Copyright © 2010 WILEY-VCH Verlag GmbH & Co. KGaA, Weinheim
ISBN: 978-3-527-31929-9

that have received the most attention in the peer-reviewed literature from an experimental, theoretical, and computational perspective. For additional historical reviews related to amorphous polymer blends published at the time of this writing, the reader is directed to References [3–15]. The current chapter will primarily focus on mixtures that form intimately mixed or miscible blends, since the behavior of individual components are most interesting in such systems, and, more importantly, miscible blends can represent completely new materials relative to their constituents. Indeed, an oft-overlooked point about polymer blends is their high value from an industrial intellectual property and applications perspective, since new materials can be created from existing polymers.

## 3.2
## Miscible Blend Dynamics and Length Scales of Mixing

Prediction of bulk behavior important to polymer processing and end-use mechanical properties, for example, shear viscosities, elongation, or impact strength, requires a molecular level understanding of polymer chain dynamics. Chain dynamics in miscible polymer blends and amorphous polymer mixtures has most likely been the most active area of amorphous blend science in recent years, involving many experimental approaches ranging from rheology to microscopy to spectroscopy. While certainly not the only contribution during the period covered by this chapter, the work of Lodge and McLeish [16] published in 2000 has sparked significant effort by many other experimental and theoretical groups. In summary, the principal tenants of the Lodge–McLeish model revolve around the relative contributions of "self-concentration" and "concentration fluctuations" to temperature and composition-dependent chain dynamics in miscible binary blends. These terms become meaningful when one considers the individual trajectories, or volume elements, that polymer chain segments sample as they move within the mixed blend environment. Individual monomeric units in the polymer are covalently bonded, that is, chain connectivity, and the "self-concentration" component arises from conformational reorientation of some chain elements relative to others within the same chain. Conversely, in a blend those same chain segments dynamically sample volume elements containing additional mobile chain segments from the other blend component. In a simple way, one might consider the former as an intramolecular or intrachain effect, and the latter as an interpolymer contribution, the magnitude of which can depend on how different the two polymer components may be in terms of their respective glass transition temperatures, for example. From a chain-level perspective, one would like to assess or determine (i) the size of the volume element or characteristic chain length involved in the dynamics that control polymer segmental relaxation, or the "local chain dynamics;" (ii) a characteristic or mean correlation time constant for that motion or, more specifically, for segmental versus terminal chain dynamics; (iii) some measure of the distribution of correlation times for polymer segments in a pure versus blended system; and (iv) the relative contributions of intrachain and interchain effects to the observed behavior.

Alternatively, one could pose the questions as: (i) What is the characteristic length scale for cooperative rearrangements of chain segments, and how does critical dimension depend on temperature? (ii) What is the length scale and time scale of the glass transition? (iii) How do we measure and describe the dynamically heterogeneous but locally concerted motions characteristic of primary and secondary relaxations in pure versus mixed polymers? From a bulk perspective, one might summarize the important questions as: (i) How do the individual polymer $T_g$s change upon formation of the amorphous blend? (ii) Do the mechanical and physical properties (e.g., viscosity, stress and strain, shear, etc.) of miscible blends follow simple composition-weighted averages of their constituents? This last question summarizes much of the historical treatment of polymer mixtures, and must be considered as biased by the fact that such an approach would represent the most simple, and economically attractive, description of polymer blends since it would only require knowledge of the independent pure component properties and their relative composition in the blend. The following sections will identify some of the original research contributions in the last several years that have addressed the above questions.

The publication by Lodge and McLeish entitled "Self concentrations and effective glass transitions in polymer blends" [16] directed attention to some of the key questions many polymer scientists were pursuing regarding the dynamic properties of miscible amorphous polymer blends as they relate to physical and glass transition properties [17–20]. Briefly, the model proposed by Lodge and McLeish utilized the Kuhn length (about 1–3 nm, and strictly defined as a function of the averaged versus maximum chain dimension) as the characteristic dimension, which when cubed reveals the relevant "dynamic volume" (which should be temperature dependent) associated with the reorienting units. The volume based on the Kuhn length is the determinant for monomeric friction factors in this model, as might be assessed via diffusion or rheological measurements. More importantly, the Lodge–McLeish model asserts that self-concentration (chain connectivity) contributions are primarily important in controlling segmental dynamics. In general, reasonable agreement exists between this model and some previous experimental studies [21–24], even though concentration fluctuation (interchain) contributions were neglected. Indeed, it was assumed that concentration fluctuations would only act to broaden the distribution of effective relaxation times, but not alter the central or mean correlation time effective for relaxation. Recently, others have shown that concentration fluctuation effects should be considered since they contribute, along with self-concentrations, to both the central correlation time value as well as the correlation time distributions [25]. Painter and Coleman have shown more recently that chain connectivity influences on self-concentration can include covalent connectivity and conformational connectivity contributions, the latter resulting from portions of the same chain bending back upon itself due to differential chain conformations characteristic of amorphous systems [26]. The authors assert that this latter contribution to self-concentration may be neglected in mixtures of macromolecules, but can be important in macromolecule/small molecule blends [26].

While reasonable agreement can exist between many of the recently proposed models and data analysis methods, the key fact is that the critical dimensions that govern the time and temperature dependent dynamics of a specific polymer, that is, the Kuhn length or "effective self-concentration" or "effective dynamic volume," depend on the polymer partner with which it is blended [25, 27]. Therefore, one cannot necessarily assume pure component properties, even for intrachain contributions, are preserved once a miscible blend is formed. Obviously, more rigorous experimental approaches that can address concentration fluctuation contributions can in turn improve understanding of operative self-concentration volumes. Careful analysis of glass transition temperatures ($T_g$) by recent experimental efforts have attempted to address this concept, both for amorphous blends as well as systems in which an amorphous polymer is mixed with a low molecular weight diluent [28, 29]. Historically, a single glass transition temperature has been used to define miscibility in polymer blends, the rationale being that homogeneous distributions of two polymer types in an intimate and equilibrium chain mixture should lead to an averaged, but equivalent, glass transition. Recent results indicate that two $T_g$s may be observed in miscible blends, or, stated differently, that the presence of two $T_g$s cannot always be used as an indicator that phase separation between the two constituent blends exists. Careful analysis of DSC results on amorphous blends is complicated by the fact that the glass transition is weak and broad, and discontinuities in the endotherm are hard to discern. Recent experimental reports in which two $T_g$s were observed for certain compositions, using calorimetric methods, include amorphous PI/PVE blends, PS/PVME, and PEO/PMMA [30–32]. Further, White and coworkers have used advanced solid-state NMR methods to detect two $T_g$s in a miscible polyolefin blend created from atactic PP and polyethylene-*co*-1-butene (PEB) [33]. The specific advantage of the approach by White and coworkers is a much higher information content in the raw data, and the ability to cleanly resolve distinct $T_g$s for each polymer component in the blend with much greater resolution than can be afforded by traditional methods, particularly for high molecular weight polymer components or for blends where one component may be silent to dielectric spectroscopy (as exemplified by blends of PIB and head-to-head polypropylene or hhPP, which have recently garnered significant attention in the literature) [34–36]. Finally, a detailed series of experiments on several amorphous polymer blends has shown that configurational entropy can drive formation of miscible polyolefin blends, and quantitative assessment of the magnitudes of configurational entropies of mixing based on chain-level experiments has been revealed [33, 35, 36, 38, 39].

In total, the aforementioned experiments clearly show that the historical view, in which individual polymer components in a miscible amorphous blend should exhibit identical glass transition (and therefore $\alpha$-relaxation chain dynamics) properties, is not always true. Qualitatively, these experimental results support the "self-concentration" idea, in that individual polymer chain dynamics for the blend constituents should depend on the relative concentrations of each of the components in the blend, as discussed in References [28, 37] in which concentration dependent results were obtained based on variations in the amounts of each

polymer in the blend. This does not mean that similar glass transition temperatures cannot exist for miscible blend components. Recently, identical chain-specific $T_g$s were observed for polyisobutylene (PIB) and head-to-head polypropylene (hhPP) using advanced solid-state NMR methods [35]. However, in that study, additional data analysis showed that while the average value of the correlation time constants describing α-relaxation chain motions in the miscible amorphous blend were identical, the breadth of the correlation time distribution was much larger for the high-$T_g$ component (hhPP), which was confirmed in subsequent studies on different amorphous polyolefin blends. Indeed, in many recent studies and reviews, the low-$T_g$ component in a miscible amorphous blend tends to preserve more of its dynamic "identity" as compared to the high-$T_g$ component. The latter exhibits increased dynamic heterogeneity in the miscible blend [33]. Such behavior is particularly evident in blends whose constituent polymers have very large (about $\geq$50 K) differences in pure-component polymer $T_g$s. Systems that exhibit unique temperature- and composition-dependent changes, and large differences in pure-component $T_g$s, have been termed "dynamically asymmetric" blends, and have recently been discussed in an excellent, detailed review by Colmenero and Arbe [5]. We note here that the review by Colmenero and Arbe includes references to older works that focused on theoretical and experimental contributions from thermally driven concentration fluctuations, and places them in context relative to recent contributions. Currently, debate continues about the relative contributions of either self-concentration or concentration fluctuation modes to overall blend behavior, as neither can reconcile all aspects of experimental observation, particularly with respect to heterogeneity and dynamic length scales at low or high temperatures. Additional experimental improvements are needed in that the *response of individual chains in the blends of any composition or concentration must be detected with high resolution*, either calorimetrically or spectroscopically; some key improved experimental approaches that have made significant advances toward this goal have been recently published or reviewed [5]. As examples representative of current capabilities, the reader is invited to examine Figures 3.1–3.4, in which results from dielectric spectroscopy and multiple-pulse magic-angle spinning solid-state NMR methods are compared for various amorphous blends. Figure 3.1 shows relaxation time distributions for the PVME component in miscible PVME/PS blends [5]. Clearly, detailed information is available on the temperature dependence of the dynamic heterogeneity of the PVME component. However, the PS component is silent in the experiment, and a total analysis of the blend components is not possible.

Complete information on the blend is accessible if both blend components are dielectrically active, as demonstrated in Figure 3.2 for the oft-studied PVE/PI blend system [5].

In contrast, Figures 3.3 and 3.4 show recent results using solid-state NMR methods that provide chain-specific information for any blend component, irrespective of whether it has a permanent dipole or sufficiently unique calorimetric signature. While complete experimental details may be found in References [33, 35], stated simply, chain dynamics are measured quantitatively based upon differences in the orientation dependent chemical shift parameters of backbone (or side group)

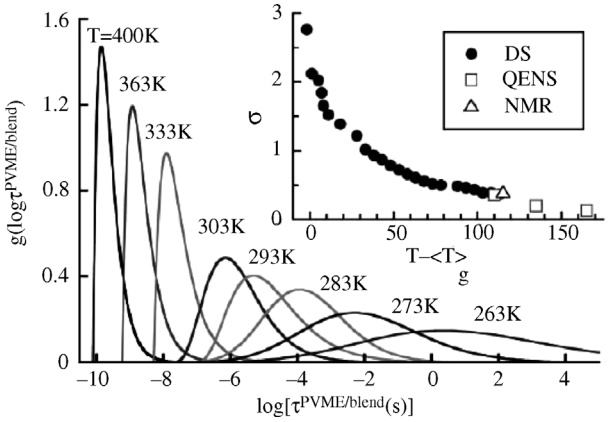


**Figure 3.1** Distributions of relaxation times describing the dynamics of PVME segments in the blend 65%PVME/35%PS at several temperatures. Inset: temperature dependence of the square root of the variance of $g(\log t^{PVME/blend})$ as observed by different techniques. Reproduced with permission from Reference [5].

carbons. Moreover, the experiment, based on a technique known as CODEX NMR [40] provides very slow-timescale information at and above the $T_g$, as shown in Figure 3.3. If no chain motion occurs, no NMR exchange signal will be detected. Figure 3.3 compares the temperature dependent response for each pure polymer and the same polymers in their miscible blend; in this case, the blend is a miscible atactic PP and PEB (polyethylene-*co*-1-butene) [33]. All that is required to interrogate glass transition properties and dynamics *for either component in the blend* is a resolved chemical shift in the solid-state $^{13}C$ spectrum.

From raw data like that shown in Figure 3.3, correlation time values (mean) and distributions may be extracted. Figure 3.4 shows the result of one such exercise for

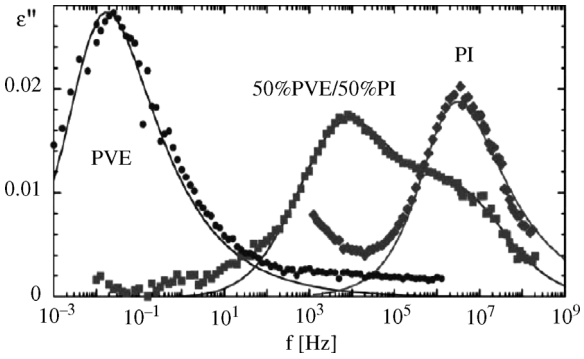


**Figure 3.2** Frequency dependence of the dielectric loss at 270 K for the homopolymers PVE and PI and for the blend 50%PVE/50%PI. Lines correspond to the estimated contributions of the α-relaxation to the spectra. Reproduced from Reference [5].

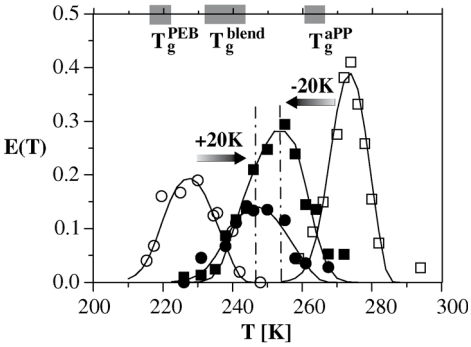


**Figure 3.3** Normalized NMR exchange intensities *E(T)* for pure (solid) PEB66 (○), PEB66 in the blend (●), pure (solid) aPP (□) and aPP in the blend (■). The smooth lines are fits to the data using an Arrhenius model as described in References [33] and [35]. Note the shifts of equal but opposite magnitude for each component upon blend formation, but a lack of complete convergence to a common temperature for the exchange intensity maximum of each polymer in the blend. The 5 K min$^{-1}$ scan DSC $T_g$ range for each polymer and the blend is plotted for reference on the top of the figure, with the box length representing the beginning and end of the endotherm. Reproduced from Reference [33].

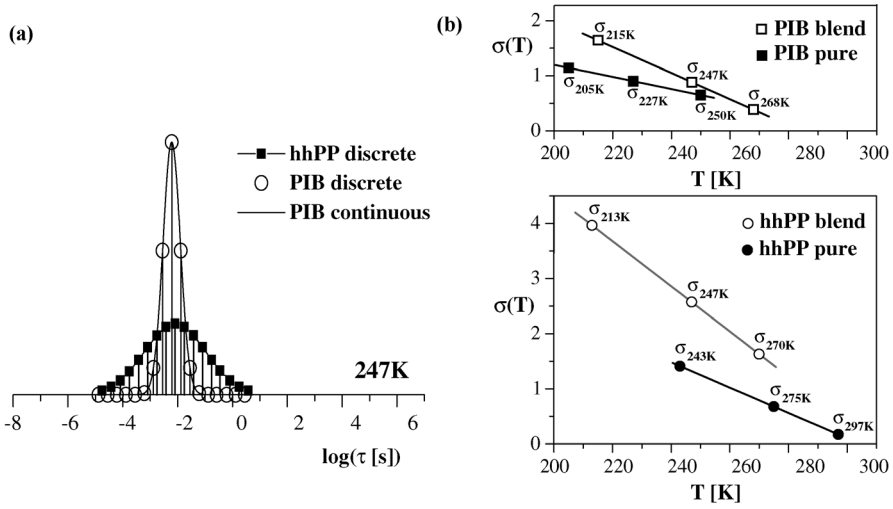


**Figure 3.4** (a) Correlation time distributions for individual polymer components in the miscible hhPP/PIB blend of Reference [35], at the temperature of maximum exchange intensity $E(T)_{max}$, showing the same central correlation time value $\tau_c$ but largely different correlation time distribution widths σ, (b) correlation time distribution widths $\sigma(T)$ for pure PIB and PIB in blend and for pure hhPP and hhPP in blend. Reproduced from References [33] and [35].

each component in the miscible blend of PIB and hhPP [35]; the reader should recognize that PIB is dielectrically silent, and such detailed information on its behavior in the miscible blend is difficult to obtain by any other method. In addition to central correlation time values (Figure 3.4a), the widths of the correlation time distributions σ may be obtained over the entire temperature range of interest (Figure 3.4b). In the PIB/hhPP case reviewed here, Figure 3.4a and b indicate that while central correlation time values for slow main-chain reorientation converge to identical values, their temperature dependent correlation time distributions (i.e., dynamic heterogeneity) actually diverge.

Plots like the one shown in Figure 3.4a may be extracted from any temperature point along the raw data curves of the type shown in Figure 3.3; only one temperature (247 K) is shown in Figure 3.4a for brevity. As such, directly comparable information to that shown in Figure 3.1 is accessible for any polymer component in a miscible blend, as long as a resolved signal in the $^{13}C$ spectrum exists.

## 3.3
## Amorphous Biopolymer Blends

Utilizing monomers from renewable sources (e.g., plants) to generate polymers that themselves are not tied to energy feedstocks, and that can be bioremedial, currently garners significant attention in both the research and economic development arenas [41–45]. Notable examples include monomeric feedstocks derived from corn fermentation, and there is every indication that this general class of polymers will increase in importance as discussed in detail in a recent review article in *Macromolecules* [46]. Polylactic acid (PLA, or polylactide) is the most common current example, and its status is summed up by the following quote from Gandini's recent review: "PLA represents the very paradigm of the polymer of the future in that it fits perfectly within the biomass refinery concept, within the green chemistry postulates, within the very definition of a polymer from renewable resources, within the biodegradability criteria, and all this accompanied by very adequate mechanical and thermal properties" [46]. However, the physical and mechanical properties of pure polymers derived from biomonomers can be deficient for many applications. PLA, for example, is a crystalline and very brittle polymer with low impact strength. A particularly well-studied system involves blending PLA with polycaprolactone (PCL), a highly flexible polymer, with the goal of obtaining a mixed system with high tensile strength (arising from the PLA component) and high impact strength (from the PCL) [47–49]. While generally considered immiscible, novel preparation methods have been reported which, at least for some period of time, lead to more intimately mixed blends that have little remaining crystallinity from the PLA component and may be considered as primarily an amorphous blend [50, 51]. Blends of PLA with atactic PHB (polyhydroxybutyrate) are attractive from a bioremediation and bacterial synthesis perspective; domain sizes can vary tremendously based on blend composition generally, such blends are immiscible [52]. Indeed, formation of amorphous blends

from atactic PHB and amorphous PLA or amorphous PMMA can actually enhance biodegradation of the PHB component [53].

Another emerging class of amorphous blends, in which at least one component is a biopolymer, includes polysaccharide blends (cellulose, starch, chitin). Recently, Marsono and coworkers have examined amorphous blends of cellulose with silk fibroin and found intimately mixed components at the about 2 nm level [54]. The biological properties of materials, for example, tissue growth hosting, biocompatibility, and biomimetic mechanical details, can be modified via appropriate blending of natural chitin polymers with synthetic biodegradable polymers, as recently reported for chitin/PCL blends or chitin/PVA [poly(vinyl alcohol)] [55, 56]. Given its hydrophilicity, PVA is a favorite synthetic polymer for blend formulation involving biopolymers; recent molecular level investigations have revealed that miscibility exists for PVA and PHB blends over the entire composition range in the amorphous phase [57]. Multicomponent mixtures of biopolymers, or biopolymers and synthetic polymers, are expected to continue growth as both an environmentally and economically attractive alternatives to fully synthetic polymers derived from petroleum feedstocks.

## 3.4 Conclusions

Amorphous polymer blends present unique challenges to both the experimentalist and the theorist, and, from an experimental perspective, often demand more creativity in extracting useful metrics than crystalline materials. Amorphous macromolecules, and their mixtures, challenge our notions on thermodynamic equilibrium, and require a time-dependent perspective. However, amorphous blends play key roles not only in materials and composites science but also in biological and life sciences where the transient structure of proteins and enzymes, membranes, lipid arrays, and many other dynamic structures control function. Fundamental insights gained from investigating the unique aspects of synthetic amorphous blends directly relate to complex systems in the life sciences, and also provide new directions for materials science development.

## References


1 National Science Foundation, Interdisciplinary Globally-Leading Polymer Science and Engineering (2007) available via the Web at http://www.nsf.gov/mps/dmr/reports.jsp.

2 Ober, C.K., Cheng, S.D., Hammond, P.T., Muthukumar, M., Reichmanis, E., Wooley, K.L., and Lodge, T.P. (2009) *Macromolecules*, **42**, 465.

3 Mark, J.E. (ed.) (2007) *Physical Properties of Polymers Handbook*, Springer Science, New York.

4 Paul, D.R. and Bucknall, C.B. (ed.) (2000) *Polymer Blends*, vols. 1 and 2, John Wiley and Sons, Inc., New York.

5 Colmenero, J. and Arbe, A. (2007) *Soft Matter*, **3**, 1474.

6 Freed, K.F. and Dudowicz, J. (2005) *Adv. Polym. Sci.*, **183**, 63.
7 Lohse, D.J. (2005) *J. Macromol. Sci. C, Polym. Rev.*, **45**, 289.
8 Yu, L., Dean, K., and Li, L. (2006) *Progr. Polym. Sci.*, **31**, 576.
9 Zhao, L. and Choi, P. (2006) *Mater. Manuf. Processes*, **21**, 135.
10 Yang, Z. and Han, C.D. (2008) *Macromolecules*, **41**, 2104.
11 Plazek, D. and Ngai, K.L. (2007) *Physical Properties of Polymers Handbook*, Springer Science, New York, pp. 187–215.
12 Paul, W. and Smith, G.D. (2004) *Rep. Prog. Phys.*, **67**, 1117.
13 Cangialosi, D., Alegria, A., and Colmonero, J. (2006) *Macromolecules*, **39**, 7149.
14 Roland, C.M. (2008) *Soft Matter*, **4**, 2316.
15 Kroy, K. (2008) *Soft Matter*, **4**, 2323.
16 Lodge, T.P. and McLeish, T.C.B. (2000) *Macromolecules*, **33**, 5278.
17 Milner, S.T. and McLeish, T.C.B. (1998) *Phys. Rev. Lett.*, **81**, 725.
18 Chung, G.C., Kornfield, J.A., and Smith, S.D. (1994) *Macromolecules*, **27**, 964.
19 Schneider, H.A. (1999) *J. Therm. Anal. Calorim.*, **56**, 983.
20 Bershtein, V.A., Egorova, L.M., and Prud'homme, R.E. (1997) *J. Macromol. Sci. B, Physics.*, **36**, 513.
21 Neelakantan, A., May, A., and Maranas, J.K. (2005) *Macromolecules*, **38**, 6598.
22 Kim, E., Kramer, E.J., and Osby, J.O. (1995) *Macromolecules*, **28**, 1979.
23 Chung, G.C., Kornfield, J.A., and Smith, S.D. (1994) *Macromolecules*, **27**, 5729.
24 Cendoya, I., Alegria, A., Alberdt, J.M., Colmonero, J., Grimm, H., Richter, D., Frick, B., Chung, G.C., Kornfield, J.A., and Smith, S.D. (1999) *Macromolecules*, **32**, 4065.
25 Kumar, S.K., Shenogin, S., and Colby, R.H. (2007) *Macromolecules*, **40**, 5759.
26 Painter, P. and Coleman, M. (2009) *Macromolecules*, **42**, 820.
27 He, Y., Lutz, T.R., and Ediger, M.D. (2004) *Macromolecules*, **37**, 9889.
28 Gaikwad, A.N., Wood, E.R., Ngai, T., and Lodge, T.P. (2008) *Macromolecules*, **41**, 2502.
29 He, Y., Lutz, T.R., and Ediger, M.D. (2005) *Macromolecules*, **38**, 9826.
30 Sakaguchi, T., Taniguchi, N., Urakawa, O., and Adachi, K. (2005) *Macromolecules*, **38**, 422.
31 Miwa, Y., Usami, K., Yamamoto, K., Sakaguchi, M., Sakai, M., and Shimada, S. (2005) *Macromolecules*, **38**, 2355.
32 Han, C.D., Chung, H.S., and Kim, J.K. (1992) *Polymer*, **33**, 546.
33 Wachowicz, M., Gill, L., Wolak, J.E., and White, J.L. (2008) *Macromolecules*, **41**, 2832.
34 Krygier, E., Lin, G.X., Mendes, J., Mukandela, G., Azar, D., Jones, A.A., Pathak, J.A., Colby, R.H., Kumar, S.K., Floudas, G., Krishnamoorti, R., and Faust, R. (2005) *Macromolecules*, **38**, 7721.
35 Wachowicz, M. and White, J.L. (2007) *Macromolecules*, **40**, 5433.
36 Wolak, J.E. and White, J.L. (2005) *Macromolecules*, **38**, 10466.
37 Lodge, T.P., Wood, E.R., and Haley, J.C. (2006) *J. Polym. Sci. B, Polym. Phys.*, **44**, 756.
38 Wolak, J., Jia, X., Gracz, H., Stejskal, E.O., Wachowicz, M., Jurga, S.J., and White, J.L. (2003) *Macromolecules*, **36**, 4844.
39 Wolak, J.E., Jia, X., and White, J.L. (2003) *J. Am. Chem. Soc.*, **125**, 13660.
40 deAzevedo, E.R., Hu, W.G., Bonagamba, T.J., and Schmidt-Rohr, K. (1999) *J. Am. Chem. Soc.* **121**, 8411.
41 Belgacem, M.N. and Gandini, A. (2008) *Monomers, Polymers, and Composites from Renewable Resources*, Elsevier, Amsterdam.
42 Snell, K.D. and Peoples, O.P. (2009) *Biofuels, Bioprod. Bioref.*, **3**, 456.
43 Vert, M. (2005) *Biomacromolecules*, **6**, 538.
44 Scott, G. (ed.) (2002) *Degradable Polymers, Principles, and Applications*, 2nd edn, Kluwer Academic Publishers, The Netherlands.
45 Martina, M. and Hutmacher, D.W. (2007) *Polym. Int.*, **56**, 145.
46 Gandini, A. (2008) *Macromolecules*, **41**, 9491.
47 Jeon, O., Lee, S.H., Kim, S.H., Lee, Y.M., and Kim, Y.H. (2003) *Macromolecules*, **36**, 5585.
48 Choi, N.S., Kim, C.H., Cho, K.Y., and Park, J.K. (2002) *J. Appl. Polym. Sci.*, **86**, 1892.

**49** Simo, C.L., Viana, J.C., and Cunha, A.M. (2009) *J. Appl. Polym. Sci.*, **112**, 345.

**50** Rusa, C. and Tonelli, A.E. (2000) *Macromolecules*, **33**, 5321.

**51** Jia, X., Wang, X., Tonelli, A.E., and White, J.L. (2005) *Macromolecules*, **38**, 2775.

**52** Kikkawa, Y., Suzuki, T., Tsuge, T., Kanesato, M., Doi, S., and Abe, H. (2006) *Biomacromolecules*, **7**, 1921.

**53** He, Y., Shuai, X., Kasuya, K., Doi, Y., and Inoue, Y. (2001) *Biomacromolecules*, **2**, 1045.

**54** Marsono, E., Canetti, M., Conio, G., Corsini, P., and Freddi, G. (2007) *J. Appl. Polym. Sci.*, **104**, 2187.

**55** Garcia Cruz, D.M., Countinho, D.F., Martinez, E.C., Mano, J.F., Ribelles, J.L.G., and Sanchez, M.S. (2008) *J. Biomed. Mater. Res. B, Appl. Biomater.*, **87**, 544.

**56** Aoi, K., Takasu, A., and Okada, M. (1995) *Macromol. Rapid Commun.*, **16**, 757.

**57** Huang, H., Hu, Y., Zhang, J., Sato, H., Zhang, H., Noda, I., and Ozaki, Y. (2005) *J. Phys. Chem. B*, **109**, 19175.

# 4
# Phase Field Modeling on Polymer Crystallization and Phase Separation in Crystalline Polymer Blends

*Thein Kyu, Haijun Xu, Taiming Guo, and Guoxiang Wang*

## 4.1
## Phase Field Theory of Crystal Solidification of a Pure Substance

The solidification phenomenon of a liquid has been one of the most fascinating first-order phase transitions, involving a complex interplay of many physical effects. The simplest solidification front is the planar interface. Usually, the solid–liquid interface is an active free boundary from which latent heat is liberated during solid–liquid phase transformation. Preferentially, this latent heat is conducted away from the convex solid–liquid tips, but it may be trapped in the case of concave interface, thereby leading to the directional growth of interfacial morphologies. Consequently, these interfaces are generally rough with convex and concave curvatures. Among them, the basic patterns are "dendrites" and "seaweeds." A structure with pronounced orientational order is termed as dendrite, and without apparent orientational order it is called seaweed. The dendritic shape is a symmetric needle crystal with a parabolic tip, the sides of which are influenced by a secondary branching. The seaweed morphology was originally introduced on the basis of experimental observations under the name of dense-branching morphology, which is characterized by repeating tip splitting at the interface front [1]. The basic element of the seaweed structure is a doublon, which consists of two fingers with a liquid channel running along the axis of the symmetry between them. Experimentally, Akamatsu *et al*. [2] showed that the seaweed growth involves a continual creation and elimination of doublons. In directional solidification, the solid–liquid interface is subjected to morphological instabilities in an externally imposed directional temperature gradient. Various interface morphologies have been observed [2–4] depending on the physical properties of the materials. Especially, the anisotropic properties of the solid–liquid interface play a particularly important role in determining the stability of the dendrites as well as the transformation between seaweed and dendrite patterns. Thus, an in-depth understanding of the interface morphology during solidification is essential to shed light on the pattern formation aspects of crystal solidification.

Theoretical investigations of the solid–liquid phase transition have long been the subject of considerable interest. Among these, there are two main streams: one is the

*Encyclopedia of Polymer Blends, Volume 1: Fundamentals*. Edited by Avraam I. Isayev
Copyright © 2010 WILEY-VCH Verlag GmbH & Co. KGaA, Weinheim
ISBN: 978-3-527-31929-9

classical "sharp interface" Stefan problem of zero interface thickness and the other is the "phase field" with smooth boundary, albeit sharp, having a finite interface thickness. The former is concerned with the free boundary problem that describes solidification of a pure material by treating solid and liquid phases individually and explicitly determining the position of the moving "sharp" interface between the two phases. Brener *et al.* [5] and Ihle and Müller-Krumbhaar [6], who calculated two-dimensional (2D) diffusional growth with this classical model, showed the morphology diagram of possible structures from the undercooled melt. They postulated that the main controlling parameters were undercooling, anisotropy of surface tension, and the strength of thermal noise. In their model, the thermal diffusion equation was used in conjunction with the Gibbs–Thomson relation at the interface where discontinuity of heat flux was imposed. The other approach presented here is the so-called phase field model that introduces a continuous transition between the two phases across a thin boundary layer of finite thickness, in which no distinction is made between the solid, the liquid, and the interface. An early phase field model was based on the Cahn–Hilliard (CH) equation that describes spinodal decomposition where the composition plays the role of the phase field [7]. However, Langer [8], who adopted the convention of a set of time-evolution equations proposed by Halperin *et al.* [9], applied the non-conserved phase field model for a solid–liquid phase transition of a pure substance. This methodology was also developed independently by Collins and Levine [10], and subject to rigorous mathematical analysis by Caginalp [11].

## 4.2
## Phase Field Modeling on Morphology Development

The phase field model under consideration involves a continuum equation for the propagation of smooth interface, albeit sharp, having a finite thickness. The advantage of this continuum approach is that the whole domain is treated in the same way numerically, and the position of interface does not have to be explicitly tracked but given implicitly by a set of scalar functions of time and space. A phase-field order parameter is introduced in which its value at a local point identifies the phase of the material as solid or liquid. In essence, compared with the classic diffusion equation, the diffusion field is expanded in the form of Kobayashi phase field free energy pertaining to a crystal phase order parameter under a non-equilibrium condition, for example, growth of a stable crystal phase from a metastable melt. Thus the classical formulation of the free boundary problem is replaced by a pair of nonlinear reaction-diffusion equations for the temperature and the phase order parameter field. This approach provides a convenient basis for calculating the realistic interfacial structures, avoiding difficult boundary integral or domain transformation methods encountered in the free boundary problems.

In the Kobayashi phase field approach [12], a phase order parameter, $\psi(r, t)$, is introduced to express explicitly the liquid and solid phases. It assumes a constant value in each bulk phase, for example, $\psi = 1$ in the solid and $\psi = 0$ in the liquid phase.

Basically, the time-dependent Ginzburg–Landau (TDGL) equation [12] relates the temporal change of a phase order parameter to a local chemical potential and a nonlocal interface gradient. With respect to a non-conserved phase field order parameter, the TDGL model A equation is customarily described as:

$$\frac{\partial\psi(r,t)}{\partial t} = -\Gamma\frac{\delta F(\psi)}{\delta\psi(r,t)} \tag{4.1}$$

Here $\psi(r, t)$ represents the phase order parameter at time $t$ and position $r$, $\Gamma$ is mobility that is inversely proportional to the viscous drag force; $\delta/\delta\psi$ is the functional derivative with respect to the crystal order parameter defined as $\delta/\delta\psi = \{\partial/\partial\psi - \nabla(\partial/\partial\nabla\psi)\}$; $F$, the total free energy of the phase ordering for overall volume ($V$), is given in terms of a local free energy density and a nonlocal gradient term, representing nucleation and growth, that is:

$$F(\psi)/Nk_{\mathrm{B}}T = f_{\mathrm{cryst}}(\psi) = \int_V [f_{\mathrm{local}}(\psi) + f_{\mathrm{grad}}(\psi)]\mathrm{d}V \tag{4.2}$$

with $Nk_{\mathrm{B}} = nR$ where $N$ is the number of molecules, $n$ is the number of moles, $R$ is the gas constant, and $k_{\mathrm{B}}$ is the Boltzmann constant.

In general, the local free energy of solidification may be expressed in accordance with the Landau expression in powers of the order parameter $\psi$ as, $f_{\mathrm{local}} = a\psi^2 + b\psi^3 + c\psi^4 + \ldots$. For the Landau free energy to be applicable to a first-order phase transition, it is necessary for the coefficient of the third power term to be finite, that is, $b \neq 0$. This free energy is characterized by an asymmetric double well that involves metastability and latent heat. However, when the coefficient of the third power term, $b$, is exactly zero, such free energy, having a symmetric double well, is applicable to a second-order phase transition or the first-order transition only at the node. According to Kobayashi, the local free energy density may be given in the form of the Landau expansion as [12]:

$$f_{\mathrm{local}}(\psi) = W\int_0^{\psi}\psi(\psi-1)(\psi-\zeta)\mathrm{d}\psi = W\left[\zeta\frac{\psi^2}{2} - (1+\zeta)\frac{\psi^3}{3} + \frac{\psi^4}{4}\right] \tag{4.3}$$

where $\zeta$ is related to supercooling, $\Delta T = T_{\mathrm{m}} - T_{\mathrm{x}}$; note that $T_{\mathrm{m}}$ is the equilibrium melting temperature, $T_{\mathrm{x}}$ is the crystallization temperature, and $W$ is a dimensionless coefficient associated with the energy penalty for the crystal solidification to overcome.

For a pure material, the local free energy density of the system is assumed to be a monotonic function of temperature, $T(r, t)$, and has the form of an asymmetric double well with respect to $\psi$. As shown in Figure 4.1, the two minima represent the free energy of the solid and liquid phases for each temperature. At the melting point $T_{\mathrm{m}}$ ($\zeta = 0.5$), the free energy density has two local minima, meaning the liquid and solid can coexist. When $T_{\mathrm{x}} < T_{\mathrm{m}}$ ($\zeta < 0.5$), the free energy density has a global minimum at $\psi = 1$. Hence, the liquid is metastable and the solid is the stable phase, the liquid will solidify by overcoming the nucleation barrier indicated by $\zeta$ on the $\psi$

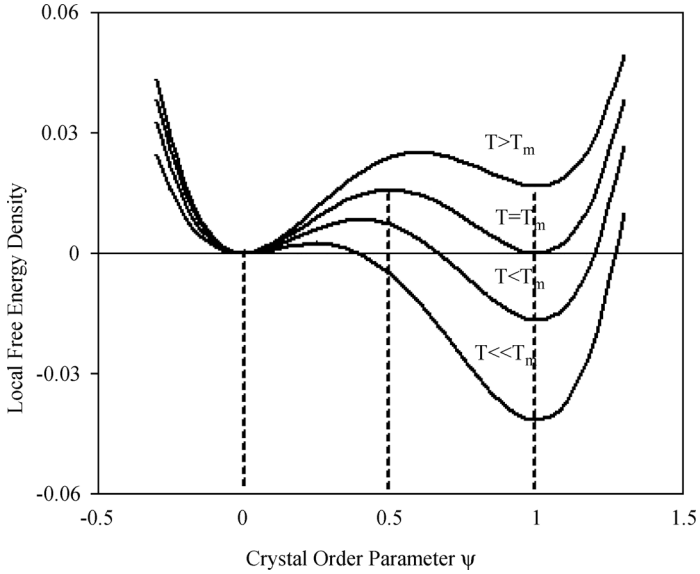


**Figure 4.1** Local free energy density as a function of crystal order parameter $\psi$ at various temperatures, showing different nucleation barrier heights and locations, $\zeta$.

axis. When $T_x > T_m$ ($\zeta > 0.5$), the solid phase becomes metastable because the global minimum of the free energy is located at $\psi = 0$, which corresponds to a stable melt phase, and thus all the solids must melt.

The total free energy is composed of local and nonlocal free energy densities. The nonlocal free energy density can be written in terms of the gradient free energy density describing the growth process as:

$$f_{\text{grad}}(\psi) = \tfrac{1}{2}\varkappa^2 \cdot |\nabla\psi|^2 \tag{4.4}$$

where $\varkappa$ is the interface gradient coefficient in the scalar form for simplicity, although it is originally defined as a tensor. Substituting Eqs. (4.2)–(4.4) into Eq. (4.1), one obtains:

$$\frac{\partial\psi(r,t)}{\partial t} = -\Gamma\frac{\delta F(\psi)}{\delta\psi} = -\Gamma\left[W\psi(\psi-1)(\psi-\zeta) - \varkappa^2\nabla^2\psi\right] \tag{4.5}$$

where $\zeta$ is the value of the phase order parameter at the energy barrier hump and $\varkappa$ is the coefficient of interface gradient [12].

In the description of the anisotropic surface energy, the coefficient of interface gradient, $\varkappa$, was allowed to depend on the crystallographic orientation, $\theta$, where $\theta = \arctan(\psi_y/\psi_x)$ is the angle between the normal to the interface (defined as $\bar{n} = \nabla\psi/|\nabla\psi|$) and the preferred axis [12]. Anisotropy, which controls the interfacial morphology drastically, is an important feature of the solidification theory. Kessler *et al.* [13] and Pomeau and Ben Amar [14] have pointed out that the interfacial property coming into play is the surface energy. The anisotropy of the surface energy

originates from the orientation of the interface with respect to the crystal lattice. Since 1980, several theoretical groups independently reached a similar conclusion that the anisotropy of surface energy plays a major part in the pattern formation [13–16]. For a certain crystallographic direction, for example, the <100> direction for a cubic crystal, the surface energy is anisotropic [17], and the morphology develops with cellular or dendritic patterns. Meanwhile, for crystalline axes along <111> direction, the surface energy is isotropic [18]; the interface development has been dominated by seaweed growth [2]. There have been several suggestions as to how to incorporate anisotropy into the phase field description. Firstly, Caginalp and Fife [19, 20] suggested that the "square gradient term" in the free energy functional could be replaced by a more general quadratic form with different coefficients in each coordinate direction. For an isothermal system this leads to an elliptical equilibrium shape. Secondly, to elucidate more complicated anisotropies, Langer [8] has proposed the gradient energy terms involving the squares of higher derivatives of the phase field, and gave an example leading to the directional growth. Cahn and Kikuchi [21] have considered discrete forms of diffuse-interface models, and included anisotropic effects through the choice of nearest-neighbor interactions.

Wheeler *et al.* [22] have incorporated the anisotropy by allowing the coefficient of the gradient energy to depend on the local orientation of the gradient of the phase order parameter. The nature of this anisotropic form has been explored by McFadden *et al.* [23]. Brener and coworkers [24] have shown that the interfacial anisotropy can be correlated to the magnitude of growth velocity in the directional solidification. According to Kobayashi [12], $\varkappa$ is proportional to the surface energy $\sigma$, thus the anisotropic function $\varkappa$ can be written in terms of the fourfold symmetry as $\varkappa = \varkappa_0[1 + \varepsilon\cos(4\theta)]$, where $\varkappa_0$ is a constant and $\varepsilon$ is the strength of surface energy anisotropy. Further, Kobayashi [12] coupled the time evolution equation pertaining to the crystal phase order parameter to the energy balance (i.e., heat conduction) equation and demonstrated the evolution of side-branched dendritic structures growing into an undercooled melt.

Based on the conservation law of enthalpy, the heat conduction equation, involving liberation of latent heat from the growth front, may be written as:

$$\varrho C_p \frac{\partial T}{\partial t} = k_T \nabla^2 T + \varrho \Delta H_u \frac{\partial \psi}{\partial t} \tag{4.6}$$

where

$\varrho$ (kg m$^{-3}$) is the density,
$C_p$ (J kg$^{-1}$ K$^{-1}$) is the heat capacity,
$k_T$ (J m$^{-1}$ s$^{-1}$ K$^{-1}$) it the thermal conductivity,
$\Delta H_u$ is the latent heat (J kg$^{-1}$).

Setting thermal diffusivity, $\alpha = k_T/\varrho C_p$ and $\Delta H_u/C_p = K$, then the heat conduction equation for the temperature evolution becomes:

$$\frac{\partial T}{\partial t} = \alpha \nabla^2 T + K \frac{\partial \psi}{\partial t} \tag{4.7}$$

More recently, Guo *et al.* [26] have evaluated the model parameters from the experimentally accessible material parameters of succinonitrile [$CN(CH_2)_2CN$] (SCN) [27, 28] in accordance with the following relationships [29, 30]:

$$W = 48\frac{\sigma}{nRT_m}\frac{1}{\delta} \tag{4.8}$$

$$\kappa^2 = \frac{3}{2}\frac{\sigma\delta}{nRT_m} \tag{4.9}$$

$$\zeta = \frac{1}{2} - \frac{\Delta H_u}{8}\left(\frac{\delta}{\sigma}\right)\left(\frac{T_m - T}{T_m}\right) \tag{4.10}$$

$$\Gamma = \nu\left[\frac{3}{2\sqrt{2}}\frac{\delta\Delta H_u}{nRT_m}\left(\frac{T_m - T}{T_m}\right)\right]^{-1} \tag{4.11}$$

where

$\delta$ is the interface thickness,
$\sigma$ is the surface tension,
$\nu$ is the growth speed.

To describe the governing Eqs. (4.5) and (4.7) in dimensionless form, the variables are renormalized with dimensionless time $\tau$ and other dimensionless variables denoted with tilde symbols as follows: $\tilde{x} = x/d^*, \tilde{y} = y/d^*, \tau = Dt/d^{*2}$, where $d^*$ is the characteristic length ($10^{-6}$ m), and $D$ is the diffusion coefficient. The temperature is rescaled to $u = T/T_m$. Then, the final governing equations are represented in dimensionless form:

$$\frac{\partial\psi}{\partial\tau} = \tilde{\Gamma}\left[\tilde{\kappa}^2\tilde{\nabla}^2\psi - \tilde{W}\psi(\psi-1)(\psi-\zeta)\right] + \eta \tag{4.12}$$

$$\frac{\partial u}{\partial\tau} = \tilde{\alpha}\tilde{\nabla}^2 u + \tilde{K}\frac{\partial\psi}{\partial\tau} \tag{4.13}$$

where:

$$\tilde{\nabla} = \tilde{i}(\partial/\partial\tilde{x}) + \tilde{j}(\partial/\partial\tilde{y})$$

$$\tilde{\Gamma} = \Gamma d^{*2}/D$$

$$\tilde{\kappa} = \kappa/d^*$$

$$\tilde{W} = W$$

$$\tilde{\alpha} = \alpha/D$$

$$\tilde{K} = K/T_{\mathrm{m}}$$

The last term of Eq. (4.12), η, is the thermal force that satisfied the fluctuation–dissipation theorem. Equations (4.12) and (4.13) may be solved numerically on a square lattice using a finite difference method with central difference for spatial steps and forward difference temporal steps. A temperature gradient field can be created between the top and bottom walls. To express the external temperature gradient field, the dimensionless model parameter $\tilde{K}$ may be rescaled with:

$$\tilde{K} = \frac{K}{T_{\mathrm{m}}}\frac{T_{\mathrm{m}}}{T_{\mathrm{H}} - T_{\mathrm{L}}} = K/(T_{\mathrm{H}} - T_{\mathrm{L}})$$

for the imposed external thermal gradient, where subscripts H and L stand for high and low temperatures, respectively.

To account for the directional solidification under the external temperature gradient, the phase field model can be modified by renormalizing the coefficients of heat conduction equation with the imposed (external) thermal gradient. In this modified model, the interface roughness was imparted by simply triggering thermal noise at the cold wall in the first iteration, and then removed in the subsequent iterations. The thermal noise thus exerted has a significant effect on the solid–liquid interface, showing a rough interface with convex and concave curvatures (Figure 4.2). The latent heat thus released upon crystallization can propagate readily through the convex parabolic tip into the intercooled melt driven by the large thermal gradient, whereas heat may be trapped in the concave region due to the lack of thermal gradients between the neighboring walls. Hence, the heat flow must be directional, which has led eventually to the directional crystal growth.

It can be anticipated that the growth of interfacial morphology is governed by the anisotropy of surface energy. When ε is small, the seaweed type interface morphology

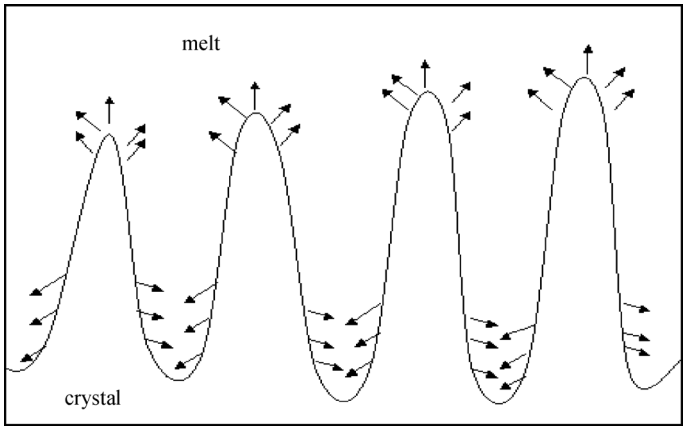


**Figure 4.2** Directional crystal growth towards the undercooled melt driven by preferential heat dissipation in the convex tip of a rough interface and heat accumulation at the concave region due to lack of thermal gradient between neighboring walls.

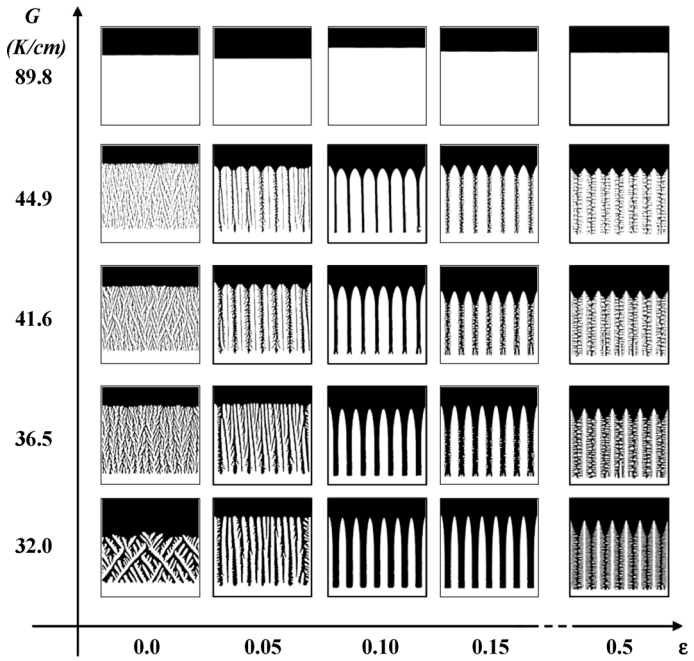


**Figure 4.3** Morphology diagram under directional solidification as a function of temperature gradient and anisotropy of surface energy.

develops through continual side-branching and tip-splitting of the growing front (Figure 4.3). The irregular side branching and tip splitting are the typical characteristics of a seaweed. As ε increases to 0.05, the frequency of tip splitting decreases and the finger structure is observed with side branching (SB). Then, as ε increases, the interface pattern slowly transits to the doublet structure. Both doublet and SB finger textures belong to the doublon structure, which is the underlying building element of the seaweed pattern. With a further increase of ε to 0.10, the interface morphology transits into a cellular pattern and such a regular cellular structure persists until $\varepsilon = 0.15$ (Figure 4.3).

When ε reaches a sufficiently high value of 0.5, the interface shows strong anisotropic character; the secondary arms branch out from the main stem. This kind of regular interface morphology is characterized as the dendritic growth pattern. The action of interfacial force, as demonstrated by Kobayashi [12], Karma *et al.* [31], and Brener *et al.* [5], as well as simulation of Guo *et al.* [26], revealed the side branching in the dendritic patterns. Of particular importance is that the crossover from the seaweed to degenerate and cellular was captured, which subsequently transited to dendrites with further increase of the surface anisotropy. The transition of the highly branched seaweed to highly branched dendrite with increasing surface energy anisotropy through the cellular structure without any branching is intriguing. It may be inferred that the interface dynamics as well as the emerged patterns are controlled sensitively by the magnitude of the anisotropy.

As illustrated in Figure 4.3, the morphology landscape clearly reveals that the dendritic patterns form predominantly at low temperature gradient $G$ and high anisotropy, $\varepsilon$, whereas seaweed patterns develop at moderately strong $G$ and weak $\varepsilon$. In the intermediate regions between the dendrite and seaweed, a cellular structure appears in manner dependent on $G$ at $\varepsilon = 0.10$ to 0.15, in which the width of each cell increases with increasing thermal gradient. The interface gap between the neighboring cells becomes closer and closer with increasing $G$. When the interfaces of the neighboring cells are in close contact, the interface boundary eventually disappears by virtue of the surface tension, thereby forming a planar interface (e.g., at $G = 89.8\,\mathrm{K\,cm^{-1}}$). A similar conclusion may be drawn for the dendrites (at $\varepsilon = 0.5$) and also for the seaweeds (at $\varepsilon = 0.05$).

When the surface energy anisotropy becomes stronger, say $\varepsilon = 0.5$, the preferred crystal orientation of the secondary arms is nearly perpendicular to the axis of temperature gradient. At the weak anisotropy of $\varepsilon = 0.05$ and $G = 41.6\,\mathrm{K\,cm^{-1}}$, the easiest growth direction is the direction of sharpest temperature gradient. Thus the secondary arms will deviate from the preferred crystal orientation by tilting to the axis of temperature gradient. It is easier for the latent heat to be liberated at the growth front to conduct away into the undercooled melt. The main branches are somewhat irregular due to frequent tip-splitting and side branching, but the growth direction remains fairly along the axis of temperature gradient. The tips split alternately on both sides. It appears that the main branch and the secondary arm are locally symmetric about the axis of temperature gradient. Such interface morphology with a slight degeneracy is called degenerate seaweed according to Utter and Bodenschatz [18].

It is intriguing to discern the morphology transformation from dendrite into seaweed occurring through the cellular structure, which has an inherently smooth surface relative to dendrites or seaweeds. Although cellular structure is a rare occurrence, it can be observed experimentally at moderate $G$ and $\varepsilon$. The cellular structures are unique in the sense that the surface instability is sufficiently small to make the cellular interface smooth. When the instability exceeds a critical size, the surface becomes rougher, eventually evolving into side branching in seaweeds and dendrites. The secondary branches in the dendrites tend to align perpendicular to the main branch due to the strong preferential crystal orientation. In the case of seaweeds, the strength of the anisotropy is very small, such that the crystal orientation loses its preferred crystallographic direction. When the competition between the thermal gradient and the anisotropy strength becomes comparable, the side branches tend to tilt in some intermediate upward angles into the undercooled melt as seen in the seaweeds.

The predicted morphological landscape is interesting in its own right; it is imperative to compare it with the experimental findings to test the rigor of the phase field theory. Guo *et al.* have performed some non-isothermal solidification experiments on succinonitrile (SCN) using traditional directional solidification apparatus [26]. The interfacial morphology landscape has been constructed as a function of anisotropy and temperature gradient. Of particular interest is that these predicted morphology patterns are in good accord with the experimental findings in the phase transitions of succinonitrile (SCN) (Figure 4.4), exhibiting (a) dendrite, (b)

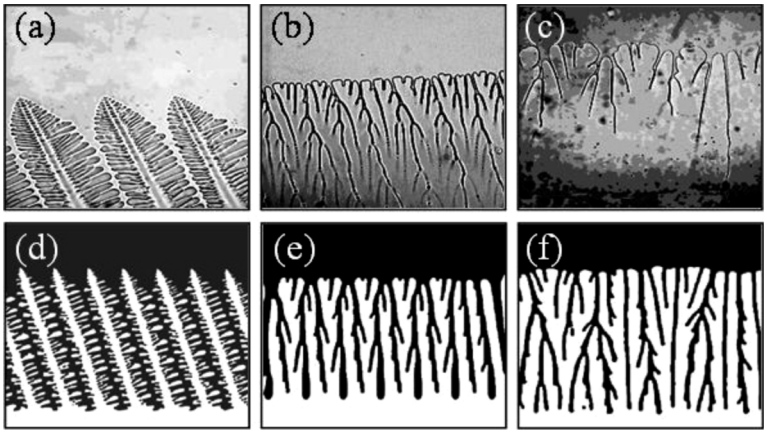


**Figure 4.4** Experimentally observed (a) dendrite, (b) degenerate ($G = 58.7\,\mathrm{K\,cm^{-1}}$), and (c) seaweed ($23\,\mathrm{K\,cm^{-1}}$) of SCN under directional solidification with temperature gradient in comparison with the corresponding patterns (d), (e), and (f) simulated in the context of the phase field model. The length scale of the calculated images is 512 μm.

degenerate (at $G = 58.7\,\mathrm{K\,cm^{-1}}$), and (c) seaweed (at $23\,\mathrm{K\,cm^{-1}}$) of SCN under directional solidification in comparison with the corresponding patterns (d), (e), and (f) simulated in the context of the Kobayashi phase field model [12].

## 4.3 Application of Phase Field Approach to Crystallization of a Homopolymer

Polymer crystallization has received immense attention for several decades because of a rich variety of crystalline morphology encompassing single crystals to hierarchical structures such as sheaf-like textures and spherulites [32, 33]. By virtue of the connectivity of polymeric chains, polymer crystallization hardly reaches thermodynamic equilibrium; therefore crystals thus formed are imperfect, containing sizable amount of defects. It has been generally known that polymer single crystals can be grown from dilute solutions, whereas spherulites develop from the melt. Recently, various single crystals were found to develop from the melt state with various fascinating patterns, including diamond, snowflakes, or faceted hexagonal shapes [34–37].

Lovinger *et al.* have examined single crystal growth from the melt of poly(trifluoroethylene) exhibiting lamellar branched morphology, which was explained in the context of the diffusion limited aggregation [34]. Reiter *et al.* observed fingerlike branched patterns during crystallization of poly(ethylene oxide), which has been attributed to the diffusion process [35]. Sakai and coworkers have found tip-splitting crystal growth in thin films of poly(ethylene terephthalate) that evolves to a novel crystal morphology, called terrace [36]. Taguchi *et al.*, who investigated the crystal growth of isotactic polystyrene (*i*-PS), have found morphology variation with de-

creasing crystallization temperature [37]. At high crystallization temperatures, a hexagonal single crystal of *i*-PS formed. However, the faceted hexagonal plate transforms to nonfaceted snowflakes, then to dense branching morphology (compact seaweed) with decreasing temperature of crystallization.

Intrigued by the experimental observations of Taguchi and coworkers, Kyu and coworkers [38–40] calculated the spatiotemporal growth of polymer single crystals based on the phase field model of Kobayashi, who applied a phase field model based on the anisotropic Landau-type potential with some free model parameters in accounting for the dendritic growth of snowflakes and successfully demonstrated the evolution of dendritic structures growing into an undercooled melt [12]. Although the Kobayashi potential is seemingly adequate for describing the dendritic growth of the small molecule systems, the extension of it to high molecular weight polymers requires appropriate modification since polymer crystallization may not achieve thermodynamic equilibrium during solidification due to the long chain nature of macromolecules. The advantage of the above phase field approach is that it describes the spatiotemporal growth rather than the conventional nucleation theory of Lauritzen–-Hoffman (LH) that considered only the kinetics, that is, the temporal growth without any spatial dependence [41, 42]. There are many criticisms of the LH theory; a fair account may be found in the review of Armistead and Goldbeck-Wood [43]. There are also several modifications, especially by Mansfield [44] as well as by Toda [45] who use the front propagation model of Frank [46] based on the sharp discrete interface approach. Although simulation with these models captured some features of curved single crystals, intricate textures such as sectorization, ripples, or other decorated patterns are not explicable because these models tracked the solid–melt interface front only. Moreover, the LH theory is too geometrically specific to polymer crystals, without general applicability to other systems such as snowflakes or metallic crystals [43].

There are newer calculations on spatiotemporal evolution of polymer crystals in the framework of Langevin dynamics by Muthukumar [47] and also by Granasy *et al*. [48, 49] and Kyu's group [38–40] who used the phase field theory of crystal solidification. The Langevin dynamic approach is based on competition between the attractions among nonbonded repeat units and the torsional energies along the polymer backbone. The notable outcomes of the Langevin dynamics are the formation of a pearl-like crystal precursor, called smectic pearls, preceding the nucleation. The latter phase field theory is a continuum approach and thus it can be regarded as a phenomenological approach, as explained in earlier sections. In this section, we focus on the extension of the phase field approach to polymer crystallization.

To capture the imperfect morphology of semicrystalline polymer crystals, Kyu and coworkers adopted the phase field approach by taking into consideration various metastable states of polymer crystallization [38–40]. That is to say, the calculation based on this modification must account for the development of less-ordered incomplete spherulitic structures to highly-ordered faceted single crystals of polymers by simply varying crystallization temperature or supercooling. A convenient starting point is deployment of the asymmetric free energy double-well of Harrowell *et al*. [29] or of Chan [30] who expressed the phase field parameter at the solidification potential as a constant, but less than unity.

The free energy density of crystal solidification of a small molecule system may be extended to polymer crystallization by modifying Eq. (4.3) in what follows [38–40]:

$$\begin{aligned} f(\psi) &= \frac{F(\psi)}{Nk_{\mathrm{B}}T} = W\int_0^{\psi}\psi(\psi-\zeta)(\psi-\zeta_0)\mathrm{d}\psi \\ &= W(T)\left[\frac{\zeta(T)\zeta_0(T_{\mathrm{m}})}{2}\psi^2 - \frac{\zeta(T)+\zeta_0(T_{\mathrm{m}})}{3}\psi^3 + \frac{1}{4}\psi^4\right] \end{aligned} \tag{4.14}$$

where the coefficients of the Landau free energy expansion in terms of the crystal order parameter ($\psi$) are treated as temperature dependent in polymer crystallization to account for the imperfect nature of polymer crystals. This crystal phase order parameter may be defined as the ratio of the lamellar thickness ($l$) to the lamellar thickness of a perfect polymer crystal ($l^0$), that is, $\psi = l/l^0$, and thus it represents the one-dimensional crystallinity, hereafter called linear crystallinity [38]. It should be cautioned that the coefficient of the cubic term should be non-zero in order to apply the aforementioned Landau double-potential to the first-order phase transition; otherwise, Eq. (4.14) is applicable only to a second-order phase transition or only at equilibrium where the two minima are equivalent. The term $\zeta$ represents the unstable hump for the crystal nucleation to overcome the barrier and $W$ is the coefficient that represents the penalty for the nucleation process; $\zeta_0$ represents the crystal order parameter at the solidification potential for crystallization given as $\zeta_0 = (T_{\mathrm{m}}^0 - T_{\mathrm{m}})/(T_{\mathrm{m}}^0 - T_{\mathrm{x}})$, where $T_{\mathrm{x}}$ is the crystallization temperature (Figure 4.5) [40].

In principle, the stable solid may vary from unity at equilibrium to some finite values of $\zeta_0$ depending on the supercooling or the crystallization temperature. At $T_{\mathrm{m}}^0$,

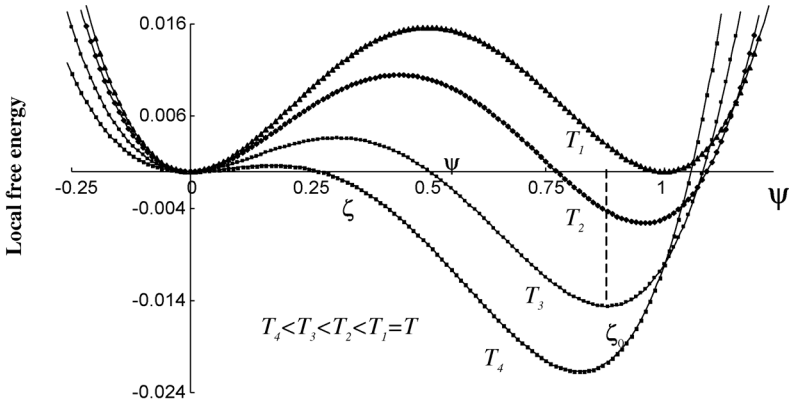


**Figure 4.5** Local free energy density as a function of crystal order parameter $\psi$ for various temperatures, showing different nucleation barrier heights and locations, $\zeta$. The order parameter at the solidification potential ($\zeta_0$) varies with the crystallization temperature, indicating the imperfection of polymer crystals.

the free energy densities of the melt and the solid are equivalent, implying the coexistence of the crystal and melt. When $T < T_m^0$, the free energy density has a global minimum at $\zeta < 1$, that is, the linear crystallinity is less than unity, which suggests that the emerged crystals are defective or some amorphous materials are entrapped in the solid phase, reflecting the metastable nature of the polymorphous crystals. Nonetheless, the metastable crystal phase is more stable than the unstable melt. Hence, the melt must solidify by overcoming the nucleation barrier peak labeled by $\zeta$ on the $\psi$-axis. As the supercooling increases, $\zeta_0$ moves to a lower value that implies imperfection of the crystal, containing a sizable amount of entrapped amorphous chains or defects. For small molecule systems, $\zeta_0$ may be taken as unity. The advantage of the present theory of polymer solidification is that these model parameters, $W$ and $\zeta$, are intimately related to the material properties of the individual components [38–40].

Xu *et al.* have established a morphological diagram of *i*-PS as a function of supercooling and anisotropy (Figure 4.6), which discriminates among different interfacial patterns [39]. At very low supercooling and high anisotropy, the faceted hexagonal pattern emerges. With increasing supercooling, the edges of the hexagon cave in, while the interface structure gradually transforms from hexagonal into nonfaceted dendrites. In the absence of anisotropy at small supercooling, a circular pattern develops. With decreasing anisotropy at the shallow supercooling, the morphology transformation occurs from the hexagonal single crystal to the circular

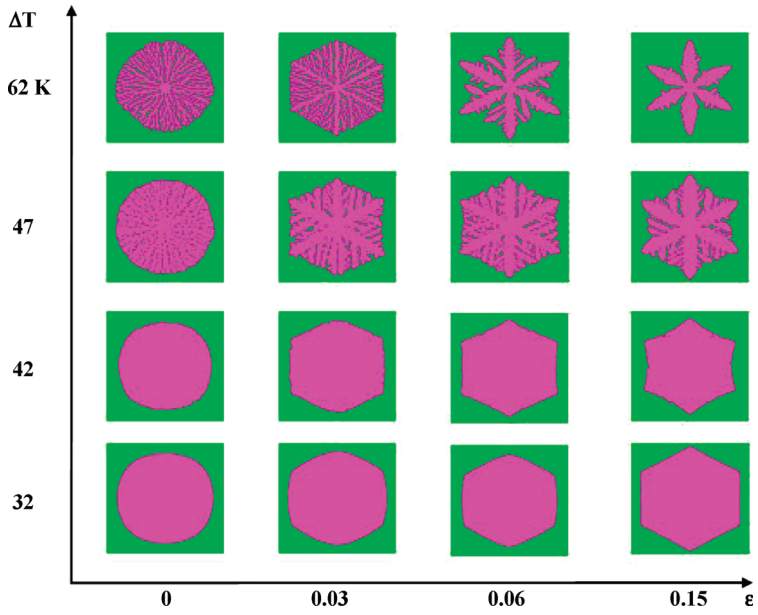


**Figure 4.6** Morphology landscape of crystalline polymer morphologies as a function of supercooling and anisotropy of surface energy.

pattern through intermediate textures such as bulged (convex) hexagons. Upon increasing the supercooling slightly, hexagonal single crystals with curved edges develop, for example, the curvature changes from circular to concave at intermediate values of anisotropy. On further increasing supercooling, the edges of the hexagon split and form irregular branches, which may be characterized by degenerate and/or seaweed structures that eventually evolve to the dense lamellar branching morphology. Notably, not only the shape of crystal morphologies changes with supercooling, but the length scale of the crystal changes, that is, the mean width of branches and the average distance between neighboring lamellar branches decrease with increasing supercooling.

Furthermore, the faceted hexagonal single crystal changes to dendritic snowflakes and non-faceted lamellar branching morphology in accordance with the combination of increasing supercooling and decreasing anisotropy of the interfacial energy. Usually, the anisotropy parameter is difficult to measure experimentally, in many cases it is unknown. In this particular case, the anisotropy of the interfacial energy must be supercooling dependent as the anisotropy decreases as the supercooling increases. Taguchi and coworkers [37] have pointed out that the experimental single-crystal structures of isotactic polystyrene (*i*-PS) were obtained by first cooling the samples below the glass transition and then crystallizing them at some elevated temperatures. Hence, it is somewhat different from the direct temperature quench to the isothermal crystallization temperatures. Moreover, the importance of the finite thickness of the thin films on the emerging morphology was emphasized by Taguchi *et al.* [37], which was not accounted for in the calculation [39]. The effects of anisotropy of surface energy and supercooling on the morphological landscape of *i*-PS have been demonstrated (Figure 4.7). With increasing supercooling and

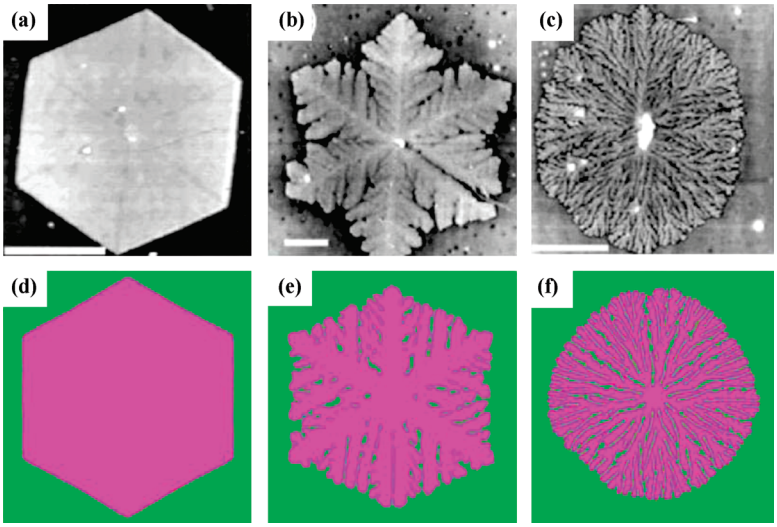


**Figure 4.7** Comparison of calculated patterns with the experimental observations of Taguchi *et al.* [37] on isotactic polystyrene.

decreasing anisotropy, the lateral surface of *i*-PS crystals becomes unstable and undergoes morphological transition from the hexagonal plate to dendrite-like snowflakes, and then to dense lamellar branching morphology. The resulting free energy expression thus accounts for metastability involving the latent heat generated at the crystal growth fronts.

In addition to the sectorization, Taguchi *et al.* observed corrugated ripple formation in these hexagonal sectors in the hexagonal single crystal of *i*-PS [50]. In an attempt to generate such sectorized hexagons, Mehta and coworkers coupled two nonlinear differential equations, pertaining to a crystal order parameter and a chain tilt angle [51, 52]. The process of chain tilting was described through the mechanical deformation field associated with a sudden change of density driven by volume shrinkage at the interface during the solid crystal–liquid melt transition. Note that mass is conserved during this melt–solid phase transformation and thus the increase in density at the interface has to be compensated by volume shrinkage. Such volume shrinkage at the interface probably occurs like a shock wave, giving rise to undulation. The similarity between the calculated sectorized single crystals with corrugated textures (Figure 4.8d–f) and the observed morphologies of *i*-PS (Figure 4.8a–c) was striking. Notably, the modified phase field model as described by the temperature dependent free energy double wells is the first to capture the various metastable states, which is mathematically simpler and physically more rigorous than that of the conventional concept of multiple-well potentials.

In practice, heterogeneous nucleation occurs in polymer crystallization. The multi-nucleation event was triggered in the crystal order parameter field based on the large density fluctuations driven by thermal perturbation. As can be witnessed in the

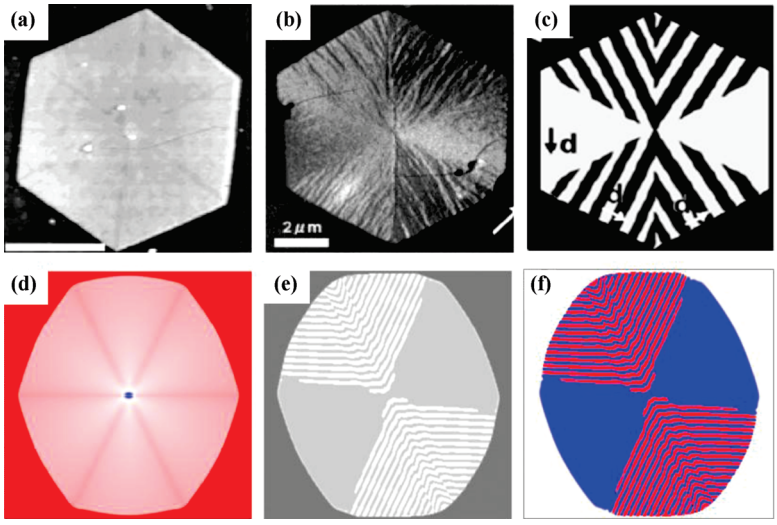


**Figure 4.8** Sectorization and ripple formation in a hexagonal single crystal of isotactic polystyrene. Experimental observations by Taguchi *et al.* for it-PS [37] (a–c) and calculated patterns in crystal order parameter and concentration fields by Mehta *et al.* [52] (d–f).

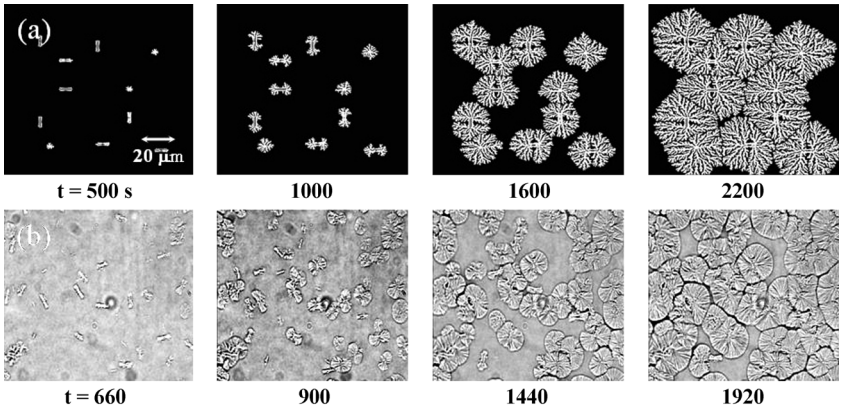


**Figure 4.9** (a) Spatiotemporal growth of multiple spherulites crystallized in the crystal order parameter field with a grid size of 1024 × 1024, exhibiting sequential growth of the anisotropic nuclei with lamellar stacks, sheaf-like, and dense lamellar branching morphology with distinct grain boundaries. The calculated length scale of the picture frame is 102.4 μm. (b) Sequential growth of the spherulitic structure of neat *s*-PP obtained at an isothermal crystallization temperature of 100 °C.

experiment as well as in the calculation [40], some nuclei that exceeded the critical size grow while others diminish. The anisotropic lamellar growth is maintained for some initial period, but it loses its character with progressive growth as manifested in the time sequence of the emerging hedrites and regular spherulites (Figure 4.9a). When the neighboring spherulites impinge on each other, the growth ceases and concurrently grain boundaries develop between these neighboring spherulites. The formation of grain boundaries may be attributed to the latent heat being released into the interstitial spherulitic regions, where the heat is seemingly accumulated, and thereby preventing further growth of the spherulites. Consequently, the impinged spherulites transform into polyhedral shapes.

The calculated trends of spherulitic growth can be confirmed in the isothermal crystallization of *s*-PP from the melt. Figure 4.9b shows the time sequence of the optical micrographs of *s*-PP spherulites crystallized at 100 °C, which is strikingly similar to what was demonstrated in the 2D calculated patterns. The initial nuclei grow into rectangular shape lamellae, reflecting the crystallographic axes of *s*-PP crystals. These lamellae tend to stack into lamellar bundles that transform into the sheaf-like structure before emerging to dense lamellar branching morphology. Some spherulites show anisotropic nuclei with dual eye-socket appearance at the core. In the case of multiple nucleation events, the neighboring spherulites impinge and form the interface grain boundaries. The heat released at the peripheral of the spherulite boundaries cannot escape since there is virtually no thermal gradient between the adjacent boundaries, which themselves are heat sources. It is reasonable to infer that the present modified phase field model captures the sequential growth of the anisotropic nuclei, leading to lamellar stacks, sheaf-like, then to spherulites, and impingement of spherulites. These calculated

morphological patterns are consistent with the experimental findings on the isothermal crystallization of *s*-PP [40]. The observed anisotropic lamellar stacked morphology with dual-eye pocket textures may be unique to polymer crystals, although the formation of dense branching morphology has been identified in small molecule organic crystals. The development of dense branched spherulitic morphology has also been computed by Granasy *et al*. using a similar phase field approach but solely based on the instability of the interface [48, 49]. In metal alloys, the grain boundary formation has been attributed to the mismatched orientations of the interface plane normals caused by the surface instability along the non-uniform interface. It appeared that the interface front growth can be influenced appreciably by the latent heat flux, especially in generating the well-known lamellar branching morphology with distinct development of the grain boundaries.

## 4.4
## Thermodynamics of Crystalline Polymer Solutions and Blends

### 4.4.1
### Prigogine's Model

Prigogine was the first to establish phase diagrams for solid–liquid transitions in binary blends theoretically based on the following assumptions: (i) solvent and solute are like molecules, that is, indistinguishable from each other; (ii) the liquid mixture is completely ideal, that is, there is no heat of mixing; and (iii) the solvent is completely immiscible with the solute phase [53]. Under these assumptions, one can directly evaluate the melting point depression by equating the chemical potential of the solid phase to the known chemical potential of the liquid phase to obtain the relation. Since the heat of crystallization is a colligative property in solutions, the chemical potential of the solid crystalline fraction ($\mu_c$) is equal to the corresponding intensive property, that is, the free energy:

$$\mu_c = \frac{\Delta H_u}{RT_m}\frac{T_m^0 - T_m}{T_m^0} \tag{4.15}$$

leading to the well-known expression:

$$\frac{1}{T_m} - \frac{1}{T_m^0} = \frac{-R}{\Delta H_u}\frac{V_u}{V_2}\phi_2 \tag{4.16}$$

which relies simply on the entropic contribution to the free energy of the mixture. Here $V_u$ is the volume of the repeating unit and $V_2$ is that of the diluent, whereas $\phi_2$ is the volume fraction of the diluent, with $\phi_1 + \phi_2 = 1$; $\phi_1$ is the volume fraction of the solute. Prigogine's model was overly simplified as it did not account for the non-ideal nature of crystals that can exist in the liquid phase [53]. The non-ideal behavior was observed in solution mixtures of hydrocarbons in carbon tetrachloride, aromatic hydrocarbons in benzene, and *o*-chloronitrobenzene/*p*-chloronitrobenzene

mixtures [54]. Hence, the entropic free energy alone cannot describe materials like polymers since long-chain hydrocarbons that contain numerous monomeric units have a large conformational energy; this has led to the modification for the real polymer solution by Flory, as discussed below [54, 55].

### 4.4.2 Flory Diluent Theory

The melting point of a solution mixture is usually lower than the melting points of its constituents in their neat states; polymer solutions and blends are no exception to this rule. This phenomenon is known as the melting point depression [54]. The most widely utilized theory for describing the melting point depression is the well-known Flory diluent theory. Flory removed the first two assumptions of Prigogine, such that (i) solvent and solute can be dissimilar molecules and are distinguishable from each other; (ii) the liquid mixture can be non-ideal and involves a heat of mixing. However, the third assumption that the solvent is completely rejected from the crystal solid phase was maintained in the Flory diluent theory to obtain an analytical solution to the Gibb's coexistence rule. The Flory diluent theory, formulated on the above premises, has found widespread adoption in both industry and academia due to its tractable analytical solution and simplicity of testing with experiments [56].

The FH free energy of liquid–liquid demixing of a crystalline polymer blend (or with polymeric solvent) may be written as [54–58]:

$$f_{\text{mixing}} = \frac{\phi \ln\phi}{r_1} + \frac{(1-\phi)\ln(1-\phi)}{r_2} + \chi_{\text{FH}}\phi(1-\phi) \tag{4.17}$$

Here $\phi_1 = \phi$ and $\phi_2 = (1-\phi)$ are volume fractions of the crystalline component and amorphous component, respectively; $r_1$ and $r_2$ represent the numbers of statistical segments of the polymer chain of crystalline and amorphous constituents, respectively, with $\chi_{aa} = \chi_{\text{FH}} = A + B/T$, where the FH interaction parameter represents the amorphous–amorphous interaction and $A$ and $B$ are constants. Let us consider a situation where a crystalline polymer is mixed with an amorphous polymer, that is, polymeric solvent. The chemical potential of the liquid phase can be calculated from the Flory–Huggins theory of liquid–liquid mixing for polymer blends as follows:

$$\frac{\partial f^i}{\partial \phi} = \mu_1 = \left[\frac{1+\ln(\phi)}{r_1} - \frac{1+\ln(1-\phi)}{r_2} + \chi_{\text{FH}}(1-2\phi)\right] \tag{4.18}$$

The complete free energy of the system is expressed as $f_{\text{mix}} = f^i + \phi f^c$. An alternative approach of determining the Gibb's coexistence points is to equate the chemical potentials of each phase simultaneously to their common tangent, which renders the following equation:

$$\left.\frac{\partial f_{\text{mix}}}{\partial \phi}\right|_{\phi^\alpha} = \left.\frac{\partial f_{\text{mix}}}{\partial \phi}\right|_{\phi^\beta} = \left[\frac{f^\alpha_{\text{mix}} - f^\beta_{\text{mix}}}{\phi^\alpha - \phi^\beta}\right] \tag{4.19}$$

Assuming that the solid crystal is pure, that is, $\phi^{\alpha} = 1$, then Eq. (4.19) can be reduced to determine an analytical expression of the liquidus line:

$$\frac{\partial f_{\text{mix}}}{\partial \phi}\Big|_{\phi^{\beta}} = \left[\frac{f_{\text{mix}}^{\alpha} - f_{\text{mix}}^{\beta}}{\phi^{\alpha} - \phi^{\beta}}\right] \tag{4.20}$$

From Eqs. (4.17) and (4.18), one obtains the following equation, called the melting point depression:

$$\frac{1}{T_{\text{m}}} - \frac{1}{T_{\text{m}}^{0}} = \frac{R}{\Delta H_{\text{u}}}\left[\frac{\ln \phi}{r_2} + \left(\frac{1}{r_2} - \frac{1}{r_1}\right)(1-\phi) + \chi_{\text{FH}}(1-\phi)^2\right] \tag{4.21}$$

In small molecule systems, the melting point depression is dominated by both entropy and euthalpy. Conversely, in the case of high molecular weight polymer blends, the entropic contributions are negligible, and thus Eq. (4.21) leads to:

$$1 - \frac{T_{\text{m}}}{T_{\text{m}}^{0}} = \frac{RT_{\text{m}}}{\Delta H_{\text{u}}}\left[\chi_{\text{FH}}(1-\phi)^2\right] \tag{4.22}$$

From the slope of a $(1 - T_{\text{m}}/T_{\text{m}}^{0})$ versus $(1-\phi)^2$ plot, along with the fusion entropy, $\chi_{\text{FH}}$ of the crystalline polymer blend can be determined.

Equation (4.22) is appealing because of its simplistic expression, from which the experimental determination of $\chi_{\text{FH}}$ of crystalline polymer blends is possible. Generally speaking, the phenomenon of melting point depression has been attributed to the plasticization effect caused by the solvent surrounding the melting crystals. Since crystalline polymer chains are interconnected mutually with their amorphous chains at the interface, the $\chi_{\text{FH}}$ parameter may be regarded as the amorphous–amorphous interaction at the crystalline interface. However, the paradox is that the experimental value of $\chi_{\text{FH}}$ as obtained from the melting point depression plot is an order of magnitude different from that of amorphous–amorphous interaction obtained by small-angle neutron scattering in the isotropic state. Moreover, there is a much evidence in the literature, notably for metallic alloys [59], fatty acid mixtures [60], and liquid crystal blends [61, 62], that the solid crystal can accommodate some solvent at some high crystalline concentrations at equilibrium.

The possible entrapment of solvent in polymer crystals has been demonstrated by Malik *et al.*, who investigated blends of syndiotactic polystyrene (*s*-PS) with organic solvents such as naphthalene, benzene, toluene, and so on [63]. Subsequently, the phase diagrams of these polymer–solvent systems, thus established, exhibited the liquidus and solidus lines, showing crystalline phases of *s*-PS and/or its modifications such as crystallo-solvates, in which the solvent molecules were trapped in the *s*-PS crystals [63–65]. The experimental evidence has led to the suggestion of possible entrapment of solvent in polymer crystals, forming solvated crystals [63].

More importantly, the crystalline–solvent phase diagrams, thus solved in the context of the Flory–Huggins theory alone, cannot account for the existence of the solidus line, because the crystal phase always coincides with the pure crystalline polymer axis due to the inherent assumption, adopted from Prigogine theory, of the complete rejection of solvent molecules from the crystalline phase [66, 67]. Thus,

the binary phase diagrams of crystalline polymer blends are at odds with those of the small molecule systems including organic compounds [60], metal alloys [68], ceramic glasses [69], and liquid crystal mixtures [70].

Matkar *et al.* have hypothesized what would happen to crystalline blend phase diagrams if one relaxes the last assumption of the Flory diluent theory of crystalline polymer solutions, namely, the complete rejection of polymeric solvent from the crystalline phase [66, 67]. In addition, Xu *et al.* have developed a new theory for a binary crystalline polymer blends based on a combination of liquid–liquid phase separation and solid–liquid phase transition by taking into consideration the coupling interaction between the solid crystal and amorphous liquid phase [71].

## 4.5 Phase Diagrams of Crystalline Polymer Blends

### 4.5.1 Phase Diagram Calculation of a Crystalline/Amorphous Polymer Blend

Matkar *et al.* have proposed a free energy description for crystalline/amorphous polymer blends by taking into consideration the interaction between the crystal phase of the crystalline constituent and the amorphous phase of the second component (i.e., polymeric solvent) while removing the assumption of complete immiscibility inherent in the Flory diluent theory [53]. The Matkar–Kyu (MK) model consists of a combination of FH free energy of liquid–liquid demixing, free energy of crystal solidification given by a Landau-type double well potential, and the free energy of coupling interaction between the amorphous and crystalline phases [66], that is:

$$f(\phi,\psi) = f_{\text{mixing}}(\phi) + \phi f_{\text{cryst}}(\psi) + f_{\text{coupling}}(\phi,\psi) \tag{4.23}$$

where $f_{\text{mixing}}(\phi)$ is given by Eq. (4.17), whereas $f_{\text{cryst}}(\psi)$ may be expressed in accordance with Eq. (4.14). The free energy of coupling interaction between the crystalline constituent and the amorphous component is given via the coupling term, viz.:

$$f_{\text{coupling}} = \chi_{\text{ca}}\phi(1-\phi)\psi^2 \tag{4.24}$$

where $\chi_{\text{ca}} \propto \Delta H_{\text{u}}/RT = \omega\Delta H_{\text{u}}/RT$, is the interaction parameter, which is directly proportional to the heat of fusion, $\Delta H_{\text{u}}$, but is inversely proportional to absolute temperature $T$ [66, 67]. The overall free energy of the crystalline/amorphous blend becomes [66]:

$$\begin{aligned} f = &\left[\frac{\phi\ln\phi}{r_1} + \frac{(1-\phi)\ln(1-\phi)}{r_2} + \chi_{\text{aa}}\phi(1-\phi)\right] \\ &+ W\phi\left[\frac{\psi^4}{4} - (\zeta+\zeta_0)\frac{\psi^3}{3} + \zeta\zeta_0\frac{\psi^2}{2}\right] + \chi_{\text{ca}}\psi^2\phi(1-\phi) \end{aligned} \tag{4.25}$$

where the first term in square brackets represents the free energy of liquid–liquid mixing, the second is the free energy of crystallization, and the third term represents the coupling interaction between the crystal phase of the crystalline constituent and the amorphous phase of the other component.

Various phase diagrams of crystalline/amorphous blends have been established under various conditions for liquid–liquid and solid–liquid phase transitions [66]. Figure 4.10a shows the occurrence of melting point depression in a hypothetical crystalline/amorphous blend. It is seen that the liquidus and solidus lines virtually overlap as the UCST (upper critical solution temperature) is suppressed far below the crystal melting temperatures. When the UCST moves up closer to the solidus line, the L + Cr coexistence gap opens up (Figure 4.10b). With increasing competition from the UCST, the solidus line breaks away and moves toward the pure crystal axis, showing the neat crystal gap at the high crystalline polymer concentrations (Figure 4.10c). When the UCST surpasses the melting temperatures of the blends, a liquid + liquid (L + L) coexistence region can be identified in addition to the

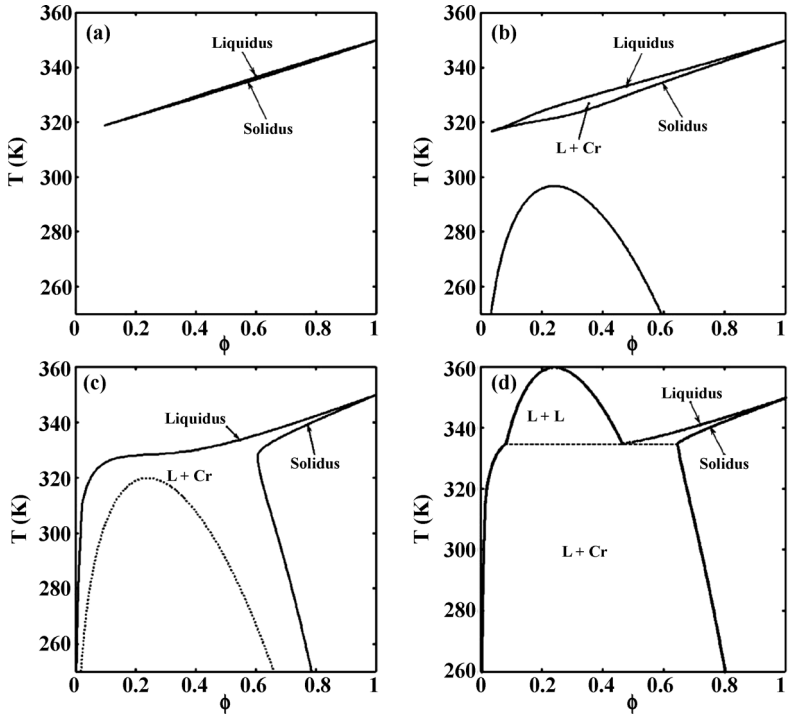


**Figure 4.10** Phase diagram of a crystalline/amorphous blend having $T_m = 350$ K, (a) showing overlap of the liquidus and solidus lines; (b) widening of the crystal + liquid coexistence gap bound by the liquidus and solidus lines with increasing influence by the UCST; (c) showing an interplay between the solid–liquid phase transition including solidus and liquidus lines with the UCST liquid–liquid phase separation; and (d) protrusion of the UCST above the solidus and liquidus lines, showing various coexistence regions such as liquid + liquid, liquid + solid, and pure solid gaps.

liquid + solid crystal region and the neat crystal region (Figure 4.10d). Although the FH interaction parameter controls the behavior of the UCST [52, 61], the trend of liquidus and solidus lines at the high crystalline content compositions is not noticeably affected by the $\chi_{aa}$ parameter. It can be inferred that these phase diagrams of crystalline polymer blends are governed by the competition between the crystalline solid–amorphous melt phase transition and the liquid–liquid phase separation.

The validity of the MK theory [66] has been tested with the melting point depression data of the crystalline/amorphous blend of poly(vinylidene fluoride) (PVDF) and poly(methyl methacrylate) (PMMA) reported by Nishi *et al.* [56]. In their calculation, the values of $r_1 = 3371$ and $r_2 = 866$ were utilized, which approximately correspond to the respective molecular weights of PVDF and PMMA. From the theoretical fit with the experimental melting points (Figure 4.11), a value of $\chi_{aa} = -0.141$ was estimated at 165 °C (based on the $\chi_{ca}$ value of 0.345), which is smaller in magnitude (i.e., a lesser attractive interaction) than the reported value of $\chi_{mp} = -0.31$ obtained by Nishi *et al.* from the melting point depression experiments in the vicinity of the melting temperature of pure PVDF [56]. In contrast, small-angle neutron scattering experiments gave much smaller values for the same PVDF/PMMA blends, for example, $\chi_{aa} \sim -0.226$ and $-0.077$ for two different concentrations of PVDF/PMMA by Hadziioannou *et al.* [72] and $-0.14$ by Canalda *et al.* [73], and $-0.03$ to $-0.16$ from SAXS by Wendorff [74]. In the Flory diluent theory, the repulsive crystal–amorphous interaction $\chi_{ca}$ was completely ignored, and thus the $\chi_{aa}$ could have been overestimated as compared to those of other experiments. Notably, the $\chi_{aa}$ value as estimated from the melting point depression may vary depending on the

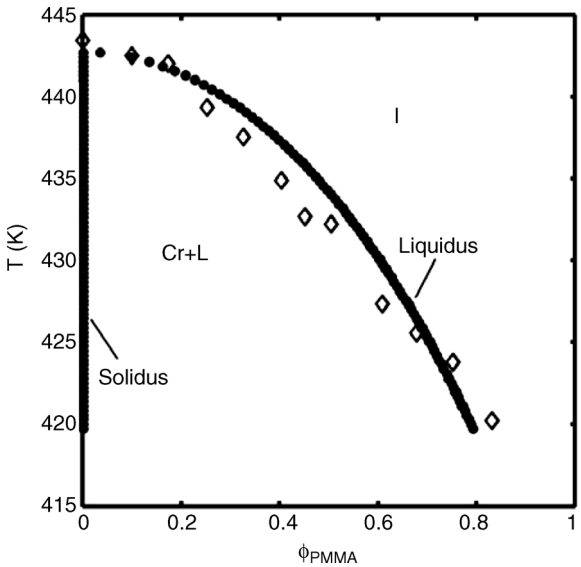


**Figure 4.11** Theoretically calculated phase diagram of PVDF/PMMA blend. Experimental and material parameters were determined by Nishi and Wang (◇) [56].

actual value of $\chi_{ca}$. This kind of uncertainty may be eliminated in a partially miscible system, where both coexistence lines of the solid–liquid phase transition and of the UCST type liquid–liquid phase separation are clearly discernable in the experimental phase diagram [66].

### 4.5.2
### Determination of Crystal–Amorphous Interaction in Crystalline/Amorphous Blends

In the Matkar–Kyu model, the crystal–amorphous interaction parameter was assumed to be inversely proportional to the absolute temperature, that is, $\chi_{ca} = \omega\Delta H_u/RT$, where $\Delta H_u$ is heat of fusion of the crystal in the pure state and $T$ is absolute temperature. However, the analytical solution for the melting point depression was not sought in their original approach [66, 67]. This deficiency has been remedied recently by Rathi *et al.* [75] for a crystalline/amorphous blend by solving the combined FH/PF free energies and obtaining an analytical expression from the equilibrium conditions, viz., $\partial f/\partial\psi = 0$ and $f(\psi) = 0$ as described below:

$$1 - \frac{T_m}{T_m^0} = \frac{RT_m}{6\Delta H_u}\left(\zeta - \tfrac{1}{2}\right)\left[\frac{\zeta_0^{\,2}}{4} - (\zeta + \zeta_0)\frac{\zeta_0}{3} + \frac{\zeta\zeta_0}{2}\right]^{-1}\chi_{ca}(1-\phi) \tag{4.26}$$

where $T_m$ is the crystal melting temperature. In small molecule systems, $\zeta_0 = 1$, but it can be less than unity in crystalline polymer solutions since polymer crystallization hardly reaches thermodynamic equilibrium. Setting $\zeta_0 \cong 1$, then Eq. (4.26) reduces to:

$$1 - \frac{T_m}{T_m^0} = \frac{k_B T_m}{\Delta H_u}\chi_{ca}(1-\phi) \tag{4.27}$$

It can be anticipated that Eq. (4.27) should be valid for a small molecule system, but in the case of crystalline polymer blends its applicability may be limited to high crystalline polymer compositions. From a plot of $1 - T_m/T_m^0$ versus $(1-\phi)$, one can determine $\chi_{ca}$ directly from the slope ($B_c$) as follows:

$$B_c = \frac{RT_m}{\Delta H_u}\chi_{ca} \tag{4.28}$$

Notably, Eq. (4.28) is the same as the empirical expression used by Matkar *et al.* [66, 67], except that Rathi *et al.* derived the analytical expression of Eq. (4.27) [75].

Figure 4.12 shows a plot of $1 - T_m/T_m^0$ against $(1-\phi)$ using the melting point depression data of poly(ethylene oxide) (PEO)/diacrylate (DA) blends [74]. As expected, a linear slope was obtained with a $B_c$ of 0.09, which gives a $\chi_{ca}$ value of 0.27 at 337 K, where DA is in the melt state (Figure 4.13). This $B_c$ value is within the range estimated by Matkar *et al.* [66]. Using the as-determined $\chi_{ca}$ along with other experimental conditions and physical parameters of the PEO/DA blend, a solid–liquid phase diagram was calculated by self-consistently solving the combined FH/PH free energies of Eq. (4.25). The calculated phase diagram reveals a close match between the liquidus line and the experimental depressed melting points of

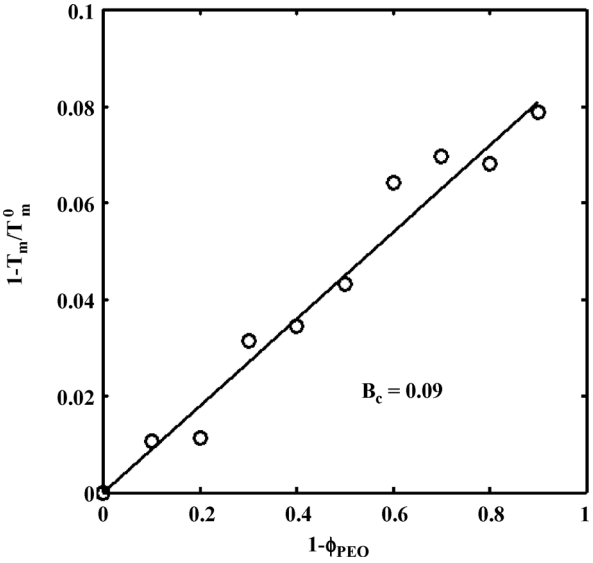


**Figure 4.12** Plot of $1 - T_m/T_m^0$ vs $(1 - \phi)$ representing the melting point depression against the amorphous content, corresponding to the phase diagram of poly(ethylene oxide)/ diacrylate blends. A linear slope was obtained by a least-squares method, from which the slope, $B_c = 0.09$, was obtained.

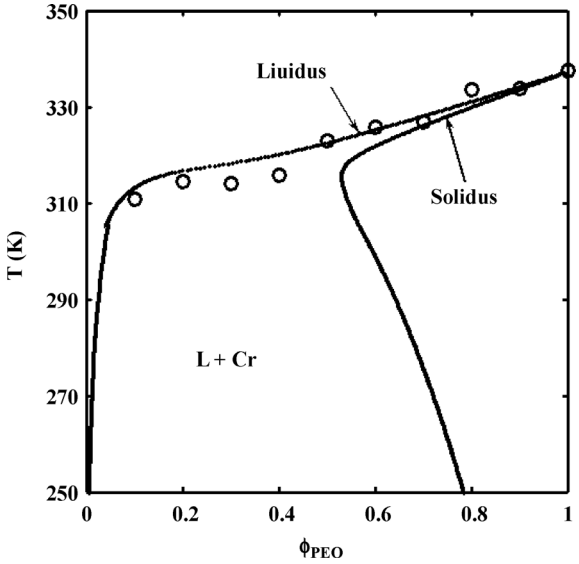


**Figure 4.13** Theoretical phase diagram calculated using the value of slope ($B_c = 0.09$) from Figure 4.12. A close match between the experimentally obtained melting points and the self-consistently calculated phase diagram signifies the validity of the present theory. Open symbols denote experimental data and solid lines indicate the theoretical coexistence curves.

the PEO crystal in its DA blends with the coexistence gap of liquid + crystal bound by the liquidus and solidus lines (Figure 4.13). Moreover, a pure solid crystal gap was predicted to be located in the high crystalline compositions. The authors further suggested that a linear slope should be drawn through the melting points of the high crystalline polymer compositions of the $1 - T_m/T_m^0$ against $(1 - \phi)$ plot. Although their approach based on Eq. (4.27) is similar to the melting point depression plot of crystalline polymer solutions (or blends) of the Flory diluent theory, the supercooling $(1 - T_m/T_m^0)$ was plotted against $(1 - \phi)$ as opposed to $(1 - \phi)^2$ of the original version. More importantly, it is the crystalline–amorphous interaction parameter that can be obtained from the slope of the above plot; this is different from the Flory–Huggins interaction parameter. Rathi *et al.* further [75] advocated evaluating the crystalline–amorphous interaction parameter from the melting point depression plot according to Eq. (4.27); it is more informative in constructing the crystalline–amorphous phase diagram, as demonstrated earlier by Matkar *et al.* [66, 67]. Notably, it is the crystal–amorphous interaction that has led to the lowering of the melting point. Hence, it is important to distinguish the types of different interactions, viz., liquid–liquid versus solid crystal–liquid interactions. Contrary to general perception [56], it is the crystal–amorphous interaction parameter that can be obtained from the experimental melting point depression data, not the FH interaction parameter.

### 4.5.3
### Phase Diagram Calculation for Binary Crystalline Polymer Blends

The total free energy density of mixing of a binary crystalline polymer blend may be expressed as the weighted sum of the free energy density pertaining to crystal solidification of the crystalline constituent with its volume fraction ($\phi$) and the free energy of liquid–liquid mixing as described by the Flory–Huggins theory of isotropic mixing [53–57] with the addition of the anisotropic interaction terms including crystal–amorphous, amorphous–crystal, and crystal–crystal mixing [67]. This leads to:

$$f(\psi_1, \psi_2, \phi) = \left\{ \phi f(\psi_1) + (1-\phi) f(\psi_2) \right\} + \left\{ \frac{\phi}{r_1} \ln(\phi) + \frac{(1-\phi)}{r_2} \ln(1-\phi) \right\} + \left\{ \chi_{aa} + \left( \chi_{ca} \psi_1^2 - 2\chi_{cc} \psi_1 \psi_2 + \chi_{ac} \psi_2^2 \right) \right\} \phi(1-\phi) \tag{4.29}$$

The first term in braces represents the Landau-type free energy of crystal solidification of each component in which the individual free energy of the constituents is weighted by the respective volume fractions to ensure that these potentials vanish at the extreme limits of zero crystallinity or if a component is non-crystallizable. The second term represents the entropic part of the free energy of mixing of the amorphous constituents. In the third term, $\chi_{aa}$ corresponds to the amorphous–amorphous interaction parameter of Flory–Huggins that characterizes the stability of the liquid phase.

The anisotropic interactions such as crystal solid–amorphous liquid or amorphous liquid–crystal solid interactions may be defined as $\chi_{ca}$ and $\chi_{ac}$, respectively. The coupling term representing the crystal–amorphous interaction with volume fraction (or concentration) may be regarded as:

$$\chi_{ca}\psi_1^2\phi(1-\phi) = \chi_{ca}\psi_1^2\phi - \chi_{ca}\psi_1^2\phi^2$$

where the linear–quadratic coupling represents the interaction between the crystal and amorphous chains at the interface, which is analogous to the surface anchoring energy. The quadratic–quadratic coupling is the interaction energy in the bulk. The same explanation may be given for the amorphous–crystal interaction. These anisotropic interactions of separate crystals and co-crystals are complementary to $\chi_{aa}$ representing isotropic interaction of amorphous materials. Note that the order of the subscript in $\chi$ denotes the crystal or amorphous phase of constituent 1 and of constituent 2, respectively, viz. $\chi_{c_1a_2} \equiv \chi_{ca}$, $\chi_{a_1c_2} \equiv \chi_{ac}$ and $\chi_{c_1c_2} \equiv \chi_{cc}$. Moreover, these interaction parameters are proportional to the fusion enthalpies, that is, $\chi_{ca} = \omega_1\Delta H_{u,1}/RT$ and $\chi_{ac} = \omega_2\Delta H_{u,2}/RT$, where $\Delta H_{u,1}$ and $\Delta H_{u,2}$ are the heat of fusions of components 1 and 2, respectively. Furthermore, the crystal–crystal interaction may be expressed as a geometric mean of the crystal–amorphous and amorphous–crystal interactions to account for the non-ideal rule of the crystalline mixture, that is:

$$\chi_{c_1c_2} = \omega_{c_{12}}\left(\sqrt{\chi_{c_1a_2}}\cdot\sqrt{\chi_{a_1c_2}}\right)$$

or:

$$\chi_{cc} = \omega_c\left(\sqrt{\chi_{ca}}\cdot\sqrt{\chi_{ac}}\right)$$

for simplicity, in which $\omega_c$ is a constant representing the anisotropic interaction, which signifies any departure from ideality (if it is different from unity). The term $B_c$ is associated only with the anisotropic interactions that are intimately related to the heat of fusions of these individual crystals as well as of the co-crystals and thus it is not directly connected to $\chi_{aa}$. This $\omega_c$ parameter is analogous to the "*c*" anisotropic interaction parameter defined for the case of nematic liquid crystal mixtures [62].

Matkar *et al*. have compared their calculated phase diagram with that reported by Smith and Manley [76] for two polyethylene fractions of different molecular weight, denoted 1000 (PE1000) and 2000 (PE2000), respectively. The melting transitions of the two PE fractions, as obtained from the DSC experiment, show a systematic variation of the melting temperatures, suggesting that the crystal solid solution may be ideal (Figure 4.14a). The two calculated lines, exhibiting convex and concave curvatures, form the liquidus and solidus loop. As may be expected, the experimental melting transition points are closer to the liquidus line. Although the solidus curve is identifiable in the self-consistent simulation, it is difficult to detect experimentally due to the broad nature of the experimental DSC peaks, which are affected by the close proximity to these solidus and liquidus lines.

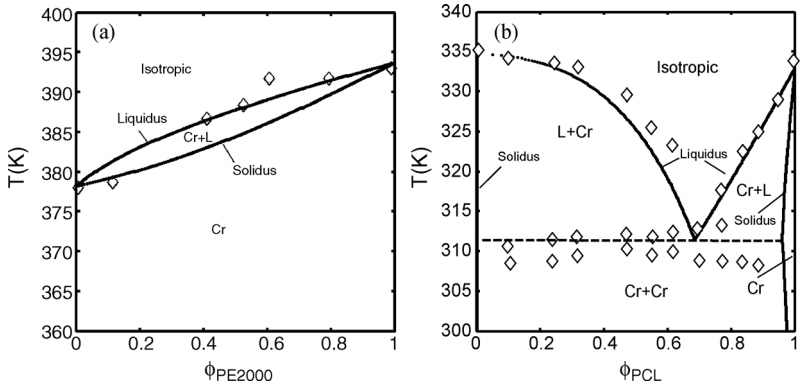


**Figure 4.14** Solid solution of polyethylene fractions in comparison with the experimental phase diagram of (a) two polyethylene fractions [76] and (b) PCL/trioxane blends [77], showing the liquidus–solidus loop and eutectic phase behavior, respectively.

Another interesting system, investigated by Wittman *et al.*, is the eutectic mixture of polycaprolactone (PCL) and trioxane; the authors solved these melting point depression data in the context of the Flory diluent theory by treating one constituent at a time without mutual interference by each other [77]. Their calculated liquidus line certainly captured the trend of the melting point depression, but the solidus lines were absent. Matkar *et al.* have made calculations based on their new free energy description [66]. As shown in Figure 4.14b, the liquidus lines exhibit a remarkable match with the experimental melting transition points, except for the anomalous double peaks observed experimentally, which were attributed to possible segregated crystals [76]. More importantly, Matkar *et al.* [66] captured the solidus lines in their calculation as located very close to, or coincident with, the pure component axis; these lines are difficult to determine experimentally [76]. Matkar *et al.* further advocated the important roles of the crystal–amorphous, amorphous–crystal, and crystal–crystal interactions in the establishment of the eutectic, peritectic, and azeotropic phase diagrams of binary crystalline polymer blends, which are consistent with other materials phase diagrams such as metal alloys and liquid crystal mixtures [67].

### 4.5.4
### Morphology Development in Relation to Phase Diagram of Crystalline/Amorphous Polymer Blends

Before examining the morphology development in crystalline polymer blends, it is important to establish the phase diagram as it provides guidance to the pathway traversed by the system in the dynamic study. Figure 4.15 shows the self-consistent solution representing a solid–liquid coexistence gap bound by the solidus and liquidus lines of a PEO/TA blend [78]. As shown, the liquidus and solidus lines merge at a dilute concentration, exhibiting a crystal + liquid coexistence gap. In principle, the melting transition would drop asymptotically at the very dilute regime, if the polymeric solvent is crystallizable or the UCST is close to the melting

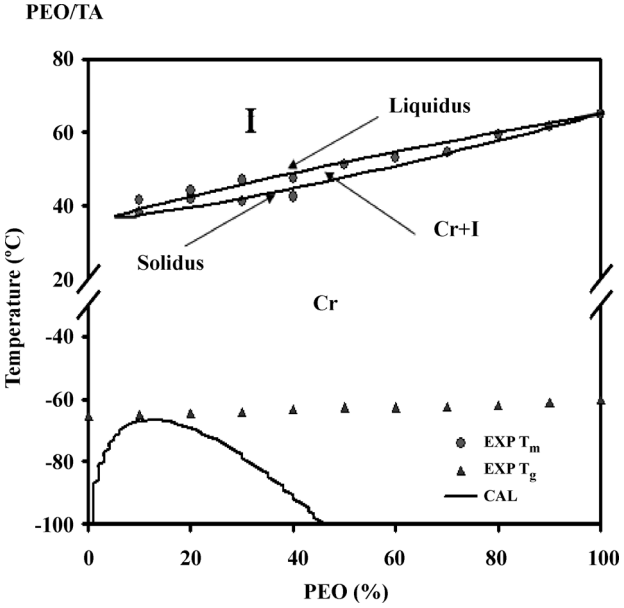


**Figure 4.15** Comparison between the calculated self-consistent solutions (solid lines) and experimental melting temperatures (filled circles) of PEO/TA blends, showing the crystal solid–liquid coexistence region bound by the liquidus and solidus lines. The parameters used were $\Delta H_u = 8.36$ kJ mol$^{-1}$, $\chi_{aa} = 0.0134$, $\chi_{ca} = 0.203$ at 40 °C, $r_1 = 110$, $r_2 = 2$, and $A = 0$ at $T_{crit} = -260$ °C. The predicted UCST falls below the glass transition temperatures of the blends.

temperature of the constituent polymer. In the present case, there is no crystal melting temperature of TA while the UCST is buried below the glass transition temperature and thus the melting point disappeared abruptly at a very dilute concentration. Such a sudden disappearance of the crystal melting in a crystalline polymer blend is not unusual, at least from the experimental point of view. For instance, PVDF crystals completely disappeared when the PMMA concentration exceeded 60 wt% and no melting transition was observed experimentally [56]. Although the close resemblance of the calculated liquidus line to the experimental melting transition points is promising, it is important to confirm the phase morphology of each region.

Various temperature quenching experiments of three PEO/TA concentrations were conducted from the melt at 80 °C to indicated temperatures corresponding to the solid–liquid coexistence gap at the 5/95, 20/80, and 50/50 compositions. Figure 4.16a displays the temporal evolution of crystalline morphologies in the blend of 5/95 PEO/TA following temperature quench to 35 °C. Multiple nuclei reminiscent of lamellar single crystals develop in the early stage that grow in size predominantly lengthwise. Subsequently, the primary lamellae branch out at both ends and then splay apart. As a result of this continuous branching and splaying, these initial lamellae eventually evolve into open spherulitic structure or sheaf-like

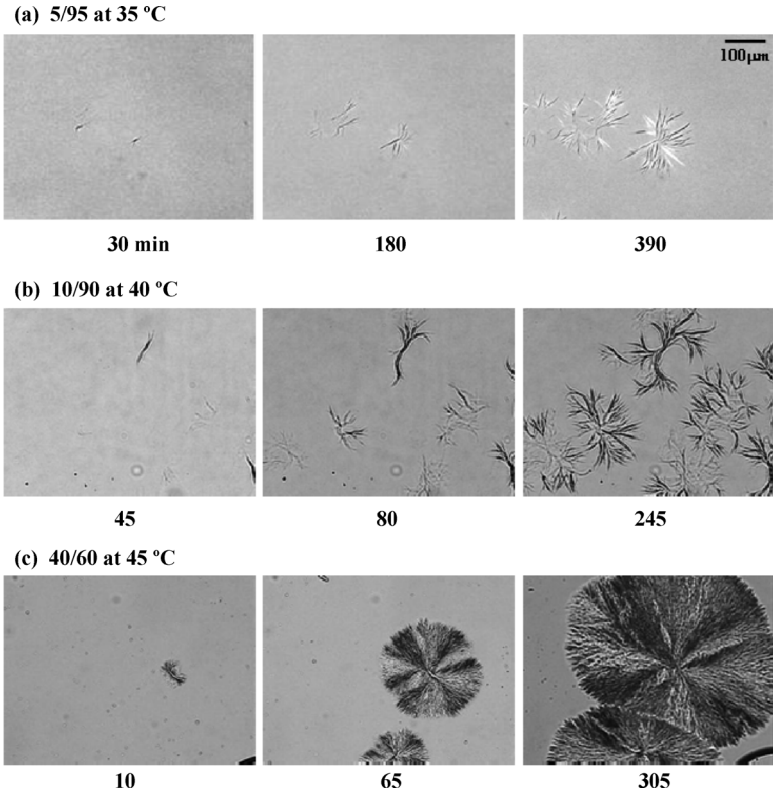


**Figure 4.16** Temporal emergence of PEO crystals in a PEO/TA blend. showing the coexistence of crystal + isotropic liquid: (a) aggregates of anisotropic lamellar structure of PEO in the continuum of a TA-rich melt of 5/95 PEO/TA blend at 35 °C; (b) sheaf-like structure in a 10/90 blend at 40 °C; (c) fully grown spherulite structure in a 40/60 blend at 45 °C.

textures; some of these nuclei show an anisotropic shape, especially in the 10/90 PEO/TA (Figure 4.16b). Likewise, the 20/80 PEO/TA mixture reveals a similar progression of branched lamellar morphology or sheaf-like crystals (picture not shown). When the PEO concentration increases to 40%, the crystal structures evolve into dense lamellar (or spherulitic) morphology (Figure 4.16c). Regardless of the PEO crystal shapes at different compositions, all these crystal morphologies were found to coexist with the surrounding isotropic TA-rich liquid at the asymptotic equilibrium, thereby confirming the solid–liquid coexistence region.

Upon quenching from the melt (80 °C) to a deeper temperature of 25 °C corresponding to the single-phase crystal region (Cr) at the same 5/95, 20/80, and 50/50 PEO/TA compositions, the emerged morphology varies with concentration (Figure 4.17). At the lower concentration of PEO (5/95), numerous needle-like lamellae developed, which are presumably swollen in TA solvent. The unambiguous assignment of such an opened lamellar structure to the single-phase crystal is

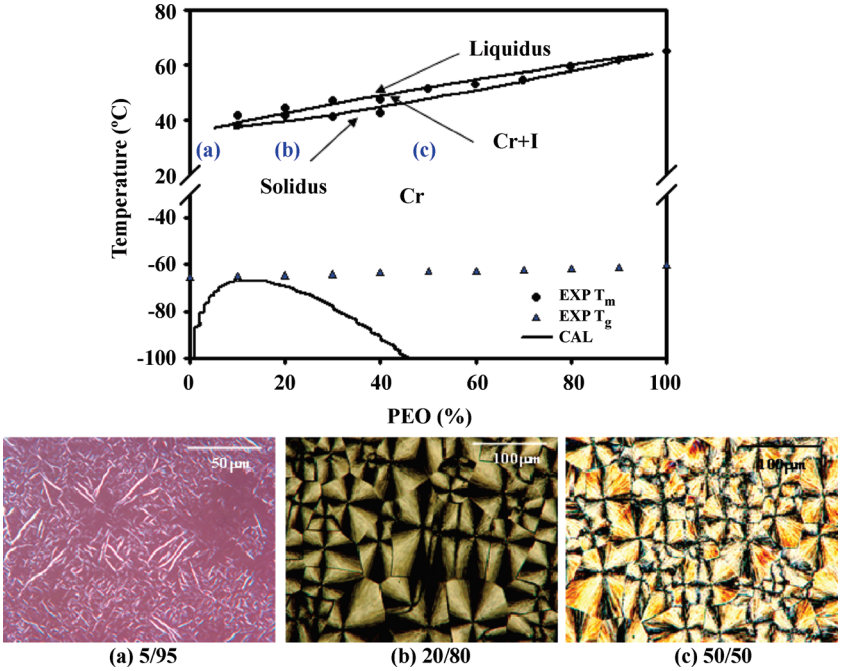


**Figure 4.17** Emerged PEO crystal structures following isothermal crystallization by quenching various PEO/TA blends to 25 °C: (a) 5/95, (b) 20/80, and (c) 50/50, showing the solvated spherulites in conformity with the predicted single-phase crystalline region of the phase diagram.

difficult in the 5/95 PEO/TA blend, because the amount of PEO materials is not sufficient to fill the entire microscopic view, especially at 1 or 2%. However, with increasing PEO content to 20/80 and 50/50 compositions, fully grown spherulites developed quickly and impinged on each other, suggestive of the single-phase crystals. The observed hierarchical PEO crystal morphologies obtained at the asymptotic equilibrium are explicable by Matkar–Kyu theory [66], including isotropic state, crystal + isotropic liquid, and single-phase crystalline regions of the crystalline–amorphous systems.

### 4.5.5
### Morphology Development in Relation to the Phase Diagram of Crystalline/Crystalline Polymer Blends

The phase diagram of two-crystalline polymer blends such as that of PEO/diacrylate (DA) reveals a solid–liquid coexistence gap bound by the solidus and liquidus lines intersecting with the upper critical solution temperature (UCST) (Figure 4.18) [79]. The liquidus closely matches with the melting transition points, showing isotropic (I), the coexistence of crystal + liquid ($Cr_1$ + I), and crystal + crystal ($Cr_1$ + $Cr_2$) regions. The two horizontal lines represent the monotectic line (upper) and the

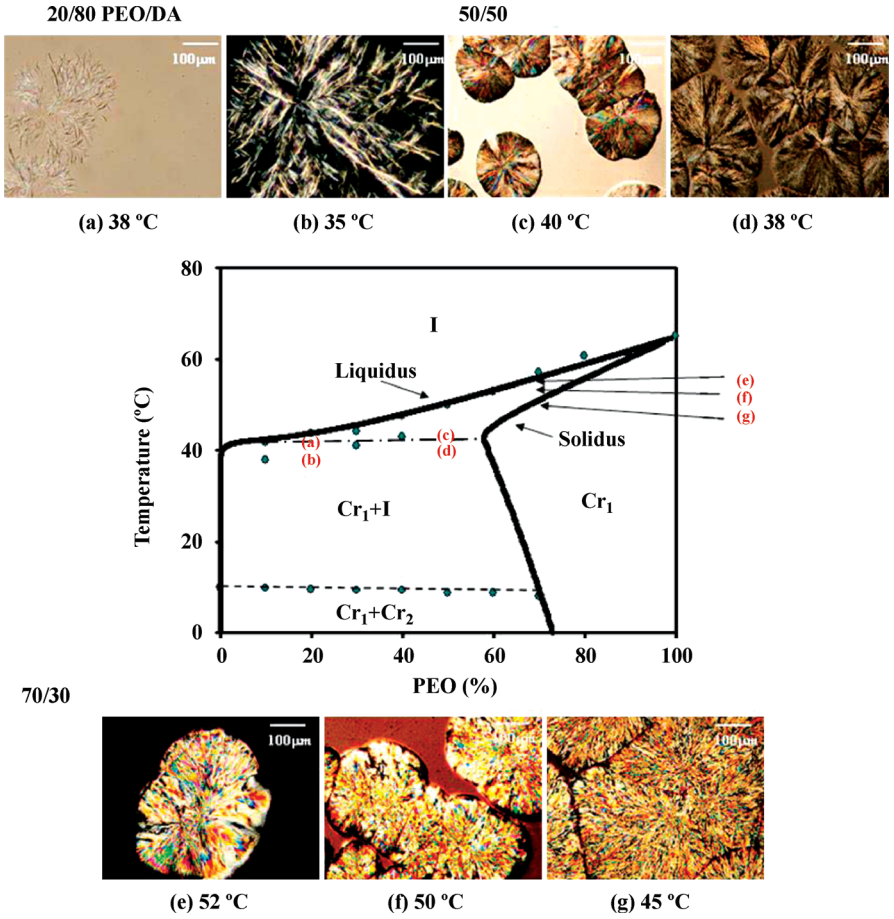


**Figure 4.18** Emerged final crystalline morphologies of PEO/DA blends following thermal quenching to various indicated temperatures, showing (a–f) the coexistence of spherulitic crystals in the continuum of isotropic melt. The impinged spherulites in Figure 4.18g represent the single phase PEO crystal region, as the quenching was performed just below the solidus line.

eutectic line (lower). At very low concentrations of PEO, the binodal line of the $Cr_1$ + I gap is virtually coincident with the pure DA axis and thus it may be regarded as $L_2$. Although the single phase crystal of PEO ($Cr_1$) is clearly discernible, the $Cr_2$ region (corresponding to the DA crystal phase) can be seen only if it is sufficiently magnified.

Figure 4.18a–f display the emerged morphologies following isothermal thermal quenching into various crystal + liquid and crystal + crystal coexistences regions of the phase diagram of the PEO/DA blends [79]. In the T-quenches of the 20/80 PEO/DA blend to 38 and 35 °C, the Cr1 + I coexistence phases can be identified in the optical micrographs obtained (a) without and (b) with the crossed polarizers; the dark

appearance under the crossed polarizers indicates the isotropic phase. The same conclusion can be drawn for the 50/50 and 70/30 blends (Figure 4.18c–f). When thermal quenching of the 70/30 blend was performed slightly below the solidus line to 45 °C, the whole microscopic view was volume-filled with solvated PEO spherulites, suggestive of the Cr1 region (Figure 4.18g). It seems that DA acts like a good solvent, which may be intimately mixed with the PEO spherulites.

The optical micrographs in Figure 4.19a–g are the emerged morphologies upon T-quenching at indicated points within the $Cr_1 + I$ and $Cr_1 + Cr_2$ regions. As may be

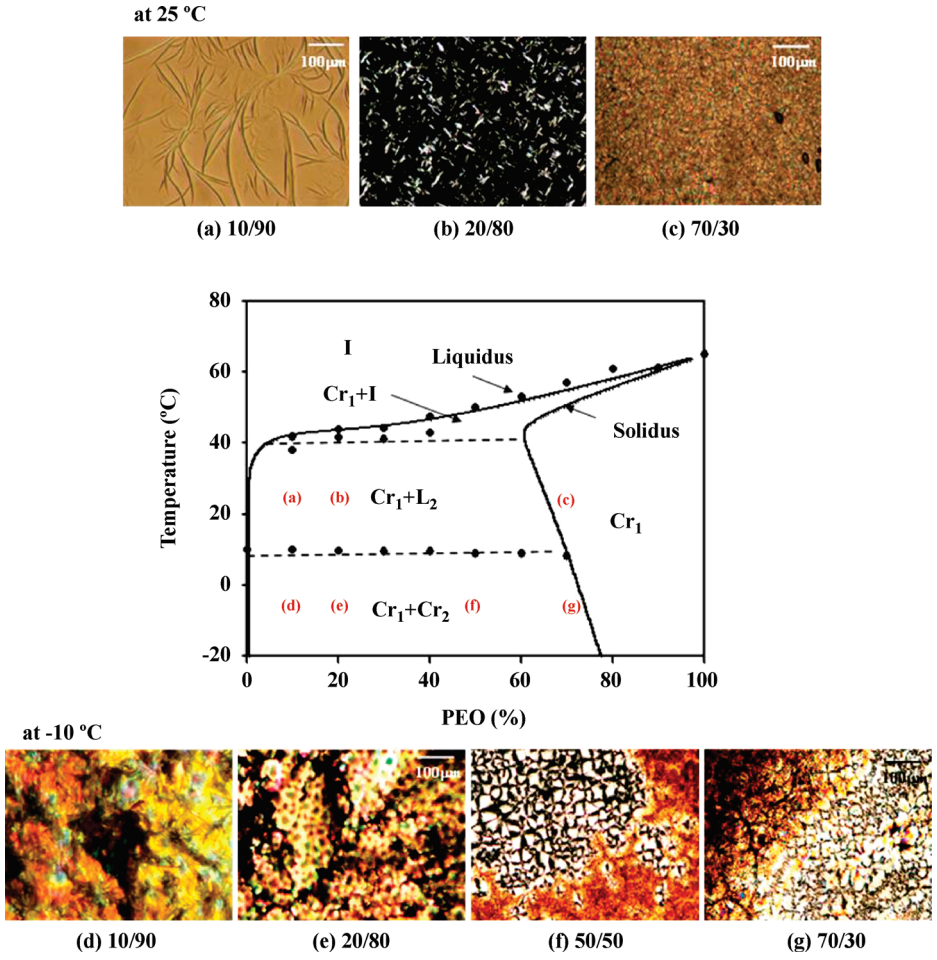


**Figure 4.19** Emerged morphologies at various PEO/DA compositions after quenching to the indicated isothermal crystallization temperatures: (a) 10/90, (b) 20/80, and (c) 70/30, confirming the ($Cr_1 + I$) regions (upper row), and the single phase crystal at 70/30 and (d) 10/90, (e) 20/80, (f) 50/50, and (g) 70/30, verifying the coexistence of ($Cr_1 + Cr_2$) regions (bottom row).

expected for the $Cr_1 + I$ region, the 10/90 and 20/80 blends show the aggregates of needle structures in the continuum of isotropic melt at 25 °C (Figure 4.19a and b). At 70/30, the fully developed spherulite PEO crystal can be seen, as expected for the $Cr_1$ region. Notably, in the T quench of 70/30 to 25 °C (Figure 4.19c), the system passes from isotropic state (I) to the crystal state ($Cr_1$) through the crystal + isotropic liquid gap ($Cr_1 + I$). The system still remembered the trajectory by which it traversed, and thus the spherulitic structure initially developed in the isotropic continuum before it reached its final congested spherulitic morphology. When these blends were quenched to around −10 °C, a different type of crystal develops in competition with the existing PEO crystals, which may be attributed to that of DA, suggesting the formation of separate crystals ($Cr_1 + Cr_2$) (Figure 4.19d–g). Based on these thermal quenched experiments, the observed crystal phase morphologies supported the calculated coexistence regions pertaining to the solid–liquid phase diagram of the PEO/DA blends.

### 4.5.6
### Phase Field Modeling on Phase Separation and Morphology Evolution

To elucidate the spatiotemporal emergence of crystalline structure and liquid–liquid phase separation in the crystalline–amorphous polymer blends, Rathi [80] employed the time dependent Ginzburg–Landau (TDGL Model-C) equations pertaining to the conserved concentration order parameter and the non-conserved crystal order parameter. Model C is a combination of TDGL Model-A and Model-B, viz.:

$$\frac{\partial \psi}{\partial t} = -\Gamma_{\psi}\frac{\delta f}{\delta \psi} \tag{4.30}$$

$$\frac{\partial \phi}{\partial t} = \nabla \Gamma_{\phi} \nabla \frac{\delta f}{\delta \phi} \tag{4.31}$$

where $\Gamma_{\psi}$ is related to the rotational mobility and $\delta/\delta\psi$ is the functional derivative defined earlier. The corresponding $\Gamma_{\phi}$ is the mutual diffusion, which is related to the self-diffusion coefficients of each constituent that obeys the Onsager reciprocal relation. The free energy of the system $f$ may be represented by the total sum of local, nonlocal, and the coupling interaction energy terms in what follows:

$$\begin{aligned} f(\phi,\psi) = {} & \phi\left[f(\psi) + \frac{\kappa_{\psi}}{2}|\nabla\psi|^2\right] \\ & + \left[\frac{\phi}{r_1}\ln(\phi) + \frac{(1-\phi)}{r_2}\ln(1-\phi) + \chi_{aa}\phi(1-\phi) + \frac{\kappa_{\phi}}{2}|\nabla\phi|^2\right] \\ & + \chi_{ca}\psi^2\phi(1-\phi) \end{aligned} \tag{4.32}$$

where:

$$f_{\text{non local}} = \phi\frac{\varkappa_\psi}{2}|\nabla\psi|^2 + \frac{\varkappa_\phi}{2}|\nabla\phi|^2$$

represents the nonlocal free energy with $\varkappa_\psi$ and $\varkappa_\phi$ being the coefficients of the interface gradients of the respective order parameter fields. As mentioned earlier, the linear($\phi$)–quadratic($\psi$) and quadratic($\phi$)–quadratic($\psi$) couplings in the third term of Eq. (4.32), that is:

$$\chi_{ca}\psi^2\phi(1-\phi) = \chi_{ca}\psi^2\phi - \chi_{ca}\psi^2\phi^2$$

represent the interactions between the crystal and amorphous materials at the interface and in the bulk, respectively. Inserting Eq. (4.32) into Eqs. (4.30) and (4.31) and subsequently non-dimensionalizing the time and space variables by $\tau = \Gamma_\phi t/\ell^2$ and $\tilde{x} = x/\ell$, one obtains a set of nonlinear reaction–diffusion equations in dimensionless form, that is:

$$\frac{\partial\psi}{\partial\tau} = -\tilde{\Gamma}_\psi\left\{\phi\left[W(\psi)(\psi-\zeta)(\psi-\zeta_0) + 2\chi_{ca}(1-\phi)\psi - \tilde{\varkappa}_\psi\tilde{\nabla}^2\psi\right]\right\} \tag{4.33}$$

$$\frac{\partial\phi}{\partial\tau} = \tilde{\nabla}^2\left\{\begin{array}{l}\dfrac{1+\ln\phi}{r_1} - \left(\dfrac{1+\ln(1-\phi)}{r_2}\right) + \chi_{aa}(1-2\phi) - \tilde{\varkappa}_\phi\tilde{\nabla}^2\phi \\ + W\left[\dfrac{\zeta(T)\zeta_0(T_m)}{2}\psi^2 - \dfrac{\zeta(T)+\zeta_0(T_m)}{3}\psi^3 + \dfrac{1}{4}\psi^4\right] \\ + \dfrac{\tilde{\varkappa}_\psi}{2}\left|\tilde{\nabla}\psi\right|^2 + \chi_{ca}(1-2\phi)\psi^2\end{array}\right\} \tag{4.34}$$

with dimensionless variables, $\tilde{\Gamma}_\psi = \Gamma_\psi\ell^2/\Gamma_\phi$, $\tilde{\varkappa}_\psi = \varkappa_\psi/\ell^2$, and $\tilde{\varkappa}_\phi = \varkappa_\phi/\ell^2$ that govern the spatiotemporal growth of domain morphology. The advantage of the present model is that these phase field model parameters can be related to the material parameters, which themselves may be supercooling dependent.

Before computing the morphology development based on a set of coupled nonlinear partial differential equations (PDEs) (4.33) and (4.34), Rathi *et al.* calculated a phase diagram of a hypothetical crystalline–amorphous polymer blend, consisting of liquid + liquid ($L_1 + L_2$), liquid + crystal ($L_1 + Cr_2$), and solid crystal ($Cr_2$) regions [79]. Furthermore, the emerged crystalline phase morphologies were computed by solving the above nonlinear PDEs in conjunction with the heat conduction equation at various compositions subjected to quenching to the indicated isothermal crystallization temperature at 375 K: (a) 30/70, (b) 55/45, (c) 86/24, and 95/5. Figure 4.20 shows the liquid–liquid phase separation (a) through spinodal decomposition (upper row), and (b) nucleation and growth. No crystallization occurs in this $L_1 + L_2$ gap. In Figure 4.20c, textureless crystal growth occurs in the metastable liquid + crystal region, which is a signature of crystalline spinodal. At point (d), fully developed spherulitic morphology can be seen. It can be noticed that some solvent pockets were seemingly trapped in the impinged

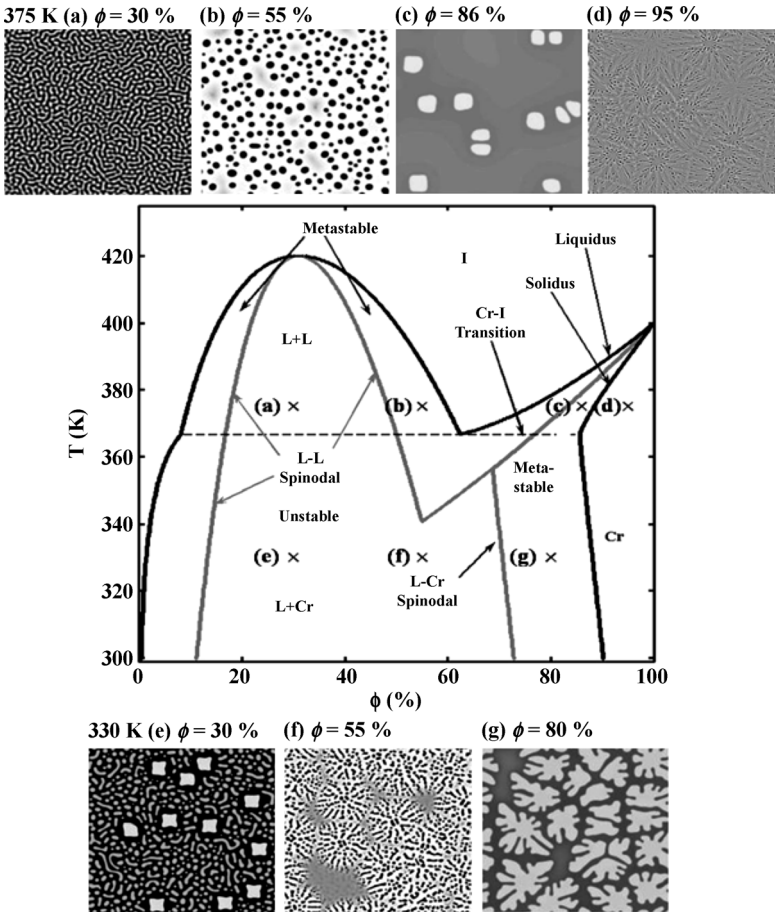


**Figure 4.20** The simulated phase separated domain morphologies in upper row were obtained at various compositions after quenching to 375 K, showing the occurence of liquid + liquid phase separation through (a) spinodal decomposition at 30/70 composition; (b) nucleation and growth at 55/45; (c) the development of textureless crystals at 86/24 and (d) the single phase crystal showing the spherulitic morphology at 95/5 (note that the whole view would be filled with impinged spherulites at longer times). The simulated crystal morphologies in the bottom row were obtained at 330 K exhibiting (e) the development of textureless crystals at 30/70 and (f) lamellar branching morphology (i.e., spherulites) at 55/45 in the continuum of phase separated matrix; and (g) the seaweed crystals at the 80/20 composition surrounded by isotropic liquid.

spherulites at the asymptotic equilibrium. Upon T-quenching to a much lower temperature of 330 K, the competition between the liquid–liquid phase separation and crystallization becomes stronger: in the quenching to point (e) (30/70) and point (f) (55/45) within the unstable liquid + crystal region; that is, the system is unstable against both liquid–liquid phase separation and liquid–solid transition. One can discern the development of textureless crystals in the matrix of liquid–

liquid phase separated spinodal-like structure in the background (Figure 4.20e). At point (f), the crystalline morphology is like the spherulite (or branching morphology), but liquid–liquid phase segregation can be seen in the background. However, the 80/20 at point (g) corresponds to the metastable liquid + crystal region, that is, it is stable against liquid–liquid phase separation, but metastable against liquid–solid phase transition. The emerged crystalline morphology at point (g) is reminiscent of seaweed type growing via tip-splitting and branching from a center without any indication of liquid–liquid phase separation in the background. The morphology at points (c) and (g) is unique to the metastable crystal + liquid coexistence region.

In summary, various phase diagrams have been solved self-consistently using the coupled Flory–Huggins free energy for liquid–liquid mixing and phase field free energy for crystallization. These theoretical phase diagrams were found to accord satisfactorily with various experimental phase diagrams. This combined free energy functional is further utilized in the time-dependent Ginzburg–Landau (TDGL Model-C) dynamics pertaining to the concentration and crystal order parameters. Then, the spatiotemporal evolution of crystalline morphology in the polymer blends was elucidated based on the competition between the liquid–liquid phase separation and solid–liquid phase transition. Of particular interest is that the development of various hierarchical morphology encompassing single crystals to lamellar branching morphology or spherulites can be explained in relation to various coexistence regions of the experimental phase diagrams.

**Acknowledgment**

Support of this work by the National Science Foundation through grant number DMR-0514942 is gratefully acknowledged.

**Symbols**

| | |
|---|---|
| $C_p$ | heat capacity |
| $F$ | total free energy |
| $f$ | local free energy |
| $G$ | temperature gradient |
| $\Delta H_u$ | latent heat |
| $\Delta H_u/C_p = K$ | thermal coefficient |
| $k_B$ | Boltzmann constant |
| $k_T$ | thermal conductivity |
| $N$ | number of molecules |
| $n$ | number of moles |
| $R$ | gas constant |
| $r$ | position |
| $r_1$ | numbers of statistical segments of the crystalline polymer chain |

| | |
|---|---|
| $r_2$ | numbers of statistical segments of amorphous polymer chain |
| $T$ | temperature |
| $\Delta T$ | supercooling |
| $T_m$ | melting temperature |
| $T_m^o$ | equilibrium melting temperature |
| $T_x$ | crystallization temperature |
| $t$ | time |
| $\nu$ | growth velocity |
| $W$ | dimensionless coefficient for free energy penalty |

### Greek Symbols

| | |
|---|---|
| $\alpha = k_T/\varrho C_p$ | thermal diffusivity |
| $\Gamma$ | mobility |
| $\delta$ | interface thickness |
| $\varepsilon$ | surface energy anisotropy |
| $\zeta$ | peak position of free energy hump |
| $\zeta_o$ | position of solidification potential well |
| $\theta$ | crystallographic orientation |
| $\varkappa$ | coefficient of interface gradient |
| $\varrho$ | density |
| $\sigma$ | surface tension |
| $\phi_1$ | volume fraction of crystalline polymer |
| $\phi_2$ | volume fraction of amorphous solvent |
| $\chi_{aa}$ | amorphous–amorphous interaction parameter |
| $\chi_{ac}$ | amorphous–crystal interaction parameter |
| $\chi_{ca}$ | crystal–amorphous interaction parameter |
| $\chi_{cc}$ | crystal–crystal interaction parameter |
| $\chi_{FH}$ | FH interaction parameter |
| $\psi$ | crystal phase order parameter |
| $\omega_c$ | coefficient of anisotropic interaction |

### References


1 Ben-Jacob, E., Deutscher, G., Garik, P., Goldenfeld, N., and Lareah, Y. (1986) *Phys. Rev. Lett.*, **57**, 1903.
2 Akamatsu, S., Faivre, G., and Ihle, T. (1995) *Phys. Rev. E*, **51**, 4751.
3 Akamatsu, S. and Ihle, T. (1997) *Phys. Rev. E*, **56**, 4479.
4 Utter, B., Ragnarsson, R., and Bodenschatz, E. (2001) *Phys. Rev. Lett.*, **86**, 4604.
5 Brener, E., Müller-Krumbhaar, H., Temkin, D., and Abel, T. (1998) *Physica A*, **249**, 73.
6 Ihle, T. and Müller-Krumbhaar, H. (1994) *Phys. Rev. E*, **49**, 2972.
7 Cahn, J.W. and Hilliard, J.E. (1958) *J. Chem. Phys.*, **28**, 258.
8 Langer, J.S. (1986) *Models of Pattern Formation in First-Order Phase Transitions. Directions in Condensed Matter* (eds G. Grinstein and G. Mazenko) World Scientific, Philadelphia, p. 165.
9 Halperin, B.I., Hohenburg, P.C., and Ma, S.-K. (1974) *Phys. Rev. B*, **10**, 139.

10 Collins, J.B. and Levine, H. (1985) *Phys. Rev. B*, **31**, 6119.
11 Caginalp, G. (1986) *Arch. Rational Mech. Anal.*, **92**, 205.
12 Kobayashi, R. (1993) *Phys. D*, **63**, 410.
13 Kessler, D.A., Koplik, J., and Levine, H. (1988) *Adv. Phys.*, **37**, 255.
14 Pomeau, Y. and Ben Amar, M. (1992) *Solids Far from Equilibrium* (ed. C. Godrèche), Cambridge University Press, Cambridge.
15 Langer, J.S. (1987) *Chance and Matter* (eds J. Souletie, J. Vannimenus, and R. Stora), Elsevier, Amsterdam.
16 Müller-Krumbhaar, H. and Kurz, W. (1991) *Phase Transformation in Materials* (ed. P. Haasen), VCH Verlag, Weinheim.
17 Kessler, D.A., Koplik, J., and Levine, H. (1984) *Phys. Rev. A*, **30**, 3161.
18 Utter, B. and Bodenschatz, E. (2002) *Phys. Rev. E*, **66**, 1604.
19 Caginalp, G. and Fife, P. (1986) *Phys. Rev. B*, **34**, 4940.
20 Caginalp, G. (1986) *Ann. Phys. (N. Y.)*, **172**, 136.
21 Cahn, J.W. and Kikuchi, R. (1985) *Phys. Rev. B*, **31**, 4300.
22 Wheeler, A.A., Murray, B.T., and Schaefer, R.J. (1993) *Phys. D*, **66**, 243.
23 Wheeler, A.A., Boettinger, W.J., and McFadden, G.B. (1992) *Phys. Rev. A*, **45**, 7424.
24 Brener, E.A., Müller-Krumbhaar, H., and Temkin, D.E. (1992) *Euro-Phys. Lett.*, **17**, 535.
25 Allen, S.M. and Cahn, J.W. (1979) *Acta Metall. Mater.*, **27**, 1085.
26 Guo, T.-M., Xu, H.-J., Kyu, T., and Wang, G.-X. (2004) Experimental Observation and Phase-Field Modeling of Interface Morphological Transition in Unidirectional Solidification, in *Solidification Processes and Microstructures* (eds M. Rappaz, C. Beckermann, and R. Trivedi), TMS, Warrendale, PA, p. 393.
27 Smithells, C.J. (1976) *Metals Reference Book*, 5th edn, Butterworths, London.
28 Prausnitz, J.M., Lichtenthaler, R.N., and de Azevedo, E.G. (1999) *Molecular Thermodynamics of Fluid-Phase Equilibria*, Prentice-Hall, New York.
29 Harrowell, P.R. and Oxtoby, D.W. (1987) *J. Chem. Phys.*, **86**, 2932.
30 Chan, S.-K. (1977) *J. Chem. Phys.*, **67**, 5755.
31 Karma, A. and Rapple, W.J. (1999) *Phys. Rev. E*, **60**, 3614.
32 Geil, P.H. (1973) *Polymer Single Crystals*, R. E. Krieger Publishing Co., Huntington, NY.
33 Bassett, B.C. (1981) *Principles of Polymer Morphology*, Cambridge University Press, Cambridge.
34 Lovinger, A.J. and Cais, R.E. (1984) *Macromolecules*, **17**, 1939.
35 Reiter, G. and Sommer, J.U. (1998) *Phys. Rev. Lett.*, **17**, 3771.
36 Sakai, Y., Imai, M., Kaji, K., and Tsuji, M. (1999) *J. Cryst. Growth*, **203**, 244.
37 Taguchi, K., Miyaji, H., Izumi, K., Hoshino, A., Miyamoto, Y., and Kokawa, R. (2001) *Polymer*, **42**, 7443.
38 Kyu, T., Mehta, R., and Chiu, H.-W. (2000) *Phys. Rev. E*, **61**, 4161.
39 Xu, H., Matkar, R., and Kyu, T. (2005) *Phys. Rev. E*, **72**, 011804.
40 Xu, H., Keawwattana, W., and Kyu, T. (2005) *J. Chem. Phys.*, **123**, 124908.
41 Hoffman, J.D. and Lauritzen, J.I. (1961) *J. Res. Natl. Bur. Stand.*, **65**, 297.
42 Hoffman, J.D. and Weeks, J.J. (1962) *J. Res. Natl. Bur. Stand.*, **66**, 13.
43 Armistead, K. and Goldbeck-Wood, G. (1992) *Adv. Polym. Sci.*, **100**, 219.
44 Mansfield, M.L. (1988) *Polymer*, **29**, 1755.
45 Tanzawa, Y. and Toda, A. (1994) *Polymer*, **37**, 1621.
46 Frank, F.C. (1974) *J. Cryst. Growth*, **22**, 233.
47 Muthukumar, M. (2004) *Advances in Chemical Physics* (ed. S.A. Rice), John Wiley & Sons, Inc., Hoboken, NJ, vol. **128**, p. 1.
48 Granasy, L., Pusztai, T., Borzsonyi, T., Warren, J.A., and Douglas, J.F. (2004) *Nat. Mater.*, **3**, 645.
49 Granasy, L., Pusztai, T., Tegze, G., Warren, J.A., and Douglas, J.F. (2005) *Phys. Rev. E*, **72**, 011605.
50 Taguchi, K., Miyamoto, Y., Miyaji, H., and Izumi, K. (2003) *Macromolecules*, **36**, 5208.
51 Guenthner, A.J. and Kyu, T. (2000) *Macromolecules*, **33**, 4463.
52 Mehta, R., Keawwattana, W., Guenthner, A.J., and Kyu, T. (2004) *Phys. Rev. E.*, **69**, 061802.

**53** Prigogine, I. and Garikian, G. (1951) *Physica*, **16**, 239.

**54** Flory, P.J. (1953) *Principles of Polymer Chemistry*, Cornell University Press, Ithaca, NY.

**55** Huggins, M.L. (1942) *J. Am. Chem. Soc.*, **64**, 1712.

**56** Nishi, T. and Wang, T.T. (1975) *Macromolecules*, **8**, 909.

**57** Burkhardt, W.R. (1989) *Macromolecules*, **22**, 2482.

**58** Konigsveld, R. and Stockmayer, W.H. (2001) *Polymer Phase Diagrams*, Oxford University Press, Oxford, New York.

**59** Kerridge, R. (1952) *J. Chem. Soc.*, 4577.

**60** Drolet, F., Elder, K.R., Grant, M., and Kosterlitz, J.M. (2000) *Phys. Rev. E*, **61**, 6705.

**61** Shen, C.S. and Kyu, T. (1995) *J. Chem. Phys.*, **102**, 556.

**62** Chiu, H.-W. and Kyu, T. (1995) *J. Chem. Phys.*, **103**, 7471.

**63** Malik, S., Rochas, C., and Guenet, J.M. (2005) *Macromolecules*, **38**, 4888.

**64** Ray, B., Elhasri, S., Thierry, A., Marie, P., and Guenet, J.M. (2002) *Macromolecules*, **35**, 9730.

**65** Daniel, C., Menelle, A., Brulet, A., and Guenet, J.M. (1997) *Polymer*, **38**, 4193.

**66** Matkar, R.A. and Kyu, T. (2006) *J. Phys. Chem. B*, **110**, 12728.

**67** Matkar, R.A. and Kyu, T. (2006) *J. Phys. Chem. B*, **110**, 16059.

**68** Gunton, J.D., San Miguel, M., and Sahni, P.S. (1983) in *Phase Transitions and Critical Phemonena*, vol. 8 (eds C. Domb and J.L. Lebowitz), Academic Press, Ch. 3, p. 267.

**69** Mazurin, O.V. and Porai-Koshits, E.A. (eds) (1984) *Phase Separation in Glass*, North-Holland, Amsterdam.

**70** Kyu, T. and Chiu, H.W. (1996) *Phys. Rev. E*, **53**, 3618.

**71** Xu, H., Matkar, R., and Kyu, T. (2005) *Phys. Rev. E*, **72**, 011804.

**72** Hadziioannou, G. and Stein, R.S. (1984) *Macromolecules*, **17**, 567.

**73** Canalda, J.C., Hoffmann, Th., and Martinez-Salazar, J. (1995) *Polymer*, **36**, 981.

**74** Wendorff, J.H. (1980) *J. Polym. Sci., Polym. Lett. Ed.*, **18**, 439.

**75** Rathi, P., Huang, T.-M., Dayal, P., and Kyu, T. (2008) *J. Phys. Chem. B*, **112**, 6460.

**76** Smith, P. and Manley, R.St.J. (1979) *Macromolecules*, **12**, 483.

**77** Wittman, J.C. and Manley, R.St.J. (1977) *J. Polym. Sci., Polym. Phys. Ed.*, **15**, 1089.

**78** Park, S.J. and Kyu, T. (2008) *J. Chem. Phys.*, **129**, 244901.

**79** Park, S.J. and Kyu, T. (2009) *Macromolecules*, **42**, 1180.

**80** Rathi, P. (2009) Theoretical Modeling of Morphology Development in Blends of Semicrystalline Polymers undergoing Photopolymerization, PhD Dissertation, University of Akron.

# 5
# Miscibility Criterion in Polymer Blends and its Determination

*Valeria Arrighi, John M.G. Cowie, Steven Fuhrmann, and Abdelsallam Youssef*

## 5.1
## Introduction

The mixing of two or more polymers is an established method used to attain new property combinations that overcomes the need to synthesize new structures with the desired characteristics [1]. The development of any polymer blend system, including selection and performance, crucially depends on our ability to predict and control phase behavior as well as blend morphology. To achieve this, understanding of the parameters that govern polymer–polymer miscibility is vital.

The term miscibility is used to describe a mixture containing two or more components able to form a one-phase (solid or liquid) system that is homogeneous down to the molecular level [2]. Thermodynamics offers an unambiguous way to predict whether a binary mixture is miscible or immiscible and provides a quantitative determination of the polymer–polymer interaction energies. This is important since the interaction between polymer–polymer pairs affects the physical and mechanical properties of miscible systems and, for immiscible ones, it determines the nature and the width of the interface between the two polymers.

While the above definition of miscibility is unequivocal as it corresponds to a precise thermodynamic description of the system, in practical terms the experimental determination of polymer blend miscibility is not free from ambiguities. This is because the experimental determination of homogeneity in a blend is dependent on the experimental probe and, consequently, while a system may appear to be one-phase if examined at sufficiently large length scales, it may not be truly miscible at the molecular level.

One of the primary tasks of the investigations carried out in the past few decades has been the control of the structure and properties of multicomponent systems. These are interrelated and therefore the control and design of the structures that develop in multicomponent systems is fundamental to produce novel properties. Understanding of phase separation and spinodal decomposition is fundamental and this involves knowledge of the thermodynamics of the system, phase transitions and critical phenomena and a general evaluation of the degree of miscibility of the polymeric blend components.

*Encyclopedia of Polymer Blends, Volume 1: Fundamentals.* Edited by Avraam I. Isayev
Copyright © 2010 WILEY-VCH Verlag GmbH & Co. KGaA, Weinheim
ISBN: 978-3-527-31929-9

There is a wealth of experimental methods that can be used to investigate polymer–polymer miscibility. One of the first and most used criterion to establish whether a polymer–polymer blend is one- or two-phase rests on the observation of a single glass transition temperature ($T_g$) that is intermediate between the $T_g$s of the components. The merging of the two $T_g$s into a single relaxation process signifies that there is intimate mixing of the polymer chains on a molecular level. In contrast, an immiscible system will display two distinct $T_g$s that correspond to the transitions in the pure components, thus indicating the existence of two distinct phases. In addition to the single glass transition method, techniques such as nuclear magnetic resonance (NMR), Fourier-transform infrared spectroscopy (FTIR), light scattering, small-angle neutron scattering, and neutron reflectivity have been employed. Some of the experimental methods are sensitive to the phase, that is, the size and structure of the blends, and techniques such as scanning electron microscopy (SEM), transmission electron microscopy (TEM), and polarized light microscopy offer a direct means to visualize the morphology of the phases.

Given the extensive literature on blends and the wide range of techniques developed to investigate polymer miscibility it would be impossible to cover each one with the same level of detail and we therefore include a comprehensive list of references. Although it may appear useful to attempt a grouping of the different methods, such as the classification used by Utracki [3], our aim here is to provide a general background to the experimental determination of miscibility. Following a brief description of the thermodynamics of mixing, the different techniques are discussed in separate sections and grouped according to the type of measurement, for example, scattering, spectroscopy, and microscopy. A separate section is dedicated to the glass transition of polymer blends.

## 5.2 Thermodynamics

The phase behavior of polymers differs considerably from that of small molecules, whether in solution or in mixtures with other polymers. This difference is a direct result of the large macromolecular size; whereas for mixtures of small molecules the large gain in entropy on mixing provides the driving force for miscibility, for polymers the entropic contribution is negligible. Based on these arguments, polymer–polymer miscibility was initially regarded as a rarity but, over the years, several miscible systems have been reported. In addition, methods for enhancing polymer–polymer miscibility have been developed such as incorporating functional groups capable of generating strong specific interaction between the polymer components or exploiting the intramolecular repulsive effect.

Thermodynamically, the necessary condition for two substances to mix is that the Gibbs free energy of the solution, $G_{12}$, is lower than the sum of the Gibbs free

energies of the two separate components, $G_1$ and $G_2$:

$$\Delta G_m = G_{12} - (G_1 + G_2) < 0 \tag{5.1}$$

Therefore, miscibility is governed by the Gibbs free energy of mixing $\Delta G_m$ and depends on the relative magnitude of the enthalpic $\Delta H_m$ and entropic $\Delta S_m$ terms:

$$\Delta G_m = \Delta H_m - T\Delta S_m \tag{5.2}$$

It follows that, for a two-component mixture to be miscible at a temperature $T$, $\Delta G_m$ needs to be negative. However, as discussed later, this is a necessary but not sufficient condition for thermodynamic miscibility to be achieved.

The two terms in Eq. (5.2) provide a measure of the number of "distinguishable" arrangements available to a system via the entropic term, $\Delta S_m$, and the extent of interactions between molecules through the enthalpic term, $\Delta H_m$. The former is a positive quantity: mixing always increases the disorder of the system. This holds true for low-molecular weight materials where the large entropic change occurring on mixing provides the driving force to miscibility. For such systems, $\Delta G_m$ becomes more negative with increasing temperature and this favors miscibility.

The enthalpic term is negative when there are attractive interactions between the components, a condition that decreases $\Delta G_m$ and favors miscibility. For an ideal solution, intermolecular forces between like and unlike molecules (i.e., the two components) are similar and $\Delta H_m = 0$.

The lattice model offers a means to derive an expression for $\Delta S_m$ and it can also be used to account for the effect of intermolecular interactions, which, within the model, are of the first neighbor type. In the absence of specific attractive forces such as hydrogen bonding and complex formation, and assuming random mixing, $\Delta H_m$ can be expressed as the product of the number of [1, 4] contacts in solution and the contact exchange energy, $\Delta W_{12}$:

$$\Delta H_m = n\, z\, N_A\, \Delta W_{12}\, x_1\, x_2 \tag{5.3}$$

where

$n$ is the total number of moles,
$x_1$ and $x_2$ are the mole fractions of the two components,
$z$ is the lattice coordination number,
$N_A$ is the Avogadro constant.

Equation (5.3) is often written in terms of the van Laar dimensionless segment–segment interaction parameter $\chi_{12}$:

$$\chi_{12} = \frac{z\Delta W_{12}}{k_B T} \tag{5.4}$$

where $T$ is the temperature and $k_B$ is Boltzmann's constant. Using the definition of the interaction parameter, Eq. (5.3) can be rewritten as:

$$\Delta H_m = RT\, \chi_{12}\, x_1\, x_2 \tag{5.5}$$

where $R$ is the gas constant.

The Flory–Huggins (FH) model [5–7] originally developed for polymer solutions can be extended to polymer–polymer mixtures by introducing the concept of a reference segment volume $V_R$, which is approximated to the smallest polymer repeat unit. For a binary polymer mixture, the combinatorial entropy of mixing $\Delta S_m$ can be expressed as:

$$\frac{\Delta S_m}{R} = -\left(\frac{V}{V_R}\right)\left[\frac{\varphi_1}{r_1}\ln\varphi_1 + \frac{\varphi_2}{r_2}\ln\varphi_2\right] \tag{5.6}$$

where

$r_i$ indicates the number of segments per chain molecule (i.e., the degree of polymerization) of component $i$ relative to the reference volume $V_R$,
$\varphi_i$ is the volume fraction of component $i$,
$V$ is the total molar volume.

Substitution of Eq. (5.6) and $\Delta H_m$ into Eq. (5.2) gives the Gibbs free energy of mixing:

$$\frac{\Delta G_m}{RT} = \left(\frac{V}{V_R}\right)\left[\frac{\varphi_1}{r_1}\ln\varphi_1 + \frac{\varphi_2}{r_2}\ln\varphi_2 + \varphi_1\varphi_2\chi_{12}\right] \tag{5.7}$$

The large size of polymer molecules is directly responsible for their thermodynamic behavior, with the combinatorial entropy of mixing being very small for polymer–polymer mixtures due to the large $r_i$ values of the high molecular weight polymer components. Thus any small interaction between the constituents that is unfavorable to mixing leads to a positive $\Delta G_m$. Miscibility is achieved if $\Delta H_m \approx 0$ that is, for systems with very similar chemical structures or when specific interactions such as dipole–dipole or hydrogen bonding are introduced among the blend components, making $\Delta H_m$ and $\Delta G_m$ negative.

As temperature increases, the specific interactions between the two components weaken due to molecular motion and a point will be reached where the system tends to separate into two different phases. Phase separation and limited solubility play a crucial role in situations of practical interest and therefore knowledge of the phase behavior of a mixture is essential. Numerous polymer blends show lower critical solution temperature (LCST) behavior, but an upper critical solution temperature (UCST) may be observed in some binary systems, particularly low molecular weight non-polar mixtures. For these, even if the entropic term is small it is still larger than $\Delta H_m$ and, thereby, $\Delta S_m$ governs the miscibility.

Figure 5.1 shows a phase diagram relative to a polymer solution that phase separates on cooling. With decreasing temperature, $\Delta G_m$ shows a local negative curvature between points A and D: the system can lower its free energy by separating into two phases of compositions $\varphi_A$ and $\varphi_D$ that correspond to free energy minima. For $T = T_1$, a common line can be drawn between points A and D where the free energy of the two separate phases lies below the curve that represents the free energy of the single phase system. Thus, for compositions between points A and D, the system can lower its free energy by separating into two phases of compositions $\varphi_A$

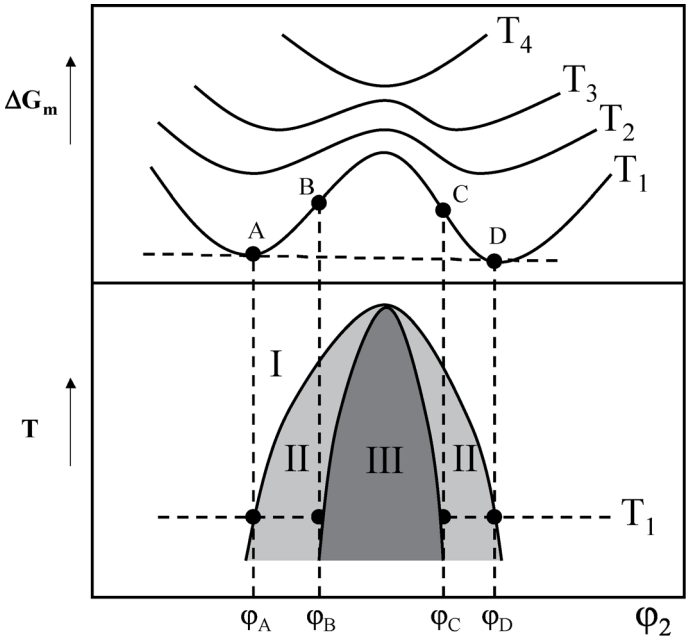


**Figure 5.1** Schematic representation of free energy of mixing versus composition curves at different temperatures, $T_1 < T_2 < T_3 < T_4$, and corresponding phase diagram. In the lower section, I refers to the one-phase region while II and III are the metastable and unstable regions of the phase diagram, respectively.

and $\varphi_D$ that correspond to free energy minima. This implies that there is a miscibility gap between these two compositions. For this condition to be achieved, the $\Delta G_m$ versus composition curve needs to show two inflexion points, here indicated as $\varphi_B$ and $\varphi_C$.

The solid, outer line in Figure 5.1 is the *binodal* that separates the stable from the metastable regions of the phase diagram whereas the inner line is the *spinodal* curve, separating the metastable and unstable regions. The latter touches the binodal at the critical point, $T_c$.

It follows from the above discussion that for miscibility to be achieved the following thermodynamic condition needs to be satisfied:

$$\left[\frac{\partial^2 \Delta G_m}{\partial \varphi_2^2}\right]_{T,p} > 0 \tag{5.8}$$

since the system becomes unstable when the second derivative is negative [8]. The recommended terminology related to polymer blends and multiphase systems is described in Reference [8] and various aspects of blend thermodynamics have been reviewed in books [1–3, 9–11].

## 5.3
## Glass Transition of Polymer Blends

The glass transition of a polymer is a reversible process associated with the motion of the polymer chains, which greatly influences the physical and mechanical properties of a polymer, for example, strength and rheology. Below the glass transition temperature ($T_g$) the available thermal energy is less than the energy required for the rotation of the main chain backbone. In this state, the motion is restricted to the rotation of the side chains and limited oscillations of the backbone. Above the $T_g$ the polymer chains are in the rubbery state and can move about with relative freedom. The change between these two states is called the glass transition and usually occurs in the temperature range 170–500 K for most polymers. The chemical structure of the polymer greatly influences the temperature where the transition from a glass to a rubber occurs and therefore $T_g$ depends on steric effects, average molar mass and chain flexibility, and other parameters such as crystallinity and degree of crosslinking.

Blending greatly affects the $T_g$ of the system and therefore the observation of the glass transition behavior is the most accepted method to assess polymer miscibility. A miscible blend shows a single glass transition intermediate to the $T_g$s of the components whereas an immiscible one will exhibit multiple transitions, reflecting either macrophase separation or the partial miscibility of the components. Figure 5.2 illustrates different types of behavior, ranging from immiscibility to complete miscibility. In intermediate cases, when the blend is partially miscible, either multiple $T_g$s shifted closer together in temperature or a broadening of the transition region is observed.

Because of the link between $T_g$ and the mechanical and thermal properties, the dependence of the glass transition temperature on blend composition is of much interest and has been the subject of many experimental and theoretical papers. The subject is particularly vast since $T_g$s can be determined using various experimental techniques, including differential scanning calorimetry, dynamic mechanical thermal analysis, and dielectric relaxation spectroscopy (DRS).

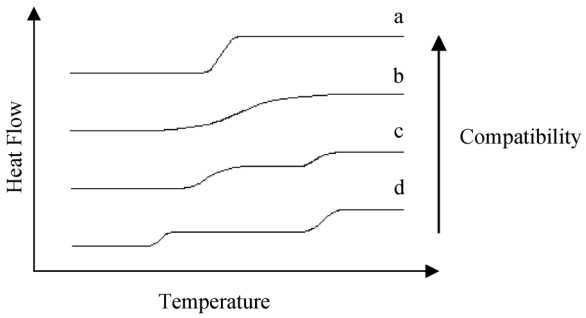


**Figure 5.2** Typical DSC thermograms for (a) a miscible blend, (b) miscible blend close to phase separation, (c) partially miscible blend close to complete immiscibility, and (d) immiscible blend.

For polymer blends that are mixtures of two miscible polymers, only one $T_g$ is observed. Thus any analytical technique that can be used to determine the $T_g$, can also be employed to distinguish between miscible and immiscible blend systems, provided that the $T_g$s of the two individual components are sufficiently far apart. Several equations are available to describe the dependence of the glass transition temperature on blend composition. A simple linear relationship between $T_g$ and composition is very seldom observed [12–15]:

$$T_g = w_1 T_{g1} + w_2 T_{g2} \tag{5.9}$$

where

$T_{g1}$ and $T_{g2}$ are the glass transitions of the two components,
$w_1$ and $w_2$ the corresponding weight fractions.

The Gordon–Taylor equation [16] is a modified version of Eq. (5.9):

$$T_g = \frac{w_1 T_{g1} + K w_2 T_{g2}}{w_1 + K w_2} \tag{5.10}$$

where the constant $K$ can either represent the volume expansion coefficients of the components at the glass transition temperature:

$$K = (\alpha_l - \alpha_g)_2 / (\alpha_l - \alpha_g)_1 = \Delta\alpha_2 / \Delta\alpha_1 \tag{5.11}$$

or the ratio of the heat capacity increments of the components:

$$K = \Delta C_{p2} / \Delta C_{p1} \tag{5.12}$$

as suggested by Couchman and Karasz [17]. Either method produces $K$ values in the range 0.8–1.2, at least for those cases to which the Gordon–Taylor equation can be applied successfully. Despite being extensively used to predict the variation of $T_g$ with blend composition, the Gordon–Taylor equation cannot be applied to cases where maxima, minima, or points of inflection are evident in the $T_g$ versus composition curve. It therefore fails to predict the behavior of some blends, particularly those where strong interactions exist between the components, for example, hydrogen bonding. For these, the Kwei equation [14] is the most effective as it involves the addition of a term ($q w_A w_B$) that accounts for the positive deviation from additivity to Eq. (5.9):

$$T_g = w_1 T_{g1} + w_2 T_{g2} + q w_1 w_2 \tag{5.13}$$

where $q$ is an adjustable parameter. The same term can also be used to modify the Gordon–Taylor equation:

$$T_g = \frac{w_1 T_{g1} + K w_2 T_{g2}}{w_1 + K w_2} + q w_1 w_2 \tag{5.14}$$

which then becomes a function of two adjustable parameters, $K$ and $q$. Once again $q$ is related to the number of stabilizing interactions that exist between the polymer components in the blend, while $K$ is usually close to unity. If these interactions are

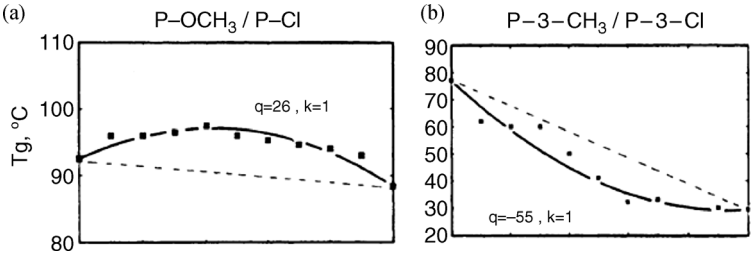


**Figure 5.3** Glass transition temperature versus blend composition (weight fraction of the electron-donor substituted component) for a blend of two substituted poly(vinyl cinnamate) polymers (a) with $OCH_3$ and Cl groups in the para position of the phenyl ring and (b) with $CH_3$ and Cl groups in the para position of the phenyl ring and with $(CH_2)_3$ spacer groups between the backbone and cinnamoyl groups. Reproduced with permission from Reference [18].

stronger in the blend than in the pure components, $q$ is positive and the resultant $T_g$ will be higher than predicted for an ideal blend. This is shown in Figure 5.3a, where the glass transition temperatures of blends of two substituted poly(vinyl cinnamate) polymers with $OCH_3$ and Cl groups in the para position of the phenyl ring are plotted versus composition.

However, should the interactions immobilize the polymer chains in the blend less than the pure components, then a negative deviation is expected, with the blend $T_g$ being lower than the weighted mean of the homopolymers (Figure 5.3b). The Gordon–Taylor equation can be treated as a special case of the Kwei equation, where $q$ is negligible, meaning there is no difference in the interactions of the polymer chains in the blend in comparison to those interactions in the pure component. By adjusting the values of the parameters $q$ and $K$, Eq. (5.14) provides an effective method for modeling the variation in $T_g$ with blend composition, for a large variety of different polymer blend combinations [18].

### 5.3.1
### Determination of the Glass Transition of Polymer Blends

Various experimental techniques can been used to determine the polymer glass transition, including differential scanning calorimetry (DSC), dynamic mechanical analysis (DMA), dielectric relaxation spectroscopy (DRS), and NMR. All these techniques can be employed to assess the phase behavior of a blend but DSC is by far the most common. This technique provides a simple, efficient way to measure the $T_g$, width of the glass transition, heat capacity, as well as the melting temperature ($T_m$) and the enthalpy of fusion ($\Delta H_f$), and it is therefore suitable to investigate binary mixtures of amorphous or crystalline polymers. As an example of the wealth of information obtained from the DSC measurements, Figure 5.4a shows thermograms for blends of poly(L-lactide) (PLLA) with a high molecular weight poly(ethylene oxide) sample (PEO).

Similar to other semicrystalline blends [19, 20], the melting temperatures of PEO and PLLA decrease with increasing the amount of the second component in the blend

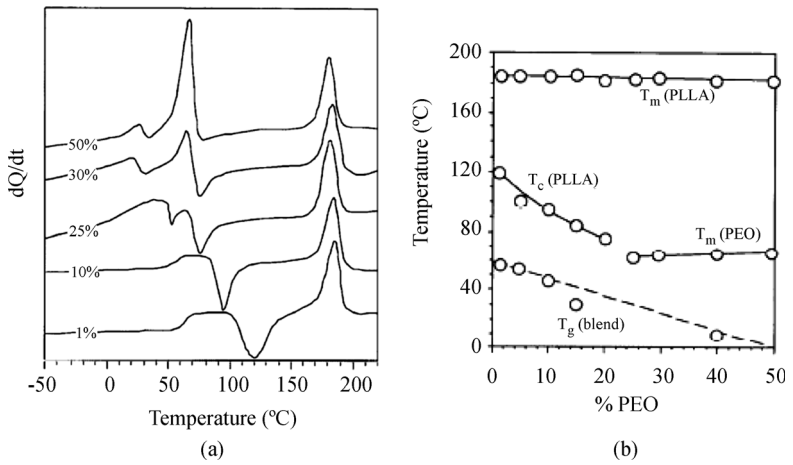


**Figure 5.4** (a) Thermograms of PLLA/PEO blends as a function of PEO concentration (wt%); (b) phase diagram of PLLA/PEO blends [dotted line = dependence of $T_g$ on blend composition, solid lines = $T_C$ (critical point) and $T_m$]. Reproduced with permission from Reference [21].

(Figure 5.4b). As commented by the authors, this is usually indicative of miscibility but similar changes have also been observed in systems that are immiscible [21]. However, the glass transition behavior with blend composition provides an unambiguous proof that the system is miscible since the blend $T_g$ is proportional to composition.

The use of calorimetric methods to assess blend miscibility has various limitations. First of all, for the technique to provide a reliable assessment of phase behavior the difference between the $T_g$s of the polymer components needs to be larger than 10 °C, although annealing experiments can be helpful in discriminating between miscibility/immiscibility when the two $T_g$s are close (Chapter 6). Furthermore, DSC is generally limited to the determination of domain sizes larger than 100 Å [22] and this limitation has sometimes been at the origin of contradictory results reported in the literature [23–27]. This is the case for blends of poly(methyl methacrylate) (PMMA) and poly(vinylphenol) (PVPh) that were at first reported to be miscible, on the basis of DSC measurements [28–33] but immiscible based on NMR results [34]. In the latter work, the $^1$H spin–lattice relaxation times measured in both the rotating frame ($T_{1\rho}$) and laboratory frame ($T_1$) indicated that miscibility in PVPh/PMMA blends is poor, contrary to PVPh/poly(methy1 acrylate) (PMA) blends that were found to be mixed on a scale of 20–30 Å. To clarify the issue of the miscibility in PVPh/PMMA blends, Li and Brisson have carried out dynamic mechanical thermal analysis (DMTA) as a function of blend composition and frequency [27]. The DMTA data, particularly the loss moduli and tan δ, showed evidence of a second relaxation (Figure 5.5), in addition to the main transition. This supports the idea that the blends are not homogeneous, when observed on the smaller domain scale probed by the DMTA technique. The DSC measurements are not sensitive to small domain sizes and so the

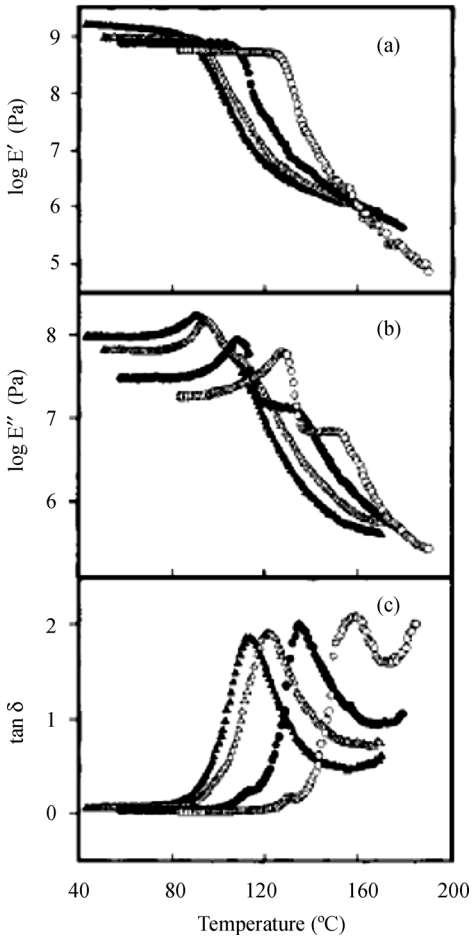


**Figure 5.5** Temperature dependence of the storage (a) and loss (b) moduli, and the loss tangent (c) , as determined by DMTA for PVPh-PMMA blends at 10 Hz: (▲) pure PMMA, (△) 10 wt% PVPh, (●) 30 wt% PVPh, and (○) 54.5 wt% PVPh.

blends display a single $T_g$ by DSC. This was further supported by SAXS (small-angle X-ray scattering) measurements, which showed a peak at 30 Å.

## 5.4 Phase Equilibria Methods

The phase behavior of polymer blends is of both commercial and academic interest. For a given polymer–polymer system, the phase diagram provides all necessary information on phase behavior, including temperature values at which phase separation takes place. A wide range of experimental methods is available to either

assess the degree of miscibility of a sample or map the whole temperature–composition space.

The morphology of the blend and the kinetics of the phase separation process can be investigated using static techniques such as light scattering and electron microscopy whereas other methods such as small-angle X-ray scattering (SAXS), small-angle neutron scattering (SANS), ellipsometry, and neutron reflectivity (NR) allow for determination of the interaction parameters in miscible or immiscible systems.

Based on the method of analysis employed, one can distinguish between real or reciprocal-space techniques. The first class includes optical microscopy, transmission electron microscopy (TEM), scanning electron microscopy (SEM) and atomic force microscopy (AFM). Techniques such as light scattering and neutron and X-ray scattering are part of the latter category. All these experimental methods are discussed in the following sections.

### 5.4.1
### Scattering Techniques

Scattering techniques such as light, X-ray, and neutron scattering offer unique information on polymer blends as they provide a measure of interaction parameters and also conformation, local structure, domain sizes, crystalline order, and crystallinity.

Figure 5.6 gives a schematic representation of a scattering experiment. The setup consists of (i) a radiation source, (ii) a system of collimation and/or monochromation, (iii) the sample, and (iv) a detector. As shown in Figure 5.6, the incident radiation of wavelength $\lambda_0$, wavevector $\boldsymbol{k}_0(|k_0| = 2\pi/\lambda_0)$, and energy $E_0$ is scattered and detected at scattering angle $\theta$. If the process is elastic then there is no energy change during the process, but simply a change in the direction of traveling of the wave, defined in terms of the wavevector change, $\boldsymbol{Q} = \boldsymbol{k} - \boldsymbol{k}_0$, also referred to as the *scattering vector* or

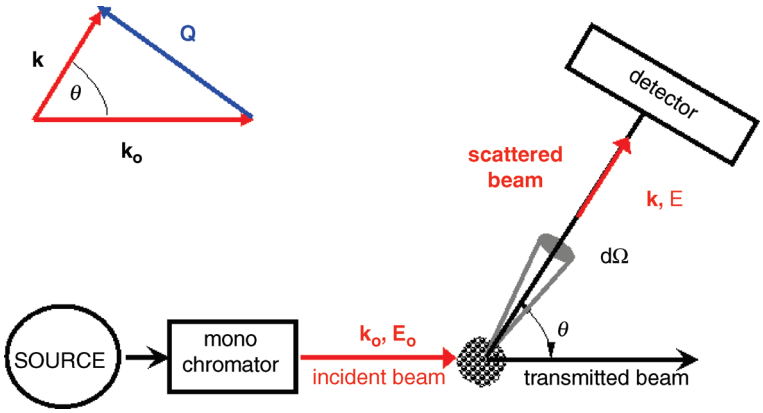


**Figure 5.6** Schematic of a scattering experiment and the relationship between wavevectors and momentum transfer.

*momentum transfer*. For elastic scattering, the magnitude of the initial and final wavevectors coincides, that is, $|k_0| = |k|$ and $Q = 4\pi/\lambda_0 \sin(\theta/2)$ (Figure 5.6).

Structural investigations involve measurements of the scattered intensity as a function of the scattering angle. A relationship between structure in real space and scattering in $Q$-space can be derived from Bragg's law:

$$n\lambda = 2d \sin\left(\frac{\theta}{2}\right) \tag{5.15}$$

where $d$ is the distance between two crystallographic planes and $n$ is the order of reflection, and defines $Q$. This leads to:

$$d = \frac{2\pi}{Q} \tag{5.16}$$

indicating that $d$ is inversely proportional to $Q$, meaning that to probe the large distances corresponding to chain dimensions, lamellar spacing, and domain structures one needs to approach low $Q$ values. Conversely, large $Q$ values give information on short distances, for example, the local polymer structure.

All scattering techniques are used for polymer studies and characterization of blend behavior. The choice of technique depends on various factors, particularly the length scale of interest and the type of contrast available between the components. X-Ray and neutron wavelengths are of the order of interatomic distances (Table 5.1) and, in order to reach small $Q$ values, instruments need to operate at low angles. Typically, the $Q$ range probed by conventional small-angle scattering instruments ranges between $10^{-3}$ and $10^{-1}$ Å$^{-1}$, with scattering angles from 0.1° to 10° and the techniques are then referred to as small-angle neutron and X-ray scattering (SANS, SAXS). These can probe length scales of 1 to a few thousand ångströms, which is comparatively smaller than those accessed by light scattering, and within the range of polymer chain dimensions. Additional information on length scales of a few ångströms are obtained in the wide-angle regime from 0.6 to 15 Å$^{-1}$, which is typical of crystal structures, local conformation, and orientation.

In addition to the size range explored, scattering techniques differ in the way they interact with matter (Table 5.1). Both X-rays and light are scattered by electrons: phase

**Table 5.1** Characteristics of the different types of radiation employed in small-angle scattering experiments. Adapted from Reference [35].

| Parameter | Small-angle scattering | | |
|---|---|---|---|
| | **Neutrons** | **X-Rays** | **Light** |
| Radiation scattered by | Nuclei | Electrons | Electrons |
| Availability | Large-scale facility | Laboratory or large-scale facility | Laboratory |
| Wavelength (nm) | 0.15–2.5 | 0.154 | 400–700 |
| Length scale probed | 1–2000 Å | 1–3000 Å | 1–100 μm |

separation studies with light or X-rays are limited to systems where a difference between refractive indices or electron densities exists between the polymer components. Neutrons instead interact with the nuclei and the SANS technique can be applied to any blend system, provided that at least one of the components can be deuterated. By exploiting the labeling method it has been possible, using SANS, to obtain detailed thermodynamic information on several polymer blends, in the homogeneous state.

SANS is an expensive tool and, whenever possible, SAXS or light scattering should be used. It is the judicious use of deuterium labeling that usually justifies SANS measurements, giving access to structural features unavailable through other scattering methods or complementary results.

#### 5.4.1.1 Turbidity Measurements and Light Scattering

Turbidity measurements represent one of the oldest methods used to monitor phase behavior. Experiments involve preparing samples of varying compositions by dissolving known weights of the two polymer components in a suitable solvent, followed by solvent evaporation to create thin polymer films. The determination of phase boundaries involves heating the samples at a controlled heating rate in order to measure the temperature at which the sample becomes opaque.

When investigating a large number of samples, direct visual observation of temperature induced changes in the degree of transparency of the films provide a good first indication of whether a blend is miscible. For example, the method has been used to compare experimental data and calculated phase diagrams in several copolymer systems [37]. One simple way to assess polymer miscibility is by direct visual observation, or through an optical microscope, of a sample, usually in the form of a thin film. Amorphous, one-phase blends form a transparent film whereas two-phase systems should be opaque if the difference between the refractive indices of the two components is sufficiently large.

However, such a simple approach has various limitations. Problems may be encountered when the film is thinner than the wavelength of the light used ($<$100 nm) or the difference between the refractive indices of the components is too small, in which case there will not be sufficient contrast between the components. Therefore, when the difference between the refractive indexes of the polymer components is less than a critical value of 0.01, it is not possible to detect phase separation by optical observation [38]. Studies carried out on blends of chlorinated polyethylene with poly(methyl methacrylate) (PMMA) indicate that inconsistent results can be obtained when using turbidity as the sole criterion for miscibility [39]. For 27% chlorination, the blend with PMMA appeared opaque below 70 °C, clear up to 80 °C, and then opaque once again at higher temperature. While these results were at first believed to be due to the blend displaying upper critical as well as lower critical solution temperatures [40], it later became clear that the appearance of a clear region was a result of the two polymers having similar refractive indices in the range 70–80 °C due to different temperature dependencies of their refractive indices.

Recent work by Haggard *et al.* [38] on co-polycarbonate blends with styrene–acrylonitrile (SAN) copolymers has shown that one should always bear in mind

refractive index differences when interpreting the blend behavior via optical observations. In this respect, as the authors did, it is helpful to calculate values of refractive index, if experimental data are not avaliable.

Complete characterization of the miscibility behavior of a binary polymer mixture would generally involve determination of the associated phase diagram, that is, the mapping of whether the blend is one or two phase, as a function of temperature and blend composition. Cloud point (CP) measurements are particularly useful in this respect as they define the point at which a homogenous, one-phase mixture starts developing composition fluctuations whose size become comparable to the wavelength of light. Therefore, if a sample is heated at a constant rate and the scattered intensity is monitored as a function of time, the CP identifies the onset of phase separation and coincides with the point at which the measured scattered intensity begins to deviate from the baseline. An example of the power of these relatively simple measurements is given by the experiments of Hindawi *et al.* [41], who were able to follow phase changes in polymer blends undergoing shear flow between parallel plates, during controlled heating. An example of the CP changes observed by these authors for blends of poly(butylene acrylate) (PBA) and solution chlorinated polyethylene (SCPE) as a function of shear is given in Figure 5.7. As shown in

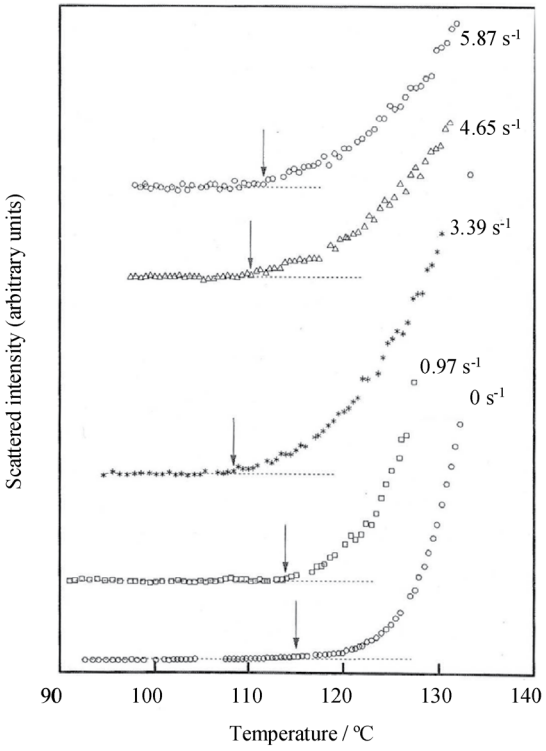


**Figure 5.7** Dependence of the CP of a 55/45 PBA/SCPE12 blend on the applied shear rate. The CP is indicated by an arrow on each curve. Reproduced with permission from Reference [41].

Figure 5.7, the CP first decreases, indicating demixing and, above a critical shear rate, it increases, suggesting shear-induced mixing, a behavior that was later confirmed for other blend systems.

Various experimental setups can be used, with different levels of sophistication. The sample can be illuminated using a laser beam (He-Ne) or UV source or simply white light. Changes in turbidity can be monitored visually, under a microscope or by using a photomultiplier or photodiode.

For blends for which the glass transition is strongly dependent upon blend composition, the cloud points are better obtained by extrapolation to a zero heating rate to avoid errors due to kinetic effects [42]. Generally, the CP curve obtained by extrapolating the cloud point temperature to zero heating rate can be taken as a measure of the binodal, at least for samples with small polydispersity [44]. The spinodal line can be determined experimentally by considering that the reciprocal of the scattered intensity extrapolaterd to zero scattering angle, $1/\left[R_\theta^c\right]_{\theta=0}$, is proportional to the second derivative of the Gibbs free energy. Therefore, a plot of $1/\left[R_\theta^c\right]_{\theta=0}$ versus temperature can be used to determine the spinodal temperature, by extrapolation to zero, which satisfies the condition that:

$$\left[\frac{\partial^2 \Delta G_m}{\partial \varphi_2^2}\right]_{T,p} = 0 \tag{5.17}$$

Although the application of light scattering measurements is generally restricted to those systems where a sufficiently large contrast exists between the components, that is, a sufficiently large difference between the refractive indices, methods exists that can overcome this problem. For example, Wang *et al.* [45] were able to study the phase behavior of blends of ethylene/hexane and ethylene/butene copolymers, which have nearly identical refractive indices. For these conventional methods of determination of phase diagrams such cloud-point measurements are not applicable but the authors were able to demonstrate that techniques such as diffuse and small-angle light scattering and light transmission are suitable for determining liquid–liquid phase separation boundaries, thanks to the contrast that arises due to crystallization (degree of inhomogeneity).

An interesting variation of the light scattering technique has been developed by Gordon *et al.* [46, 47]. This consists of heating or cooling very rapidly a small sample size into the metastable region and then measuring the scattered intensity. Measurements are made at equilibrium and before phase separation occurs, so that the sample can be brought back into the homogenous region and then the cycle can be repeated. The method has been used to investigate polymer solutions or short-chain polymers but the high viscosity of high polymer blends makes it very difficult to obtain homogeneous mixtures, although use of a low speed centrifuge has been shown to overcome these problems [48].

Small-angle light scattering has also been used extensively to investigate the kinetics of the phase separation process in a range of blends such as polystyrene (PS)/poly(vinyl methyl ether) (PVME) [49], PS/poly(*ortho*-chlorostyrene) (PoClS) [50], and polycarbonate (PC)/poly(methyl methacrylate) (PMMA) [51, 52].

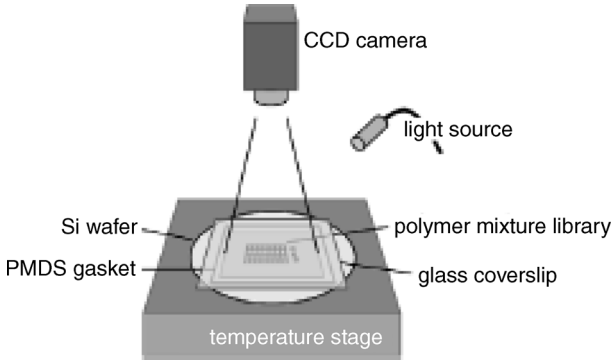


**Figure 5.8** Schematic of the cloud point detection setup used by Cabral *et al.* [54].

A new development in the determination of blend phase behavior is the use of high-throughput techniques. The few reports that have been published clearly illustrate the power of combinatoirial methods in describing, in a fast efficient manner, the complex behavior of polymer mixtures. For example, Meredith *et al.* [53] were able to determine the cloud point curve of PS/PVME using a single thin polymer film with a continuous composition gradient, to which an orthogonal temperature gradient was applied. An alternative procedure has been developed by Cabral *et al.* [54], who carried out cloud point measurements on PS/polybutadiene blends using discrete rather than continuous composition libraries. In this case the samples consisted of a series of microwell arrays that contained the polymer mixtures. Figure 5.8 shows the detection system. The system, which displays a UCST, is first equilibrated above its critical temperature and then cooled at a controlled rate while the cloud point curve is determined by parallel imaging.

#### 5.4.1.2 **Small-Angle Neutron Scattering**

Neutrons interact with the nuclei and are efficiently scattered by light elements such as hydrogen. This makes it advantageous compared to light and X-ray scattering and it is a feature that has been exploited in many polymer blend investigations [55]. In contrast to X-rays for which the scattering increases with increasing atomic number, the neutron scattering length, $b$, which characterizes the nucleus–nuclear interaction varies randomly across the periodic table. In addition, isotopes of the same element have different scattering lengths, and of particular significance in polymer studies is the difference between the scattering length of hydrogen and its isotope deuterium. Isotopic labeling was first used in pioneering experiments carried out in the 1970s on atactic polystyrene (PS) and poly (methyl methacrylate) (PMMA) [56, 57], which confirmed Flory's hypothesis [58] that polymer dimensions in bulk are unperturbed.

Figure 5.9 gives a schematic representation of a SANS instrument: a collimated beam is transmitted through the sample and the scattering is monitored by a large area detector. Long wavelengths and large sample to detector distances afford small $Q$ values. Conventional SANS spectrometers make it possible to probe structures over a length scale from near to atomic (10 Å) dimensions to a few microns. The

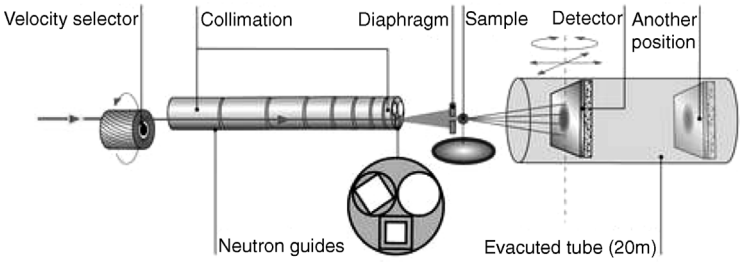


**Figure 5.9** Schematic representation of the D22 instrument at the Institut Laue-Langevin (Grenoble, France).

ultrasmall-angle neutron scattering (USANS) instruments that have recently become available have extended the experimental $Q$ range down to $2 \times 10^{-5}$ Å$^{-1}$, reaching distances up to about 30 μm.

SANS can be employed to study both homogeneous as well as heterogenous blends and various information can be derived by analysis of the differential scattering cross-section, $d\Sigma(Q)/d\Omega$ (cm$^{-1}$), where $d\Sigma(Q)$ (neutron s$^{-1}$) is the number of neutrons scattered per second into a small solid angle, $d\Omega$. The measured intensity, $I(Q)$, is related to $d\,\Sigma(Q)/d\,\Omega$ and depends on various parameters such as the incident flux, resolution of the detector, detector efficiency, and so on. It is also a function of the contrast factor $(\Delta\varrho)^2$, which is defined as the square of the difference of the scattering length density of the scattering centers, for example, the particle and the matrix. This quantity is calculated from:

$$\varrho = \sum b_i \quad \frac{\delta\, N_A}{m} \tag{5.18}$$

by adding the coherent scattering lengths $b_i$ of the nuclei in the polymer repeat unit (here $\delta$ is the density, $m$ is the mass of the repeat unit, and $N_A$ is the Avogadro constant).

For a binary blend in the one phase region:

$$\frac{d\,\Sigma(Q)}{d\,\Omega} = \left(\frac{b_1}{\nu_1} - \frac{b_2}{\nu_2}\right)^2 S(Q) \tag{5.19}$$

where the term in brackets on the right-hand side is the contrast factor that determines the magnitude of scattering through the difference between the scattering lengths of the two monomer units, $b_i$ ($\nu_i$ are the monomeric volumes of the two components). The large difference between the scattering lengths of hydrogen ($b = -3.74 \times 10^{-13}$ cm) and deuterium ($b = +6.67 \times 10^{-13}$ cm) offers a means of enhancing the natural contrast between two polymers and for this reason SANS measurements on blends are usually performed by deuterating one of the two components. Bear in mind that isotopic substitution may affect the phase behavior, as first noted for blends of PVME and deuterated PS [59] and predicted by Buckingham and Hentschel [60]. Isotopic effects have also been observed in mixtures of hydrogenous and deuterated polymers having the same chemical structure [61–63] and need

to be accounted for to correctly interpret the SANS interaction parameters [64]. Isotopic and microstructural effects may combine in a complicated manner, as shown by the large differences in critical temperatures that result from the exchange of the isotopic labeling [65].

There are various ways of extracting the polymer–polymer interaction parameters from SANS data. One of these is based on the mean-field random phase approximation (RPA) derived by de Gennes [66, 67] and Binder [68], according to which the differential scattering cross section is given by:

$$\frac{\mathrm{d}\,\Sigma(Q)}{\mathrm{d}\,\Omega} = \frac{(1/\nu)\,(b_1 - b_2)^2}{[\varphi_1\, n_1\, P_1(Q)]^{-1} + [\varphi_2\, n_2\, P_2(Q)]^{-1} - 2\chi} \tag{5.20}$$

where

$n_i$ and $\varphi_i$ are the degree of polymerization and the volume fraction of component $i$, respectively,
$\chi$ is the Flory–Huggins interaction parameter,
$\nu = \sqrt{\nu_1\, \nu_2}$ is a reference volume.

The form factors $P_i(Q)$ depend on the conformation of the polymer chains, and equations are available for several cases, such as Gaussian chains [69], spheres, discs, and rods [35, 55]. As pointed out by various authors [70, 71], the form factors $P_1(Q)$ and $P_2(Q)$ are correlated, meaning that the two $R_{g,i}$ values cannot be determined independently. Therefore, strictly speaking, the single component $R_{g,i}$ can only be determined from measurements on samples at dilute concentration [72].

As noted earlier, the scattered intensity at $Q = 0$, and therefore $S(Q = 0)$, is related to the free energy of mixing, $\Delta G_m$, and, using Flory and Huggins theories, can be used to determine the $\chi$ parameter:

$$\frac{1}{S(Q=0)} = \frac{\partial^2 \Delta G_m}{\partial \varphi_1^2} = \frac{1}{n_1\, \varphi_1} + \frac{1}{n_2(1-\varphi_1)} - 2\chi \tag{5.21}$$

Extrapolation to $Q = 0$ yields the interaction parameter $\chi$ if the degrees of polymerization $n_i$ are known. By fitting the SANS data to the RPA equation the $\chi$ parameter can be determined as a function of blend composition, temperature, and molecular weight of the components [73]. Studies on selectively deuterated PS [74] have shown that deuteration in the main chain of the PS component does not alter the phase diagram and this has confirmed that it is the interaction between PVME and the phenyl rings that is thermodynamically favorable.

One area where SANS has greatly contributed to the understanding of phase behavior is that of polyolefin blends [75–77]. For these systems, one would expect to measure a positive $\chi$ value but, contrary to these expectations, SANS experiments have revealed complex thermodynamic interactions of both attractive and repulsive type [75–77]. This is illustrated by the example in Figure 5.10 where the SANS data for a blend of saturated poly(ethylbutadiene) with elevated 3,4 content and deuterated polypropylene, at three different temperatures, are plotted and compared with the predicted intensity for the same blend without interactions ($\chi = 0$). The experimental

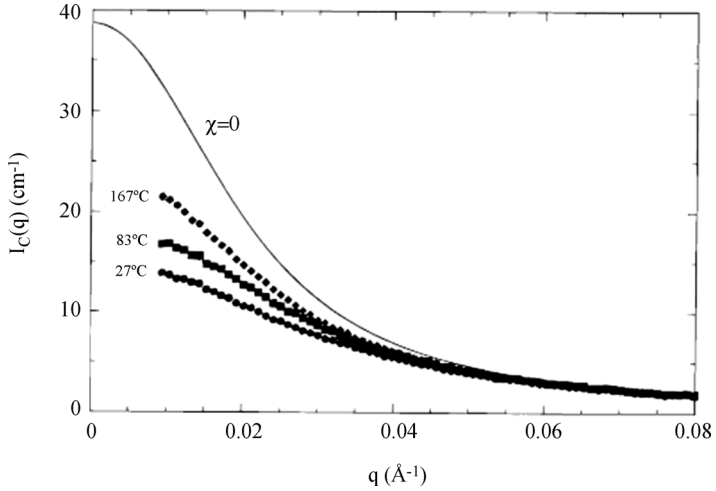


**Figure 5.10** Experimental SANS scattered intensity of a blend of saturated poly (ethylbutadiene) with high 3,4 content and deuterated polypropylene at three different temperatures. The solid line represents the predicted scattering profiles in the absence of any interactions between the polymer components. Reprinted with permission from Reference [75].

profiles are lower than expected and this suggests suppression of concentration fluctuations due to a net attraction between the components, that is, a negative $\chi$. Similarly, SANS experiments on blends of linear and branched polyolefins [78–80] have shown that high density polyethylene (HDPE) and low density polyethylene (LDPE) are miscible [78, 79], whereas for mixtures of HDPE and linear low density polyethylene (LLDPE) the miscibility depends on the LLDPE branch content.

In addition to the $\chi$ parameter, detailed analysis of SANS data through the RPA gives a measure of the radii of gyration ($R_{g,i}$). The determination of the molecular dimensions of the polymer components is particularly useful and this approach has been used by us to investigate mixtures of linear and cyclic poly(dimethylsiloxane)s [81, 82].

While the RPA equation gives a very satisfactory description of the scattering of miscible polymer blends, other, simpler approaches have been used such as the Ornstein–Zernike equation [83], which is applicable in the limit of small $Q$ values:

$$S(Q) = \frac{S(Q=0)}{1 + Q^2\,\xi^2(T,\phi)} \tag{5.22}$$

where $\xi(T,\phi)$ is the composition fluctuation correlation length at temperature $T$ and composition $\phi$.

This approach has been used to test the applicability of the mean-field theory to binary polymer mixtures.

The lowest $Q$ value accessible with SANS means that particle sizes up to 5000 Å can be studied. Hence, in addition to the conformation and interaction parameters,

SANS may also be employed to study molecular aggregates and sample morphology. It is not unusual to find that blends that appear to be homogenous by light scattering show evidence of immiscibility by SANS, as a result of the smaller length scale probed by the technique. Discrepancies between light scattering (LS) and SANS results have been reported for some blends, including mixtures of the lithium salt of sulfonated polystyrene ionomer (Li-SPS) and a methylated polyamide (mPA) [84]. Although the system was found to be miscible by light scattering, SANS revealed a peak for sulfonation levels below 20 mol% that was attributed to either microphase separation or concentration fluctuations correlated with a characteristic distance between complexation points.

Generally, the two most useful approaches dealing with the scattering of phase separated systems are those due to Debye–Bueche and Porod. For a non-homogeneous blend where the two phases have random shape and size with sharp phase boundaries, the scattering is described by the Debye–Bueche model [85–87]:

$$\frac{\mathrm{d}\,\Sigma(Q)}{\mathrm{d}\,\Omega} = \frac{8\pi\,\xi^3\,\varphi(1-\varphi)\left(\frac{b_1}{V_1}-\frac{b_2}{V_2}\right)^2}{(1-Q^2\,\xi^2)^2} \tag{5.23}$$

where $V_i$ is the average volume of phase $i$. This model is valid when $\xi \approx Q^{-1}$ and, for neutron scattering, this condition is satisfied for correlation lengths, $\xi$, of approximately 100 nm. In the more general case, when $Q \gg \xi^{-1}$, Porod's law applies and the scattering varies as [55]:

$$\frac{\mathrm{d}\,\Sigma(Q)}{\mathrm{d}\,\Omega} = \frac{2\pi}{Q^4}\left(\frac{b_1}{V_1}-\frac{b_2}{V_2}\right)^2 \frac{S_\mathrm{p}}{V_\mathrm{p}} \tag{5.24}$$

where $S_\mathrm{p}/V_\mathrm{p}$ is the average surface area to volume ratio of the phases. Deviations from Porod's law have been observed, and have been attributed to diffuse phase boundaries as well as void scattering and thermal density fluctuations, and modifications to the above equation have been proposed to treat a number of domain morphologies such as spherical, cylindrical, and lamellar [88].

Increased neutron flux and instrument optimization have made it possible to perform time-resolved neutron scattering measurements. By combining the SANS data with those obtained from time-resolved light scattering experiments, the time evolution of hierarchical structures in two-component mixtures can be studied over a wide range length scales, from 1 nm to 10 μm [89]. The wealth of information that can be obtained from these experiments is schematically shown in Figure 5.11 for a binary mixture during the late stage of the phase separation process.

The scattering pattern provides information on the space–time evolution of the hierarchical structures as shown in Figure 5.11b for a deuterated polybutadiene/hydrogenous polyisoprene (DPB/HPI) blend, which exhibits lower critical solution temperature behavior in the late stage of the phase separation process. The four different regimes observed correspond to those identified in Figure 5.11a. The scattering maximum that is initially evident in the SANS data has shifted towards smaller $Q$ values and is detected in the LS regime (for $Q < 10^{-2}\,\mathrm{nm}^{-1}$). Therefore,

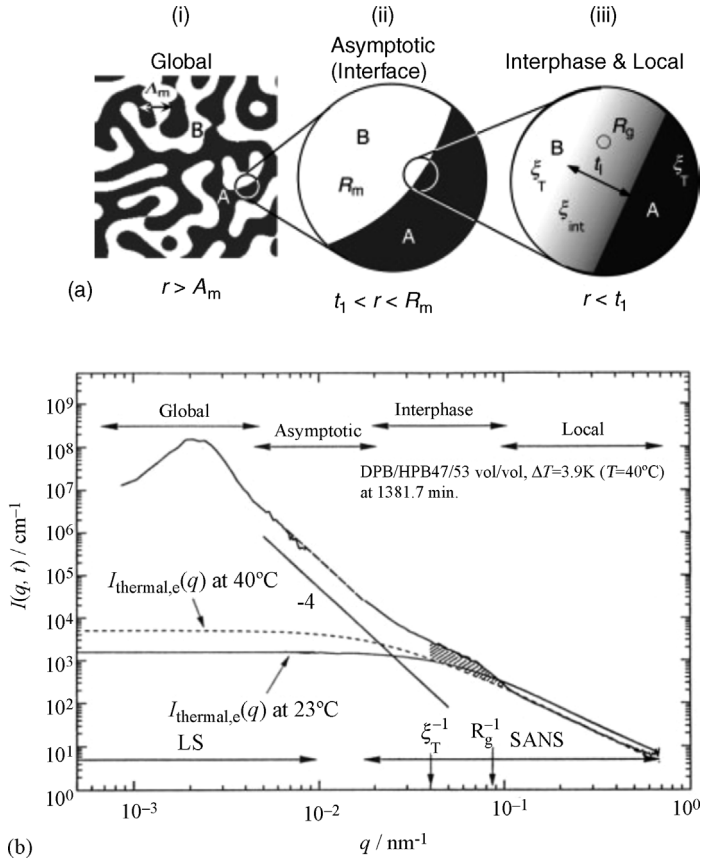


**Figure 5.11** t(a) Schematic representation of the hierarchical structures that develop during the late stage of spinodal decomposition (SD): (i) global, (ii) asymptotic (or interface), and (iii) interphase and local scale; (b) LS and SANS profile in the late stage of SD for a DPB/HPI sample. Reproduced with permission from Reference [89].

while SANS plays a crucial role in the detection of the early and intermediate stages of the spinodal decomposition (SD) process, time-resolved LS is vital to follow the late stages.

#### 5.4.1.3 Small-Angle and Wide-Angle X-Ray Scattering

X-Rays are available both as laboratory equipment and at large-scale facilities. Laboratory instrumentation makes use of the Cu $K_\alpha$ line with $\lambda = 1.54$ Å while synchrotron sources offer a wavelength range from 0.6 to 3 Å. In both cases, the wavelength is much smaller than typical polymer dimensions but, when operating at small scattering angles of the order of 1°, structural features at length scales larger than the separation between crystal planes can be accessed.

The scattered intensity, $I(Q)$, is the Fourier transform of the correlation function $\varrho(r)$, which gives the probability of finding a scatterer at position $r$ relative to another

scatterer at position 0. Therefore, elastic X-ray scattering experiments reveal the spatial correlations in the sample.

The intensity of scattering can be modeled by the same equations developed for light scattering and used in analyzing SANS data, provided that account is taken of the different matter–radiation interaction. In a similar way to SANS, the scattered intensity is proportional to the total sample volume and the contrast, which in this case is given by the difference between the mean electron densities of the two components, for example, for a polymer solution, the polymer and the solvent. For X-rays the scattering length density is given by a modification of Eq. (5.18). Since the scattering is only due to the electrons, the scattering length is given by:

$$\varrho_{\text{X-ray}} = \frac{b_e \delta\, N_A}{m} \sum n_i z_i \tag{5.25}$$

where

$b_e$ is the scattering length of an electron ($2.85 \times 10^{-5}$ Å$^{-1}$),
$n_i$ is the number of atoms of type $i$
$z_i$ is the atomic number of $i$.

It follows from the above equation that investigations similar to those performed with SANS would also be possible using SAXS, if there is sufficient contrast between the polymer components. This condition is achieved only when one of the blend components contains heavy atoms. For example, SAXS has been used to study blends of polycaprolactone (PCL) and poly(vinyl chloride) (PVC) [90] and poly(2-chlorostyrene) and PVME [91]. In both cases, data analysis in terms of Eq. (5.23) made it possible to extract values of correlation length. Tran-Cong *et al.* [91] have also determined the spinodal temperature from their data, as a function of blend composition, by exploiting the linear dependence of $1/\xi^2$ versus $1/T$ and extrapolating to zero.

Studies such as those described above are limited and SAXS is more appropriately used to investigate the morphology of semicrystalline polymers. The technique can also be applied to blends where one of the components is crystalline. Numerous systems have been investigated, among which are blends of PCL with PVC [92–96], polycarbonate [97], and polystyrene [98].

Crystallization of a miscible blend containing crystalline and amorphous polymer components must involve the segregation of the amorphous phase. Segregation can take place in different forms, leading to various types of morphology: interlamellar, interfibrillar, or interspherulitic. The latter, which can be observed using optical microscopy, occurs when the diluent is segregated to the regions between spherulites whereas in the other two cases the amorphous component is located between the lamellae (interlamellar) or between stacks of lamellae (interfibrillar). Often, different types of morphology may coexist, the amorphous diluent being located in different regions.

Several morphological parameters can be derived from the SAXS intensities, including the long period ($L$), crystal thickness ($l_c$), and amorphous layer thickness ($l_a$). These can be determined from either the one-dimensional correlation

function [99]:

$$\gamma(z) = \frac{1}{\gamma(0)} \int_0^\infty I(Q) Q^2 \cos(Qz) \mathrm{d}Q \tag{5.26}$$

where $\gamma(0)$ is the scattering invariant, that is, $\int_0^\infty I(Q) Q^2 \mathrm{d}Q$, which normalizes the correlation function to unity, or the interphase distribution function, which corresponds to the second derivative of $\gamma(z)$. Evaluation of $L$, $l_c$, and $l_a$ as a function of composition, supported by optical microscopy and WAXS (wide-angle X-ray scattering) data, can provide useful insight into the segregation morphology. For example, interlamellar segregation should be accompanied by an increase of the long period $L$, and a swelling of the amorphous layer, with increasing concentration of the amorphous component.

The morphology and melting and/or crystallization behavior of polyethylene (PE) blends has also been extensively studied using light scattering, optical microscopy, electron microscopy, and differential scanning calorimetry (DSC). SAXS measurements at a synchrotron source, with their high signal to noise ratio, offer low counting times and make it possible to study the crystallization kinetics. Making use of time-resolved SAXS measurements, Tashiro *et al.* [100] have demonstrated that similarity of crystallization rates is linked to co-crystallization.

One other area where SAXS has been very useful is in studies of the phase separation behavior of homopolymer/block copolymer mixtures such as styrene–butadiene diblock copolymers with polystyrene [101], polystyrene-*block*-polyisoprene (SI) diblock blended with polystyrene [102], and binary blends of polystyrene-*block*-polyisoprene (SI) copolymers [103].

Compared to SAXS, WAXS is of limited use in investigating blends but the technique has been employed in some cases in conjunction with small-angle scattering to determine the degree of crystallinity or to determine changes in unit cell parameters with blending [104].

#### 5.4.1.4 **Neutron Reflectivity**

Neutron reflection (NR) has played a major role in the study of polymer surfaces and interfaces, offering several advantages over other techniques such as TEM, infrared densitometry, X-ray microanalysis, or ion-beam techniques [105–107]. It offers the high depth resolution of about 10 Å that is required to characterize the shape and size of polymer interfaces combined with the high penetration power of neutrons, making it possible to investigate buried interfaces.

NR provides information on the composition profile normal to a surface and data can be treated using the same formalism developed to describe reflection and refraction phenomena of light or X-rays [55]. In principle, if measured up to sufficiently high wave vector, the reflectivity data could be Fourier transformed to a real space profile consisting of the scattering length density in the direction perpendicular to the surface, but in practice this is rarely possible due to the limited $Q$ range. Thus it is common practice to perform data analysis by calculating the reflectivity profiles by assuming that the interfacial shape can be described as a sequence of thin homogeneous layers [108]. Comparison between experimental

and calculated reflectivity curves yields the composition profile normal to the surface. Thus NR provides a measure of the interfacial width, $l$, from which the interaction parameter, $\chi$, can be calculated from the degrees of polymerization $n_1$ and $n_2$ of the two polymers, and the average statistical segment length, $b_k$ [109]:

$$\chi = \left(\frac{b_k}{l\sqrt{6}}\right)^2 + \frac{\pi^2}{6}\left(\frac{1}{n_1} + \frac{1}{n_2}\right) \tag{5.27}$$

Several studies have investigated the interface between immiscible and partially miscible amorphous polymers and the results have been reviewed [110, 111]. As the molecular weight of the components increases, the second term in Eq. (5.27) becomes negligible and therefore $\chi$ will solely depend on $b_k$ and $l$.

Experimental values of interfacial widths between incompatible polymers are larger than expected and there has been considerable discussion as to the origin of this discrepancy. Capillary wave fluctuations are considered to be responsible for the difference between calculated and experimental results [112]. Detailed discussion of these effects can be found in Reference [107].

For a miscible or partially miscible mixture annealing in the one-phase region results in polymer–polymer interdiffusion. Numerous investigations have been performed using NR to monitor the increase in interfacial width as a function of time and, therefore, investigate the initial stages of the diffusion process [105, 113–118]. By observing the development of the interfacial profile between hydrogenous and deuterated polymers it has been possible to test de Gennes' theoretical predictions [119] in support of the theory of reptation. These NR measurements had to be performed on amorphous polymer films that were annealed prior to the experiment at temperatures above the glass transition and subsequently quenched. Nowadays, using a white beam at a pulsed neutron source, reflectivity profiles of sufficient statistical accuracy for data analysis can be obtained in a few tens of seconds. Thus, *in situ* NR measurements are possible and special sample cells have been developed for this purpose [120]. Improvements in neutron flux have made not only *in situ* studies of polymer/polymer interfusion possible [121] but also extended these measurements to the diffusion of small molecules into polymer matrices [122, 123].

### 5.4.2 Microscopy

The morphology of polymer blends can vary greatly from system to system and the presence of various additives such as fillers, pigments, and compatibilizers often brings about morphological changes that affect the physical and mechanical properties. Microscopy plays a major role in the characterization of phase separated blends, offering a means to understanding key structure–property relationships.

Nowadays a wide range of microscopic instruments is available, which allow the characterization of various polymeric micro-structural features at different length scales. In addition to optical and light microscopy (Section 5.4.1.1), techniques such

as scanning electron microscopy (SEM), transmission electron microscopy (TEM), and atomic force microscopy (AFM) have been extensively used to study phase separated blends. These are discussed below and more extensive reviews can be found elsewhere [124–126].

#### 5.4.2.1 Transmission Electron Microscopy

TEM is one of the main microscopy techniques for the characterization of polymer blends. Use of an electron beam allows for high resolution down to 0.2 nm, making it possible to resolve smaller sample's features at length scales much smaller than when using optical microscopy. Generally, very thin samples (<100 nm thick) need to be used and, due to the low contrast display by polymer samples, staining methods need to be used [127]. Of those that are available, staining with osmium tetroxide is particularly useful for unsaturated polymers such as rubbers whereas ruthenium oxide is a more versatile staining agent that reacts with polymers containing ether, alcohol, amine, or aromatic groups. In some cases, differential uptake of the staining agent by the different components of a multiphase blend has allowed the identification of the spatial distribution of the components, indicating that spontaneous partitioning may take place in these systems.

TEM has played a major role in the characterization of the ordered structures developed by block copolymers and in following the changes in morphology that accrue in homopolymer/block copolymer mixtures such as (styrene-*b*-isoprene) (SI)/polystyrene blends [128–130].

TEM can also be used to follow the development of structural features during spinodal decomposition [131] and reaction-induced phase separation [1].

Additional information can be obtained from energy-filtering transmission electron microscopy (EFTEM), a technique that makes it possible to create elemental distribution images through the analysis of the elemental compositions by electron energy loss spectroscopy. As shown by Horiuchi *et al*. for the PMMA/SAN immiscible blend, the technique can provide information on the blend composition in the interfacial region of a phase separated blend.

#### 5.4.2.2 Scanning Electron Microscopy

Similar to TEM, SEM offers improved resolution compared to light microscopy. In a scanning electron microscope a finely focused electron beam is scanned across the specimen and the emitted electrons are detected and amplified, forming an image. SEM images may be formed by using either secondary or back-scattered electrons. Both methods offer advantages and disadvantages: images of more uniform illumination are obtained from backscattered electrons but are of lower resolution than those resulting from secondary electrons. The latter are generated from the sample's thin top layer; the interaction volume is small in this case and comparable to the area irradiated by the incident beam, leading to higher resolution.

SEM instruments have a resolution better than 5 nm and are useful for the characterization of surfaces and the determination of surface topography. Unlike TEM, little sample preparation is required. For polymers that are poor conductors problems associated with charge build-up need to be overcome.

The technique has found widespread use in the analysis of fracture surfaces, giving information on the internal structure of polymer blends. In these investigations, samples with internal phases that are poorly bonded are best. Microtoming and chemical etching (solvent or acid) were used in early investigations of rubber particles in HIPS (high impact polystyrene) and ABS (acrylonitrile–butadiene–styrene) to develop contrast between the different phases [133–135] though it was shown by Hobbs that the internal structure of dispersed rubbers can be studied by using samples that are microtomed at low temperature, without the need for chemical etching [136].

Solvent etching can be employed to investigate the morphology of polymer blends by SEM. Usually, this treatment causes complete removal of the soluble phase and this can be used advantageously to monitor morphological changes [137]. For example, treatment of cryogenically microtomed PET/PE and PC/PE blends using hot xylene leads to removal of the PE component [138], making it possible to investigate the morphology of the PET [poly(ethylene terephthalate)] or PC phases of the specimens.

In addition to detecting backscattered and secondary electrons, SEM instruments may also offer information on the elemental composition of the sample. Interaction of the primary beam with the sample results in the emission of X-rays. Since the energy of the emitted X-rays is a specific feature of an atom, by measuring the energy or the wavelength of the X-rays that are produced it is possible to achieve quantitative analysis of elemental composition (energy dispersive X-ray spectroscopy or EDS).

#### 5.4.2.3 Scanning Probe Microscopy – Atomic Force Microscopy (AFM) and Scanning Tunneling Microscopy (STM)

The main feature of a scanning probe microscope (SPM) is the presence of a probe with a sharp tip. During measurements, this is brought very close to the specimen surface and the interaction between the probe and the sample is monitored. The physical or chemical property of the material that is measured by the SPM depends on the structure of the probe and the detecting system: electronic properties can be studied using scanning tunneling microscopy (STM), surface topography and roughness with scanning force microscopy (SFM) or atomic force microscopy (AFM), frictional properties with frictional force microscopy (FFM, frictional force microscopy; LFM), and so on. Techniques such as STM and AFM offer advantages over electron microscopy since no sample preparation is required such as coating or microtoming.

Among the various SPM techniques, AFM has become a popular tool for the study of polymer surfaces as it provides information on the morphology and molecular structure of crystalline and oriented polymers, block copolymers, and polymer blends [139–143] while STM is limited to studies of conducting or metal-coating polymers. Three imaging modes can be used to produce topographic images of sample surfaces: contact mode, non-contact mode, and tapping mode AFM (TMAFM). In the repulsive "contact" mode, vertical deflections of the cantilever caused by surface variations are monitored. This imaging mode is used to study "hard" samples. TMAFM is generally applicable to soft samples, such as biological and polymeric materials.

AFM measurements have greatly contributed to our understanding of the interplay between phase separation and surface dewetting in thin films of miscible polymer blends [144–149].

An example of AFM measurements is given in Figure 5.12 for blends of deuterated PS and a random copolymer of poly(styrene-*co*-4-bromostyrene) (PBrS). Affrossman *et al.* [150] have investigated the phase behavior of deuterated PS blends with a PBrS copolymer having a degree of bromination of 1.0, which are incompatible in the bulk. As shown in Figure 5.12, blending results in very marked topographical features, which alter progressively with increaseasing the concentration of $P(Br_{1.0}S)$.

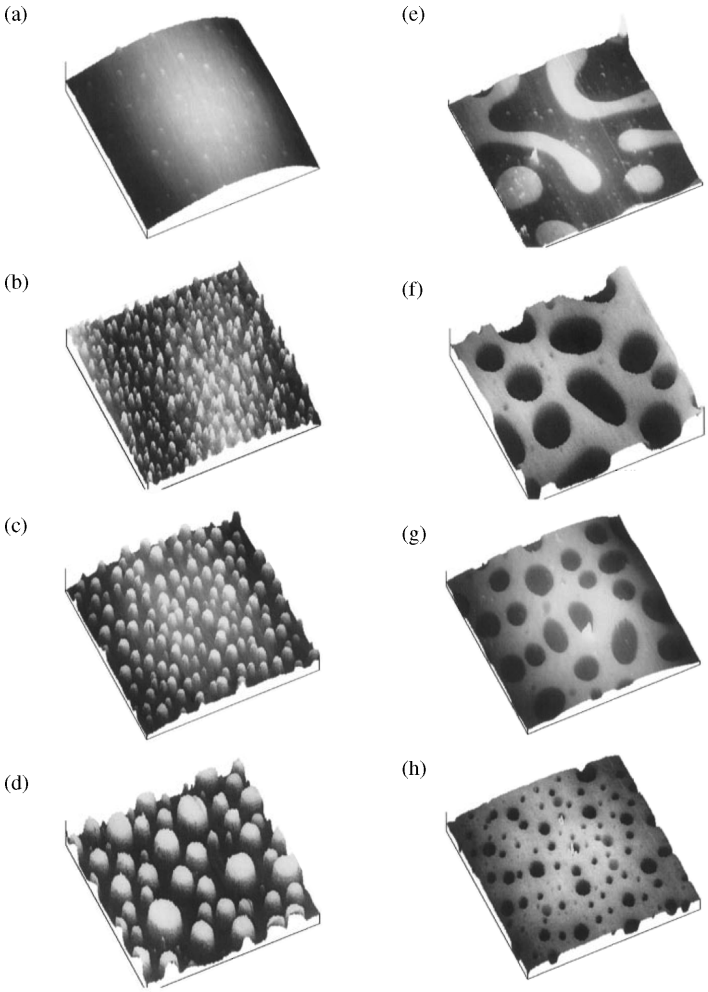


**Figure 5.12** AFM images of poly(styrene-$d_8$)/poly($Br_{1.0}S$) blends. P(Br1.0S) (wt%): (a) 100, (b) 10, (c) 30, (d) 50, (e) 60, (f) 70, (g) 75, and (h) 90. Reproduced with permission from Reference [150].

Bulk spinodal decomposition in TMPC/PS [TMPC = poly(tetramethyl-Bisphenol-A-polycarbonate)] films was also studied by Cabral *et al.* [151] using AFM. These authors were able to show that the topography observed by AFM is related to the spinodal morphology, although the periodicity of the structure determined by AFM appears to be larger than expected from LS measurements. Since the AFM structure factor is obtained by Fourier transform of an image of a cross-section (2D) whereas the LS data are 3D Fourier transform of the spinodal structure, such a discrepancy between AFM and LS results is not surprising.

Studies of phase separation that combine experimental data acquired in real and reciprocal space have been carried out using laser scanning confocal microscopy (LSCM) by Hashimoto and coworkers [131, 152]. This technique overcomes one of the problems with AFM measurements, namely, its large focal depth, which may cause out-of-focus information from neighboring planes. Using LSCM, Hashimoto *et al.* [131, 152] were able to reconstruct the 3D spinodal structure by superposition of successive layers of LSCM images (Figure 5.13a). The resulting morphologies were Fourier transformed and compared to the LS structure factors [152]. As shown in Figure 5.13b, there is quantitative agreement between the Fourier transform of the image and the LS structure factor.

## 5.5 Spectroscopic Methods

### 5.5.1 Dynamics above the Glass Transition

As discussed earlier, the presence of a single $T_g$ intermediate between those of the components is one of the first proofs of miscibility for binary blends. This is a useful but limited criterion and deeper insight into the level of homogeneity of a polymer–polymer mixture can be gained by analyzing in detail the relaxation processes, particularly the α-relaxation. The broad glass transition events that are detected by DSC for miscible blends compared to the relatively narrow $T_g$s of the pure components provide a first evidence of the dynamic effect due to blending [153–155]. Similarly, broad α-relaxation processes have been measured using DMTA or DRS [155–157] where the width of the loss curves give a measure of the concentration fluctuations in the blend as well as the degree of intermolecular coupling [157–159].

When comparing experimental data from different techniques, it is important to bear in mind that each method is designed to probe a specific length and frequency scale [160]. Compared to DMTA, which is limited to a frequency range from approximately 0.01 to 100 Hz and probes cooperative motions that may involve up to 50 bonds, DRS covers a very wide frequency range, $10^{-5}$–$10^{9}$ Hz, and gives information on local segmental motions of a few units up to ten bonds [161]. There are other important differences. Since DRS measures the response of dipoles to an electric perturbation, the technique is limited to investigations of chemical species possessing a permanent dipole. While this generally means that not all blends can be

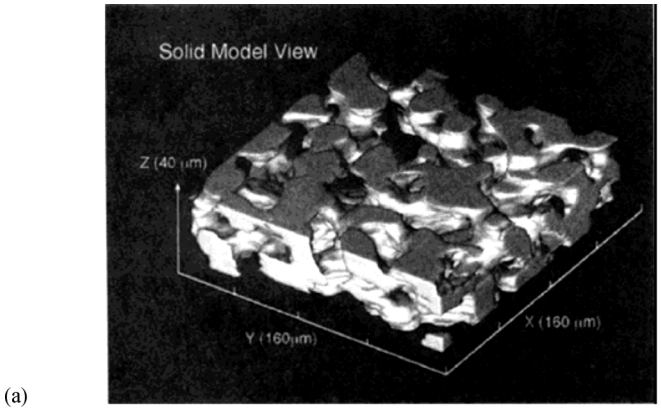


(a)

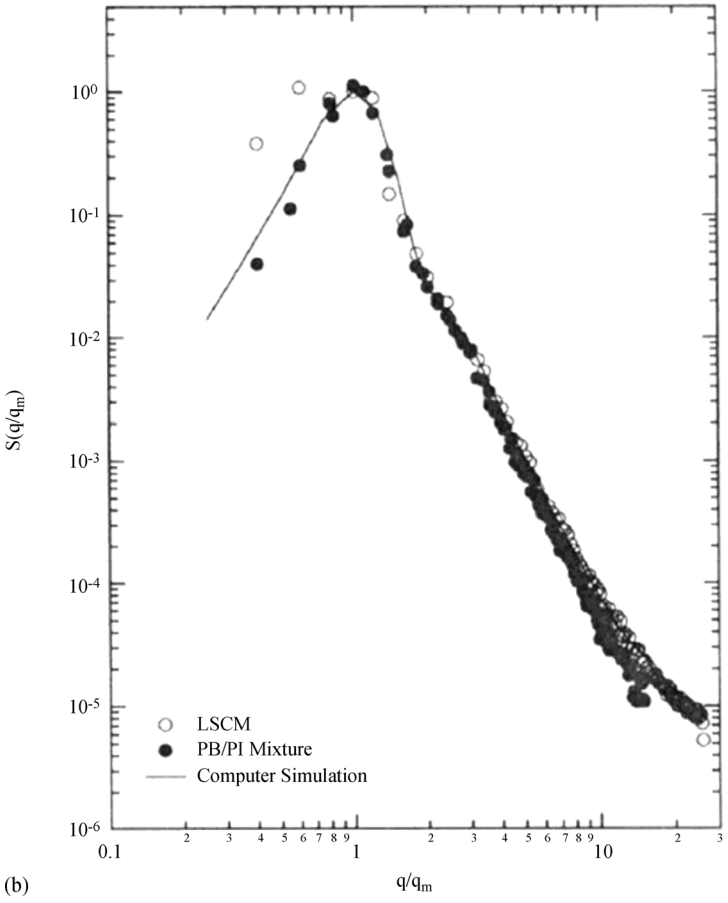


(b)

**Figure 5.13** (a) Solid modeling view of the SBR/PB phase-separating structure, reconstructed from 40 slices of image-processed LSCM scans; (b) comparison between structure factors $S(q/q_m)$ obtained from Fourier transform of the LSCM image (○), LS results of a PB/PI 50/50 wt% mixture (●), and a representative computer simulation (solid line). Reproduced with permission from Reference [152].

investigated by DRS, it may also prove advantageous when studying the dynamics of a polar component in a blend with a second polymer that is non-polar. By contrast, the DMTA technique gives the global material response and cannot be used to separate the component's dynamics.

One of the first detailed studies of compatibility in polymer blends was performed on miscible and immiscible blends of poly(2,6-dimethyl-1,4-phenylene oxide) (PPO) and copolymers of styrene and 4-chlorostyrene, poly(styrene-*co*-4-chlorostyrene) [154, 155]. For this system, miscibility can be drastically changed by varying the copolymer composition, that is, copolymers with 4-chlorostyrene content below 67.1 mol% are compatible with PPO. Although the transition from one- to two-phase behavior occurs over a narrow copolymer composition range, subtle differences in blend homogeneity were detected on a relatively wide composition range. For example, the width of the calorimetric glass transition increased with increasing 4-chlorostyrene content in the copolymers, with a maximum occurring at 67.1 mol. %, just before phase separation [154]. DRS measurements [155] revealed broad relaxations with width at half-height that extended over three decades for the miscible blends compared to about two decades for the copolymers. As expected, the immiscible PPO blends showed a second $\alpha$-relaxation peak, and relatively narrow peaks compared to the miscible mixtures. This result implies that the broadening is a characteristic of the residual heterogeneity in miscible blends that disappears upon phase separation. Similar conclusions were drawn by Alexandrovich *et al.* [162] for blends of polystyrene (PS) and poly(2-chlorostyrene) (PoClS). Figure 5.14 shows the dielectric spectra for a 40/60 (by weight) PS/PoClS blend, indicating that the spectrum in the one-phase region is much broader than for the phase separated sample. Because the polarity of PS is negligible compared to PoClS, the dielectric measurements mainly reflect the dynamics of the PoClS component. As shown in Figure 5.14, the loss peaks of the phase separated blend and the pure PoClS sample coincide.

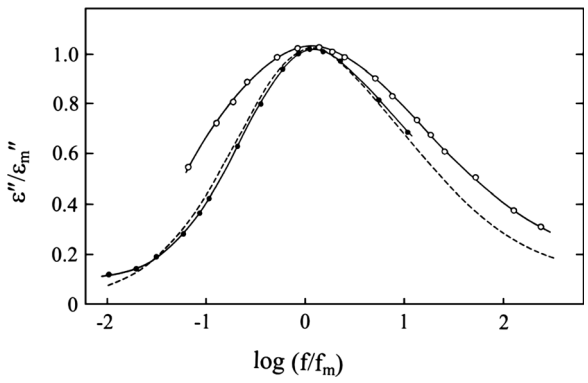


**Figure 5.14** Normalized dielectric relaxation spectra for a 40/60 (by weight) PS/PoClS blend: (○) annealed at 150.3 °C, below the LCST, and (●) annealed at 171.8°C, in the two-phase region, above the LCST. The dashed line is the relaxation spectrum of pure PoClS. Adapted from Reference [162].

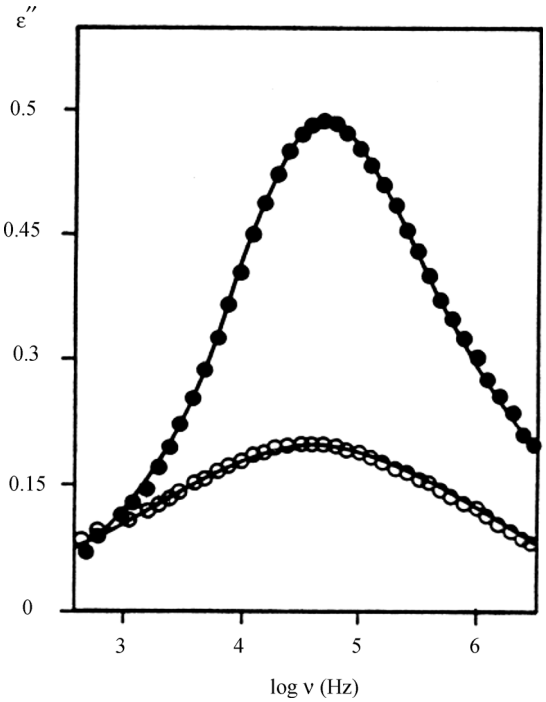


**Figure 5.15** Dielectric α-relaxations (●) in pure PVME at $T = 291.53$ K and (○) for a 40/60 (by weight) PS/PVME blend at $T = 299.55$ K. The lines indicate fits to the experimental data using the Havriliak–Negami equation with $\alpha = 0.65$, $\beta = 0.68$, and $\tau = 5.8 \times 10^{-6}$ s for PVME and $\alpha = 0.44$, $\beta = 1$, and $\tau = 4 \times 10^{-6}$ s for the blend. Adapted from Reference [156].

One of the main goals of experimental studies carried out on polymer blends is to resolve the dynamics of the individual components. For dielectric measurements this can be achieved when one of components has a high dipole moment, for example, PVME, poly(chlorostyrene), or poly(tetramethyl-Bisphenol-A-polycarbonate) (TMPC) [163, 164], compared to the second polymer, for example, polystyrene.

For miscible blends, the broadening of the α-relaxation increases with increasing distance between the $T_g$s of the components. This is evident when comparing the DRS data in Figure 5.14 with the dielectric loss peaks for the miscible PVME/PS blends (Figure 5.15), which are much broader than those of pure PVME, owing to the large difference between the $T_g$s of PVME (255 K) and PS (380 K) [$T_g$(PS) and $T_g$(PoClS) differ by only 30 K].

Other aspects of the dynamic behavior of polymer blends that are not observed in the pure components are a breakdown of time–temperature superposition [156, 158] and a pronounced asymmetry of the relaxation spectrum. This is evident in the dielectric spectra of PS/PVME as well as other miscible blends that are strongly temperature dependent and display an asymmetric shape towards lower frequencies that becomes more pronounced with decreasing temperature [156, 157]. This differs

from the behavior of pure amorphous polymers, which show a slight asymmetry towards higher frequencies. The immediate consequence of this strong temperature dependence of relaxation time distribution is that the technique of master-curve construction, which is commonly used to describe the relaxation behavior of pure polymers, is no longer valid. For miscible blends, this leads to a failure of the time–temperature superposition principle [156, 158].

In addition to DRS and DMTA, nuclear magnetic resonance has also been extensively used to study molecular motion and the effect of intermolecular interactions in binary blends. For example, high resolution solid state $^{13}C$ NMR [165, 166] has been employed to identify the individual dynamics of the components in blends. By combining the techniques of magic-angle spinning with high power proton decoupling it is possible to observe well-resolved $^{13}C$ NMR signals for specific C atoms. The dynamics of each component can then be followed through measurements of line broadening. Contrary to DRS and DMTA, this is a highly selective method, and it offers the advantage that the dynamics of the individual components can be observed simultaneously. Other NMR techniques, such as two-dimensional solid state NMR, have been used to obtain information on one of the blend components using deuterium or $^{13}C$-labeling. For example, Chin *et al.* have employed 2D solid-state NMR [167, 168] to compare the chain motion of PS and PPO in miscible PS/PPO blends. The dynamics of each component in the blend was monitored by either using $^{13}C$ NMR on $^{13}C$-labeled poly(2,6-dimethyl-1,4-phenylene oxide) or $^{2}H$ NMR on polystyrene samples deuterated in the chain backbone (PS-$d_3$). In agreement with the DRS measurements of Wetton *et al.* [154, 155], the distribution of correlation times from NMR was found to be broader in the blend compared to the pure polymers. The 2D patterns could not be described by either a single-exponential correlation function or a single stretched exponential: a multimodal distribution (bimodal or trimodal) was found more appropriate where the relative weighting of the components was correlated with local concentration fluctuations.

Combining information from different experimental methods is often a very useful approach employed to characterize the dynamics of the individual blend components. For example, Alegria *et al.* [169] were able to resolve the dynamics of poly(vinylethylene) (PVE) and polyisoprene (PIP) in PVE/PIP blends by exploiting the fact that the dielectric strength of PVE is more than twice that of PIP whereas PIP makes a stronger contribution to the mechanical loss modulus of the blend. The PVE vinyl units attached to the chain backbone impose strong intermolecular constraints to the molecular motion and are responsible for the unusually broad dynamic mechanical spectrum [170]. Blends of PVE with PIP, a polymer with weaker intermolecular coupling, present similar broad loss peaks in the dynamic mechanical spectra, particularly at high PVE concentrations [171]. $^{13}C$ NMR [170] and dielectric spectroscopy [169] measurements indicate that the PVE and PIP components have their own intrinsic mobility but, due to local composition fluctuations in the blend, the distribution of the relaxation frequencies differs from those found in the pure polymers.

Similar behavior has been observed for many blend systems [165, 166]. Generally, even though the blend may appear to be homogeneous, as indicated by a single glass

transition, the constituents display different segmental mobilities [165, 166]. The primary, α-relaxation of the individual components in a binary, miscible blend shift closer to one another but are not identical. These results are usually explained in terms of dynamically heterogeneous environments that exist even for macroscopically homogenous blends.

As pointed out by Lodge and McLeish [172], a major goal of the dynamic studies carried out on polymer mixtures is to be able to predict the viscoelastic response of a blend based on the behavior of the pure components. These authors have proposed a model that accounts for many of the experimental observations discussed above. This model rests on the idea that, due to chain connectivity, the local environment of monomer A in an A/B blend will be, on average, richer in A, and the same is true for component B. Thus the local dynamics of the two chains will generally differ, giving rise to different temperature and composition dependencies. The "self concentration," $\phi_s$ can be calculated from the Kuhn length of the chain and the effective glass transitions of the components estimated by comparison with the experimental data. Generally, the larger the self-concentration, the closer the average dynamics of that component in the blend will be to that of the pure polymer. The model has been found to provide an excellent description of the experimental data (segmental or global component dynamics) using a single temperature and composition independent $\phi_s$ parameter [172–177], but a few exceptions have been reported [173].

### 5.5.2 Sub-$T_g$ Relaxations

The effect of blending on the dynamics of the components below the glass transition temperature has also been investigated in detail using various techniques, including dielectric relaxation spectroscopy (DRS), dynamic mechanical thermal analysis (DMTA), NMR, and quasi-elastic neutron scattering. Because these secondary relaxations are correlated with the mechanical properties of the blends, such as ductility, impact strength, and toughening, studies of sub-$T_g$ blend dynamics are of considerable practical interest. Similar to studies on the addition of low molecular weight plasticizers, one may anticipate that the addition of a second polymer should suppress secondary relaxations [178]. However, Fischer *et al.* [178] have suggested that because the local free volume fluctuations are responsible for the antiplastization observed in polymer–additive mixtures, a similar dynamic effect is not to be expected for polymer blends, due to the much lower volume fluctuations in these systems. Studies on BPA-PC/TMPC (BPA = Bisphenol A) blends appear to support this hypothesis [178–180].

Specific interactions among the blend components also affect sub-$T_g$ motions and so, generally, it is not surprising to find that the dynamic effect that is observed is system dependent. This is supported by experiments that range from little or no evidence of antiplasticization [178] to a strong suppression of the β-relaxation [181–183]. Evidence for cooperative motion of the aromatic rings of PPO and PS, probably due to a strong π–π interaction between them, in the blend has been given by Feng *et al.* [184] using $^{13}C$ NMR. The ability of the PS chains to undergo rapid

conformational transitions in the PS/PPO blends could explain the improved impact strength of PS chains upon addition of PPO.

### 5.5.3 Infrared and Raman Spectroscopy

Fourier-transform infrared (FTIR) spectroscopy is an invaluable characterization technique used to confirm the chemical structure of a polymer, particularly through the observation of vibrational transitions associated with specific functional groups [185, 186]. The technique has been extensively used for the characterization of polymer blends and several reviews have appeared in the literature [187–190]. FTIR measurements can help identify the mechanism of interaction between the components of a polymer blend. For example, FTIR studies carried out by Hsu and coworkers [191] have shown that the favorable interaction between PS and PVME can be monitored through the C−H out-of-plane vibration of the phenyl ring at 698 $cm^{-1}$ in PS and the $COCH_3$ vibration of PVME (doublet at 1085 and 1107 $cm^{-1}$). Changes in the position and intensity of the IR bands can be used to monitor changes in miscibility behavior [192, 193].

Blends in which hydrogen bonding interactions exist between the components offer ideal systems for FTIR investigations [187–190]. For example, IR spectroscopy has provided the main proof for the presence of a strong interactions between poly(4-hydroxystyrene), P4HS, and the carbonyl groups of polyacrylates [194], polymethacrylates [195–197], polyesters [198], and polylactides [199], as well as with the ether groups of polyethers [200]. The H-bond interaction clearly affects the hydroxyl region of the IR spectra (3100–3700 $cm^{-1}$) and three distinct contributions are usually observed due to "free," intra- and inter-associated O−H vibrations [196]. Deconvolution of the different contributions using a curve fitting procedure yields semiquantitative information due to the strong overlap of the different vibrations [196]. However, as clearly shown in Figure 5.16 for PVPh/PMMA blends, the relative proportion of the different components is composition dependent: intra-association dominates in the PVPh spectrum but in blends rich in PMMA most hydroxyl groups are involved in inter-associating hydrogen bonds.

The carbonyl stretching vibration region (1650–1800 $cm^{-1}$) and the region varying from 1000 to 1650 $cm^{-1}$ are also affected by strong intermolecular interactions. In blends with PVPh, the carbonyl band at 1730 $cm^{-1}$ can be resolved into two distinct contributions, attributed to hydrogen bonding (1706 $cm^{-1}$) and free carbonyls (1730 $cm^{-1}$) (Figure 5.17). It has been shown that temperature has a pronounced effect on hydrogen bonds, with the relative proportion of free to hydrogen bonded carbonyl group vibration generally increasing with temperature [197]. A shift of the hydrogen bonded C=O vibration to a higher frequency with increasing temperature has also been reported and attributed to weakening of the hydrogen bonds [195].

Coleman and Painter have reported that the miscibility in hydrogen bonded blends is primarily dictated by the balance between unfavorable physical and favorable chemical interactions [187, 190]. They have developed a model, called the association model, that makes use of the self- and inter-association equilibrium constants

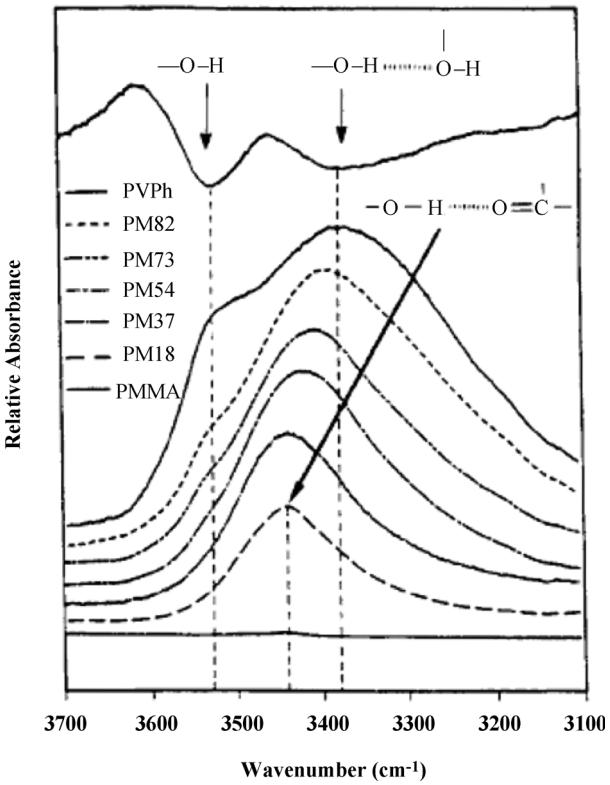


**Figure 5.16** FTIR spectra of hydroxyl vibration region for blends of PMMA with poly(4-vinylphenol) (PVPh). Lines from bottom to top are pure PMMA, blends with increasing PVPh content (PM19, PM37, PM54, PM73, PM82), pure PVPh, and the second differential of the PVPh spectrum. Reprinted from Reference [196].

determined from the FTIR spectra to predict polymer–polymer miscibility [201–203]. In general terms, one expects miscibility when inter-association is favored over the self-association, for example, for PVPh/poly(*N*-vinylpyrrolidone), [204, 205], whereas the system may be immiscible or partially miscible when this condition is not met, for example, for blends of PVPh and poly(*p*-acetoxystyrene) [206].

Studies similar to those described above can be carried out on polyamides [207] and polyurethanes [208, 209]. Moreover, infrared spectroscopy has been used to study intermolecular interactions in amorphous/crystalline binary blends such as mixtures of poly(caprolactone) [210] or (polyethylene oxide) [211] and poly(vinylphenol).

A more recent development in this area is FTIR imaging. This technique is a powerful tool that can be used to study a range of polymer systems, including multilayer polymer films, composite materials, fibers, and blends [212]. By selecting the characteristic bands of a chemical species, its spatial distribution can be mapped. Conventional infrared microspectroscopy uses apertures to limit the examined area

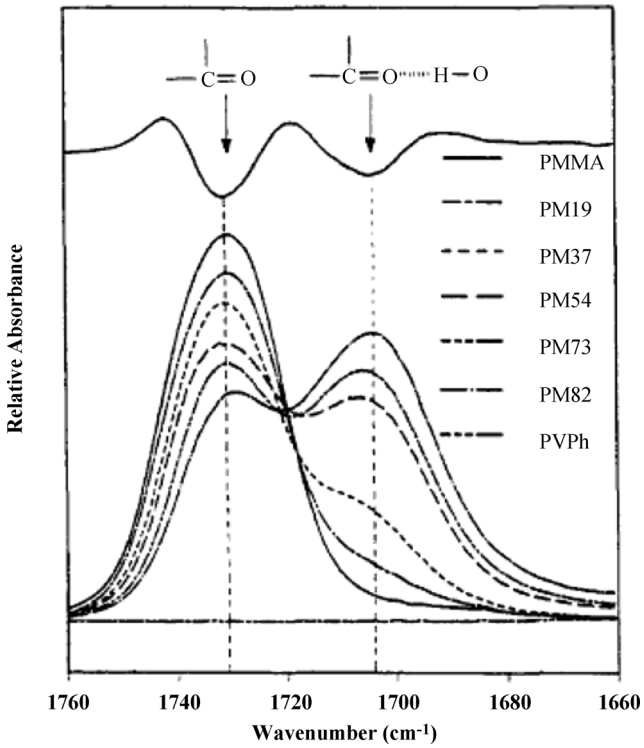


**Figure 5.17** FTIR spectra of carbonyl vibration region for blends of PMMA with poly(4-vinylphenol). Lines from bottom to top are pure PVPh, blends with decreasing PVPh content (PM82, PM73, PM54, PM37, PM19), pure PMMA, and the second differential of the PM73 spectrum. Reprinted from Reference [196].

and a map is obtained via sequential steps [213]. This technique is time-consuming and of limited spatial resolution. With FTIR imaging using a focal plane array detector (FPA) data can be obtained within a few minutes, and thousands of spectra accumulated. The technique has been used to investigate polymer dispersed liquid crystals (PDLCs) composed of low molecular weight liquid crystal (LC) microdomains in a polymeric matrix [214]. Figure 5.18 gives representative IR data, for samples cured after a prepolymerization rest time at 255 K.

Compared to IR, Raman and Fourier-transform Raman spectroscopy (FTRS) are less commonly employed in polymer blend studies but may prove useful in the characterization of crystalline polymer morphology and studies of conjugate polymers. A confocal Raman spectrometer with high spatial resolution has been used by Hashida *et al.* [215] to study the morphological changes in blends of a crystallizable polyester with a noncrystallizable polyether. In that case, Raman spectroscopy gave information on the local composition of the rich phase within a region of 40–80 μm diameter, offering additional information to that provided by optical microscopy and DSC.

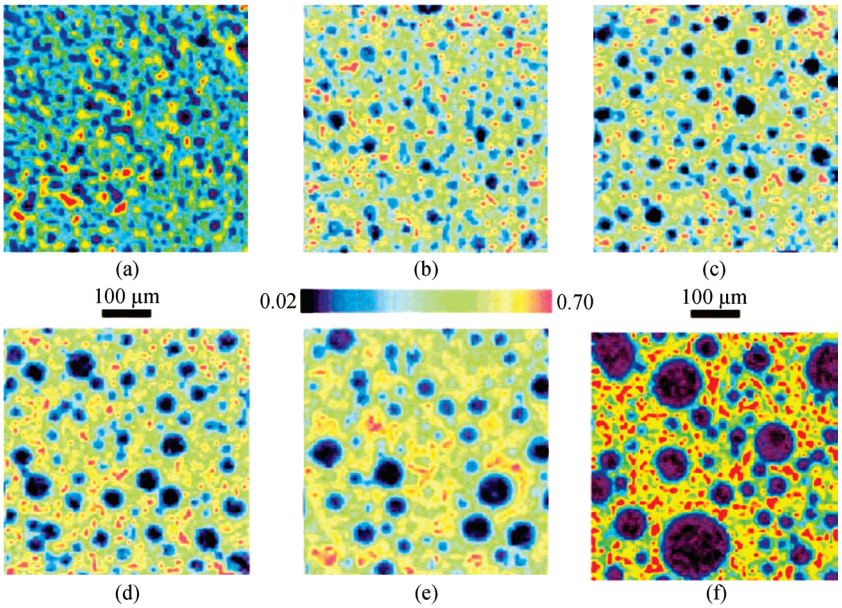


**Figure 5.18** Infrared images of PDLCs formed by curing at 255 K after a prepolymerization cooling time of (a) 30 min, (b) 1 h, (c) 2 h, (d) 4 h, (e) 6 h, and (f) 8 h. Reprinted from Reference [214].

## 5.6 Summary and Conclusions

The determination of polymer–polymer miscibility is a very important aspect of blending. In this chapter we have reviewed the main techniques now in use for the assessment of blend miscibility. Owing to the delicate balance between entropic and enthalpic terms as well as the large size of polymer molecules, miscibility is often difficult to assess. In some cases this difficulty has led to apparently contradictory results being reported in the literature. For this reason, whenever possible, multiple experimental probes should be used to unequivocally assess if a blend is miscible.

### Abbreviations and Symbols

#### Abbreviations

| | |
|---|---|
| ABS | acrylonitrile-butadiene-styrene |
| AFM | atomic force microscopy |
| BPA | Bisphenol A |
| CP | cloud point |
| DMA | dynamic mechanical analysis |
| DMTA | dynamic mechanical thermal analysis |

| | |
|---|---|
| DRS | dielectric relaxation spectroscopy |
| DSC | differential scanning calorimetry |
| EDS | energy dispersive X-ray spectroscopy |
| EFTEM | energy-filtering transmission electron microscopy |
| FFM | frictional force microscopy |
| FH | Flory–Huggins |
| FPA | focal plane array detector |
| FTIR | Fourier-transform infrared spectroscopy |
| HDPE | high density polyethylene |
| HIPS | high impact polystyrene |
| LC | liquid crystal |
| LCST | lower critical solution temperature |
| LDPE | low density polyethylene |
| LLDPE | linear low density polyethylene |
| LS | light scattering |
| LSCM | laser scanning confocal microscopy |
| NMR | nuclear magnetic resonance |
| NR | neutron reflectivity |
| mPA | methylated polyamide |
| PBA | poly(butylene acrylate) |
| PBrS | poly(styrene-*co*-4-bromostyrene) |
| PC | polycarbonate |
| PCL | polycaprolactone |
| PDLC | polymer dispersed liquid crystal |
| PE | polyethylene |
| PEO | poly(ethylene oxide) |
| PET | poly(ethylene terephthalate) |
| PIP | polyisoprene |
| PLLA | poly(L-lactide) |
| PMA | poly(methyl acrylate) |
| PMMA | poly(methyl methacrylate) |
| PoClS | poly(*ortho*-chlorostyrene) |
| PPO | poly(2,6-dimethyl-1,4-phenylene oxide) |
| PS | polystyrene |
| PVC | poly(vinyl chloride) |
| PVE | poly(vinyl ethylene) |
| PVME | poly(vinyl methyl ether) |
| PVPh | poly(vinylphenol) |
| RPA | random phase approximation |
| SAN | styrene-acrylonitrile copolymer |
| SANS | small-angle neutron scattering |
| SAXS | small-angle X-ray scattering |
| SCPE | solution chlorinated polyethylene |
| SEM | scanning electron microscopy |
| SI | polystyrene-*block*-polyisoprene |

| | |
|---|---|
| SPM | scanning probe microscopy |
| SPS | sulfonated polystyrene ionomer |
| STM | scanning tunneling microscopy |
| TEM | transmission electron microscopy |
| TMAFM | tapping mode atomic force microscopy |
| TMPC | poly(tetramethyl-Bisphenol-A-carbonate) |
| UCST | upper critical solution temperature |
| USANS | ultrasmall-angle neutron scattering |
| WAXS | wide-angle X-ray scattering |

**Symbols**

| | |
|---|---|
| $b$ | neutron scattering length |
| $b_k$ | average statistical segment length |
| $C_p$ | heat capacity |
| $d$ | Bragg spacing |
| $E_0$ | Electron scattering energy |
| $G$ | Gibbs free energy |
| $\Delta G_m$ | Gibbs free energy change upon mixing |
| $H$ | enthalpy |
| $\Delta H_f$ | enthalpy of fusion |
| $\Delta H_m$ | enthalpy change upon mixing |
| $I(Q)$ | scattering intensity |
| $K$ | constant |
| $\boldsymbol{k}_0$ | wavevector |
| $k_B$ | Boltzmann's constant |
| $L$ | long period |
| $l$ | length |
| $l_a$ | amorphous layer thickness |
| $l_c$ | crystal thickness |
| $n$ | number of moles |
| $N_A$ | Avogadro constant |
| $n_i$ | degree of polymerization |
| $m$ | mass |
| $P(Q)$ | form factor |
| $\boldsymbol{Q}$ | wavevector change |
| $q$ | constant |
| $R$ | ideal gas constant |
| $r$ | number of segments per polymer chain |
| $S$ | entropy |
| $\Delta S_m$ | entropy change upon mixing |
| $T$ | temperature |
| $T_c$ | critical temperature |
| $T_g$ | glass transition temperature |
| $T_m$ | melting temperature |

| | |
|---|---|
| $V$ | volume |
| $V_R$ | reference segment volume |
| $W$ | contact exchange energy |
| $w$ | weight fraction |
| $x$ | mole fraction |
| $z$ | lattice coordination number |

### Greek symbols

| | |
|---|---|
| $\alpha$ | volume expansion coefficient |
| $\gamma$ | composition fluctuation correlation length |
| $\gamma(0)$ | scattering invariant |
| $\theta$ | scattering angle |
| $\lambda$ | wavelength |
| $\xi$ | correlation length |
| $\varrho$ | density |
| $\varrho(r)$ | correlation function |
| $d\Sigma(Q)/d\Omega$ | differential scattering cross section |
| $\phi$ | composition |
| $\varphi$ | volume fraction |
| $\chi$ | Flory–Huggins interaction parameter |

## References


1 Paul, D.R. and Newman, S. (eds) (1978) *Polymer Blends,* Academic Press, New York.
2 Olabisi, O., Robeson, L.M., and Shaw, M.T. (1969) *Polymer-Polymer Miscibility,* Academic Press, New York.
3 Utracki, L.A. (1989) *Polymer Alloys and Blends,* Hanser Publishers.
4 Patterson, D. (1967) *Rubber Chem. Technol.*, **40**, 1.
5 Flory, P.J. (1953) *Principles of Polymer Chemistry,* Cornell University Press, Chs 12 and 13.
6 Flory, P.J. (1942) *J. Chem. Phys.*, **10**, 51.
7 Huggins, M.L. (1942) *Ann. N.Y. Acad. Sci.*, **43**, 1.
8 Work, W.J., Horie, K., Hess, M., and Stepto, R.F.T. (2004) *Pure Appl. Chem.*, **76**, 1985.
9 Utracki, L.A. (ed.) (2002) *Polymer Blends Handbook,* vol. 1 and 2, Kluwer Academic Publishers, Dordrecht.
10 Paul, D.R. and Bucknall, C.B. (eds) (2000) *Polymer Blends,* John Wiley & Sons, Inc., New York.
11 Robeson, L.M. (2007) *Polymer Blends. A Comprehensive Review,* Hanser Gardner Publications.
12 Lu, X. and Jiang, B. (1991) *Polymer,* **32**, 471.
13 Aubin, M. and Prud'homme, R. (1988) *Polym. Eng. Sci.*, **28**, 1355.
14 Kwei, T.K. (1984) *J. Polym. Sci., Polym. Lett. Ed.*, **22**, 307.
15 Painter, P.C., Graf, J.F., and Coleman, M.M. (1991) *Macromolecules,* **24**, 5630.
16 Gordon, M. and Taylor, J.S. (1952) *J. Appl. Chem.*, **2**, 493.
17 Couchman, P.R. and Karasz, F.E. (1978) *Macromolecules,* **11**, 117.
18 Lin, A.A., Kwei, T.K., and Reiser, A. (1989) *Macromolecules,* **22**, 4112.
19 Avella, M. and Martuscelli, E. (1988) *Polymer,* **29**, 1731.
20 Guo, Q. (1990) *Makromol. Chem.*, **191**, 2639.
21 Nijenhuis, A.J., Colstee, E., Grijpma, D.W., and Pennings, A.J. (1996) *Polymer,* **37**, 5849.

**22** Cowie, J.M.G. (1989) *Encyclopedia of Polymer Science and Engineering – Supplement Volume*, 2nd edn, John Wiley & Sons, New York, p. 456.

**23** Zhang, X., Takegoshi, K., and Hikichi, K. (1991) *Macromolecules*, **24**, 5756.

**24** MacKnight, W.J., Stoelting, J., and Karasz, F.E. (1971) *Adv. Chem. Series*, **99**, 29.

**25** Stoelting, J., Karasz, F.E., and MacKnight, W.J. (1970) *Polym. Eng. Sci.*, **10**, 133.

**26** Cesteros, L.C., Quintana, J.R., Fernandez, J.A., and Katime, I.A. (1989) *J. Polym. Sci., B: Polym. Phys.*, **27**, 2567.

**27** Li, D. and Brisson, J. (1996) *Macromolecules*, **29**, 868.

**28** Serman, C.J., Painter, P.C., and Coleman, M.M. (1991) *Polymer*, **32**, 1049.

**29** Landry, C.J.T. and Teegarden, D.M. (1991) *Macromolecules*, **24**, 4310.

**30** Goh, S.H. and Siow, K.S. (1987) *Polym. Bull.*, **17**, 453.

**31** Serman, C.J., Xu, Y., Painter, P.C., and Coleman, M.M. (1989) *Macromolecules*, **22**, 2015.

**32** Pomposo, J.A., Calahorra, E., Eguiazabal, I., and Cortazar, M. (1993) *Macromolecules*, **26**, 2104.

**33** Pomposo, J.A., Eguiazabal, I., Calahorra, E., and Cortazar, M. (1993) *Polymer*, **34**, 95.

**34** Zhang, X., Takegoshi, K., and Hikichi, K. (1991) *Macromolecules*, **24**, 5756.

**35** King, S.M. (1999) in *Modern Techniques for Polymer Characterisation* (eds R.A. Pethrick and J.V. Dawkins), John Wiley & Sons., Ch. 7.

**36** Kim, Y., Yoo, J.E., and Kim, C.K. (2003) *Polymer*, **44**, 5439.

**37** Brannock, G.R., Barlow, J.W., and Paul, D.R. (1991) *J. Polym. Sci., Polym. Phys.*, **29**, 413.

**38** Haggard, K.W. and Paul, D.R. (2002) *Polymer*, **43**, 3727.

**39** Walsh, D.J., Shi, L., and Chai, Z. (1981) *Polymer*, **22**, 1005.

**40** Walsh, D.J., Higgins, J.S., and Chai, Z. (1982) *Polymer*, **23**, 336.

**41** Hindawi, I.A., Higgins, J.S., and Weiss, R.A. (1992) *Polymer*, **33**, 2522.

**42** Kwak, K.D., Okada, M., and Nose, T. (1991) *Polymer*, **32**, 864.

**43** Hashimoto, T., Kumaki, J., and Kawai, H. (1983) *Macromolecules*, **16**, 641.

**44** Beaucage, G., Stein, R.S., and Koningsveld, R. (1993) *Macromolecules*, **26**, 1603.

**45** Wang, H., Shimizu, K., Hobbie, E.K., Wang, Z.-G., Meredith, J.C., Karim, A., Amis, E.J., Hsiao, B.S., Hsieh, E.T., and Han, C.C. (2002) *Macromolecules*, **35**, 1072.

**46** Gordon, M., Goldsbrough, J., Ready, B.W., and Derham, K. (1973) *Industrial Polymers* (eds J.H.S. Green and R. Dietz), Transcripta Books, London.

**47** Gordon, M., Kleintjens, L.A., Ready, B.W., and Torkington, J.A. (1979) *Br. Polym. J.*, **10**, 170.

**48** Koningsveld, R., Ondin, M.H., and Kleintjens, L.A. (1982) *Polymer Compatibility and Incompatibility: Principles and Practices* (ed. K. Solc) MMI Press Symposium Series, vol. 2, Harwood Academic Publishers, New York, p. 25.

**49** Synder, H.L., Meakin, P., and Reich, S. (1983) *Macromolecules*, **16**, 757.

**50** Gilmer, J., Goldstein, N., and Stein, R.S. (1982) *J. Polym. Sci.: Polym. Phys. Ed.*, **20**, 2219.

**51** Kyu, T. and Lim, D.S. (1991) *Macromolecules*, **24**, 3645.

**52** Kyu, T. and Saldanha, J.M. (1988) *Macromolecules*, **21**, 1021.

**53** Meredith, J.C., Karim, A., and Amis, E. (2000) *Macromolecules*, **33**, 5760.

**54** Cabral, J.T. and Karim, A. (2005) *Meas. Sci. Technol.*, **16**, 191.

**55** Higgins, J.S. and Benoit, H.C. (1993) *Polymers and Neutron Scattering*, Oxford University Press, Oxford.

**56** Cotton, J.P., Decker, D., Benoit, H., Farnoux, B., Higgins, J.S., Jannink, G., Ober, R., Picot, C., and des Cloizeaux, J. (1974) *Macromolecules*, **7**, 863.

**57** Kirste, R.G., Kruse, W.A., and Ibel, K. (1975) *Polymer*, **16**, 120.

**58** Flory, P.J. (1949) *J. Chem. Phys.*, **17**, 303.

**59** Yang, H., Hadziioannou, G., and Stein, R.S. (1983) *J. Polym. Sci.: Polym. Phys. Ed.*, **21**, 159.

**60** Buckingham, A.D. and Hentschel, H.G.E. (1980) *J. Polym. Sci.: Polym. Phys. Ed.*, **18**, 853.

**61** Bates, F.S., Wignall, G.D., and Koehler, W.C. (1985) *Phys. Rev. Lett.*, **55**, 2425.

**62** Bates, F.S., Fetters, L.J., and Wignall, G.D. (1988) *Macromolecules*, **21**, 1086.

**63** Lapp, A., Picot, C., and Benoit, H. (1985) *Macromolecules*, **18**, 2437.

**64** Budkowski, A., Klein, J., Eiser, E., Steiner, U., and Fetters, L.J. (1993) *Macromolecules*, **26**, 3858.

**65** Balsara, N.P., Fetters, L.J., Hadjichristidis, N., Lohse, D.J., Han, C.C., Graessley, W.W., and Krishnamoorti, R. (1992) *Macromolecules*, **25**, 6137.

**66** de Gennes, P.G. (1979) *Scaling Concepts in Polymer Physics*, Cornell University Press, Ithaca, New York.

**67** de Gennes, P.G. (1989) *C.R. Acad. Sci. Paris Ser. B.*, **308**, 13.

**68** Binder, K. (1983) *J. Chem. Phys.*, **79**, 6387.

**69** Debye, P. (1947) *J. Phys. Colloid Chem.*, **51**, 18.

**70** O'Connor, K., Pochan, M., and Thiyagarajan, P. (1991) *Polymer*, **32**, 195.

**71** Shibayama, M., Yang, H., Stein, R.S., and Han, C.C. (1985) *Macromolecules*, **18**, 2179.

**72** Chou, S., Liu, X., and Briber, R.M. (1998) *J. Polym. Sci., Part B: Polym. Phys.*, **36**, 1.

**73** Han, C.C., Bauer, B.J., Clark, J.C., Muroga, Y., Matsushita, Y., Okada, M., Qui, T.C., Chang, T.H., and Sanchez, I.C. (1988) *Polymer*, **29**, 2002.

**74** Larbi, F.B.C., Leloup, S., Halary, J.L., and Monnerie, L. (1986) *Polym. Commun.*, **27**, 23.

**75** Reichart, G.C., Graessley, W.W., Register, R.A., Krishnamoorti, R., and Lohse, D.J. (1997) *Macromolecules*, **30**, 3036.

**76** Krishnamoorti, R., Graessley, W.W., Dee, G.T., Walsh, D.J., Fetters, L.J., and Lohse, D.J. (1995) *Macromolecules*, **28**, 1252.

**77** Krishnamoorti, R., Graessley, W.W., Balsara, N.P., and Lohse, D.J. (1994) *Macromolecules*, **27**, 3073.

**78** Alamo, R.G., Londono, J.D., Mandelkern, L., Stehling, F.C., and Wignall, G.D. (1994) *Macromolecules*, **27**, 411.

**79** Londono, J.D., Narten, A.H., Wignall, G.D., Honnell, K., Hsieh, E.T., Johnson, T.W., and Bates, F.S. (1994) *Macromolecules*, **27**, 2864.

**80** Wignall, G.D., Alamo, R.G., Ritchson, E.J., Mandelkern, L., and Schwahn, D. (2001) *Macromolecules*, **34**, 8160.

**81** Arrighi, V., Gagliardi, S., Dagger, A.C., Semlyen, J.A., Higgins, J.S., and Shenton, M. (2004) *Macromolecules*, **37**, 8057.

**82** Arrighi, V., Gagliardi, S., Ferguson, R., Dagger, A.C., Semlyen, J.A., and Higgins, J.S. (2005) *J. Chem. Phys.*, **122**, 064904.

**83** Ornstein, L.S. and Zernike, F. (1914) *Proc. Acad. Sci., Amsterdam*, **17**, 793.

**84** Tucker, R.T., Han, C.C., Dobrynin, A.V., and Weiss, R.A. (2003) *Macromolecules*, **36**, 4404.

**85** Debye, P. and Bueche, M.A. (1949) *J. Appl. Phys.*, **20**, 518.

**86** Debye, P., Anderson, H.R., and Brumberger, H. (1957) *J. Appl. Phys.*, **28**, 679.

**87** Wignall, G.D., Child, H.R., and Samuels, R. (1982) *J. Polym.*, **23**, 957.

**88** Richards, R.W. and Thomason, J.L. (1983) *Polymer*, **24**, 1089.

**89** Hashimoto, T. (2004) *J. Polym. Sci.: Polym. Phys. Ed.*, **42**, 3027.

**90** Russell, T.P. and Stein, R. (1982) *J. Polym. Sci.: Polym. Phys. Ed.*, **20**, 1593.

**91** Tran-Cong, Q., Kawakubo, R., and Sakurai, S. (1994) *Polymer*, **35**, 1236.

**92** Warner, F.P., MacKnight, W.J., and Stein, R.S. (1977) *J. Polym. Sci.: Polym. Phys. Ed.*, **15**, 2113.

**93** Khambatta, F.B., Warner, F., MacKnight, W.J., and Stein, R.S. (1976) *J. Polym. Sci.: Polym. Phys. Ed.*, **14**, 1391.

**94** Russell, T.P. and Stein, R.S. (1980) *J. Macromol. Sci.*, **B17**, 617.

**95** Russell, T.P. and Stein, R.S. (1983) *J. Polym. Sci.: Polym. Phys. Ed.*, **21**, 999.

**96** Nojima, S., Tsutsui, H., Urushihara, M., Kosaka, W., Kato, N., and Ashida, T. (1986) *Polym. J.*, **18**, 451.

**97** Cheung, Y.W., Stein, R.S., Chu, B., and Wu, G. (1994) *Macromolecules*, **27**, 3589.

**98** Li, Y. and Jungnickel, B.-J. (1993) *Polymer*, **34**, 9.

**99** Strobl, G.R. and Schneider, M. (1980) *J. Polym. Sci.: Polym. Phys. Ed.*, **18**, 1343.

**100** Tashiro, K., Imanishi, K., Izumi, Y., Kobayashi, M., Kobayashi, K., Satoh, D.M., and Stein, R.S. (1995) *Macromolecules*, **28**, 8477.

**101** Zin, W.C. and Roe, R.J. (1984) *Macromolecules*, **17**, 183.

**102** Bodycomb, J., Yamaguchi, D., and Hashimoto, T. (2000) *Macromolecules*, **33**, 5187.

**103** Sakurai, S., Irie, H., Umeda, H., Nomura, S., Lee, H.H., and Kim, J.K. (1998) *Macromolecules*, **31**, 336.

**104** Xing, P., Dong, L., An, Y., and Feng, Z. (1997) *Macromolecules*, **30**, 2726.

**105** Russell, T.P. (1996) *Phys. B*, **221**, 267.

**106** Bucknall, D.G. and Higgins, J.S. (1998) *Polymers and Surfaces – a Versatile Combination* (ed. H. Hommell), Research Signpost, Trivandrum, India, pp. 161–199.

**107** Bucknall, D.G. (2004) *Prog. Mater. Sci*, **49**, 713.

**108** Lekner, J. (1987) *Theory of Reflection*, Martinus Nijhoff, Dordrecht.

**109** Schubert, D.W., Abetz, V., Stamm, M., Hack, T., and Siol, W. (1995) *Macromolecules*, **28**, 2519.

**110** Stamm, M. and Schubert, D.W. (1995) *Ann. Rev. Mater. Sci.*, **25**, 325.

**111** Jones, R.A.L. (1997) *Curr. Opin. Solid State Mater. Sci.*, **2**, 673.

**112** Shull, K.R., Mayes, K.R., and Russell, T.P. (1993) *Macromolecules*, **26**, 3929.

**113** Russell, T.P., Karim, A., Mansour, A., and Felcher, G.P. (1988) *Macromolecules*, **21**, 1890.

**114** Karim, A., Felcher, G.P., and Russell, T.P. (1994) *Macromolecules*, **27**, 6973.

**115** Fernandez, M.L., Higgins, J.S., Penfold, J., Ward, R.C., Shackleton, J., and Walsh, D.J. (1988) *Polymer*, **29**, 1923.

**116** Sferrazza, M., Xiao, C., Jones, R.A.L., Bucknall, D.G., Webster, J., and Penfold, J. (1997) *Phys. Rev. Lett.*, **78**, 3693.

**117** Stamm, M., Reiter, G., and Kunz, K. (1991) *Phys. B*, **173**, 35.

**118** Liu, Y., Reiter, G., Kunz, K., and Stamm, M. (1993) *Macromolecules*, **26**, 2134.

**119** Russell, T.P. (1990) *Mater. Sci. Rep.*, **5**, 171.

**120** Bucknall, D.G., Butler, S.A., and Higgins, J.S. (1999) *J. Phys. Chem. Solids*, **60**, 1273.

**121** Bucknall, D.G., Butler, S.A., and Higgins, J.S. (1999) *Macromolecules*, **32**, 5453.

**122** Bucknall, D.G., Higgins, J.S., and Butler, S.A. (2001) *Chem. Eng. Sci.*, **56**, 5473.

**123** Bucknall, D.G., Higgins, J.S., and Butler, S.A. (2004) *J. Polym. Sci.: Polym. Phys.*, **42**, 3267.

**124** Sawyer, L.C., Grubb, D.T., and Meyers, G.F. (2008) *Polymer Microscopy*, 3rd edn, Springer.

**125** Campbell, D., Pethrick, R.A., and White, J.R. (2000) *Polymer Characterization: Physical Techniques*, Stanley Thornes.

**126** Vesely, D. (1996) *Polym. Eng. Sci.*, **36**, 1586.

**127** Hobbs, S.Y. and Watkins, V.H. (2000) *Polymer Blends – Volume 1: Formulation* (eds D.R. Paul and C.B. Bucknall), John Wiley & Sons.

**128** Koizumi, S., Hasegawa, H., and Hashimoto, T. (1994) *Macromolecules*, **27**, 6532.

**129** Spontak, R.J., Smith, S.D., and Ashraf, A. (1993) *Macromolecules*, **26**, 956.

**130** Laurer, J.H., Smith, S.D., Samseth, J., Mortensen, K., and Spontak, R.J. (1998) *Macromolecules*, **31**, 4975.

**131** Ribbe, A.E. and Hashimoto, T. (1997) *Macromolecules*, **30**, 3999.

**132** Girard-Reydet, E., Sautereau, H., Pascault, J.P., Keates, P., Navard, P., Thollet, G., and Vigier, G. (1998) *Polymer*, **39**, 2269.

**133** Bucknall, C.B., Drinkwater, I.C., and Keast, W.E. (1972) *Polymer*, **13**, 115.

**134** Hall, R.A. and Jacoby, P. (1979) *J. Appl. Polym. Sci.*, **23**, 1453.

**135** Freeguard, G.F. (1974) *Br. Polym. J.*, **6**, 205.

**136** Hobbs, S.Y. (1978) *J. Polym. Sci.*, **16**, 1321.

**137** Chowa, W.S., Mohd Ishaka, Z.A., Karger-Kocsisb, J., Apostolov, A.A., and Ishiakud, U.S. (2003) *Polymer*, **44**, 7427.

**138** Li, Z.-M., Xie, B., Yang, S., Huang, R., and Yang, M.-B. (2004) *J. Mater. Sci.*, **39**, 433.

**139** Reneker, D.H. (1990) *New Characterization Techniques for Thin Polymer Films* (eds H.M. Tong and L.T. Nguyen), John Wiley & Sons, Inc., New York.

**140** Hobbs, J.K., Winkel, A.K., McMaster, T.J., Humphris, A.D.I., Baker, A.A., Blakely, S., Aissaoui, M., and Miles, M.J. (2001) *Macromol. Symp.*, **167**, 1.

**141** VanLandigham, M.R., Villarrubia, J.S., Guthrie, W.F., and Meyers, G.F. (2001) *Macromol. Symp.*, **167**, 15.

**142** Magonov, S.N. and Reneker, D.H. (1997) *Annu. Rev. Mater. Sci.*, **27**, 175.

**143** Jandt, K.D. (1998) *Mater. Sci. Eng. R*, **21**, 221.

**144** Karim, A., Slawecki, T.M., Kumar, S.K., Douglas, J.F., Satija, S.K., Han, C.C., Russell, T.P., Liu, Y., Overney, R., Sokolov, J., and Rafailovich, M.H. (1998) *Macromolecules*, **31**, 857.

**145** Ermi, B.D., Karim, A., and Douglas, J.F. (1998) *J. Polym. Sci.: Polym. Phys. Ed.*, **36**, 191.

**146** Heier, J., Kramer, E.J., Revesz, P., Battistig, G., and Bates, F.S. (1999) *Macromolecules*, **32**, 3758.

**147** Newby, B.Z. and Composto, R.J. (2000) *Macromolecules*, **33**, 3274.

**148** Böltau, M., Walheim, S., Mlynek, J., Krausch, G., and Steiner, U. (1998) *Nature (London)*, **3391**, 877.

**149** Nisato, G., Ermi, B.D., Douglas, J.F., and Karim, A. (1999) *Macromolecules*, **32**, 2356.

**150** Affrossman, S., Henn, G., O'Neill, S.A., Pethrick, R.A., and Stamm, M. (1996) *Macromolecules*, **29**, 5010.

**151** Cabral, J.T., Higgins, J.S., McLeish, T.C.B., Strausser, S., and Magonov, S.N. (2001) *Macromolecules*, **34**, 3748.

**152** Jinna, H., Nishikawa, J.Y., Koga, T., and Hashimoto, T. (1995) *Macromolecules*, **28**, 4782.

**153** Lau, S.F., Pathak, J., and Wunderlich, B. (1982) *Macromolecules*, **15**, 1278.

**154** Fried, J.R., Karasz, F.E., and MacKnight, W.J. (1978) *Macromolecules*, **11**, 150.

**155** Wetton, R.E., MacKnight, W.J., Fried, J.R., and Karasz, F.E. (1978) *Macromolecules*, **11**, 158.

**156** Roland, C.M. and Ngai, K.L. (1992) *Macromolecules*, **25**, 363.

**157** Zetsche, A., Kremer, F., Jung, W., and Schulze, H. (1990) *Polymer*, **31**, 1883.

**158** McGrath, K.J. and Roland, C.M. (1994) *J. Non-Cryst. Solids*, **172–174**, 891.

**159** Ngai, K.L., Roland, C.M., O'Reilly, J.M., and Sedita, J.S. (1992) *Macromolecules*, **25**, 3906.

**160** Spall, S., Goodwin, A.A., Zipper, M.D., and Simon, G.P. (1996) *J. Polym. Sci., Part B: Polym. Phys.*, **34**, 2419.

**161** Simon, G.P. (1994) *Mater. Forum*, **18**, 235.

**162** Alexandrovich, P.S., Karasz, F.E., and MacKnight, W.J. (1980) *J. Macromol. Sci., Phys.*, **B17**, 501.

**163** O'Reilly, J.M. and Sedita, J.S. (1991) *J. Non-Cryst. Sol.*, **131–133**, 1140.

**164** Mansour, A.A. and Madbouly, S.A. (1995) *Polym. Int.*, **37**, 267.

**165** Le Menestrel, C., Kenwright, A.M., Sergot, P., Laupretre, F., and Monnerie, L. (1992) *Macromolecules*, **25**, 3020.

**166** Takegoshi, K. and Hikichi, K. (1991) *J. Chem. Phys.*, **94**, 3200.

**167** Chin, Y.H., Zhang, C., Wang, P., Inglefield, P.T., Jones, A.A., Kambour, R.P., Bendler, J.T., and White, D.M. (1992) *Macromolecules*, **25**, 3031.

**168** Chin, Y.H., Inglefield, P.T., and Jones, A.A. (1993) *Macromolecules*, **26**, 5372.

**169** Alegria, A., Colmenero, J., Ngai, K.L., and Roland, C.M. (1994) *Macromolecules*, **27**, 4486.

**170** McGrath, K.J., Ngai, K.L., and Roland, C.M. (1992) *Macromolecules*, **25**, 4911.

**171** Roland, C.M. and Ngai, K.L. (1991) *Macromolecules*, **24**, 2261.

**172** Lodge, T.P. and McLeish, T.C.B. (2000) *Macromolecules*, **33**, 5278.

**173** He, Y., Lutz, T.R., and Ediger, M.D. (2003) *J. Chem. Phys.*, **119**, 9956.

**174** He, Y., Lutz, T.R., Ediger, M.D., and Lodge, T.P. (2003) *Macromolecules*, **36**, 9170.

**175** Haley, J.C., Lodge, T.P., He, Y., Ediger, M.D., Meerwall, E.D., and Mijovic, J. (2003) *Macromolecules*, **36**, 6142.

**176** Lodge, T.P., Wood, E.R., and Haley, J.C. (2006) *J. Polym. Sci. Polym. Phys.*, **44**, 756.

**177** Leroy, E., Alegria, A., and Colmenro, J. (2002) *Macromolecules*, **35**, 5587.

**178** Fischer, E.W., Hellmann, G.P., Spiess, H.W., Horth, F.J., Ecarius, U., and Wehrle, M. (1985) *Makromol. Chem.-Macromol. Chem. Phys.*, **S12**, 189.

**179** Katana, G., Kremer, F., Fischer, E.W., and Plaetschke, R. (1993) *Macromolecules*, **26**, 3075.

**180** Mansour, A.A. and Madbouly, S.A. (1995) *Polym. Int.*, **36**, 269.

**181** Landry, C.J.T. and Henrichs, P.M. (1989) *Macromolecules*, **22**, 2157.

**182** de los Santos Jones, H., Liu, Y., Inglefield, P.T., Jones, A.A., Kim, C.K., and Paul, D.R. (1994) *Polymer*, **35**, 57.

**183** Chin, Y.H., Liu, Y., Jones, A.A., Inglefield, P.T., and Kambour, R.P. (1994) *Polym. Prepr. (Am. Chem. Soc., Div. Polym. Chem.)*, **35**, 66.

**184** Feng, H., Feng, Z., Ruan, H., and Shen, L. (1992) *Macromolecules*, **25**, 5981.

**185** Koenig, J.L. (1999) *Spectroscopy of Polymers*, 2nd edn, Elsevier.

**186** Klopffer, W. (1984) *Introduction to Polymer Spectroscopy*, Springer-Verlag, Berlin.

**187** Coleman, M.M., Graf, J.F. and Painter, P.C. (1991) *Specific Interactions and the Miscibility of Polymer Blends*, Technomic, Lancaster.

**188** He, Y., Zhu, G., and Inoue, Y. (2004) *Prog. Polym. Sci.*, **29**, 1021.

**189** Painter, P.C. and Coleman, M.M. (2000) *Polymer Blends, Vol. 1: Formulation* (eds D.R. Paul and C.B. Bucknall), John Wiley & Sons, Inc., New York, p. 93.

**190** Coleman, M.M. and Painter, P.C. (1995) *Prog. Polym. Sci.*, **20**, 1.

**191** Lu, F.J., Benedetti, E., and Hsu, S.L. (1983) *Macromolecules*, **16**, 1525.

**192** Ryou, J.H., Ha, C.S., and Cho, W.J. (1993) *J. Polym. Sci. Polym. Chem.*, **31**, 325.

**193** Garcia, D. (1984) *J. Polym. Sci. Polym. Phys.*, **22**, 1773.

**194** Coleman, M.M., Yun, X., Painter, P.C., and Harrell, J.R. (1991) *Makromol. Chem. - Macromol. Symp.*, **52**, 75.

**195** Li, D. and Brisson, J. (1998) *Polymer*, **39**, 801.

**196** Li, D. and Brisson, J. (1998) *Polymer*, **39**, 793.

**197** Serman, C.J., Painter, P.C., and Coleman, M.M. (1991) *Polymer*, **32**, 1049.

**198** Pomposo, J.A., Etxeberria, A., and Cortazar, M. (1992) *Macromolecules*, **25**, 6909.

**199** Meaurio, E., Zuza, E., and Sarasua, J.-R. (2005) *Macromolecules*, **38**, 9221.

**200** Serman, C.J., Xu, Y., Painter, P.C., and Coleman, M.M. (1991) *Polymer*, **32**, 516.

**201** Painter, P.C., Park, Y., and Coleman, M.M. (1989) *Macromolecules*, **22**, 570.

**202** Coleman, M.M., Pehlert, G.J., and Painter, P.C. (1996) *Macromolecules*, **29**, 6820.

**203** Pehlert, G.J., Painter, P.C., Veytsman, B., and Coleman, M.M. (1997) *Macromolecules*, **30**, 3671.

**204** Hu, Y., Motzer, H.R., Etxeberria, A.M., Fernadez-Berridi, M.J., Iruin, J.J., Painter, P.C., and Coleman, M.M. (2000) *Macromol. Chem. Phys.*, **201**, 705.

**205** Kuo, S.W. and Chang, F.-C. (2001) *Macromolecules*, **34**, 5224.

**206** Kuo, S.W. and Chang, F.-C. (2002) *J. Polym. Sci. Polym. Phys.*, **40**, 1661.

**207** Garcia, D. and Starkweather, H.W. (1985) *J. Polym. Sci. Polym. Phys.*, **23**, 537.

**208** Koberstein, J.T. and Gancarz, I. (1986) *J. Polym. Sci.: Polym. Phys.*, **24**, 2487.

**209** Wang, F.C., Feve, M., Lam, T.M., and Pascault, J.-P. (1994) *J. Polym. Sci.: Polym. Phys.*, **32**, 1305.

**210** Wang, J., Cheung, M.K., and Mi, Y. (2002) *Polymer*, **43**, 1357.

**211** Moskala, E.J., Varnell, D.F., and Coleman, M.M. (1985) *Polymer*, **26**, 228.

**212** Kazaian, S. and Higgins, J.S. (2002) *Chem. Ind.*, **10**, 21.

**213** Schafer, R., Zimmermann, J., Kressler, J., and Mülhaupt, R. (1997) *Polymer*, **38**, 3745.

**214** Bhargava, R., Wang, S.Q., and Koenig, J.L. (1999) *Macromolecules*, **32**, 2748.

**215** Hashida, T., Jeong, Y.G., Hua, Y., Hsu, S.L., and Paul, C.W. (2005) *Macromolecules*, **38**, 2876.

# 6
# Physical Aging of Polymer Blends

*John M.G. Cowie and Valeria Arrighi*

## 6.1
## Introduction to Physical Aging

When a polymeric material is processed, fabricated, and placed in its working environment it cannot be regarded, automatically, as being stable, as it is subject to a wide range of possible changes, collectively known as "aging processes." The polymer can react with its environment (light, oxygen, water, etc.) and undergo several non-reversible chemical reactions. These lead to changes in the polymer structure such as chain scission, oxidation, decarboxylation, hydrolysis, dehalogenation, crosslinking, and so on, leading to degeneration of the polymer physical properties, for example, discoloration, brittleness, or loss of tensile strength. This type of aging will not be considered here.

More subtle changes can also take place that do not involve chemical modification. These are a consequence of small-scale relaxation events that take place predominantly in the amorphous regions of glassy polymers, at temperatures below the glass transition temperature, $T_g$. The resulting effects are referred to as physical aging and, unlike chemical aging, are reversible.

In physical aging the chemical structure of the polymer chain remains unchanged but the local packing of the chains alters over a period of time, leading to changes in the bulk properties of the material [1].

When an amorphous, or semi-amorphous, polymer is quenched from the melt to a temperature $T_a$, below $T_g$, there is insufficient time for the chains to relax fully to their lowest energy configurations and a vitreous state is formed that is not in equilibrium with its surroundings. Such a state will have an excess enthalpy, entropy, and volume, and if the material is held at that temperature it will attempt to move towards a state of thermodynamic equilibrium by losing those excess quantities over a period of time. This is achieved through a series of localized molecular relaxation processes that is termed physical aging and is manifest as the time dependent alteration in polymer properties (density, modulus, compliance, $T_g$, material dimensions, and fracture toughness) at zero stress and constant temperature. Clearly, such changes will have an impact on the use and long-term stability of materials like high-performance thermoplastics and composites that are manufactured using techniques involving

*Encyclopedia of Polymer Blends, Volume 1: Fundamentals.* Edited by Avraam I. Isayev
Copyright © 2010 WILEY-VCH Verlag GmbH & Co. KGaA, Weinheim
ISBN: 978-3-527-31929-9

quenching high-temperature melts to low (usually ambient) temperatures. It is important, therefore, to measure the effects, understand the processes involved, and identify the specific molecular relaxation events that occur during physical aging.

Physical aging studies on homopolymers and copolymers have received considerable attention. In contrast, fewer investigations of physical aging in polymer blends have been carried out and there are still important aspects of the physical aging process, for example, the role of intermolecular interactions, that are still unclear. This lack is somewhat surprising given the practical importance of the phenomenon and is certainly a consequence of a still incomplete understanding of the molecular processes that govern physical aging even in the case of relatively simple homopolymers. Extending our current knowledge to complex systems such as blends or composites is not trivial. However, a detailed knowledge of the glassy state of polymeric materials is necessary if we are to measure and model the aging process and then use the results to design more stable materials.

In the following sections, aging data for blend systems is reviewed, including our own work, and compared to the relevant homopolymer data.

## 6.2
## Experimental Measurements

During the physical aging process there is a long, continuous, slow relaxation of the non-equilibrium glass towards a final equilibrium state. This can be followed by measuring the decrease in the enthalpy and specific volume or the changes in the creep compliance and stress relaxation of the sample over time. While these have been the most widely used measurements, spectroscopic and scattering methods have also been adopted to follow physical aging. A brief description of these techniques follows. A more comprehensive review has been given by Hutchinson [2].

### 6.2.1
### Enthalpy Relaxation

Calorimetry has been one of the most commonly used techniques to follow the enthalpy relaxation observed during physical aging. This can be measured using a differential scanning calorimeter (DSC), which is a convenient and widely available instrument. If accurate and meaningful results are to be obtained the thermal history of the sample must be controlled and reproducible. The principles underpinning the measurements are summarized in Figure 6.1. The sample is first heated to a temperature $T_2$ (point A) above the polymer $T_g$ to ensure that any previous thermal history is completely erased.

The sample is then cooled at a rate $q$, to the annealing temperature $T_a$ (point B) in the glass. The rate $q$ must be controlled and be the same for all the measurements, if results are to be consistent, as the distance of the sample from its "equilibrium state" at $T_a$ depends on the rate at which the material is cooled. The sample is then held at $T_a$ for a specified time $t_a$, during which physical aging occurs, as seen by the loss of

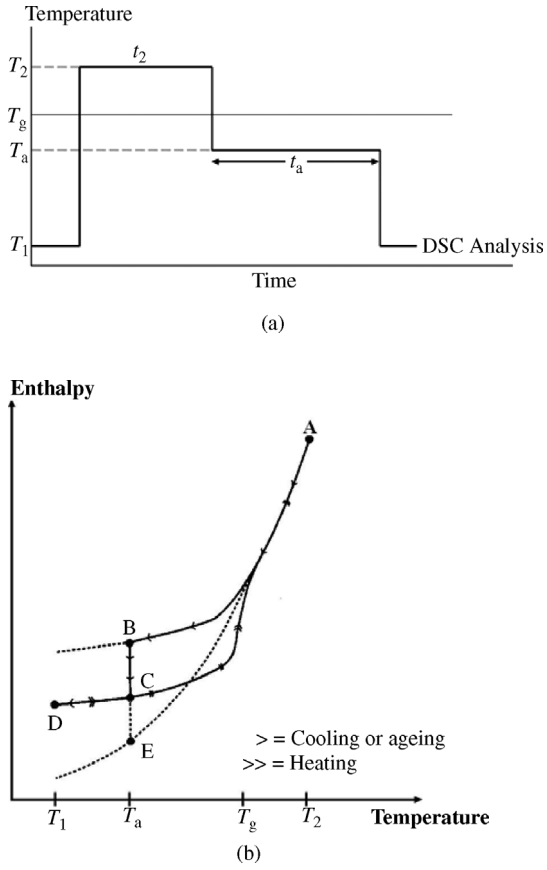


**Figure 6.1** (a) Schematic diagram of the time–temperature profile used in enthalpy relaxation experiments and (b) schematic representation of cooling, aging, and heating cycles using the time–temperature profile in (a).

excess enthalpy (line B-C). This loss ($H_B - H_C$) will depend on the length of the aging time, $t_a$, that is, the longer $t_a$ the closer the sample will approach its equilibrium state at point E. The sample is then quenched from $T_a$, followed by heating at a rate $q_2$. This causes the enthalpy to overshoot the equilibrium curve by an amount proportional to ($H_B - H_C$) along line (C-A) and this is illustrated in Figure 6.2 as it is manifest in the DSC curves.

The enthalpy difference (Figure 6.2) is expressed as:

$$(H_B - H_C) = \Delta H(t_a, T_a) = \int_{T\alpha}^{T\beta} \{C_p(\text{aged}) - C_p(\text{unaged})\} dT \qquad (6.1)$$

and it is equivalent to the area (A-B) in Figure 6.2. As DSC measures the specific heat, $C_p$, and $C_p = (\partial H/\partial T)_p$, the enthalpy change can be obtained by integration of

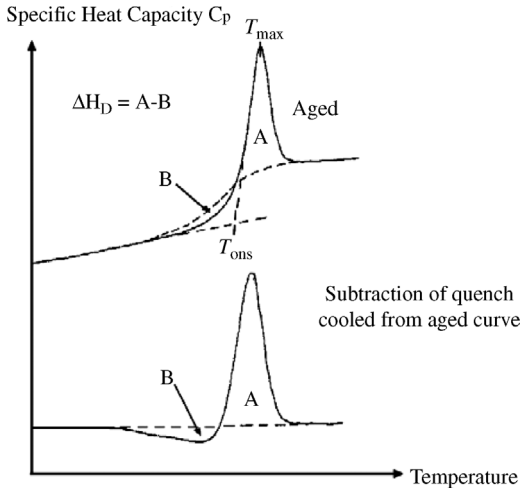


**Figure 6.2** Schematic diagram of DSC curves for an aged (full line) and unaged (dashed line) polymer sample before (top diagram) and after (bottom diagram) subtraction.

the DSC curves. From a practical point of view the aging temperatures $T_a$ are normally close to $T_g$ because the greater $(T_g - T_a)$ the slower the aging processes become and the time scales for the relaxation events are too long for accurate measurement. It is necessary to carry out accelerated aging at temperatures close to $T_g$, so that measurements can be made over periods of a few hours up to several days at the most.

### 6.2.2 Theoretical Approaches

Most models developed to describe the physical aging process are based on the idea of free volume in the polymer. Some only attempt to model the observed behavior, while others take a more holistic approach and try to understand the relationship between the molecular relaxation events and the distribution of free volume in the sample.

#### 6.2.2.1 Phenomenological Models

As the observed enthalpy relaxation is used extensively to follow the physical aging process, many of the earlier attempts at modeling were developed in terms of the heat capacity. The phenomenological models tend to use curve fitting procedures to try and reproduce the heat capacity changes as measured during DSC. The most important of these were proposed by Narayanaswamy [3], Moynihan *et al.* [4], and Hodge *et al.* [5–7]. These use the concept of the fictive temperature ($T_f$) first introduced by Tool and defined as the temperature at which the equilibrium value of a macroscopic property of the system would be an equilibrium one. Making use of $T_f$, Narayanaswamy [3] and Moynihan *et al.* [4] modeled the kinetics of the aging in terms of a non-equilibrium decay function. To allow for the fact that the kinetics are

nonlinear, an average relaxation time, $\tau$, was defined:

$$\tau = \tau_o \exp\left[\frac{x\Delta E^*}{RT} + \frac{(1-x)\Delta E^*}{RT_f}\right] \tag{6.2}$$

where $\tau_o$ is the relaxation time at equilibrium, that is, $T = T_f$ and $x$ is a structural parameter, introduced to account for nonlinearity effects, with values $0 < x < 1$. The activation energy for the relaxation process, $\Delta E^*$, is assumed to have an Arrhenius temperature dependence

The weakness of this approach as first introduced by Narayanaswamy [3] is the assumption that a single relaxation time can describe the physical aging process accurately. Some improvement can be achieved by introducing the Kohlrausch–Williams–Watts (KWW) stretched exponential function [8] to describe the distribution of relaxation times expressed as:

$$\phi(t) = \exp\left\{-(t/\tau)^{\beta}\right\} \tag{6.3}$$

where $t$ is the time and $\beta$ is inversely proportional to the breadth of the distribution of relaxation times. Following these arguments, the phenomenological treatment of Moynihan *et al.* [4] accounts for the non-exponential and nonlinear character of the structural relaxation during physical aging.

In a similar way, Kovacs [9] has invoked a distribution of relaxation times to account for multiple relaxation events in the aging polymer, where each relaxation time depends on the glass structure and the temperature. The difference is that rather than trying to fit the observed heat capacity data, the movement of the enthalpy recovery peak in the DSC curves was followed, as discussed by Hutchinson [10]. This approach obviated the need to define a specific distribution of relaxation times.

A purely thermodynamic interpretation of the glassy state was proposed by Gibbs and Di Marzio [11] (GD). In this they defined a thermodynamic transition temperature $T_2$, below $T_g$, where the configurational entropy of the system $S_c$ was zero. This was developed further by Adam and Gibbs [12] who proposed the concept of a "minimum co-operative region" in which a configurational entropy change can take place without affecting the surroundings. At $T_2$ only one configuration is possible, so $S_c = 0$.

By using the GD theory, Hodge [13] was able to show that the structural factor $x$ was equal to $x = (T_f/T_2)$. The curve fitting approach has been developed further by Gomez-Ribelles and Monleon-Pradas (G-M) [14]. The authors replaced $T_f$ with $S_c$ and found marked improvements when fitting experimental data to the theory. In this approach the authors have adopted the concept introduced by Cowie and Ferguson [15] that the physical restrictions imposed by chain entanglement lead to inefficient chain packing in quenched polymer matrices and the glass may be physically unable to achieve the limiting value of $C_p$ as predicted by a linear extrapolation of the liquid $C_p$ curve, because of chain entanglement.

Several criticisms can be leveled at the phenomenological models; the distribution of relaxation times is not easily defined, they give no information about the molecular relaxation processes involved and recently Simon and Bernazzani [16] found that

volume relaxation times depend on $T_f$ and the relation is nonlinear. Interpretation of data, using these models, must be viewed critically.

#### 6.2.2.2 Petrie–Marshall and Cowie–Ferguson Models

The models described above offer a means to describe the phenomenology of the glassy state during aging, accounting for its non-exponential, nonlinear character. Empirical models such as the Petrie–Marshall [17] (P-M) or the Cowie–Ferguson (C-F) [15, 18] treatments are less rigorous but, due a simpler approach, make it possible to quickly compare the behavior of different materials as well as predict the effect of physical aging over time periods well beyond reasonable experimentation times. In both models, the loss of enthalpy during the aging process is given by:

$$\Delta H(t_a, T_a) = \Delta H(\infty, T_a)[1 - \phi(t_a)] \tag{6.4}$$

While the P-M model uses the linear extrapolation of the liquid polymer enthalpy–temperature dependence to measure $\phi(t_a)$, the C-F approach is different. It considers $\Delta H(\infty, T_a)$ to be an adjustable parameter and is measured by curve fitting the $\Delta H(t_a, T_a)$ versus $\log t_a$ plots. The function $\phi(t_a)$ is also redefined as:

$$\phi(t_a) = \exp\left\{-(t/t_c)^{\beta}\right\} \tag{6.5}$$

where $t_c$ is a characteristic time, that is, $t_a = t_c$ when the glass has aged to 63.2% of the fully aged glass. The C-F model also allows one to predict the time $t_e$ required to reach 99.9% of the thermodynamic equilibrium state of the infinitely aged glass, from accelerated aging experiments.

As discussed below, the C-F model has been extensively used to compare the aging behavior of polymer blends to that of the corresponding homopolymers, because of its simplicity. However, notably, this model cannot adequately describe all of the phenomenology associated with the glass transition, namely, its nonlinear character. The consequences of this when describing the physical aging process have been discussed in the literature [19, 20].

#### 6.2.2.3 Molecular Models

Most models developed are based on the idea that significant free volume exists in the glass state of a polymer. Some only attempt to model the consequences of the reduction in this free volume during physical aging, while others try to understand the relationship between the molecular relaxation processes that are responsible for the change in free volume and the distribution of this free volume in the aging sample. The latter approach is much more sensible and desirable if a deeper understanding of the glassy state is to be achieved.

Simha, Robertson, and their coworkers have pursued this line of attack with commendable results, using the Simha–Somcynsky "hole" theory [21] (S-S) as a starting point. The theory uses the formalism of a polymer lattice in which vacant cells or "holes" constitute the free volume arising from inefficient chain packing. An equation of state was developed to calculate the fraction of occupied lattice sites and hence the fractional free volume.

This approach has been expanded by Robertson [22, 23] to encompass the molecular relaxation events that occur via small, simple trans and gauche confor-

mational changes in the chains. These are assumed to be coupled with the free volume environment, which will also be subject to thermal fluctuations.

Robertson and coworkers [24] also view the structural relaxation as a free volume reduction via the mechanism of a diffusion of holes, in response to molecular relaxation events along the chains.

Other coupling models have been proposed by Ngai [25] and by Kubát *et al.* [26, 27]. Kubát's group has proposed that, while the available free volume will restrict the molecular motion, the activation energy of the relaxing unit is capable of precipitating molecular relaxation events in neighboring parts of the polymer chains.

### 6.2.3
### Enthalpic Relaxation in Polymer Blends

Physical aging studies have been performed on several polymer–polymer mixtures; Tables 6.1 and 6.2 list the systems investigated. Most of these studies have made use of DSC and enthalpic data to assess physical aging behavior in blends.

Early enthalpy relaxation studies of PMMA/SAN blends carried out by Naito *et al.* [33] indicated a single endothermic aging peak for the 50/50 blend and the pure

**Table 6.1** Physical aging in homopolymer systems: qualitative treatment.

| Polymer | Technique | Reference |
|---|---|---|
| ABS/BPAPC | Mech | Maurer [28] |
| ABS/BPAPC | DSC, FTIR | Tang [29] |
| BPAPC/SAN | DSC | Belloch [30] |
| Aromatic polyamides | DSC | Ellis [31] |
| Nylon 6,6/PPE | Mech | Laverty [32] |
| PMMA/SAN | DSC | Naito [33] |
| PMMA/SAN | DSC | Mijovic [34] |
| PMMA/SAN | Dil, DSC, Mech | Robertson [35] |
| PMMA/SAN | DSC | Cowie [36] |
| PMMA/SAN | Mech | Cowie [37] |
| Poly(lactide) blends | DSC | Jorda [38] |
| PS/P(2-VP) | DSC | Grooten [39] |
| PSF/CPSF | DSC | Lau [40] |
| PVC/PiPMA | DSC | ten Brinke [41], Bosma [42] |
| PVC/PMMA | DSC | Bosma [42] |
| PPE/PVME | PALS, Mech | Chang [43] |
| PMMA/PEG | PALS, Mech | Chang [43] |
| PS/PPE | Dil, DSC, Mech | Robertson [44] |
| PEEK/PPS | Mech | Guo [45] |
| PVP/PVAc | PALS | Cowie [46] |
| PVP/P(VAc-co-VA) | PALS | Cowie [46] |
| PMMA/PEO | Dil, DSC, Mech | Vernel [47] |
| PS/NR | Mech | Asaletha [48] |
| PEO/PPO | DSC | Morales [49] |
| Polymide blends | DSC | Goodwin [50] |
| Polyimide/PEI | DSC | Campbell [51] |

**Table 6.2** Physical aging in blends: quantitative treatment.

| Polymer | Technique | Model | Reference |
|---|---|---|---|
| PEEK/PEI | DSC | KWW | Hay [52] |
| PES/epoxy | DSC | C-F | Breach [53] |
| PES/epoxy | DSC | C-F | Hay [52] |
| PMMA/PVDF | E(t) | KWW | Mijovic [54] |
| PMMA/SAN | DSC | Hodge | Mijovic [55] |
| PMMA/SAN | DSC | Hodge | Mijovic [56] |
| PMMA/SAN | Mech | Stress relaxation | Mijovic [55] |
| PMMA/SAN | Mech | KWW | Mijovic [54] |
| PS/PVME | DSC | C-F | Cowie [57] |
| PS/PPE | DSC | Hodge | ten Brinke [58] |
| PS/PPE | Mech | KWW | Mijovic [54] |
| PHS/PVME | DSC, PALS | C-F | Arrighi [59] |
| PHS/PMMA | DSC | C-F | Cowie [60] |
| PMMA/SMA | DSC | C-F | Cameron [61] |
| PMMA/SAN | DSC | G-M | Cameron [62] |
| PEO/PPO | DSC | C-F | Morales [63] |
| Epoxy/PES | DSC | C-F | Jong [64] |
| sPS/aPS | DSC | C-F | Hong [65] |

components. No measurable changes in the magnitude of the enthalpy relaxation peak after blending were observed and the authors concluded that this was a result of a weak interaction between the two polymers.

The expectation that homogeneous, one-phase, blends should show a single recovery peak has been used extensively to investigate the miscibility of polymer–polymer systems. Implicit is the assumption that, for a miscible blend, the kinetics of the aging process is an average of those of the pure components. On the other hand, the appearance of multiple enthalpy recovery peaks is characteristic of heterogenous systems in which the components age at their own individual rates. Based on these ideas, isothermal aging experiments have been used to determine phase behavior in systems where the close proximity of the component glass transition temperatures make it difficult to discriminate between the presence of one or two $T_g$s in a DSC measurement at normal scan rates [38, 42].

The applicability of the method in the assessment of polymer–polymer miscibility was first demonstrated by comparing the behavior of poly(vinyl chloride), PVC, blended with atactic poly(methyl methacrylate), PMMA, and poly(isopropyl methacrylate), PiPMA. As shown in Figure 6.3a, despite the proximity of the glass transition temperatures [$T_g$(PVC) = 80 °C; $T_g$(PiPMA) = 82.5 °C], the immiscible PVC/PiPMA develops two distinct enthalpy recovery peaks with increasing aging time $t_a$ at 60 °C, that is, ($T_g - T_a$) ~ 20 °C, a clear signature that phase separation had occurred [42]. In contrast, the miscible PMMA/PVC blend displays a single enthalpy recovery peak, indicating a one-phase system [42] (Figure 6.3b).

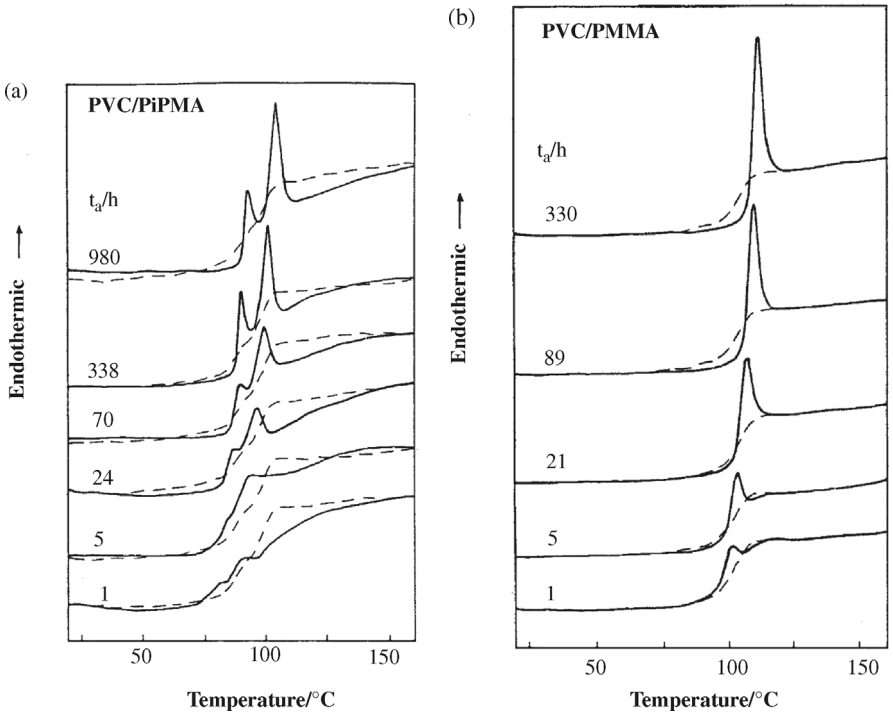


**Figure 6.3** (a) DSC thermograms for aged polymer blends: (a) poly(vinyl chloride)/poly(isopropyl methacrylate), immiscible blend, aged at 60 °C; (b) poly(vinyl chloride)/poly(methyl methacrylate), miscible blend, aged at 80 °C. Time of aging, $t_a$ in hours, is shown alongside each curve. Broken lines represent the unaged samples for comparison. Adapted from Reference [42].

As suggested by Grooten and ten Brinke [39] the most appropriate range of aging temperature for this type of experiment is $T_g$ to $\sim(T_g - 20\,^\circ\text{C})$. As for the aging time required to assess polymer–polymer miscibility this does not necessarily need to be long. It was noted [66] that the ability to distinguish between one- and two-phase systems as the $T_g$ values approach one another depends on the effective aging times, $t_{eff}$:

$$t_{eff} = t_a/\tau \tag{6.6}$$

Since $\tau$ is related to $x$, $\Delta E^*$, and $\tau_o$ [Eq. (6.6)], even if the two blend components have a similar $T_g$, when these kinetic parameters differ so will the enthalpy relaxation at $T_a$. Therefore it is the difference in the enthalpy relaxation of the single components that is crucial when investigating polymer–polymer miscibility.

Analysis of the kinetics of the recovery process in terms of $T_{max}$, $T_{on}$ (Figure 6.2) provides a further means to assess quantitatively phase behavior. The structural dependence of these parameters has made it possible to investigate the phase

behavior of blends containing aromatic polyamides [31]. Despite the similarity in structure of the blend components and therefore the close proximity of the glass transition temperatures, Ellis [31] was able to confirm the immiscibility behavior predicted using the mean field binary interaction model [67, 68]. Interestingly, the enthalpy difference $\Delta H_D$ did not prove to be a useful parameter to investigate phase behavior in these systems as similar values were found for all pure polymers and blends.

The ability to discriminate between miscible and immiscible blends using DSC has also been demonstrated by Jorda and Wilkes [38] who showed, after aging, that blends of racemic polylactide ($T_g = 53\,^\circ C$) and its optically active L-form ($T_g = 65\,^\circ C$) were two-phase, a convincing demonstration that two stereoregular forms of a polymer may be immiscible.

The first comprehensive study of physical aging in a miscible blend system using enthalpy relaxation was reported by Cowie and Ferguson [57] for blends of polystyrene (PS) and poly(vinyl methyl ether), PVME. The enthalpic aging data were analyzed using both the P-M and C-F models; comparison of the blend behavior with that of the pure components led to the conclusions that, when aging was conducted at a comparable temperature below $T_g$, the blends aged more slowly than PVME. As shown in Figure 6.4, this conclusion is supported by a comparison of the C-F parameters of a 50/50 wt% blend. In the case of random mixing, one may expect $\Delta H_\infty$ for a blend to have intermediate values between those of the two pure components. This is not the case for this system and in fact $\Delta H_\infty$ for the blend lies below the PVME values (Figure 6.4).

The component with the lower $T_g$, that is, PVME, was responsible for most of the aging effects seen in this blend, as indicated by the similarity of $t_c$ values of the blend and PVME. The PS component did not appear to contribute significantly to the total aging because the relaxation processes were much slower than for PVME at the aging temperature. Thus, even though this is a miscible blend, its components seem to relax independently. Notably, while this blend does display a single $T_g$ it is quite broad and the $T_g$ region may span up to 23 K. When such a broad transition region exists, then aging close to the enthalpic $T_g$ might impinge on the onset region of the glass transition process and show an accelerated aging for the more flexible component.

This idea was further addressed by Oudhuis and ten Brinke [58] by examining the aging of blends of PS with poly(2,6-dimethyl-1,4-phenylene ether), PPE, where both components are relatively rigid, although there is still about 100 °C difference between the $T_g$s. In agreement with the work of Cowie and Ferguson [57], the amount of enthalpy relaxation observed in the blends was considerably lower than that for the corresponding homopolymers and was attributed to the large difference in the $T_g$s of the blend components. The similarity in $\Delta H_\infty$ values of blends of various compositions led the authors to the conclusion that there was no evidence for faster relaxation by the component with the lower $T_g$, viz. PS. They concluded that the blend behaves as a pure component but the presence of concentration fluctuations is responsible for a range of $T_g$ values, some of which may be above the onset $T_g$ and therefore result in lower $\Delta H_\infty$ values.

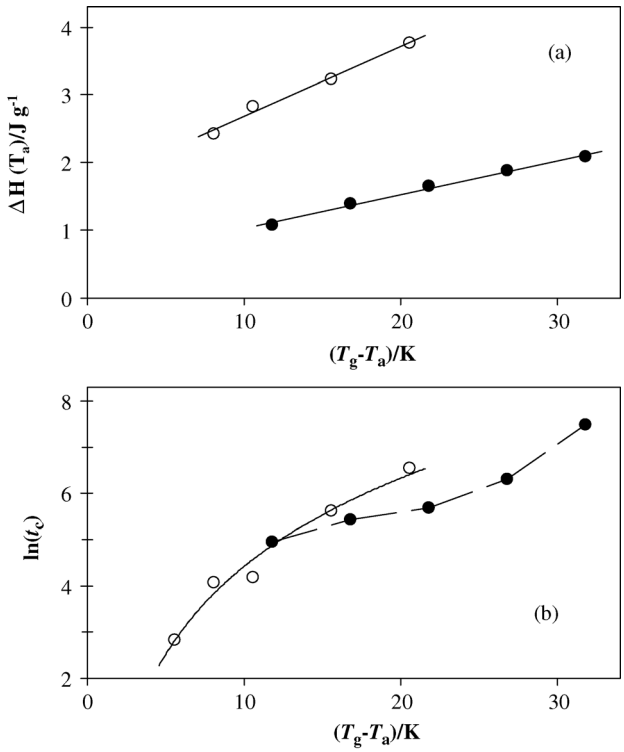


**Figure 6.4** (a) $\Delta H_\infty(T_a)$ versus $(T_g - T_a)$ plot for 50/50 wt% PS/PVME blend (●) and PVME (○) homopolymer; (b) $\ln(t_c)$ (min) versus $(T_g - T_a)$, plot for 50/50 wt% PS/PVME blend (●) and PVME homopolymer (○); the dashed curve is a guide to the eye through the blend data, and the solid line is the William–Landel–Ferry equation fit to the PVME homopolymer data.

The "sequential aging theory" proposed by Chai and McCrum [69] may provide an alternative explanation to the PS/PVME results. These authors postulated that at a given $T_a$ and $t_a$ the viscoelastic elements with relaxation times equivalent to $t_a$ will be aging, but that elements with $t < t_a$ will already have reached equilibrium and those with $t > t_a$ will not yet have begun to move towards equilibrium. Thus, in the PVME/PS case, the more flexible PVME, which will also be closer to its own $T_g$, will possess more elements with shorter $t$ than the PS. Consequently, the PVME relaxation spectrum will tend to move more rapidly towards equilibrium than the PS and so would age more rapidly.

Blends of PMMA and poly(styrene-*stat*-acrylonitrile), SAN, have been studied by several authors [33–37, 55]. These blends are of special interest since the miscibility is a result of the "copolymer repulsion effect" rather than intermolecular interactions. Mijovic *et al.* [34] as well as Cowie and Ferguson [36] have investigated PMMA blends containing a commercial copolymer of 25 wt% AN (acrylonitrile), using enthalpy [34, 36] and stress relaxation [55] measurements. Blends rich in SAN were

observed [34, 55] to relax faster than those having higher PMMA content but this effect was observed to be temperature dependent.

A comprehensive study of this system was carried out by Cowie and Ferguson [36] who followed the enthalpy and stress relaxation of a series of PMMA/SAN blends with SAN compositions spanning the miscibility window, that is, from 13.3 to 30 wt% AN. Figure 6.5 shows examples of $\Delta H(t_a, T_a)$ versus $\log t_a$ plots together with fits obtained using the P-M and C-F models. Evidently, the C-F model provides a better estimate of the long-term aging effects whereas overestimates of the time taken to reach equilibrium are made when using the P-M model. In agreement with findings

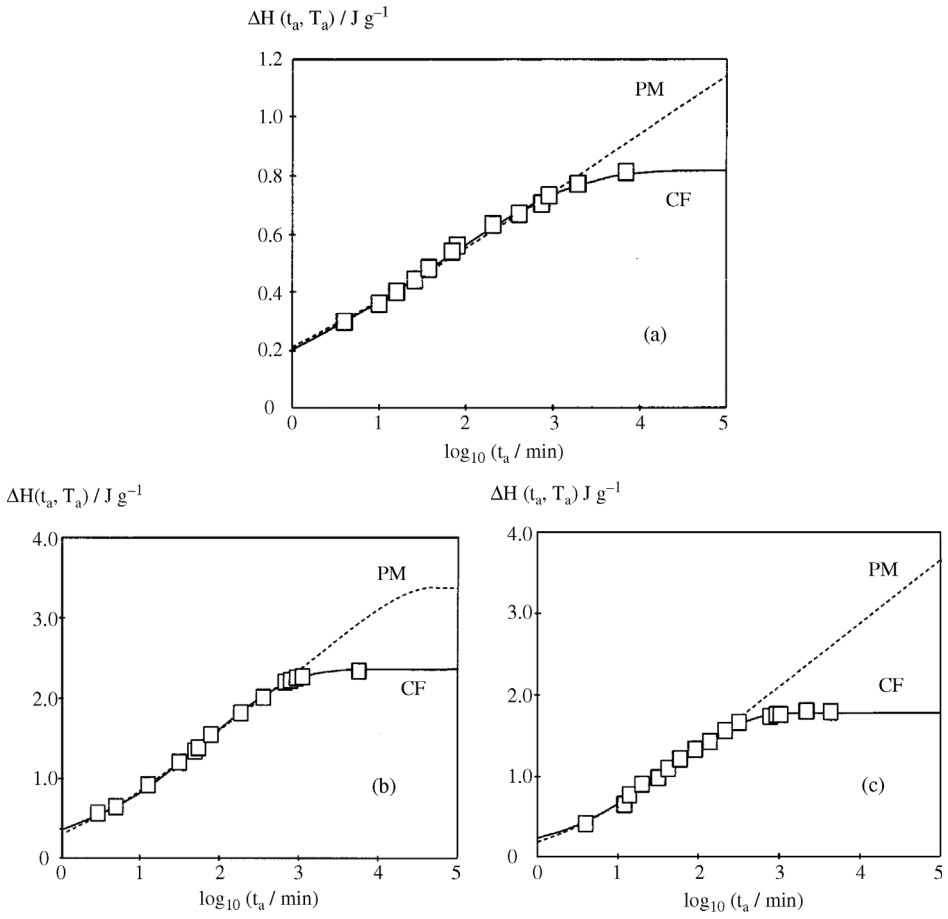


**Figure 6.5** Comparison of the experimental enthalpy change on aging for $t_a$ minutes for (a) PMMA, (b) SAN containing 26.6 wt% AN, and (c) a 50/50 blend of these two polymers, with the theoretical curves derived from the Petrie–Marshall (P-M) and Cowie–Ferguson (C-F) models. Adapted from Reference [36].

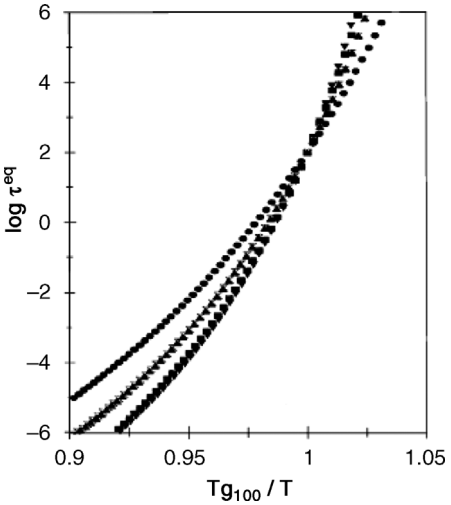


**Figure 6.6** Temperature dependence of the equilibrium relaxation times, $\tau^{eq}(T)$ from the G-M model, calculated for PMMA (●), SAN13 (▲), SAN17 (X), SAN26 (■) and SAN30 (▼). Reproduced with permission from Reference [62].

of Mijovic *et al.* [34], temperature affects the enthalpic relaxation behavior of the blend: at an aging temperature ($T_g - T_a$) of 10 °C, blends were found to relax faster than either of the components, but blend aging was intermediate to both components at $T_g - T_a = 20$ °C.

Modeling of the structural relaxation provides further insight into the physical aging process. As discussed in previous sections several models are available to quantitatively describe the aging, including those of Narayanaswamy [3] and Moynihan *et al.* [4]. All these models have been used to describe structural relaxations in polymers and have also been applied to blends (Table 6.2).

Cameron *et al.* [62] have applied the model proposed by Gomez-Ribelles and Monleon-Padras [14] to blends of PMMA and SAN copolymers. By using this model, various parameters can be extracted from the enthalpic data, including the equilibrium relaxation time, $\tau_{eq}$, $\beta$, and $T_2$. The temperature dependence of $\tau_{eq}$ is particulalry informative. Log $\tau_{eq}$ versus $T_{g100}/T$ (where $T_{g100}$ is the temperature at which the relaxation time in equilibrium is 100 s) are shown in Figure 6.6 for three PMMA blends with copolymers having different AN content. Blends that are far from the upper limit of miscibility (blends of SAN13 and SAN17) have nearly identical behavior whereas PMMA/SAN26 has a significantly lower slope. This feature has been attributed to blend microheterogeneity due to the AN content being close to the miscibility limit. This is reflected in a distribution of glass transition temperatures, broader than in pure polymers. Such an effect, which is evident in the enthalpy relaxation studies, cannot be observed by conventional DSC measurements, and it does not manifest itself in enthalpic aging data that display a single aging peak.

The Gomez-Ribelles theoretical approach has been used to reproduce the enthalpy relaxation of several blends of PS/poly(2,6-dimethyl-1,4-phenylene oxide) (PPO) [70]. Results show that the distribution of relaxation times is broader in the blends than in the individual components. In terms of the Angell [71] concept of "fragile-strong" classification of materials, the blends were "stronger" than the component parts.

Enthalpy relaxation studies have also been used to assess the aging of poly(ether ether ketone) (PEEK) blends with poly(ether imide) (PEI), PEEK/PEI = 50/50 [52]. The preparation of the blend produced an amorphous system with $T_g \sim 215\,^{\circ}C$, but crystallization of the PEEK occurred after raising the temperature above $T_g$. Enthalpic relaxation could only be observed in the temperature range $T_g$ to $(T_g - 50)$ and no aging could be detected at temperatures below 150 °C. The system was analyzed using the KWW equation, which yielded $\beta = 0.4$, intermediate between those of the component polymers. When the blends were examined using dielectric relaxation measurements, which probe the dipole relaxation spectrum, values of β were found to be much lower (0.1–0.22). This was interpreted as indicating the development of heterogeneity at the molecular level caused, probably, by the crystallization of the PEEK component.

Poly(ether sulfone), PES, can be blended with epoxy resins in certain combinations that do not lead to phase separated systems, and Breach *et al.* [72] have investigated the aging characteristics of Epikote 828 (Shell) and Victrex 5003P. Comparison of aged and unaged samples allowed the enthalpy relaxation to be calculated from the peak areas. The blends aged at a faster rate than the components, and this increased with increasing PES content. It was observed that β also increased and these effects were explained by considering that the incorporation of PES loosened the epoxy resin network, thereby increasing the free volume. As this would change the size distribution of the free volume "holes," the presence of larger holes would accelerate the relaxation process and narrow the relaxation time distribution.

### 6.2.4
### Volume Relaxation

The decrease in volume that accompanies physical aging is known as *volume recovery* or *volume relaxation*. Dilatometry (Dil) can be used to follow the volume relaxation in glasses by monitoring the time-dependence of the volume change on aging. The material is either cooled from above $T_g$ to the aging temperature $T_a$ (down-jump) and the isothermal volume contraction is measured or the sample is heated in the glassy state (up-jump), in which case an expansion follows.

The simplest volume recovery experiment is the down-jump. Volumetric data collected at a series of aging temperatures are normalized to examine the relative departure from equilibrium (δ), which is defined as:

$$\delta = \frac{V - V_\infty}{V_\infty} \tag{6.7}$$

where $V$ represents the volume at a specific aging time and $V_\infty$ is the volume at equilibrium density. Pioneering work by Tool [73, 74] showed that a simple kinetic model in which the relaxation time $\tau$ depended solely on the temperature could not describe adequately the isothermal recovery that followed a temperature jump from an equilibrium state. He proposed that $\tau$ had to be a function of the structure of the glass and that it was necessary to introduce the idea of a fictive temperature ($T_f$) to help describe the process. As the idea can be applied to enthalpic as well as volume relaxations, $T_f$ can be defined generally as the temperature at which the equilibrium value of a macroscopic property of the system would be an equilibrium one.

Work by Kovacs [75] on the volume relaxation of poly(vinyl acetate) highlighted the nonlinearity in the kinetics of isothermal recovery processes, and that the distribution of relaxation times, $\tau$, was necessary if the memory effects in glasses were to be explained. These ideas are incorporated in some of the phenomenological models developed to describe the aging of a glass and met in earlier sections.

As pointed out earlier, most aging studies of blends have employed enthalpy relaxation and very few measurements have been made using volume relaxation. Notably, the volume changes during isothermal volume recovery are small, typically of the order of 1% or less and require high-precision measurements.

Isothermal, isobaric volume relaxation can be described in terms of the volume relaxation rate ($b_V$) [1]:

$$b_V = -\frac{1}{V}\frac{dV}{d\log t_a} \tag{6.8}$$

which is valid for isothermal volume relaxation following a fast quench (or down-jump) into the glassy state from the equilibrium liquid state. This parameter can be used to follow changes with blend composition and aging temperature [35, 44].

For PS/PPE blends, negative deviations from simple addittivity have been observed, for small undercoolings. To verify whether this behavior was to be attributed to concentration fluctuations and the breadth of the glass transition, as suggested by Oudhuis and ten Brinke [58], Robertson and Wilkes [44] scaled the volume relaxation rates by the onset temperature ($T_{onset}$) and $T_g$ and concluded that the data provided no evidence of concentration fluctuations being responsible for the trends in volume relaxation rate. Measurements of specific volume data indicated that the existence of interactions between the PS and PPE components led to more densely packed blends compared to expected values based on the densities of the pure polymers. Better packing in the blends was considered to be the more likely cause of the observed slower aging of the blends.

The same authors also studied PMMA/SAN blends where the SAN copolymer contained 25 mol.% AN [35]. The dependence of the volume relaxation rate on blend composition appeared to be consistent with the enthalpic measurements of Mijovic *et al.* [34] on the same system. In fact, volume relaxation rates were found to be intermediate for the blends compared to the pure components and were composition dependent, except for $T_g - 50\,^\circ C$.

### 6.2.5 Mechanical Relaxation

The effect of physical aging on the mechanical properties of polymer–polymer systems is undoubtedly of primary importance for applications. Changes in viscoelastic properties with aging time were first reported for poly(vinyl acetate) (PVAc) by Kovacs *et al.* [76] and later investigated by Struik [1]. Generally, with increasing aging time, a shift in the viscoelastic relaxation spectrum to longer times is observed. This process can be followed using either stress relaxation or creep measurements.

Figure 6.7 gives a schematic representation of a creep experiment: the sample is quenched from above $T_g$ to the annealing temperature ($T_a$). A series of load–unload tests are performed whose duration is short in comparison to the aging time (typically less than 10% of $t_a$). As shown in Figure 6.7, the stress, $\sigma_o$, is constant and the time-dependent response, the strain, is measured following both load and unload. Since creep times, $t_e$, are kept relatively short, the creep response can be viewed as a "snapshot" of the viscoelastic response at a particular aging time.

The momentary creep compliance, $D(t)$, can be calculated:

$$D(t) = \frac{\varepsilon(t) - \varepsilon_{\text{unload}}(t)}{\sigma_o} \tag{6.9}$$

where $\varepsilon$ is the measured strain value and $\varepsilon_{\text{unload}}(t)$ is the extrapolated strain from the previous unload step. The momentary creep compliance curves can be described in terms of the KWW function and so the equation proposed originally by Struik [1] is:

$$D(t) = D_o e^{(t/\tau)^{\beta}} \tag{6.10}$$

where $D_o$ is the compliance at zero time, $\tau$ is the relaxation time, and $\beta$ is the shape parameter as defined earlier.

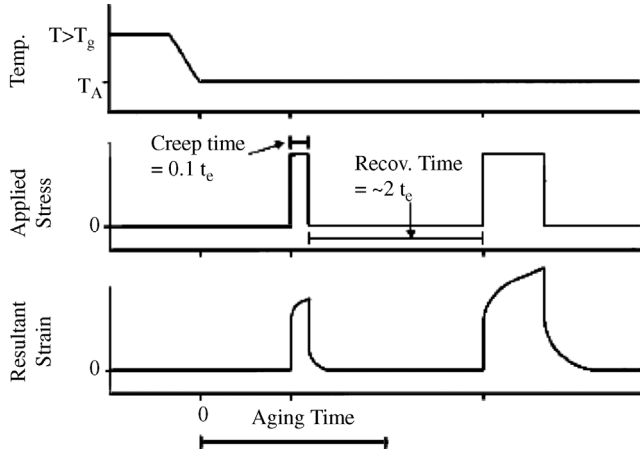


**Figure 6.7** Schematic representation of temperature, strain and stress program for a single aging time test. Reproduced with permission from Reference [77].

Stress relaxation measurements are carried out in a similar way but in this case small strains rather than small stresses are applied to measure the effect of aging on the viscolestic properties. The momentary modulus $E(t)$ is obtained, which can also be modeled using the KWW equation:

$$E(t) = E_o e^{(t/\tau)^{\beta}} \tag{6.11}$$

It has been shown that momentary creep or stress relaxation curves usually have a universal shape and a master curve can be constructed using either time–aging time $(t - t_a)$ or time–temperature $(t - T)$ superposition. A small vertical shift is sometimes needed to achieve this.

Similarly to time–temperature superposition, time–aging time superposition implies structural-rheological simplicity and rests on the idea of a constant distribution of relaxation times. As long as the measuring time is short compared with the relaxation or retardation times the aging process can be studied effectively. For small values of an applied deformation, the shift factors that are required to superimpose isothermal data at increasing aging times are found to depend on aging time according to:

$$\mu = \frac{d(\log \tau)}{d(\log t_a)} \tag{6.12}$$

where $\log \tau$ is the shift along the logarithmic relaxation time necessary to superimpose compliance or modulus data determined at increasing aging times $t_a$. Thus, $\mu$ can be considered as a measure of the rate of aging in a mechanical experiment, and a useful indication of long-term behavior can be derived from measurements made over relatively short periods of time.

Several polymer–polymer systems have been investigated. Among these, measurements of the effect of aging on the viscoelastic properties of PMMA/SAN blends have been reported by different research groups. Short-term stress–relaxation measurements have been carried out by Ho *et al.* [54] on blends of PMMA/SAN and PS/PPE and these authors found that $\tau$ could be expressed by:

$$\ln \tau = A + C_T \ln(T_g - T_a) + C_t \ln t_a \tag{6.13}$$

where $A$ is a function of the weight fraction of one of the components in the blend, while $C_T$ and $C_t$ are adjustable temperature and time coefficients. Ho *et al.* [54, 55] also observed that the stress relaxation response was well represented by the KWW function, with $\beta$ values centered within a narrow range around 0.41. While this, as well as many other reports, suggests $\beta$ does not vary significantly, there have been contrasting reports and views as to the behavior of the shape parameter $\beta$ during aging. By analogy to other relaxations, one might expect $\beta$ to be an increasing function of $(T_g - T_a)$, reaching a plateau at temperatures well below the glass transition.

Mijovic and Ho have attempted to link the results of enthalpy relaxation and tensile mechanical testing [56]. They reported similar dependencies of the relaxation times

from enthalpic and viscoelastic measurements. As for the general composition dependence of the aging process, the enthalpy relaxation data of PMMA/SAN had indicated that, at aging temperatures well below the $T_g$ of the blends, the recovery behavior appeared to be independent of blend composition. This was not the case in the tensile mechanical test results. Similar differences in response between enthalpic and mechanical tests have been observed by Brunacci *et al.* [78, 79] in polystyrene and substituted polystyrenes, a result that was attributed to the different perturbating effects used to measure the aging.

In some cases, when one blend component is in excess of the other, the aging of the blend appears to match that of the major component. This was observed by Cowie *et al.* [80] for (50/50) blends of PMMA/SAN using stress relaxation measurements. In this blend the rate of aging was similar to that of PMMA rather than being intermediate between the two components. It was concluded that the PMMA component was more responsive to the mechanical stresses than SAN, and spectroscopic evidence for stressed blends indicates that PMMA is more oriented than the SAN component [80].

Changes in mechanical properties during isothermal physical aging of three miscible blend systems, PS/PPE, PS/PVME, and PMMA/PEO [PEO = poly(ethylene oxide)], have been monitored by Chang *et al.* [43] using stress relaxation, for compositions in which one of the components was always in excess. For PS/PPE and PS/PVME, the stress relaxation rates were found to be faster for the blends than with PS alone, whereas the opposite was true for a PMMA/PEO blend when compared with pure PMMA. In attempting to explain these observations, the authors discussed the importance of two effects, namely, packing density and concentration fluctuations. It is observed that addition of the second component leads to a decrease in the packing density of the blend for PS/PPE and PS/PVME but an increase for PMMA/PEO. The presence of concentration fluctuations in the blend, detected via changes in width of the stress relaxation time distribution, appeared to be particularly significant in the PS/PVME system.

While time–aging time superposition has been extensively used to analyze creep and stress relaxation data, failure to achieve this has been reported in some cases. For example, Robertson and Wilkes [35] have questioned the applicability of time–aging time superposition to the creep data of PMMA and PMMA/SAN blends. It has been argued that failure to produce a master curve was due to overlapping, for the PMMA component, of primary and secondary mechanical relaxations. The extent to which this will affect the mechanical aging data depends on the annealing temperature and it is expected to become more pronounced at lower temperatures.

### 6.2.6
### Positron Annihilation Lifetime Spectroscopy

The decrease in volume that accompanies the physical aging process can be associated to a change of the distribution of free volume holes. Since the size and concentration of free volume holes in amorphous polymers is closely linked to the

thermal expansion, direct measurements of the free volume are very informative and can be used to monitor the aging processes.

One of the most useful tools for the detection of free volume "holes" or "voids," free volume, and free volume distribution, at an atomic scale, is positron annihilation lifetime spectroscopy (PALS). The technique exploits the fact that the positively charged positron ($e^+$), the antiparticle to the electron, preferentially samples regions of low positive charge density. When injected in a polymer matrix, thermalized positrons can combine with an electron to form a bound state, known as positronium (Ps). This species can only exist in a void and it rapidly annihilates on contact with the electron cloud of a molecule. For polymer studies using PALS, it is ortho-positronium (oPs, a triplet state) that is of main interest. The oPs spin exchanges with electrons of opposite spin on the walls of the cavity and it is annihilated. Thus, the oPs lifetime, $\tau_3$, gives a measure of the mean free volume cavity radius whereas the relative intensity of the oPs component, $I_3$, can be related to the number of cavities. A semiempirical equation has been derived that correlates $\tau_3$ with the cavity radius, $r$ [81]:

$$\tau_3 = \tfrac{1}{2}\left[1 - \frac{r}{r+\Delta r} + \frac{1}{2\pi}\sin\left(\frac{2\pi r}{r+\Delta r}\right)\right]^{-1} \tag{6.14}$$

which was obtained by using a spherical potential of radius $r_o$ with an electron layer of thickness $(r - r_0)$ of 1.656 Å.

As mentioned earlier, Chang *et al.* [43] have studied PS/PPE blends using stress relaxation measurements and PALS. As aging tends to be accompanied by changes in the packing density of the system, PALS can provide a qualitative estimate of the free volume in the system and its changes due to blending. For PS/PPE, the stress relaxation results were confirmed qualitatively using PALS and it was found that PS/PPE and PS/PVME blends were less dense than PS while PMMA/PEO was denser than PMMA, thereby making chain relaxation easier in the former and more difficult in the latter.

PALS has been used to examine the interactions in copolymers and blends. The technique has proven to be particularly useful when attempting to correlate physical aging data of a series of hydrogen bonded blends. Investigations carried out by Cowie *et al.* [82, 98] on polymer and copolymer blends with varying amount of hydrogen bonding illustrate the advantages of the PALS measurements. The first system to be studied by the Cowie group consisted of copolymers of poly(vinyl acetate-*co*-vinyl alcohol) (PVAc-co-VOH) and blends of these copolymers with poly(vinylpyrrolidone) (PVP) [82]. Infrared spectroscopy had revealed the presence of hydrogen bonding in these blends as a shift to lower wavenumbers of the pyrrolidone carbonyl and the alcohol hydroxyl bands. PALS measurements indicated that low levels of hydrogen bonding gave rise to open structures with increased free volume [82]. As the hydrogen bond concentration increased, a dramatic "collapse" in the free volume was observed (Figure 6.8), and it was suggested that this change should affect the physical aging properties.

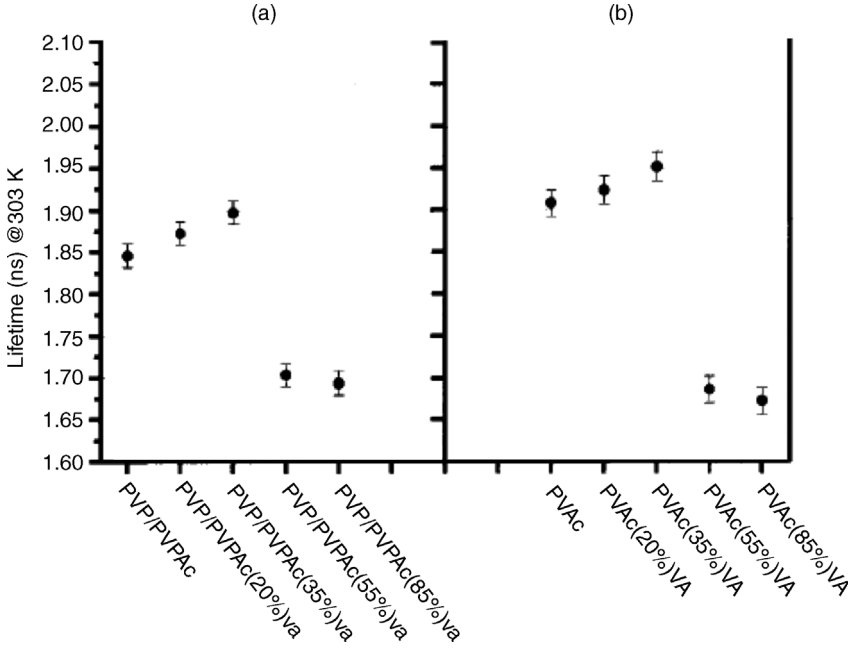


**Figure 6.8** Positron annihilation lifetimes at 303 K for poly(vinylacetate-*co*-vinylalcohol) (PVAc-co-VOH) copolymers (b) and blends of these copolymers with poly(vinylpyrrolidone) (PVP) (a). Reproduced with permission from Reference [82].

### 6.2.7
### Other Spectroscopic Techniques

In addition to PALS, other spectroscopic techniques that have been used to investigate physical aging are electron spin resonance spectroscopy (ESR) [83], fluorescence spectroscopy [84–86], dielectric spectroscopy [87], and Fourier-transform infrared spectroscopy (FTIR) [88].

Both ESR and fluorescence spectroscopy give an indirect measure of motion in polymers as they make use of either spin label or probe methods. In the case of ESR, nitroxyl radicals dispersed (spin probe) in a polymer matrix or covalently bonded to the polymer chains (spin label) are employed to probe the local environment. Therefore, ESR spectra provide information on molecular motion and microstructure of polymer matrices. Similarly, fluorescent probes are sensitive to the glass structure. This is because photon emission increases when non-radiative processes are hindered by lack of mobility of the probe. Interestingly, studies on poly (vinyl acetate) (PVAc) have shown that changes in the fluorescence intensities with aging time and temperature follow closely those observed by volumetric relaxation [85].

While various spectroscopic techniques have been used to investigate physical aging in amorphous polymers, very few studies have been reported on blends. As shown by studies on polymer–silica nanocomposites [89–91], fluorescence and

dielectric spectroscopy can provide insight into the molecular processes that are responsible for changes in physical aging. For example, Priestly *et al.* [91] have reported that addition of 0.4 vol.% silica to PMMA gives a reduction in the rate of aging of more than a factor of 20 compared to the pure polymer and that this was accompanied by a reduction in the β-relaxation process monitored by dielectric spectroscopy.

The idea that conformational changes occur during aging has been tested by means of FTIR and, for sample polymers, it was shown that the ratio of the trans to gauche conformations changes with decreasing temperature and aging [88]. Schmidt *et al.* [92] have shown that the carbonyl stretching band of polycarbonate contains contributions from trans-trans (t-t) and trans-cis (t-c) conformers present at 1767 and 1785 $cm^{-1}$, respectively. These assignments were confirmed by Lu *et al.* [93] who also reported the occurrence of conformational changes upon aging from high energy t-c to lower energy t-t conformations. However, Tang and Lee-Sullivan [94] did not observe similar changes upon aging of the PC component in a blend with ABS (acrylonitrile–butadiene–styrene copolymer).

### 6.2.8
### Scattering Techniques

Among the scattering techniques, small-angle X-ray scattering (SAXS) is the most used for aging studies, though only a few reports have been published [95–97]. Scattering of X-rays at small angles from amorphous, single-phase materials arises from density fluctuations caused by the disordered, liquid-like arrangement of atoms. The density fluctuation can be defined as:

$$\psi(v) = \frac{\left\langle (N - \langle N \rangle)^2 \right\rangle}{\langle N \rangle} \tag{6.15}$$

where $N$ is the number of particles in volume $v$, which fluctuates around the mean value $\langle N \rangle$. At equilibrium, the amount of density fluctuation is related to the isothermal compressibility, $\beta_T$, and can be evaluated from the extrapolated intensity at $Q = 0$, $I(0)$, according to:

$$I(0) = kT\,\varrho^2\,\beta_T \tag{6.16}$$

where $\varrho$ is the average electron density, expressed in electron units per unit volume.

An X-ray study of polystyrene samples subjected to volume changes using different methods has shown that large-scale density fluctuations correlate well with the specific volume but this is not the case on smaller length scale (0.25–0.4 nm) when the density fluctutations are sensitive to the method used to induce the volume changes [96]. As discussed by the authors, the results suggest that the properties of glassy materials are not simply described in terms of the amount of free volume but also depend on the state of local segmental packing of chains. This observation may also explain some of the discrepancies observed when monitoring aging using different experimental methods.

## 6.3
## Discussion of Physical Aging in Blends

### 6.3.1
### Effect of Intermolecular Interactions

As discussed in previous sections, the kinetics of the structural relaxation in miscible polymer blends can show significant differences with respect to that of pure amorphous polymers. Use of physical aging experiments as a means of assessing polymer–polymer miscibility relies on the assumption that the kinetics of the aging process is, for miscible blends, intermediate between that of the pure polymers. When considering a well-investigated blend system such as PS/PVME, aging studies suggest that blending causes the enthalpy change to decrease compared to the pure components, at similar undercoolings. As for the effect of blending on the rate of aging, this may depend on the specific system under study, even when equally large differences between the $T_g$s of the components exist (as is the case for PS/PVME and PS/PPO). This is probably because polymer–polymer mixtures show different levels of microheterogeneity, manifested in a distribution of relaxation times that is generally broader in blends than for the pure components. As discussed earlier this may be particularly important for homopolymer/copolymer blends that display transitions from miscibility to immiscibility as a function of copolymer composition.

The effect of blending on secondary relaxations (e.g., β process) may also need to be considered in some cases and it has been invoked to explain the changes of volume and enthalpy relaxation [35] in PMMA/SAN blends with aging temperature ($T_a$).

Polymer–polymer interactions would be expected to play a crucial role in determining the physical aging properties of a blend and this would be particularly evident when the blend components can interact strongly, for example, via hydrogen bonding. Relatively few reports of the effect of hydrogen bonding and other secondary interactions on the physical aging of polymer blends have appeared in the literature. Among these, blends of poly(4-hydroxystyrene) (PHS) with PVME [59] and PMMA [60] have been examined in detail, over a range of compositions. In discussing these systems one should bear in mind that the hydroxyl group in PHS can act as both a proton donor and acceptor, forming self-associated hydrogen bonds between either two PHS repeat units of the same chain (intra-chains) or two adjacent ones (inter-chain). In contrast, the PVME or PMMA components can only act as a proton acceptor, through their ether or carbonyl linkages, participating in intermolecular hydrogen bonds. FTIR analysis of the PHS/PVME blends showed that at 5 mol.% PHS only intermolecular hydroxyl groups are present but, upon increasing the PVME content in the blend, the band associated with the free hydroxyl groups becomes undetectable. Owing to the strong intermolecular interactions a considerable increase in glass transition temperature of the blend is observed compared to that of PVME. PALS measurements suggested that 59/41 (mol.%) PHS/PVME may be an optimum blend composition in terms of both strength of interaction and packing, with a minimum mean free volume hole size [59].

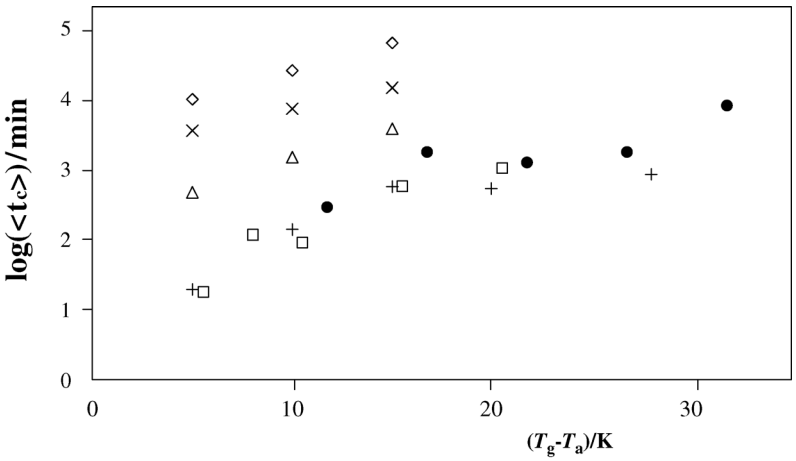


**Figure 6.9** Average relaxation times as a function of $(T_g - T_a)$ for the PHS/PVME blends: (△) (81/19), (×) (33/67), and (ε) (59/41), and for (◇) PVME, (+) PHS and (●) PS/PVME. Replotted from data reported in Reference [59].

For both PVME and PMMA blended with PHS the rate of physical aging was retarded compared to that of pure PVME or PMMA, due to the intermolecular hydrogen bonding. This is evident in Figure 6.9 where the average relaxation time, $\langle t_c \rangle$, for the KWW distribution:

$$\langle t_c \rangle = t_c \, \Gamma(1 + 1/\beta) \tag{6.17}$$

of blends and pure polymers are compared.

The rate of aging of PHS is comparable to that of PVME and PS/PVME, thus indicating that, at similar undercoolings, the presence of strong inter- and intra-H-bonding has little effect on the aging rate.

In contrast to the behavior of the PHS component, the presence of hydrogen bonds considerably hinders the enthalpic relaxation (Figure 6.9). The results are consistent with PALS measurements [59] carried out on the same PHS/PVME blends, where there was a steady free volume contraction in the blends with increasing PHS content, except for the 59 : 41 composition, where the free volume was less than that of the PHS alone. As illustrated in Figure 6.9, this blend aged more slowly than any of the other systems investigated, confirming that an optimum strength of the interaction is realized at approximately equimolar composition. At compositions where intermolecular hydroxyl–ether interactions are greatest, the C-F enthalpy parameters for PHS/PVME blends were found to be higher than those of the PHS/PMMA blends, reflecting the higher strength of the former interactions compared to the hydroxyl–carbonyl interactions.

Comparison between the enthalpic parameters $\log(\tau)$ and $\Delta H_\infty(T_a)$ for PVME or PMMA blends with PHS or styrene–hydroxystyrene (SHS) copolymers makes it possible to discuss the effect of hydrogen bond strength on aging. For example, FTIR measurements on a SHS copolymer with 71 mol.% hydroxystyrene (SHS71) indicated that the strength of the interaction increased in the order SHS71/PMMA

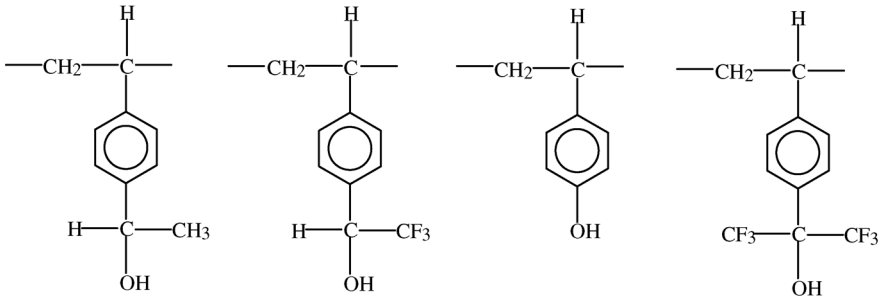


**Figure 6.10** Modified polystyrene systems: poly[4-(2-hydroxyethyl)styrene] (**6.1**, HES), poly[4-(1,1,1-trifluoro-2-hydroxyethyl)styrene] (**6.2**, TFHS), poly(4-hydroxystyrene) (**6.3**, PHS), poly[4-(hexafluoro-2-hydroxyisopropyl)styrene] (**6.4**, HFHS). The hydrogen bond strength of the donor site increases as **6.1** < **6.2** < **6.3** < **6.4**.

< SHS71 < SHS71/PVME. This is consistent with the finding that the SHS71/PVME blend exhibited the slowest relaxation while SHS/PMMA blends relaxed faster than the corresponding SHS copolymers close to $T_g$.

Cowie and coworkers have also examined in detail the effect of hydrogen bond strength on the physical aging in PVME and PMMA blends [59, 60] and copolymers [98] based on modified polystyrenes (Figure 6.10) that had been previously investigated by the same group [99]. The introduction of fluorine atoms (Figure 6.10) increases the inductive effect and the relative hydrogen bond strength. In blends of SHS, hydrogen bond formation is influenced by the strong acidity of the phenol groups resulting from resonance effects with the benzene ring.

In stark contrast with the SHS systems, the relaxation of the SHFHS/PMMA blends was generally slower than that of the copolymers [60], at comparable undercoolings. Another noteworthy difference was that the enthalpic parameters, $\Delta H_\infty(T_a)$, were generally found to be greater for the SHFHS/PMMA blends than for the SHFHS copolymers. This was attributed to a stronger interaction in the blends and it was speculated that the blends with the lower hydroxyl content SHFHS components would have higher free volumes and a greater degree of disorder. These facts would also contribute to the greater values of $\Delta H_\infty$. Moreover, most of the PMMA blends had higher $\Delta C_p$ values than the corresponding copolymers, which also indicates that there is a greater degree of disorder in the blend.

Some of these results highlight the fact that differences in aging behavior are probably consequential of structural differences rather than fully accounted for by the strength of the hydrogen bonding. Therefore, it may be concluded that it is difficult to establish a simple structure–property relationship in hydrogen bonded blends. Nevertheless, the enthalpy relaxation technique is sensitive to the structural features of these systems and it shows that H-bonding provides a reliable method of stabilizing polymer blends to the effects of long-term physical aging.

### 6.3.2
### Phase Separated Blends

The behavior of the two-phase systems may be rather complex and responses on aging can be affected by the thermal history and aging temperature. One of the most investigated systems is the two-phase blend of the acrylonitrile–butadiene–styrene copolymer (ABS) and Bisphenol-A polycarbonate (BPAPC). The effect of physical aging in a 75 : 25 polycarbonate/ABS blend has been studied by Tang and Lee-Sullivan [94] using enthalpy relaxation. Owing to the phase separated nature of the blend, two enthalpy recovery peaks were detected and attributed to the two separate components. However, the authors noted that aging had little effect on the ABS component even though the aging temperature was closer to the $T_g$ of ABS.

Maurer *et al.* [100] have examined the two-phase blend of ABS ($T_g = 110\,^\circ$C) and BPAPC ($T_g = 151\,^\circ$C) using stress relaxation measurements. Four regimes of behavior were found. Below 70 °C both ($t - T$) and ($t - t_a$) superpositions were possible, because the aging rates ($\mu$) of both components were equal. Between 70 °C and 100 °C only ($t - t_a$) superposition was achieved. However, close to the glass transition of ABS, and between the $T_g$s of both components, neither was valid. While a relationship similar to Eq. (6.11) has been used by other workers, Booij and Palmen [101] reported that a more precise form was:

$$G(t,\tau) = G_o(t/\tau)^{\alpha} \exp[-(t/\tau)^{\beta}] \tag{6.18}$$

where $\beta = 0.4$ was regarded as a constant (although this might be structure dependent) and $\alpha$ was normally a very small number. This form was used to analyze the ABS/BPAPC blend data.

Polycarbonate has been found to lose its toughness when aged at temperatures below its $T_g$ and impact modifiers are often added to counteract this effect of physical aging. Blends of BPAPC with several core–shell methacrylate–butadiene–styrene impact modifiers have been studied after aging at 125, 130, and 135 °C [102]. Tests for changes in impact strength, tensile strength, dynamic mechanical response, and fracture morphology were complicated by the simultaneous chemical degradation of the samples when aged in air, but the modifiers did appear to slow down the sample embrittlement caused by physical aging. The increase in toughness life-time of the modified BPAPC depended on the amount and nature of the impact modifier used, and the aging environment conditions. The effectiveness of the modifiers was reduced by their chemical degradation at elevated temperatures, particularly in the region of the sample surface.

## 6.4
## Concluding Comments

On a simplistic level one might expect that the physical aging behavior of blends could be predicted from that of the component polymers on an additive basis. This is clearly

not the case and examination of the available data suggests that several other factors can influence the behavior of a blend.

In weakly interacting systems the differences in chain stiffness, reflected in the $T_g$ values, can determine the aging characteristics of a blend. This can be quite variable, however, and no clear cut predictions can be made because different factors also come into play.

The most obvious of those is the presence of secondary specific interactions, such as hydrogen bonding. In blends where there is significant intermolecular H-bonding, there is a noticeable effect on the rate of aging. The H-bonded blend is a reversibly crosslinked system in which the available free volume is changed, the molecular relaxation processes can be impeded or retarded, and the extent of aging in the system is reduced.

Comparable results are obtained in some heterogeneous nanocomposite systems. Inclusion of an additive to the polymer, where there is no interaction between the components, has little or no effect on the aging behavior of the host polymer. The situation changes dramatically when the additive can interact with the polymer through secondary bonding, and the rate of aging of the polymer host is decreased significantly.

Thus systems that include effective intermolecular interactions are stabilized and the physical aging effects are reduced, providing a material whose properties are less likely to alter significantly over time.

Generally speaking, at our present level of knowledge, each blend is a unique system with its own unique aging behavior. This is determined by a combination of the relative flexibility of the component polymers and the extent and strength of the intermolecular interactions between them. Further studies are necessary if a full understanding of how these factors interact is to be obtained and to use this knowledge to help design new and stable materials.

## Abbreviations and Symbols

### Abbreviations

| | |
|---|---|
| ABS | acrylonitrile-butadiene-styrene |
| AN | acrylonitrile |
| BPAPC | Bisphenol-A polycarbonate |
| C-F | Cowie–Ferguson model |
| CPSF | carboxylated polysulfone |
| Dil | dilatometry |
| DSC | differential scanning calorimetry |
| $e^+$ | positively charged positron |
| ESR | electron spin resonance spectroscopy |
| FTIR | Fourier-transform infrared spectroscopy |
| HES | poly[4-(2-hydroxyethyl)styrene] |
| HFHS | poly[4-(hexafluoro-2-hydroxyisopropyl)styrene] |

| | |
|---|---|
| KWW | Kohlrausch–Williams–Watts function |
| Mech | mechanical |
| NR | natural rubber |
| PALS | positron annihilation lifetime spectroscopy |
| PEEK | poly(ether ether ketone) |
| PEG | poly(ethylene glycol) |
| PEI | poly(ether imide) |
| PEO | poly(ethylene oxide) |
| PHS | poly(hydroxystyrene) |
| PiPMA | poly(isopropyl methacrylate) |
| P-M | Petrie–Marshall model |
| PMMA | poly(methyl methacrylate) |
| PPE | poly(2,6-dimethyl-1,4-phenylene ether) |
| PPS | poly(phenylene sulfide) |
| PS | polystyrene (atactic) |
| Ps | positronium |
| PSF | polysulfone |
| PVAc | poly(vinyl acetate) |
| PVC | poly(vinyl chloride) |
| PVDF | poly(vinylidene fluoride) |
| PVME | poly(vinyl methyl ether) |
| PVP | poly(*N*-vinylpyrrolidone) |
| S | styrene |
| SAN | poly(styrene-*stat*-acrylonitrile) |
| SAXS | small angle X-ray scattering |
| SMA | styrene-*co*-maleic anhydride |
| TFHS | poly[4-(1,1,1-trifluoro-2-hydroxyethyl)styrene] |
| VA | vinyl alcohol |
| VAc | vinyl acetate |

**Symbols**

| | |
|---|---|
| $A$ | fitting constant |
| $b_V$ | volume relaxation rate |
| $C_p$ | heat capacity |
| $C_T$ | adjustable temperature coefficient |
| $C_t$ | adjustable time coefficient |
| $\Delta C_p$ | heat capacity change |
| $D_o$ | creep compliance at zero time |
| $D(t)$ | creep compliance at time $t$ |
| $E_o$ | modulus at zero time |
| $E(t)$ | modulus at time $t$ |
| $\Delta E^*$ | activation energy |
| $G_o$ | stress relaxation moduli at zero time |
| $G(t)$ | stress relaxation moduli at time $t$ |

| | |
|---|---|
| $H$ | enthalpy |
| $H(\infty)$ | equilibrium enthalpy value |
| $\Delta H$ | enthalpy change |
| $I_3$ | relative intensity of the oPs component |
| $I(0)$ | extrapolated intensity at $Q=0$ |
| oPs | ortho positronium |
| $q$ | cooling rate |
| $R$ | gas constant |
| $r$ | cavity radius |
| $S_c$ | configurational entropy |
| $T$ | temperature |
| $t$ | time |
| $T_a$ | annealing temperature |
| $t_a$ | annealing time |
| $t_c$ | characteristic time |
| $T_f$ | fictive temperature |
| $T_g$ | glass transition temperature |
| $V$ | specific volume |
| $V_\infty$ | specific volume at equilibrium, at temperature $T$ |
| $x$ | structural parameter |

### Greek Symbols

| | |
|---|---|
| $\beta$ | parameter of KWW function |
| $\beta_T$ | isothermal compressibility |
| $\delta$ | departure from equilibrium |
| $\varepsilon$ | strain |
| $\varrho$ | electron density |
| $\varrho(\tau)$ | relaxation time distribution |
| $\sigma$ | stress |
| $\tau$ | relaxation time |
| $\tau_3$ | oPs lifetime |
| $\tau_o$ | equilibrium relaxation time |
| $\phi(t)$ | KWW relaxation function |

## References


1 Struik, L.C.E. (1978) *Physical Ageing in Amorphous Polymers and Other Materials*, Elsevier, Amsterdam.

2 Hutchinson, J.M. (1995) Physical ageing of polymers. *Prog. Polym. Sci.*, **20**, 703.

3 Narayanaswamy, O.S. (1971) A model of structural relaxation in glass. *J. Am. Ceram Soc.*, **54**, 491.

4 Moynihan, C.T., Macedo, P.B., Montrose, C.J., Gupta, P.K., DeBolt, M.A., Dill, J.F., Dom, B.E., Drake, P.W., Easteal, A.J., Elterman, P.B., Moeller, R.P., Sasabe, H., and Wilder, J.A. (1976) Structural relaxation in vitreous materials. *Ann. N. Y. Acad. Sci.*, **279**, 15.

5 Hodge, I.M. and Berens, A.R. (1981) Calculation of the effect of annealing on sub-$T_g$ endotherms. *Macromolecules*, **14**, 1598.

6 Hodge, I.M. and Berens, A.R. (1982) Effects of annealing and prior history on enthalpy relaxation in glassy polymers. 1. Mathematical modeling. *Macromolecules*, **15**, 762.

7 Hodge, I.M. and Huvard, G.S. (1983) Effects of annealing and prior history on enthalpy relaxation in glassy polymers. 3. Experimental and modeling studies of polystyrene. *Macromolecules*, **16**, 371.

8 Williams, G. and Watts, D.C. (1970) Non-symmetrical dielectric relaxation behaviour arising from a simple empirical decay function. *Trans. Faraday Soc.*, **66**, 80.

9 Kovacs, A.J. (1963) Transition vitreuse dans les polymeres amorphes. Etude phenomenologique. *Fortschr. Hochpolym. Forsch*, **3**, 394.

10 Hutchinson, J.M. (1992) Interpretation of structural recovery of amorphous polymers from DSC data. *Progr. Colloid Polym. Sci.*, **87**, 69.

11 Gibbs, J.H. and Di Marzio, E.A. (1958) Nature of the glass transition and the glassy state. *J. Chem. Phys.*, **28**, 373.

12 Adam, G. and Gibbs, J.H. (1965) On the temperature dependence of cooperative relaxation properties in glass-forming liquids. *J. Chem. Phys.*, **43**, 139.

13 Hodge, I.M. (1987) Effects of annealing and prior history on enthalpy relaxation in glassy polymers. 6. Adam-Gibbs formulation of nonlinearity. *Macromolecules*, **20**, 2897.

14 Gomez-Ribelles, J.L. and Monleon-Pradas, M. (1995) Structural relaxation of glass-forming polymers based on an equation for configurational entropy. 1. DSC experiments on polycarbonate. *Macromolecules*, **28**, 5867.

15 Cowie, J.M.G. and Ferguson, R. (1986) The ageing of poly(vinyl methyl ether) as determined from enthalpy relaxation measurements. *Polym. Commun.*, **27**, 258.

16 Simon, S.L. and Bernazzani, P. (2006) Structural relaxation in the glass: Evidence for a path dependence of the relaxation time. *J. Non-Cryst. Solids*, **352**, 4763.

17 Marshall, A.S. and Petrie, S.E.B. (1975) Rate-determining factors for enthalpy relaxation of glassy polymers. Molecular weight. *J. Appl. Phys.*, **46**, 4223.

18 Cowie, J.M.G. and Ferguson, R. (1989) Physical ageing studies in poly(vinyl methyl ether). 1. Enthalpy relaxation as a function of ageing temperature. *Macromolecules*, **22**, 2307.

19 Li, Q. and Simon, S.L. (2006) Enthalpy recovery of polymeric glasses: is the theoretical limiting liquid line reached? *Polymer*, **47**, 4781.

20 Hutchinson, J.M. and Kumar, P. (2002) Enthalpy relaxation in poly(vinyl acetate) *Thermochim. Acta*, **391**, 197.

21 Simha, R. and Somcynsky, T. (1969) On the statistical thermodynamics of spherical and chain molecule fluids. *Macromolecules*, **2**, 342.

22 Robertson, R.E. (1978) Effect of free-volume fluctuations on polymer relaxation in the glassy state. *J. Polym. Sci. Polym. Symp.*, **63**, 173.

23 Robertson, R.E. (1979) Effect of free volume fluctuations on polymer relaxation in the glassy state. II. Calculated results. *J. Polym. Sci. Polym. Phys. Ed.*, **17**, 597.

24 Robertson, R.E., Simha, R., and Curro, J.G. (1984) Free volume and the kinetics of aging of polymer glasses. *Macromolecules*, **17**, 911.

25 Ngai, K.L. (1979) Universality of low-frequency fluctuation, dissipation and relaxation properties of condensed matter I. *Comments Solid State Phys.*, **9**, 127.

26 Kubát, M.J., Ríha, P., Rychwalski, R.W., and Uggla, S. (1999) A Kohlrausch type equation based on a simplified cooperative model. *Mechan. Time-dependent Mater*, **3**, 31.

27 Kubát, M.J., Riha, P., Rychwalski, R.W., and Kubat, J. (2000) Stochastic approach to cooperative relaxation processes in solids. *Europhys. Lett.*, **50**, 507.

28 Maurer, F.H.J., Palmen, J.H.M., and Booij, H.C. (1985) Generalized stress relaxation behaviour and physical aging

in heterogeneous amorphous polyblends. *Rheol. Acta*, **24**, 243.
29 Tang, J.K.Y. and Lee-Sullivan, P. (2008) Observation of physical aging in a polycarbonate and acrylonitrile-butadiene-styrene blend. *J. Appl. Polym. Sci.*, **110**, 97.
30 Belloch, G.P., Sanchez, M.S., Ribelles, J.L.G., Pradas, M.M., Duenas, J.M.M., and Pissis, P. (1999) Conformational motions in immiscible blends of polycarbonate and styrene acrylonitrile copolymers. *Polym. Eng. Sci.*, **39**, 688.
31 Ellis, T.S. (1990) Aromatic polyamide blends: enthalpy relaxation and its correlation with phase phenomena. *Macromolecules*, **23**, 1494.
32 Laverty, J.J. (1988) Effect of heat aging on the properties of a nylon 6,6/poly (phenylene oxide) blend. *Polym. Eng. Sci.*, **28**, 360.
33 Naito, K., Johnson, G.E., Allara, D.L., and Kwei, T.K. (1978) Compatibility in blends of poly(methyl methacrylate) and poly(styrene-co-acrylonitrile). 1. Physical properties. *Macromolecules*, **11**, 1260.
34 Mijovic, J., Ho, T., and Kwei, T.K. (1989) Physical aging in poly(methyl methacrylate)/poly(styrene-co-acrylonitrile) blends. Part II: enthalpy relaxation. *Polym. Eng. Sci.*, **29**, 1604.
35 Robertson, C.G. and Wilkes, G.L. (2001) Physical aging behavior of miscible blends of poly(methyl methacrylate) and poly(styrene-co-acrylonitrile). *Polymer*, **42**, 1581.
36 Cowie, J.M.G. and Ferguson, R. (1991) Physical ageing studies in a series of SAN copolymers and a blend of PMMA/SAN. Paper presented at IUPAC, Montreal.
37 Cowie, J.M.G., McEwen, I.J., and Matsuda, S. (1998) Stress relaxation and physical ageing in a blend of poly(styrene-co-acrylonitrile) and poly(methyl methacrylate). *J. Chem. Soc., Faraday Trans.*, **94**, 3481.
38 Jorda, R. and Wilkes, G.L. (1988) A novel use of physical aging to distinguish immiscibility in polymer blends. *Polym. Bull.*, **20**, 479.
39 Grooten, R. and ten Brinke, G. (1989) Enthalpy relaxations in blends of polystyrene and poly(2-vinylpyridine). *Macromolecules*, **22**, 1761.
40 Lau, W.W.Y., Jiang, Y.G., and Tan, P.P.K. (1993) Miscibility and enthalpy relaxations in polysulfone-carboxylated polysulfone blends. *Polym. Int.*, **31**, 163.
41 ten Brinke, G. and Grooten, R. (1989) Enthalpy relaxations in polymer blends and block copolymers: Influence of domain size. *Colloid Polym. Sci.*, **267**, 992.
42 Bosma, M., ten Brinke, G., and Ellis, T.S. (1988) Polymer-polymer miscibility and enthalpy relaxations. *Macromolecules*, **21**, 1465.
43 Chang, G.-W., Jamieson, A.M., Yu, Z.B., and McGervey, J.D. (1997) Physical ageing in the mechanical properties of miscible polymer blends. *J. Appl. Polym. Sci.*, **63**, 483.
44 Robertson, C.G. and Wilkes, G.L. (2000) Physical aging behavior of miscible blends containing atactic polystyrene and poly(2,6-dimethyl-1,4-phenylene oxide). *Polymer*, **41**, 9191.
45 Guo, Y.L. and Bradshaw, R.D. (2007) Isothermal physical aging characterization of polyether-ether-ketone (PEEK) and polyphenylene sulfide (PPS) films by creep and stress relaxation. *Mech. Time-Dependent Mater.*, **11**, 61.
46 Cowie, J.M.G., McEwan, I., McEwen, I.J., and Pethrick, R.A. (2001) Investigation of hydrogen-bonding structure in blends of poly(N-vinylpyrrolidone) with poly(vinyl acetate-co-vinyl alcohol) using positron annihilation. *Macromolecules*, **34**, 7071.
47 Vernel, J., Rychwalski, R.W., Pelisek, V., Saha, P., Schmidt, M.K., and Maurer, F.H.J. (1999) Physical aging in poly (ethylene oxide)/atactic-poly(methyl methacrylate) blends. *Thermochim. Acta*, **342**, 115.
48 Asaletha, R., Bindu, P., Aravind, I., Meera, A.P., Valsaraj, S.V., Yang, W.M., and Thomas, S. (2008) Stress-relaxation behavior of natural rubber/polystyrene and natural rubber/polystyrene/natural rubber-graft-polystyrene blends. *J. Appl. Polym. Sci.*, **108**, 904.
49 Morales, E. and Acosta, J.L. (1995) Enthalpy relaxation in poly(propylene oxide)/poly(ethylene oxide) blends. *Polym. J.*, **27**, 226.

**50** Goodwin, A.A. (1999) Thermal properties of a thermoplastic polyimide blend. *J. Appl. Polym. Sci.*, **72**, 543.

**51** Campbell, J.A., Goodwin, A.A., Mercer, F.W., and Reddy, V. (1997) Studies on a miscible polyimide blend. *High Perform. Polym.*, **9**, 263.

**52** Hay, J.N. (1992) Enthalpy relaxation in amorphous and crystalline polymers. Polyaryl ether ether ketone blends. *Prog. Colloid. Polym. Sci.*, **87**, 74.

**53** Breach, C.D., Folkes, M.J., and Barton, J.M. (1992) Physical ageing of an epoxy resin/polyethersulphone blend. *Polymer*, **33**, 3080.

**54** Ho, T., Mijovic, J., and Lee, C. (1991) Effect of structure on stress relaxation of polymer blends in glassy state. *Polymer*, **32**, 619.

**55** Mijovic, J., Devine, S.T., and Ho, T. (1990) Physical aging in poly(methyl methacrylate)/poly(styrene-co-acrylonitrile) blends. Part I: stress relaxation. *J. Appl. Polym. Sci.*, **39**, 1133.

**56** Mijovic, J. and Ho, T. (1993) Proposed correlation between enthalpic and viscoelastic measurements of structural relaxation in glassy polymers. *Polymer*, **34**, 3865.

**57** Cowie, J.M.G. and Ferguson, R. (1989) Physical ageing studies in polymer blends. 2. Enthalpy relaxation as a function of ageing temperature in a poly (vinyl methyl ether)/polystyrene blend. *Macromolecules*, **22**, 2312.

**58** Oudhuis, A.A.C.M. and ten Brinke, G. (1992) Enthalpy relaxations and concentration fluctuations in blends of polystyrene and poly(oxy-2,6-dimethyl-1,4-phenylene). *Macromolecules*, **25**, 698.

**59** Arrighi, V., Cowie, J.M.G., Ferguson, R., McEwen, I.J., McGonigle, E.-A., Pethrick, R.A., and Princi, E. (2006) Physical ageing in poly(4-hydroxy styrene)/poly (vinyl methyl ether) blends. *Polym. Int.*, **55**, 749.

**60** Cowie, J.M.G., Arrighi, V., and McGonigle, E.-A. (2005) Enthalpy relaxation in poly(4-hydroxystyrene)/poly (methyl methacrylate) blends. *Macromol. Chem. Phys.*, **206**, 767.

**61** Cameron, N.R., Cowie, J.M.G., Ferguson, R., and McEwan, I. (2001) Enthalpy relaxation of styrene–maleic anhydride (SMA) copolymers. 2. Blends with poly (methyl methacrylate) (PMMA). *Polymer*, **42**, 6991.

**62** Cameron, N., Cowie, J.M.G., Ferguson, R., Ribelles, J.L.G., and Estelles, J.M. (2002) Transition from miscibility to immiscibility in blends of poly(methyl methacrylate) and styrene-acrylonitrile copolymers with varying copolymer composition: a DSC study. *Eur. Polym. J.*, **38**, 597.

**63** Morales, E. and Acosta, J.L. (1995) Enthalpy relaxation in poly(propylene oxide)/poly(ethylene oxide) blends. *Polym. J.*, **27**, 226.

**64** Jong, S.R. and Yu, T.L. (1997) Physical aging of poly (ether sulfone)-modified epoxy resin. *J. Polym. Sci. Polym. Phys.*, **35**, 69.

**65** Hong, B.K., Jo, W.H., and Kim, J. (1998) Miscibility of syndiotactic polystyrene/ atactic polystyrene blends by crystallization kinetics and enthalpy relaxation. *Polymer*, **39**, 3753.

**66** ten Brinke, G., Oudhuis, L., and Ellis, T.S. (1994) The thermal characterization of multi-component systems by enthalpy relaxation. *Thermochm. Acta*, **238**, 75.

**67** ten Brinke, G., Karasz, F.E., and MacKnight, W.J. (1983) Phase-behavior in co-polymer blends – poly(2,6-dimethyl-1,4-phenylene oxide) and halogen-substituted styrene co-polymers. *Macromolecules*, **16**, 1827.

**68** Paul, D.R. and Barlow, J.W. (1984) A binary interaction model for miscibility of copolymers in blends. *Polymer*, **25**, 487.

**69** Chai, C.K. and McCrum, N.G. (1980) Mechanism of physical ageing in crystalline polymers. *Polymer*, **21**, 706.

**70** Cowie, J.M.G., Harris, S., Gomez-Ribelles, J., Mesegner, J.M., Romero, F., and Torregrosa, C. (1999) Glass transition and structural relaxation in polystyrene poly(2,6-dimethyl-1,4-phenylene oxide) miscible blends. *Macromolecules*, **32**, 4430.

**71** Angell, C.A. (1991) Relaxation in liquids, polymers and plastic crystals – strong

fragile patterns and problems. *J. Non. Cryst. Solids*, **131**, 13.
**72** Breach, C.D., Folkes, M.J., and Barton, J.M. (1992) Physical ageing of an epoxy resin/polyethersulphone blend. *Polymer*, **33**, 3080.
**73** Tool, A.Q. (1946) Relation between inelastic deformability and thermal expansion of glass in its annealing range. *J. Am. Ceram. Soc.*, **29**, 240.
**74** Tool, A.Q. (1948) Effect of heat-treatment on the density and constitution of high-silica glasses of borosilicate type. *J. Am. Ceram Soc.*, **31**, 177.
**75** (a) Kovacs, A.J. (1963) Transition vitreuse dans les polymeres amorphes. Etude phenomenologique. *Fortschr. Hochpolym. Forsch.*, **3**, 394; (b) Kovacs, A.J., Aklonis, J.J., Hutchinson, J.M., and Ramos, A.R. (1979) Isobaric volume and enthalpy recovery of glasses. II. A transparent multiparameter theory. *J. Polym. Sci. Polym. Phys. Ed.*, **17**, 1097.
**76** Kovacs, A.J., Stratton, R.A., and Ferry, J.D. (1963) Dynamic mechanical properties of polyvinyl acetate in shear in the glass transition temperature range. *J. Phys. Chem.*, **67**, 152.
**77** Bernatz, K.M., Giri, L., Simon, S.L., and Plazek, D.J. (1999) Physical aging by periodic creep and interrupted creep experiments. *J. Chem. Phys.*, **111**, 2235.
**78** Brunacci, A., Cowie, J.M.G., and McEwen, I.J. (1998) Enthalpy relaxation in glassy polystyrenes – Part 3 – stress and enthalpy relaxation in poly(4-methylstyrene) and poly(4-chlorostyrene). *J. Chem. Soc., Faraday Trans.*, **94**, 1105.
**79** (a) Brunacci, A., Cowie, J.M.G., Ferguson, R., and McEwen, I.J. (1997) Enthalpy relaxation in glassy polystyrenes: 1. *Polymer*, **38**, 865; (b) Brunacci, A., Cowie, J.M.G., Ferguson, R., and McEwen, I.J. (1997) Enthalpy relaxation in glassy polystyrenes: 2. *Polymer*, **38**, 3263.
**80** Cowie, J.M.G., McEwen, I.J., and Matsuda, S. (1998) Stress relaxation and physical ageing in a blend of poly(styrene-co-acrylonitrile) and poly(methyl methacrylate). *J. Chem. Soc., Faraday Trans.*, **94**, 3481.
**81** Eldrup, M., Lightbody, D., and Sherwood, J.N. (1981) The temperature dependence of positron lifetimes in solid pivalic acid. *Chem. Phys.*, **63**, 51.
**82** Cowie, J.M.G., McEwan, I., McEwen, I.J., and Pethrick, R.A. (2001) Investigation of hydrogen-bonding structure in blends of poly(N-vinylpyrrolidone) with poly(vinyl acetate-co-vinyl alcohol) using positron annihilation. *Macromolecules*, **34**, 7071.
**83** Bartos, J., Müller, J., and Wendorff, J.H. (1990) Physical ageing of isotropic and anisotropic polycarbonate. *Polymer*, **31**, 1678.
**84** Meyer, E.F., Jamieson, A.M., Simha, R., Palmen, J.H.M., Booij, H.C., and Maurer, F.H.J. (1990) Free volume changes in polyvinyl acetate measured by fluorescence spectroscopy. *Polymer*, **31**, 243.
**85** Royal, J.S. and Torkelson, J.M. (1992) Molecular-scale asymmetry and memory behavior in poly(vinyl acetate) monitored with mobility-sensitive fluorescent molecules. *Macromolecules*, **25**, 1705.
**86** Royal, J.S. and Torkelson, J.M. (1993) Physical ageing effects on molecular-scale polymer relaxations monitored with mobility-sensitive fluorescent molecules. *Macromolecules*, **26**, 5331.
**87** McGonigle, E.-A., Daly, J.H., Jenkins, S.D., Liggat, J.J., and Pethrick, R.A. (2000) Influence of physical ageing on the molecular motion and structural relaxation in poly(ethylene terephthalate) and related polyesters. *Macromolecules*, **33**, 480.
**88** Atkinson, J.R., Biddlestone, F., and Hay, J.N. (2000) An investigation of glass formation and physical ageing in poly (ethylene terephthalate) by FT-IR spectroscopy. *Polymer*, **41**, 6965.
**89** Rittigstein, P., Priestley, R.D., Broadbelt, L.J., and Torkelson, J.M. (2007) Model polymer nanocomposites provide an understanding of confinement effects in real nanocomposites. *Nat. Mater.*, **6**, 278.
**90** Rittigstein, P. and Torkelson, J.M. (2006) Polymer-nanoparticle interfacial interactions in polymer nanocomposites: confinement effects on glass transition temperature and suppression of physical

ageing. *J. Polym. Sci. Polym. Phys.*, **44**, 2935.

**91** Priestley, R.D., Rittigstein, P., Broadbelt, L.J., Fukao, K., and Torkelson, J.M. (2007) Evidence for the molecular-scale origin of the suppression of physical ageing in confined polymer: fluorescence and dielectric spectroscopy studies of polymer–silica nanocomposites. *J. Phys. Condens. Matter*, **19**, 205120.

**92** Schmidt, P., Dybal, J., Turska, E., and Kulczycki, A. (1991) Conformational structure of bisphenol A polycarbonate studied by infra-red spectroscopy. *Polymer*, **32**, 1862.

**93** Lu, J., Wong, Y., and Shen, D. (2000) Infrared spectroscopic and modulated differential scanning calorimetric study of physical aging in bisphenol A polycarbonate. *Polym. J.*, **32**, 610.

**94** Tang, J.K.Y. and Lee-Sullivan, P. (2008) Observation of physical ageing in a polycarbonate and acrylonitrile-butadiene-styrene blend. *J. Appl. Polym. Sci.*, **110**, 97.

**95** Roe, R.J. and Curro, J.J. (1983) Small angle X-ray scattering study of density fluctuation in polystyrene annealed below the glass transition temperature. *Macromolecules*, **16**, 428.

**96** Song, H.-H. and Roe, R.-J. (1987) Structural change accompanying volume change in amorphous polystyrene as studied by small and intermediate angle X-ray scattering. *Macromolecules*, **20**, 2723.

**97** Faivre, A., David, L., Vassoille, R., Vigier, G., Etienne, S., and Geissler, E. (1996) Electronic density fluctuations in disordered systems. 1. Effect of thermal treatments on the dynamics and local microstructure of poly(methyl methacrylate). *Macromolecules*, **29**, 8387.

**98** McGonigle, E.-A., Cowie, J.M.G., Arrighi, V., and Pethrick, R.A. (2005) Enthalpy relaxation and free volume changes in aged styrene copolymers containing a hydrogen bonding co-monomer. *J. Mater Sci.*, **40**, 1869.

**99** Cowie, J.M.G., Devlin, B.G., and McEwen, I.J. (1993) Surface enrichment in PS PVME blends. 2. The effect of specific interactions in the bulk mixture. *Polymer*, **34**, 4130.

**100** Maurer, F.H.J., Palmen, J.H.M., and Booij, H.C. (1985) Generalized stress relaxation behaviour and physical ageing in heterogeneous amorphous polyblends. *Rheol. Acta*, **24**, 243.

**101** Booij, H.C. and Palmen, J.H.M. (1978) Viscoelasticity of ABS samples differing in thermal history. *Polym. Eng. Sci.*, **18**, 781.

**102** Cheng, T.W., Keskkula, H., and Paul, D.R. (1992) Thermal ageing of impact-modified polycarbonate. *J. Appl. Polym. Sci.*, **45**, 531.

# 7
# Nanoparticle/Polymer Blends: Theory and Modeling

*Valeriy V. Ginzburg*

## 7.1
## Introduction

In recent years, the use of nanoparticles as modifiers to polymeric materials has become more and more widespread [1–8] (see Table 7.1 for selected examples). Although, strictly speaking, "nanoparticles" have been used as additives for many years (e.g., medieval stained-glass windows were painted with the use of submicron colloidal glass particles, and the personal care industry used submicron-sized oxide particles for decades), it was only in the last 20 or so years that "nanotechnology" became a specialized field. In particular, polymer–inorganic "nanocomposites" have received special attention since the pioneering work of Toyota researchers [9] in which particles of montmorillonite clay were successfully compounded ("exfoliated") with a Nylon-6 polymer matrix. The resulting composite was characterized by a 2–4× increase in Young's modulus (compared to the pristine polymer) with only 3–6 wt% filler loading (in a conventional composite, a similar increase in modulus or strength would require at least 25–30 wt% filler loading). Similar advances were obtained with other matrices (epoxy, polyurethane, polyethylene, and polypropylene), even though, in most instances, achieving a good nanoparticle dispersion or exfoliation was a non-trivial chemical engineering problem. Now, the issues of the clay particle dispersion in polymer matrices, as well as the properties of resulting composite materials, are fairly well understood; we refer the readers to several reviews discussing both experimental and theoretical developments in the field [10–19]. Note, however, that most research concentrated on idealized homopolymer/clay systems; later in this chapter, we touch on the subject of clay/polymer blend ternary composites and briefly discuss corresponding thermodynamic and dynamic aspects.

Of course, clay particles are not the only nanofillers used today. Other nanofillers include carbon particles (carbon black and carbon nanotubes), various inorganic oxides (zirconia, titania, silica, etc.), metal nanoparticles (gold, silver), and some other, more exotic ones (e.g., polymeric nanoparticles such as dendrimers). In general, we can distinguish nanoparticles by:

*Encyclopedia of Polymer Blends, Volume 1: Fundamentals.* Edited by Avraam I. Isayev
Copyright © 2010 WILEY-VCH Verlag GmbH & Co. KGaA, Weinheim
ISBN: 978-3-527-31929-9

**Table 7.1** Nanofillers for polymer/particle blends and their applications (selected examples).

| Particle type | Particle shape and size | Applications |
|---|---|---|
| Carbon black | Sphere, radius $R \sim 20$ nm (primary particles) | Conductive coatings and paints |
| | Fractal aggregates (secondary clusters) | Automotive sealants and adhesives |
| Carbon nanotubes | Rods, length $L > 100$ nm, thickness $T \sim 1$ nm | Conductive coatings and materials |
| Silica particles | Spheres, radius $R \sim 5$–$100$ nm | Toughened, flame retardant polymer materials |
| Nanoclays | Platelets, width $H \sim 50$–$5000$ nm, thickness $T \sim 1$ nm | Hardened, toughened, flame retardant polymer materials |
| Metal (Au, Ag, Pt) nanoparticles | Spheres, radius $R \sim 2$–$100$ nm | Sensors, electronic applications, catalysts |

1) characteristic size ($R_P$) and aspect ratio $A$ (ratio of the largest particle dimension to the smallest),
2) surface chemistry,
3) surface charge density.

In colloidal science, particles are often characterized by means of the so-called Hamaker constant [20] that characterizes the strength of the particle–particle attraction in a particular medium, as well as the so-called Zeta-potential (see, e.g., Tadros [21]) that characterizes the strength of electrostatic repulsion. Typically, electrostatic forces are more significant in water and polar solvents, and play a less important role when nanoparticles are blended with polymers; however, it is conceivable that electrostatic interactions (including charge–dipole and dipole–dipole) could impact local molecular arrangements near particle surfaces. For particles dispersed in polar solvents, physics of electrostatic interaction is reasonably well understood [21–25], even though calculation of all relevant parameters and prediction of the dispersion stability is often technically challenging. For particles dispersed in polymers, such theoretical understanding is still in its infancy. Thus, in this chapter, we concentrate less on the influence of surface charge and more on the role of surface chemistry and particle size.

The size of the particles is critically important in judging the morphology of the final composite material. In general, colloidal particles have a strong tendency to aggregate (or precipitate) when mixed with polymers. The attractive force between two particles depends, as mentioned above, on the electrostatic interaction between the particles, as well as on the van der Waals attractive forces (as characterized by Hamaker constant); in addition, there is also a strong entropic force pushing the polymer away from the particle surfaces. The latter force (sometimes known as depletion attraction) is universal (independent of the polymer and particle chemistry) and stems from the fact that the number of possible conformations of long polymer chains is substantially restricted as the chain sites near a surface. In the case

when entropic forces are the only ones present (e.g., polystyrene nanospheres in a polystyrene melt – see Mackay *et al.* [26]), it was shown that spherical nanoparticles disperse uniformly in a polymer if their radius, $R_P$, is smaller than the radius of gyration of the matrix polymer chains, $R_g$. On the other hand, those particles whose radius was larger than $R_g$ aggregated into large "chunks" or agglomerates, leading to opaque, non-homogeneous materials. Similar results have been obtained in several theoretical and experimental studies of nanoparticles in block copolymers [27–33] – smaller nanoparticles were predicted to "fit into" the microphase-separated structures, while the larger ones could either template new structures or result in a macrophase separation. Similar thermodynamic analysis has been performed recently for the mixture of spherical nanoparticles and binary polymer blend, and several other systems. Thus, in Section 7.2, we describe theoretical and modeling approaches to prediction of equilibrium phase behavior and morphologies of polymer/nanoparticle systems, emphasizing mesoscale simulations and theories (1–50 nm range).

Of course, morphology of the composite is important mainly as it serves to shape and determine the ultimate physical or mechanical properties of the material. Thus, particle arrangements could play a role in determining modulus and strength (in the case of polymer/clay nanocomposites), electrical conductivity or dielectric constant (polymer/metal or polymer/carbon composites), increased viscosity of melts or solutions (polymer/carbon black adhesives), and so on. In many instances, it is not enough to have a good dispersion of the particles; it is also important to have specific morphology to achieve desired properties. This is an exciting topic, and there are numerous studies aimed at elucidating the morphology–property relationships. We review some of those models in Section 7.3.

To conclude this brief introduction, we note that there are many other aspects not covered in this chapter that are nevertheless important for practical applications. Those include material purity and polydispersity, processing, environmental health and safety, toxicology, and others. Clearly, as we understand more and more about the specific mechanisms of nanoparticle/human cell interactions, there will be new changes in the chemical engineering, processing, and preparation of nanocomposite materials. For the purposes of this chapter, however, we concentrate mainly on the simplified "equilibrium" aspects of nanocomposite polymer blends, from morphology and phase diagrams to mechanical and physical properties.

## 7.2
## Morphology of Polymer Blends with Nanoparticles

### 7.2.1
### Phase Behavior of Binary Polymer Blends

Before discussing the phase behavior of ternary nanoparticle/polymer/polymer mixtures it is useful to briefly recall the fundamentals governing the phase behavior of binary polymer blends. The simplest model describing phase behavior of such

blends is due to Flory [34] and Huggins [35]. According to Flory–Huggins theory, the free energy, $F$, of a binary blend is given by a simple expression:

$$\frac{F v_{\text{ref}}}{k_B T V} = \frac{\varphi_A}{N_A} \ln \varphi_A + \frac{\varphi_B}{N_B} \ln \varphi_B + \chi_{AB} \varphi_A \varphi_B \tag{7.1}$$

where

$N_A$ and $N_B$ are chain lengths of the A- and B-homopolymers,
$\varphi_A$ and $\varphi_B$ are volume fractions of the A- and B-homopolymers ($\varphi_A + \varphi_B = 1$),
$v_{\text{ref}}$ is the "reference" volume of one monomer unit (it is assumed that monomer units of A and B have the same sizes),
$V$ is the total volume of the system,
$T$ is temperature (in kelvin),
$k_B$ is the Boltzmann's constant.

The Flory–Huggins interaction parameter, $\chi_{AB}$, has the meaning of mixing enthalpy divided by the absolute temperature. Sometimes, it is related to solubility parameters of polymers A and B via the following expression [36, 37]:

$$\chi_{AB} = \frac{v_{\text{ref}}}{k_B T} (\delta_A - \delta_B)^2 \tag{7.2}$$

However, in practice, to fit experimental phase diagrams, one has to make $\chi$ a more complex (often, non-monotonic) function of $T$. Sometimes, researchers use a concentration-dependent Flory–Huggins interaction parameter – while this is clearly contrary to the spirit of the original Flory–Huggins theory, it can be useful to successfully fit experimental diagrams (see, e.g., Reference [38]). For more detailed discussion see, for example, References [38–40].

The above theory is based on the idea of incompressible polymer melt. Various alternative formalisms have been proposed where free energy explicitly depended on the pressure and the densities of pure components (see, e.g., Ruzette *et al.* [41]):

$$\frac{\Delta G}{V} = k_B T \left[ \frac{\varphi_A}{N_A v_A} \ln \varphi_A + \frac{\varphi_B}{N_B v_B} \ln \varphi_B \right] + \varphi_A \varphi_B [\tilde{\varrho}_A \delta_{A0} - \tilde{\varrho}_B \delta_{B0}]^2 \tag{7.3}$$

Here, $\Delta G$ is the Gibbs free energy of mixing. The "equal volume restriction" for A and B monomers has been removed, and $v_A$ and $v_B$ now represent the "nominal" volumes of A and B monomers, respectively. At a given pressure (say, 1 atm), the actual volume per monomer is greater than the "nominal" volume; the inverse of the ratio of "actual" to "nominal" volume is called reduced density, $\tilde{\varrho}$, and it can be determined from thermodynamic data for a pure homopolymer. Therefore, effective interactions could depend not only on "ideal" solubility parameters but also on the polymer equation of state and compressibility. Thus, while the conventional Flory–Huggins theory typically predicts a so-called upper critical solution temperature (UCST) behavior (Figure 7.1a), the pressure-dependent approach allows, in principle, for other phase diagrams such as lower critical solution temperature (LCST) (Figure 7.1b) or mixed (combined LCST and UCST) diagrams (Figure 7.1c and d). Despite their potential utility, "compressible" extensions of Flory–Huggins theory

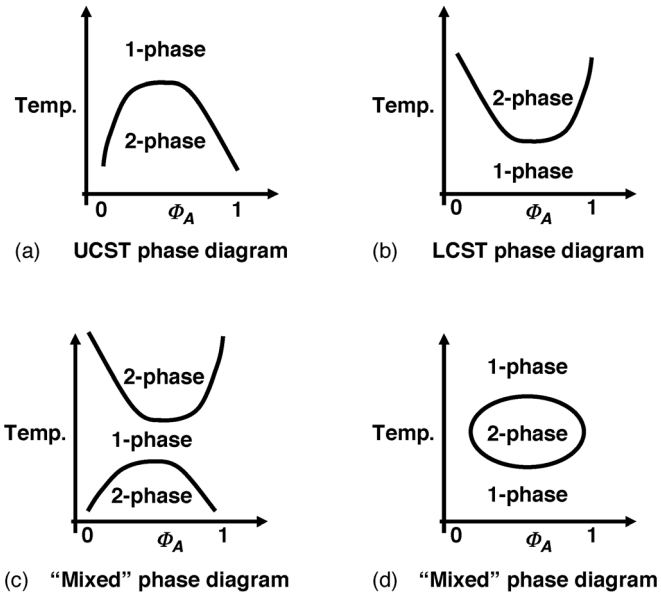


**Figure 7.1** Schematic of various types of phase diagrams in binary polymer mixtures: (a) upper critical solution behavior (UCST); (b) lower critical solution behavior (LCST); (c) and (d) mixed phase diagrams with both upper and lower critical temperatures.

still have not found widespread application. Below, we will be mainly using the classical "incompressible" Flory–Huggins theory and consider its possible extensions when nanoparticles are introduced into the system.

### 7.2.2
### Simple Arguments for Nanoparticles as Compatibilizers

Consider a two-component (A + B) polymer blend in a two-phase region. Even if the mixture was homogeneous at time $t = 0$, as time goes on it will undergo spontaneous phase separation into A-rich and B-rich domains. The interfaces between these domains cost energy (one denotes this energy per unit area as interfacial tension, $\gamma_{AB}$), so the domains undergo coarsening with time so as to reduce the density of interfaces [the quantity $L(t)$ defined as the total volume divided by the total interfacial area in this volume can serve as a good measure of characteristic domain size; its increase as function of time is a measure of the speed with which the phase separation proceeds]. Reducing the interfacial tension by adding "compatibilizers" (e.g., AB diblock copolymers, AB random copolymers, etc. [42]) could lead to a reduction in the rate of domain growth and perhaps even to its saturation. In particular, when interfacial tension is reduced to zero, the system forms a unique phase called a microemulsion, where A and B homopolymers are locally separated into domains, but these domains – like in the case of block copolymer melts – have finite average sizes [43–45]. It has been shown both

theoretically [44] and experimentally [45] that a ternary A-homopolymer/B-homopolymer/AB-diblock copolymer mixture could form microemulsions in some narrow composition ranges.

Could nanoparticles act in a similar fashion as compatibilizers? As discussed by Glogowski *et al.* [46] and Chung *et al.* [47], such a mechanism is certainly feasible. According to a simple model first proposed by Pieranski [48] and later extended by Binks and Clint [49], a single spherical particle, P, favors being positioned at the interface between the two homopolymer domains, A and B, provided that the polymer–polymer interfacial tension, $\gamma_{AB}$, is greater than the absolute value of the difference between the two particle–polymer interfacial tensions, $\gamma_{AP}$ and $\gamma_{BP}$: $\gamma_{AB} > |\gamma_{AP} - \gamma_{BP}|$. If this condition is satisfied, the energy change, $\Delta E$, for moving a particle from a bulk phase (A) to the interface is given by:

$$\Delta E = -\pi R_P^2 \frac{[\gamma_{AB} + (\gamma_{AP} - \gamma_{BP})]^2}{\gamma_{AB}} \tag{7.4}$$

where $R_P$ is the particle radius. The distribution of nanoparticles between the interface and the bulk phases is dictated by the usual Boltzmann factor:

$$\frac{n(\text{int})}{n(\text{bulk})} = \exp\left[-\frac{\Delta E}{k_B T}\right]$$

where $n$(int) is the number of nanoparticles segregated to the interfaces, and $n$(bulk) is the number of nanoparticles dispersed within bulk A and B phases. Thus, the probability of finding a nanoparticle at an interface increases dramatically if: (i) the particle is sufficiently amphiphilic, $|\gamma_{AP} - \gamma_{BP}| << \gamma_{AB}$, and (ii) particle radius is sufficiently large. In particular, changing particle radius could have a great impact on the probability of particle "hopping" between the interface and the bulk versus particles "immobilized" at the interface and creating a strong, rigid monolayer. The latter scenario, obviously, is more conducive to the formation of microemulsions (or, at least, well-stabilized emulsions). Similarly, the type of particle surface treatment helps to determine the interfacial tension balance, as discussed by Glogowski *et al.* [46]. Some possible nanoparticle surface treatments are sketched in Figure 7.2. An unmodified nanoparticle 1 (e.g., metal) would likely segregate into the polymeric phase with which it has lower interfacial tension (probably the more polar polymer of the pair). To change the particle preference, one could attach (covalently or otherwise) non-polar ligands; such a particle (2 in Figure 7.2) would have a preference to a less polar polymer. By attaching A-type and B-type ligands that can segregate along the particle surface ("Janus" particles) (4), or by grafting random AB-copolymer ligands (3), one can design particles with strong preference to the interface.

The above discussion mainly applied to nanospheres. It can also be adapted to nanorods and nanoplatelets, where the drive towards the interfaces could be even stronger. Preliminary evidence (see, e.g., Gelfer *et al.* [50]) shows that clay nanoplatelets dispersed in polymer blends indeed have a tendency to segregate to interfaces and "jam" them, thus effectively compatibilizing the blend. However, theoretical understanding of this process is not yet fully developed.

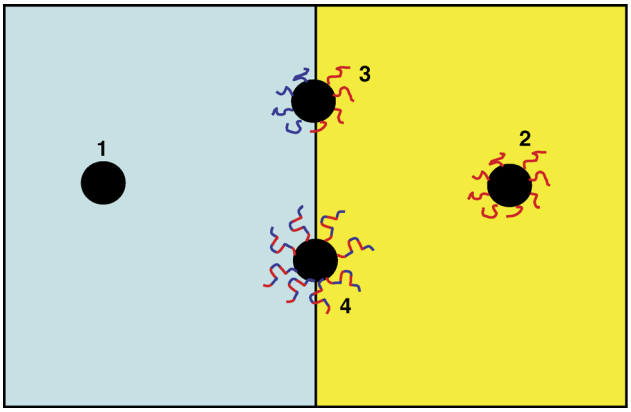


**Figure 7.2** Influence of surface coverage of a nanoparticle on its localization in a binary polymer blend. Here, the light blue region corresponds to a more polar polymer, and the yellow region to a more hydrophobic polymer. Unmodified metal nanoparticle (1) would tend to segregate into the more polar (light blue) phase. A similar particle covered with a hydrophobic ligand (2) would segregate into the more hydrophobic (yellow) phase. Particles covered with random amphiphilic copolymer (3) or "Janus" particles (4) would tend to localize at or near the interfaces.

The enthalpic considerations on which Eq. (7.4) is based are probably sufficient to describe relatively large nanoparticles with "amphiphilic" surface chemistry (e.g., particles covered with random AB-copolymers). However, for a particle with smaller radii (comparable to the polymer radius of gyration) and/or more preferential surface treatment, interfacial segregation is not very strong. In modeling their dynamic and thermodynamic behavior in polymers, we need to consider carefully both enthalpic and entropic factors, as will be discussed in the following sections.

### 7.2.3
### Influence of Nanoparticles on the Dynamics of Phase Separation in Polymer Blends

Before reviewing thermodynamic models of particle/polymer mixtures, we consider a slightly different *dynamic* problem: how can the addition of particles influence the phase separation of two polymers? Such a problem statement assumes that: (i) particle addition does not impact the incompatibility of the polymers in the blend and (ii) particles can impact the mobility of nearby polymer molecules. Numerous papers and reviews deal with this subject, and our discussion here certainly will not be exhaustive, but will provide a brief overview of the major results.

When a binary polymer blend (A-polymer and B-polymer) is rapidly quenched from one-phase to the two-phase region of the phase diagram (e.g., by a rapid temperature change), the system undergoes phase separation into A-rich and B-rich domains. It is often convenient to characterize the extent of phase separation by measuring the characteristic domain size as function of time, $L(t)$. (Characteristic domain size could be defined as, for example, total volume divided by the total

interfacial area.) In the 1980s, extensive simulations showed that if the dynamics of the phase separation are conserved and purely diffusive (Model B of the Hohenberg–Halperin classification – see References [51, 52]), at late times $L(t)$ *asymptotically* grows as $t^{1/3}$. [The behavior at early times can be more complicated and depends on whether the initial phase separation proceeds via spinodal decomposition (SD) or nucleation and growth (N&G) mechanism – but we will not go into such details here.] This Lifshitz–Slyozov [53] exponent of $^1/_3$ is observed in both two- and three-dimensional systems with conserved diffusive dynamics. If one includes hydrodynamics in addition to diffusion, phase separation could dramatically speed up, resulting in almost linear growth, $L(t) \propto t^1$ [54].

The addition of particles provides interesting complications to the problem. In 1994, Tanaka, Lovinger, and Davis [55] observed experimentally that the rate of phase separation dramatically slows down in the presence of immobile glass particles. Karim and coworkers have observed similar effects in both blends [56] and microphase-separating block copolymers [57]; they also were able to visualize (by means of transmission electron microscopy) that the particles nucleate transient circular phase-separation patterns that later transform into the bicontinuous or lamellar patterns. Several simulation studies [58–61] provided insight into the mechanism of the observed particle-induced slowing down of the phase separation dynamics, suggesting that the immobile particles can pin the interfaces. Immobile point-like particles create obstacles for the interface growth, so that there is a "saturation" domain size, $L^* \cong n_P^{-1/d}$, where $n_P$ is the number density of particles, and $d$ is the space dimensionality.

The picture becomes more complicated when particles are mobile. Experimental studies of nanoparticles in binary polymer films (see, for example, Composto *et al.* [47, 62]) have demonstrated some slowing down of the phase separation dynamics compared to the pure blend – although the trend was not as pronounced as in the case of "pinned" particles. Ginzburg *et al.* [63–68] have developed a hybrid simulation formalism combining a cell dynamical systems (CDSs) model for the polymers with appropriate Langevin dynamics for the particles. Their simulations mainly concerned the particles with affinity to one of the polymers (A-polymer). In the original studies [63, 64], particles were allowed to move in a purely diffusive fashion, leading to the substantial slowing down of the phase separation. Subsequently, it was recognized that the movement of the particles must also incorporate the driving force pushing them towards the middle of the A-rich domains ("strong coupling" in the notation of Balazs *et al.* [68]). In that case, particles with affinity towards one of the polymers provide little if any slowing down of the phase separation. This analysis has been essentially confirmed by large-scale Langevin dynamics, molecular dynamics and dissipative particle dynamics (DPD) simulations of Laradji and coworkers [69–72] (see Figure 7.3 for simulated blend morphologies with and without nanoparticles, as well as optical micrographs of similar experimental system). Laradji and coworkers concluded also that nanoparticles with "neutral" surfaces (equal affinity towards A-polymer and B-polymer) could slow down the phase separation by "crowding" the interfaces and acting as weak surfactants. In Figure 7.4, the experimentally measured rate of domain

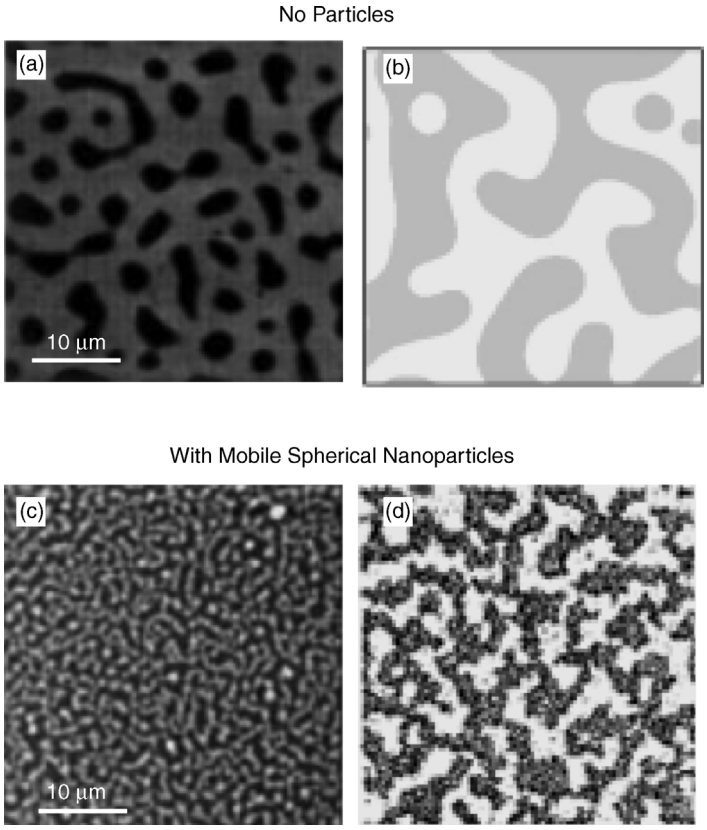


**Figure 7.3** Transient morphologies of phase-separating polymer blends with and without nanoparticles. (a) Optical micrograph of a phase-separating deuterated polystyrene (dPS)/polybutadiene (PB) 70 : 30 critical mixture after coarsening for 1510 min at 25 °C [40]; (b) snapshot of a Langevin dynamic simulation of a critical (50 : 50) AB-mixture, with A-rich phase as white, B-rich phase as gray [71]; (c) optical micrograph of a polystyrene (PS)/poly(vinyl methyl ether) (PVME) 80 : 20 critical mixture, with a very low amount of 100 nm silica beads, after coarsening at 145 °C for 30 min [56]; (d) snapshot of a Langevin dynamic simulation of a critical (50 : 50) AB mixture with a small fraction of B-coated nanospheres [71].

growth in a thin dPMMA/SAN film with and without nanoparticles [47] is contrasted with predictions from simulations of Laradji *et al.* [70, 71].

Laradji *et al.* [69–72] have also proposed that phase separation could be slowed down or even stopped completely if nanoparticles are strongly anisotropic (e.g., nanorods) – the latter result also agrees with the simulations of Peng *et al.* [73]. In that case, the interplay between enthalpic interactions (rods favoring the A-polymer) and steric interactions (strong anisotropy of the rods acting as templating agents for polymer domain morphology) creates metastable structures resembling microphase separated lamellae of block copolymers (Figure 7.5). Whether these structures represent thermodynamic equilibrium, mestastable states, or just kinetically trapped states is not yet fully understood.

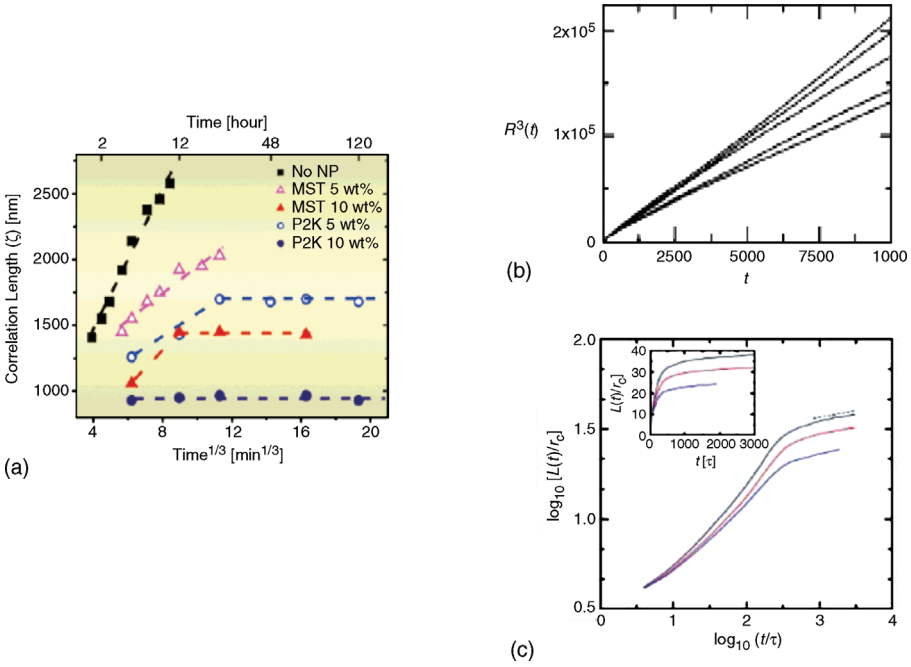


**Figure 7.4** Diffusion-controlled domain growth in phase-separating blends with and without nanoparticles. (a) Experimental data on phase separation dynamics in deuterated poly (methyl methacrylate) (dPMMA)/styrene-acrylonitrile (SAN) thin films, as a function of nanoparticle surface chemistry and loading [47]; (b) Langevin dynamics calculations of domain growth as a function of particle loading for the case of mobile spherical particles preferring one of the two components [71]; (c) dissipative particle dynamics (DPDs) simulations of domain growth as a function of particle loading for the case of mobile spherical particles preferring the interfaces [70].

### 7.2.4
### Thermodynamics of Binary Nanoparticle/Polymer Blends

Until recently, mixtures of nanoparticles and polymers were considered in the same way as mixtures of colloids and polymers. It has long been known that colloidal particles, when mixed with polymer melt or solution, exhibit a strong tendency to aggregate due to so-called depletion attraction [21, 74–76]. According to depletion–attraction theories, in the absence of enthalpic interactions, entropic restrictions placed on the polymer due to the presence of colloidal particles promote strong phase separation into (fluid) polymer-rich and (solid) particle-rich phases. These theories treat polymers effectively as spheres of radius $R_g$ and thus, as pointed out by Ramakrishnan *et al.* [77], fail as the particle radius, $R_P$, approaches $R_g$ from above. For mixtures of nanoparticles and polymers, however, $R_P$ and $R_g$ are of the same order of magnitude (1–50 nm), so new approaches are needed.

In their pioneering work, Mackay *et al.* [26] investigated dispersion of polymeric nanoparticles with polymer matrix of the same chemistry (PE, polyethylene; PS,

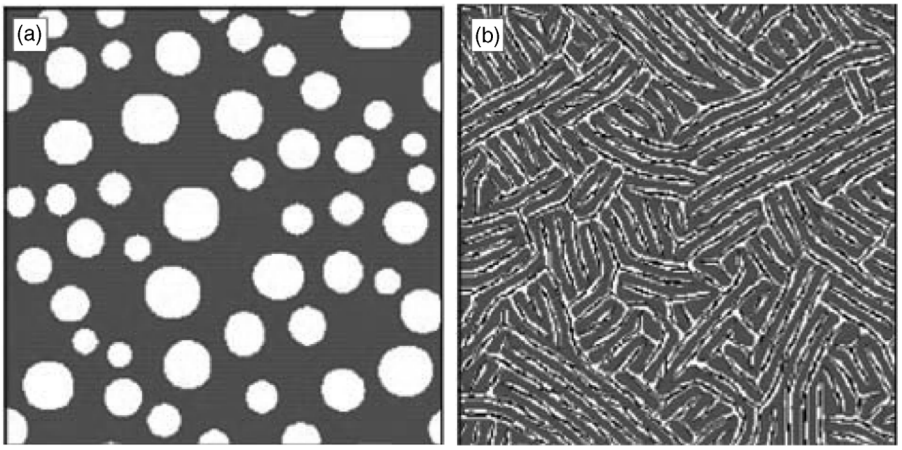


**Figure 7.5** Cell dynamical systems (CDSs) simulation of nanoscale rods in binary mixtures. (a) Late-stage morphology of a 30 : 70 AB-mixture without rods; (b) same system in which rods (with enthalpic preference to the minority A-polymer) have been added. The system with rods appears to form a metastable lamellar structure in which the rods form a percolated network [73].

polystyrene). By varying nanoparticle size and homopolymer molecular weight, they clearly demonstrated that the ratio $R_P/R_g$ is crucial in determining the dispersability of the particles (Figure 7.6a). Particles whose radius was larger than the matrix $R_g$ (region above the solid line) tended to precipitate; those whose radius was smaller (region below the solid line) tended to disperse. It was also found (Figure 7.6b) that when nanoparticles dispersed well they tended to swell the polymer molecules, thereby dramatically increasing their effective radius of gyration. A theoretical model of this behavior has been proposed recently by de Luzuriaga *et al.* [87, 88] (Figure 7.6c). In this model, the Flory–Huggins framework was adopted, and additional terms were introduced to account for the conformational entropy changes due to polymer–particle contacts and for particle–particle correlations at large particle volume fractions. While the agreement between theory and experiment is very encouraging, more research is still needed.

So far, the discussion centered on the "hard" spherical particles; the role of surface-grafted chains, if any, was not considered explicitly. Such chains, when grafted onto the particle surface, add both enthalpic and entropic contributions to the overall free energy. In a limit when particle radius, $R_P$, is large, the problem becomes similar to that of a flat sheet with grafted polymer brushes, dispersed in a polymer melt. This problem has been investigated extensively, primarily in the context of polymer–clay nanocomposites [13–19, 89–100]. Thus, it was shown by means of lattice self-consistent field theory (SCFT) [89–97], mesoscale density functional theory (DFT) [98, 100], and mesoscale Monte Carlo simulations [99] that the interaction between the particles can be repulsive ("exfoliation") or attractive ("aggregation") depending on the grafting density of the short chains on the particle surfaces, as well as the interaction parameter between the grafted chains and the matrix, and the ratio of the grafted chain

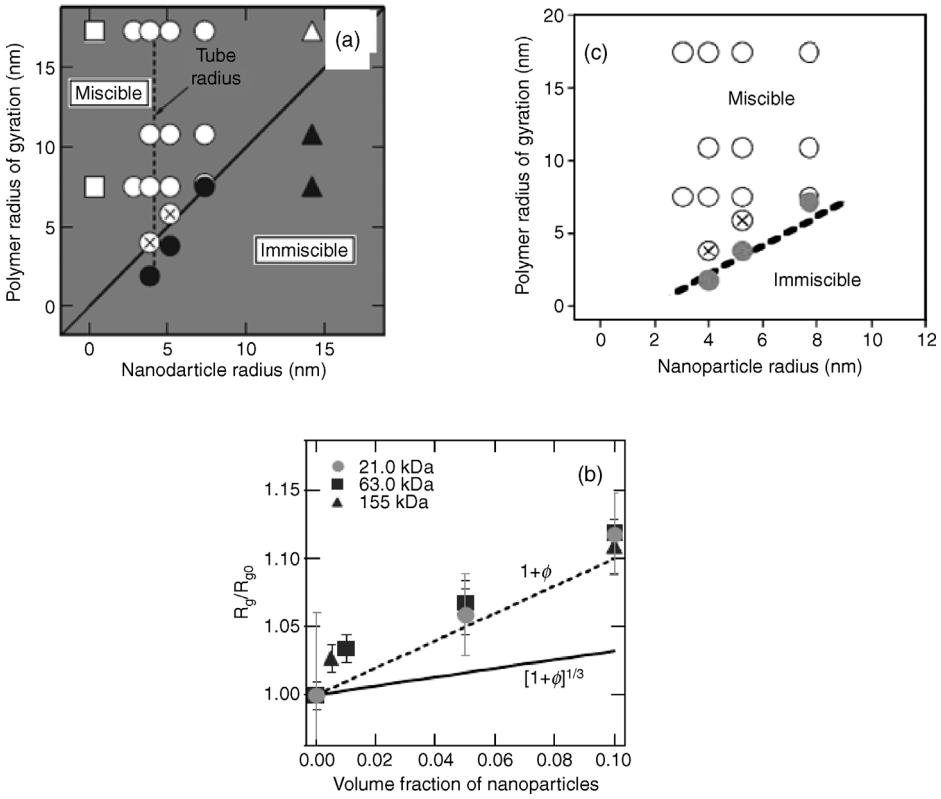


**Figure 7.6** Thermodynamics of nanospheres in homopolymers. (a) Experimental miscibility phase map for binary mixtures of polymer nanoparticles (PS, PP) with their chemically identical homopolymers [26]. (b) Estimated (from small-angle neutron scattering) polymer radius of gyration as function of nanoparticle loading [26]. (c) Theoretical interpretation of the miscibility map, based on the mean-field theory model of de Luzuriaga *et al.* [87].

length to the matrix chain length. For particles whose size is now comparable to the characteristic polymer dimensions, the analysis becomes even more complicated. Recently, Akcora *et al.* [101] have demonstrated that spherical nanoparticles with grafted polystyrene oligomers, when mixed into polystyrene melt, can form various anisotropic structures, from spherical aggregates to nanowires to nanosheets. In their study, experimental observations were compared with implicit solvent mesoscale Monte Carlo simulations. The interactions between grafted chains and matrix, as well as between the grafted monomers themselves, were set to be pure hard sphere, while those between the particles were described by means of a square-well attractive potential combined with hard sphere repulsive wall. Simulations and experiments were shown to be in a good qualitative agreement. The variety of structures demonstrated in this study is also consistent with earlier computational investigations of Glotzer and coworkers [102–105]. Still, our understanding of the mechanisms leading to the formation of various anisotropic structures is at a very early stage.

The above discussion concentrated mainly on the behavior of nanospheres. Understanding the thermodynamics of nanoplatelets and nanorods in polymers is even more complicated, since their anisotropy often leads to the breaking of orientational symmetry and formation of various ordered phases (nematic, smectic, columnar, etc.). We refer the readers to recent reviews [13, 78] for more information of these topics.

### 7.2.5
### Phase Behavior of Ternary Nanoparticle/Polymer/Polymer Mixtures

Let us now return to the case of a ternary mixture (nanoparticle/homopolymer A/homopolymer B) and consider its thermodynamic phase behavior. From dynamic simulations, we have already determined that nanoparticles can change at least the dynamics of phase separation if the polymers are immiscible. Can the particles modify the phase boundaries itself?

The true answer to this question is that everything depends on the particle size (and shape but, for simplicity, we concentrate on spherical particles here). If particle sizes are well in excess of characteristic polymer dimensions ($R_P \gg 50$ nm), particles would always aggregate and likely precipitate; thus, the system would separate into three phases: A-polymer-rich, B-polymer-rich, and particle-rich. (Note that in the particle-rich phase, interstitial volume needs to be occupied by the polymer; whether this is A-polymer, B-polymer, or a mixture of A and B would depend on the particle surface chemistry.) On the other hand, particles that are sufficiently small ($R_P < 10$ nm) can uniformly disperse in a polymer matrix, provided that van der Waals interactions between the particle and the polymer are not unfavorable.

One interesting result of this understanding is that, under some conditions, addition of nanoparticles to the binary blend could result in a two- to one-phase system transition. Such effects had been observed by Lipatov and coworkers [79, 80] as they added silica nanoparticles to a weakly incompatible binary blend and measured the critical temperature as function of the nanoparticles loading. It was shown that the transition temperature ("cloud point") could shift either up or down, depending on the specific system (Figure 7.7). Similar observations were made by several other groups [81–83].

To model such effects, Ginzburg [84], and He, Ginzburg, and Balazs [85] have formulated a simple theory that provides a description of the phase behavior of these three-component systems. This theory begins by writing a modified Flory–Huggins [34, 35] free energy for the three-component system:

$$\begin{aligned} f = \frac{F}{k_B T V} = {} & \frac{\varphi_A}{V_A}\ln\varphi_A + \frac{\varphi_B}{V_B}\ln\varphi_B + \frac{\varphi_P}{V_P}\ln\varphi_P \\ & + \chi_{AB}\varphi_A\varphi_B + \chi_{AP}\left(\frac{a}{R_P}\right)\varphi_A\varphi_P + \chi_{BP}\left(\frac{a}{R_P}\right)\varphi_B\varphi_P \\ & + \left[p\left(\frac{a}{R_P}\right)\right]\frac{\varphi_P}{V_P}\left[\Psi_{HS}(\varphi_P) + f_{entr}\right] \end{aligned} \tag{7.5}$$

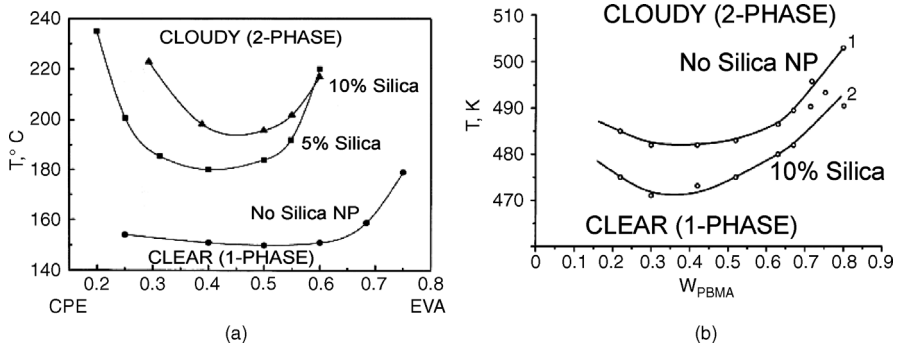


**Figure 7.7** Influence of nanoparticles on the phase behavior of binary blends. (a) Chlorinated polyethylene (CE)/poly(ethylene vinyl acetate) (EVA) blend shows an upward shift in the cloud point curve upon addition of fumed silica [79]; here, silica particles stabilize homogeneous phase. (b) Polystyrene (PS)/poly(butyl methacrylate) (PBMA) blend shows a downward shift upon addition of fumed silica [80]; here, silica particles destabilize the homogeneous phase and promote phase separation.

Here, most definitions are the same as in Eq. (7.1); $V_A$, $V_B$, and $V_P$ denote the volumes of A-homopolymer, B-homopolymer, and particle, respectively. The first line is the ideal mixing entropy contribution, and the second line sums up the enthalpic contributions, taking into account that particles interact with the polymers only at the surfaces. The third line describes two additional contributions due to the nature of the particles. The function $\Psi_{HS}(\varphi_P)$ is the Carnahan–Starling [86] non-ideal contribution to the free energy of hard spheres, given by:

$$\Psi_{HS}(x) = \frac{4x - 3x^2}{(1-x)^2} \tag{7.6}$$

Finally, the term called $f_{entr}$ deals with the changes in the conformational entropy of the polymers due to the presence of the particles. Mackay *et al.* [26], and Ginzburg and coworkers [84, 85], stipulated that $f_{entr}$ was mainly due to chain stretching in the vicinity of the particles. In particular, Ginzburg and coworkers [84, 85] used a simple scaling formula:

$$f_{entr} \cong (1-\varphi_P)\frac{3R_P^2}{Na^2} \tag{7.7}$$

where $N = N_A = N_B$ is the homopolymer chain length (assuming for simplicity that the lengths of the two homopolymers are equal). Finally, the function $p(x)$ serves to distinguish between a "solvent" ($R_P = a$, then $p = 0$) and "nanoparticle" ($R_P \gg a$, then $p \to 1$). For more details, see References [84, 85]. (Recently, a more complicated expression for $f_{entr}$ was proposed by Pomposo and coworkers [87, 88]; in their approach, both chain stretching and chain compression are accounted for; also, the reference state for the nanoparticle fluid is modified compared to the previous models.)

Note that the influence of particle surface chemistry is taken into account by means of introducing simple Flory–Huggins parameters between the particle and polymers

($\chi_{AP}$ and $\chi_{BP}$). We discuss various methods of determining those parameters in Section 7.2.7. In addition, the above model does not consider long-range particle–particle interactions, which could become fairly strong at moderate-to-high particle volume fractions. Even so, the model could provide at least a qualitative guidance regarding particle influence on the phase behavior of polymer blends.

In general, phase behavior of three-component systems is complicated and includes one-, two-, and three-phase regions. The analysis of the whole phase behavior of a system described by Eq. (7.1), then, is fairly complicated. Ginzburg [84], and He, Ginzburg, and Balazs [85] considered a simpler problem of determining the spinodal boundaries, that is, the boundaries of stability of homogeneous (one-phase) systems. The condition of stability of the homogeneous phase could be written as:

$$\begin{aligned} &\frac{\partial^2 f}{\partial \varphi^2} > 0 \\ &\frac{\partial^2 f}{\partial \psi^2} > 0 \\ &J = \det \begin{Vmatrix} \dfrac{\partial^2 f}{\partial \varphi^2} & \dfrac{\partial^2 f}{\partial \varphi \partial \psi} \\ \dfrac{\partial^2 f}{\partial \varphi \partial \psi} & \dfrac{\partial^2 f}{\partial \psi^2} \end{Vmatrix} = \left[\frac{\partial^2 f}{\partial \varphi^2}\right]\left[\frac{\partial^2 f}{\partial \psi^2}\right] - \left[\frac{\partial^2 f}{\partial \varphi \partial \psi}\right]^2 > 0 \end{aligned} \tag{7.8}$$

where $\psi = \varphi_P$ and $\varphi = \varphi_A/(\varphi_A + \varphi_B) = \varphi_A/(1 - \psi)$.

After solving Eq. (7.8), one could obtain spinodal boundaries; this analysis, while incomplete, provides a good indication under which conditions nanoparticles can either stabilize or destabilize a homogeneous blend. In particular, it has been found that when the particles are sufficiently small, and polymers have sufficiently high molecular weight, they can have a compatibilizing effect even when they have a strong preference for one of two polymers.

More recently, Abad *et al.* [106, 107] have used the above theory to describe experimental data on the phase behavior of nanoparticle/epoxy/polystyrene mixtures. The authors expanded the formalism of He, Ginzburg, and Balazs, and solved co-existence equations to determine not just spinodal boundaries but also two-phase coexistence boundaries. The results appear to demonstrate that sufficiently small spherical nanoparticles (e.g., silica nanospheres with diameter less than 15 nm) can substantially reduce the size of the two-phase regions. For example, as shown in Figure 7.8, addition of 18 vol.% of silica NP (nanoparticle) shifts the upper critical temperature downward by 2–3 °C, and also narrows the two-phase region boundaries. Several other recent publications have been devoted to the investigation of thermodynamics of binary polymer blends in the presence of small nanospheres [83, 108]. At the time of writing, this is still a relatively new topic and more theoretical and experimental analysis would be needed to improve our understanding.

The above theories concentrated on the influence of nanospheres. What about nanotubes or nanoplatelets? There have been various simulations of nanorods or nanoplatelets in polymer blends, although no simple picture had emerged so far.

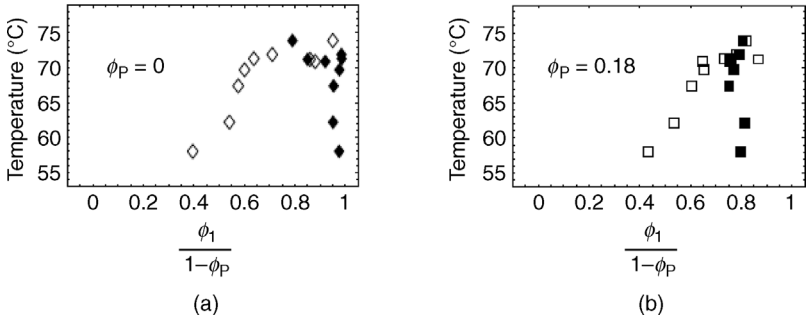


**Figure 7.8** Representative theoretical phase diagram of a ternary polymer/polymer/particle mixture, from Reference [106]): (a) coexistence lines for an epoxy/polystyrene mixture without particles; (b) coexistence lines for the same mixture in the presence of 18 vol.% of nanoparticles with $R_P = 20$ nm, covered with epoxy-philic ligand. In both (a) and (b) the area between the filled and open symbols corresponds to the two-phase region. The addition of nanoparticles, therefore, reduces the two-phase region and promotes miscibility.

Laradji and Hore [72] have simulated the dynamics of phase separation in binary blends in the presence of nanorods; the simulations predicted that rods would dramatically slow down, and possibly stop, the phase separation, leading to the stabilization of a single-phase morphology. Still, it is not clear whether this morphology is a simple homogeneous structure or, more likely, a complicated phase like a microemulsion. Similarly, there have been some experimental studies [50] suggesting that nanoplatelets could lead to microemulsion-like behavior, when platelets occupy interfaces between A-rich and B-rich domains and stabilize them. At present, to our knowledge, there is no satisfactory theory to describe this behavior, and more research is needed.

### 7.2.6
### Phase Behavior of Nanoparticle/Block-Copolymer Mixtures

Finally, we note that nanoparticles can also play an interesting role in *ordered* multicomponent polymer systems. These could include microemulsions, block copolymer (and block copolymer/homopolymer) melts, micelles of block copolymers in solvents or homopolymers, and so on. Once again, the thermodynamic behavior of the mixture depends strongly on the nanoparticles size: if the nanoparticle radius is smaller than a characteristic feature of the ordered structure (e.g., lamellar period or micellar radius), nanoparticles can modify the structure, possibly leading to phase transitions. For binary mixtures of nanoparticles and diblock copolymers, it has been observed that the presence of the particles modified the morphology of the polymer film [27–31, 109–112]. Thus, for example, when particles were added to diblocks with lamellar morphology [109], they could enter one of the domains and swell it; depending on the nanoparticle size, the distribution within the domain could be uniform (smaller particles), Gaussian with maximum probability near the center (larger particles), or Gaussian with maximum probability near the edges (interme-

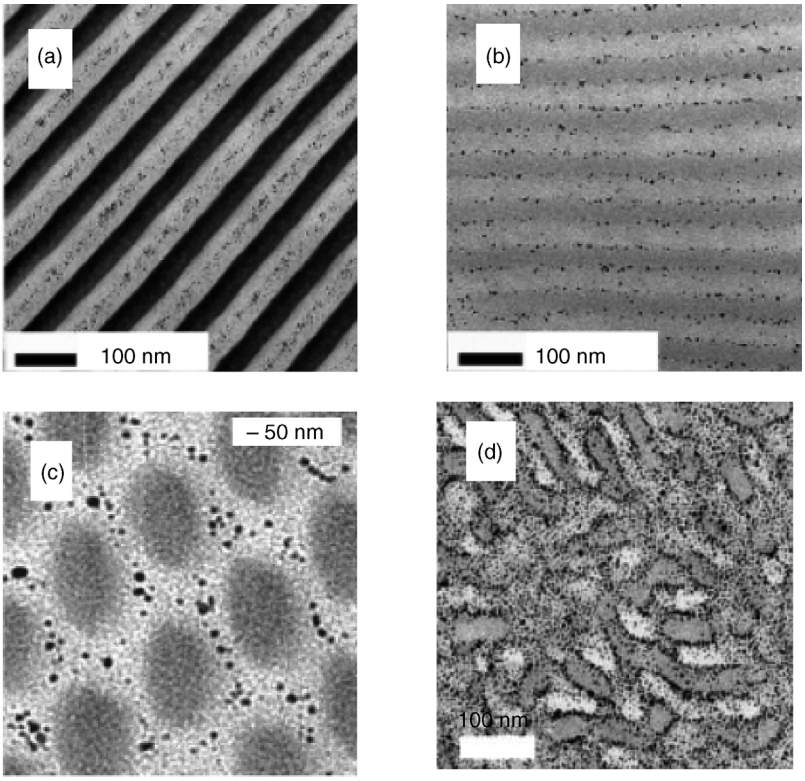


**Figure 7.9** Equilibrium morphologies of block copolymer/nanoparticle thin films: (a) 15 vol.% PS-coated gold nanoparticles (Au-NP) ($R_p \sim 4$ nm) in a symmetric PS-b-PVP block copolymer [111]; (b) 15 vol.% Au-NP with mixed PS/PVP ligands in the same block copolymer [111]; (c) same as (a) but with 35 vol. % particles [113], which produces a transition from lamellar to deformed hexagonal morphology; (d) 28 vol.% Au-NP with extremely strong segregation towards the interfaces produces bicontinuous morphology [120].

diate size particles with "mixed" ligands). It was also found that increasing the nanoparticle loading (volume fraction) could cause a transition from one morphology to another (Figure 7.9). Huh, Ginzburg, and Balazs addressed this problem theoretically using Monte Carlo modeling and strong segregation theory (SST). The phase diagram obtained on the basis of their SST theory predicted the possibility of nanoparticle-induced transitions from lamellar to cylindrical, or cylindrical to lamellar – transitions that were indeed later observed by Sides *et al.* [113], and Lo *et al.* [114]. Figure 7.10 shows the SST phase diagram of Huh, Ginzburg, and Balazs [33] and the experimental phase map of Lo *et al.* [114] side by side; clearly, the two diagrams are in good qualitative agreement. A subsequent, more elaborate version of the SST approach for the nanoparticle/block copolymer systems has been developed by Ganesan and Pryamitsyn [115]; this approach successfully described the spatial distribution of nanoparticles in the lamellae as a function of nanoparticle size. A more comprehensive analysis, based on the combination of numerical

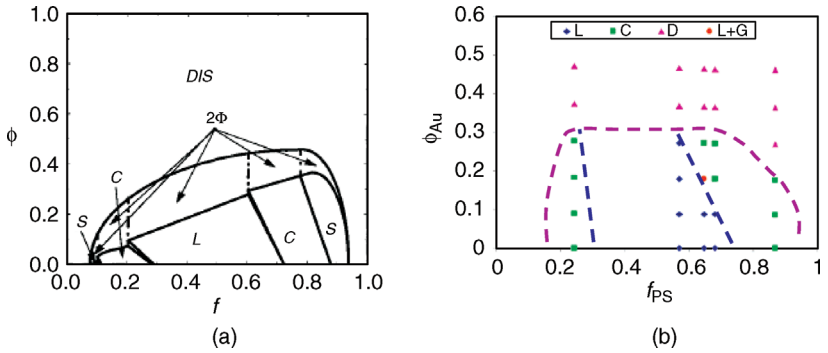


**Figure 7.10** Theoretical (a, [33]) and experimental (b, [114]) phase diagrams of diblock copolymer/nanoparticle mixtures. In both cases the ratio $R_P/(aN^{1/2}) \sim 0.2$–$0.3$, and $\chi N \sim 30$–$40$. Note that the experimental phase diagram does not distinguish one-phase from two-phase regions.

self-consistent-field theory (SCFT) and density functional theory (DFT) formalism for hard spheres, was proposed by Thompson, Ginzburg, Matsen, and Balazs (TGMB) [32, 116]. Within the TGMB approach, the free energy of the nanoparticle/polymer system can be described with the help of the SCFT free energy, provided that the nanoparticle free energy contribution contains both ideal and non-ideal terms (to account for the non-deformability and excluded volume conditions for the particles).

The example of the TGMB free energy in a binary mixture of nanospheres (P) and AB-diblocks (D) is given in Eq. (7.9):

$$
\begin{aligned}
f = \frac{N_{AB} F v_0}{k_B T V} = &-\frac{\varphi_P}{\alpha}\ln\left[\frac{Q_P \alpha}{V\varphi_P}\right] - (1-\varphi_P)\ln\left[\frac{Q_d}{V(1-\varphi_P)}\right] \\
&+ V^{-1}\int d\boldsymbol{r}\left[(\chi N)_{AB}\phi_A(\boldsymbol{r})\phi_B(\boldsymbol{r}) + (\chi N)_{AP}\phi_A(\boldsymbol{r})\phi_P(\boldsymbol{r}) + (\chi N)_{BP}\phi_B(\boldsymbol{r})\phi_P(\boldsymbol{r})\right] \\
&+ V^{-1}\int d\boldsymbol{r}\left[-\sum_{i=A,B} w_i(\boldsymbol{r})\phi_i(\boldsymbol{r}) - w_P(\boldsymbol{r})\varrho_P(\boldsymbol{r}) - \xi(\boldsymbol{r})\left(1 - \sum_{i=A,B,P}\phi_i(\boldsymbol{r})\right)\right. \\
&\left. + \varrho_P(\boldsymbol{r})\Psi_{HS}\left(\overline{\phi}_P(\boldsymbol{r})\right)\right]
\end{aligned}
\tag{7.9}
$$

Here $\alpha = V_P/V_d = (4/3)\pi\ R_P^3/(N_{AB}v_0)$ is the ratio of particle volume to the diblock volume. The partition functions of diblock and particle are given by:

$$Q_P = \int d\boldsymbol{r}\exp[-w_P(\boldsymbol{r})]$$
$$Q_d = \int d\boldsymbol{r}\, q(\boldsymbol{r}, s=1)$$

As usual in SCFT, partition function of the diblock must be evaluated by solving modified diffusion equations and finding the propagators $q$ and $q\dagger$. To correctly capture the spherical geometry of the particle, one has to introduce the relationship between the particle volume fraction, $\phi_P(\boldsymbol{r})$, and the particle center probability

density, $\varrho_P(\boldsymbol{r})$:

$$\phi_P(\boldsymbol{r}) = \frac{\alpha}{V_P} \int_{|\boldsymbol{r}'|<R_P} \mathrm{d}\boldsymbol{r}' \varrho_P(\boldsymbol{r}+\boldsymbol{r}')$$

Finally, to correctly evaluate the non-ideal contribution to the free energy of the nanospheres, the weighted-density Carnahan–Starling term is added. (For the reasoning behind its inclusion in the overall free energy, see Reference [32].) The weighted particle density is calculated via:

$$\overline{\overline{\phi}}_P(\boldsymbol{r}) = \frac{\alpha}{2^d V_P} \int_{|\boldsymbol{r}'|<2R_P} \mathrm{d}\boldsymbol{r}' \varrho_P(\boldsymbol{r}+\boldsymbol{r}')$$

($d = 2$ for a two-dimensional system and 3 for a three-dimensional one).

To calculate the morphology of a given multicomponent system, one needs to calculate the density and chemical potential fields that correspond to a "saddle point" of the free energy density functional of Eq. (7.8). Thus, as in a conventional SCFT (see, for example, Fredrickson *et al.* [117–119]), we obtain the so-called self-consistency equations that can be solved iteratively. The result of the calculation is the "morphology map," describing the distribution of particles and various polymeric species. A morphology map can be analyzed to understand its symmetry [e.g., whether it corresponds to a lamellar, hexagonal, face-centered cubic (FCC), or body-centered cubic (BCC) phase). Figure 7.11 depicts one-dimensional density maps for

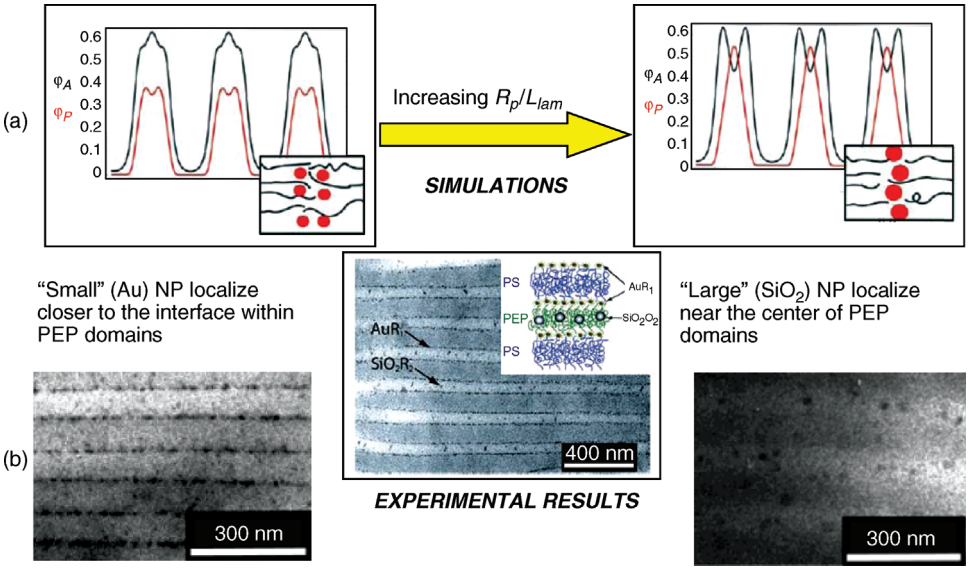


**Figure 7.11** Influence of particle size on their distribution within a lamellar domain. As the size of the A-coated particle is increased, the particle distribution becomes sharply localized near the center of the A-lamellae. (a) TGMB simulations [32] for small (left) and large (right) nanoparticles; red curves are the particle densities, black curves are the A-block densities. (b) Experimental pictures from Bockstaller *et al.* [29], demonstrating similar trends.

nanoparticles and A-block (assuming A-ligand covered particles) for the case of small (Figure 7.11a, left-hand side) and large (Figure 7.11a, right-hand side) nanoparticles; it can be seen that as the nanoparticle size is increased they tend to aggregate more strongly near the center of the A-block lamella [32]. These results are consistent with experimental observations of Bockstaller *et al.* (Figure 7.11b) [29].

Other modifications of this approach could include different boundary conditions to study different types of problems (e.g., periodic for bulk, fixed for thin films, or reflective for a prescribed interface). In principle, this method could be also modified to describe grand canonical, rather than canonical, ensembles. Certainly – although it has not been done so far – the method could be adapted to study nanoparticles in polymer blends, and, in particular, their compatibilizing effects and their ability to cause the system to form a bicontinuous microemulsion [120]. While these problems still remain to be addressed, below we review some systems where the TGMB approach has been already applied. Balazs and coworkers [121–125] have investigated several types of block copolymer/particle mixtures; in particular, they demonstrated that nanoparticles could segregate to the interface in thin films, giving rise to "self-healing" films. Ginzburg *et al.* [126] have demonstrated that nanoparticles could help create interesting hybrid micellar morphologies in spin-coated polymer films where solvent evaporation, polymerization, and phase separation all competed in real time. In the cases of block copolymer solutions, Zhang *et al.* [127] have adapted the TGMB approach to investigate the phase behavior of nanoparticle/nonionic surfactant micellar solutions and predicted the phase diagram (Figure 7.12), demonstrating that particles could lead to transitions between spherical micelles, rods, and vesicles. Ginzburg and Balijepalli [128] have applied the TGMB model to analyze the thermodynamics of nanoparticle/cell membrane interaction, modeling cell

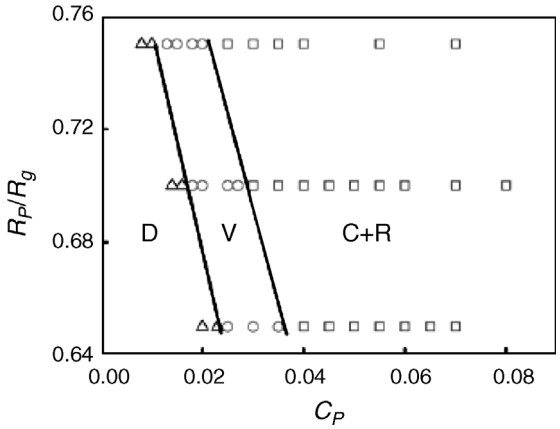


**Figure 7.12** Theoretical phase diagram of hybrid nanoparticle/block copolymer surfactant micelles in solution. Here, $c_P$ is the particle volume fraction (volume fraction of the surfactant is fixed at 5%), D stands for disordered state, V for vesicles, C for circles, and R for rods. Simulations were performed using a slightly modified TGMB approach. For more details, see Reference [127].

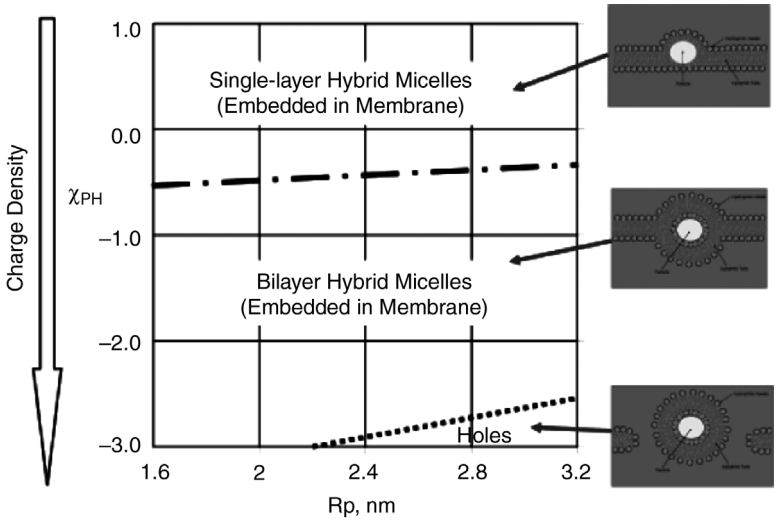


**Figure 7.13** Theoretical phase diagram of the structures resulting from the interaction of nanoparticle and cell membrane (modeled as a block copolymer in solution). Sketches on the right-hand side demonstrate the meaning of various structures (single-layer hybrid micelles, bilayer hybrid micelles, and holes). Simulations were performed using a slightly modified TGMB approach. For more details, see Reference [128].

membrane as a diblock copolymer, with lipophilic and hydrophilic blocks. It was shown that depending on the nanoparticle size and type of its surface chemistry it could lodge itself in a membrane, or, possibly, rip a hole in the membrane (Figure 7.13). These results were shown to be in a qualitative agreement with experiments of Leroueil *et al.* [129].

Other recent contributions to the understanding of block copolymer/nanoparticle systems include a different SCFT-based model in which particles are modeled as "cavities" or constraints for the density fields (see Reister and Fredrickson [130], Sides *et al.* [113], Matsen and Thompson [131], Kim and Matsen [132]); DPD simulations (Smith, Jasnow, and Balazs [133]), DFT studies (Cao and Wu [134], McGarrity, Mackay, and Frischknecht [135, 136]); as well as coarse-grained Monte Carlo [33, 137, 138] and molecular dynamics [139, 140] simulations. Figure 7.14 demonstrates how the hybrid ("cavity") model of Sides *et al.* can qualitatively reproduce experimental micrographs of PS-P2VP [poly(2-vinlypyridine)] block copolymer films with the addition of gold nanoparticles. Both model and experiment show that as the nanoparticle loading is increased the morphology changes from lamellar to hexagonal. (A comprehensive review discussing these and other approaches to polymer/nanoparticle modeling has been published recently by Allegra, Raos, and Vacatello [141].)

Most of the above studies were devoted to the particles with a uniform surface chemistry, so that any particle possesses full rotational symmetry. In principle, one could adapt these methods to more complex situations where part of the particle is "A-philic" and another part is "B-philic," so that the overall particle is "Janus"-like and

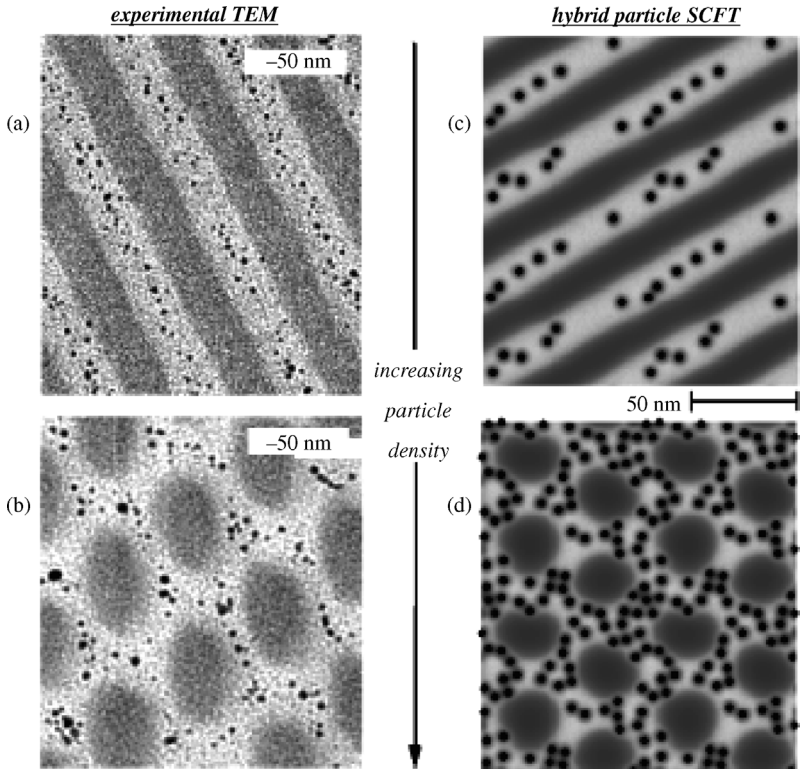


**Figure 7.14** Experimental and simulated morphologies of block copolymer/nanoparticle systems at two different particle volume fractions (10 and 35 vol.%). Simulations were performed using a "hybrid" SCFT method [113].

could act as a surfactant or compatibilizer. However, calculating phase diagrams of such systems remains a formidable task because of the need to evaluate additional (rotational) degrees of freedom. We expect these studies to be forthcoming in the near future.

### 7.2.7
### Determination of Polymer–Particle Flory–Huggins Interaction Parameters

Most of the above theories assumed that one knows the interaction parameter between particle and polymer, $\chi_{AP}$ (here A, again, denotes a matrix homopolymer or a block in a block copolymer). However, this is not trivial. There are several ways of estimating this parameter, depending on the surface chemistry of the particle:

- If the particle is covered with a brush of an oligomeric ligand B, then $\chi_{AP} = \chi_{AB}$, since the interior of the particle is not accessible to the polymer.
- If the particle does not have any ligand attached to its surface, one could use the surface tension data or estimates to derive the "interfacial tension" between

the particle and the polymer using Owens–Wendt [142], Girifalco–Good [143], or Wu [144] equations (see Reference [2] for more details). Once this "interfacial tension," $\gamma_{AP}$, is evaluated, it can be converted into a Flory–Huggins parameter via $\chi_{AP} = \gamma_{AP}(v_0/a)$, where $v_0$ is the "reference" monomer volume and $a$ is the "reference" Kuhn length. (Note that the "interfacial tension" evaluated in this fashion contains mainly enthalpic, not entropic, contributions.)

As already mentioned, the Flory–Huggins approach does not take into account long-range interaction between the particles and captures only the short-range interactions between the particle surface and its surroundings. As the particle concentration increases, the role of direct particle–particle interactions, such as van der Waals–Hamaker attraction [20] or perhaps electrostatic repulsion [21], becomes more important in determining the blend morphology and structure. However, quantifying these effects (especially electrostatic) is somewhat challenging, especially as the particle surface itself is subjected to various physicochemical changes when the particles are blended with the polymers.

With this, we conclude the discussion of the morphology of polymer/nanoparticle blends. Obviously, this is still a relatively new – and rapidly growing – area of science, and today we understand only general principles and several specific simple cases. More studies – experimental and theoretical – are likely to come in the next several years and provide new insights into this fascinating subject.

## 7.3
## Physical Properties of Filled Polymer Blends

The morphology of nanocomposites, of course, is not the goal in itself but the means to the goal (the goal being nanocomposite performance and therefore specific physical or mechanical properties). Thus, when dealing with nanocomposites, it is important to be able to predict how the particular morphology can impact the properties. Below, we discuss some aspects of this morphology–property link. As examples, we consider only mechanical and electrical properties; many other characteristics (thermal expansion coefficients, gas permeability, flame retardancy, viscoelastic behavior, etc.), while extremely important for many applications, are deliberately left outside the scope of this chapter. (Readers are encouraged to consult References [2, 5, 10, 11] for more detailed discussion on these and other topics.)

### 7.3.1
### Mechanical Properties (Modulus, Strength, and Toughness)

Mechanical properties of nanocomposites in general have been extensively reviewed in recent years [10–13, 145–148]. It has been shown that the inorganic fillers typically increase modulus and strength of the composite, compared to the unmodified pristine polymer. The magnitude of the increase depends on the aspect ratio of the fillers, the filler loading, and – assuming the filler is anisotropic – its orientation.

For the case of anisotropic and aligned fillers in a single polymer matrix, elastic properties such as modulus could be predicted using composite theories such as Halpin–Tsai [149, 150] or Mori–Tanaka [151]. In general, it is held that the same approaches used for conventional composites could be applied to nanocomposites. Fornes and Paul [147] have investigated the properties of polymer/clay nanocomposites and found reasonable agreement between experiment and Mori–Tanaka prediction for the Young's modulus. Gusev and coworkers [152, 153] have utilized the finite element analysis (FEA) approach to investigate the modulus of two- and three-component (filler-1/filler-2/polymer matrix) nanocomposites as a function of filler loading. Brune and Bicerano [154] have investigated the influence of the morphology on mechanical properties in homopolymer/clay nanocomposites. Using modified Halpin–Tsai equations, they showed that the in-plane elastic modulus for the perfectly exfoliated, perfectly aligned nanocomposite was substantially greater than the modulus for an intercalated or partially exfoliated system with the same clay loading. A similar calculation was performed by Bicerano *et al.* [146] using Gusev's finite element scheme (Figure 7.15).

While there has been limited investigation of mechanical properties of three-component (polymer/polymer/filler) nanocomposites, it would appear that the final result is strongly dependent on the morphology of the system. For example, if two polymers are immiscible, and nanoparticles are localized in one of the domains, the modulus could be evaluated in two stages: (i) separately calculate the modulus of the phase containing particles and (ii) utilize composite theories to determine the overall modulus of the entire system.

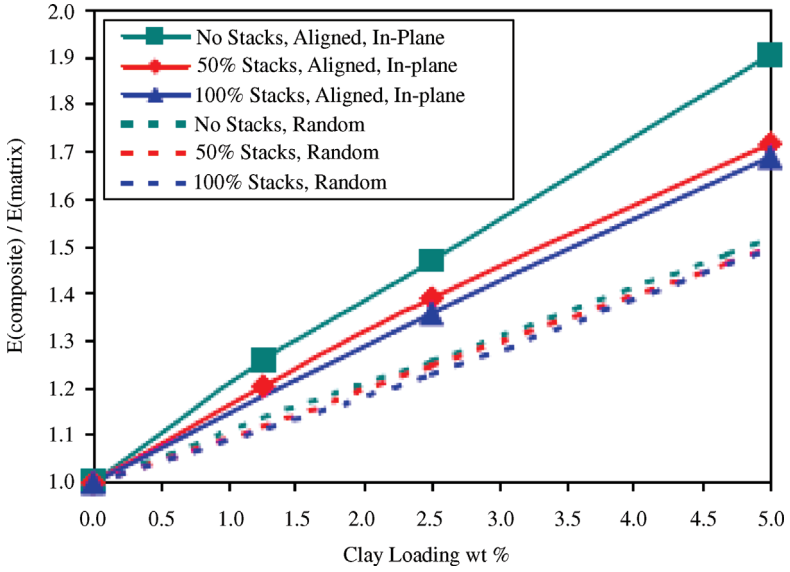


**Figure 7.15** Finite element analysis simulations of elastic modulus of polymer/clay composites as a function of clay loading. Clay particles are modeled as discs with $D = 60$ nm, $T = 1$ nm, $\varrho = 2.7\ \mathrm{g\,cm^{-3}}$, and $E_{clay}/E_{polymer} = 1000$. In modeling stacks, it is assumed that the distance between platelets ("gallery") equals 1 nm. For more details, see Reference [146].

Prediction of strength and toughness present many additional challenges. Indeed, in nanocomposites, toughness often decreases as the filler loading is increased. While the reasons for this are not fully understood at present, one hypothesis is that the fillers introduce weak interfaces precisely at the points where stress concentration is the highest. As a result, the mechanism of failure could change from cohesive to interfacial. The dependence of toughness on the filler loading can be nonlinear and even non-monotonic, depending on various factors. For more details, the reader is referred to a recent review [155]. For the case of multicomponent blends, toughness often could be improved if the two phases are better compatibilized (smaller domain size and lower interfacial tension at the domain boundaries). In that case, compatibilizing nanofillers could contribute to the increase in both modulus and toughness (see discussion in Reference [2] for more details).

### 7.3.2 Electrical Conductivity

In many composites, conducting fillers (carbon black, carbon nanotubes, or metal nanoparticles) are added to make material conductive. The relationship between composite morphology and electrical conductivity has been studied extensively, especially in the context of carbon black filled polymers [156–162]. It is well known that the dependence of conductivity on the loading of conductive filler, $\varphi_P$, can be described on the basis of percolation theory: there is some threshold filler loading below which there is no conductive pathway through the system and conductivity is zero; above the threshold, conductivity grows very rapidly as:

$$\sigma = k(\varphi_P - \phi_c)^n \tag{7.10}$$

with $\phi_c$ being the so-called percolation threshold, and $n$ being the so-called percolation exponent. Both $\phi_c$ and $n$ could depend on the shape of the conducting fillers, as well as on the interparticle interactions. As discussed by Bicerano, Douglas, and Brune [163], percolation threshold is generally the highest for spherical particles, and decreases rapidly as the particles become more and more anisotropic:

$$\phi_c = \frac{9.875\,A + A^2}{7.742 + 14.61\,A + 12.33\,A^{1.5} + 1.763\,A^2 + 1.658\,A^3} \tag{7.11}$$

Thus, composites with high-aspect-ratio carbon nanotubes become conductive at filler loadings of less than 1 vol.%, while composites with spherical particles like carbon black begin to conduct at much higher loadings (>15 vol.%).

The percolation threshold can be further reduced, and conductivity increased, if one makes use of the concept of "double percolation," first theoretically studied by Levon, Margolina, and Patashinsky [164], and experimentally observed by Sumita and coworkers [161], as well as other researchers [157, 158, 162] for the dispersion of carbon black in binary polymer blends. To obtain double percolation, one needs to have a ternary system, with two phase-separating polymers and conducting filler with strong affinity to one of the polymers (we denote it as A, and the second polymer as B). Then, the system could be conducting if (i) filler loading in the A-domain is above percolation threshold and (ii) the volume fraction of the filled A-domains is above

percolation threshold, that is, filled A-domains represent a continuous phase. Conductivity in such "double-percolation" system is given by:

$$\sigma \approx k\left(\varphi_P - \phi_c'\right)^{n'} \tag{7.12}$$

Here, the new percolation exponent $n' \approx 2n$; assuming a "standard" percolation exponent of 2 [164], we conclude that, for the double percolation, conductivity growth should be described by the power exponent close to 4. In an analogous fashion, the percolation threshold, $\phi'_c$, becomes equal to the product of the percolation threshold for the system in a homopolymer, $\phi_c$, and the volume fraction of the A-polymer in the blend (as long as A-domains are themselves percolated). Thus, if we take a geometrical percolation threshold to be equal to 0.16, the threshold for a double percolation becomes equal to $0.16^2 = 0.0256$, or 2.5 vol.%. As shown experimentally, for example, by Gubbels *et al.* [157], double percolation indeed decreases the percolation threshold (Figure 7.16). Within the same "double percolation" paradigm, Gubbels *et al.* demonstrated that percolation threshold could be reduced well below 1%, provided that CB particles are segregated at interfaces between polystyrene and polyethylene domains.

As already mentioned, another way of reducing percolation threshold is to use high-aspect-ratio particles, for example, carbon nanotubes instead of carbon black.

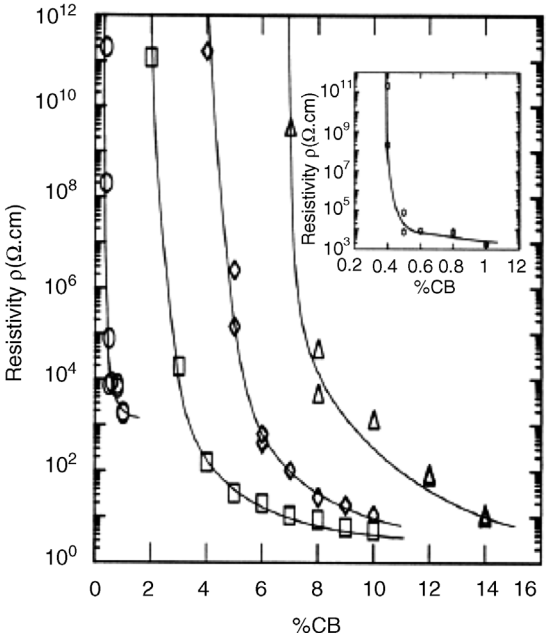


**Figure 7.16** Resistivity of ternary polymer/polymer/carbon black mixture as function of carbon black (CB) content and morphology. The percolation threshold is the highest for uniformly dispersed CB particles (open triangles), lower for the case of particles localized in one of the two polymer phases (PS – diamonds, PE – squares), and the lowest for the case of particles localized at the interfaces (circles). Inset shows the latter case in more detail. Reprinted from Reference [157].

The impact of aspect ratio and alignment of the carbon nanotubes on the nanocomposite conductivity has been studied recently (both experimentally and computationally) by Winey and coworkers [165–167]. In particular, Du *et al.* [165] demonstrated that in a poly(methyl methacrylate) (PMMA)/single wall carbon nanotube (SWCNT) nanocomposite, conductivity increases as a function of the SWCNT loading as predicted by Eq. (7.10), with a power-law exponent of 2.3 and percolation threshold of 0.39 wt%. Interestingly, the rapid increase in conductivity was accompanied by a rapid increase in the storage modulus, $G'$ (Figure 7.17). In fact,

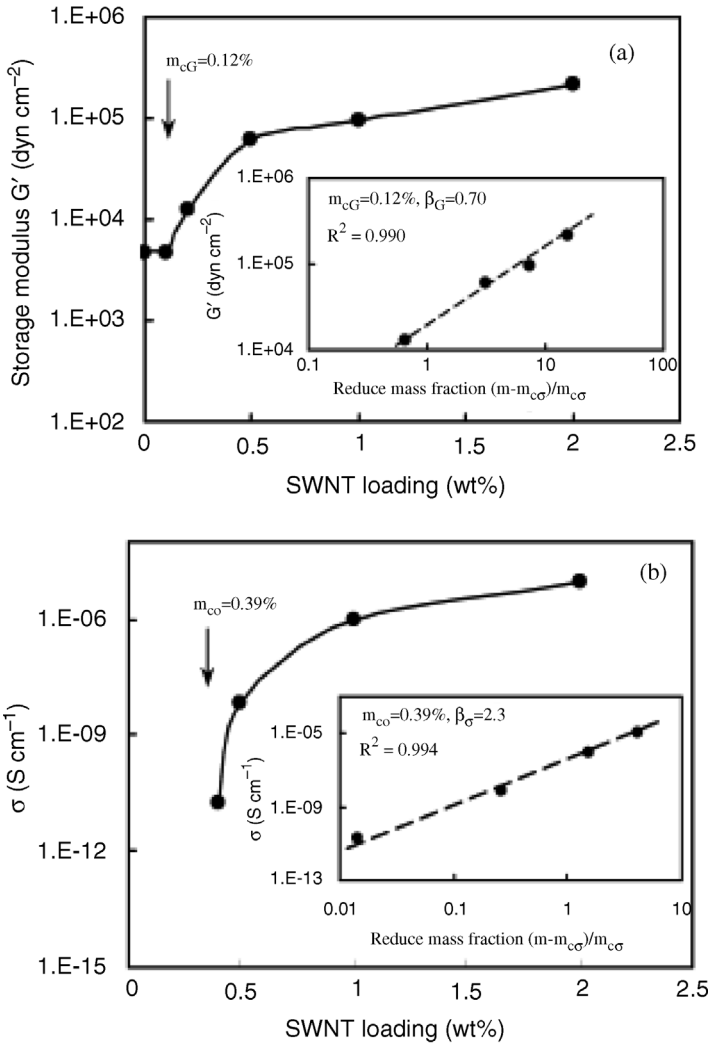


**Figure 7.17** Storage modulus (a) and electrical conductivity (b) of poly(methyl methacrylate) (PMMA)/SWCNT nanocomposites. Insets: power-law percolation model fits to experimental data. (Reprinted from Reference [165]).

the threshold for the "rheological" ($G'$) percolation was found to be lower than that for the electrical percolation (0.12 versus 0.39 wt%). It was hypothesized that the onset of rheological percolation is lower because the elastic network contains not just nanotubes (or, to be more precise, nanotube bundles) but also some "bridging" polymer chains. In addition, conductivity is strongly impacted by the alignment of the nanotube bundles; as predicted by White *et al.* [167], for any given aspect ratio and particle loading, there is an optimal degree of alignment corresponding to the maximum conductivity. Obviously, predicting conductivity in the blends of CNTs (carbon nanotubes) and polymer mixtures is an even more complex problem; one that awaits resolution.

## 7.4 Summary and Outlook

The development of hybrid organic–inorganic materials has accelerated rapidly in the past two decades and, undoubtedly, they will play an increasingly prominent role in the future. As demonstrated in this chapter, addition of nanoparticles can dramatically expand the range of desired attributes for many polymer systems; hybrid materials could be stronger, tougher, lighter, and more conductive than conventional polymer blends or composites. Recent studies also suggest new applications for the hybrid nanocomposites, including solar cells [168, 169], ignition resistant materials [170], and others.

One of the critical attributes of the nanocomposite systems – unlike conventional composites – is the increased importance of thermodynamic considerations in designing new materials. The effective interactions between particles and polymers (combined enthalpic and entropic "surface tension") influence the morphology of the material as strongly as the processing history. Thus, surface modification of nanoparticles (grafting of appropriate ligands) becomes the critical step in nanocomposite preparation. Thermodynamic modeling helps us understand how to appropriately choose the grafting agents and what morphologies we could obtain.

The relationship between morphology and properties is very important and is understood at present for only a limited number of systems and only for some properties (elastic modulus, electrical conductivity, coefficient of thermal expansion, gas permeability). As the complexity of the system increases, accurate prediction of properties becomes more difficult and would require more elaborate computational and experimental techniques.

Finally, we emphasize that this chapter is by no means exhaustive; it is our hope, however, that it provides some general idea of recent developments in the theory and modeling of polymer/nanoparticle blend systems.

### Acknowledgment

This work was supported by The Dow Chemical Company.

## Abbreviations and Symbols

### Abbreviations

| | |
|---|---|
| CDS | cell dynamical systems (method of mesoscale simulations) |
| CNT | carbon nanotube |
| DFT | density functional theory |
| DPD | dissipative particle dynamics (method of mesoscale simulations) |
| dPMMA | deuterated poly(methyl methacrylate) |
| EVA | poly(ethyl vinyl acetate) |
| NP | nanoparticle |
| PBMA | poly(butyl methacrylate) |
| PE | polyethylene |
| PMMA | poly(methyl methacrylate) |
| PS | polystyrene |
| P2VP | poly(2-vinylpyridine) |
| SAN | poly(styrene acrylonitrile) |
| SCFT | self-consistent field theory |
| SST | strong segregation theory |
| SWCNT | single-wall carbon nanotube |

### Symbols

| | |
|---|---|
| $A$ | aspect ratio |
| $a$ | Kuhn length (one lattice unit) |
| $\Delta E$ | Energy change upon particle move from the bulk to the interface |
| $F$ | Helmholtz free energy |
| $f$ | Helmholtz free energy density |
| $f_{\mathrm{entr}}$ | entropic component of the Helmholtz free energy density |
| $\Delta G$ | Gibbs free energy of mixing |
| $J$ | jacobian |
| $k$ | prefactor in the formula for the dependence of conductivity on particle loading |
| $k_{\mathrm{B}}$ | Boltzmann's constant |
| $L(t)$ | time-dependent characteristic domain size in binary phase-separating polymer blend |
| $n$, $n'$ | percolation exponents for the dependence of conductivity on particle loading (single and double percolation models, respectively) |
| $n$(int), $n$(bulk) | number of particles located at the interfaces or in the bulk, respectively, in a binary polymer blend or in a microphase-separated block copolymer |
| $N$, $N_{\mathrm{A}}$, $N_{\mathrm{B}}$ | degree of polymerization (chain length) of a polymer |

| | |
|---|---|
| $Q_j$ | partition function of a component (particles, solvent, or polymer) within self-consistent field theory |
| $R_g$ | polymer radius of gyration |
| $R_P$ | particle radius |
| V | total volume of a system |
| $v_{ref}$ | reference volume used in calculating Flory–Huggins interaction parameters |
| $v_0$ | volume of a lattice unit in Flory–Huggins or self-consistent field theory (in general, should be equal to $v_{ref}$) |
| $w_i(\boldsymbol{r})$ | chemical potential-type field for $i$-th species in self-consistent field theory |

**Greek Symbols**

| | |
|---|---|
| $\alpha$ | ratio of particle volume to block copolymer volume in self-consistent field theory |
| $\gamma_{ij}$ | interfacial tension between two phases, $i$ and $j$, where $i$ and $j$ could denote various polymers or nanoparticles |
| $\delta_A$ | solubility parameter of polymer labeled A (incompressible model) |
| $\delta_{A0}$ | solubility parameter of polymer labeled A (compressible model, at reference temperature and density) |
| $\zeta(\boldsymbol{r})$ | pressure field in self-consistent field theory |
| $\varrho_P(\boldsymbol{r})$ | particle center distribution function in self-consistent field theory |
| $\tilde{\varrho}_A$ | reduced density of polymer labeled A (in a compressible version of Flory–Huggins theory) |
| $\sigma$ | electrical conductivity |
| $\varphi$ | volume fraction of the first polymeric component in a binary blend to which nanoparticles are added |
| $\varphi_A$ | volume fraction of component labeled A in the overall mixture (A could denote polymers or nanoparticles) |
| $\phi_c$ | percolation threshold |
| $\phi_i(\boldsymbol{r})$ | local volume fraction of species $i$ at position $\boldsymbol{r}$ in self-consistent field theory ($i$ can denote any monomer or nanoparticle) |
| $\overline{\overline{\phi}}_P(\boldsymbol{r})$ | weighted particle density (used to calculate free energy of inhomogeneous polymer–particle mixtures using hybrid SCFT-DFT approach) |
| $\chi_{AB}$ | Flory–Huggins interaction parameters between polymers A and B |
| $\psi$ | nanoparticle volume fraction in a ternary polymer/polymer/nanoparticle blend |
| $\Psi_{HS}$ | Carnahan–Starling excess free energy for the hard-sphere fluid |

## References


1 Balazs, A.C., Emrick, T., and Russell, T.P. (2006) *Science*, **314**, 1107, and references therein.
2 Fenouillot, F., Cassagnau, P., and Majeste, J.-C. (2009) *Polymer*, **50**, 1333, and references therein.
3 Shenhar, R., Norsten, T.B., and Rotello, V.M. (2005) *Adv. Mater.*, **17**, 657, and references therein.
4 Sanchez, C., Julian, B., Belleville, P., and Popall, M. (2005) *J. Mater. Chem.*, **15**, 3559, and references therein.
5 Winey, K.I. and Vaia, R.A. (2007) *MRS Bull.*, **32**, 314, and references therein.
6 Bockstaller, M.R., Mickiewicz, R.A., and Thomas, E.L. (2005) *Adv. Mater.*, **17**, 1331, and references therein.
7 Rozenberg, B.A. and Tenne, R. (2008) *Prog. Polym. Sci.*, **33**, 40, and references therein.
8 Szleifer, I. and Yerushalmi-Rozen, R. (2005) *Polymer*, **46**, 7803, and references therein.
9 Okada, A., Kawasumi, M., Usuki, A., Kojima, Y., Kurauchi, T., and Kamigaito, O. (1990) Synthesis and properties of nylon-6/clay hybrids, in *Polymer Based Molecular Composites* (eds D.W. Schaefer and J.E. Mark), MRS Symposium Proceedings, vol. **171**, Materials Research Society, Pittsburgh, p. 45.
10 Sinha Ray, S. and Okamoto, M. (2003) *Prog. Polym. Sci.*, **28**, 1539, and references therein.
11 Schadler, L.S. (2003) Polymer-based and polymer-filled nanocomposites, in *Nanocomposite Science and Technology* (eds P.M. Ajayan, L.S., Schadler, and P.V. Braun), Wiley-VCH Verlag GmbH, Weinheim, and references therein.
12 Sheng, N., Boyce, M.C., Parks, D.M., Rutledge, G.C., Abes, J.I., and Cohen, R.E. (2004) *Polymer*, **45**, 487, and references therein.
13 Balazs, A.C., Bicerano, J., and Ginzburg, V.V. (2008) Polyolefin/clay nanocomposites: theory and simulations, in *Polyolefin Composites* (eds D. Nwabunma and T. Kyu), Wiley-VCH Verlag GmbH, New York, and references therein.
14 Giannelis, E.P., Krishnamoorti, R., and Manias, E. (1999) *Adv. Polym. Sci.*, **138**, 107, and references therein.
15 LeBaron, P.C., Wang, Z., and Pinnavaia, T. (1999) *J. Appl. Clay Sci.*, **15**, 11, and references therein.
16 Alexandre, M. and Dubois, P. (2000) *Mater. Sci. Eng. R*, **28**, 1, and references therein.
17 Krishnamoorti, R. and Vaia, R. (2002) *Polymer Nanocomposites: Synthesis, Characterization, and Modeling*, Oxford University Press, Oxford.
18 Pinnavaia, T. and Beall, G.(eds) (2000) *Polymer-Clay Nanocomposites*, John Wiley & Sons, Inc., New York.
19 Vaia, R. and Giannelis, E.P. (2001) *Mater. Res. Soc. Bull.*, **5**, 394, and references therein.
20 Hamaker, H.C. (1937) *Physica*, **4**, 1058.
21 Tadros, T.F. (1980) *Adv. Colloid Interface Sci.*, **12**, 141, and references therein.
22 Gouy, G. (1910) *J. Phys.*, **9**, 457.
23 Chapman, D.L. (1913) *Philos. Mag.*, **25**, 475.
24 Deryaguin, B. (1934) *Kolloid Z.*, **69**, 155; (1939) *Acta Phys.-Chem. USSR*, **10**, 333.
25 Verwey, E.J.W. and Overbeek, J.T.G. (1949) *Theory of the Stability of Lyotropic Colloids*, Elsevier, Amsterdam.
26 Mackay, M., Tuteja, A., Duxbury, P.M., Hawker, C.J., van Horn, B., Guan, Z., Chen, G., and Krishnan, R.S. (2006) *Science*, **311**, 1740.
27 Lin, Y., Böker, A., He, J., Sill, K., Xiang, H., Abetz, C., Li, X., Wang, J., Emrick, T., Long, S., Wang, Q., Balazs, C., and Russell, T.P. (2005) *Nature*, **434**, 55.
28 Lopes, W.A. and Jaeger, H.M. (2001) *Nature*, **414**, 735.
29 Bockstaller, M.R., Lapetnikov, Y., Margel, S., and Thomas, E.L. (2003) *J. Am. Chem. Soc.*, **125**, 5276.
30 Thurn-Albrecht, T., Schotter, J., Kastle, G.A., Emley, N., Shibauchi, T., Krusin-Elbaum, L., Guarini, K., Black, C.T., Tuominen, M.T., and Russell, T.P. (2000) *Science*, **290**, 2126.
31 Lauter-Pasyuk, V., Lauter, H.J., Ausserre, D., Gallot, Y., Cabuil, V., Hamdoun, B.,

and Kornilov, E.I. (1998) *Phys. B (Amsterdam)*, **248**, 243.
32 Thompson, R., Ginzburg, V., Matsen, M., and Balazs, A.C. (2001) *Science*, **292**, 2469.
33 Huh, J., Ginzburg, V.V., and Balazs, A.C. (2000) *Macromolecules*, **33**, 8085.
34 Flory, P.J. (1941) *J. Chem. Phys.*, **9**, 660.
35 Huggins, M. (1941) *J. Chem. Phys.*, **9**, 440.
36 Bicerano, J. (2002), in *Prediction of Polymer Properties*, 3rd edn, Marcel Dekker, New York–Basel, Ch. 5.
37 Brandrup, J., Immergut, E.H., Grulke, E.A., Abe, A., and Bloch, D.R. (2005) *Polymer Handbook*, 4th edn, John Wiley & Sons, Inc., New York.
38 Balsara, N.P. and Eitouni, H.B. (2007) Thermodynamics of polymer blends, in *Physical Properties of Polymers Handbook*, 2nd edn, (ed. J.E. Mark), Springer, New York, Ch. 19, pp. 339–356.
39 Bates, F.S. (1991) *Science*, **251**, 898, and references therein.
40 Sung, L., Karim, A., Douglas, J.F., and Han, C.C. (1996) *Phys. Rev. Lett.*, **76**, 4358.
41 Ruzette, A.V.G., Banerjee, P., Mayes, A.M., and Russell, T.P. (2001) *J. Chem. Phys.*, **114**, 8205.
42 Lyatskaya, Y., Gersappe, D., Gross, N.A., and Balazs, A.C. (1996) *J. Phys. Chem. B*, **100**, 1449, and references therein.
43 Rosen, M.J. (1989) in *Surfactants and Interfacial Phenomena*, 2nd edn, John Wiley and Sons, Inc., New York, Ch. 8 and references therein.
44 Fredrickson, G.H. and Bates, F.S. (1997) *J. Polym. Sci Part B: Polym. Phys.*, **35**, 2775.
45 Bates, F.S., Maurer, W.W., Lipic, P.M., Hillmyer, M.A., Almdal, K., Mortensen, K., Fredrickson, G.H., and Lodge, T.P. (1995) *Phys. Rev. Lett.*, **79**, 849.
46 Glogowski, E., Tangirala, R., Russell, T.P., and Emrick, T. (2006) *J. Polym. Sci. Part A: Polym. Chem.*, **44**, 5076, and references therein.
47 Chung, H.J., Ohno, K., Fukuda, T., and Composto, R.J. (2005) *Nano. Lett.*, **5**, 1878.
48 Pieranski, P. (1980) *Phys. Rev. Lett.*, **45**, 569.
49 Binks, B.P. and Clint, J.H. (2002) *Langmuir*, **18**, 1270.
50 Gelfer, M.Y., Song, H.H., Liu, L., Hsiao, B.S., Chu, B., Rafailovich, M., Si, M., and Zaitsev, V. (2003) *J. Polym. Sci., Part B: Polym. Phys.*, **41**, 44.
51 Chaikin, P.M. and Lubensky, T.C. (1995) *Principles of Condensed Matter Physics*, Cambridge University Press, Cambridge–New York.
52 Hohenberg, P.C. and Halperin, B.I. (1977) *Rev. Mod. Phys.*, **49**, 435.
53 Lifshitz, I.M. and Slyozov, V.V. (1961) *J. Phys. Chem. Solids*, **19**, 35.
54 Siggia, E. (1979) *Phys. Rev. A*, **20**, 595.
55 Tanaka, H., Lovinger, A.J., and Davis, D.D. (1994) *Phys. Rev. Lett.*, **72**, 2581.
56 Karim, A., Douglas, J.F., Nisato, G., Liu, D.W., and Amis, E.J. (1999) *Macromolecules*, **32**, 5917.
57 Zhang, X., Lacerda, S.H.D.P., Yager, K.G., Berry, B.C., Douglas, J.F., Jones, R.L., and Karim, A. (2009) *ACS Nano*, **3**, 2115.
58 Huse, D.A. and Henley, C.L. (1985) *Phys. Rev. Lett.*, **54**, 2708.
59 Srolovits, D.J. and Hassold, G.N. (1987) *Phys. Rev. B*, **35**, 6902.
60 Gyure, M.F., Harrington, S.T., Strilka, A., and Stanley, H.E. (1995) *Phys. Rev. E*, **52**, 4632.
61 Lee, B.P., Douglas, J., and Glotzer, S.C. (1999) *Phys. Rev. E*, **60**, 5812.
62 Chung, H.J., Taubert, A.H., Deshmukh, R.D., and Composto, R. (2004) *J. Europhys. Lett.*, **68**, 219.
63 Ginzburg, V.V., Qiu, F., Paniconi, M., Peng, G., Jasnow, D., and Balazs, A.C. (1999) *Phys. Rev. Lett.*, **82**, 4026.
64 Ginzburg, V.V., Peng, G., Qiu, F., Jasnow, D., and Balazs, A.C. (1999) *Phys. Rev. E.*, **60**, 4352.
65 Qiu, F., Ginzburg, V.V., Peng, G., Balazs, A.C., Chen, H.-C., and Jasnow, D. (2001) *J. Chem. Phys.*, **115**, 3779.
66 Qiu, F., Ginzburg, V.V., Paniconi, M., Peng, G., Jasnow, D., and Balazs, A.C. (1999) *Langmuir*, **15**, 4952.
67 Ginzburg, V.V., Qiu, F., and Balazs, A.C. (2002) *Polymer*, **43**, 461.
68 Balazs, A.C., Ginzburg, V.V., Peng, G., Qiu, F., and Jasnow, D. (2000) *J. Phys. Chem. B*, **104**, 3411.
69 Laradji, M. and MacNevin, G. (2003) *J. Chem. Phys.*, **119**, 2275.

**70** Laradji, M. and Hore, M.J.A. (2004) *J. Chem. Phys.*, **121**, 10641.

**71** Laradji, M. (2004) *J. Chem. Phys.*, **120**, 9330.

**72** Laradji, M. and Hore, M.J.A. (2008) *J. Chem. Phys.*, **128**, 054901.

**73** Peng, G., Qiu, F., Ginzburg, V.V., Jasnow, D., and Balazs, A.C. (2000) *Science*, **288**, 1802.

**74** Asakura, S. and Oosawa, F. (1958) *J. Polym. Sci.*, **33**, 183.

**75** Gast, A.P., Hall, C.K., and Russel, W.B. (1983) *J. Colloid Interface Sci.*, **96**, 251.

**76** Lekkerkerker, H.N.W., Poon, W.C.K., Pusey, P.N., Stroobants, A., and Warren, P.B. (1992) *Europhys. Lett.*, **20**, 559.

**77** Ramakrishnan, S., Fuchs, M., Schweizer, K.S., and Zukoski, C.F. (2002) *J. Chem. Phys.*, **116**, 2201.

**78** Szleifer, I. and Yerushalmi-Rozen, R. (2005) *Polymer*, **46**, 7803, and references therein.

**79** Lipatov, Y.S., Nesterov, A.E., Ignatova, T.D., and Nesterov, D.A. (2002) *Polymer*, **43**, 875.

**80** Lipatov, Y.S. (2002) *Prog. Polym. Sci.*, **27**, 1721, and references therein.

**81** Karim, A., Liu, D.W., Douglas, J.F., Nakatani, A., and Amis, E. (2000) *Polymer*, **41**, 8455.

**82** Hrnjak-Murgić, Z., Jelčić, Z., Kovačević, V., Mlinać-Miŝak, M., and Jelenčić, J. (2002) *Macromol. Mater. Eng.*, **287**, 684.

**83** Gharachorlou, A. and Goharpey, F. (2008) *Macromolecules*, **41**, 3276.

**84** Ginzburg, V.V. (2005) *Macromolecules*, **38**, 2362.

**85** He, G., Ginzburg, V.V., and Balazs, A.C. (2006) *J. Polym. Sci. Part B: Polym. Phys.*, **44**, 2389.

**86** Carnahan, N.F. and Starling, K.E. (1969) *J. Chem. Phys.*, **51**, 635.

**87** de Luzuriaga, A.R., Etxeberria, A., Rodriguez, J., and Pomposo, J.A. (2008) *Polym. Adv. Technol.*, **19**, 756.

**88** Pomposo, J.A., de Luzuriaga, A.R., Etxeberria, A., and Rodriguez, J. (2008) *Phys. Chem. Chem. Phys.*, **10**, 650.

**89** Vaia, R.A. and Giannelis, E.P. (1997) *Macromolecules*, **30**, 7990.

**90** Vaia, R.A. and Giannelis, E.P. (1997) *Macromolecules*, **30**, 8000.

**91** Balazs, A.C., Singh, C., and Zhulina, E. (1998) *Macromolecules*, **31**, 8370.

**92** Balazs, A.C., Singh, C., Zhulina, E., and Lyatskaya, Y. (1999) *Acc. Chem. Res.*, **32**, 651.

**93** Lyatskaya, Y. and Balazs, A.C. (1998) *Macromolecules*, **31**, 6676.

**94** Ginzburg, V.V., Singh, C., and Balazs, A.C. (2000) *Macromolecules*, **33**, 1089.

**95** Ginzburg, V.V. and Balazs, A.C. (2000) *Adv. Mater.*, **12**, 1805.

**96** Kuznetsov, D. and Balazs, A.C. (2000) *J. Chem. Phys.*, **112**, 4365.

**97** Kuznetsov, D. and Balazs, A.C. (2000) *J. Chem. Phys.*, **113**, 2479.

**98** Cao, D. and Wu, J. (2006) *Langmuir*, **22**, 2712.

**99** Pandey, R. and Farmer, B. (2008) *Macromol. Theory Simul.*, **17**, 208.

**100** Jain, S., Ginzburg, V.V., Jog, P., Weinhold, J., Srivastava, R., and Chapman, W.G. (2009) *J. Chem. Phys.*, **131**, 044908.

**101** Akcora, P., Liu, H., Kumar, S.K., Moll, J., Li, Y., Benicewicz, B.C., Schadler, L.S., Acehan, D., Panagiotopoulos, A.Z., Pryamitsyn, V., Ganesan, V., Ilavsky, J., Thiyagarajan, P., Colby, R.H., and Douglas, J.F. (2009) *Nat. Mater.*, **8**, 354.

**102** Zhang, Z.L., Horsch, M.A., Lamm, M.H., and Glotzer, S.C. (2003) *Nano Lett.*, **3**, 1341.

**103** Iacovella, C.R., Horsch, M.A., Zhang, Z., and Glotzer, S.C. (2005) *Langmuir*, **21**, 9488.

**104** Iacovella, C.R., Keys, A.S., Horsch, M.A., and Glotzer, S.C. (2007) *Phys. Rev. E*, **75**, 40801.

**105** Tang, Z.Y., Zhang, Z.L., Wang, Y., Glotzer, S.C., and Kotov, N.A. (2006) *Science*, **314**, 274.

**106** Gomez, C.M., Porcar, I., Monzo, I.S., Abad, C., and Campos, A. (2007) *Eur. Polym. J.*, **43**, 360.

**107** Figueruelo, J.E., Gomez, C.M., Monzo, I.S., Abad, C., and Campos, A. (2007) *Macromol. Theory Simul.*, **16**, 458.

**108** Soul, E.R., Borrajo, J., and Williams, R. (2007) *Macromolecules*, **40**, 8082.

**109** Chiu, J., Kim, B.J., Yi, C.R., Bang, J., Kramer, E.J., and Pine, D. (2007) *Macromolecules*, **40**, 3361.

**110** Park, S.C., Kim, B.J., Hawker, C.J., Kramer, E.J., Bang, J., and Ha, J.S. (2007) *Macromolecules*, **40**, 8119.

**111** Chiu, J., Kim, B.J., Kramer, E.J., and Pine, D. (2005) *J. Am. Chem. Soc.*, **127**, 5036.

**112** Kim, B.J., Fredrickson, G.H., and Kramer, E.J. (2008) *Macromolecules*, **41**, 436.

**113** Sides, S.W., Kim, B.J., Kramer, E.J., and Fredrickson, G.H. (2006) *Phys. Rev. Lett.*, **96**, 250601.

**114** Lo, C.T., Lee, B., Pol, V.G., Rago, N., Seifert, S., Winans, R.E., and Thiyagarajan, P. (2007) *Macromolecules*, **40**, 8302.

**115** Pryamitsyn, V. and Ganesan, V. (2006) *Macromolecules*, **39**, 8499.

**116** Thompson, R.B., Ginzburg, V.V., Matsen, M., and Balazs, A.C. (2002) *Macromolecules*, **35**, 1060.

**117** Fredrickson, G.H. (2006) *The Equilibrium Theory of Inhomogeneous Polymers*, Oxford University Press, Oxford.

**118** Fredrickson, G.H., Ganesan, V., and Drolet, F. (2002) *Macromolecules*, **35**, 16.

**119** Drolet, F. and Fredrickson, G.H. (1999) *Phys. Rev. Lett.*, **83**, 4317.

**120** Kim, B.J., Fredrickson, G.H., Hawker, C.J., and Kramer, E.J. (2007) *Langmuir*, **23**, 7804.

**121** Lee, J.Y., Thompson, R.B., Jasnow, D., and Balazs, A.C. (2003) *Faraday Trans.*, **123**, 121.

**122** Lee, J.Y., Balazs, A.C., Thompson, R.B., and Hill, R.M. (2004) *Macromolecules*, **37**, 3536.

**123** Lee, J.Y., Shou, Z., and Balazs, A.C. (2003) *Phys. Rev. Lett.*, **91**, 136103.

**124** Lee, J.Y., Shou, Z., and Balazs, A.C. (2003) *Macromolecules*, **36**, 7730.

**125** Lee, J.Y., Buxton, G., and Balazs, A.C. (2004) *J. Chem. Phys.*, **121**, 5531.

**126** Ginzburg, V.V., Myers, K., Malowinski, S., Cieslinski, R., Elwell, M.J., and Bernius, M.T. (2006) *Macromolecules*, **39**, 3901.

**127** Zhang, L., Lin, J., and Lin, S. (2007) *Macromolecules*, **40**, 5582.

**128** Ginzburg, V.V. and Balijepalli, S. (2007) *Nano Lett.*, **7**, 3716.

**129** Leroueil, P., Hong, S., Mecke, A., Baker, J. Jr., Orr, B.G., and Banaszak Holl, M.M. (2007) *Acc. Chem. Res.*, **40**, 335, and references therein.

**130** Reister, E. and Fredrickson, G.H. (2004) *Macromolecules*, **37**, 4718.

**131** Matsen, M.W. and Thompson, R.B. (2008) *Macromolecules*, **41**, 1853.

**132** Kim, J.U. and Matsen, M.W. (2008) *Macromolecules*, **41**, 4435.

**133** Smith, K.A., Jasnow, D., and Balazs, A.C. (2007) *J. Chem. Phys.*, **127**, 084703.

**134** Cao, D. and Wu, J.J. (2007) *Chem. Phys.*, **126**, 144912.

**135** McGarrity, E.S., Frischknecht, A.L., Frink, L.J., and Mackay, M.E. (2007) *Phys. Rev. Lett.*, **99**, 238302.

**136** McGarrity, E.S., Frischknecht, A.L., and Mackay, M.E. (2008) *J. Chem. Phys.*, **128**, 154904.

**137** Vacatello, M. (2001) *Macromolecules*, **34**, 1946.

**138** Sharaf, M.A. and Mark, J.E. (2004) *Polymer*, **45**, 3943.

**139** Smith, J.S., Bedrov, D., and Smith, G.D. (2003) *Compos. Sci. Technol.*, **63**, 1599.

**140** Bedrov, D., Smith, G.D., and Smith, J.S. (2003) *J. Chem. Phys.*, **119**, 10438.

**141** Allegra, G., Raos, G., and Vacatello, M. (2008) *Prog. Polym. Sci.*, **33**, 683, and references therein.

**142** Owens, D.K. and Wendt, R.C. (1969) *J. Appl. Polym. Sci.*, **13**, 1741.

**143** Adamson, A.W. and Gast, A.P. (1997) *Physical Chemistry of Surfaces*, 6th edn, John Wiley & Sons, Inc., New York, Ch. 10.

**144** Wu, S. (1974) *J. Macromol. Sci. C: Rev. Macromol. Chem.*, **10**, 1.

**145** Bicerano, J. (2002) *Prediction of Polymer Properties*, 3rd edn, Marcel Dekker, Basel-New York, Ch. 20.

**146** Bicerano, J., Balijepalli, S., Doufas, A., Ginzburg, V., Moore, J., Somasi, M., Somasi, S., Storer, J., and Verbrugge, T. (2004) *J. Macromol. Sci. Polym. Rev.*, **44**, 53.

**147** Fornes, T. and Paul, D.R. (2003) *Polymer*, **44**, 4993.

**148** Odegard, G.M., Clancy, T.C., and Gates, T.S. (2005) *Polymer*, **46**, 553.

**149** Halpin, J.C. and Kardos, J.L. (1972) *J. Appl. Phys.*, **43**, 2235.

**150** Halpin, J.C. and Kardos, J.L. (1976) *Polym. Eng. Sci.*, **16**, 344.

**151** Mori, T. and Tanaka, K. (1973) *Acta Metall. Mater.*, **21**, 571.

**152** Gusev, A.A. (2001) *Macromolecules*, **34**, 3081.

**153** Wissler, M., Lusti, H.R., Oberson, C., Widmann-Schupak, A.H., Zappini, G., and Gusev, A.A. (2003) *Adv. Eng. Mater.*, **5**, 113.

**154** Brune, D.A. and Bicerano, J. (2002) *Polymer*, **43**, 369.

**155** Thosteson, E.T., Li, C., and Chou, T.W. (2005) *Compos. Sci. Technol.*, **65**, 491, and references therein.

**156** Ponomarenko, A.T., Shevchenko, V.G., and Enikolopyan, N.S. (1990) *Adv. Polym. Sci.*, **96**, 125, and references therein.

**157** Gubbels, F., Jerome, R., Teyssie, P., Vanlathem, E., Deltour, R., Calderone, A., Parente, V., and Bredas, J.L. (1994) *Macromolecules*, **27**, 1972.

**158** Gubbels, F., Blacher, S., Vanlathem, E., Jerome, R., Deltour, R., Brouers, F., and Teyssie, P. (1995) *Macromolecules*, **28**, 1559.

**159** Huang, J.C. (2002) *Adv. Polym. Technol.*, **21**, 299, and references therein.

**160** Mamunya, E.P. (2001) *Macromol. Symp.*, **170**, 257, and references therein.

**161** Sumita, M., Sakata, K., Hayakawa, Y., Asai, S., Miyasaka, K., and Tanemura, M. (1992) *Colloid. Polym. Sci.*, **270**, 134.

**162** Zhang, M.Q., Yu, G., Zeng, H.M., Zhang, H.B., and Hou, Y.H. (1998) *Macromolecules*, **31**, 6724.

**163** Bicerano, J., Douglas, J., and Brune, D.J. (1999) *Macromol. Sci. - Rev.*, **C39**, 561.

**164** Levon, K., Margolina, A., and Patashinsky, A.Z. (1993) *Macromolecules*, **26**, 4061.

**165** Du, F., Scogna, R.C., Zhou, W., Brand, S., Fischer, J.E., and Winey, K.I. (2004) *Macromolecules*, **37**, 9048.

**166** Moniruzzaman, M. and Winey, K. (2006) *Macromolecules*, **39**, 5194, and references therein.

**167** White, S.I., DiDonna, B.A., Mu, M., Lubensky, T.C., and Winey, K.I. (2009) *Phys. Rev. B*, **79**, 024301.

**168** Godovsky, D.Y. (2000) Device applications of polymer nanocomposites, in *Biopolymers/PVA Hydrogels/Anionic Polymerisation/Nanocomposites, Advances in Polymer Sciences*, vol. **153**, Springer-Verlag, Berlin, p. 163, and references therein.

**169** Saunders, B.R. and Turner, M.L. (2008) *Adv. Colloid Interfac.*, **138**, 1, and references therein.

**170** Winey, K., Kashiwagi, T., and Mu, M. (2007) *MRS Bull.*, **32**, 348, and references therein.

# 8
# Modeling the Self-Assembly of Ternary Blends that Encompass Photosensitive Chemical Reactions: Creating Defect-Free, Hierarchically Ordered Materials

*Olga Kuksenok, Rui D.M. Travasso, Pratyush Dayal, and Anna C. Balazs*

## 8.1
## Introduction

There is a significant drive to harness self-assembling polymers in various microelectronic devices; the fact that the materials are polymers reduces the cost of fabrication and the self-assembling aspect reduces the number of processing steps, which again reduces cost. However, several critical requirements, typically, must be met before self-assembling polymers can be implemented in the production of electronic components. In particular, the following conditions must be satisfied:

1) the system should form hierarchical structures, with some domains being on the sub-micron or nanoscale scale, while other domains are on the micron scale;
2) the material should be defect free on the mm to cm length scale;
3) it should be possible to form a wide variety of patterns.

Researchers have addressed these issues, particularly conditions (2) and (3), by directing the self-organization of block copolymer films with an underlying patterned substrate [1–5]. In this manner, the systems exhibited nanoscale features and macroscopic order (with ordered regions that are 1 $cm^2$ in size) [2–4]. In addition, the substrate could be patterned into non-regular shapes and the overlying copolymers or copolymer/homopolymer mixture could be made to replicate the underlying design [2–4].

In recent studies [6–8], we proposed an alternative approach that does not rely on self-assembling copolymers to address the issues listed above. In particular, we used a computational model to demonstrate how homopolymer blends undergoing a photo-induced chemical reaction can yield structures with long-range order in thin films [6, 7] and bulk materials [8]. The process is initiated by shining a spatially uniform light over a photosensitive AB binary homopolymer blend, which thereby undergoes both a reversible chemical reaction and phase separation. We then introduce a well-collimated, higher intensity light source. By rastering this secondary light over the sample we could "comb out" any defects in the material and thereby create spatially regular, periodic structures. These binary structures resemble either the lamellar or hexagonal phases of microphase-separated diblock copolymers [9, 10].

*Encyclopedia of Polymer Blends, Volume 1: Fundamentals.* Edited by Avraam I. Isayev
Copyright © 2010 WILEY-VCH Verlag GmbH & Co. KGaA, Weinheim
ISBN: 978-3-527-31929-9

We then add a non-reactive homopolymer C, which is immiscible with both A and B. We showed that this component migrates to regions that are illuminated by a secondary, higher intensity light, allowing us to effectively write a pattern of C onto the AB film [6–8]. Rastering over the ternary blend with a collimated, high intensity light now leads to defect-free, hierarchically ordered patterns of A, B, and C [6–8].

In addition to addressing conditions (2) and (3) above, the approach allows one to readily create various hierarchical patterns, where some features are on the sub-micron size scale, while other domains are on the micron scale. Furthermore, the resulting structures exhibit periodicity over multiple length scales. Since our approach involves homopolymers rather than block copolymers, it introduces a new way of creating ordered, periodic structures from these simpler systems. Overall, these findings point to a facile, non-intrusive process for manufacturing high quality polymeric devices in a low cost, efficient manner.

More recently [11, 12], we have extended these concepts to formulate another method for creating defect-free, hierarchically structured thin films. In particular, we could drive a film of the photosensitive, immiscible ABC blend into more than one regular, periodic structure with the use of light and just one photomask [11, 12]. The first pattern is established by irradiating the sample through a mask, which serves to pin the C regions; the A and B self-assemble around these pinned regions and, consequently, the system forms an ordered structure. When the mask is removed, the photo-activity of the AB blend leads to different periodic patterns. The various morphologies can be locked into the film by quenching the system at the appropriate time.

Notably, in all these studies, and particularly in the studies involving the photomask, we can form novel square structures, which are particularly important for the microelectronics industry. Additionally, we can form structural motifs that combine hexagonal and rectangular patterns [11, 12]. Prior work by Epstein *et al.* [13, 14] revealed that the application of light and masks to a photosensitive reaction–diffusion system could produce such distinctive "superlattices." In the later work, the small molecule system underwent the chlorine dioxide–iodine–malonic acid (CDIMA) reaction, which is more complicated than the simple interconversion considered here and discussed further below. Nevertheless, certain patterns seen in our study [11, 12] qualitatively resemble some of the images uncovered by these researchers [13, 14]. The later experimental studies on the small molecule systems clearly demonstrate the utility of combining light, masks, and reaction–diffusion systems to manipulate the regularity of the pattern formation.

Recently, Hur *et al.* [15] have used self-consistent field theory to study the equilibrium phase behavior of thin films composed of blends of AB diblock copolymers and A homopolymers laterally confined in square wells. By using suitable homopolymer additives and appropriately sized wells, the researchers observed superlattices that consisted of square lattices and cylindrical structures.

What is distinct in our system is that the patterns involve three different domains (as opposed to the binary motifs found in the above studies [13–15]). Furthermore, in the case involving the photomask [11, 12], we demonstrate that the system evolves

to another hierarchically ordered, periodic structure when the mask is lifted and the entire sample is irradiated.

In the following discussion, we specifically focus on a binary AB blend that undergoes the following photo-induced reversible chemical reaction:

$$A \underset{\Gamma_-}{\overset{\Gamma_+}{\Longleftrightarrow}} B \tag{8.1}$$

where the parameters $\Gamma_+$ and $\Gamma_-$ represent the forward and reverse reaction rate coefficients, respectively. In addition, A and B components undergo phase separation. There are several examples of reaction-induced phase separation in photosensitive systems. Blends of *trans*-stilbene labeled polystyrene and poly(vinyl methyl ether) (PSS/PVME) constitute one well-known example [16–21]. Upon irradiation, the stilbene moieties on the PSS chains undergo a reversible trans–cis photoisomerization. Once the reaction reaches a certain threshold, the mixture undergoes phase separation since the cis-labeled polystyrene and PVME are immiscible. Thus, a reversible chemical reaction and phase separation taking place simultaneously within this binary blend. Other photosensitive pendent groups can also be used to yield a similar behavior [16–21].

An important feature of our model is that we assume that the above reaction rates coefficients can be controlled through an external light source and, consequently, the reaction rate coefficients vary in both space and time, that is, $\Gamma_\pm \equiv \Gamma_\pm(\boldsymbol{r}, t)$. In the corresponding experiments, this would mean, for example, that different regions of the sample would be exposed to light of different intensities and the intensity of the irradiating light would be altered with time. We note that the behavior of binary mixtures that undergo phase separation and chemical reaction, as in Eq. (8.1), has been well studied (see, for example, References [9, 10, 22, 23]). In particular, it is well known that the morphologies in such mixtures resemble the morphologies observed in microphase-separated diblock copolymers [9, 22, 23]. There has also been significant progress in understanding the kinetics of ternary phase-separating mixtures in the absence of chemical reactions (see, for example, References [24–36] and references therein). To date, however, the behavior of reactive ternary mixtures has received considerably less attention [37–42]. Researchers have examined diblock/homopolymer mixtures [43] that display structures similar to patterns described below (i.e., those in which the reaction rate coefficients are constant throughout the sample). Other than our previous studies [6–8], to the best of our knowledge, there have been no studies of phase-separating ternary mixtures undergoing the reaction in Eq. (8.1), where the reaction rate coefficients are varied in space and in time.

In what follows below, we first provide a description of our theoretical model. We then show how one can control the evolution of such systems by varying the reaction rate coefficients in a specified manner. In subsequent sections, we discuss the formation of defect-free structures in the binary and ternary systems via a combination of stationary and moving light sources. We then go on to describe the use of a photomask to control the structure formation within thin films of the ABC blends.

## 8.2 The Model

As noted above, we investigate the structural evolution of ABC ternary mixtures, where the AB binary blend undergoes the photo-induced, reversible chemical reaction described by Eq. (8.1). The C component in the mixture is non-reactive; it is simply immiscible with both A and B. The volume fraction of each component is given by $\varrho_i$, where $i = \mathrm{A}, \mathrm{B}, \mathrm{C}$, and the mixture is assumed to be incompressible, that is, $\sum_i \varrho_i = 1$. To describe the concentration distributions in our system, we define two order parameters; the first order parameter is the difference between the volume fractions of the A and B components, $\varphi = \varrho_\mathrm{B} - \varrho_\mathrm{A}$, and the second order parameter is the volume fraction of the C component, $\psi = \varrho_\mathrm{C}$.

The evolution of the two order parameters is described by the following two modified Cahn–Hilliard equations [6, 12, 32]:

$$\frac{\partial \varphi}{\partial t} = M_\phi \nabla^2 \frac{\delta F(\phi, \psi)}{\delta \phi} - \Gamma[\varphi - \varphi_0(1-\psi)] \tag{8.2}$$

$$\frac{\partial \psi}{\partial t} = M_\psi \nabla^2 \frac{\delta F(\varphi, \psi)}{\delta \psi} \tag{8.3}$$

where $\Gamma = \Gamma_+ + \Gamma_-$ and $\varphi_0 = (\Gamma_+ - \Gamma_-)/(\Gamma_+ + \Gamma_-)$ [1]. Here, we assume that the viscosity of the mixture is sufficiently high so that hydrodynamic effects do not play a role in the system's behavior (see Reference [44]); hence, we neglect hydrodynamics in Eqs. (8.2)–(8.3). We also neglect cross-diffusion [45] in the above system of equations. We note that the expressions describing the dynamics of ternary, phase-separating mixtures in the absence of a chemical reaction were previously derived in References [24, 25] and we refer the reader to these publications for further details.

If the forward and reverse reaction rate coefficients are equal, that is, $\Gamma_+ = \Gamma_- \equiv \Gamma$, Eq. (8.2) reduces to:

$$\frac{\partial \varphi}{\partial t} = M_\varphi \nabla^2 \frac{\delta F(\varphi, \psi)}{\delta \varphi} - 2\Gamma \varphi \tag{8.4}$$

Here, $M_\varphi$ and $M_\psi$ are the respective mobilities of the two order parameters and are taken to be constants.

The form of the free energy functional $F(\varphi, \psi)$ is taken to be [32, 38]:

$$F(\varphi, \psi) = \frac{1}{V} \int \mathrm{d}\boldsymbol{r} \left[ \begin{array}{l} -a_{20}\varphi^2 + a_{40}\varphi^4 + a_{02}\psi^2 - a_{03}\psi^3 + a_{04}\psi^4 + a_{22}\varphi^2\psi^2 \\ + \varkappa_\varphi (\nabla\varphi)^2 + \varkappa_\psi (\nabla\psi)^2 \end{array} \right] \tag{8.5}$$

We determine the values of the coefficients $a_{ij}$ in Eq. (8.5) by requiring the local free energy to have equal minima at $\varphi = \pm 1; \psi = 0$ [which corresponds to the pure A(B) phase] and $\varphi = 0; \psi = 1$ (which corresponds to the pure C phase). Moreover, we

1) Alternatively, one can define the first order parameter as $\varphi = \varrho_\mathrm{A} - \varrho_\mathrm{B}$; with this definition, however, one would need to correspondingly switch the signs of $\Gamma_+$ and $\Gamma_-$ in the numerator of $\varphi_0$.

require the free energy to be symmetric with respect to all three of the components. In particular, we choose [32]:

$$a_{40} = 0.5a_{20}, a_{02} = 3a_{20}, a_{03} = 8a_{20}, a_{04} = 4.5a_{20}, a_{22} = 3a_{20}, a_{20} = 0.5 \quad (8.6)$$

The two gradient terms in Eq. (8.5) are related to the interfacial tension, $\gamma_{ij}$, between the different components; these two terms are sufficient for describing the interfacial energy if $\gamma_{AC} = \gamma_{BC}$. We consider the latter case in most of the following sections. (We note, however, that if $\gamma_{AC} \neq \gamma_{BC}$, one must include an additional term proportional to $\nabla\varphi \cdot \nabla\psi$ in Eq. (8.5); we consider this scenario in Section 8.3.6.) The additional constraint that $\gamma_{AB} = \gamma_{AC} = \gamma_{BC}$ gives the ratio between the coefficients in the gradient terms as $\kappa_\varphi = \kappa_\psi/3$ [32]. The constraint that the mobilities of all the phases are equal yields $M_\varphi = 3M_\psi$ [32]. We note that these constraints on the values of the interfacial tensions and mobilities are not necessary conditions to observe the behavior described below. In fact, as we discuss in the next section, a range of different interfacial tensions and mobilities will yield results similar to those presented herein.

To numerically solve Eqs. (8.2) and(8.3), we used either the cell dynamical system (CDS) method [46–48] or a lattice Boltzmann model (LBM) [49], as specified further in Section 8.3 (Results and Discussion). Details on how the CDS method was implemented for a reactive system with two order parameters in three dimensions are given in Reference [8]. Details on the LBM we used to study ternary, reactive systems are given in Reference [38]. Both the CDS method and the free-energy-based LBM [50–53] constitute two different approaches for simulating the phase-field dynamics described by Eqs. (8.2) and (8.3). By using the LB approach, one can readily study the effect of hydrodynamic interactions in such reactive, multicomponent systems. In the studies discussed here [6, 7], however, we focused on mixtures with high viscosities, where hydrodynamic effects can be neglected [44]. The effects of hydrodynamic interactions on the dynamics of a reactive AB system with the reaction given in Eq. (8.1) were studied in detail in References [54, 55].

We emphasize that when the C component is absent $(\psi = 0)$ the above model reduces to the well-known model for block copolymers [56–59] or reactive polymer blends [9, 10]. In this case, the evolution of the reactive AB system is governed solely by Eq. (8.2) and the morphology of the mixture resembles the lamellar structure formed by microphase-separated symmetric diblock copolymers [9]. (In the context of our work, we only consider reactive blends, and do not consider diblock copolymers.) When $\Gamma_+ = \Gamma_- \equiv \Gamma$ for such reactive binary mixtures, a linear stability analysis gives the growth rate, $w_\varphi(k)$, for the $k_{th}$ mode of the fluctuations of the order parameter around the homogeneous value $\varphi = 0$ as:

$$w_\varphi(k) = 2M_\varphi\left(a_{20}k^2 - \kappa_\varphi k^4\right) - 2\Gamma \quad (8.7)$$

The roots of this characteristic equation give two critical wavenumbers:

$$k^2_{crit,\pm} = \frac{a_{20}}{2\kappa_\varphi}\left[1 \pm \sqrt{1 - \frac{4\Gamma\kappa_\varphi}{M_\varphi a_{20}{}^2}}\right]$$

if the reaction rate coefficient is sufficiently small that $\Gamma < a_{20}^2 M_\varphi / 4\varkappa_\varphi$. The existence of a lower critical wavenumber due to the reaction term means that fluctuations with the small wavenumbers $k < k_{\text{crit},-}$ are suppressed. In other words, only fluctuations with wavelengths in the range:

$$\frac{2\pi}{k_{\text{crit},+}} < \lambda < \frac{2\pi}{k_{\text{crit},-}}$$

can grow in such systems. Thus, reactions such as those in Eq. (8.1) arrest domain growth in binary mixtures at a characteristic wavelength $\lambda$, which is defined by the parameters $\Gamma$, $M_\varphi$, and $\varkappa_\varphi$, and can be found by minimizing the total free energy in the system (which includes the reactive term). If, however, $\Gamma > a_{20}^2 / 4\varkappa_\varphi M_\varphi$, any fluctuations of the order parameter are suppressed, so that the mixture will remain homogeneously mixed. A linear stability analysis for the more general case in which the reaction rate coefficients for the forward and backward reactions in Eq. (8.1) are not equal is provided in Reference [12].

To estimate the total free energy of the reactive ternary system (Section 8.3.2), we first write the effective free energy potential of the binary blend that takes into account not only the free energy defined in Eq. (8.5) but also the reactive contribution on the right-hand side of Eq. (8.4). Hence, we define the effective chemical potential, $\tilde{\mu} = \left(\delta \tilde{F}(\varphi, \psi)\right)/\delta\varphi$, that accounts for the reactive term in Eq. (8.4), and rewrite this equation as (see References [10, 56]):

$$\frac{\partial \varphi}{\partial t} = M_\varphi \nabla^2 \frac{\delta \tilde{F}(\varphi, \psi)}{\delta \varphi} \tag{8.8}$$

where:

$$\tilde{F}(\varphi, \psi) = F(\varphi, \psi) + \frac{\Gamma}{M_\varphi V} \int \mathrm{d}\boldsymbol{r}\, \mathrm{d}\boldsymbol{r} G(\boldsymbol{r} - \boldsymbol{r}') \varphi(\boldsymbol{r}) \varphi(\boldsymbol{r}') \tag{8.9}$$

and the Green's function $G(\boldsymbol{r} - \boldsymbol{r}')$ can be found from the Poisson's equation $\nabla^2 G(\boldsymbol{r} - \boldsymbol{r}') = -\delta(\boldsymbol{r} - \boldsymbol{r}')$ with the appropriate boundary conditions [10, 56]. As we show bellow (see also Reference [10, 56]), the use of the effective potential in Eq. (8.9) is beneficial because it allows one to write the analytical expressions for both the bulk value of the order parameter and the equilibrium value of the characteristic wavenumber (in the single mode approximation).

Finally, we note that a linear stability analysis of both Eqs. (8.3) and (8.4) for the ternary case gives a growth rate $w_\psi(k)$ for the $k_{\text{th}}$ mode of the fluctuations of the second order parameter around the homogeneous value $\psi = 0$ as:

$$w_\psi(k) = 2M_\psi \left(a_{02} k^2 - \varkappa_\psi k^4\right) \tag{8.10}$$

while the growth rate $w_\varphi(k)$ for the $k_{\text{th}}$ mode of the fluctuations of the first order parameter is still given by Eq. (8.7). In other words, there is no lower critical wavenumber for the second order parameter fluctuations and all large wavelength fluctuations will grow. This means that, in our ternary system, a suppression of the large wavelength fluctuations (i.e., a freezing of the evolution of the domains at some

characteristic wavelength) is only expected to occur within the A/B domains, and the growth of the C domains is not suppressed. Similar behavior was observed in earlier simulations (in two dimensions) on copolymer/homopolymer blends [43].

## 8.3
## Results and Discussion

### 8.3.1
### Combing with Light: Creating Patterned, Defect-Free Thin Films

We first consider a thin film of a binary AB system (i.e., C is absent). To model the behavior of the thin film we carry out the simulations in two dimensions. We assume that this 2D sample is irradiated with a uniform background light. In addition, we introduce a spatially localized, secondary light source, moving at a constant speed, $v$, along the $y$-direction (dark stripe in Figure 8.1a). The secondary light source is assumed to have a higher intensity and, therefore, it locally increases the reaction rate coefficients. Thus, Eq. (8.4) is now solved for both spatially and temporally varying values of these coefficients. (Here, we used the lattice Boltzmann technique adapted for a reactive, phase separating ternary mixture with two order parameters [38]; however, we considered the diffusive limit and neglected hydrodynamic interactions in the system.)

Figure 8.1b and c show the system's morphology at early and late times, respectively; here $\Gamma_+ = \Gamma_- = \Gamma_1$ everywhere within the sample and $\Gamma_+ = \Gamma_- = \Gamma_2 >> \Gamma_1$ within the moving secondary light region. We observe that the intermixing is higher (i.e., the absolute value of the order parameter in the bulk is lower) and the width of the lamellar domains is smaller within the $\Gamma_2$ region then in the $\Gamma_1$ areas (in agreement with previous studies [9, 10, 22]).

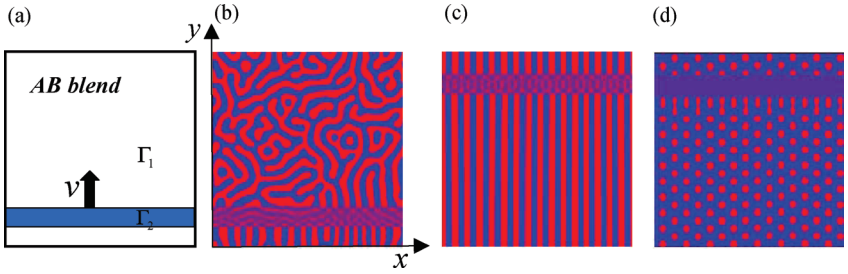


**Figure 8.1** (a) Schematic of the binary AB system. The size of the simulation box is $198 \times 198$, the width of rastering domain is 25 lattice sites, and the rastering velocity is $v = 10^{-3}$. (b, c) Morphologies at early times ($t = 2 \times 10^4$) and late times ($t = 3.7 \times 10^5$), respectively; here, $\Gamma_1 = 0.0003$ and $\Gamma_2 = 0.003$. (d) Morphology at late times for $\Gamma_1^+/\Gamma_1^- = \Gamma_2^+/\Gamma_2^- = 7/3$, where $\Gamma_1^- = 0.0003$ and $\Gamma_2^- = 0.004$. A and B are shown in red and blue, respectively.

By observing the evolution of the structure as the light is moved over the sample, we see that the lamellar domains within the $\Gamma_1$ region align perpendicular to the $\Gamma_2$ boundary and the structure becomes more spatially regular. In effect, the light acts as a "comb" that straightens out the domains as it is passed over the sample.

One can understand this phenomenon in the following manner. Consider the perspective from a wide A (or B) domain on the lower portion of Figure 8.1b (i.e., below the moving horizontal zone). At the interface, this wide domain "sees" several thin A and B neighbors. In addition, the thinner AB domains within the moving $\Gamma_2$ region are more intermixed. In effect, the moving region that comes into contact with the wide A (or B) domain on the lower portion of Figure 8.1b can be thought of as a nonselective or "neutral" domain of some effective homopolymer. It has been shown that when lamellar stripes of diblock copolymers come into contact with a neutral surface, the stripes form perpendicular to the surface [60]. The scenario considered here is somewhat analogous to the latter situation [60], where symmetric diblocks were confined between two surfaces, which were coated with AB random copolymers. On the length scale of a lamellar block of the confined diblocks, the random copolymer appeared as a nonselective "homopolymer." Consequently, the diblocks viewed the surface as being effectively neutral, and aligned with the lamellar stripes being perpendicular to the substrates [60].

In addition to this analogy with the behavior of diblock copolymers, the findings in Figure 8.1 can be understood by recalling that a fluid will form a 90° contact angle with a neutral interface [61]. As the secondary light source is moved across the sample, it effectively creates a *moving* neutral interface. The lamellar domains align perpendicular to the mobile, neutral boundary and, in this manner, the perpendicular orientation propagates throughout the sample (Figure 8.1c).

To better understand the above findings, it is important to note that the phenomenon is a free-energy minimizing process. Since A and B are immiscible, the ordered structure has a lower free energy because the total interfacial length between the A and B domains is smaller in the ordered system than in a disordered one. Consequently, once the rastering light has performed its "combing" function and is subsequently removed, this mixture will retain its defect-free morphology as long as the background illumination is in place. (It was shown in previous studies [62] that thermal fluctuations in the systems described by Eq. (8.8) lead to a higher degree of ordering of the lamellar domains; hence, we anticipate that the structures observed above will retain their high degree of order even for moderately high thermal fluctuations in the system.) Moreover, the structure can be permanently locked into the material by quenching the sample into the solid state.

Both, the ratio $\Gamma_2/\Gamma_1$ and the rastering speed, $v$, affect the degree of order in the sample; the efficient ordering requires relatively high values of $\Gamma_2$ and relatively slow rastering so that the morphology within the $\Gamma_2$ region can reach its steady-state during the time this region is illuminated with the secondary light [6, 7]. Finally, the image in Figure 8.1d illustrates how the proposed approach can also be used to order hexagonal patterns; in this case, we chose different values for the forward and backward reaction rate coefficients.

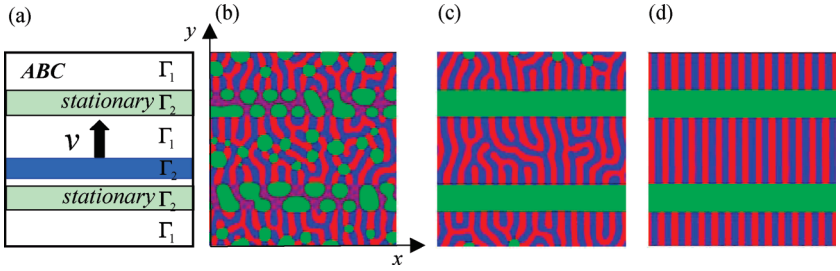


**Figure 8.2** (a) Schematic of the ternary ABC system. (b, c) Morphologies before combing at early times ($t = 8 \times 10^4$) and late times ($t = 3 \times 10^5$), respectively; here, $\Gamma_1 = 0.0003$ and $\Gamma_2 = 0.003$, and the volume fraction of C is 25%. (d) Late time morphology after combing of the sample in (c). All the parameters of the ternary mixture are given in Reference [7]. A, B, and C are shown in red, blue, and green, respectively.

Having examined the binary mixture, we turn our attention to the ternary blend. In addition to the background irradiation (which gives rise to a reaction rate coefficient of $\Gamma_1$), we focus a stationary, higher intensity light on specific areas ($\Gamma_2$ areas in Figure 8.2a). Owing to the higher intensity of the focused light, $\Gamma_2 > \Gamma_1$, and, consequently, we observe thinner and more intermixed domains of A and B within this region than within the rest of the sample. The mixture with the thinner, more intermixed stripes has a higher total free energy. (In the following section, we show quantitatively that the total energy of the AB reactive system gradually increases with the reaction rate, $\Gamma$.) Therefore, in the system that consists of two regions, one with a higher and one with a lower reaction rate, C component migrates into the region with the higher reaction rate. In doing so, it displaces the A and B domains, pushing them into the less intermixed areas and thereby the free energy of the entire system decreases. The diffusion of the C component into the higher intensity regions means that we can essentially "write" any pattern of C onto the AB film by focusing the stationary, higher intensity light in a specified location, as long as the concentration of C is just sufficient to completely cover the $\Gamma_2$ regions [6, 7].

The morphologies of the initially homogeneous A/B/C mixture at early and later times are shown in Figure 8.2b and c, respectively. Even though the C component is ordered in Figure 8.2c, the AB lamellar domains still remain disordered. By "combing" this sample with a moving higher intensity light we obtain a multi-scale, hierarchically ordered A/B/C pattern (Figure 8.2d).

The width of the AB stripe is defined by the polymer properties (e.g., the molecular weight of the chains) and the light intensity, and can be on the sub-micron scale. The size of the C domains is limited by the wavelength of the light; thus, the C domains can be on the microscale. By shining light into areas of different shapes, one can control the shape of the C domains and create a variety of the hierarchically ordered structures [6, 7]. The observed patterns are stable as long as the sample remains illuminated; however, as noted above, the structure can be locked into the material by rapidly quenching the melt into the solid state.

### 8.3.2
### Modeling the Bulk Behavior of Photosensitive Blends under Non-uniform Illumination

We now turn our attention from thin films to bulk materials; to model the latter systems, we utilize a three-dimensional simulation box, which is shown schematically in Figure 8.3a. Unless specified otherwise, the dimensions of the simulation box (in lattice units) are: $L_x = 120$, $L_y = 120$ and $L_z = 150$. Periodic boundary conditions

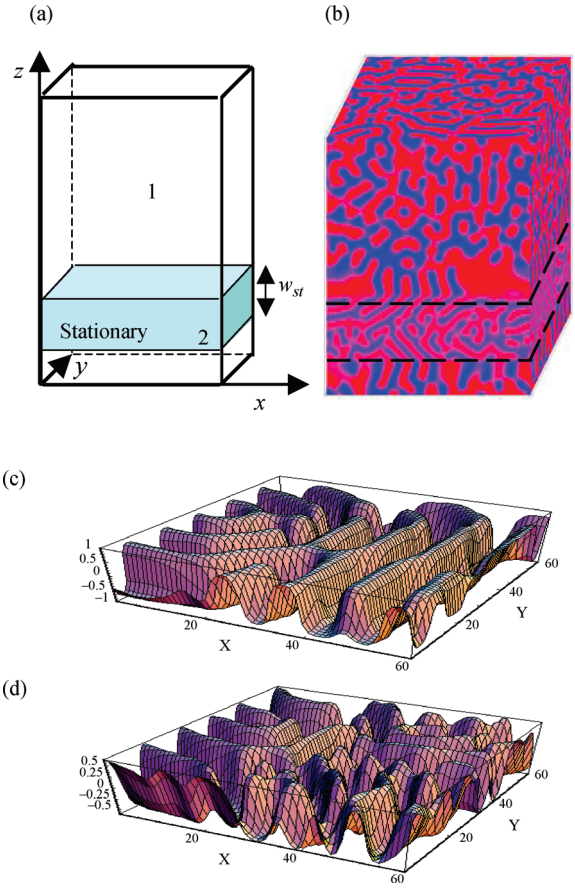


**Figure 8.3** (a) Schematic of the bulk system. The simulation box is $120 \times 120 \times 150$ lattice sites in size and the width of the $\Gamma_2$ region is $w_{st} = 40$ lattice sites (the positions of the lower and upper boundaries of the $\Gamma_2$ region are at $z = 20$ and at $z = 60$ respectively). (b) Morphology of binary blend in the simulation box shown in (a) at late times ($t = 7 \times 10^4$). Here, $\Gamma_1 = 0.003$ and $\Gamma_2 = 0.01$. (c) Order parameter distribution within the $\Gamma_1$ region at the horizontal cross-section at $z = 70$. (d) Order parameter distribution within the $\Gamma_2$ region at the horizontal cross-section at $z = 40$. For clarity in both (c) and (d), only a quarter of the $xy$ plane is shown.

are applied in the $x$, $y$, and $z$ directions. We assume that the entire box is irradiated with a uniform background light [8]. We again refer to the reaction rate coefficient corresponding to the background light as $\Gamma_1$. In all the simulations described herein, we fix $\Gamma_1 = 0.003$. To this uniformly irradiated system, we introduce a spatially localized, secondary light source, which is represented by the cyan stripe in Figure 8.3a. This higher intensity light source locally increases the reaction rate coefficients to $\Gamma_2 > \Gamma_1$. (Within both $\Gamma_1$ and $\Gamma_2$regions, we again assume that the rate coefficients for the forward and reverse reactions are the same, i.e., $\Gamma_1^+ = \Gamma_1^- \equiv \Gamma_1$ and $\Gamma_2^+ = \Gamma_2^- \equiv \Gamma_2$.) For the simulations described in this section, the secondary light source is held fixed in position. Here, we used the cell dynamical systems method (CDSs) [46–48] to simulate the behavior of the reactive ternary blend in three dimensions. Details of how the CDS method was implemented for a reactive system with two order parameters are given in Reference [8].

To facilitate our understanding of the behavior of ternary reactive mixtures under such spatially non-uniform irradiation, we first consider the response of a binary reactive blend to the same conditions. The initial condition for these simulations is a homogeneous AB mixture with a random fluctuation of the order parameter around its average value, $\langle\varphi\rangle = 0$. (We chose the standard deviation to be equal to 0.03; however, any reasonably small value ($\ll 1$) can be chosen.) In this simulation, $\Gamma_1 = 0.003$ and $\Gamma_2 = 0.01$. Figure 8.3b shows the morphology of the reactive binary blend at late times; in addition, Figure 8.3c and d show the order parameter profiles within a specific plane within the $\Gamma_1$ and $\Gamma_2$ regions, respectively. Figure 8.3b and d clearly reveals that the thickness of the lamellae are smaller and the intermixing is higher (i.e., the bulk value of the order parameter is lower) within the $\Gamma_2$ region than in the rest of the sample. The above results agree with earlier studies on AB binary reactive mixtures [9, 10]. Moreover, it has been shown [10] that for the binary case it is possible to use a single mode approximation (in 1D) for the order parameter, $\varphi = \varphi_0 \cos kx$, to successfully estimate the bulk value of the order parameter[2)], $\varphi_0$, and the equilibrium value of the wavenumber, $k$, for a given value of $\Gamma$. (Note that this approximation is valid for small $\varphi$ or relatively high $\Gamma$.) Choosing the Green's function in Eq. (8.9) to be of the form $G(x-x') = -(|x-x'|)/2$ [10, 56] and minimizing the total free energy with respect to $k$ and $\varphi_0$ [10] we obtain:

$$k = \sqrt[4]{\frac{\Gamma}{M_\varphi \kappa_\varphi}}$$

and:

$$\varphi_0 = \sqrt{\frac{2a_{20}}{3a_{40}}}\sqrt{1-\frac{2}{a_{20}}\sqrt{\frac{\kappa_\varphi \Gamma}{M_\varphi}}}$$

2) Here, we use the notation $\varphi_0$ to specify the value of the order parameter in the bulk; this notation is consistent with previous studies [8] and is distinctly different from the notation of $\varphi_0$ we introduced in Section 8.2.

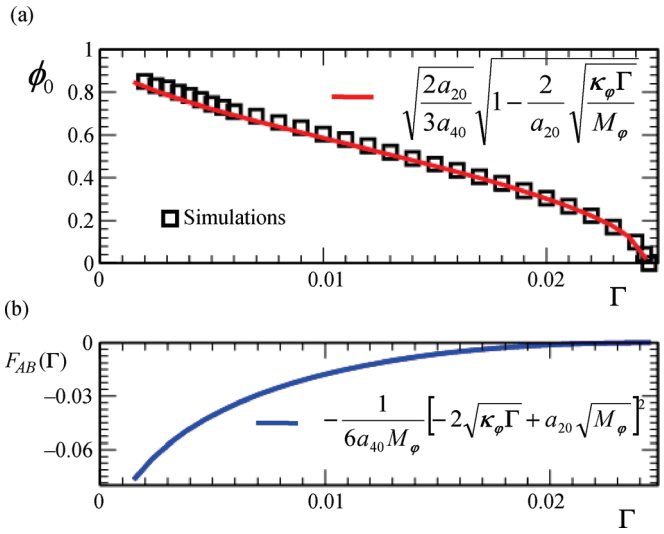


**Figure 8.4** (a) Dependence of the bulk values of the order parameter, $\varphi_0$, on the reaction rate coefficient, $\Gamma$. The squares show simulation data, and the line is described by the equation shown, with $\varkappa_\varphi = 0.25$, $M_\varphi = 0.076$, $a_{20} = 0.569$ and $a_{40} = 0.398$ (see Reference [8]). (b) Dependence of free energy of the binary reactive blend $F_{AB}(\Gamma)$ on the reaction rate coefficient, $\Gamma$, as given by Eq. (8.11).

The latter expression clearly indicates that $\varphi_0$ decreases with increases in $\Gamma$. In addition, using the above expressions for $k$ and $\varphi_0$, we write the total free energy density for this 1D single mode approximation as:

$$F_{AB}(\Gamma) = -\frac{1}{6a_{40}\,M_\varphi}\left(-2\sqrt{\varkappa_\varphi \Gamma}+a_{20}\sqrt{M_\varphi}\right)^2 \tag{8.11}$$

Figure 8.4a shows the dependence of the bulk value of the order parameter, $\varphi_0$, on the values of $\Gamma$; the open squares mark the simulations and the solid line is the analytical expression for $\varphi_0$ given above. The good agreement between the simulation results and analytical expression for $\varphi_0$ indicates that the above approximation is valid for the wide range of $\Gamma$ in our 3D simulations [8]. This result also suggests that the formula in Eq. (8.11) can be used to estimate the free energy of such binary reactive systems. Equation (8.11) indicates that the total free energy of a binary blend undergoing the interconversion reaction in Eq. (8.1) monotonically increases with an increase in the reaction rate constant, $\Gamma$ (Figure 8.4b).

In the next series of simulations, we examine the evolution of the ternary blends under the spatially non-uniform, constant light irradiation. Figure 8.5 shows the time evolution of the ternary system within the same simulation box as in Figure 8.3a. In this case, the initial condition is a homogeneous ABC mixture with a random fluctuation of both order parameters around their average values, $\langle\varphi\rangle = 0$, and $\langle\psi\rangle = 0.27$, respectively. (Here again, the standard deviation around the average value is taken to be to 0.03.) Strictly speaking, to fully represent the morphology in

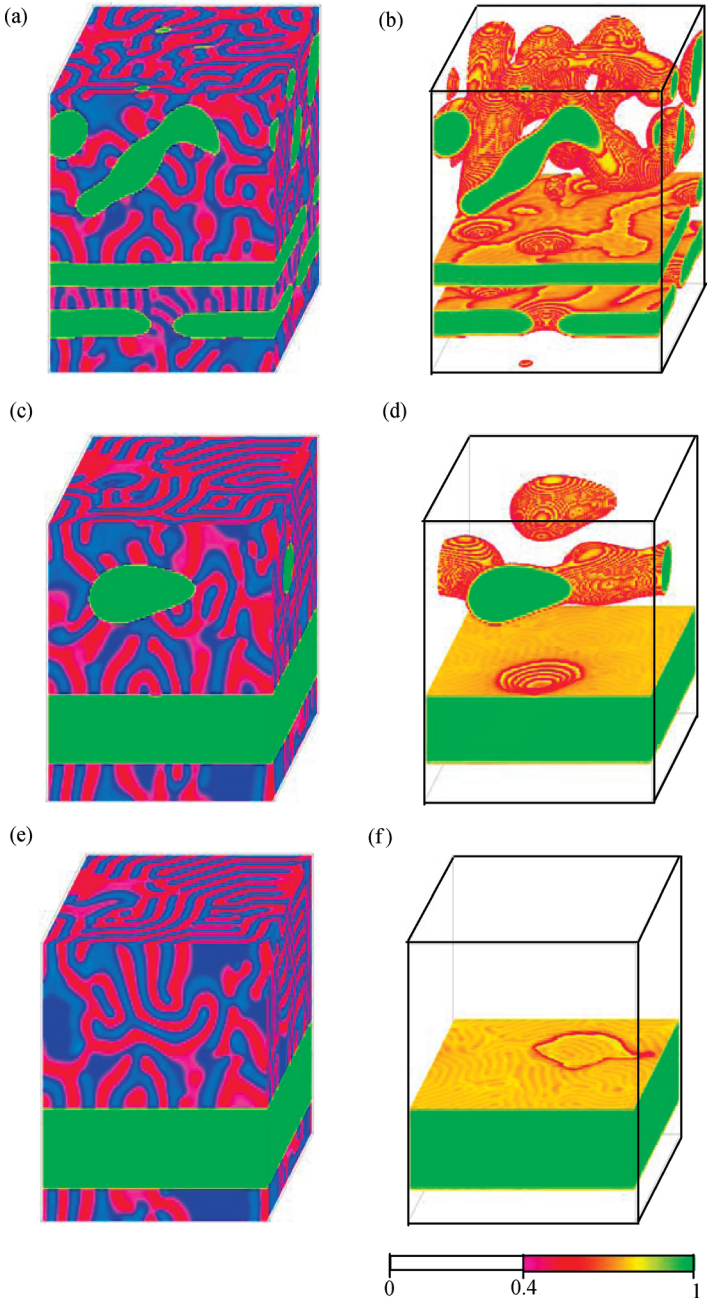


**Figure 8.5** Evolution of the ternary system within the simulation box shown in Figure 8.3a. Here, $\Gamma_1 = 0.003$, $\Gamma_2 = 0.01$. The images in (a), (c), and (e) show morphologies of the ternary mixture (A, B and C are shown in red, blue and green, respectively). Images (b), (d), and (f) show the distribution of C only [according to the scaling bar shown in (f)] for the same run shown in (a), (c), and (e). Corresponding times are: (a, b) $t = 5 \times 10^4$, (c, d) $t = 2 \times 10^5$, and (e, f) $t = 5 \times 10^5$.

the system, one should plot the distribution of both order parameters, $\varphi$ and $\psi$; however, since the C component phase separates from the AB mixture (i.e., within the C domains, $\psi \approx 1$ and $\varphi \approx 0$), here we show the evolution of the system by plotting the value of $\varphi$ for all the points in space for which the condition $\psi < \tilde{\psi} = 0.65$ is satisfied and by plotting the distribution of $\psi$ for all the points in space for which $\psi \geq \tilde{\psi}$ [8]. In other words, in the morphologies shown in the left-hand column of Figure 8.5, as well as in all the following graphical representations of the 3D ternary blends, we plot only the C component when the AB components are predominantly absent, and plot only the AB order parameter when the C component is predominantly absent. (This graphical representation leads to the interface between C and AB looking somewhat sharper than it is in the data.) To provide a clearer picture of the structural evolution inside the 3D sample, in the right-hand column of Figure 8.5 we plot only the distributions of the C component for each of the respective morphology snapshots shown in the left-hand column.

The snapshots of the structural development of the mixture illustrate several processes that are occurring simultaneously: (i) phase separation among all three components, (ii) competition between the reaction and phase separation that defines the characteristic mixing and length scale within the AB domains (for both the $\Gamma_1$ and $\Gamma_2$ regions), and (iii) migration of the C component to the $\Gamma_2$ region (the region with the higher reaction rate coefficient). At late times, we observe saturation of the $\Gamma_2$ region with the C component (Figure 8.5e and f). We also observe that the AB domains are preferentially oriented perpendicular to the boundaries of the C stripe. We note that the amount of C was chosen such that C fills the $\Gamma_2$ region. If there is too much of the C component in the system, the final C domain still forms around the $\Gamma_2$ stripe, but the positions of the interfaces between the C and AB domains are influenced by the concentration of C. If there is too little of the C component in the system, it will not completely fill the stripe, and a droplet of C is formed within the $\Gamma_2$ region.

As noted in the previous section, the C component migrates to the higher intensity region (as shown in Figure 8.5) because, in this manner, the total free energy of the system is minimized. As can be seen from Eq. (8.11), the free energy of the binary blend monotonically increases with increasing $\Gamma$ (Figure 8.4b). Therefore, the total free energy density of the *binary* AB mixture is higher in the $\Gamma_2$ region than in the $\Gamma_1$ region. In the *ternary* case, the A and B components diffuse to the lower free energy region (i.e., to the $\Gamma_1$ region or, in the other words, away from the $\Gamma_2$ region); thus, the $\Gamma_2$ region becomes more and more "depleted" of AB domains and "enriched" with the non-reactive C component. At late times, the C component will be always located in the region with the higher reaction rate coefficient, since this leads to a minimization of the total free energy.

To characterize quantitatively the migration of the C component to the $\Gamma_2$ regions, we plot the actual volume fraction of C within this region, $C_0$, as a function of time for different values of $\Gamma_2$. Specifically, we calculate:

$$C_0 = \frac{1}{V_{\Gamma_2}} \oint_{\Gamma_2} \psi(\boldsymbol{r}, t) \mathrm{d}\boldsymbol{r} \tag{8.12}$$

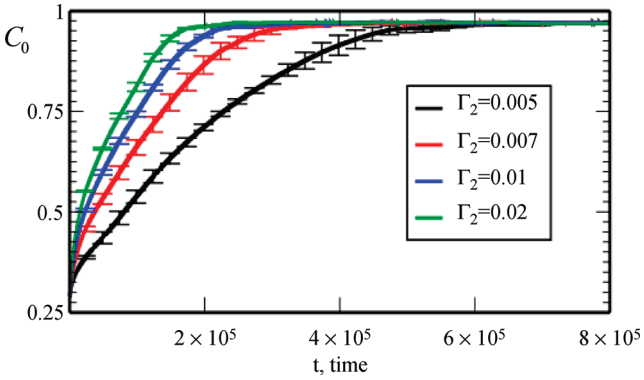


**Figure 8.6** Time evolution of the volume fraction of the C component within the $\Gamma_2$ stripe, $C_0$, for the system shown schematically in Figure 8.3a.

Figure 8.6 shows that at late times, C always diffuses to the $\Gamma_2$ region; however, the rate at which this region becomes saturated strongly depends on $\Gamma_2$. In particular, the domain saturates faster for higher values of $\Gamma_2$. The gain in the total free energy for "replacing" the AB domains with the C domains within the $\Gamma_2$ region increases with increasing values of $\Gamma_2/\Gamma_1$; the greater gain in free energy provides a driving force for the more rapid migration of the C component [8].

Notably, the effect of the migration of C to the higher intensity regions remains robust even if we significantly vary the properties of the local free energy of the C component. For example, we varied the depth of the minima of free energy that corresponds to the pure C component [i.e., we altered the appropriate coefficients in Eq. (8.5)]. We found that the migration of C to the $\Gamma_2$ regions is observed for any chosen parameters. These observations support the above theoretical arguments; that is, the migration of C to the higher $\Gamma$ region happens because the AB blend is diffusing away from this region, and C simply occupies available space[3)]. In other words, the effect of migration of the C component into the higher intensity region is robust and occurs for a wide range of parameters explored in this study.

In the next series of simulations, we examine the migration of C in the case where the $\Gamma_2$ region is a rectangular parallelepiped, which is located in the center of the $xz$ plane and spans the simulation box in the $y$ direction (as indicated by the white rectangle in Figure 8.7a). Figure 8.7a shows early time (left-hand image) and the late time (middle and right-hand images) morphologies for the case where $\Gamma_2 = 0.02$ and $\varkappa_\psi = 0.75$. The late time image on the right-hand side in Figure 8.7a shows only the distribution of the C component. One can clearly see that the C component diffuses to

3) In the limiting case of $\Gamma_2 = \Gamma_1$, the phase separation between the A, B, and C components also occurs. In this case, however, there is no distinction between the $\Gamma_2$ and $\Gamma_1$ regions; hence there is no free energy benefit for the C domain to form at the $\Gamma_2$ region. In this study, we specifically focus on relatively high ratios of $\Gamma_2$ to $\Gamma_1$, because it is only in these cases that clear "writing" with the C component is possible (as illustrated by the above criteria), and, more generally, the effects of the non-uniform illumination are more pronounced.

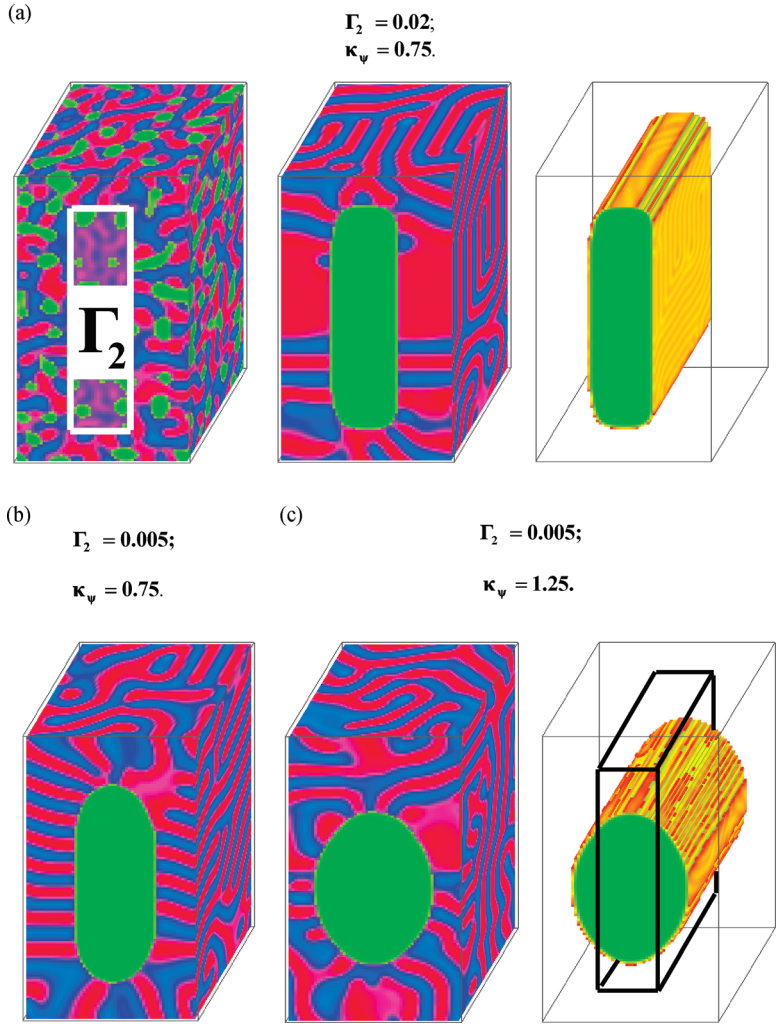


**Figure 8.7** Saturation of the $\Gamma_2$ region, which occupies a rectangular parallelepiped of $22 \times 60 \times 94$ lattice sites and is located within a simulation box of $60 \times 60 \times 120$ lattice sites. (This region is marked by the white rectangular in (a).) (a) $\Gamma_2 = 0.02$, $\varkappa_\psi = 0.75$, and times are: $t = 10^3$ (left-hand image), and $t = 10^6$ (middle and right-hand images); (b) $\Gamma_2 = 0.005$, $\varkappa_\psi = 0.75$, $t = 10^6$; (c) $\Gamma_2 = 0.005$, $\varkappa_\psi = 1.25$, $t = 10^6$. For clarity, the images on the right-hand side in (a) and (c) show only the distributions of the C component (A and B are not shown) for the ternary cases shown in the middle of (a) and on the left in (c), respectively.

the $\Gamma_2$ region at such late times. These simulations illustrate how one can utilize a non-uniform light illumination to effectively write with the non-reactive component C within a ternary blend. In the case shown in Figure 8.7a, the writing is successful; here, the C component is located within the $\Gamma_2$ region at late times with the only imperfections in the corners of the parallelepiped being comparable in size to the

interfacial width. At the lower value of $\Gamma_2 = 0.005$, Figure 8.7b indicates that the writing is less successful. Although the C component still migrates to the $\Gamma_2$ region, the imperfections become much more distinct. Finally, Figure 8.7c shows the late time morphology for the case of the least successful writing, where the C domain forms a cylinder instead of the rectangular parallelepiped. In the latter case, in addition to a decreased value of $\Gamma_2 = 0.005$, we chose a relatively high value of the interfacial tension between the A (B) and C components, namely, $\varkappa_\psi = 1.25$ [8].

To predict which situation will occur for a given set of parameters (i.e., as in Figure 8.7a–c), one has to consider the relative magnitudes of the two distinct contributions to the total free energy. In the case shown in Figure 8.7a, the free energy within the cube is minimized because the A and B components are essentially absent within the $\Gamma_2$ region (except for a relatively small amount within the corners of the $\Gamma_2$ region; we assume this amount to be negligibly small in the following estimates). There is, however, some increase in the total free energy due to the relatively large interfacial area between the A(B) and C domains. The total free energy of the configuration shown in Figure 8.7a can be estimated as:

$$\Psi_{\text{tot}}^{\text{sharp}} \approx F_{\text{AB}}(\Gamma_1)(V - V_{\Gamma_2}) + A_{\Gamma_2}\gamma_{\text{AC}} + F_{\text{C}}V_{\Gamma_2}, \tag{8.13}$$

where $F_{\text{AB}}(\Gamma_1)$ is the free energy density of the A and B domains within the $\Gamma_1$ region, and $V_C$ and $V_{\Gamma_2}$ are the volumes of the simulation box and the $\Gamma_2$ region, respectively. The parameter $V_{\Gamma_2}$ is the surface area of the $\Gamma_2$ region and $F_{\text{C}}$ is the free energy density within the C domain. Note that the volume $V_{\text{C}}$ and the surface area $A_{\text{C}}$ of the C domain in the above case are taken to be equal to the respective volume $V_{\Gamma_2}$ and to the surface area $A_{\Gamma_2}$ of the $\Gamma_2$ region. (Recall that in these calculations we set $\gamma_{\text{AC}} = \gamma_{\text{BC}}$.)

In contrast, in the case of Figure 8.7c, the interfacial area between the A(B) and C domains is at a minimum value; however, there is some loss in the total free energy due to the presence of A and B domains within the $\Gamma_2$ region. The total free energy of the configuration shown in Figure 8.7c can be estimated as [8]:

$$\Psi_{\text{tot}}^{\text{cyl}} \approx F_{\text{AB}}(\Gamma_1)(V - V_{\Gamma_2} - \Delta V) + F_{\text{AB}}(\Gamma_2)\Delta V + A_{\text{C}}\gamma_{\text{AC}} + F_{\text{C}}V_{\text{C}} \tag{8.14}$$

where $\Delta V$ is the volume of the $\Gamma_2$ region occupied by A and B domains. Note that in this case the volumes and the surface areas of the C domain and of the respective values for the $\Gamma_2$ region are distinctly different.

A sharper domain of C (as in Figure 8.7a) is formed if the decrease in the total free energy due to the A and B domains migrating out of the $\Gamma_2$ region exceeds the increase of the free energy due to the formation of a relatively large interface, that is, if $\Psi_{\text{tot}}^{\text{sharp}} < \Psi_{\text{tot}}^{\text{cyl}}$, which, using the above estimates, can be rewritten as:

$$\Delta V[F_{\text{AB}}(\Gamma_2) - F_{\text{AB}}(\Gamma_1)] > (A_{\Gamma_2} - A_{\text{C}})\gamma_{\text{AC}} \tag{8.15}$$

The above condition allows us to pinpoint the system parameters that ensure a successful writing process, that is, an effective migration of the C component to the rectangular $\Gamma_2$ region. For example, Eq. (8.15) shows that, to write a sharper C domain, one should use a relatively high intensity for the secondary light (high $\Gamma_2$) and choose blends with relatively low interfacial tensions between the C and A(B)

components (low $\gamma_{AC}$). For our simulation values and for the geometry in Figure 8.7, the condition in Eq. (8.15) is only satisfied for the case shown in Figure 8.7a; specifically, in this case we have:

$$\Delta V[F_{AB}(\Gamma_2) - F_{AB}(\Gamma_1)] \approx 2.3(A_{\Gamma_2} - A_C)\gamma_{AC}$$

We also note that for the parameters used for the case shown in Figure 8.7b, even though the condition in Eq. (8.15) is not satisfied, the actual values on the left- and right-hand sides of the inequality are relatively close:

$$(\Delta V[F_{AB}(\Gamma_2) - F_{AB}(\Gamma_1)] \approx 0.7(A_{\Gamma_2} - A_C)\gamma_{AC})$$

The latter values indicate that there is a strong competition between the two mechanisms that contribute to the decrease of the total free energy (i.e., the migration of the A and B domains from the $\Gamma_2$ regions and the decrease of the interfacial area of the C domain); this competition yields the final shape of the C domain.

Finally, for the case shown in Figure 8.7c, we have:

$$\Delta V[F_{AB}(\Gamma_2) - F_{AB}(\Gamma_1)] \approx 0.4(A_{\Gamma_2} - A_C)\gamma_{AC}$$

In this case, the cylindrical configuration clearly corresponds to the minimum of the total free energy. We note that even though we have written Eq. (8.15) for the specific case where the $\Gamma_2$ region has the form of a rectangular parallelepiped, and shown that the above condition describes our simulation results, the arguments we used to derive Eq. (8.15) are quite general and the same condition can be used to estimate the sharpness of the written pattern for basically any chosen shape of the $\Gamma_2$ region.

### 8.3.3
### Combing Out Defects in Bulk Binary Blends

As shown in Section 8.3.1, by rastering the secondary light over a 2D sample (i.e., a thin polymeric film), we could effectively "comb out" the defects within the system, provided that the $\Gamma_2/\Gamma_1$ ratio is sufficiently high and the "combing" speed is lower than a specified critical value [6, 7]. In this section, we examine the ordering in three-dimensional binary systems as we move the secondary, higher intensity light (the cyan $\Gamma_2$ region in Figure 8.3a) with a velocity $v$ from the bottom to the top of the entire sample.

Figure 8.8a shows the time evolution in an AB system that is being ordered or "combed" with the moving light (the $\Gamma_2$ region). Here, $\Gamma_2 = 0.02$ and the thickness of this region is $w_{mov} = 20$ lattice sites. This slab is moved with a velocity of $v = 0.001$ lattice sites per simulation unit of time. As the $\Gamma_2$ region passes through the sample, it acts as a mobile, neutral interface and the underlying domains reorient perpendicular to this slab. [Recall that the domains are smaller and more intermixed within the $\Gamma_2$ region (Figure 8.3b–d); consequently, these domains are relatively neutral with respect to the $\Gamma_1$ domains.] As the $\Gamma_2$ stripe is moved from the bottom to the top of the sample, the underlying $\Gamma_1$ domains become more oriented along $z$ and, in this manner, the defects along this direction are effectively "combed out" of the material.

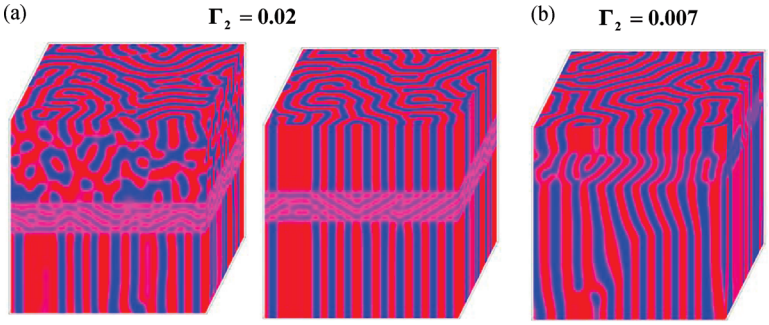


**Figure 8.8** (a) Evolution of the binary system, combed with a rastering speed of $v = 0.001$; $\Gamma_2 = 0.02$, and the corresponding simulation time steps are $t = 5 \times 10^4$ and $t = 3 \times 10^5$ for the images on the left and on the right, respectively. Here and in all the following simulations, we set the width of the moving $\Gamma_2$ region to $w_{mov} = 20$ lattice sites. (b) Late time morphology (at $t = 6 \times 10^5$) for unsuccessful combing with $\Gamma_2 = 0.007$; here, the rastering velocity is $v = 5 \times 10^{-4}$.

Similar to the 2D case [6, 7], the efficiency of the combing process depends on the velocity of the moving stripe and on the value of $\Gamma_2$relative to $\Gamma_1$. For example, in the case shown in Figure 8.8a, $\Gamma_2$ is sufficiently high that the A and B phases are almost intermixed within the stripe; consequently, the combing is highly efficient. For lower $\Gamma_2$ within the stripe (where we still maintain the constraint that $\Gamma_2 > \Gamma_1$), the efficiency of the combing strongly depends on the combing velocity [8]. Figure 8.8b represents a case of the unsuccessful combing that can occur with a relatively low rastering velocity at a fixed value of $\Gamma_2 = 0.007$. We note, however, that the above values of the rastering speeds, as well as all the values used later in this work, are lower than the critical velocity $v_{max} \approx 2\Gamma_2 w_{mov}$ [6, 7]. If $v$ is on the order of or greater than $v_{max}$, then the secondary light is being rastered too quickly for the lamellar domains within the $\Gamma_2$ stripe to reach both their equilibrium size and bulk order parameter (i.e., for the domains to become intermixed). Given this constraint, we found that at lower values of $\Gamma_2$ the ordering is significantly better for the higher rastering velocity. This is because, at the lower rastering velocity, the stripe is moving sufficiently slowly for the $\Gamma_2$ domains to reorient and to coincide with the domains in the neighboring $\Gamma_1$ region (Figure 8.8b). Owing to the difference in sizes, a perfect match between the different domains is not possible and, therefore, the motion of the stripe leads to the formation of the distorted domains [8].

To quantitatively characterize the ordering along the z-direction, we use the following measure:

$$\beta_z(t) = \left\langle <\varphi(t)>_z^2 / <\varphi(t)^2>_z \right\rangle_{x,y} \tag{8.16}$$

The system is completely ordered along $z$ when $\beta_z = 1$. We emphasize that this measure only allows us to calculate the ordering in the $z$ direction, and does not account for any order/disorder in the $x$,$y$ directions. In other words, the ordering

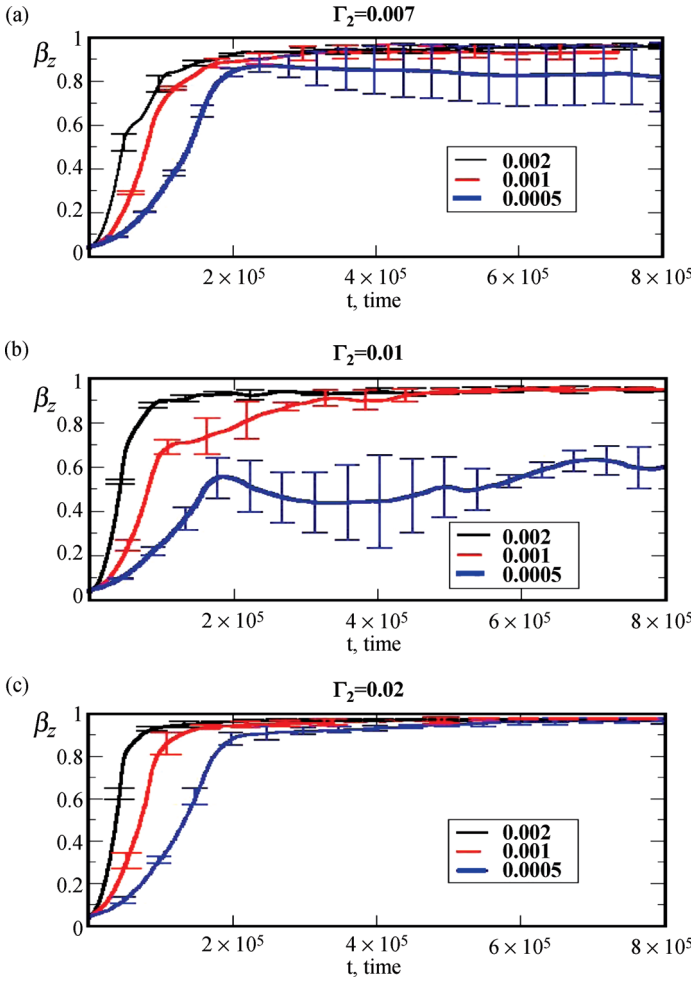


**Figure 8.9** Evolution of the ordering along the combing direction, $\beta_z$, for $\Gamma_2 =$ (a) 0.007, (b) 0.01, and (c) 0.02. For all the cases, black, red, and blue curves represent an average over three independent runs with the values of rastering velocities taken to be $\nu = 0.002$, 0.001, and 0.0005, respectively (see corresponding legends).

along $z$ is complete if all the AB interfaces are oriented along the $z$ direction, independent of the thickness and orientation of these domains in the $x$, $y$ directions. Note that in Eq. (8.16), the average values $(< \ldots >_z, < \ldots >_{x,y})$ are calculated everywhere within the box except within the moving $\Gamma_2$ region.

In Figure 8.9, we plot the evolution of $\beta_z$ within the system as regions with $\Gamma_2 = 0.007$, 0.01, or 0.02 are rastered through the sample. For each value of $\Gamma_2$, we calculate the ordering for three different rastering velocities; each data point (with error bars) represents an average over three independent runs. A common feature of

all the plots in Figure 8.9 is the fast growth of the ordering within the sample during the first passage of the $\Gamma_2$ region over the sample. In each curve, the saturation of the ordering (i.e., when $\beta_z$ reaches its equilibrium value for the given rastering speed and the value of $\Gamma_2$) happens at the beginning of the second passage of the $\Gamma_2$ region over the sample. In fact, we observed that a single passage is enough to obtain a value of $\beta_z$ that is close to its equilibrium value everywhere within the sample, except at the bottom portion of the simulation box, where the ordering is slightly distorted due to the periodic boundary conditions. The latter observation explains the improved ordering during the beginning of the second passage.

Another common feature of all the examples in Figure 8.9 is the high degree of ordering that is obtained at relatively high velocities (see black curves in Figure 8.9a–c). The ordering at the lowest rastering velocity is the poorest for both intermediate values of $\Gamma_2$(i.e., for $\Gamma_2 = 0.007$ and $\Gamma_2 = 0.01$). As was shown in the example in Figure 8.8b, when the $\Gamma_2$ region is moved sufficiently slowly and $\Gamma_2$ is relatively small (compared to $\Gamma_1$), the domains within this stripe undergo a rearrangement to "match up" with the domains in the neighboring $\Gamma_1$ region; this behavior effectively reduces the ordering in $z$ since this matching is not possible for domains with different sizes. In addition, the increase in the ordering of the domains in the $z$ direction can be slightly reduced because the domains are observed to reorient in the $x,y$ directions. The situation is different for the slow movement of the slab with a relatively high value of $\Gamma_2$ (see blue curve in Figure 8.9c). In the latter case, the intermixing is sufficiently high that the $\Gamma_2$ region is relatively neutral with respect to the $\Gamma_1$ region; hence, the perpendicular orientation of the domains in the $\Gamma_1$ region is realized at each moment in time and is propagated along the sample. We also note here that the error bars in Figure 8.9 are small for the cases of successful combing, indicating that the combing is robust and does not depend on the initial conditions. In contrast, the error bars are relatively large for the cases of non-successful combing; this indicates that if a structure with defects is formed, the actual morphology, and therefore the degree of ordering, depends to some extent on the initial conditions. Finally, while the actual morphology also depends on the size of the box to satisfy the periodic boundary conditions, all the above features of the combing process (i.e., dependence of the average degree of ordering on the rastering velocities) remain the same for the larger simulation boxes.

Summarizing this section, we found that rastering of the $\Gamma_2$ region throughout the sample in a selected direction can be used to introduce an ordering in this direction (the $z$ direction in the above example). However, rastering along one direction cannot be used to introduce order in all directions. To achieve ordering in all directions, a similar technique can be applied a second time in the $x$ direction. In additional simulation studies, we selected a sample that is ordered in the $z$ direction (as in the image on the right in Figure 8.8a), removed the $\Gamma_2$ region that was used during the first stage of the process and, instead, introduced another $\Gamma_2$ region, which was rastered along the $x$ direction, from the left to the right. The late time morphology in these cases exhibited a high degree of order in all directions since the rastering along $x$ aligns the AB interfaces along this direction (due to the moving "neutral" boundary effect discussed above). In the other words, as the $\Gamma_2$ stripe moves from the

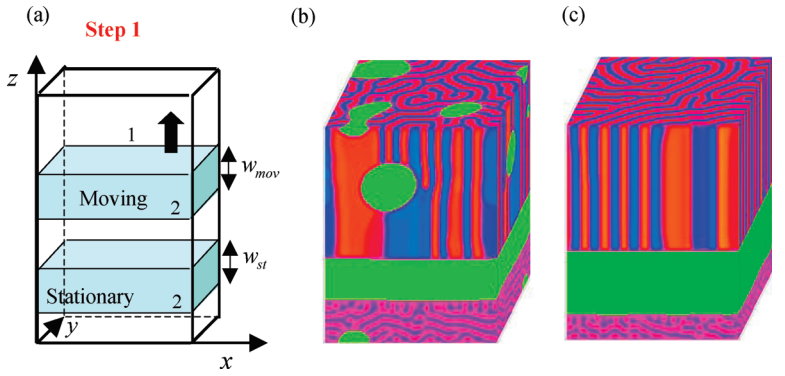


**Figure 8.10** (a) Schematic of the system with two $\Gamma_2$ regions. The width of the stationary $\Gamma_2$ region (lower cyan region) is $w_{st} = 40$ lattice sites with the positions of the lower and upper boundaries at $z = 20$ and 60, respectively. The width of the moving $\Gamma_2$ region (upper cyan region) is $w_{mov} = 20$ lattice sites. (b, c) Evolution of the ordering in the ternary system, rastered with a high intensity region with $\Gamma_2 = 0.02$ along the $z$ direction with a rastering velocity $v = 0.001$. The corresponding times are: $t =$ (b) $1.5 \times 10^5$ and (c) $6 \times 10^5$.

left to right it effectively "transfers" the ordering along $z$ on its left side throughout the sample. Below, we illustrate how to apply such a two-step process to introduce ordering within the ternary systems.

### 8.3.4 Creating Order within the Ternary Mixtures

In this section, we consider a ternary system similar to the one described in Section 8.3.2, except that we now introduce a moving slab, characterized by the higher reaction rates coefficients, to introduce ordering within the AB domains [8]. In particular, we consider the system shown schematically in Figure 8.10a. The images in Figure 8.10b and c illustrate the structural evolution in this system. The two major effects that we described above occur simultaneously in this system: (i) the C component migrates to the stationary $\Gamma_2$ region and (ii) the moving $\Gamma_2$ region combs out the defects within the AB domains along the combing direction.

To achieve ordering within all three directions, we introduce a second step, as shown schematically in Figure 8.11a. Here, we take the morphology that was ordered along the $z$ direction during the first step (as in Figure 8.10c), remove the mobile $\Gamma_2$ region that was utilized in this first step and, instead, introduce another $\Gamma_2$ region, which we now raster along the $x$ direction, from left to right (Figure 8.11a). We keep the stationary $\Gamma_2$ region in the same position as in the first step (Figure 8.10a). An example of the structural evolution in this system is shown in Figure 8.11b and c. As the initial state for this simulation, we took the late time morphology from the example shown in Figure 8.10 (at time $t = 6.25 \times 10^5$). The images in Figure 8.11b and c illustrate that rastering along the $x$ direction aligns the A/B interfaces along $x$; this behavior is attributable to the "neutral" moving boundary, as described above.

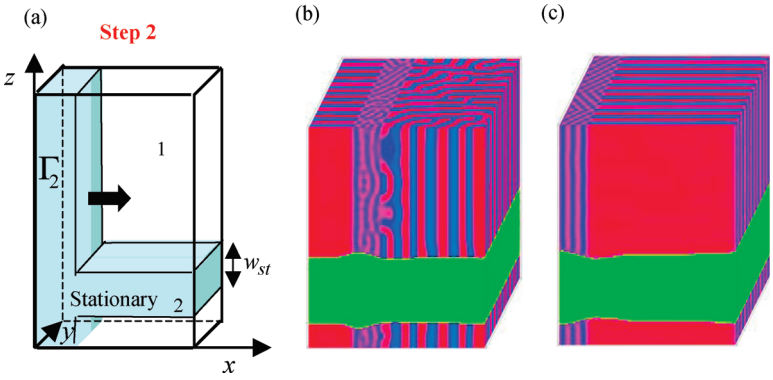


**Figure 8.11** (a) Schematic of the second step of the two-step combing process: the horizontal $\Gamma_2$ region remains the same as in the schematic shown in Figure 8.10a, but the moving $\Gamma_2$ region ($w_{mov} = 20$) is oriented vertically and moves along the $x$ direction (from left to right). (b, c) Snapshots of the ternary morphology at the simulation time steps $t =$ (b) $3 \times 10^4$ and (c) $6 \times 10^5$.

The late time morphology (Figure 8.11c) exhibits a high degree of order in all three directions.

Notable is the distortion of the C region at the places where the moving $\Gamma_2$ region crosses the stationary $\Gamma_2$ region and the fact that these distortions relax away from the moving $\Gamma_2$ region. These distortions appear for the following reason: at each moment of time, some portion of the C component from the stationary $\Gamma_2$ region diffuses to the moving $\Gamma_2$ region because the minimization of the total free energy is the same when the C component occupies either of these $\Gamma_2$ regions. As the mobile $\Gamma_2$ region is swept across the remainder of the sample, the C component returns back to its position within the stationary $\Gamma_2$ region (Figure 8.11b and c). Therefore, one can expect that the above distortions are smaller for a more rapidly moving $\Gamma_2$ region and for a lower mobility, $M_\psi$, of the C component, which does not have enough time to "respond" to the moving $\Gamma_2$ region; this is in fact what we observe in additional simulation studies.

The images in Figures 8.10 and 8.11 illustrate the fact that two steps are needed to create the final, ordered 3D structure (Figure 8.11c). We note that the critical role of the first step (combing along $z$) in the formation of the final structure lies in ordering only within the left side of the image in Figure 8.11b. In other words, as the $\Gamma_2$ stripe moves from the left to right, it effectively "transfers" the ordering along $z$ on its left side throughout the sample. Therefore, to create the morphology shown in Figure 8.11c in an efficient manner, one does not necessarily have to carry out the vertical "combing" for the entire sample; it is sufficient to "comb" along $z$ for only a small longitudinal section of the sample.

To quantify the degree of order within a sample such as that in Figure 8.11c, we calculate the ordering in the $x$ direction in the same way that we calculated the ordering in the $z$ direction,

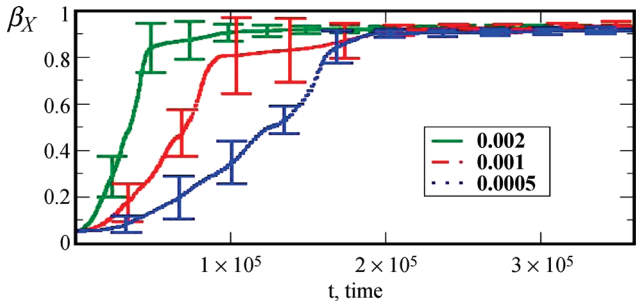


**Figure 8.12** Evolution of the ordering, $\beta_x$, in the ternary system shown schematically in Figure 8.11a. Green, red, and blue curves represent an average over three independent runs with the values of rastering velocities $\nu = 0.002$, 0.001, and 0.0005, respectively. Here, we use $\Gamma_2 = 0.02$.

$$\beta_x(t) = \left\langle <\varphi(t)>_x^2 / <\varphi(t)^2>_x \right\rangle_{y,z} \tag{8.17}$$

In Figure 8.12, we plot the evolution of $\beta_x$ within the system as a region with $\Gamma_2 = 0.02$; $\Gamma_2 = 0.02$ is rastered from left to right (as in Figure 8.11a) through the sample at three different rastering velocities; each curve is an average of three independent runs. As one would expect, the overall behavior of $\beta_x$ is very similar to the behavior of $\beta_z$ for the same parameters as the binary case (Figure 8.9c) because the origin of the ordering process is the same for both procedures. However, there are some differences between the graphs in Figure 8.9c and Figure 8.12. In particular, relative to the binary case, the plots for the ternary case exhibit larger error bars, a less smooth increase of the ordering at the early and intermediate times, and smaller absolute values of the ordering at late times. We attribute these differences to distortions of the *C* region due to the moving $\Gamma_2$ region (Figure 8.11b and c). Since the latter distortions decay away from the moving $\Gamma_2$ region, the ordering away from these regions is high (i.e., it is higher than the saturation value in Figure 8.12). In other words, the local distortions decrease the final value of the ordering in Figure 8.12.

The patterns obtained using the proposed technique are stable under the conditions imposed on the system (i.e., as long as the reaction rate coefficients are held at the specified values). With rapid quenching, for example, the systems described above can be frozen to form a solid that exhibits the morphology of the molten state.

Finally, we note that in the above calculations we assumed that the absorption of light is small and can be neglected over the entire thickness of the sample. In other words, the applied light leads to a constant value of $\Gamma_2$ at each point within the sample. We have, however, examined the evolution of the ternary blends (for the geometry shown in the schematic in Figure 8.10a) in cases where the absorption of light within the sample is explicitly taken into account and refer the reader to Reference [8] for more details. Here we note that, as one expects, the AB lamellar thickness at the back of the sample (i.e., away from the light source) becomes larger as $R_0$, the distance that characterizes the light attenuation within the A and B components, becomes smaller than $L_\gamma$. The moving $\Gamma_2$ region introduces an ordering within the "combing"

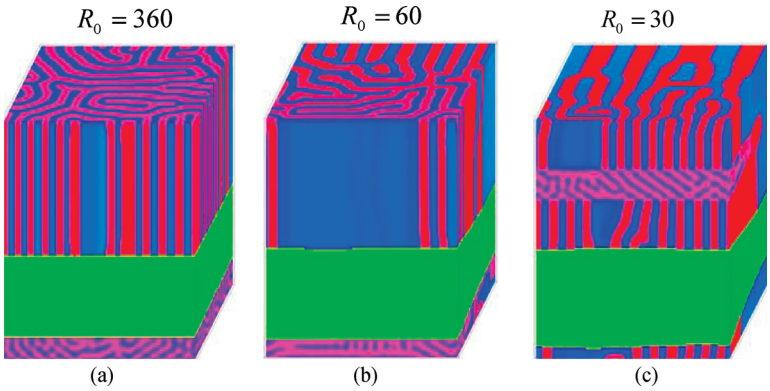


**Figure 8.13** Late time morphologies in the ternary system (its schematic is shown in Figure 8.10a), for values of the characteristic length scales (in lattice sites) of light attenuation, $R_0$, as provided above each image. The corresponding simulation times and rastering velocities are $t = 6 \times 10^5$ and $\nu = 0.001$ for (a) and (b) and $t = 8 \times 10^5$ and $\nu = 0.0005$ for (c); in all the cases, $\Gamma_2 = 0.02$.

direction; however, this ordering becomes more imperfect as $R_0$ is decreased. Figure 8.13 illustrates the latter point; it clearly shows that while at $R_0 = 360$ the degree of ordering remains high, it significantly decreases with decreasing $R_0$. For example, the combing clearly becomes unsuccessful at $R_0 = 30$ (Figure 8.13c). This is mostly because the average reaction rate coefficient within the moving region becomes smaller. In addition, we note that, due to the mismatch between the lamellae thickness at the front and at the back of the sample, the three-dimensional ordering of the form shown in Figure 8.11c would no longer be possible for relatively small $R_0$, even after the second combing step along the $x$ direction. Rather, in this scenario, a gradient material could potentially be formed. Notably, the effect of migration of the C component to the stationary $\Gamma_2$ region remains robust even at relatively low values of $R_0$; the sharpness of writing, however, decreases with decreasing $R_0$ due to widening of the C domain close to the front of the sample (Figure 8.13).

We also note that in additional preliminary studies we probed effects due to the adsorption of light within the C component. In particular, we simulated cases where the light adsorption within the C component is the same as within the AB domains and we found that for the intermediate values of $R_0 \approx L_\gamma$ the late time morphologies are similar to the morphologies shown in Figure 8.13, except for the distinctively greater widening of the C domain close to the front of the sample.

### 8.3.5
### Relating the Dimensionless Simulation Parameters to Physical Values

In the following, we give an example of the relationship between our dimensionless simulation parameters and physical dimensional values. In particular, if we equate

the distance between two lattice sites to $\zeta \approx 10^{-7}$m; then the choice of the dimensional diffusion constant $D$ gives the time scale for one simulation time step as $\tau \approx \zeta^2 2M_\varphi a_{20}/D \approx \zeta^2 0.07/D$ (where we use the dimensionless value for the diffusion constant from our simulation [8], $2M_\varphi a_{20} \approx 0.076$). If we take the value of $D \approx 10^{-14}\,\mathrm{m^2\,s^{-1}}$, we find that the time step in our simulations corresponds to $\tau \approx 0.076\,\mathrm{s}$ and the dimensional combing speed, $\nu\zeta/\tau \approx 2.6 \times 10^{-9}\,\mathrm{m\,s^{-1}}$ (where $\nu = 0.002$ is the dimensionless value of the combing speed). In other words, in the above example, our 3D sample can be "combed out" in $\approx 5.7 \times 10^3$ s with the smallest features being on $10\zeta \approx 1\mu$ (note, that the height of the sample is $150\zeta \approx 15\mu$).

To roughly estimate the effective length for the light intensity attenuation due to the reaction, we assume that both the forward and backward reactions consume a single photon with energy $h\nu$ (i.e., here, we neglect the fact that the adsorption wavelengths for the forward and the backward reactions could be different, and we also neglect any interference between the two light sources [8]). Therefore, the change in the intensity of light, $I$, passing through the sample of thickness $\mathrm{d}y$ can be found as $\mathrm{d}I = -\Gamma h\nu N_\mathrm{R}\mathrm{d}y$. The concentration of the reaction centers, $N_\mathrm{R}$, is defined by the molar mass of the A (B) component ($M_\mathrm{w}$), as $N_\mathrm{R} = N_\mathrm{A}\varrho/M_\mathrm{w}$. Here $N_\mathrm{A}$ is Avogadro's constant and $\varrho$ is a mass density; it is also assumed that there is a single reaction center per molecule. In addition, we assume a linear dependence between the reaction rate coefficient and the light intensity, $I$, so that $\Gamma = \alpha I$. In the estimates below, we use the following physical values: the intensity and the wavelength of the light are taken to be $I = 3 \times \mathrm{mW} \times \mathrm{cm^{-2}}$ and $\lambda = 400\,\mathrm{nm}$, respectively, for the mass density we take $\varrho = 1\,\mathrm{g\,cm^{-3}}$ and for the molar mass of the A(B) we take $M_\mathrm{w} = 1.4 \times 10^4$. Finally, we find the proportionality constant, $\alpha$, using the above value for the light intensity and the dimensional value for the reaction rate constant, $\Gamma = 0.003/\tau$ (here we take 0.003 as the dimensionless value of the reaction rate coefficient used in the simulations [8]). Taking into account all the physical values given above, we find that the characteristic length for the light attenuation within the sample is $(\alpha h\nu N_\mathrm{R})^{-1} \approx 3L_y$ (here $L_y = 120\zeta$ is the dimensional thickness of the sample) [8]. Therefore, the parameters chosen above correspond to the case shown in the left image in Figure 8.13. We also note that by choosing higher values for the molecular weight, lower values for the diffusivity, and higher values for the characteristic length scale one can significantly (e.g., by a couple of orders of magnitude) increase the effective characteristic length for the light attenuation within the sample; however, the latter parameters will also cause a slower evolution of the system.

Above, we gave one example of the relationship between our dimensionless simulation parameters and physical dimensional values. The characteristic time scales given in the first paragraph in this section can be rescaled for different values of the diffusion coefficient and for different length scales in the system. (Namely, the distance between two lattice sites, $\zeta$, could be chosen to be a different value; one should, however, keep in mind that the model is a mesoscale model.)

Finally, we summarize our assumptions and indicate the limitations of our model. In particular the model (i) is valid for polymer blends at a constant temperature, which is chosen above the glass transition temperature, (ii) does not take into account hydrodynamic interactions and cross-diffusion in the system, and (iii) considers

blends undergoing the interconversion reaction in Eq. (8.1) and is not applicable to blends with photo-controlled crosslinking. (Hence, our model does not account for the reaction-induced elasticity, which has been shown to be important for systems undergoing photo-induced crosslinking [63, 64].) To design experiments based on our model systems, one would first need to perform the control experiments for a binary reactive blend to obtain data on the dependence of both the bulk value of the order parameter (similar to the data shown in Figure 8.4a) and the characteristic length scale (e.g., calculated from the expression for the wavenumber in Section 8.3.2) on the intensity of light illumination. Such control experiments would allow one to match the characteristic time scale and length scale in the particular experimental system and the dimensionless values in our simulations. We also note that the computer-assisted irradiation (CAI) method [63] recently used to create a two-dimensional light pattern to illuminate polymer blends undergoing photo-crosslinking could also provide an excellent opportunity for modifying intensity to "write" with the non-reactive C component in a controlled manner.

### 8.3.6
### Using a Single Photomask to Create Multiple Patterns in the Ternary Films

The approach described above uses a combination of stationary and mobile light sources to create the ordered structures. In the following, we use an alternative approach that involves irradiating ternary mixtures through a mask and thereby creating thin films with spatially periodic ABC structures that are hierarchically ordered on different length scales [11, 12].

The proposed approach encompasses two distinctive features that allow us to create various well-controlled morphologies. First, as we show below, irradiation through the mask results not only in the migration and pinning of the C component to the light-exposed regions, but also in the pinning of both the A and B domains, thus yielding a defect-free arrangement of the ABC components. With the removal of the mask, the entire sample becomes uniformly irradiated, and we observe the second distinctive aspect of this system: it evolves to a clearly different *ordered* pattern. If the system is quenched at the appropriate time, one can lock either the first or subsequent regular structures into the material. This approach provides a facile method for producing unique morphologies that could encompass both nanoscopic features and long-range order.

Our system consists of the same ternary blend described above; namely, the photosensitive A and B components undergo the interconversion reaction given by Eq. (8.1), and the C component is not photoactive. Additionally, all three components are mutually immiscible. Since most polymer pairs are immiscible, the C component can in fact be chosen from a large class of compounds. We note that while the size of the AB domains can be tailored by both modifying the molecular weight of these chains and/or the light intensity, the size and the arrangements of the C domains is now dictated by the size and arrangement of the apertures in the photomask [11, 12].

Since our focus is on the behavior of thin films, we carry out the simulations in two dimensions. The size of the simulation box is taken to be $400 \times 400$ lattice sites (unless

specified otherwise) and periodic boundary conditions are imposed along all the edges. The mixtures are assumed to be initially intermixed and homogeneous; the average initial values of $\langle\varphi\rangle$ and $\langle\psi\rangle$ are given for each of the cases below. (Recall that we define $\varphi = \varrho_B - \varrho_A$.)

Through the above model, we simulate the irradiation of a ternary blend through an overlying mask, which contains a periodic arrangement of square holes[4]. The light passes through the holes and initiates the reaction in Eq. (8.1) within these exposed regions. In terms of the simulation, $\Gamma$ is set to a specific value in areas that represent the holes and $\Gamma = 0$ in the non-illuminated regions (i.e., those areas covered by the mask).

Within the illuminated regions, the A/B domains are smaller and more intermixed than in the unexposed areas (where $\Gamma = 0$). Recall that the smaller domain sizes give rise to more interfaces and, consequently, a higher free energy. As discussed in the previous sections, the system's free energy is lowered when the non-reactive C component displaces these A/B domains. This free energy minimization drives C to saturate the illuminated regions. In effect, the reaction pins the C component to the irradiated regions and, in this manner, the C effectively transfers the pattern in the mask onto the AB field. The latter behavior can be seen in Figure 8.14a, which reveals the morphology of the system in the presence of the mask and shows the system at relatively early times. Here, $\Gamma = 0.1$ in the irradiated region and the mixture's composition is given by $\langle\varphi\rangle = 0.3$ and $\langle\psi\rangle = 0.2$; initially, all three components were uniformly intermixed.

Irradiation through the mask, however, is not sufficient for the formation of the ordered structure. Two other critical factors are the interfacial tension ($\gamma_{ij}$) between the different components and the initial composition of the blend. To model mixtures with $\gamma_{AC} \neq \gamma_{BC}$, we added the term $\varkappa_\delta \nabla\varphi \cdot \nabla\psi$ in Eq. (8.5); here, $\varkappa_\delta$ is proportional to the difference between the interfacial tension coefficients for the BC and AC mixtures [11, 12]. In the scenario shown in Figure 8.14, the interfacial tension between A and C is less than that between B and C, that is, $\gamma_{AC} < \gamma_{BC}$. (This is satisfied in Figure 8.14 by setting $\varkappa_\varphi = 0.90$, $\varkappa_\psi = 3.0$, and $\varkappa_\delta = 0.30$.) Under these conditions, the A component acts as a compatibilizer, localizing between the C and B domains and thereby lowering the free energy of the system. Again, free energy minimization drives the system from the morphology in Figure 8.14a, where some of the C and B are still in contact, to the late time structure in Figure 8.14b, where the C is completely shielded from the B by the regular arrangement of A. Notably, such a regular arrangement is possible only for a finite range of A and B volume fractions. Thus, the pinning of the C domains in the system imposes an effective pinning of the A and B domains and, consequently, a global order in the system, as can be seen in Figure 8.14b. This regular structure can be locked into the system by rapidly quenching the film (see discussion below).

**4)** Taking into account that we have periodic boundary conditions, we choose this periodic arrangement of the holes in such a way that the distances between all the neighboring holes are the same (including the distances between the holes close to the boundaries). Hence, the size of the simulation box in this and the following simulations is chosen to satisfy the above requirement for such periodic arrangements of holes with the specified distance between the holes.

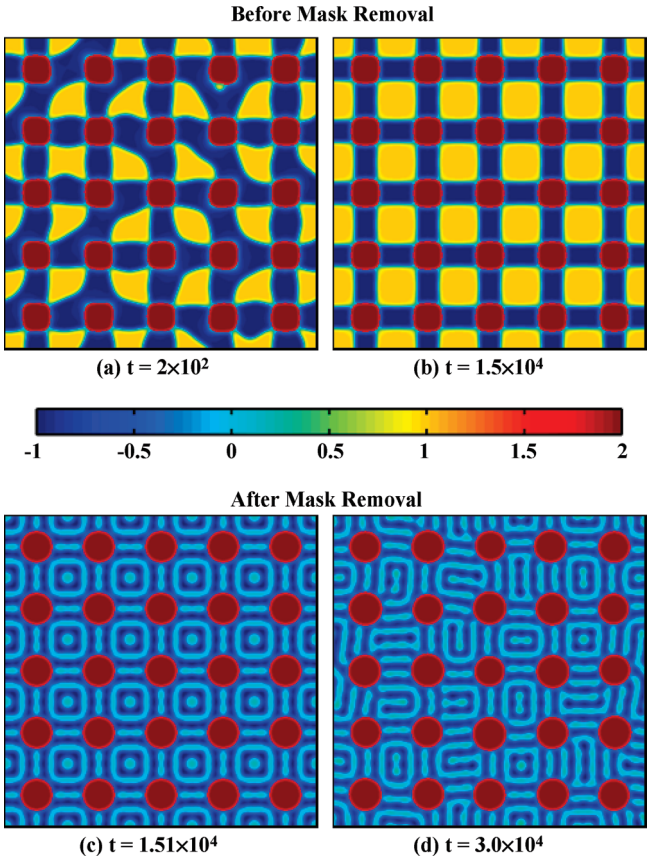


**Figure 8.14** Spatio-temporal evolution of a ternary blend with $\Gamma = 0.10$, $\varkappa_{\varphi} = 0.90$, $\varkappa_{\psi} = 3.0$ and $\varkappa_{\delta} = 0.3$. Initially, all three components were intermixed with $\langle\varphi\rangle = 0.30$ and $\langle\psi\rangle = 0.20$. Simulation times are $2 \times 10^2$, $1.5 \times 10^4$, $1.51 \times 10^4$ and $3 \times 10^4$ in (a), (b), (c) and (d), respectively. The mask is removed at time $1.5 \times 10^4$. The size of the mask's hole is 10% of the sample size. Values $< 1$ in the color bar indicate the A and B components (i.e., the value of $\varphi$), while values $> 1$ mark the C component [i.e., the value of $(\psi + 1)$]. For example, in (a) and (b), the A and B components are represented by blue and yellow, respectively, and the C component is represented by dark red. In (c) and (d), C remains dark red, but the colors marking A and B (i.e., $\varphi$) change because of an intermixing that is caused by the reaction. The same color scheme is used for subsequent figures.

Another remarkable feature of the system is uncovered if, instead of quenching this ordered film, we remove the mask and allow the mixture to coarsen for a relatively short period of time. Namely, the blend evolves to a different periodic pattern, as can be seen in Figure 8.14c. With the removal of the mask, the entire system becomes illuminated and, thus, the reaction in Eq. (8.1) occurs throughout the film. The alternating AB stripes appear because, as already noted in the previous sections, at $\Gamma_+ = \Gamma_- \equiv \Gamma$ the system forms structures that resemble the lamellar morphology created by symmetric diblock copolymers [9, 10]. Even in this uniformly irradiated sample, the prior pinning of the C and the compatibilizing activity of the A impose

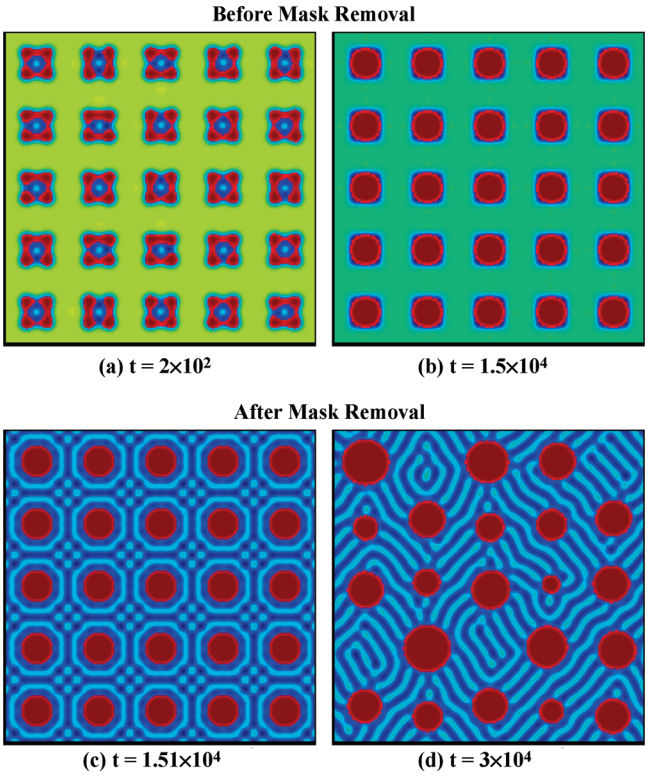


**Figure 8.15** Effect of changing the initial composition of the mixture on morphology development. The initially homogeneous mixture is composed solely of B and C, with $\langle\varphi\rangle = 0.8$ and $\langle\psi\rangle = 0.20$. All other parameters are identical to those in Figure 8.14. The mask was removed at time $1.5 \times 10^4$.

rather strict constraints, which hinder the mobility and rearrangement of the different domains [11, 12]. In response to the latter influences, the film forms the complex pattern in Figure 8.14c, which can also be locked into the system by quenching at the appropriate time (see Figure 8.16). Thus, depending upon the time of the quench, this particular mixture can provide two distinct, highly ordered morphologies. Furthermore, to the best of our knowledge, these regular morphologies have not been previously predicted or observed in ternary blends. It is important to note that if the system in Figure 8.14c continues to coarsen, it will ultimately lead to the disordered system in Figure 8.14d.

The examples that follow illustrate that a simple change in the initial composition of the A and B provides an effective means of tailoring the resulting pattern. For the case in Figure 8.15, the A component is initially absent and the mixture consists of just B and C; all other parameters are identical to those in Figure 8.14. When the sample is illuminated through the mask, A is formed as a product of the reaction within the holes; the masked regions, however, remain pure B. During the initial stages (Figure 8.15a and b), C migrates from the bulk to the illuminated, square

domains and is surrounded by the compatibilizing A component. The small amount of B that would be present in the illuminated area is expelled to bulk of the B phase since this lowers the system's free energy. The morphology in Figure 8.15b is distinctly different from that in Figure 8.14b, indicating that variations in the mixture's composition provide a means of tuning the morphology of the masked film.

More dramatic structural variations occur, however, when the mask is lifted from the above system. As the whole sample is exposed to light, A is formed in the bulk of the material and AB target patterns appear around each C domain. The periodic array of such circular patterns, however, is not space filling, posing a difficult tiling problem [64]. The system appears to solve this problem by self-assembling into an A/B checkerboard-like arrangement at the interstitial sites and thereby forms the complex, ordered pattern in Figure 8.15c.

To quantify the degree of ordering in these systems, we define the effective ordering parameter:

$$\beta = \left\langle \left\langle \langle \varphi \rangle_{\Lambda x}^2 / \langle \varphi^2 \rangle_{\Lambda x} \right\rangle_x \right\rangle_y$$

where $\Lambda$ is the periodicity of the masks and $\langle \ldots \rangle_j$ represents the average values computed in $j$-direction. When the system is completely disordered, $\beta = 0$, while for the perfectly ordered film, $\beta = 1$. This definition of $\beta$ is similar to the one we introduced in previous sections for the degree of ordering along the combing direction; here, however, $\beta$ explicitly accounts for the periodicity of the mask.

Figure 8.16 depicts the evolution of $\beta$ for the examples given in Figures 8.14 and 8.15. For the case corresponding to Figure 8.14, $\beta$ approaches unity as the system becomes ordered, while for the case corresponding to Figure 8.15, $\beta$ remains close to

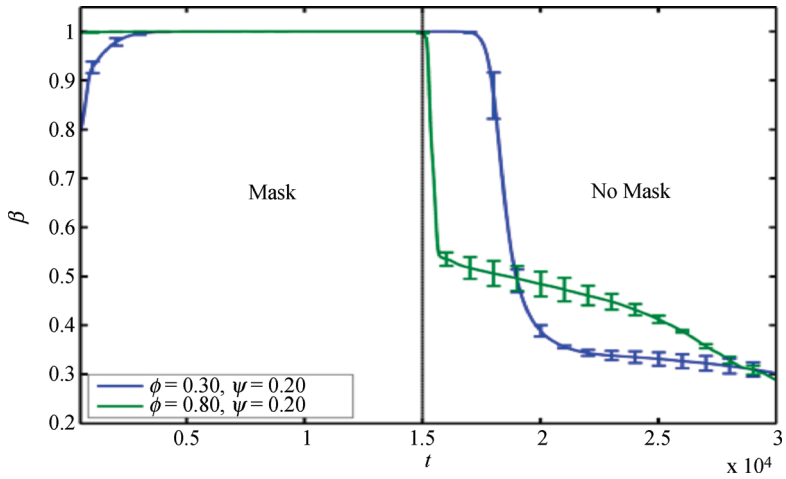


**Figure 8.16** Time evolution of the degree of order in the system, $\beta$, for parameters used in Figures 8.14 and 8.15. The solid vertical line marks the moment in time when the masks were removed. The values of $\beta$ are average values computed over three independent simulations.

unity even at early times due to the different initial conditions (Figure 8.15a). When the masks are removed (marked by the vertical line in Figure 8.16), there exists a finite time interval before $\beta$ drops significantly in both cases; however, this time is much larger for the case in Figure 8.14c than for the case in Figure 8.15c (the lifetimes of the ordered structures in Figures 8.14c and 8.15c are approximately 1700 and 100 dimensionless units of time, respectively). This difference in the lifetimes of the ordered structures can be attributed to the fact that the AB part of the pattern formed in Figure 8.14c is closer to the equilibrium lamellar-like morphology for this reaction–diffusion system than the more exotic AB distribution in Figure 8.15c. The latter pattern tends to promptly form the more energetically favorable lamella-like domains and, thus, speeds up the coarsening of the C domains (as in Figure 8.15d). By relating the dimensionless simulation unit of time to characteristic dimensional experimental parameters [11], we find that the lifetime of the ordered structures after removing the mask can range from seconds to hours, depending, for example, on the components' mobilities, which can be tailored by varying the respective molecular weights. Note that, in contrast to the structures in Figures 8.14c and 8.15c, the ordered structures in Figures 8.14b and 8.15b remain indefinitely until the mask is removed.

Varying the size and separation between the holes in the masks, as well as the arrangement of these holes, provides another means of altering the film's morphology. For the image in Figure 8.17a, the inter-hole distance and the hole-size are increased to 20% and 13% of the sample size, respectively. Here, we have an initially homogeneous mixture of just B and C, with $\langle\varphi\rangle = 0.775$, $\langle\psi\rangle = 0.225$. The other parameters are $\Gamma = 0.05$, $\varkappa_\varphi = 0.90$, $\varkappa_\psi = 3.0$ and $\varkappa_\delta = 0.50$. Again, the striking structural changes occur when the mask is lifted. In contrast to the unmasked structures in Figures 8.14 and 8.15, a greater number of lamellae are localized between the C domains due to the greater inter-hole distance; furthermore, the self-assembling system now solves the tiling problem by forming a diamond shaped pattern between the target-like morphologies. The boundaries of a unit cell resemble structures formed by the combination of stamping and reaction–diffusion [65]; here, however, the film is flat and interactions among A, B, and C lead to a complex design within each cell.

When the arrangement of the holes is changed from rectangular to hexagonal, as shown in Figure 8.17b, perfect hexagonally ordered structures are formed. What is most remarkable here is that two distinct periodic morphologies are produced as the system coarsens, with the late-time structure forming a hexagonal honeycomb pattern. Another essential feature of this system is its very long lifetime; in the simulations, we observed no degradation of the honeycomb pattern in Figure 8.17b even after $4 \times 10^5$ simulation time steps.

## 8.4 Conclusions

Our goal was to establish facile methods for creating defect-free, multicomponent materials that show hierarchical ordering, with the structural features being on

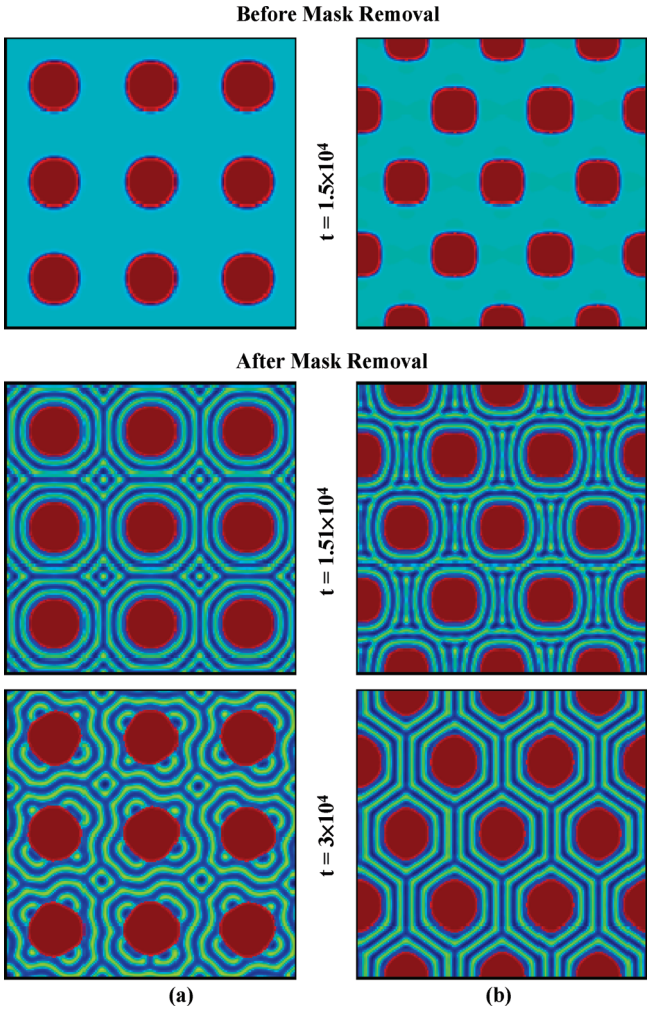


**Figure 8.17** Spatio-temporal evolution of a ternary blend with $\Gamma = 0.05$, $\varkappa_{\varphi} = 0.90$, $\varkappa_{\psi} = 3.0$ and $\varkappa_{\delta} = 0.50$. The initially homogeneous mixture is composed solely of B and C, with $\langle\varphi\rangle = 0.775$ and $\langle\psi\rangle = 0.225$. Morphologies for different arrangements of holes in the mask: (a) for a rectangular arrangement and (b) for the analogous hexagonal arrangement. The mask is removed at time $1.5 \times 10^4$. Effect of changing the initial composition of the mixture on the morphology development: The initially homogeneous mixture is composed solely of B and C, with $\langle\varphi\rangle = 0.8$ and $\langle\psi\rangle = 0.20$. All the other parameters are identical to parameters in Figure 8.14. The mask is removed at time $1.5 \times 10^4$.

distinctly different length scales. We considered thin films and bulk samples of AB binary and ABC ternary blends where the A and B undergo a reversible photochemical interconversion reaction, and the C component is non-reactive. All three components, A, B, and C, are mutually immiscible. By using computer simulation,

we demonstrated two distinct ways of creating regular, periodic structures within these materials. In the first approach, we exposed the mixtures to both spatially and temporally dependent light irradiation [6–8]. Experimentally, this would correspond to using both a uniform background light and a localized, well-collimated light source. The well-collimated light is taken to have a higher intensity than the background light and, thus, the rate coefficient in the latter region, $\Gamma_2$, is higher than $\Gamma_1$, the rate coefficient in the rest of the sample. (Here, we assumed that the forward and reverse rate coefficients for the reversible reaction are equal.)

For the AB binary blend, we demonstrated how moving the $\Gamma_2$ region through the sample could lead to spatially ordered morphologies. In experiments, such motion would correspond to rastering over the sample with the well-collimated light source. We showed that for a specified range of the rastering velocities the mobile light "combs out" defects within the AB lamellar domains and the system becomes ordered along the combing direction. This ordering occurs because the $\Gamma_2$ region creates a moving "neutral" boundary, which drives the re-orientation of the AB domains perpendicular to this interface (i.e., along the rastering direction). The results also reveal that a three-dimensional bulk sample of the AB blend can be ordered in all three directions by applying the proposed technique twice, that is, by rastering the higher intensity light along $z$ and then along $x$.

We next considered the effect of illuminating ABC ternary samples with a background light and a stationary, collimated light (again characterized by a rate coefficient of $\Gamma_2$). We found that the reactive AB mixture will diffuse out of the $\Gamma_2$ regions, while the non-reactive C component will diffuse into these regions. Thus, by focusing the higher intensity light onto selected regions, one can write a pattern of C on the AB reactive blend. This approach provides a non-invasive, robust means of writing with the C "ink" and is effective for a wide range of system parameters.

To successfully write the desired C pattern, it is necessary to have a sufficient amount of C to effectively fill the higher intensity region (or regions). We derived a criterion that allows us to predict, for different system parameters, the sharpness of the written pattern (i.e., how closely the shape of the C domain replicates the geometry of the $\Gamma_2$ region). We showed that the writing is sharper for relatively high values of $\Gamma_2$ and relatively low values of the interfacial tension between the A(B) and C components.

By combining the two effects described above (the migration of C to stationary $\Gamma_2$ domains and the combing of the AB domains with the moving $\Gamma_2$ regions), one can create various defect-free, hierarchically ordered, multicomponent materials. For example, one can create ordered materials that exhibit a periodicity over two distinct length scales, where one length scale is defined by the thickness of the AB lamellae, and the second length scale is defined by the size of the C-filled stationary $\Gamma_2$ regions.

In the second approach described herein, we again exploited the photochemical reaction within the ternary ABC mixture. Here, however, we irradiated a thin film of the blend through a photomask [11, 12]. For a range of interfacial tensions between the different components, we found that the system not only forms an ordered pattern in the presence of a periodic mask, but also coarsens to a different spatially regular structure when the mask is removed (before ultimately forming a disordered mixture). In essence, the use of a single mask can lead to two or even three different patterns for a chosen mixture, any of which can be trapped in the material by

quenching at the appropriate time. The observed patterns are highly complex, forming a rich variety of superlattices. The size scale of the features can be tailored by varying the molecular weight of the components, with, for example, sub-micron AB domains forming around microscopic C regions. We showed that a simple change in the initial composition of such reactive blends can provide an effective means of tailoring resulting morphologies. The proposed approach could provide a robust technique for creating patterned films with long-range order and, thus, could enable low-cost production methods for nanoscale devices.

Since our approaches involve homopolymers they significantly expand the range of materials that can be used to form periodic structures. Furthermore, these methods could potentially provide advantages over current photolithographic processes from several vantage points. First, functionality or contrast can be selectively placed on a surface in just two processing steps, eliminating the need for conventional multistep processes. For photovoltaic, sensor, and media applications, the ability to select the lateral placement on materials is key. Second, the process is fully reversible, thereby producing "read-write" media in a straightforward way. Third, since light is used, the process is non-invasive, eliminating the need to physically contact the film. Fourth, the technique points to a novel means of writing patterns in three dimensions within polymeric materials.

One area where these techniques could have important consequences is in the fabrication of organic photovoltaic (PV) devices. The active material in these devices is usually a blend of two materials, one is good at transporting holes and the other is good at transporting electrons. The two materials should lie in close proximity (i.e., on the order of 10 nm apart) and there should be a large interfacial area between these two domains. In addition, the morphology must provide a percolating path for both holes and electrons. The spatially regular lamellar morphology shown here for the binary blends could potentially provide the desired structure for the organic component of a PV cell. While microphase-separated diblock copolymers could also be harnessed for this application, it is relatively challenging and limiting to create diblocks that have the necessary electronic properties. By using blends, rather than diblocks, the designer has a greater range of materials that can be utilized to create the PV devices.

## Acknowledgments

The authors gratefully acknowledge financial support from the DOE. RDMT acknowledges support from Fundação para a Ciência e Tecnologia through the Ciência 2007 program.

## Abbreviations and Symbols

### Abbreviations

CDS cell dynamical system
LBM lattice Boltzmann model

**Symbols**

| | |
|---|---|
| $a_{ij}$ | coefficients in free energy |
| $A_{\Gamma_2}$ | surface area of high intensity region |
| $C_0$ | volume fraction of the C component within the high intensity region |
| $D$ | diffusion constant |
| $F(\varphi, \psi)$ | free energy functional |
| $F_{AB}(\Gamma)$ | free energy of AB reactive blend in a single mode approximation |
| $G(\boldsymbol{r}-\boldsymbol{r}')$ | Green's function |
| $I$ | light intensity |
| $k$ | wavenumber |
| $k_{crit,\pm}$ | critical wavenumber |
| $L_i$ | length of simulation box in $i$-direction |
| $M_\varphi$ | mobility of the first order parameter |
| $M_\psi$ | mobility of the second order parameter |
| $N_A$ | Avogadro's constant |
| $N_R$ | concentration of reaction centers |
| $R_0$ | characteristic length scale of light attenuation |
| $v$ | combing velocity |
| $v_{max}$ | critical combing velocity |
| $w_{mov}$ | width of moving $\Gamma_2$ region |
| $w_{st}$ | width of stationary $\Gamma_2$ region |
| $w_\varphi(k)$ | growth rate of the fluctuations |
| $V_{\Gamma_2}$ | volume of the high intensity region |

**Greek Symbols**

| | |
|---|---|
| $\beta_i$ | degree of ordering in the $i$-direction |
| $\gamma_{ij}$ | interfacial tension between the $i$ and $j$ components |
| $\Gamma_1$ | reaction rate coefficient under background illumination |
| $\Gamma_2$ | reaction rate coefficient within higher intensity domain |
| $\Gamma_+$ | forward reaction rate coefficient |
| $\Gamma_-$ | reverse reaction rate coefficient |
| $\delta(\boldsymbol{r}-\boldsymbol{r}')$ | Delta function |
| $\zeta$ | characteristic length scale |
| $\varkappa_\varphi$ | coefficient in front of $\nabla\varphi$ term in free energy |
| $\varkappa_\psi$ | coefficient in front of $\nabla\psi$ term in free energy |
| $\lambda$ | characteristic wavelength |
| $\varrho_A, \varrho_B, \varrho_C$ | volume fractions of components A,B, and C |
| $\tau$ | characteristic time scale |
| $\varphi$ | first order parameter |
| $\psi$ | second order parameter |

## References


1 Rockford, L., Mochrie, S.G.J., and Russell, T.P. (2001) *Macromolecules*, **34**, 1487–1492.
2 Kim, S.O., Solak, H.H., Stoykovich, M.P., Ferrier, N.J., de Pablo, J.J., and Nealey, P.F. (2003) *Nature*, **424**, 411–414.
3 Stoykovich, M.P., Muller, M., Kim, S.O., Solak, H.H., Edwards, E.W., de Pablo, J.J., and Nealey, P.F. (2005) *Science*, **308**, 1442–1446.
4 Edwards, E.W., Montague, M.F., Solak, H.H., Hawker, C.J., and Nealey, P.F. (2004) *Adv. Mater.*, **16**, 1315–1319.
5 Darling, S.B. (2007) *Prog. Polym. Sci.*, **32**, 1152–1204.
6 Travasso, R.D.M., Kuksenok, O., and Balazs, A.C. (2005) *Langmuir*, **21**, 10912–10915.
7 Travasso, R.D.M., Kuksenok, O., and Balazs, A.C. (2006) *Langmuir*, **22**, 2620–2628.
8 Kuksenok, O., Travasso, R.D.M., and Balazs, A.C. (2006) *Phys. Rev. E*, **74**, 011502.1–011502.13.
9 Glotzer, S.C., Dimarzio, E.A., and Muthukumar, M. (1995) *Phys. Rev. Lett.*, **74**, 2034–2037.
10 Christensen, J.J., Elder, K., and Fogedby, H.C. (1996) *Phys. Rev. E*, **54**, R2212–R2215.
11 Dayal, P., Kuksenok, O., and Balazs, A.C. (2008) *Langmuir*, **24**, 1621–1624.
12 Dayal, P., Kuksenok, O., and Balazs, A.C. (2009) *Soft Matter*, **5**, 1205–1213.
13 Yang, L.F., Dolnik, M., Zhabotinsky, A.M., and Epstein, I.R. (2006) *Chaos*, **16**, 053802.1–4.
14 Berenstein, I., Yang, L., Dolnik, M., Zhabotinsky, A.M., and Epstein, I.R. (2003) *Phys. Rev. Lett.*, **91**, 058302.1–4.
15 Hur, S.-M., Garca-Cervera, C.J., Kramer, E.J., and Fredrickson, G.H. (2009) *Macromolecules*, **42**, 5861–5872.
16 Tran-Cong, Q., Kawai, J., and Endoh, K. (1999) *Chaos*, **9**, 298–307.
17 Tran-Cong-Miyata, Q. (2000) *Macromol. Symp.*, **160**, 91–97.
18 Nishioka, H., Kida, K., Yano, O., and Tran-Cong, Q. (2000) *Macromolecules*, **33**, 4301–4303.
19 Ohta, T., Urakawa, O., and Tran-Cong, Q. (1998) *Macromolecules*, **31**, 6845–6854.
20 Nakanishi, H., Satoh, M., Norisuye, T., and Tran-Cong-Miyata, Q. (2004) *Macromolecules*, **37**, 8495–8498.
21 Tran-Cong-Miyata, Q., Nishigami, S., Ito, T., Komatsu, S., and Norisuye, T. (2004) *Nat. Mater.*, **3**, 448–451.
22 Glotzer, S.C. and Coniglio, A. (1994) *Phys. Rev. E*, **50**, 4241–4244.
23 Puri, S. and Frisch, H.L. (1994) *J. Phys. A-Math. Gen.*, **27**, 6027–6038.
24 Huang, C., de la Cruz, M.O., and Swift, B.W. (1995) *Macromolecules*, **28**, 7996–8005.
25 Huang, C. and de la Cruz, M.O. (1996) *Phys. Rev. E*, **53**, 812–819.
26 Huang, C. and de la Cruz, M.O. (1996) *Europhys. Lett.*, **34**, 171–175.
27 Huang, C. and de la Cruz, M.O. (1996) *Macromolecules*, **29**, 6068–6070.
28 Laradji, M., Mouritsen, O.G., and Toxvaerd, S. (1994) *Europhys. Lett.*, **28**, 157–162.
29 Puri, S. and Kumar, D. (2004) *Phys. Rev. Lett.*, **93**, 025701.1–4.
30 Puri, S. and Kumar, D. (2004) *Phys. Rev. E*, **70**, 051501.1–12.
31 Tafa, K., Puri, S., and Kumar, D. (2001) *Phys. Rev. E*, **64**, 056139.1–10.
32 Travasso, R.D.M., Buxton, G.A., Kuksenok, O., Good, K., and Balazs, A.C. (2005) *J. Chem. Phys.*, **122**, 194906–194917.
33 Ma, Y.Q. (2000) *J. Phys. Soc. Jpn.*, **69**, 3597–3601.
34 Lakshmi, K.C. and Kumar, P.B.S. (2003) *Phys. Rev. E*, **67**, 011507.
35 Ma, Y.Q. (2001) *J. Chem. Phys.*, **114**, 3734–3738.
36 Smith, K.A., Solis, F.J., Tao, L., Thornton, K., and de la Cruz, M.O. (2000) *Phys. Rev. Lett.*, **84**, 91–94.
37 Okuzono, T. and Ohta, T. (2003) *Phys. Rev. E*, **67**, 056211.1–10.
38 Good, K., Kuksenok, O., Buxton, G.A., Ginzburg, V.V., and Balazs, A.C. (2004) *J. Chem. Phys.*, **121**, 6052–6063.
39 Tong, C.H. and Yang, Y.L. (2002) *J. Chem. Phys.*, **116**, 1519–1529.

**40** Liu, B., Tong, C.H., and Yang, Y.L. (2001) *J. Phys. Chem. B*, **105**, 10091–10100.

**41** Tong, C.H., Zhang, H.D., and Yang, Y.L. (2002) *J. Phys. Chem. B*, **106**, 7869–7877.

**42** Zhu, Y.J. and Ma, Y.Q. (2003) *Phys. Rev. E*, **67**, 021804.1–7.

**43** Ohta, T. and Ito, A. (1995) *Phys. Rev. E*, **52**, 5250–5260.

**44** Bray, A.J. (1994) *Adv. Phys*, **43** 357–459.

**45** Vanag, V.K. and Epstein, I.R. (2009) *Phys. Chem. Chem. Phys.*, **11**, 897–912.

**46** Oono, Y. and Puri, S. (1988) *Phys. Rev. A*, **38**, 434–453.

**47** Shinozaki, A. and Oono, Y. (1993) *Phys. Rev. E*, **48**, 2622–2654.

**48** Oono, Y. (1997) *Phys. Rev. E*, **55**, 3792–3792.

**49** Succi, S. (2001) *The Lattice Boltzmann Equation for Fluid Dynamics and Beyond*, Oxford University Press, Oxford.

**50** Swift, M.R., Orlandini, E., Osborn, W.R., and Yeomans, J.M. (1996) *Phys. Rev. E*, **54**, 5041–5052.

**51** Orlandini, E., Swift, M.R., and Yeomans, J.M. (1995) *Europhys. Lett.*, **32**, 463–468.

**52** Osborn, W.R., Orlandini, E., Swift, M.R., Yeomans, J.M., and Banavar, J.R. (1995) *Phys. Rev. Lett.*, **75**, 4031–4034.

**53** Swift, M.R., Osborn, W.R., and Yeomans, J.M. (1995) *Phys. Rev. Lett.*, **75**, 830–833.

**54** Furtado, K. and Yeomans, J.M. (2006) *Phys. Rev. E*, **73**, 066124.1–7.

**55** Huo, Y.L., Jiang, X.L., Zhang, H.D., and Yang, Y.L. (2003) *J. Chem. Phys.*, **118**, 9830–9837.

**56** Liu, F. and Goldenfeld, N. (1989) *Phys. Rev. A*, **39**, 4805–4810.

**57** Bahiana, M. and Oono, Y. (1990) *Phys. Rev. A*, **41**, 6763–6771.

**58** Hamley, I.W. (2000) *Macromol. Theor. Simul.*, **9**, 363–380.

**59** Ren, S.R. and Hamley, I.W. (2001) *Macromolecules*, **34**, 116–126.

**60** Kellogg, G.J., Walton, D.G., Mayes, A.M., Lambooy, P., Russell, T.P., Gallagher, P.D., and Satija, S.K. (1996) *Phys. Rev. Lett.*, **76**, 2503–2506.

**61** de Gennes, P. (1985) *Rev. Mod. Phys.*, **57**, 827–863.

**62** Ren, S.R. and Hamley, I.W. (2002) *Phys. B*, **322**, 110–115.

**63** Nakanishi, H., Fujiki, D., Van-Pham, D.-T., and Tran-Cong-Miyata, Q. (2009) *Nonlinear Dynamics with Polymers*, Wiley-VCH Verlag GmbH, Weinheim.

**64** Tran-Cong, Q., Harada, A., Kataoka, K., Ohta, T., and Urakawa, O. (1997) *Phys. Rev. E*, **55**, R6340–R6343.

**65** Campbell, C.J., Klajn, R., Fialkowski, M., and Grzybowski, B.A., (2005) *Langmuir*, **21**, 418–423.

# Index


***a***

*ab-initio* simulations 22, 34
activation energy 203, 205
amorphous 101–105, 108, 109, 125, 130–139, 142, 145, 146, 160, 165, 174–176, 184, 187, 199, 212, 216, 218–220
amorphous–amorphous interaction parameter 130, 131, 137
amorphous polymers 101–104, 109, 130, 132, 139, 145, 146, 174, 176, 184, 199, 216, 218, 220
analytical techniques for determining blend miscibility:
– dielectric relaxation spectroscopy 160
–– for determining miscibility 161
–– limits thereof 161
–– of polymer blends 158, 160
annealing temperature 200, 214, 216
atomistic models 1, 6, 8, 15, 16, 30, 31, 33–36
attractive intermolecular forces 48

***b***

background illumination 276
Beeman's algorithm 22
binary blends 102, 129, 169, 175, 184, 187, 236, 245, 246, 248, 271, 272, 274, 278–280, 282, 286, 302, 303
binodal curve 59, 65, 68–70
biopolymer 8, 30, 76, 77, 108, 109
biphasic region 51, 53, 65–67, 69–74, 79, 80, 88
blends
– PHS/PMMA 206, 221
– PHS/PVME 206, 220, 221
– PMMA/PEO 205, 216, 217
– PMMA/SAN 177, 205, 206, 210, 211, 213, 215, 216, 220, 241
– PS/PPE 205, 206, 213, 215–217
– PS/PPO 184, 186, 220
– PS/PVME 104, 168, 183, 206, 209, 216, 217, 220, 221
– (PVAc-co-VOH)/PVP 217, 218
– SHFHS/PMMA 222
– SHS/PMMA 222
– SHS/PVME 222
block copolymers 30, 175, 177, 178, 235, 237, 238, 240, 241, 248–250, 252–254, 269–271, 273, 276, 297, 303
Boltzmann constant 47, 115
bond fluctuation model 7, 36
Bragg's law 164

***c***

Cahn–Hilliard theory 85
calorimetry 158, 160, 175, 200
carbon dioxide 3, 5, 13, 20
characteristic length scale 103, 293–295
chemical aging 199
chemical potential 10, 11, 18, 22, 47, 50, 52, 60, 81, 82, 115, 129, 130, 251, 274
chitin 109
coarse-grained model 5, 6, 13–18, 20, 23, 32–37
coefficient of anisotropic interaction 138
coefficient of interface gradient 116
coexistence curve 3, 58, 59, 136
combing process 287, 289, 291
common tangent construction 51, 53, 65, 66
compatibilizer 176, 237, 238, 254, 296
composite theories
– Halpin–Tsai 256
– Mori–Tanaka 256
concentration fluctuation 33, 46, 80, 83–87, 93, 102–105, 171, 172, 180, 184, 208, 213, 216
configurational bias Monte Carlo 10


*Encyclopedia of Polymer Blends, Volume 1: Fundamentals.* Edited by Avaraam I. Isayev
Copyright © 2010 WILEY-VCH Verlag GmbH & Co. KGaA, Weinheim
ISBN: 978-3-527-31929-9

configurational entropy 104, 203
conformational entropy 16, 243, 246
conformational reorientation 102
concentration-induced spinodal decomposition 85
conserved order parameter 46, 78–81
contact angle 5, 16–18, 276
cooperative rearrangement 103
copolymers aging 200, 203
coupling model 205
Cowie–Ferguson model 204, 210
correlation time distribution 103, 105, 107, 108
critical point $T_c$ 3, 4, 10–12, 14, 17, 56, 65, 67, 68, 73, 74, 157, 161
critical wave numbers 273, 274
crystallization temperature 115, 123, 124, 126, 128, 144, 146,
crystallographic orientation 116
crystalline phase 45, 55, 56, 70, 75, 76, 79, 83, 94, 131, 132, 146
crystal phase order parameter 114, 117, 124
cumulants 11

*d*

Debye–Bueche model 172
degree of ordering 276, 289, 293, 299
density 1, 5, 11–20, 24, 25, 27, 28, 34, 47, 50–52, 56, 59, 60, 75, 80, 81, 115–117, 124, 125, 127, 137, 169, 171, 172, 174, 175, 199, 213, 216, 217, 219, 234, 236, 237, 240, 243, 250, 251, 253, 280, 282, 285, 294
density functional theory 34, 59, 75, 243, 250
depletion attraction 234, 242
detailed-balance 9
diblock copolymers 175, 237, 238, 248, 250, 253, 269–271, 273, 276, 297, 303
dielectric spectroscopy 104, 105, 184, 218, 219
differential scanning calorimetry 158, 160, 175
– for determining miscibility 158
–– limits thereof 158
– of polymer blends 158, 160
dilatometry 212
director 46, 54, 71, 76–78, 80, 87–93
dissipative particle dynamics 24, 25, 34, 240, 242
distribution function 33, 47–49, 55, 56, 60, 62, 71, 72, 83, 175
DNA 27, 30, 31, 76, 77
dynamically asymmetric blends 105
dynamic mechanical thermal analysis 158, 161, 185
– for determining miscibility 158
–– limits thereof 158
– of polymer blends 158, 161

*e*

EBBA 56, 57, 59, 69
electron spin resonance spectroscopy (ESR) 218
energy-driven nematic ordering 54, 55
enthalpy relaxation 200–202, 205–208, 211, 212, 213, 215, 216, 220, 222, 223, 227
entropy-driven nematic ordering 45, 54
entropy-induced fluid-crystalline phase transition 55
equilibrium melting temperature 115
ergodic hypothesis 21
Ewald summation 22
excluded volume 2, 6, 7, 27, 28, 48, 50, 54, 55, 59–62, 70, 250
external field 67, 92, 93

*f*

fd virus 74–77, 87
FENE potential 7
fibrillar network 89, 90
fictive temperature, $T_f$ 202, 213
filler loading 233, 255–257
finite element analysis 256
finite-size effects 11, 18
first-order nematic-isotropic phase transition 58, 77
Flory–Huggins interaction parameter 61, 137, 170, 236, 254
Flory–Huggins lattice model 1
Flory–Huggins model 1, 156
Flory lattice model 45, 54, 59
Fourier-transform infrared (FITR) 154, 186, 218
Frank elastic constant 81, 91
free energy 1, 12, 13, 16, 18–20, 47, 48, 50–56, 59–64, 66, 69–72, 75, 76, 80, 81, 83, 89, 91, 93, 114–117, 123–125, 127, 129, 130, 132, 133, 137, 139, 145, 146, 148, 154–157, 167, 170, 236, 243, 245, 246, 250, 251, 272–274, 276, 277, 279, 280, 282, 283, 285, 286, 291, 296, 299
free energy functional 117, 148, 272
free energy of mixing 59, 60, 71, 137, 155, 156, 157, 170, 236
free energy penalty 118, 124
free volume 1, 30, 31, 54, 185, 202, 205, 212, 216, 217, 219–222, 224

**g**

Gaussian thread model 4
generalized Born algorithm 22
Gibbs free energy 154–156, 167, 236
– of mixing of polymers 156
glass transition 30–32, 35, 36, 102, 103–106, 126, 140, 154, 158–161, 167, 176, 180, 182, 185, 199, 204, 206, 208, 211, 213, 215, 220, 223, 294
– mathematical model for blends dynamics of 180
– as a miscibility criteria 32, 104, 154, 158, 161
– sub-$T_g$ relaxations 185
glass transition temperature, $T_g$ 30–32, 35, 102, 104, 105, 140, 154, 158–160, 185, 199, 206, 208, 211, 220, 294
Gordon–Taylor equation 159, 160
grandcanonical Monte Carlo simulations 21
growth velocity 117

**h**

Hamaker constant 17, 234
heat capacity 30, 117, 159, 160, 202, 203
hexadecane 13, 14, 20
hexagonal pattern 125, 276
hierarchically ordered patterns 270
homeotropic anchoring 88, 91, 92, 93
HP model 7
hydrodynamic effect 88, 91–93
hydrodynamics 23, 24, 26–28, 78, 81, 86, 90, 93, 240, 272, 273, 275, 294

**i**

importance sampling 8
inflection point of the free energy 53, 66
infrared spectroscopy 154, 187, 217, 218
– for determining miscibility 154, 187
– of polymer blends 154
interacting SAW model 7
interface thickness 114, 118
interfacial tension 16–20, 81, 237, 238, 254, 255, 257, 273, 285, 296, 302
internal-rebridging algorithm 9
3d-Ising universality class 11
isotropic–isotropic phase separation 66, 68, 73
isotropic unstable region (Iu) 65

**k**

Kelvin equation 18
Kohlrausch–Williams–Watts (KWW) function 203
Kwei equation 159, 160

**l**

Langevin thermostat 24
lamella 252
lamellar phase 74, 75
Landau–de Gennes expansion 59
latent heat 113, 115, 117, 119, 121, 127–129
lattice Boltzmann method 24
LBM 273
leap-frog algorithm 22
Lennard–Jones potential 7, 17, 36
linear stability analysis 273, 274
liquid crystal 45, 46, 55, 56, 58, 59, 63, 65, 69–71, 73, 75, 76–79, 82–84, 86, 88–91, 93, 94, 131, 132, 138, 139, 188
local displacements 9
Lorentz–Berthelot combining rule 14
lower critical solution temperature (LCST) 156, 165, 172, 236

**m**

Maier–Saupe free energy 55
McMillan model 55
mean correlation time 102, 103
mean-field random phase approximation 170
mean field theory 34, 59, 69, 81, 93, 171, 244
mechanical properties 29, 34, 35, 56, 102, 108, 153, 158, 176, 185, 214, 216, 235, 255, 256
melting temperature 30, 115, 133–135, 138, 140, 160
mesoscale simulations and theories 235
– CDS 273, 279
– DFT 75, 76, 243, 250, 253
– DPD 25–28, 34, 240, 253
– Flory–Huggins theory 3, 35, 36, 59, 61, 68, 71, 75, 93, 130, 131, 137, 236, 237
– interaction parameter 61, 130, 134, 137, 170, 236, 254
– Langevin dynamics 123, 240–242
– molecular dynamics 5, 6, 8, 21, 23, 28, 30, 31, 33, 36, 37, 240, 253
– Monte Carlo 1, 3, 5–10, 18, 21, 29, 30, 36, 88, 244, 253
– SCFT 36, 243, 250, 251, 253, 254
metastable region 50, 53, 65, 80, 157, 167
Metropolis criterion 9
microemulsions 237, 238, 248, 252
microscopy
– cloud point measurements of blends 167, 168
–– limitations thereof 168
–– of polymer blends 167, 168
–– setup 168
– laser scanning confocal microscopy 180

–– of polymer blends 180
– light scattering and turbidity 83, 86, 154, 163–165, 167, 172, 174, 175
– of polymer blends atomic force microscopy 163, 177, 178
–– limitations of 178
–– of polymer blends 163
– scanning electron microscopy 154, 163, 177
–– of polymer blends 154
– scanning tunneling microscopy 178
–– of polymer blends 178
– transmission electron microscopy 178
–– of polymer blends 178
miscibility
– definition of 153
– determination via real time or reciprocal-space techniques 163
– thermodynamics 155
mobility 81, 115, 145, 184, 218, 239, 291, 298
modulus 45, 184, 199, 215, 233, 235, 255, 256, 257, 259, 260
molecular dynamics 5, 6, 8, 21, 23, 28, 30, 31, 33, 36, 240, 253
Monte Carlo 1, 3, 5–11, 18, 21, 29, 30, 88, 244, 253
morphology
– bicontinuous 249
– cylindrical 18, 172, 249, 270, 286
– lamellar 141, 248, 297, 303
multicanonical sampling 13
multi-particle collision dynamics 27

***n***

nanocomposites
– dielectric constant 235
– electrical conductivity 235, 257, 259, 260
– electrical properties 255
– mechanical properties 235
– modulus 233, 235, 255–257, 259, 260
– strength 233–235, 255, 257
– toughness 255, 257
nanoparticle
– aggregation 243
– aspect ratio 234, 255, 257–260
– carbon black 233–235, 257, 258
– carbon nanotubes 233, 234, 257–260
– characteristic size 234
– charge density 217, 234
– clay 233, 235, 238, 243, 256
– dispersion 233
– exfoliation 233, 243
– gold 249, 253
– silica 218, 233, 245, 247
– silver 233
– surface chemistry 234, 239, 242, 245, 246, 253, 254
– surface modification 260
– titania 233
– zirconia 233
nanoplatelets 238, 245, 247, 248
nanorods 238, 241, 245, 247, 248
nanospheres 235, 238, 241, 244, 245, 247, 250, 251
nematic–isotropic interface 90, 91
nematic–isotropic phase separation 51, 56, 57, 66, 68, 70, 71, 73, 76, 94
nematic–isotropic phase transition(NIT) 50, 63
nematic phase 45, 46, 48, 50–56, 58, 63, 64, 66, 67, 69, 70, 72–77, 79, 82, 89, 92, 93
nematic unstable region(Nu) 65
non-conserved order parameter 46, 78, 79, 81
non equilibrium molecular dynamics 5, 23
nuclear magnetic resonance 154, 184
– of polymer blends 154, 184
nucleation and growth 115, 146, 147, 240

***o***

order parameter 11, 46, 48–51, 53, 60, 62–65, 72, 73, 78–83, 85, 86, 90, 92, 114–117, 124, 127, 128, 145, 146, 148, 272–275, 278, 279, 280, 282, 287, 295
orientational distribution function 47, 48, 55, 60, 62
orientational entropy 48, 49, 54
orientation fluctuation 80, 83–86, 88, 93
orientation-induced spinodal decomposition 85, 92
Ornstein–Zernike equation 171
osmotic pressure 52
Onsager model 46, 48

***p***

PAA 56
packing entropy 48, 49
particle-mesh Ewald algorithm 22
PBLG 70, 71
percolation
– double percolation 257, 258
– percolation threshold 257–259
persistence length 76, 77
Petrie–Marshall model 204, 210
phase behaviour 1, 5, 9, 14, 15, 18, 35, 45, 55, 56, 59, 67, 69–71, 74, 76, 88, 93, 94, 139, 153, 154, 156, 160–162, 165, 167–170, 179, 182, 206–208, 23, 245–248, 252, 270

phase diagram 4, 8, 14, 53, 54, 56–59, 65–71, 73–76, 78, 79, 93, 129, 131–143, 157, 161, 162, 165, 166, 167, 170, 235, 236. 237, 239, 248, 250, 252
phase separation 5, 16, 25, 34, 45, 46, 52, 56, 58, 68, 71, 74, 79, 88, 93, 148, 162, 175, 239, 240, 282
phase separation kinetics 56, 84
phenomenological models 202, 203, 213
photosensitive chemical reactions 269
pivot algorithm 9
planar anchoring 91, 92
polycarbonate 15, 34, 165, 167, 174, 180, 183, 219, 223
polycaprolactone (PCl) 108, 109, 139, 174
poly(2,6-dimethyl-1,4-phenylene ether) 208
poly(2,6-dimethyl-1,4-phenylene oxide) 182, 184, 212
polyether ether ketone 212
polyetherimide 212
poly(ether sulfone) 212
polyethylene-*co*-butene (PEB) 104, 106
poly(ethylene oxide) (PEO) 33, 56, 104, 135, 140–143, 145, 216
poly[4-(hexafluoro-2-hydroxyisopropyl) styrene] 222
polyhydroxybutyrate (PHB) 108, 109
poly[4-(2-hydroxyethyl)styrene] 222
poly(hydroxystyrene) 186, 220, 222
polyisobutylene (PIB) 30, 104, 107, 108
polyisoprene (PI) 9, 104–106, 181
poly(isopropyl methacrylate) 206, 207
polymer blend phase behavior 132, 168
– critical point $T_c$ polymer-stabilized liquid crystal (PSLC) 56
polymer blends
– chlorinated polyethylene
–– blends with poly(butyl acrylate) 166
–– CP of 166
–– blends with poly(methyl methacrylate) 165
–– light scattering of 165
– hydrogenous polyisoprene
–– blends with poly(butadiene) 172
–– SANS of 172
– poly(butadiene)
–– blends with chlorinated polystyrene 32
–– light scattering of 167
–– blends with hydrogenous polyisoprene
–– SANS of 172
– poly(butyl acrylate)
–– blends with chlorinated polyethylene 166
–– CP of 167
– poly(carbonates)
–– blends with polyethylene:
–– SEM of 34
–– blends with poly(methyl methacrylate):
–– CP of 34
–– blends with styrene–acrylonitrile copolymers
–– CP of 165
– poly(carprolactone)
–– blends with poly(vinyl chloride):
–– SAXS of 174
– poly(2,6-dimethyl-1,4-oxide)
–– blends with polystyrene:
–– $^{13}$C-NMR 184
–– blends with styrene-*co*-*para*-chlorostyrene:
–– DRS of 182
– polyethylene
–– blends of different molecular weights:
–– SANS of 138
–– blends of linear and branched:
–– SANS of 171
–– blends with poly(carbonates):
–– SEM of 34
–– blends with poly(ethylene terephthalate):
–– SEM of 34
– poly(ethylene butadiene)
–– blends with polypropylene
–– SANS of 171
– poly(ethylene oxide)
–– blends with poly(L-Lactide)
–– DSC of 160
– poly(ethylene terephthalate)
–– blends with polyethylene
–– SEM of 178
– poly(4-hydroxystyrene)
–– blends with acrylates, polyesters, polyethers and polylactides
–– IR spectroscopy of 186
– poly(isoprene)
–– blends with poly(vinylethylene)
–– DRS of 184
– poly(L-Lactide)
–– blends with poly(ethylene oxide) 160
–– DSC of 160
– poly(methyl methacrylate)
–– blends with chlorinated polyethylene
–– light scattering of 166, 167
–– blends with poly(carbonates)
–– light scattering of 167
–– blends with polystyrene
–– SANS of 168
–– blends with poly(vinylphenol) 32, 161, 187
–– DMTA of 161
–– DSC of 161

–– IR spectroscopy of 187
–– NMR of 161
–– blends with styrene–acrylonitrile copolymers
–– TEM of 177
– poly(*ortho*-chlorostyrene)
–– blends with polystyrene
–– light scattering of 167
–– DRS of 182
–– blends with poly(vinyl methyl ether)
–– SAXS 167
– poly(polypropylene)
–– blends with poly(ethylene butadiene)
–– SANS of 170
– polystyrene
–– blends with polybutadiene
–– light scattering of 172
–– blends with poly(2,6-dimethyl-1,4-oxide):
–– $^{13}$C NMR of 184
–– blends with poly(methyl methacrylate)
–– SANS of 165, 210
–– blends with poly(vinyl methyl ether)
–– DRS of 183
–– IR spectroscopy of, 186
–– light scattering of 167
–– SANS of 241
–– blends with poly(*ortho*-chlorostyrene)
–– DRS of 182
–– light scattering of 167
–– blends with styrene-*block*-butadiene copolymers
–– SAXS of 175
–– blends with styrene-*block*-polyisoprene copolymers
–– SAXS of 175
–– blends with styrene-*co*-4-bromostyrene copolymers
–– AFM of 179
– poly(vinyl chloride) 34, 174, 206, 207
–– blends poly(carprolactone)
–– SAXS of 174
– poly(vinyl cinnamate) 160
–– blends of isomeric forms
–– DSC of 160
– poly(vinylethylene) 184
–– blends with polyisoprene
–– $^{13}$C-NMR of 184, 185
– poly(vinyl methyl ether) 32, 167, 208, 241, 271
–– blends with poly(*ortho*-chlorostyrene)
–– SAXS 167
–– blends with polystyrene
–– DRS of 158
–– IR spectroscopy of 186
–– light scattering of 167
–– SANS of 168
– poly(vinyl phenol) 32, 161, 187
–– blends with poly(methyl methacrylate)
–– DSC of 161
–– NMR of 161
–– DMTA of 161
–– IR spectroscopy of 187
– styrene–acrylonitrile copolymers 165
–– blends with polycarbonates
–– light scattering of 165
–– blends with poly(methyl methacrylate)
–– TEM of 165
polymer brushes 26, 28, 243
polymer dispersed liquid crystal (PDLC) 56, 58, 59, 79, 83, 88, 90, 93, 188, 189
polymerization-induced phase separation 58, 59, 90
polymer reference interaction site model 4, 36
polymer-solid interface 15
poly(methyl methacrylate) (PMMA) 56, 104, 109, 134, 161, 165, 186, 188, 209, 211, 216, 217, 222, 259
polypropylene (PP) 29, 32, 34, 35, 171, 233
polystyrene (PS) 34, 56, 241, 243, 246
poly(styrene-*co*-4-hydroxystyrene) 186, 220
polyvinyl acetate (PVA) 109
poly(vinyl alcohol) (PVA) 109, 217
poly(vinyl chloride) (PVC) 174, 206
poly(vinylethylene) (PVE) 104–106, 184
poly(vinyl methyl ether) 32, 167, 208, 241, 271
poly(vinylmethylethylene) (PVME) 105, 106, 167–170, 174, 183, 186, 208, 209, 216, 217, 220–222, 271
poly(vinyl pyrrolidone) 217, 218
Porod's law 172
position of solidification potential well 123, 124
positron annihilation lifetime spectroscopy (PALS) 217, 218, 220, 221
predictor-corrector algorithms 22
pretransitional behavior 50

**r**

Raman spectroscopy
– of polymer blends 186, 188
reactive polymer blends 273
relaxation time 29, 31, 36, 103, 105, 106, 161, 184, 203, 209, 211, 212–216, 220, 221
relaxation time distribution 105, 184, 212, 216
Rouse model 29

**s**
scattering techniques
– basic setup 163
– characteristics of 164
– neutron reflectivity 154, 163
–– of polymer blends 175–176
– small-angle neutron scattering 76, 131, 134
–– of polymer blends 244
–– setup 168–173
– small-angle X-ray scattering 219
–– morphology parameters derived from SAXS 163
–– of polymer blends 162
– WAXS
–– of polymer blends 175
second virial approximation 47, 59, 61
self-avoiding walk 6, 36
self-concentration 102–105, 185
self-consistent field theory 4, 36, 250, 270
sequential aging theory 209
shear alignment 23
shear thinning 23
Simha–Somcynsky (S-S) theory 204
single mode approximation 274, 279, 280
slithering snake algorithm 9
small-angle X-ray scattering 87, 162, 163
smectic A–isotropic phase transition (SIT) 73
smectic A–nematic phase transition (SNT) 73
smectic A phase 55, 71
soft matter 55
spinodal boundaries 247
spinodal curve 3, 58, 65, 80, 85, 157
spinodal decomposition (SD) 78, 173, 240
statistical segments 16, 130, 176
– amorphous polymer chain 130, 176
– crystalline polymer chain 131
steric interaction 48, 54, 63, 241
stochastic rotational dynamics 24, 27
stress relaxation 200, 209, 210, 214–217, 223
stripe domain 92
structure factor 83–86, 180, 181
successive umbrella sampling 12
surface energy anisotropy 117, 120, 121
surface tension 16, 17, 19, 33, 93, 114, 118, 121, 254

**t**
temperature gradient 113, 119, 121, 122, 168
ternary blends 292, 298, 301
thermal coefficient 117–119
thermal conductivity 117
thermal diffusivity 117
thermal equilibrium state 45, 53, 54, 75
thermodynamical inequality 53
thermodynamic integration 20
thermostat 23–26, 28
three-phase equilibrium 73
time-dependent Landau–Ginzburg equation (TDLG) 80
time–temperature (t–T) superposition principle 184
translational entropy 2, 47, 54, 55
triple point(TP) 66, 70, 73
two-phase coexistence boundaries 247
two-phase equilibrium 65

**u**
united atom model 8
unstable region 53, 65, 66, 79, 80, 157
upper critical solution temperature (UCST) 74, 133, 142, 156, 236

**v**
van der Waals interactions 31, 245
van Laar dimensionless interaction parameter 155
velocity-Verlet algorithm 22
Verlet algorithm 22
Verlet list 22
volume fraction 1, 31, 49–53, 56, 60, 63–65, 68, 70, 79, 80, 89, 91, 129, 130, 137, 138, 156, 236, 243, 247, 249, 250, 252, 254, 258, 272, 277, 282, 283, 296
– amorphous solvent 129, 130
– crystalline polymer 129, 130, 137
volume relaxation 204, 212, 213

**w**
Wertheim's perturbation theory 4
wetting 5, 14–17, 19, 21, 179

**y**
Young's equation 16
Young's modulus 233, 256

**z**
Zeta-potential 234